NASA CONTRACTOR REPORT 177507 USAVSCOM TR-88-A-008

Wake Model for Helicopter Rotors in High Speed Flight

Wayne R. Johnson

Johnson Aeronautics

Prepared for
Ames Research Center
under Contract NAS2-12767

November 1988

NASA CONTRACTOR REPORT 177507

USAVSCOM TR-88-A-008

Wake Model for Helicopter Rotors in High Speed Flight

Wayne R. Johnson

CONTRACT NAS2-12767

November 1988

National Aeronautics and
Space Administration

Ames Research Center
Moffett Field, California 94035

US ARMY
AVIATION
SYSTEMS COMMAND

AVIATION RESEARCH AND
TECHNOLOGY ACTIVITY
MOFFETT FIELD, CA 94305-1099

TABLE OF CONTENTS

SYMBOLS AND ABBREVIATIONS

b	wing or blade semichord
c	wing or blade chord
c_ℓ	section lift coefficient, $L/(\frac{1}{2}\rho U^2 c)$
c_m	section moment coefficient, $M/(\frac{1}{2}\rho U^2 c^2)$; or blade mean chord
C_{mt}/σ	dimensionless torsion moment, $M_t/(\rho(\Omega R)^2 R^2 c_m)$
c_p	pressure coefficient, $p/(\frac{1}{2}\rho U^2)$
c_s	speed of sound
C_T	rotor thrust coefficient, $T/(\rho(\Omega R)^2 \pi R^2)$
C_X	rotor drag force coefficient, $X/\rho(\Omega R)^2 \pi R^2)$
d	radial resolution of trailed vorticity in discretized wake
$d(C_T/\sigma)/dr$	blade section lift, $L/(\rho(\Omega R)^2 c_m) = (c/2c_m)u_T^2 c_\ell$
h	vertical separation between vortex and wing
k	reduced frequency, $\omega b/U$
L	wing or blade section lift (force per unit span)
M	wing or blade section moment (moment per unit span); or Mach number, U/c_s
M_{at}	advancing tip Mach number, $(1+\mu)M_{tip}$
M_t	blade structural torsion moment
M_{tip}	rotor tip Mach number, $\Omega R/c_s$
N	number of blades
p	blade surface pressure
q	dynamic pressure, $\frac{1}{2}\rho V^2$
r	blade radial station, measured from center of rotation
R	blade radius
r_c	tip vortex core radius (defined by maximum circumferential velocity)

T	rotor thrust
U	wing or blade section velocity
u_T	blade tangential velocity, $r/R+\mu\sin\psi$
V	flight speed
x	blade chordwise position, measured from leading edge
X	rotor drag force
y	wing spanwise coordinate
α_s	rotor shaft angle of attack, positive aft
α_{tpp}	rotor tip-path-plane angle of attack, positive aft
β_{1c}	rotor longitudinal tip-path-plane tilt relative shaft, positive forward
β_{1s}	rotor lateral tip-path-plane tilt relative shaft, positive toward retreating side
Γ	wing or blade bound circulation; or line vortex strength
μ	rotor advance ratio, $V/(\Omega R)$
ρ	air density; or blade radial station
σ	rotor solidity, $Nc_m/\pi R$
ϕ	velocity potential; or rotor wake age
ψ	rotor azimuth angle, measured from downstream, in direction of rotor rotation
ω	frequency of wing or loading oscillation
Ω	rotor rotational speed
$(..)'$	spanwise derivative

WAKE MODEL FOR HELICOPTER ROTORS IN HIGH SPEED FLIGHT

SUMMARY

An improved rotor wake model for helicopter rotors is developed, and applied to airloads data from several tests, including the Boeing model 360 scale rotor test. The emphasis is on wake effects (including blade-vortex interaction) in high speed flight, considering in particular cases with negative loading on the blade advancing tip. The capability is developed to model the wake created by dual-peak span loading (inboard and outboard circulation peaks, of opposite sign), optionally with multiple rollup of the trailed vorticity. Two alternative approaches for blade-vortex interaction are considered: second order lifting-line theory, and a lifting-surface theory correction. The common approach of using a larger vortex core radius to account for lifting-surface effects is quantified. The second order lifting-line theory also improves the modeling of yawed flow, swept tips, and low aspect-ratio blades. Calculated rotor airloads are compared with measured data from tests of the model 360, SA349/2, H-34, and AH-1G rotors. The correlation illustrates the features and effects of the wake model, provides an assessment of the importance of the wake to high speed rotor airloading, and shows the capability to calculate the airloading. In addition, the requirements for future airloads measurements are defined.

1. INTRODUCTION

1.1 Background

The vortex wake of the rotor is a factor in most problems of helicopters, including blade loads, vibration, noise, and even performance (Johnson, 1980a). The wake, particularly the discrete tip vortices, are a principal source of the higher harmonic loading on the blades. Hooper (1984) provides a summary of rotor airloads measurements in forward flight, including tests of the H-34, UH-1, NH-3A, XH-51A, CH-53A, and AH-1G rotors. The H-34 rotor tests in flight (Scheiman, 1964) and the wind tunnel (Rabbott, Lizak, and Paglino, 1966a) have been particularly fruitful, exhibiting several phenomena that are unusual, and as yet not fully explained.

Hooper (1984) observed relatively consistent behavior in all the data sets examined. At transition speeds, there was impulsive loading of the blade tip, on both the advancing and retreating sides of the rotor disk. Considering the locus of the tip vortex from the preceding blade, this loading was attributed in certain cases to blade-vortex interaction. At high speed, there was an impulsive (up-down) loading on the tip of the advancing blade. The locus of the tip vortex was similar to the locus of the peak loading, but the impulse was the opposite sign from the low speed case. This suggested that significant negative vorticity was being produced by the negative lift region on the advancing tip at high speed. Miller (1985) discussed the implications of the negative loading on the advancing tip. The trailing wake may be expected to roll up into two vortices of opposite sign: a negative tip vortex; and a stronger, positive inboard vortex. A simple three-trailer model of the wake was developed and applied by Miller and Ellis (1986).

Johnson (1971a) observed in the H-34 low speed flight test data that the vortex-induced loads on the advancing side are generally high when the blade first encounters the vortex from the preceding blade, but decrease inboard as the blade sweeps over the vortex. Evidently there is some phenomenon limiting the loads. Several possibilities have been proposed: local distortion of the vortex geometry; bursting of the vortex core, induced by the blade (Scully, 1975); vortex interaction with the trailed wake it induces behind the blade, with the effect of diffusing the circulation in the vortex; and local flow separation produced by the high radial pressure gradients on the blade (Ham, 1975). The exact physical mechanism involved remains speculative. The phenomena (or at least their effect on the blade airloads) can be modelled by increasing the vortex core size as the blade-vortex interaction progresses.

The computer code "Comprehensive Analytical Model of Rotorcraft Aerodynamics and Dynamics" (CAMRAD) introduced a new wake model for helicopter rotor airloads calculations (Johnson, 1986a). This model has been applied with considerable success in calculations of important rotor phenomena, including:

correlation with flight test measurements of blade loads and airloading (Yamauchi, Heffernan, and Gaubert, 1988); lateral flapping as influenced by the wake geometry (Johnson, 1981); and hover loading calculations using prescribed wake geometry (Johnson, 1986a). A major advance was the coupling of the CAMRAD wake analysis with finite-difference calculations for advancing blade tip transonic flow (Tung, Caradonna, and Johnson, 1986). These various applications have established the capabilities and limitations of the CAMRAD models.

The Aeroflightdynamics Directorate of the U.S. Army Aviation Research and Technology Activity has recently acquired a new set of blade pressure data, from a wind tunnel test of a Boeing model 360 scaled rotor. This data set is notable for the use of modern instrumentation; the inclusion of scaled blade dynamics in the model rotor; and the advanced design of the rotor system, intended for high speed operation. The next step in the model 360 scale rotor project must be to apply analyses to the rotor system, and compare the results with the measured data.

1.2 Objectives

The objectives of the present investigation were to develop an improved rotor wake analysis capability for helicopter rotors, and to apply the analysis in particular to the data from the model 360 scale rotor test. The emphasis was on wake effects (including blade-vortex interaction) in high speed flight. Much of the existing rotor airloads data from high speed tests was examined. The product of the investigation is an advanced and demonstrated wake and aerodynamics model for the calculation of rotor airloads.

1.3 Approach

Rotor blade airloads are considered in the present investigation, since they provide the most detailed information available about the aerodynamic phenomena involved. Wake geometry measurements would be very useful, but are seldom available. Blade structural bending and torsion loads are of interest, but provide only an indirect picture of the aerodynamics. Performance data are of interest themselves, and because errors in performance prediction will produce errors in blade loads predictions also. Moreover, as has been remarked for the lateral flapping problem (Johnson, 1981), if the mean and 1/rev airloading can not be predicted, it is unreasonable to claim to know much about the higher harmonic loading.

The starting point for the investigation was the existing code CAMRAD (Johnson, 1986a). This code is applicable to a wide range of rotorcraft configurations and rotor types. It has had numerous successful applications to rotorcraft aerodynamics and dynamics problems. The code can calculate performance, airloads, response, loads, and stability. It has a highly developed rotor

aerodynamic model, and a wake model with many unique features. The present work extends this aerodynamic and wake model to improve the prediction of airloads, blade loads, and performance.

Key aspects of the aerodynamics and wake models in CAMRAD are as follows. The rotor aerodynamic model is based on lifting line theory, using steady two-dimensional airfoil characteristics and a vortex wake. The model includes a correction for close blade-vortex passage loading using a linear lifting-surface theory solution; an empirical dynamic stall model; a yawed flow correction; and unsteady aerodynamic forces from thin airfoil theory. The aerodynamic model is applicable to axial and nonaxial flight, with high inflow and large angles. The induced velocity is obtained from momentum theory or a vortex wake model.

The CAMRAD rotor wake model is based on a vortex lattice (straight line segment) approximation for the wake. A small viscous core radius is used for the tip vortices. A large core size is used for the inboard wake elements, not as a representation of a physical effect, but to produce an approximation for sheet elements. Sheet elements are available in CAMRAD for the inboard wake, but have not proved necessary in applications so far. The wake influence coefficients are calculated for incompressible flow. A model of the wake rollup process is included. Eventually the tip vortex has strength equal to the maximum bound circulation of the azimuth where the wake element was trailed. A number of parameters allow the tip vortex to have only a fraction of this maximum strength when it encounters the following blade, with the remainder of the vorticity still in the inboard wake. The radial location of the tip vortex formation at the generating blade is also prescribed in the model. Close blade-vortex passage loading is calculated using a small viscous core radius for the vortex and a lifting-surface theory correction for the induced loads. In addition, it is possible to increase the core radius after the first encounter with a blade, in order to model the phenomena limiting vortex-induced loads on a rotor blade.

The CAMRAD wake geometry models include simple undistorted geometry; hover prescribed wake models based on experimental measurements; and a calculated free wake. The free-wake analysis (Scully, 1975) calculates the distorted tip vortex geometry for a single rotor in forward flight, using modelling features consistent with the CAMRAD wake analysis.

The present investigation developed and implemented several major improvements in the wake model. The focus on high speed flight requires consideration of cases with negative loading on the blade advancing tip. Hence the capability was introduced to model the wake created by dual-peak span loading, perhaps with multiple rollup of the trailed vorticity. If the wake effects are important, it follows that the blade-vortex interaction loads must be properly calculated. Two approaches for blade-vortex interaction were considered. For the first approach, the capability to use a second order lifting-line theory was

introduced. For the second approach, a lifting-surface theory correction was implemented. The second order lifting-line theory is also applicable to swept tips, and improves the calculation of the loading in yawed flow and for low aspect-ratio blades.

The airloading calculated using the improved wake model was compared with measured data from the model 360 scale rotor test, as well as with data from other wind tunnel and flight tests. This correlation illustrates the features and effects of the wake model, provides an assessment of the importance of the wake to high speed rotor airloading, and shows the capability to calculate the airloading. In addition, the requirements for future airloads measurements are defined.

2. HIGH SPEED WAKE MODEL

2.1 Rotor Blade Loading

On a lifting rotor in hover or low speed flight, the bound circulation is positive along the entire blade length. In such flight conditions there may be local minima and maxima of the circulation, such as produced by blade-vortex interaction or blade twist, but generally the circulation monotonically increases to a maximum value at a radial station near the tip.

It is common for helicopter rotors in high speed forward flight to encounter negative lift on the advancing tip, particularly in the second quadrant of the rotor disk. With a flapping rotor, the net pitch and roll moment acting on the rotor hub must be small (zero for an articulated rotor with no flap hinge offset). In forward flight, the lifting capability of the retreating side is limited by the combination of low dynamic pressure and stall of the blade airfoil. Consequently the lift on the advancing side must be small also, in order to maintain roll moment balance. At sufficiently high speed, the lift on the advancing tip can become negative. Large twist, either built-in or elastic, will increase the negative loading. In such cases, the bound circulation is still positive along the entire blade length for most of the rotor disk, but in the second quadrant there is a negative maximum near the tip and a positive maximum inboard. Hence in this region the tip vortex rolls up with negative strength (i.e., opposite sign from normal rollup), with a region of positive vorticity trailed between the positive and negative circulation peaks. This positive vorticity might also rollup somewhat, but normally the peaks are widely separated, so the circulation gradient is not large and the rollup will not be as strong as for the tip vortex.

Figures 2-1 to 2-3 illustrate the phenomenon. The radial distribution of the blade bound circulation (dimensionless, $\Gamma/\Omega R^2$) is shown for azimuth angles around the rotor disk. These are calculated results, for several cases that are considered in detail later. Figure 2-1 is a typical low speed case. The bound circulation is always positive, and generally concentrated at the tip, implying strong rollup of the tip vortex. Note the blade-vortex interaction on the advancing and retreating tips. Figure 2-2 and 2-3 are typical high speed cases. For azimuth angles between 90 and 135 degrees, the tip loading is negative. In this region, the positive circulation peak occurs well inboard on the blade. The objective is to develop a wake model that encompasses the rollup implied by such loading distributions.

Other cases with major positive and negative circulation peaks can be encountered. For example, a tiltrotor has a large twist that is far from optimum for most of its flight conditions. For a tiltrotor in cruise the twist is generally smaller than optimum, hence the blade circulation is negative inboard and positive outboard. For a tiltrotor in helicopter mode the twist

is larger than optimum, hence the blade circulation is negative on the advancing tip, even for relatively low speed flight. The loading distribution of a helicopter rotor will also exhibit local minima and maxima, such as from blade-vortex interaction and the reverse flow region.

For the present wake analysis, the rollup process is modelled rather than calculated. The rollup is determined by the spanwise distribution of the bound circulation where the wake is created, and by certain input parameters. Regarding the basic configuration of the circulation distribution, $\Gamma(r)$ at a given ψ, only two major cases are considered:

a) Γ the same sign all along the length of the blade (single-peak model);

b) Γ with one positive region and one negative region (dual-peak model).

More complicated circulation distributions (more than one zero-crossing, or local minima and maxima) imply more complicated rollup processes, which will likely require detailed calculation.

2.2 Far Wake Model

The wake model of CAMRAD is described by Johnson (1980b). CAMRAD assumes a single peak of the bound circulation. The radial maximum of the blade bound circulation is $\Gamma_{max}(\psi)$. The vorticity distribution of the rolled up wake is described entirely by Γ_{max}. It is assumed that all of Γ_{max} rolls up into a tip vortex, which is represented by discrete line segments. The corresponding negative trailed vorticity (of total strength $-\Gamma_{max}$) is in an inboard sheet. Since the rollup process is not being calculated, there is no information on the distribution of vorticity in this sheet. Hence it is assumed that the trailed vorticity has constant strength spanwise (at each ψ). This wake configuration can be viewed as arising from a circulation distribution that is linear from $\Gamma = 0$ at the root to $\Gamma = \Gamma_{max}$ at the tip. The equivalent circulation distribution and resulting wake segment models for the CAMRAD far wake are shown in figure 2-4. (The equivalent circulation distribution is not the actual blade loading, but rather it is a way to represent the rollup process.)

CAMRAD also includes a rolling-up wake model, defined by Γ_{max} at radial station ρ_{RU}, and $f\Gamma_{max}$ at the tip (figure 2-4). The parameters ρ_{RU} and f vary from r_{RU} and f_{RU} at the blade, to 1 at ϕ_{RU} (the wake age of the rollup process). The values of r_{RU}, f_{RU}, and ϕ_{RU} are input parameters. The resulting wake model consists of a tip vortex line and two inboard sheet segments. Note that the strength of this wake model is still described solely by Γ_{max}.

This CAMRAD model assumes that Γ has the same sign (positive or negative) along the entire blade length. Consider the application of this model to a case where $\Gamma(r)$ changes sign (figure 2-5). The maximum bound circulation Γ_{max} is obtained from the peak (positive or negative) with maximum magnitude. If Γ_{max} is the most outboard peak, then the sign of the tip vortex will be correct. However, the single trailed sheet will be too weak outboard and of wrong sign inboard. Getting the correct sign for the tip vortex might be sufficient though. The more common circumstance is that Γ_{max} is the inboard peak (for example, small negative circulation at the tip and large positive circulation inboard). Then the CAMRAD model will produce a tip vortex of the wrong sign and too large magnitude. Such a result is not acceptable.

To accommodate more complex loadings, consider a representation of the bound circulation distribution by two peaks of opposite sign (negative and positive peaks of $\Gamma(r)$). The outboard peak (positive or negative) is Γ_O and the inboard peak is Γ_I, at r_{GO} and r_{GI} respectively. Figure 2-5 illustrates the following possibilites for the wake model:

a) A single-peak model, using Γ_{max}. This is the CAMRAD model described above.

b) A single-peak model, using Γ_O. This model gives the correct sign and magnitude for the tip vortex, which is usually the first priority.

c) A dual-peak model, using both Γ_O and Γ_I.

d) A dual-peak model, with a rolled-up inboard trailed wake. Whether or not such rollup occurs, and its extent (core size), are defined by input parameters, not calculated.

It is assumed that $\Gamma(r)$ has at most one zero crossing between the root and tip. The influence of two or more zero crossings, or local peaks produced by blade-vortex interaction, is not dealt with. Such complexities require detailed calculations.

In summary, two wake configurations are now possible for the far wake and rolling up wake: single-peak or dual-peak. For the single-peak model, either Γ_{max} or Γ_O can be used (with the same influence coefficients). For the dual-peak model, the inboard trailed vorticity can be rolled up or not.

The equivalent circulation distributions for the dual-peak wake model are shown in figure 2-6. The rolling up wake has a line tip vortex, and three inboard sheet element (from radial stations ρ_{GI} and ρ_{RU}). The far wake has a line tip vortex, and two inboard sheet elements (from radial station ρ_{GI}). Typically the slope from Γ_I to Γ_O is small, so strong rollup of the inbaord trailed wake is unlikely. Still, the analysis includes the option for rollup of the trailed sheet from ρ_{GI} to the tip, which

will then be a line segment in the middle of the panel, with an appropriate core radius (input). The shed wake for this panel is still a sheet (a trailed line implies that the shed vorticity has a stepped rather than linear strength variation radially). Note that vortex lines (with large cores) are commonly used as approximations for the sheet panels. Here however, the vortex line in the inboard wake model is intended to represent an actual physical configuration.

The radial station ρ_{GI} in the dual-peak model is a wake geometry parameter. It can be input, or the analysis can use the calculated location r_{GI} of the inboard circulation peak, from the latest wake iteration. It will be important that ρ_{GI} in the wake geometry (and hence influence coefficients) be consistent with r_{GI} of the current circulation solution. This consistency must be checked (by the user, not the computer). It may be necessary to iterate on the influence coefficient calculation in order to achieve consistency (see Johnson, 1980b, section 5.3.5). Such iteration is required when the wake geometry varies significantly with the loading solution. Generally the wake geometry is influenced by parameters such as the rotor thrust and tip-path-plane incidence, which are constrained by the rotor trim. With the dual-peak model the wake geometry is also influenced by ρ_{GI}, which will be different for the uniform inflow and nonuniform inflow solutions.

The analysis must also consider the case where the inboard peak exists in either the wake geometry or the circulation distribution, but not the other. If the inboard peak is absent in the wake geometry (input ρ_{GI} not available, or no peak in the last circulation solution), then the influence coefficients will be calculated as for a single-peak model, and Γ_I will be ignored in calculating the inflow. If the inboard peak is absent in the circulation distribution, then Γ_I will be the circulation at ρ_{GI} obtained by interpolating between 0 and Γ_0, so the dual-peak wake model will give the single-peak result.

2.3 Geometry

The description of the wake geometry follows the CAMRAD documentation (Johnson, 1980b), which defines the parameters in the equations below. The dual-peak model requires r_{GI}, which may be obtained from one of two sources:

a) input (including the possibility that the inboard peak does not exist);

b) the position of Γ_I from the latest calculation.

Then for each wake panel, ρ_{GI} is the average of the leading edge and trailing edge values:

$$\rho_{GI} = \frac{1}{2} \left(r_{GI}(\psi_m - \phi_k) + r_{GI}(\psi_m - \phi_{k+1}) \right)$$

For the wake geometry, $\vec{r}_w$ at the inside and outside edges is interpolated to ρ_{GI} (Johnson, 1980b, section 3.1.3).

It will also be required that ρ_{RU} be greater than ρ_{GI} for the rolling up wake:

single-peak model $\quad r_{ROOT}+.05 \leq \rho_{RU} \leq 1$

dual-peak model $\quad \rho_{GI}+.05(1-\rho_{GI}) \leq \rho_{RU} \leq 1$

For the rolled-up inboard trailed wake, the line vortex will be placed midway between the panel edges:

$$\rho_{TL} = \frac{1}{2}(\rho_{GI} + 1)$$

By using the line aproximation for a sheet (Johnson, 1980b, section 3.1.8), this is automatically accomplished.

2.4 Induced Velocity Calculation

The evaluation of the induced velocity follows the CAMRAD documentation (Johnson, 1980b), which defines the parameters in the equations below. The circulation peaks are located by searching $\Gamma(r)$ at each ψ. The search is conducted between r_{Gmax} (an input limit) and r_{TV} (the location of the tip vortex rollup at the blade). The search is restricted to inboard of r_{TV} since otherwise a small negative circulation at the tip might be considered an outboard peak. The positive and negative peaks, and their corresponding radial stations are identified. Then the positive and negative peaks are assigned to the inboard and outboard peaks as appropriate. Finally, Γ_{max} is the positive or negative peak with maximum absolute value.

If an inboard peak is not found but ρ_{GI} exists (i.e. the inboard peak was used in the wake geometry, for the dual-peak model), then the inboard peak value is obtained by interpolation:

$$\Gamma_I = \Gamma_O (\rho_{GI} - r_{ROOT})/(1 - r_{ROOT})$$

so the dual-peak wake geometry gives nearly the single-peak result.

The induced velocity is obtained from the blade bound circulation and the influence coefficients as follows:

$$v = \sum_{j=1}^{J} \Gamma_{Oj} C_{Oj} + \sum_{j=1}^{J} \Gamma_{Ij} C_{Ij} + \sum_{j=\ell-K_{NW}}^{\ell} \sum_{i=1}^{M_L} \Gamma_{ij} C_{NWij}$$

The following three options are considered:

a) for the single-peak model using Γ_{max}, the second term is

absent and Γ_{max} replaces Γ_0 in the first term;

b) for the single-peak model using Γ_0, the second term is absent;

c) for the dual-peak model, all three terms are used.

The wake geometry, either prescribed (section 3.1.3) or free (section 3.2), is based on Γ_{max} for option (a) or on Γ_0 for options (b) and (c). The circulation convergence test (section 5.1.12) is based on Γ_{max} for option (a); on Γ_0 for option (b); or on both Γ_0 and Γ_I for option (c).

3. SECOND ORDER LIFTING-LINE THEORY

3.1 Objective

With the focus of this investigation on improving the rotor wake model, it is important that the analysis accurately calculate the airloading produced by blade-vortex interaction. With the CAMRAD model it has been necessary to use an unrealistically large vortex core radius in order to obtain good correlation between measured and calculated rotor airloads (Johnson, 1986a). Such an empirical approach has limitations that are unacceptable in the long term, such as not being able to select the correct core size until after the data has been measured, and not being able to account for other effects such as swept or yawed flow. The long term goal must be to improve the wing and wake models to the point where the vortex core in the analysis simply represents the actual physical core and nothing else.

The present investigation introduces two alternative methods for improving the wing model for blade-vortex interaction: second order lifting-line theory, and a lifting-surface theory correction (the latter developed in the next chapter). The intent is to improve the calculation of the airloads without actually resorting to methods such as lifting-surface theory, which require more computation and still need some development for rotary wing applications. Several investigations have shown that second order lifting-line theory gives nearly the same result as lifting-surface theory, including the lift produced in close blade-vortex interactions (Johnson, 1986b). In addition, second order lifting-line theory should improve the loads calculated for swept tips, yawed flow, and low aspect-ratio blades.

Formal lifting-line theory is the solution of the three-dimensional wing loading problem using the method of matched asymptotic expansions. Based on the assumption of large wing aspect-ratio, the problem is split into separate outer (wake) and inner (wing) problems, which are solved individually and then combined through a matching procedure. For a rotor in forward flight it is also necessary to consider a swept and yawed planform, and unsteady, compressible, and viscous flow. The lowest order fixed wing solution is Prandtl's theory (steady and no sweep). The development of higher order lifting line theories originated with Weissinger for intuitive methods, and with Van Dyke for singular perturbation methods.

The lifting-line theories generally found in the literature, even including unsteady, transonic, and swept flow, are analytical methods, i.e. they obtain analytical solutions for both the inner and outer problems. For the rotary wing however, it is necessary to include stall (high angle-of-attack) in the inner solution, and the helical, distorted, rolled-up wake geometry in the outer solution. Hence for the rotor problem the

objective is to obtain from lifting-line theory a separate formulation of the inner (wing) and outer (wake) problems, with numerical not analytical solutions, and a matching procedure that will be the basis for an iterative solution.

Lifting-line theory contains so many approximations and assumptions that ultimately it must be replaced by a more accurate method; but that is in the future. Now lifting-line theory is still the only practical method for including viscous effects in the analysis, allowing two-dimensional experimental data containing information on stall and compressibility to be combined with three-dimensional theory. So it is important to develop the best possible lifting-line theory for the rotor. Higher order perturbation methods are not directly applicable, since they involve analytical solutions and quadrature rather than integral form. The objective is to define a practical method, one that gives the best accuracy without convergence problems or singularities. For this purpose the perturbation solutions provide a guide and a sound mathematical foundation for the approach.

3.2 Outline of Second Order Lifting-Line Theory

This section summarizes the development and results of higher order lifting-line theory. Johnson (1986b) provides a more detailed description, and cites the sources responsible for developing various aspects of the theory. The intent here is to concentrate on presenting the basis for the analysis to be implemented (i.e. a practical version of higher order lifting-line theory), with enough information to justify its use.

The method of matched asymptotic expansions for this problem is based on the small parameter $\epsilon = c/R = 1/(\text{aspect-ratio})$. The inner (wing) and outer (wake) solutions are expanded as series, with each term order ϵ smaller than its predecessor. Then the n-term/m-order inner solution is matched to the m-term/n-order outer solution. At each level, the matching provides boundary conditions for the next term in the inner or outer expansion, from the solution at previous levels. For the high aspect-ratio wing, the inner problem has simpler geometry (two-dimensional) but complex flow (Navier-Stokes equations). In the outer limit, the inner solution can be considered irrotational. The outer problem has complex geometry (the vortex wake), but irrotational flow. In the inner limit, the outer solution has simple geometry. In the matching domain, there is both simple geometry and irrotational flow. Hence it is appropriate to represent the order-n inner or outer solution by ϕ_n; ϕ can be considered the velocity potential, or just a symbolic representation of the solution.

3.2.1 Steady, Unswept, Incompressible Fixed Wing

The method of matched asymptotic expansions produces the following results for a fixed wing at speed U. The steady, unswept, incompressible case is considered first.

a) Inner ϕ_0: two-dimensional airfoil with thickness, camber, and the geometric angle of attack (boundary conditions on the surface), in free stream U (boundary conditions at infinity).

b) Outer ϕ_1: line of dipoles from inner bound circulation Γ_0, i.e. a lifting line.

c) Inner ϕ_1: two-dimensional airfoil with zero boundary conditions on the surface; in a uniform flow at infinity that is the induced velocity v_i produced by the outer ϕ_1; v_i is the regular part, i.e. excludes the bound vortex contribution.

d) Outer ϕ_2: dipole line from Γ_1 and quadrupole line from Γ_0; note that ϕ_2 is more singular than ϕ_1 in the inner limit, hence this is a singular perturbation.

e) Inner ϕ_2: inhomogeneous equation with a particular solution produced by second spanwise derivatives of the inner ϕ_0; zero boundary conditions on surface; boundary conditions at infinity from outer ϕ_1 and ϕ_2, consisting of a singular term (proportional to Γ_0'') and a regular term (a linear variation of induced velocity); note that ϕ_2 is more singular than ϕ_1 in the outer limit.

Consider the outer ϕ_2 quadrupole line from Γ_0. The outer limit of the inner ϕ_0 solution is unchanged if the quadrupole line has zero strength and instead the dipole line (bound vortex) is offset. For a thin airfoil the bound vortex must be at the quarter-chord. (Camber introduces an additional chordwise shift, and thickness a vertical shift, but these are not proportional to Γ, so the position of the bound vortex would depend on the lift. These effects will be neglected.) With the bound vortex at the quarter-chord, only a dipole line solution is needed in the outer problem, i.e. a wake of vortex sheets.

Consider the inner ϕ_2 boundary condition at infinity that corresponds to an induced velocity that varies linearly in space. For a thin airfoil, the same lift will be obtained with a boundary condition at infinity that is a uniform induced velocity, if the value at the three-quarter-chord is used. However, a linear induced velocity variation (chordwise) produces a section moment about the quarter chord, while the uniform induced velocity does not. Also, the inner ϕ_2 has a particular solution, as well as other terms in the boundary conditions.

Consider the remainder problem, consisting of the inner ϕ_2 solution after accounting for the induced velocity at the three-quarter-chord. This remainder problems has been solved by Van Dyke for constant geometric angle of attack (spanwise), and by

Van Holten for constant chord. In practice this part of the second order theory is neglected, so such solutions provide an error estimate. Generally the lift error is small (second order); and the moment error is also small, except perhaps for the term that would be produced by the linearly varying induced velocity.

The perturbation solution alternates between the inner and outer problems, using only the solution up to the previous order. Combining the inner problems and combining the outer problems, to solve at all orders simultaneously, is an alternative that is equivalent in terms of the perturbation expansions. For the inner problem, the airfoil (ϕ_0) and wake-induced velocity (ϕ_1) boundary conditions are combined. This is logical and easy, since the ϕ_1 boundary condition is just an angle of attack increment from the wake-induced velocity. For the outer problem, the wake strength is obtained from the total bound circulation, $\Gamma_0+\Gamma_1$ rather than Γ_0. Using the total bound circulation changes the solution from direct quadrature to an integral equation, i.e. Prandtl's formulation. It is found that the solution of the integral equation is actually better behaved; the direct solution is singular at the tips for normal wing planforms.

In general, the integral formulation of lifting-line theory will be used here. Another general feature will be the neglect of the solution of the remainder problem, as described above. This is justified by the fact that an analytical inner solution will not be used, and is consistent with other approximations that are made. Experience shows that the resulting three-dimensional wing theory is second order accurate for lift, but less accurate for moments.

Hence a practical second order lifting-line theory has for the inner problem a two-dimensional airfoil in a uniform flow, consisting of the free stream U and the wake induced velocity. The outer problem is a vortex wake from the bound vortex at the quarter-chord, with distorted wake geometry if necessary. The induced velocity (all three components in general) is evaluated at the three-quarter-chord, excluding the contribution of the bound vortex (which is already accounted for in the matching).

A comparison of the various formulations is useful. Let θ be the geometric angle of attack of the wing. The inner problem problem can be solved analytically, as for a thin airfoil; or numerically, perhaps using airfoil tables:

thin airfoil $\qquad \Gamma = \pi c(U\theta - v)$

tables $\qquad \Gamma = \frac{1}{2} U c c_\ell (\theta - v/U)$

The outer problems calculates the induced velocity v at the quarter-chord or three-quarter-chord, excluding the bound vortex. Note that for a thin planar wake, the induced velocity at the quarter-chord is:

$$v_{c/4} = \frac{1}{4\pi} \int \frac{(d\Gamma/d\eta)d\eta}{y - \eta}$$

The first order perturbation method obtains v from $\Gamma_0 = \pi c U\theta$:

$$\frac{\Gamma}{\pi c} = U\theta - v_{c/4}(\theta)$$

Prandtl's integral equation is also first order, but obtains v from Γ:

$$\frac{\Gamma}{\pi c} = U\theta - v_{c/4}(\Gamma)$$

The common implementation of lifting-line theory for rotors is also first order (using $v_{c/4}$), but airfoil tables are used instead of thin airfoil theory for the inner solution:

$$\frac{\Gamma}{\pi c} = \frac{U}{2\pi} c_\ell(\theta - v_{c/4}(\Gamma)/U)$$

which is the method used in CAMRAD. For the present investigation, second order lifting-line theory is introduced, in which the induced velocity is evaluated at the three-quarter-chord:

$$\frac{\Gamma}{\pi c} = \frac{U}{2\pi} c_\ell(\theta - v_{3c/4}(\Gamma)/U)$$

This comparison should also consider Weissinger's L-theory, in which the induced velocity is calculated at the three-quarter-chord, including the contribution from the bound vortex at the quarter-chord, and equated to the geometric angle of attack. This is equivalent to using thin airfoil theory for the inner solution in second order lifting-line theory:

$$\left(\frac{\Gamma}{\pi c} + v_{3c/4}(\Gamma) \right) = U\theta$$

3.2.2 Sweep and Yawed Flow

A fixed wing with sweep and yawed flow is shown in figure 3-1. The spanwise line m(y) and the chord c(y) are both measured perpendicular to the y-axis. The free stream has yaw angle Λ_U, and the wing sweep is $m' = \tan\Lambda_W$. Large sweep and yaw are allowed, but it is assumed that the wing curvature is small enough so its effects are second order: m' and Λ_U order 1, m'' order ϵ^2. This assumption on the curvature is required in order for the inner ϕ_1 problem (the wake-induced velocity effect) to remain two-dimensional. It is generally a good assumption for rotor blades, except at kinks. At kinks the expansion is invalid to any order (the integral formulation and spanwise discretization are relied on to keep the loading solution well behaved).

The matching process gives for the inner ϕ_1 a new term in the boundary condition at infinity, which is proportional to $\Gamma' \tan\Lambda$ (an effect of the edge of the wake vortex sheet). It can be shown that if these sweep terms are neglected and the induced velocity is calculated at the three-quarter-chord, then the

second order solution gives the correct lift but introduces a moment error. Experience shows that this is a good approximation for the second order theory applied to swept wings.

Hence a practical theory has for the inner problem a two-dimensional airfoil in a uniform flow, consisting of the swept free stream and the wake induced velocity. The outer problem is a vortex wake from the bound vortex at the quarter-chord. The induced velocity is evaluated at the three-quarter-chord, excluding the contribution of the bound vortex. The inner problem is an infinite wing with crossflow. It is preferable however to define the geometry relative to the straight y-axis, which gives an infinite wing with yaw and crossflow for the inner problem.

3.2.3. Unsteady Loading

The matching process produces the following results for the case of a fixed wing with unsteady loading.

a) Inner ϕ_0: unsteady two-dimensional airfoil with shed wake, in a yawed free stream.

b) Outer ϕ_1: a lifting line; the shed wake matches the inner solution.

c) Inner ϕ_1: the boundary condition at infinity has a regular part from the wake-induced velocity, and a singular part from sweep; both the bound vortex and the inner shed wake must be excluded in evaluating the induced velocity.

If the shed wake is considered as part of the inner solution boundary conditions, instead of part of the inner problem, then only the bound vortex is excluded in evaluating the induced velocity. In this case, the shed wake is omitted from the inner ϕ_0 problem.

It is natural to include all of the wake in the outer problem when the induced velocity is being calculated numerically. Then the shed and trailed wake are treated identically: the induced velocity is evaluated at the three-quarter-chord and treated as a uniform flow for the inner problem. The assumption that the shed-wake induced velocity is constant over the chord is a significant approximation however. With the induced velocity evaluated at a single point, the shed wake model should be modified as required to obtain unsteady loads correctly. It is found (Johnson, 1980a) that if the shed wake is started a quarter-chord aft of the collocation point, then the Theodorsen and Sears functions are well approximated (at least for small reduced frequency k, and reasonably well up to about k = 1).

For small reduced frequency, k order ϵ, the unsteady part of the induced velocity is of the same order as the steady part;

while for k order 1, the unsteady part of the induced velocity (three-dimensional effect) is higher order. Hence it is consistent to have the unsteady inner solution accurate to k order 1, and the unsteady outer solution accurate to k order ϵ.

Hence a practical theory has for the inner problem a two-dimensional airfoil with no shed wake. The outer problem is a vortex wake from the bound vortex at the quarter-chord. The induced velocity is evaluated at the three-quarter-chord, including all the shed wake but excluding the contribution of the bound vortex. The trailed wake starts at the bound vortex, while the shed wake is created a quarter-chord aft of the collocation point.

3.2.4 Compressible, Transonic, and Viscous Flow

For an unswept wing with steady loading, the compressible solution is obtained simply using the Prandtl-Glauert scaling. For the swept and unsteady case, compressibility introduces new terms but does not change the basic structure and order of the solution. A practical lifting-line theory includes compressibility in the inner solution, and calculates the induced velocity from an incompressible wake model.

For transonic flow, it is necessary to first introduce transonic scaling of the equations, and expand the potential in $\tau^{2/3}$ (where τ is a measure of the disturbance produced by thickness or angle of attack). Then the solution can be expanded in $\epsilon = \tau^{-1/3} c/R$ (note that a larger aspect ratio is required in transonic flow for the same order lifting-line expansion). Transonic scaling requires moderately small sweep and small reduced frequency as well. Matching gives the following results:

a) Inner ϕ_0: transonic two-dimensional equation.

b) Outer ϕ_1: subsonic equation (linear).

c) Inner ϕ_1: transonic two-dimensional equation, linearized about ϕ_0.

Nonlinearity does not enter the matching at first order. The outer ϕ_1 solution is still a lifting-line, and the inner ϕ_1 boundary condition is still the induced velocity. If the inner ϕ_0 and ϕ_1 solutions are not combined, then it is also necessary to introduce perturbations of the shock jump relation and shock position. A practical lifting-line theory includes transonic flow in the inner solution, and calculates the induced velocity from an incompressible wake model.

For viscous flow, it is assumed that the outer limit of the inner problem is still irrotational, so the matching results are the same as for inviscid flow. The inner boundary conditions on the wing are now no-slip, which introduces new effects for a yawed wing. For a practical method it is required that with

viscous flow the inner problem still be an infinite wing (yawed and swept, unsteady, transonic). To achieve this in the equations of motion (spanwise derivatives second order or smaller) requires only that the Reynolds number be order ϵ^{-1} for a swept wing. In fact the Reynolds number is much larger, so the lifting-line assumption is good as far as viscous transport is concerned. It is also necessary to consider the geometry of the flow field that results from the introduction of viscous effects (e.g. large scale separation). The lifting-line assumption requires that such geometry vary slowly in the spanwise direction.

3.2.5 Rotary Wing

Rotation as well as translation of the wing introduces some extra complications, but does not significantly increase the level of approximation (because so much has been assumed or neglected already). Using a rotating and translating coordinate frame, the wing geometry can still be described as in figure 3-1. Now the free stream velocity U and yaw angle Λ_U vary with y. Small curvature is still assumed. Note that k_U is order ϵ for 1/rev variations, while k is order 1 for higher harmonics. For the incompressible case only the boundary conditions and wake configuration change; moreover, the inner limit of the outer problem is the same as for the fixed wing. For compressible flow, there are additional Coriolis and centrifugal type terms in the equations.

3.3 Summary of Wake and Wing Model

The following is a practical implementation of second order lifting-line theory for rotors. The outer problem is an incompressible vortex wake behind a lifting-line, with distorted geometry and rollup. The lifting-line (bound vortex) is at the quarter-chord (the quadrupole-line approximation, for second order loading). The trailed wake begins at the bound vortex, while the shed wake is created a quarter-chord aft of the collocation point on the wing (the lifting-line approximation for unsteady loading). Three components of wake-induced velocity are evaluated at the collocation points, excluding the contribution of the bound vortex. The collocation points are at the three-quarter-chord, in the direction of the local flow (the approximation for linearly varying induced velocity, from the second order wake).

The inner problem consists of unsteady, compressible, viscous flow about an infinite aspect-ratio wing; in a uniform flow consisting of the yawed free stream and three components of induced velocity. This problem is split into several parts: two-dimensional, steady, compressible, viscous flow (airfoil tables); plus corrections for unsteady flow (small angle non-circulatory loads, but without any shed wake), dynamic stall, and yawed flow (equivalence assumption for a swept wing).

This formulation is generally second order (in $\epsilon = c/R$) accurate for lift, including the effects of sweep and yaw, but less accurate for moment. Note that placing the collocation points at the quarter-chord gives a first order lifting-line theory.

The geometry of the wing will be defined by the quarter-chord (aerodynamic center) and chord as a function of r, measured perpendicular to a straight reference span axis. The inner problem (at radial station r) is an infinite aspect-ratio wing with the local chord and sweep, in yawed flow. The outer problem has the bound vortex at the quarter-chord, and the collocation points at the three-quarter-chord (in the trailed wake direction, i.e. the direction of the local velocity).

3.4 Near Wake Model

Implementation of this lifting-line theory primarily involves the CAMRAD near wake, which is defined as the wake lattice directly behind the reference blade (where the induced velocity is being calculated). The circulation distribution and resulting wake panels for the near wake are illustrated in figure 2-4. The blade bound circulation $\Gamma(r,\psi)$ is evaluated at the aerodynamic radial stations (where the induced velocity is calculated also) and at a discrete set of azimuth angles. A piecewise-linear variation of Γ implies vortex sheet panels, with shed and trailed vorticity that have strength varying linearly along their direction (see Johnson, 1980b, figures 14 and 16).

With a stepped variation of Γ, or as an approximation for the sheets, vortex lines in the middle of the panels are obtained.

It follows that the geometry in the near wake is defined in terms of these wake panels; that the vortex lines should be placed in the middle of the panels (radially and azimuthally); and that the vorticity strength varies linearly along its direction. However, sheet elements are not used for the near wake model being developed here. The discretization of the wake is not well controlled using sheet elements, because of edge and corner singularities, particularly when planar-rectangular elements are used. Also, the most important case of the downwash from the two sheet panels adjoining the collocation point would require a higher order element or some other special treatment. Hence a vortex lattice representation of the near wake is used.

The wake panel geometry is defined by the positions of the blade root, tip, and aerodynamic radial stations, convected from azimuth stations $\psi-\phi_k$ and $\psi-\phi_{k+1}$ (with self-induced distortion), where ψ is the current blade azimuth (time) and ϕ is the wake age. The trailed lines are placed in the middle of the panels (interpolated from the positions of the corners), or at the root/tip for the most inboard/outboard panels. Specifically, the end points of the trailed line are on the panel leading and trailing edges, at the radial stations that define the edges of the aerodynamic segments of the blade (see Johnson, 1980b, section 2.4.1). Then the collocation points (in the middle of the aerodynamic segments) are always equidistant from the nearest trailed lines.

The shed lines are placed in the middle of the panels (interpolated from the positions of the corners), and moved aft by 3c/4 (c/4 if the collocation points are on the quarter-chord). Specifically, the end points of the shed line are on the panel side edges, 3c/4 aft of the mid points.

The collocation points are at the three-quarter-chord, for the aerodynamic radial stations. Specifically, they are on the side edges of the first wake panels, c/2 aft of the leading edge (the geometry of the wake is thus being used to obtain the local flow direction).

The lifting-line is placed at the quarter-chord of the blade, i.e. x_A aft of the blade reference axis. Hence an increment in the blade position of $\Delta\vec{r}_b = x_A\vec{i}$ is required (see Johnson, 1980b, section 3.1.3). The c/2 shift of the aerodynamic center in reverse flow is ignored here (only for the purpose of defining the wake geometry; the loads are properly applied to the blade in reverse flow). The option of a straight lifting-line is also implemented, by omitting this x_A term.

The geometry of this discretization is well controlled. Still, with vortex lines and the distorted, skewed, helical geometry of the rotor wake it is necessary to be concerned about the singular velocities that could occur with lines too near

collocation points (most likely to occur near the reverse flow boundary). A solid-body-rotation viscous core is used for the near wake line segments in order to avoid such singularities. The baseline core size is

$$r_c = \text{(panel width)}/5$$

so the core should not influence the induced velocities in normal situations.

The tip vortex is rolled up substantially by the time it reaches the trailing edge, even with highly tapered tips. Most of the effects of this rollup can not be obtained with lifting-line theory, but it is important that radial station of the rollup, r_{TV}, be included in the model. The near wake model has trailed lines at the aerodynamic segment boundaries and at the tip. Hence it is possible to force the bound circulation to be trailed at r_{TV} by using the factor

$$\max(0,\ \min(1,\ (r_{TV}-r_i)/(r_{i+1}-r_i)\ ))$$

on the lift coefficient c_ℓ at aerodynamic radial station r_{Ai} (r_{Ai} is midway between the aerodynamic segment edges r_i and r_{i+1}). Note that if r_{TV} equals some r_i, then there will be exactly zero bound circulation and hence zero strength wake outboard of that r_i. This factor is similar to that used for the tip loss factor in the uniform inflow model (Johnson, 1980b, section 2.4.5), but here it actually models the physical rollup position.

4. LIFTING-SURFACE THEORY CORRECTION

4.1 Objective

This chapter describes a second method for improving the wing model for blade-vortex interactions: a lifting-surface theory correction. Note that the lifting-surface correction is an alternative to the second order lifting-line theory developed in the preceding chapter; the two methods should not be used simultaneously.

The basis for the lifting-surface theory correction is the model problem shown in figure 4-1: an infinite wing encountering a straight infinite vortex with intersection angle Λ. The wing and vortex lie in parallel planes with separation h. The wing semichord is b. The intersection angle Λ is 90 deg for a perpendicular encounter and 180 deg for a parallel encounter (angles between 0 and 90 deg are treated by symmetry considerations). The wing spanwise variable r is measured from the intersection with the vortex; so ($r \sin\Lambda$) is the distance to the vortex line.

Johnson (1971b) derived a lifting-surface theory solution for this model problem, and developed an approximation suitable for vortex-induced loads. By applying a Fourier transform to the vortex-induced downwash and lift, the problem becomes finding the loading produced by a sinusoidal gust. A numerical solution to this problem was approximated by a series that has an analytical inverse transform. This produced an approximate lifting-surface solution L_{ls} for vortex-induced loads.

CAMRAD uses this lifting-surface solution in the following manner (Johnson, 1980b, section 3.1.7). A similar expression is introduced for the vortex-induced load that would be obtained from lifting-line theory, L_{ll}. Then the induced-velocity of each line segment of the tip vortex in the wake model is multiplied by the factor L_{ls}/L_{ll}. By this means, the lifting-line calculation of the vortex-induced loads should give the lifting-surface theory result. Calculations performed with CAMRAD do not however show a significant effect of this lifting-surface theory correction (e.g. Yamauchi, Heffernan, and Gaubert, 1988). Therefore the method has been reviewed and revised in the present investigation.

4.2 Lifting-Surface Theory Expression

This section summarizes the results of the lifting-surface theory solution for the model problem (Johnson, 1971b). The vortex-induced downwash on the wing, for the perpendicular interaction, is:

$$\frac{w/V}{\Gamma/2\pi bV} = \frac{-r}{r^2 + h^2}$$

where r and h are scaled with b. To include a viscous core, a distributed vorticity model is used, such that the circulation at a distance r from the vortex is $\gamma = \Gamma r^2/(r^2+r_c^2)$. Then the vortex-induced downwash is still given by the above expression, if an effective separation distance h_{eff} is used:

$$h_{eff}^2 = h^2 + r_c^2$$

The Fourier transform decomposes the downwash w(r) into sinusoidal gust of amplitude $\bar{w}(\nu)$, where ν is the wave number:

$$w(r) = \int_{-\infty}^{\infty} e^{i\nu r}\ \bar{w}(\nu)\ d\nu$$

Application of the Fourier transform gives the spectrum of the vortex-induced downwash:

$$\frac{\bar{w}/V}{\Gamma/2\pi bV} = \frac{i}{2}\ e^{-\nu h}$$

Based on this equation, wavenumbers in the range ν = 0 to 5 were considered relevant for vortex-wing separations greater than a quarter-chord ($h \geq .5$)

The lift produced by a sinusoidal gust can be written in terms of a lift deficiency function g_L:

$$\bar{L}(\nu) = -2\pi\rho V b\ \bar{w}(\nu)\ g_L(\nu)$$

for the perpendicular interaction. The lift deficiency function is similarly defined for all intersection angles Λ. For the parallel intersection (two-dimensional unsteady airfoil), the wavenumber becomes the reduced frequency k, and g_L is the Sears function.

The lift deficiency function is approximated by a sum of exponentials:

$$g_L \cong \exp(-c_0\nu) - i\ \sin(b_0\nu)\ a_0'\ \exp(-c_0'\nu)$$
$$+ \exp(i(b_1\nu - b_2))\ (-a_1\nu^2\exp(-c_1\nu) + a_2\nu^4\exp(-c_2\nu))$$

This form is chosen because it (and its product with the vortex sprectrum) has an analytical inverse (see Johnson, 1980b, section 3.1.7 for the result). The exponentials decay too quickly, so any finite series of this form will be too small at high ν. The approximation is acceptable however over the required range of ν (i.e. because g_L is multiplied by $\exp(-\nu h)$ from the vortex spectrum). Linear lifting-surface theory was solved numerically for g_L, and the results used to identify the coefficients in this expression as a function of intersection angle Λ and Mach number.

CAMRAD uses this expression for zero Mach number (an incompressible interaction). Note that there is an error in the coefficients used by CAMRAD; b_0 should be

$$b_0 = 8.88 - 1.88\ (\Lambda/90)$$

(Johnson, 1980b, page 167). This correction has no effect for the perpendicular interaction, and does not greatly change the peak blade-vortex interaction loads in any case. If there is a problem with this method, it must be sought in the corresponding lifting-line solution used by CAMRAD.

4.3 Lifting-Line Theory Expression

The lifting-line theory equation for an infinite wing with downwash w (the perpendicular interaction) is:

$$\Gamma = 2\pi b w - \frac{1}{2}\int_{-\infty}^{\infty} \frac{d\Gamma}{d\rho}\frac{d\rho}{r-\rho}$$

For a sinusoidal gust, $w = \bar{w}e^{i\nu r}$, the solution is

$$g_L = \bar{\Gamma}/2\pi b\bar{w} = 1/(1+\frac{\pi}{2}\nu)$$

This result assumes a continuous trailed wake sheet. For a discretized wake, with trailed lines uniformly spaced a distance d apart, the result is

$$g_L = 1/(1 + \frac{\pi}{2}\nu \frac{\sin \nu d/c}{\nu d/c})$$

For rotor analyses, usually d/R = .02 to .06 on the outer part of the blade, so d/c = .6 is typical.

For the parallel interaction, it is necessary to consider the lifting-line approximation for two-dimensional unsteady aerodynamics (Johnson, 1980a). With the induced velocity calculated at a single point, the Theodorsen function is approximately matched by starting the shed wake c/4 behind the collocation point:

$$C(k) \cong 1/(1+kI), \quad I = i\int_{1/2}^{\infty} e^{-ik(\xi-3/2)}\frac{d\xi}{\xi}$$

For a sinusoidal gust, the corresponding approximation for the Sears function is

$$g_L = S(k) \cong e^{ik/2}\ (C + ik/2)$$

This is a low frequency approximation, good to about k = 1/2. Note that to order k, the real part of g_L is

$$Re(g_L) \cong 1/(1+\frac{\pi}{2}k)$$

which is identical to the perpendicular interaction result.

For the perpendicular interaction, CAMRAD approximates the lift deficiency function as

$$g_L \cong \exp(-\frac{\pi}{2}\nu) - a_1\nu^2\exp(-c_1\nu)$$

with $a_1 = -.662$ and $c_1 = 1.296$ obtained by matching g_L at $\nu = 1$ and $\nu = 2$.

Figure 4-2 shows the lift deficiency function g_L for the perpendicular interaction; figure 4-3 shows the normalized gust spectrum, $\exp(-\nu h)$; and figure 4-4 shows the product, $g_L \exp(-\nu h)$, for $h/b = 1$. The lifting-surface solution is significantly smaller than the lifting-line solution, particuarly with a discretized wake. It is observed that the spanwise resolution in the discretized wake should be less than $d/c = .5$ for a blade-vortex separation of about 1/2 chord; a corresponding azimuthal resolution is also required. The CAMRAD expression for the lifting-line solution is reasonable to about $\nu = 2$, but is too small for larger wavenumbers (figure 4-2). When multiplied by the gust spectrum, the errors in the CAMRAD expression are not very important though (figure 4-4), as long as d/c is not too large. A better approximation can be developed, by matching the discretized lifting-line result for d/c and using a third term. The revision is not expected to have much of an effect on the peak vortex-induced loads however.

For non-perpendicular interactions, the CAMRAD lifting-line expression was obtained by simply replacing r by $(r \sin\Lambda)$. For the parallel interaction, this is equivalent to assuming that

$$g_L = 1/(1 + \frac{\pi}{2}k)$$

which is a good approximation to order k for the real part of the Sears function, but ignores the phase shift. It is the phase shift that leads to a significant asymmetry in the blade-vortex interaction peak loads for the parallel interaction, with the first peak (in time) being much larger than the second peak, particularly for small separation. By using a real g_L, this asymmetry is absent in the CAMRAD lifting-line expression used in the lifting-surface correction. The result in fact is that L_{1s}/L_{1l} as calculated in CAMRAD is greater than one for the first peak, which CAMRAD then replaces by $L_{1s}/L_{1l} = 1$, i.e. there is no lifting-surface correction for the first peak. A nonzero phase exists for any non-perpendicular interaction, and is significant even for interactions 30 deg from perpendicular. Consequently, for most interactions the CAMRAD lifting-line expression results in no lifting-surface correction for the first peak. This is the major problem that must be corrected.

4.4 Revised Lifting-Line Theory Expression

The revised lifting-line theory expression will be based directly on the lifting-surface theory expression for g_L, assuring that the phase shift will exist, and improving the approximation at higher wavenumbers as well. The approach was to adjust the constants from the lifting-surface expression in order to match the lifting-line g_L for the perpendicular interaction (the discretized wake result for d/c about .6) and the parallel

interaction (up to about k = 1, the limit of the validity of the lifting-line approximation). The low frequency limit in both cases gives $c_0 = \pi/2$. The factors a_1 and a_2 were increased in order to match the magnitude of g_L for wavenumbers around 1. The factor a'_0 was decreased for the parallel interaction, in order to match the peak phase shift at very low frequency. Finally, for the parallel interaction $b_2 = 0$ and $b_1 = .5$ are used, to match the phase of g_L for wavenumbers around 1. Hence the expression for the lifting-surface theory lift L_{1s} (Johnson, 1980b, page 167) is used with:

$$c_0 = 1.571$$

$$a_1 = (1.25 + .5 \sin\Lambda)\ (a_1)_{1s}$$

$$a_2 = (2.5 + \sin\Lambda)\ (a_2)_{1s}$$

$$a'_0 = .75\ (a'_0)_{1s}$$

$$b_2 = 0$$

$$b_1 = .5\ (b_1)_{1s}$$

The result is a revised expression for L_{11}.

Figure 4-5 shows the revised lift deficiency function for the perpendicular interaction, and figure 4-6 shows the corresponding vortex-induced load. The revised lifting-line expression is an improvement (compare figures 4-5 and 4-2), but still the product of g_L and the vortex spectrum shows that the difference is not too important, as long as d/c is not too large.

Figure 4-7 shows the magnitude and phase of the lift deficiency function for the parallel interaction. The CAMRAD lifting-line expression has no phase shift, and its magnitude is close the the lifting-surface theory expression. The revised lifting-line expression has a nonzero phase, and matches both the magnitude and phase reasonably well. It should be noted that the lifting-surface theory phase shows some distortion that is a result of the approximate expression used; and that the accuracy of the lifting-line theory result is deteriorating at k = 1.

The vortex-induced loads along the wing span can be calculated from the lifting-surface theory and lifting-line theory expressions, and the peak loads found as a function of vortex-blade separation h/b. The normalized section lift is $L/\rho V\Gamma$, where Γ is the strength of the vortex. Note that the two-dimensional lift is $L_{2D} = -\rho V b 2\pi w$, so for the vortex-induced downwash

$$L_{2D}/\rho V\Gamma = r/(r^2 + h^2)$$

and the peak loads are $L_{2D}/\rho V\Gamma = \pm 1/2h$, occuring at $r = \pm h$. The vortex-wing separation should be considered the effective value h_{eff}, which has a minimum value equal to the core size r_c.

Figure 4-8 shows the peak lift magnitude and its spanwise location for the perpendicular interaction. The effect of the revised lifting-line expression is evident only for very small h. The lifting-surface correction is L_{ls}/L_{ll} = .74 for the peaks at h = .5b. Figure 4-9 shows the peak lift for the parallel interaction. The negative peak occurs first (in time), then the lift goes through zero and the positive peak occurs. With no phase shift, the CAMRAD lifting-line expression gives the same magnitude for the positive and negative peaks, and hence implies a correction factor greater than one for the negative peak. The revised lifting-line theory always gives a correction factor less than one. The lifting-surface correction is .61 for the positive peak at h = .5b.

Figure 4-10 shows the peak lift for an interaction with the vortex 30 deg from perpendicular, which may be considered a typical rotor blade-vortex interaction case. Again the CAMRAD lifting-line expression gives a lifting-surface correction greater than one for the negative peak, while the revised expression gives a correction significantly less than one. Hence with the phase shift accounted for in both the lifting-surface and lifting-line expressions, this result is similar to that for the perpendicular interaction. The lifting-surface correction is here .70 for the positive peak and .78 for the negative peak at h = .5b.

5. OUTLINE OF CALCULATIONS AND CORRELATIONS

5.1 CAMRAD Modifications

The new wake model described above has been incorporated into the CAMRAD computer program. Appendix A describes the code modifications, and defines the new input parameters. The analysis was run for nine test cases, to check that the modifications were functioning as intended. These checks established the following results.

a) With the three-quarter-chord collocation point, a smaller value of the relaxation factor for the circulation iteration is required (compared to that required with the quarter-chord collocation point).

b) Near wake core sizes from .0005 to .5 times the panel width were tried (the default value is .2). For the low speed cases, the results were identical for .0005 to .2, but different for .5; there were no convergence problems. For the high speed cases, the analysis would not converge with the smallest factors, and the results for .05 to .2 differed somewhat. (An influence of this core size on the results usually means potential problems with the discretization.) It was concluded that the baseline value of .2 is appropriate: small enough not to affect normal configurations, and large enough to ensure convergence.

c) With the dual-peak wake model, two iterations between the wake geometry and trim solutions were sufficient for r_{GI} to converge. It was noted that changes in the mean inflow (which defines the vertical convection for rigid wake geometry) had as much effect in these iterations as changes in r_{GI}.

5.2 Rotors Analyzed

The capabilities and limitations of the new wake model were established by comparison of the calculations with measured helicopter rotor airloads data. Outlined below are the investigations that will be described in the remainder of this report.

The focus of this investigation was on high speed forward flight, but at high speed there are many factors besides the wake that influence the rotor loads. Therefore specific features of the new wake model, particularly the treatment of blade-vortex interaction, were initially examined by considering low speed cases:

1) Hovering rotor circulation distribution. This case was used only to establish the influence and proper use of r_{TV}, the parameter defining the radial location of the tip vortex at the blade trailing edge.

2) Lateral flapping wind tunnel test. Lateral flapping in low speed forward flight is a sensitive measure of blade-vortex interaction. No airloads data were available for this case.

3) SA349/2 helicopter flight test. One low speed case that exhibits significant blade-vortex interaction was considered. This case and the lateral flapping data were used to examine the capabilities of the new wake model: the second order lifting-line theory (three-quarter-chord collocation point), and the lifting-surface theory correction.

4) Swept tip calculations. No measured data from a rotor with a swept tip is available. Calculations were performed to examine the capabilities of the new wake model: first order or second order lifting-line theory, straight or swept bound vortex.

Then the modified analysis was used to calculate the airloads for comparison with several flight tests and wind tunnel tests:

5) Boeing model 360 scale rotor test. Application of the new wake model to the high speed results of this wind tunnel test was a primary objective of the investigation.

6) H-34 rotor wind tunnel test. This test has been a primary source of information and speculation about rotor airloads at high speed. Model 360 and H-34 cases were therefore used to examine the influence of various features of the new wake model on the calculated airloads at high speed.

7) AH-1G helicopter flight test. Although only one radial station was instrumented in this test, it includes high speed operating conditions.

8) H-34 helicopter flight test. This test has long been a standard for rotor airloads data, but did not include the high speed conditions that are of interest for the present investigation. For completeness, and in order to re-examine the quality of the measured data, the airloads were calculated for low speed and moderate speed cases.

9) UH-60A rotor calculations. No data is available yet for this rotor. The calculations were performed to examine the results of the new wake model for a rotor with a swept tip and a large (and unusual) twist.

The report concludes by considering some special topics.

10) Harmonic content of airloads data. The available data are examined to determine the azimuthal resolution required for airloads tests.

11) Review of measured rotor airloads data. A summary of the problems and limitations observed in the existing rotor airloads data sets is provided. The review included tests that were not the subject of correlation in the present investigation: NACA

model wind tunnel test; and CH-47, HU-1A, XH-51A, NH-3A, and CH-53A flight tests.

5.3 Format of Data Presentation

Most of the correlation between the measured and calculated aerodynamics will be for the rotor blade section lift. The section lift at a particular radial station is obtained experimentally by measuring the pressure at several chordwise stations, and numerically integrating along the chord. The wind tunnel and flight tests considered vary greatly in the number of radial stations, number of chordwise stations, and use of differential or absolute pressure measurements. The correlation will concentrate on the loading on the outboard part of the blade, typically for radial stations near 75%, 85%, and 95% R. The section lift will be presented in dimensionless form:

$$\begin{aligned} d(C_T/\sigma)/dr &= L/(\rho(\Omega R)^2 c_m) \\ &= (c/2c_m)u_T^2 c_\ell \\ &= (c/2c_m M_{tip}^2)M^2 c_\ell \end{aligned}$$

where L is the section lift in lb/ft, and c_ℓ is the lift coefficient. The quantity obtained from the measured pressures is actually the normal force coefficient, while the analysis gives $d(C_T/\sigma)/dr$ in shaft axes; this difference is ignored.

The experimental data is presented with the best azimuthal resolution available, which ranges from 10 harmonics to 1024 samples per rev. The analysis gives the calculated blade lift at twenty-four azimuth stations, i.e. 15 deg resolution. The calculated lift is plotted by connecting the points every 15 deg with straight lines and then smoothing the corners slightly. This is accomplished by using a 15-harmonic respresentation of the piecewise-linear curve connecting the calculated points. The resulting smooth curve nearly passes through all the calculated points, without introducing spurious overshoots or oscillations.

Blade torsional moments are also presented in dimensionless form:

$$C_{mt}/\sigma = M_t / (\rho(\Omega R)^2 R^2 c_m)$$

where M_t is the moment in ft-lb.

6. HOVERING ROTOR CIRCULATION DISTRIBUTION

This case is considered to establish the influence and proper use of r_{TV}, the parameter defining the radial location of the tip vortex at the blade trailing edge. Ballard, Orloff, and Luebs (1979) obtained the bound circulation for a model rotor in hover, using a two-component laser velocimeter to measure the circulation around a box enclosing the blade at various radial stations. The rotor properties and operating condition are as follows.

number of blades	2
radius	3.43 ft
solidity	.0464 (rectangular), .0396 (ogee)
chord, c/R	.073
twist	-11 deg
airfoil	NACA 0012
C_T/σ	.10
M_{tip}	.22

Figure 6-1 compares the measured and calculated circulation, $\Gamma/\Omega R^2$, for rectangular and ogee tip planforms. Two values of r_{TV} are used for the calculations in each case.

The near wake model consists of a vortex lattice, with the trailers at the edges of the blade aerodynamic segments and the collocation points in the midpoints of the blade aerodynamic segments. The most outboard trailer is at the tip, r/R = 1. With r_{TV} = 1., this most outboard trailer is the tip vortex. Figure 6-1 shows that the loading is not accurately calculated using r_{TV} = 1. With r_{TV} less than 1, the analysis sets the blade section lift to zero for aerodynamic segments outboard of r_{TV}. The complete near wake lattice still exists, but the trailers outboard of r_{TV} have zero strength, so effectively the tip vortex is formed on the blade at radial station r_{TV}. When in figure 6-1 r_{TV} is set to the measured tip vortex rollup position, good correlation with the measured circulation is obtained. It is also found that r_{TV} has a significant influence on the calculated induced power.

Care must be taken in positioning r_{TV} relative to the blade aerodynamic segments. If there are one or more segments completely outboard of r_{TV}, hence outboard of the tip vortex, they will see a large positive induced angle-of-attack, which will increase the profile power and decrease the figure of merit. For a rectangular planform blade this effect should be avoided, which can be accomplished by having the last aerodynamic segment large enough to include r_{TV}. For a highly tapered tip (such as the ogee planform of figure 6-1) the effect may be realistic, although it is a detail that is probably beyond the capability of lifting-line theory.

The calculations shown in figure 6-1 were obtained with first order lifting-line theory (quarter-chord collocation point) and without the lifting-surface theory correction. Second order lifting-line theory or the lifting-surface theory correction reduces the loading variation produced by the vortex, hence reduces the peak circulation. The result is worse correlation than shown in figure 6-1.

7. LATERAL FLAPPING WIND TUNNEL TEST

Lateral flapping in low speed forward flight is a sensitive measure of the effects of the rotor wake. The lateral tip-path-plane tilt of an articulated rotor depends primarily on the longitudinal gradient of the induced velocity distribution over the disk. The induced velocity in forward flight is larger at the rear of the disk than at the front, which produces larger loads at the front, hence an aerodynamic pitch moment on the rotor. An articulated rotor responds to this moment like a gyro, so the tip-path-plane tilts laterally, toward the advancing side. In forward flight there is also a small lateral flapping contribution proportional to the coning angle.

The lateral flapping is underpredicted when uniform inflow is used, and even when nonuniform inflow based on undistorted wake geometry is used. Below an advance ratio of about 0.16, it is necessary to include the free wake calculation in order to obtain a good estimate of the lateral flapping (Johnson, 1986a). There is significant self-induced distortion of the tip vortices, resulting in numerous blade-vortex interactions in which the vertical separation is a faction of the blade chord. The result of such distortion is a much larger longitudinal gradient of the induced velocity, which produces the observed lateral flapping. In the case considered here, the free wake geometry places the tip vortices so close to the blades that the calculated flapping is sensitive to the value of the tip vortex core radius, which determines the maximum velocity induced by the vortex. There are a number of factors that influence the magnitude of the vortex-induced loading, including: the extent of the tip vortex rollup; the tip vortex strength; the viscous core size; lifting-surface effects on the induced blade loading; and possibly even vortex bursting or vortex-induced stall on the blade. The core size used in the analysis accounts for all such effects that are not otherwise modelled. The present investigation improves the calculation of the vortex-induced loading, using methods equivalent to lifting-surface theory. Hence it is expected that a smaller core size, closer to the physical viscous core radius, will be needed for good correlation with the improved model.

The flapping in low speed was measured by Harris (1972), on a model rotor in a wind tunnel. The rotor parameters and operating condition are as follows.

number of blades	4
radius	2.73 ft
solidity	.0891
chord, c/R	.070
twist	-9.14 deg
airfoil	V23010-1.58
C_T/σ	.08
α_{tpp}	1 deg
M_{tip}	.40

Figure 7-1 compares the measured and calculated lateral flapping, for three models of the blade-vortex interaction loads:

a) First order lifting-line theory (c/4 collocation point) and no lifting-surface correction. This model will require a larger core size.

b) Second order lifting-line theory (3c/4 collocation point) and no lifting-surface correction.

c) First order lifting-line theory (c/4 collocation point), with the lifting-surface theory correction.

For each case the tip vortex core size is varied. Figure 7-2 shows the corresponding longitudinal flapping.

For case (a), a core size of about .05R (70% chord) appears best; but at low advance ratio the lateral flapping magnitude is overpredicted, and the longitudinal underpredicted, regardless of the core size. With either the 3c/4 collocation point or the lifting-surface correction, a core size of about .035R (50% chord) appears best. These two approaches produce about the same results, but with differences in details. The lifting-surface theory correction is nearly equivalent to simply increasing the core size by Δr_c = .015 R = .43 b (20% chord). For advance ratios below about .06, the lifting-surface correction does not improve the correlation, while the 3c/4 collocation point gives good results over the entire speed range shown.

In general therefore the best model is the second-order lifting-line theory. The core size appropriate with this model is still relatively large, which might be a Reynolds number effect on the actual viscous core.

The calculations were performed using four revolutions of the rotor wake for all speeds. The free wake geometry (self-induced distortion) was calculated for the first two revolutions, and extrapolated for the last two. Using three revolutions of calculated free wake geometry produced poorer correlation with the measurements. Below an advance ratio of about .04 the free wake geometry used is not accurate. It is possible that the large errors in flapping prediction at advance ratios below .06 with the c/4 collocation point are associated with the influence of the core size (directly or through the circulation) on the wake geometry. Airloads and wake geometry measurements are needed to pursue these questions.

8. SA349/2 HELICOPTER FLIGHT TEST

In order to examine the capability of the wake model to calculate blade-vortex interactions without the additional complications of high speed flight, a low speed case that exhibits significant blade-vortex interaction is considered.

Flight tests of an SA349/2 helicopter were reported by Heffernan and Gaubert (1986). Flight test case 2 is considered here (condition number 1 of Yamauchi, Heffernan, and Gaubert, 1988). The lift coefficient was measured at radial stations 75%, 88%, and 97% R. There were 9-11 pressure gages on the upper surface and 6-7 on the lower surface. Heffernan and Gaubert (1986) present 10 harmonics of the lift, for six revolutions and averaged over the six revolutions. Time histories of the lift with an azimuthal resolution of 2 deg were obtained from the Rotary Wing Aeromechanics Branch, NASA Ames Research Center. The measured lift shows considerable variation from rev to rev for this flight condition. However, an examination of the blade-vortex interaction peaks in the individual revolutions showed that the amplitude of the peaks in the averaged data were only 3-5% less than the mean of the amplitude of the peak in the original data; and the peak amplitudes in the original data vary by ±7-16% from the mean amplitudes. Hence it is acceptable to base the correlation with analysis on the averaged lift data.

The principal characteristics of the rotor and the operating condition are as follows.

number of blades	3
radius	5.25 m
solidity	.0637
chord, c/R	.0667
airfoil	OA209
twist	-7.3 deg (0 outboard 91% radius)
C_T/σ	.065
advance ratio	.14
M_{at}	.72

Heffernan and Gaubert (1986) give CAMRAD input parameters for this rotor.

It is known that the free wake geometry must be used in order to accurately calculate the blade-vortex interaction loads for this low speed flight condition (Yamauchi, Heffernan, and Gaubert, 1988). Figure 8-1 compares the measured airloads with calculations using the present wake model, showing the influence of nonuniform inflow and the free wake geometry. Figure 8-2 shows the corresponding calculated wake geometry. These calculations involved the following features:

a) c/4 collocation point, with lifting-surface correction;

b) tip vortex core size .015 R (22.5% chord);

c) core size of .100 R for radial stations inboard of 80% R (transitioning to .015 R at 90% R), to suppress the blade-vortex interactions inboard.

The amplitudes of the blade-vortex interaction peaks are well predicted. The calculated load is low in the second quadrant for 97% R, and high in the third quadrant for 88% R.

Figures 8-3 to 8-5 compare the measured airloads with calculations using tip vortex core sizes of .015, .025, .035, and .045 R (22.5% to 67.5% chord). For these calculations the same core size was used for both inboard and outboard portions of the blade. Three wake models are considered:

a) first order lifting-line theory (c/4 collocation point), and no lifting-surface correction;

b) second order lifting-line theory (3c/4 collocation point), and no lifting-surface correction;

c) first order lifting-line theory, with the lifting-surface theory correction.

For the loading at 97% R, the best core size is .025 R (37.5% chord) for case (a), or .015 R (22.5% chord) with either the 3c/4 collocation point or the lifting-surface correction. The correlation suggests that the actual core radius varies with azimuth, being larger for vortices created on the retreating side of the disk. The calculations also significantly overpredict the blade-vortex interactions for the inboard radial stations (particularly 75% R here). The core size is increased for collocation points on the inboard part of the blade in order to eliminate (but not explain) this problem. Note that the calculations of Yamauchi, Heffernan, and Gaubert (1988) used a model similar to (a); they concluded that the best core size was 0.035 R, considering inboard stations as well as the tip.

Figure 8-6 shows the loading calculated using these three wake models, with the best core radius for each. All three models give similar results, although the details of the calculated loading vary. Note that the lifting-surface theory correction is nearly equivalent to simply increasing the core radius by Δr_c = .01 R = .3 b (15% chord). With either second order lifting-line theory or the lifting-surface theory correction, the required core size of 22.5% chord is in the expected range for the physical viscous core radius.

Application of the lifting-surface theory correction is controlled by the parameter d_{ls}. The correction is calculated and applied for a vortex line segment if the distance between the collocation point and the center of the segment is less than d_{ls}R. Using the correction for all segments in the tip vortices doubles the time required to compute the wake influence

coefficients. For this case it was found that the calculated loads were unchanged for d_{ls} varying from 100. to 0.5, and were nearly the same for $d_{ls} = 0.2$; however, with $d_{ls} = 0.1$ the loads were often the same as without the correction. Hence it is concluded that it is possible to apply the lifting-surface correction with $d_{ls} = 0.5$, which increases the influence coefficient computation time by only 5%.

Figure 8-7 shows the effect of the core size used for inboard collocation points on the calculated loads. If the same tip vortex core size is used for all blade collocation points, then the blade-vortex interaction loads are significantly overpredicted at 75% R. While the existence of this effect has been known for a long time (Johnson, 1971a), the physical nature of the phenomenon remains speculative. Figure 8-7 shows that using a larger core size when the collocation points are on the inboard part of the blade will improve the correlation; no explanation of the physics is intended. More detailed measurements, including measurements of the wake geometry, are needed to explore this phenomenon.

Figure 8-8 compares the calculations (using the lifting-surface correction) with three revolutions of the unaveraged data. The unsteadiness and noise in the measured data do not change the basic conclusions of the correlation, but it is clear that fine details must be ignored. The data for 75% R suggest that the unsteadiness may be partially responsible for the decreased blade-vortex interaction peaks in the averaged data.

9. SWEPT TIP CALCULATIONS

The new wake model improves the capability to analyze rotors with swept tips, by introducing the second order lifting-line theory. No measured airloads data are available for rotors with swept tips. Calculations were performed to examine the effects of the features in the wake model. The rotor considered had the following properties and operating condition:

number of blades	4
solidity	.0748
C_T/σ	.10
α_{top}	-5 deg
advance ratio	.2

(similar to the S-76 main rotor). Three tip configurations were analyzed:

1) tapered planform, 30 deg sweep at 95%R;
2) rectangular planform, 30 deg sweep at 95%R;
3) rectangular planform, 45 deg sweep at 90%R.

In the tip region, the edges of the blade aerodynamic panels are at r/R = .88, .91, .935, .955, .97, .985, and 1. The only blade motion included was coning and first harmonic rigid flapping. The influence of a swept tip on the dynamics of a rotor blade, particularly the elastic torsion motion, is significant. That influence is suppressed here so that the influence of the wake model on the aerodynamic load can be assessed separately.

The analysis options that implement the near wake model allow four cases:

a) c/4 collocation point, straight lifting-line;

b) 3c/4 collocation point, straight lifting-line;

c) c/4 collocation point, swept lifting-line;

d) 3c/4 collocation point, swept lifting-line.

For a swept tip, model (a) is first order lifting-line theory and model (d) is second order lifting-line theory. The second order theory also has an influence in yawed flow, which will be given by model (b) as well as model (d).

Figure 9-1 shows the calculated loading at two stations on the tip, 92% and 98% R. Note that even for the tapered, 30 deg swept tip, model (c) has a significant effect on the calculated load. Model (c) however is not a consistent implementation of lifting-line theory, and should not be used. Comparing models (a) and (d), it is seen that second order lifting-line theory has a significant effect on the tip loading. A concern with discretized lifting-line models in yawed or swept flow is the

posibility of singular behavior of the loads, particularly near the kinks in the span axis. No such problems were encountered with the cases investigated.

The wake model has some influence on the calculated rotor induced power, as shown in the following table.

	ratio induced power to ideal induced power			
model =	(a)	(b)	(c)	(d)
tip 1	1.38	1.49	1.20	1.44
tip 2	1.38	1.49	1.19	1.45
tip 3	1.37	1.46	1.00	1.32

Again, model (c) is not appropriate.

The 3c/4 collocation point and the lifting-surface correction are alternative methods to improve the calculation of blade-vortex interaction loads. The results of the preceding chapters show that these two methods are indeed comparable. However, only second order lifting-line theory influences the swept tip loads; the lifting-surface theory correction has no role in the aerodynamics of the swept tip or yawed flow.

10. BOEING MODEL 360 SCALE ROTOR TEST

A scaled model of the Boeing model 360 main rotor was tested in the DNW wind tunnel (Dadone, Dawson, Boxwell, and Ekquist, 1987). The high twist and low aspect ratio of the blades should increase the effects of negative loading on the advancing tip (for a given blade loading C_T/σ, the bound circulation is proportional to the blade chord). Hence this is a good choice for application of the new wake model for high speed flight.

The preliminary test data, rotor properties, CAMRAD input parameters, and airfoil tables were obtained from the Aeroflightdynamics Directorate, U.S. Army Aviation Research and Technology Activity. The data provided were section lift at 88% and 95% R radial station (including plots of the individual pressures), and the torsional moment at 23% R. There were 6-8 pressure gages on the upper surface and 5-6 on the lower surface, at the following chordwise locations:

upper x/c = .06, .12, .18, .25, .35, .50*, .70, .85*
lower x/c = .03‡, .06, .28, .35, .50, .85*

(* not for 95% R)
(‡ at 89% and 94% R)

Airloads data averaged over 64 revolutions, and two revolutions of the torsional moment data were provided, with 1024 points per revolution.

The model 360 rotor has tapered planform, high twist blades with dynamics optimized for high speed flight. The principal characteristics of the rotor are as follows:

number of blades	4
radius	5.052 ft
solidity	.10725
chord, c/R	.0872 inboard 90% R, .0279 at tip
twist	-11.65 deg inboard 86% R, -17.28 deg outboard 86% R
airfoil	VR12 inboard 85% R, VR15 at tip

The blade had the pitch axis at 20.2% chord; the center of gravity and elastic axis at approximately 25% chord; and the aerodynamic center and tension center at approximately 27% chord. As the control system stiffness was unknown, the blade rigid pitch motion was not used and the pitch axis was ignored. The baseline analysis assumed that the center of gravity, tension center, elastic axis, and airfoil table reference axis were all at 25% chord (the airfoil tables account for the aerodynamic center shift from the airfoil table reference axis). The rotor had no lag damper.

The five operating conditions (identified by run number) considered are as follows. Run 195 was in the open test section, and the other runs were in the closed section.

Run	195	222	244	250	279
α_s	-5.60	-6.70	-7.95	-12.01	-10.23
C_T/σ	.0699	.0695	.0507	.0508	.0691
C_Q/σ	.00541	.00557	.00607	.00687	.01078
advance ratio	.356	.359	.398	.366	.456
M_{at}	.86	.83	.87	.93	.90
C_X/σ	-.0042	-.0041	-.0049	-.0051	-.0067
force angle	-3.43	-3.40	-5.54	-5.73	-5.50
rotor L/D	6.4	6.1	4.9	3.7	4.1

The propulsive force $-X/q$ is about 0.65 ft^2 for run 250, and about 0.55 ft^2 for the other runs. The "force angle" is the angle of the resultant rotor force from vertical, postive aft. The angle of the resultant force relative the shaft is thus 2.2 to 6.3 deg aft for these runs. It was reported that run 195 had a split tip-path-plane. Generally, the rotor was operated with the tip-path-plane normal to the shaft, but the rotor flapping was not measured. Non-zero flapping was observed for some runs. In particular, it was reported that $\beta_{1c} \cong 1.6$ deg for run 244.

The calculations trimmed the rotor thrust to the measured value, and the first-harmonic flapping relative the shaft to zero. The rotor shaft angle of attack was set to the measured value. (The calculated power matches the measured power better for fixed shaft angle than with the drag force trimmed to the measured value.) The blade motion considered was ten harmonics of the first six flap-lag bending modes (including the rigid flap and lag modes) and the first elastic torsion mode.

Figure 10-1 shows the influence of the far wake model on the calculated airloads at radial stations 80%, 88%, and 95% R for run 222 (advance ratio .36). The wake model has a significant effect on the tip loading. A single peak model using the maximum bound circulation has both the sign and strength of the vorticity wrong when the tip loading is negative. The dual peak model has a different inboard wake structure than the model using the outboard circulation peak; in addition, changes in the loading will feed into the tip vortex strength and increase the differences between these two models. Consequently the minimum loading and the azimuth at which it occurs varies greatly for the three models. Figure 10-2 examines the convergence of the dual-peak model, for which the wake structure depends on the radial station of the inboard peak. The rotor is first trimmed using uniform inflow; this solution provides a mean inflow and the location of inboard peaks, to be used in calculating the nonuniform inflow influence coefficients. Then the rotor is trimmed using nonuniform inflow (the first iteration). With the

resulting updated mean inflow and location of the inboard peaks, the influence coefficients are recalculated. The the rotor is again trimmed using nonuniform inflow (the second iteration). The wake structure for the dual-peak model is converged if the radial location of the inboard peak in the current circulation solution matches that used in the wake geometry to calculate the influence coefficients. Figure 10-2 shows that two iterations are required for such convergence, with some differences between the airloads from the two iterations. Figures 10-3 and 10-4 give the corresponding results for run 279 (advance ratio .46). The influence of the wake model is still significant, even with a tip-path-plane angle of attack of -10.2 deg.

Figures 10-5 to 10-7 show for runs 222 and 279 the influence on the airloads of the near wake model; rollup of the inboard trailed wake; and blade elastic motion. The effect of the near wake model (figure 10-5) is significant. This is the effect of second order lifting-line theory for this low aspect-ratio blade, and for the large yawed flow that the blade sees in high speed forward flight. The calculations used a tip vortex core size of 0.02 R (23% chord). Decreasing the core size to .01 R had no effect: close blade-vortex interaction is not a factor for these high speed cases. Similarly, rollup of the inboard trailed wake when the tip loading is negative had little effect in the loading (figure 10-6; an inboard core size of .03 R was used). Restricting the calculated blade motion to just 1/rev rigid flapping had some effect on the loads (figure 10-7). This effect is primarily produced by the large elastic torsion calculated for the blade, as shown in figure 10-8.

The measured and calculated airloads are compared for the five runs in figure 10-9. The behavior of the measured airloads, of the calculated airloads, and of the difference between the two is consistent. The calculated mean loads tend to be high. All the measured loads have a peak around 60 deg azimuth, while the calculated loads are decreasing in the first quadrant. Regarding the minimum loading at azimuths from 90 to 135 deg, the measurements have oscillations and are sometimes relatively flat; while the calculations are smoothly varying with a distinct minimum. For high advancing tip Mach number (runs 250 and 279), the measured loading is much more negative than the calculated loading for 95% R; and the differences between the measured and calculated loading are greater for 95% R than for 88% R.

The time histories of the blade pressures were examined to determine what is occuring in the measured lift. The features of interest are the constant or increasing lift for azimuths from 45 to 75 deg; the negative loading at azimuths 90 to 135 deg, with a flat or reversed minimum; and the oscillations at azimuths from 105 to 150 deg. Basically these effects are being produced by shocks, which cause jumps in the pressure as a function of ψ.

Upper surface shocks appear when the section Mach number reaches .72-.74, hence at ψ = 20 to 45 deg, depending on r and M_{at}. The shock moves aft as the Mach number increases with

azimuth. Thus there is a large negative pressure at the nose, with a sharp drop somewhere in the first 25% or 35% of the chord. The result is a positive lift, the effect of the shock countering the effect of the angle of attack decreasing with ψ. Lower surface shocks occur for ψ = 90 to 135 deg, the negative pressure ahead of the shock producing negative lift. The shock occurs on the first or second, or even third quarter of the chord, depending on M_{at}. For low M_{at}, the upper surface shock disappears at ψ around 100 deg, which helps produce a sharp drop in the lift. For high M_{at}, the upper surface shock disappears at ψ around 150 deg, producing oscillations in the lift.

The analysis being used sees the effects of transonic aerodynamics only through the airfoil tables. Figure 10-10 plots the airfoil table data for this case (the airfoil at 88% and 95% R is the VR15), which exhibit the expected behavior. What the measured lift implies is c_ℓ roughly constant with decreasing angle of attack but increasing Mach number, after shocks first appear around M = .73. It is possible that the measured lift reflects three-dimensional transonic effects, requiring a CFD analysis to capture.

While the pressure measurements are accurate, it is questionable for these runs whether there is sufficient chordwise resolution to obtain the section lift. The shocks tend to remain between two pressure gages for many degrees of azimuth. Without information about the movement of the shock between gages, the chordwise integration produces nearly constant lift coefficient, which is responsible for the flat c_ℓ in the first quadrant (from upper surface shocks) and near the negative minimum (from lower surface shocks). When a shock passes a gage, it produces a rapid change in the pressure there, which then appears in the integrated lift also. It is concluded that the chordwise resolution of the measured pressures on the forward 25% to 50% of the airfoil is not sufficient to obtain an accurate lift coefficient.

Figure 10-11 compares the measured and calculated torsion moment at 23% radius (the analysis and data correspond to the airloads comparison in figure 10-9). The operating condition does not influence much the shape of either the calculated or measured moment, and even the amplitudes are similar (except for the highest speed, run 279). The measured and calculated results are quite different however. Note that a moment coefficient of $\Delta C_{mt}/\sigma$ = .0002 corresponds to a blade elastic twist deflection at the tip of about 1 deg. Two observations can be made: the oscillations of the measured moment on the retreating side are at around 4.6/rev, while the calculated torsion frequency is 6.0/rev; and the measured behavior looks like a blade approaching pitch-flap flutter. The calculations were made assuming that there was no flexibility in the control system; a control system soft enough to lower the fundamental torsion/pitch mode frequency below 5/rev would not be unreasonable. To investigate the influence of the torsion frequency, the blade GJ was reduced to give a calculated elastic torsion frequency of 4.8/rev (still

with no control system flexibility). In addition, the blade center of gravity was shifted aft from 25% chord to 27% chord in the analysis. Figure 10-12 compares the original and modified calculations with the measured torsion moment for run 222, and shows the influence of the modified input parameters on the calculated lift. The input parameter changes do improve the correlation with the torsion moment. The increased oscillation of the calculated torsion moment is also evident in the calculated blade airloads. To proceed further it would be necessary to obtain a better description of the rotor physical proerties.

11. H-34 ROTOR WIND TUNNEL TEST

An H-34 main rotor was tested in the 40- by 80-Foot Wind Tunnel (Rabbott, Lizak, and Paglino; 1966a, 1966b). This test covered a large range of operating conditions (advance ratios from .29 to .45, tip-path-plane angles from -5 to 5 deg), and has been the focus for much work on high speed rotor airloads (Hooper, 1984).

The section lift was measured at nine radial stations: r/R = .25, .40, .55, .75, .85, .90, .95, .97, .99. For radial stations from 75% to 95%, differential pressure measurements were made at 7 chordwise locations:

$$x/c = .017,\ .090,\ .168,\ .233,\ .335,\ .625,\ .915$$

except for 85% radius, which used 4 additional gages (11 total) at:

$$x/c = .040,\ .130,\ .500,\ .769$$

The other radial stations had only 3-5 gages. The report gives 10 harmonics of the integrated section lift at these radial stations. For presentation here, a measurement system phase lag of $\Delta\psi = 5.3$ deg was accounted for.

The properties of the H-34 rotor blade are given by Rabbott, Lizak, and Paglino (1966a). The principal characteristics of the rotor are as follows:

number of blades	4
radius	28 ft
solidity	.0622
chord, c/R	.0488
twist	-8 deg
airfoil	NACA 0012

The operating conditions for shaft angle of attack $\alpha_s = 0$ are as follows:

advance ratio	.284	.394	.450
M_{at}	.73	.79	.83
C_L/σ	.0570	.0594	.0497
C_X/σ	.00022	.00169	.00289
β_{1c}	.5	-.5	-1.0
β_{1s}	-2.8	-3.6	-3.7

and for $\alpha_s = -5$ deg:

advance ratio	.288	.396	.449
M_{at}	.73	.79	.83
C_L/σ	.0573	.0596	.0484
C_X/σ	-.00529	-.00443	-.00172
β_{1c}	.7	1.0	-.2
β_{1s}	-3.5	-4.4	-4.4

The calculations trimmed the rotor thrust, and the longitudinal and lateral flapping to the measured values. The rotor shaft angle of attack was set to the measured value. With this trim method, the calculated rotor drag force and power were close to the measured data. The blade motion considered was ten harmonics of the first seven flap-lag bending modes (including the rigid flap and lag modes) and the first elastic torsion mode. Rigid wake geometry with a tip vortex core size of .03 R was used.

Figure 11-1 shows the influence of the far wake model on the calculated airloads at radial stations 75%, 85%, and 95% R for μ = .39 and α_s = 0. The wake model has a significant effect on the loading. The dual peak model and the single peak model using the outboard circulation peak give similar results, implying that the inboard wake structure is not very important. The wake model also influences the calculated induced power:

ratio induced power to ideal induced power	μ = .29	.39	.45
dual-peak model	1.64	2.41	2.36
single-peak, Γ_0	1.65	2.18	2.29
single-peak, Γ_{max}	1.79	2.42	3.17
dual-peak, 1st iter	1.44	2.19	2.33

Figure 11-2 examines the convergence of the dual-peak model, for which the wake structure depends on the radial station of the inboard peak. The wake structure for the dual-peak model is converged if the radial location of the inboard peak in the current circulation solution matches that used in the wake geometry to calculate the influence coefficients. Figure 11-2 shows that two iterations are required for such convergence, with some differences between the airloads from the two iterations.

Figures 11-3 and 11-4 show the influence on the airloads of the near wake model; blade elastic motion; tip vortex core size; and rollup of the inboard trailed wake. Each of these has some effect on the airloads. The near wake model (c/4 or 3c/4 collocation point) influences the lifting-line calculation of the loads in yawed flow. The rigid blade analysis only used first harmonic rigid flap motion. Decreasing the tip vortex core size had only a small effect, but rollup of the inboard trailed wake changed the loads significantly (figure 11-4). For the latter case, a core size of .05 was used for the inboard trailed wake when the tip loading was negative. These features also influenced the calculated induced power (for α_s = 0):

ratio induced power to ideal induced power	μ = .29	.39	.45
baseline	1.64	2.41	2.36
c/4 coll point	1.52	1.96	2.24
smaller core size	1.64	2.23	2.37
inboard rolled up	0.70	2.34	2.45

Note that the induced power was less than ideal for μ = .29 and the inboard trailed wake rolled up; that would not be an appropriate model.

Calculations were also performed using a free wake geometry; trimming the rotor drag force to the measured value; and with a dynamic stall model. Little change in the calculated airloads was found.

The measured and calculated airloads are compared in figure 11-5 for μ = .39 and α_s = 0. The dual-peak wake model is needed for the negative loading at 95% R (see figure 11-1). The measured and calculated airloads are compared in figure 11-6 for μ = .39 and α_s = -5 deg. For the this case, with a tip-path-plane angle of attack of -6 deg, the rigid wake geometry keeps the tip vortices well below the blades; the free wake geometry calculation give the same result. Figure 11-6 also shows the calculated airloads with the prescribed wake geometry adjusted to leave the wake in the tip-path-plane, in order to maximize the influence of the wake. Note that the measured time histories are constructed from only 10 harmonics, so the high frequency oscillations observed in figures 11-5 and 11-6 do not fully reflect the actual events. Figure 11-7 compares the measured and calculated airloads (c_{ℓ}) for all six cases considered here.

The correlation between calculated and measured airloads is not very good. The following factors may be involved.

a) The wake geometry used by the calculations may be incorrect. Figure 11-6 suggests that the wake might be closer to the rotor disk. The free wake geometry method being used has not been modified to include the dual-peak model. Hence while it is using the correct tip vortex sign and strength, it does not have the correct inboard wake model; i.e. the wake geometry calculation is based on a single peak model, using the outboard peak value at best. With a dual peak model in the wake geometry calculation, the increased strength of the inboard (positive) trailed wake would tend to push the tip vortex closer to the rotor disk. A less likely possibility is that the proximity of the wind tunnel walls affects the wake geometry.

b) The wake may not be a major influence. Figure 11-8 shows the influence of shaft angle (hence tip-path-plane angle of attack) on the measured airloads. The zero shaft angle data is expected to show much more wake influence than the -5 deg (forward tilt) data. Differences between the two cases could be attributed to wake effects. In fact the measured airloads for the two shaft

angles are very similar.

c) The chordwise resolution of the pressure measurements may not be sufficient for an accurate section lift with shocks on the blade. Generally the measured lift in the first quadrant is higher than the calculated lift. Some of the cases (e.g. figure 11-5) have nearly constant lift coefficient on the tip in the first quadrant, similar to the behavior observed on the model 360 rotor (chapter 10). With an NACA 0012 airfoil at these speeds, there are certainly shocks on the blade, although they are difficult to discern in differential pressure measurements.

d) The pressure measurements may be incorrect. The chordwise pressure distributions exhibit some unusual behavior. Examples are given in figure 11-9. The presence of shocks might produce some of this behavior, but systematic errors are also possible.

e) The test was conducted with a split tip-path-plane (Rabbott, Lizak, and Paglino, 1966b). A rotor control system modification produced kinematic coupling such that two adjacent blades (the instrumented blade and the blade proceding it) had different cyclic pitch than the other two. Hence there was a split tip-path-plane when cyclic pitch was applied, typically about 1 deg difference in the flapping. The longitudinal cyclic pitch used increased with speed and with forward shaft tilt. The unusual aerodynamic environment of a split tip-path-plane was not included in the analysis. Moreover, the control system might have introduced higher harmonics of control, in addition to the differences in 1/rev pitch.

12. AH-1G HEICOPTER FLIGHT TEST

An AH-1G helicopter was tested in flight with three blade sets having different airfoils (Morris, 1978). The three airfoils had the following properties:

	NLR-1T	10-64C	RC-SC2
M_{dd} at c_ℓ=0	.84	.83	.83
$c_{\ell max}$ at M=.4	1.1	<1.0	1.1
c_m at c_ℓ=0, low M	-.01 to -.02	-.015 to -.020	-.02
thickness ratio	.087	.10	.10

It was found that the airfoil used had an effect on the measured pitch moment coefficients and oscillatory pitch link loads (the latter were high enough with the RC-SC2 to limit the flight speed). The airfoil used had little effect on the measured power, mean pitch link load, lift coefficients, and torsion moment. The flight tests were conducted for advance ratios from 0.12 to 0.37; negative loading on the advancing tip was measured for advance ratios of 0.33 and above.

The data were reported by Morris, et al. (1979-1982). The section lift was measured at a single ratial station, 90% R. There were 7-8 pressure gages on the upper surface and 6 gages on the lower surface:

upper x/c = .02, .10, .20, .35, .50, .70, .80, .90
lower x/c = .02, .10, .20, .50, .70, .90

The 35% chord upper surface gage was inoperable for the NLR-1T airfoil. The 70% chord lower surface gage was inoperable for the RC-SC2 airfoil, and replaced by interpolated data. Time histories of the pressures, lift coefficient, and moment coefficient are given with an azimuthal resolution of 2 deg.

The properties of the modified AH-1G rotor blades tested are given by Morris, Tomaine, and Stevens (1979, 1980a, 1980b). The principal characteristics of the teetering rotor are as follows:

number of blades	2
radius	22 ft
solidity	.0651
chord, c/R	.1023
twist	-10 deg

The blade torsion frequency was 15.5 Hz (2.86/rev) with the NLR-1T airfoil, and 16.7 Hz (3.13/rev) with the other two sections. The RC-SC2 blade needed counterweights on the pitch horns, to counter larger mean torsion moments in hover; oscillatory pitch link loads limited the maximum advance ratio to 0.35 with this section.

One case, at the highest speed tested, is considered here for each of the three blades. The operating conditions are as follows.

	NLR-1T	10-64C	RC-SC2
flight and run	63-11	81-13	94-11
advance ratio	.370	.371	.345
M_{at}	.96	.91	.89
C_T/σ	.0677	.0840	.0808
α_s	-6.3	-5.5	-6.1
β_{1c}	2.4	1.1	1.3
β_{1s}	1.1	.9	1.1
C_Q/σ	.00705	.00739	.00657

Note that the measured tip-path-plane angles imply an aircraft drag area of 14-17 ft^2.

The calculations trimmed the rotor thrust, and the longitudinal and lateral flapping to the measured values. The rotor shaft angle of attack was set to the measured value. Because of the lack of two-dimensional data, particularly at the proper Reynolds numbers, no airfoil tables were available for these three sections. The calculations were performed using the table for the VR15 airfoil of the Boeing model 360 rotor (M_{dd} = 0.835, $c_{\ell max}$ = 1.2), with drag and moment coefficient increments. The blade motion considered was ten harmonics of the teeter mode, the first six flap-lag bending modes, and the first elastic torsion mode. Rigid wake geometry with a tip vortex core size of 0.02 R was used. Using free wake geometry or dynamic stall had little effect on the calculated tip airloads.

Figure 12-1 compares the measured and calculated airloads for the three cases. The correlation was improved by adding a nose-down pitch moment increment to the airfoil table data. A drag increment was also used, in order to match the measured rotor power:

	NLR-1T	10-64C	RC-SC2
Δc_m	-.04	-.03	-.05
Δc_d	-.0030	-.0030	-.0030

The measured lift coefficients are similar in character to the other high speed test data examined in this investigation. Note the roughly constant lift in the first quadrant. The oscillations around ψ = 120 deg are caused by shocks moving past individual pressure gages (particularly lower surface gages at 20% and 50% chord).

Figure 12-2 shows the influence of the far wake model on the calculated airloads. The wake model has some effect even for the large tip-path-plane angles of these cases. The inboard wake appears to be as important as the tip vortices. The wake influence on the first-quadrant airloads can be increased by

moving the prescribed geometry closer to the rotor disk. Figure 12-3 shows the influence of the near wake model (c/4 or 3c/4 collocation point). Figure 12-4 shows the influence of the blade motion, which is substantial. The blade is relatively soft in torsion (frequency about 3/rev), so the calculated elastic torsion motion is very large. Figure 12-5 shows the blade elastic deflection at the tip, which has the following composition:

mean	-4 to -5 deg
1/rev amplitude	2 to 3 deg
2/rev amplitude	1.3 deg
3/rev amplitude	0.4 deg

This torsion deflection is produced by the aerodynamic pitching moments on the blade, so the lack of airfoil tables is a serious problem. Figure 12-6 shows the measured and calcuated pitch moment coefficients. The measured c_m shows more higher harmonic content than the calculated data, implying that a uniform c_m increment is not sufficient. It is also likely however that the chordwise resolution of the pressure data is not sufficient for an accurate measurement of c_m.

Typical measured chordwise pressure distributions are shown in figure 12-7. The absolute pressures in particular show the presence of shocks, on the aft part of the chord for these sections and high M_{at}.

13. H-34 HELICOPTER FLIGHT TEST

An H-34 helicopter was tested in flight (Scheiman and Ludi, 1963; Scheiman, 1964). This test has long been a standard for rotor airloads data, but did not include the high speed conditions that are of interest in the present investigation. For completeness, and in order to re-examine the quality of the measured data, the airloads were calculated for low speed and moderate speed cases from this data.

The section lift was measured at seven radial stations: r/R = .25, .40, .55, .75, .85, .90, .95 (the wind tunnel test added radial stations .97 and .99). For radial stations from 75% to 95%, differential pressure measurements were made at 7 chordwise locations; except for 85% radius, which used 11 gages. The other radial stations had only 5 gages. The data from oscillograph records was averaged over three revolutions. Time histories of the lift are given with an azimuthal resolution of 15 deg. For presentation here, a measurement system phase lag of $\Delta\psi$ = 4.5 deg was accounted for, as well as a 6 deg shift of the zero azimuth position for some cases.

The properties of the H-34 rotor blade are given by Scheiman (1964), including data on the control system flexibility, pitch horn geometry, and lag damper characteristics. The principal characteristics of the rotor are as follows:

number of blades	4
radius	28 ft
solidity	.0622
chord, c/R	.0488
twist	-8 deg
airfoil	NACA 0012

The blade had a trailing edge tab, deflected 4 deg upward, between 85% and 90% R.

The low speed case considered is condition III of Scheiman and Ludi (1963); the high speed case is flight 19 of Scheiman (1964). The operating conditions are as follows.

advance ratio	.178	.287
M_{at}	.70	.78
C_T/σ	.0817	.0907
α_s	-2.5	-6.8
β_{1c}	.55	-.97
β_{1s}	-.58	-.61

The calculations trimmed the rotor thrust (obtained by integrating the airloads data), and the longitudinal and lateral flapping to the measured values. The rotor shaft angle of attack was set to the measured value. The blade motion considered was ten harmonics of the first seven flap-lag bending modes

(including the rigid flap and lag modes), the rigid pitch mode, and the first elastic torsion mode. To account for the trim tab, a pitch moment increment of Δc_m = .03 was used outboard of 75% R. The blade was relatively stiff in torsion: the calculated frequencies were 15.6/rev for the rigid pitch motion (control system flexibility), and 7.1/rev for the elastic torsion mode. Three revolutions of the wake were used, with a tip vortex core size of .01 R (20.5% chord). For collocation points on the inboard part of the blade, the core size was increased to .100 R (with a transition region from 72% to 86.5% R).

Figure 13-1 compares the measured and calculated airloads at radial stations 75%, 85%, 90%, and 95% R for μ = .18, showing the influence of nonuniform inflow and the free wake geometry. Figure 13-2 shows the corresponding calculated wake geometry. These calculations used the lifting-surface theory correction, with the quarter-chord collocation point. A larger core size on the retreating side and a smaller core size on the advancing side would improve the correlation.

Figure 13-3 shows the influence of the near wake model, i.e. the three methods for treating blade-vortex interaction: the lifting-surface correction, 3c/4 collocation point, or a larger core size. All three give generally similar results, but with differing details. With the lifting-surface correction or the 3c/4 collocation point, a core size of about 20% chord is good, just as for the SA349/2 calculation. The lifting-surface correction is roughly equivalent to increasing the core size by Δr_c = .007 R = .3 b (15% chord, as for the SA349/2). Figure 13-4 shows the effect of the core size for inboard collocation points on the calculated loads. Suppressing the blade-vortex interaction inboard is essential for good correlation. Figure 13-5 shows the influence of blade elastic motion, by considering calculations using only first harmonic rigid flap motion.

Figure 13-6 compares the measured and calculated airloads at radial stations 75%, 85%, 90%, and 95% R for μ = .29, showing the influence of nonuniform inflow. At high speed there is less blade-vortex interaction apparent (so free wake geometry has little effect), but nonuniform inflow is still required to predict the loads. Note that the "uniform inflow" inflow results shown include the effect of a linear variation of the inflow across the rotor disk. These calculations used the lifting-surface theory correction, with the quarter-chord collocation point. Figure 13-7 shows the influence of the near wake model. Since there is little blade-vortex interaction, the differences shown are produced by the treatment of yawed flow using first order (c/4 collocation point) and second order (3c/4 collocation point) lifting-line theory. Figure 13-8 shows the effect of blade elastic motion on the calculated airloads, which is greater for this moderate speed case than for the low speed case.

14. UH-60A ROTOR CALCULATIONS

The UH-60A rotor has a swept tip and a large (and unusual) twist, so is an interesting case for application of the new wake model. No test data is available for this rotor, although both small scale wind tunnel and full scale flight tests are planned. CAMRAD input parameters for the UH-60A helicopter are given by Shanley (1986), and airfoil decks were provided by the Aeroflightdynamics Directorate, U.S. Army Aviation Research and Technology Activity. The principal characteristics of the rotor are as follows:

number of blades	4
radius	26.83 ft
solidity	.0821
chord, c/R	.0645
airfoil	SC1095 for 0 to 30% R, SC1095R8 for 30% to 87.4% R, SC1095 for 87.4% R to tip
tip sweep	20 deg at 92.9% R

Figure 14-1 shows the blade built-in twist distribution. To ensure that the analysis has the pitch bearing outboard of the flap and lag hinges, r_{FA} = .047 was used. Noncirculatory blade loads were included, as they are a principal source of pitch damping. The number of collocation functions for the blade modes were increased to 12 for bending and 5 for torsion. For a free flight trim case, other changes to the input parameters would also be required. Whether the input parameters represent a good physical description of the aircraft was not assessed.

Two operating conditions were considered, low speed and high speed cases at typical thrust and propulsive force:

	V = 60 knots	160 knots
advance ratio	.140	.373
M_{at}	.74	.89
C_T/σ	.075	.075
fuselage drag, D/q (ft^2)	24.	24.

The calculations trimmed the rotor lift and propulsive forces (wind axes) to the required values, and the longitudinal and lateral flapping to zero, by adjusting the collective and cyclic pitch and the rotor shaft angle.

The blade motion considered for the baseline cases was ten harmonics of the first six flap-lag bending modes (including rigid flap and lag motion), the rigid pitch motion, and the first two elastic torsion modes. Two revolutions of rigid wake geometry were used for the high speed case, and three revolutions of free wake geometry for the low speed case, with a tip vortex core size of .015 R (23% chord). The baseline calculations use the dual-peak wake model, 3c/4 collocation point, and no lifting-

surface correction.

Figure 14-2 shows the influence of nonuniform inflow and wake geometry on the calculated airloads at radial stations 75%, 86.5%, and 95% R, for V = 60 knots. As expected, the free wake geometry increases the blade-vortex interaction loads. Because of the large twist, the blade-vortex interaction produces negative loading on the tip at ψ = 75 deg. Figure 14-3 shows the radial bound circulation distribution around the disk, for the free wake geometry case. The influence of both blade-vortex interaction and the reflexed twist is evident at the blade tip. Note that on the advancing side the peak circulation occurs around 40% R, and that the tip loading changes rapidly from positive to negative to positive around ψ = 75 deg. Such behavior probably does not produce a strongly rolled-up tip vortex.

Figure 14-4 shows the influence of the far wake model, i.e. for this case whether the tip vortex strength from ψ = 75 deg is positive (single-peak, maximum bound circulation) or negative (the other two cases). The effect shown might be measurable, although a larger tip vortex core could eliminate the negative loading. Figure 14-5 shows the influence of elastic blade motion on the calculated load; the effects are comparable to those of the wake model.

Figure 14-6 shows the influence of the swept tip aerodynamic model on the airloads at 91% and 95% R (the sweep occurs at 92.9% R). Only the first harmonic rigid flap motion is considered for these calculations, in order to examine just the aerodynamic effects without changes associated with the torsion dynamics. There is little difference between the swept and straight lifting-line models. The c/4 collocations point increases the blade-vortex interaction loads, because the tip vortex core size was not changed (chapters 8 and 13 showed that the core size should be increased by 15% chord for this option). In general, 20 deg sweep is not large enough to produce significant aerodynamic effects associated with the wake model.

Figures 14-7 to 14-11 show the corresponding results for the high speed case, V = 160 knots. Free wake geometry has little effect now, but nonuniform inflow is still required (figure 14-7). The radial circulation distribution shows the effect of reverse flow inboard, with little blade-vortex interaction (figure 14-8). The effect of the reflexed twist at the tip is evident. The peak circulation occurs around 35% R on the advancing side (a result of the large twist), again suggesting that the tip vortex rollup would be relatively weak. The influences of the far wake model (figure 14-9) and blade elastic motion (figure 14-10) are comparable. Different wake rollup would affect the results in figure 14-9. The effect of the swept tip aerodynamic model is still small for this high speed case (figure 14-11).

15. HARMONIC CONTENT OF AIRLOADS DATA

An important issue in planning and executing a rotor airloads test is the question of the azimuthal resolution needed for a complete, or at least sufficient, representation of the aerodynamics. The quantity of interest here is the section lift or circulation, which determines the rotor wake characteristics. Moreover, most present rotary wing analyses use lifting-line theory for the blade aerodynamics and a nonlinear beam theory for the blade structural dynamics, hence need the section lift for correlation. The harmonic content of the predictions from such analyses suggest that 10 or 12 harmonics is sufficient.

A different approach is to examine the harmonic content of the measured airloads, to see what actually occurs on rotors. Several of the existing airloads data sets have azimuth resolutions of 2 deg or less, and so are appropriate examples. The time histories of this data will be compared with representations consisting of 10 or 15 harmonics.

Figure 15-1 shows the averaged airloads data measured on the SA349/2 helicopter, and figure 15-2 shows the unaveraged data. It appears that 15 or more harmonics would be required in this case, but figure 15-3 shows that conclusion to be inappropriate. The unaveraged data exhibits significant unsteadiness and high frequency noise.

Figure 15-4 shows the airloads data measured on the Boeing model 360 scale rotor. In order to capture the oscillations around 120 deg azimuth, 15 or more harmonics are needed. However, these measured oscillations in lift are produced by shocks moving past individual pressure gages. The measured oscillations would probably be smoother with gages at more chordwise locations. Figure 15-5 shows a similar result for the airloads data measured on the AH-1G helicopter.

Too few harmonics can produce undesirable effects however. Figure 15-6 shows the airloads data measured in flight on the H-34 helicopter. While 10 harmonics clearly contain all the information of the original data (with a 15 deg azimuthal resolution), the Fourier analysis produces high frequency oscillations that are misleading.

The above results suggest that 15 or 20 harmonics are sufficient to describe the aerodynamic phenomenon of rotor airloads. Several factors require that more data be taken:

a) Unanticipated phenomena may be encountered that produce faster changes in the blade section lift.

b) Oscillations produced by the Fourier analysis rather than by the aerodynamics are undesirable.

c) A high sample rate allows analog filters to be used

simply for noise attenuation rather than for antialiasing purposes.

It is concluded that a sample rate of 64 or 72 per revolution, with a filter corner frequency of 30-40/rev, is sufficient for airloads data (5-6 deg resolution of the filtered data).

Other considerations are as important as the azimuthal resolution:

a) Unsteadiness and high frequency noise must be minimized.

b) The chordwise resolution must be sufficient to accurately obtain the section lift and moment, particularly with shocks or blade-vortex interaction.

c) The radial resolution must be sufficient to define the wake structure and measure the total rotor lift.

16. REVIEW OF MEASURED ROTOR AIRLOADS DATA

The present investigation involved correlation between measured and predicted rotor airloads data, using many of the published data sets. In all cases this effort was made more difficult by the lack of some information or data. This chapter summarizes the problems and limitations observed in these data sets. For completeness, tests that were not part of the current correlation work are also included in the summary. This summary will be the basis for recommendations regarding future rotor airloads tests.

A general consequence of any airloads correlation work is questions about wake geometry and rollup. None of the published airloads data sets includes information on the rotor wake structure.

The following identifies the problems and limitations observed in the airloads data sets.

A) SA349/2 helicopter (Heffernan and Gaubert, 1986)

1) only three radial stations
2) unsteadiness and high frequency noise
3) shaft angle of attack and flapping measurements not accurate
4) control system stiffness not measured

B) Boeing model 360 scale rotor (Dadone, Dawson, Boxwell, and Ekquist, 1987)

1) insufficient chordwise resolution of pressure measurements to obtain section lift when shocks are present
2) concern about structural dynamic properties
3) control system stiffness not measured

C) H-34 wind tunnel test (Rabbott, Lizak, and Paglino, 1966a)

1) only 10 harmonics
2) concern about chordwise pressure distribution
3) split tip-path-plane during test
4) control system stiffness not measured

D) AH-1G helicopter (Morris, 1978)

1) only one radial station
2) no airfoil tables
3) control system stiffness not measured

E) H-34 flight test (Scheiman, 1964)

1) azimuthal resolution only 15 deg
2) rotor torque not measured

F) NACA model wind tunnel test (Rabbott and Churchill, 1956)

1) propulsive force not accurate
2) no structural dynamic properties given

G) HU-1A helicopter (Burpo and Lynn, 1962)

1) azimuthal resolution at best 15 deg; 30 deg for most of the data
2) rotor torque not measured

H) CH-47 helicopter (Pruyn, et al, 1967)

1) no tabulated data

I) XH-51A compound helicopter (Bartsch and Sweers, 1968)

1) propulsive force not measured
2) shaft angle of attack measurement not accurate
3) problem with zeros of pressure measurements
4) instrumented blade operating at lower lift than other blades
5) no structural dynamic properties given

J) NH-3A compound helicopter (Fenaughty and Beno, 1970)

1) shaft angle of attack measurement not accurate (propulsive force not accurate)
2) only 5 chordwise pressure measurements
3) concern about chordwise pressure distribution
4) no structural dynamic properties given

K) CH-53A helicopter (Beno, 1970)

1) similar to NH-3A
2) no microfiche of tabulated data available

17. CONCLUSIONS AND RECOMMENDATIONS

17.1 Conclusions

An improved rotor wake model for helicopter rotors has been developed. The emphasis was on wake effects (including blade-vortex interaction) in high speed flight, considering in particular cases with negative loading on the advancing tip.

Two alternative approaches for blade-vortex interaction were considered: second order lifting-line theory, and a lifting-surface theory correction. Good correlation with measured rotor data was shown for cases involving significant blade-vortex interaction. For full scale data, the vortex core size required for the correlation was about 20% chord. This is in the range of measured core sizes for rotors, but is probably still too large. The core size must account for not only the physical viscous core radius, but also all those aspects of the blade-vortex interaction that are not otherwise included in the analysis. Factors that would cause the core size in the analysis to be too large include:

a) Discretization of the wake: generally the radial and azimuthal resolution in the discretized wake are too large, producing an overprediction of vortex-induced loads.

b) Partial tip vortex rollup: contrary to the assumptions of the analysis, the tip vortex may not be completely rolled up by the time it reaches the following blade; i.e. the strength may be less than the value of the peak bound circulation.

c) Unsteadiness and noise in the data: particularly if the azimuth angle of the blade-vortex interactions changes from rev to rev, the averaging process will reduce the measured peak loads.

Factors that would cause the core size in the analysis to be too small include:

a) Discretization of calculated lift: the blade section loading is calculated here with an azimuthal resolution of 15 deg, which would generally have the effect of reducing the apparent peak loads.

The common approach of using a larger vortex core radius to account for lifting-surface effects was quantified: the core radius should be increased by about 15% chord if neither second order lifting-line theory nor the lifting-surface correction is used.

The capability was developed to model the wake created by dual-peak span loading (inboard and outboard circulation peaks,

of opposite sign), optionally with multiple rollup of the trailed vorticity. The calculated airloads showed a significant effect of this wake model. By using the outboard circulation peak rather than the maximum bound circulation, the tip vortex has the correct sign and strength. While that is a major factor in calculating the advancing tip loads, the inboard wake is also influential. Hence the dual-peak model is best for these cases. The wake structure for the dual-peak model depends on the radial location of the inboard peak. Two iterations between the influence coefficient calculation and the trim solution were required for convergence of the inboard peak location. In some cases, the calculated loads were affected by the extent of the rollup of the inboard (positive) trailed wake.

Generally the correlation with measured airloads at high speed was not good however. The measured data showed some consistent behavior:

a) The measured loading in the first quadrant is higher than the calculated loading. Often there is a peak in the measured loading, or at least relatively constant lift coefficient, while the calculated loads tend to decrease with azimuth.

b) The model 360 data often show a flat or even reversed lift behavior in the middle of the negative loading region on the advancing tip. The calculated loading shows a distinct minimum.

c) The measured loading in the second quadrant has sharp changes and oscillations, while the calculated loading is smoothly varying.

This behavior of the measured loading is generally associated with shocks occurring on the blade. It appears likely that the chordwise resolution of the measured pressures is not sufficient to obtain an accurate lift coefficient in the presence of shocks. However, if the chordwise resolution is sufficient, then errors in the analytical wake geometry and rollup are possible causes of the discrepancies. It is clear in any case that the effects of compressibility and blade dynamics are as important as wake effects for high speed flight.

The dual-peak wake model is relevant to flight conditions besides high speed helicopter operation. With a large enough twist, blade-vortex interaction at low speed can result in small areas of negative loading on the blade. Also, a tiltrotor in airplane mode cruise can have negative loading on the inboard part of the blade and positive loading on the tip; and in helicopter mode flight it will have negative loading on the advancing tip even at low speed.

The second order lifting-line theory also improves the modeling of yawed flow, swept tips, and low aspect-ratio blades. The influence of the theory in yawed flow is significant for

rotors at high advance ratio. While the analysis is apparently functioning properly, test data are not available to verify the treatment of yawed flow and swept tips.

17.2 Recommendations: Lift Measurement at High Mach Number

It has been postulated here that the existing airloads data at high speed are inaccurate because the chordwise resolution of the pressure measurements is not sufficient to obtain the section lift in the presence of shocks. It is recommended that an investigation be conducted with the following objectives:

a) Establish whether or not the existing section lift data are accurate.

b) Establish requirements for measurements in future tests.

The approach would be to calculate the airfoil pressure distribution using existing two-dimensional finite-difference codes. Then the calculated pressures at a set of chordwise positions gives an equivalent experimental measurement, which can be integrated to obtain a lift coefficient. Comparing the calculated and equivalent-experimental lift coefficients gives a quantitative assessment of the accuracy of the process.

The airfoils, operating conditions, and chordwise stations used in previous and proposed rotor airloads tests should be considered. It would also be useful to examine the calculated differential pressure distributions, to resolve some of the concerns about existing measured data.

If there proves to be a problem with the chordwise resolution in previous tests, it would be possible to use the above approach to define a tranform to be applied to the calculated section lift. Then meaningful comparisons of experiment and theory could be made.

17.3 Recommendations: Wake Geometry and Rollup

Discrepancies between analysis and test data suggest that the distorted wake geometry, tip vortex formation, and wake rollup must be investigated further. This conclusion is a universal conclusion of any airloads correlation work. Information is needed about the self-induced distortion of the entire wake; the tip vortex core sizes and strength; and the structure of the inboard wake.

Questions and observations from the present investigation include the following. The correlation for blade-vortex interaction cases suggests that the core size is larger for vortices formed on the retreating side than for those formed on the advancing side. Something is happening on the inboard part of the blade to reduce measured the vortex-induced loads. The

wake geometry may be incorrect for the high speed airloads calculations, particularly since the free wake geometry method was not revised to include a dual-peak model (with a dual-peak model the inboard trailed wake strength would be increased, tending to push the tip vortex upward). The distorted geometry of the inboard wake is not being calculated at all. Examination of the spanwise circulation distributions for both low and high speed, particularly with highly twisted blades, suggests that the tip vortices may not be strongly rolled up on the advancing side. With a dual-peak circulation distribution however, multiple rollup of the trailed wake is a possibility.

Both theoretical and experimental investigations are recommended. The phenomena involved in rotor wakes will remain speculative until measurements are available for at least:

a) the positions of the tip vortices;

b) the structure and extent of the wake rollup.

Wake measurements should be made simultaneously with airloads measurements, and at full scale Reynolds numbers. The theoretical work need not wait for the test data however, since there are clear deficiencies in the existing wake geometry and rollup calculations.

17.4 Recommendations: Airloads Measurements and Correlation

The rotor airloads data sets examined in the present investigation will continue to be useful:

a) Boeing model 360 scale rotor test. A better definition of the rotor structural dynamic properties is needed.

b) SA349/2 helicopter flight test. The unsteadiness and noise in the data limits correlation to the major events.

c) H-34 rotor wind tunnel test. The fact that the test was run with a split tip-path-plane makes it difficult to draw conclusions from poor correlation, and raises questions about good correlation.

d) H-34 helicopter flight test. The large azimuthal resolution limits correlation to the major events.

e) AH-1G helicopter flight test. Airfoil tables are needed for the three sections tested, and might be obtained using two-dimensional finite-difference computations.

The data sets include many flight conditions, and structural load measurements. All the information available should be used (by the research community, if not in any single investigation).

Further correlations are recommended. First however it must be established whether the lift coefficient data at high Mach numbers is accurate. Improvements in the wake geometry and rollup calculations are a logical next step.

There is a clear need for further rotor airloads measurements, particularly considering the deficiencies observed in the available data sets. For high speed flight conditions, measurements must be made with sufficient chordwise resolution of the pressure gages. It is also recommended that high advance-ratio wind tunnel tests be conducted at both design tip speeds and at Mach numbers low enough to avoid shocks. By this means information will be available to separate the effects of the rotor wake, blade dynamics, and transonic flow at high speed.

17.5 Recommendations: Future Airloads Tests

Finally, the requirements for future airloads tests are summarized, based on the deficiencies observed in existing data sets.

a) Accurately measure the rotor operating condition, including: shaft angle-of-attack, flapping, torque; lift and drag in a wind tunnel; data on the helicopter drag and engine thrust for flight tests; rotor cyclic and collective pitch.

b) Collect sufficient data: enough chordwise pressure measurements to obtain lift and moment coefficients, particularly with shocks; enough radial stations to define the wake structure and for a reasonable measure of the rotor thrust; 64 to 72 samples per revolution.

c) Report sufficient data: use a good chordwise integration method; present 15-20 harmonics of data, along with the time histories.

d) Document the rotor and aircraft properties: the usual quantities; control system stiffness and torsion stiffness; airfoil tables. This information should be checked for consistency by using it in calculations.

e) Publish all performance data, much structural loads and airloads data, and a few good points of the pressure data. Use a medium that ensures the data will be available in the future.

Appendix A. CAMRAD PROGRAM MODIFICATIONS

A.1 New and Revised Input

The complete CAMRAD input is given in the user's manual (Johnson, 1980c). The new input parameters are read in namelist NLWAKE (they are not included in the binary input file). Parameters in namelist NLWAKE that are not used by the new model are: MRL, NL, MRG, NG, OPRTS, OPNWS, FNW. The new input parameters are as follows.

OPNW	integer	wake configuration: near wake and lifting-line 0 collocation point at c/4, straight lifting-line 1 collocation point at 3c/4, straight lifting-line 2 collocation point at c/4, swept lifting-line 3 collocation point at 3c/4, swept lifting-line
OPBPXA	integer	0 to suppres twist in x_A offset of swept lifting-line
FRCNW	real	factor on near wake core size; 1. for baseline value
RTVTX	real	radial station of tip vortex at blade
OPFW	integer	wake configuration: far wake rollup 0 one circulation peak, Γ_{max} 1 one circulation peak, outboard Γ 2 two circulation peaks
OPRGI	integer	source of inboard circulation peak radial station (r_{GI}) for wake geometry: 0 to calculate, 1 to use input
RGI(MPSI)	real	input r_{GI}; -1. for single peak model
OPIVTL	integer	inboard rolled up trailed wake model 0 use WKMODL(7) 1 stepped line segment 2 linear line segment
RCIVTL	real	core radius for inbaord rolled up trailed wake (line model only)

A.2 New and Revised Common Blocks

The following common block for the wake influence coefficients was revised. The influence coefficients CI for the inboard peak were added. The matrix sizes were increased, to allow the use of more radial stations and a larger near wake extent.

```
COMMON /WKC1CM/MR,ML,MI,MW,MH,MV,MO,CO(3,30000),CI(3,30000),
              CNW(3,45000)
```

The following new common blocks contain the new input parameters for the far wake and near wake models.

```
COMMON /WN1DAT/OPNW,OPBPXA,RTVTX,FRCNW
INTEGER OPNW,OPBPXA

COMMON /WF1DAT/OPFW,OPRGI,OPIVTL,RCIVTL,RGI(36)
INTEGER OPFW,OPRGI,OPIVTL
```

The following new common block contains the blade position $r_b(r_{Ai},\psi_j)$ at the aerodynamic radial stations and all azimuth stations, which is required for the near wake model.

```
COMMON /WN1CM/RBRA(3,30,36)
```

The following new common block contains the circulation peak information (as a function of azimuth station) required for the far wake model.

```
COMMON /WF1CM/CIRCO(36),CIRCI(36),
              RCIRC(36),RCIRCO(36),RCIRCI(36),
              RHOGI(36),COOLD(36),CIOLD(36)
```

where

CIRCO	Γ_O
CIRCI	Γ_I
RCIRC	r for Γ_{max}
RCIRCO	r for Γ_O
RCIRCI	r for Γ_I
RHOGI	ρ_{GI} used in wake geometry
COOLD	old Γ_O for inflow (lagged)
CIOLD	old Γ_I for inflow (lagged)

A.3 Revised Subroutines

General revisions

INPTW1	namelist read of new input parameters (NLWAKE)
PRNTW1	print new input parameters
FILEJ	store new commons; change C to CO, use CI;
INITR1	check input RGI; zero RCIRCO, RCIRCI; set RHOGI=-1.; set MRL=MRA, MRG=MRA
CHEKR1	increase dimension of influence coefficients

Far wake model

PERFR1	print CIRC's, RCIRC's, RHOGI
AEROF1	calculate circulation peaks
RAMF	use CIRCO, CIRCI in circulation convergence
GEOMR1	calculate RHOGI; use Γ_{max} or Γ_0 for wake geometry
GEOMF1	use Γ_{max} or Γ_0 for wake geometry
WAKEC1	change C to CO; calculate CO and CI for rolling up and far wake models
WAKEN1	change C to CO; lag CIRCO, CIRCI; calculate inflow from Γ_0 and Γ_I

Near wake model

GEOMR1	calculate FTIP from RTVTX; call WAKEB1; calculate RBRA
WAKEB1	use OPBPXA, calculate x_A terms; always calculate at all aerodynamic radial stations
GEOME1	calculate wake geometry at aerodynamic radial stations
GEOMP1	call GEOME1
LOADR1	call GEOME1
WAKEC1	call GEOME1; calculate collocation points; calculate CNW for near wake model
WAKEC2	call WAKEB1

REFERENCES

Ballard, J.D.; Orloff, K.L.; and Luebs, A.B. (1979) "Effect of Tip Planform on Blade Loading Characteristics for a Two-Bladed Rotor in Hover." NASA TM 78615, November 1979.

Bartsch, E.A., and Sweers, J.E. (1968) "Inflight Measurement and Correlation with Theory of Blade Airloads and Responses on the XV-51A Compound Helicopter Rotor." U.S. Army Aviation Materiel Laboratories, USAAVLABS TR 68-22, May 1968.

Beno, E.A. (1970) "CH-53A Main Rotor and Stabilizer Vibratory Airloads and Forces." Sikorsky Aircraft, Report SER 65593, June 1970.

Burpo, F.B., and Lynn, R.R. (1962) "Measurement of Dynamic Airloads on a Full-Scale Semirigid Rotor." U.S. Army Transportation Research Command, TCREC 62-42, December 1962.

Dadone, L.; Dawson, S.; Boxwell, D.; and Ekquist, D. (1987) "Model 360 Rotor Test at DNW -- Review of Performance and Blade Airload Data." Annual National Forum of the American Helicopter Society, 1987.

Fenaughty, R., and Beno, E. (1970) "NH-3A Vibratory Airloads and Vibratory Rotor Loads." Sikorsky Aircraft, Report SER 611493, January 1970..

Ham, N.D. (1975) "Some Conclusions from an Investigation of Blade-Vortex Interaction." Journal of the American Helicopter Society, vol 20, no 4 (October 1975).

Harris, F.D. (1972) "Articulated Rotor Blade Flapping Motion at Low Advance Ratio." Journal of the American Helicopter Society, vol 17, no 1 (January 1972).

Heffernan, R.M., and Gaubert, M. (1986) "Structural and Aerodynamic Loads and Performance Measurements of an SA349/2 Helicopter with an Advanced Geometry Rotor." NASA TM 88370, November 1986.

Hooper, W.E. (1984) "The Vibratory Airloading of Helicopter Rotors." Vertica, vol 8, no 2 (1984).

Johnson, W. (1971a) "Application of a Lifting-Surface Theory to the Calculation of Helicopter Airloads." Annual National Forum of the American Helicopter Society, 1971.

Johnson, W. (1971b) "A Lifting-Surface Solution for Vortex-Induced Airloads." AIAA Journal, vol 9, no 4 (April 1971).

Johnson, W. (1980a) Helicopter Theory. Princeton University Press, Princeton, New Jersey, 1980.

Johnson, W. (1980b) "A Comprehensive Analytical Model of Rotorcraft Aerodynamics and Dynamics." NASA TM 81182, June 1980.

Johnson, W. (1980c) "A Comprehensive Analytical Model of Rotorcraft Aerodynamics and Dynamics." NASA TM 81183, July 1980.

Johnson, W. (1981) "Comparison of Calculated and Measured Helicopter Rotor Lateral Flapping Angles." Journal of the American Helicopter Society, vol 26, no 2 (April 1981).

Johnson, W. (1986a) "Assessment of Aerodynamic and Dynamic Models in a Comprehensive Analysis for Rotorcraft." Computers and Mathematics with Applications, vol 12A, no 1, (January 1986).

Johnson, W. (1986b) "Recent Developments in Rotary-Wing Aerodynamic Theory." AIAA Journal, vol 24, no 8 (August 1986).

Miller, R.H. (1985) "Methods for Rotor Aerodynamic and Dynamic Analysis." Progress in Aerospace Science, vol 22 (1985).

Miller, R.H., and Ellis, S.C. (1986) "Prediction of Blade Airloads in Hovering and Forward Flight Using Free Wakes." European Rotorcraft Forum, Germany, September 1986.

Morris, C.E.K., Jr. (1978) "Rotor-Airfoil Flight Investigation: Preliminary Results." Annual National Forum of the American Helicopter Society, 1978.

Morris, C.E.K., Jr. (1981) "A Flight Investigation of Blade-Section Aerodynamics for a Helicopter Main rotor Having 10-64C Airfoil Sections." NASA TM 83226, November 1981.

Morris, C.E.K., Jr. (1982) "A Flight Investigation of Blade-Section Aerodynamics for a Helicopter Main rotor Having RC-SC2 Airfoil Sections." NASA TM 83298, March 1982.

Morris, C.E.K., Jr.; Stevens, D.D.; and Tomaine, R.L. (1980) "A Flight Investigation of Blade-Section Aerodynamics for a Helicopter Main rotor Having NLR-1T Airfoil Sections." NASA TM 80166, January 1980.

Morris, C.E.K., Jr.; Tomaine, R.L.; and Stevens, D.D. (1979) "A Flight Investtigation of Performance and Loads for a Helicopter with NLR-1T Main Rotor Blade Section." NASA TM 80165, October 1979.

Morris, C.E.K., Jr.; Tomaine, R.L.; and Stevens, D.D. (1980a) "A Flight Investtigation of Performance and Loads for a Helicopter with 10-64C Main Rotor Blade Section." NASA TM 81871, October 1980.

Morris, C.E.K., Jr.; Tomaine, R.L.; and Stevens, D.D. (1980b) "A Flight Investtigation of Performance and Loads for a Helicopter with RC-SC2 Main Rotor Blade Section." NASA TM 81898, December 1980.

Pruyn, R.R., et al. (1967) "Inflight Measurement of Rotor Blade Airloads, Bending Moments, and Motions, Together with Rotor Shaft Loads and Fuselage Vibration, on a Tandem Rotor Helicopter." U.S. Army Aviation Materiel Laboratories, USAAVLABS TR 67-9, May 1967.

Rabbott, J.P., Jr., and Churchill, G.B. (1956) "Experimental Investigation of the Aerodynamic Loading on a Helicopter Rotor Blade in Forward Flight." NACA RM L56I07, October 1956.

Rabbott, J.P., Jr.; Lizak, A.A.; and Paglino, V.M. (1966a) "A Presentation of Measured and Calculated Full-Scale Rotor Blade Aerodynamic and Structural Loads." U.S. Army Aviation Materiel Laboratories, USAAVLABS TR 66-31, July 1966.

Rabbott, J.P., Jr.; Lizak, A.A.; and Paglino, V.M. (1966b) "Tabulated Sikorsky CH-34 Blade Surface Pressures Measured at the NASA/Ames Full-Scale Wind tunnel." Sikorsky Aircraft, Report SER-58399, January 1966.

Scheiman, J. (1964) "A Tabulation of Helicopter Rotor-Blade Differential Pressures, Stresses, and Motions as Measured in Flight." NASA TM X-952, 1964.

Scheiman, J., and Ludi, L.H. (1963) "Qualitative Evaluation of Effect of Helicopter Rotor-Blade Tip Vortex on Blade Airloads." NASA TN D-1637, May 1963.

Scully, M.P. (1975) "Computation of Helicopter Rotor Wake Geometry and Its Influence on Rotor Harmonic Airloads." Massachusetts Institute of Technology, ASRL TR 178-1, March 1975.

Shanley, J.P. (1986) "Application of the Comprehensive Analytical Model of Rotorcraft Aerodynamics and Dynamics to the UH-60A Aircraft." Sikorsky Aircraft, Report SER 72126, February 1986.

Tung, C.; Caradonna, F.X.; and Johnson, W. (1986) "The Prediction of Transonic Flows on an Advancing Rotor." Journal of the American Helicopter Society, vol 31, no 3 (July 1986).

Yamauchi, G.K.; Heffernan, R.M.; and Gaubert, M. (1988) "Correlation of SA349/2 Helicopter Flight Test Data with a Comprehensive Rotorcraft Model." Journal of the American Helicopter Society, vol 33, no 2 (April 1988).

Figure 2-1a. Rotor blade loading at low speed

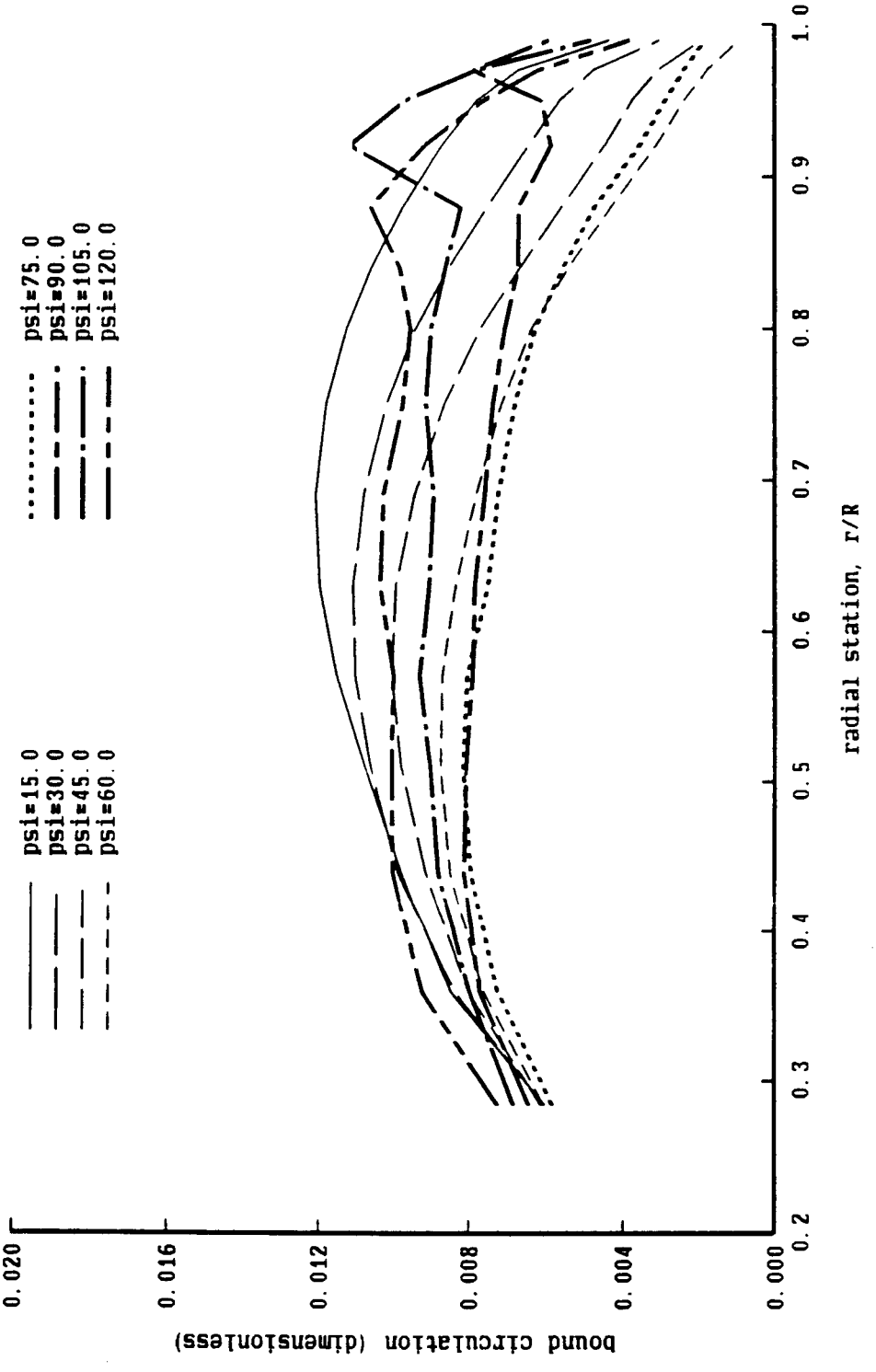

Figure 2-1b. Rotor blade loading at low speed

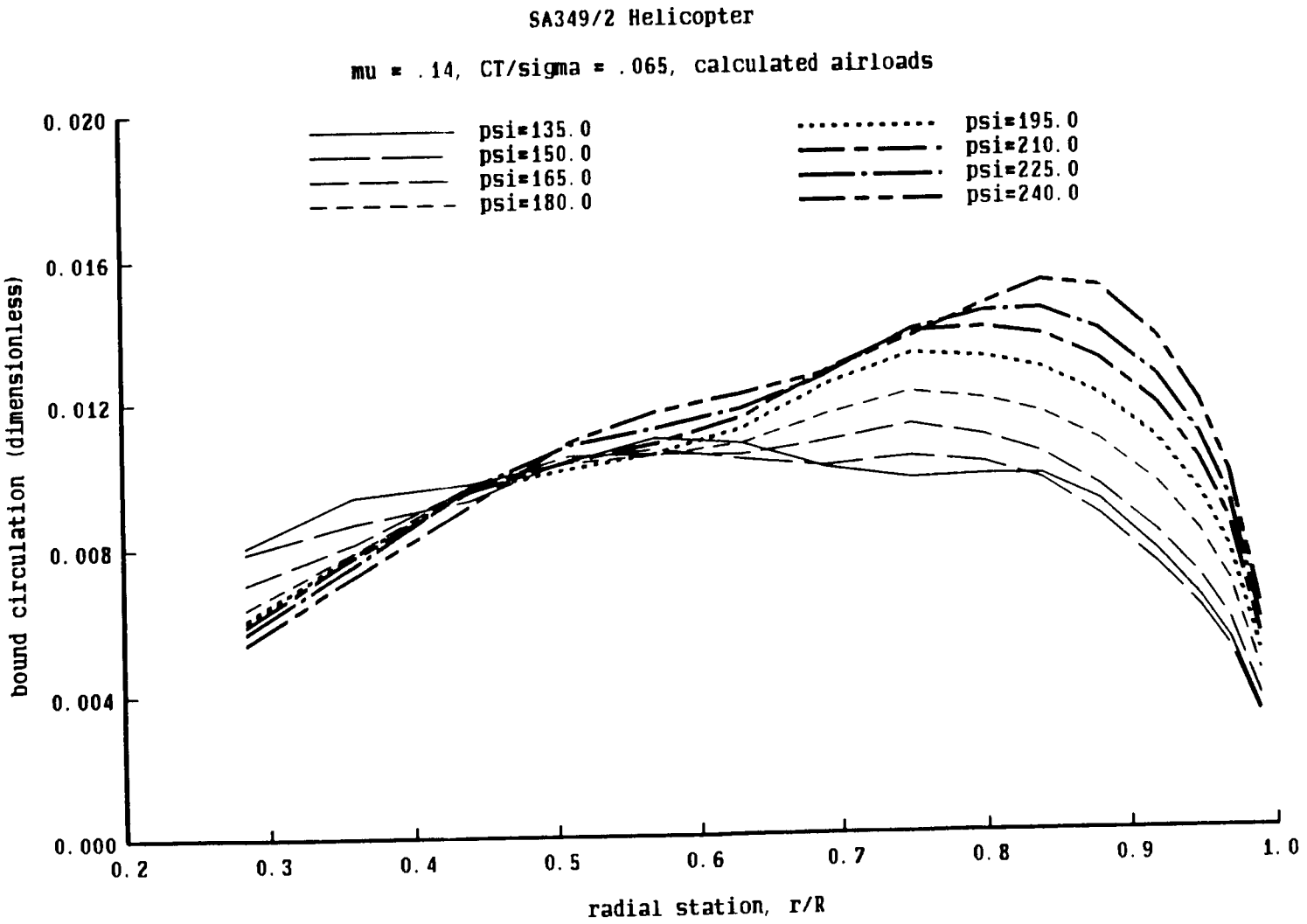

Figure 2-1c. Rotor blade loading at low speed

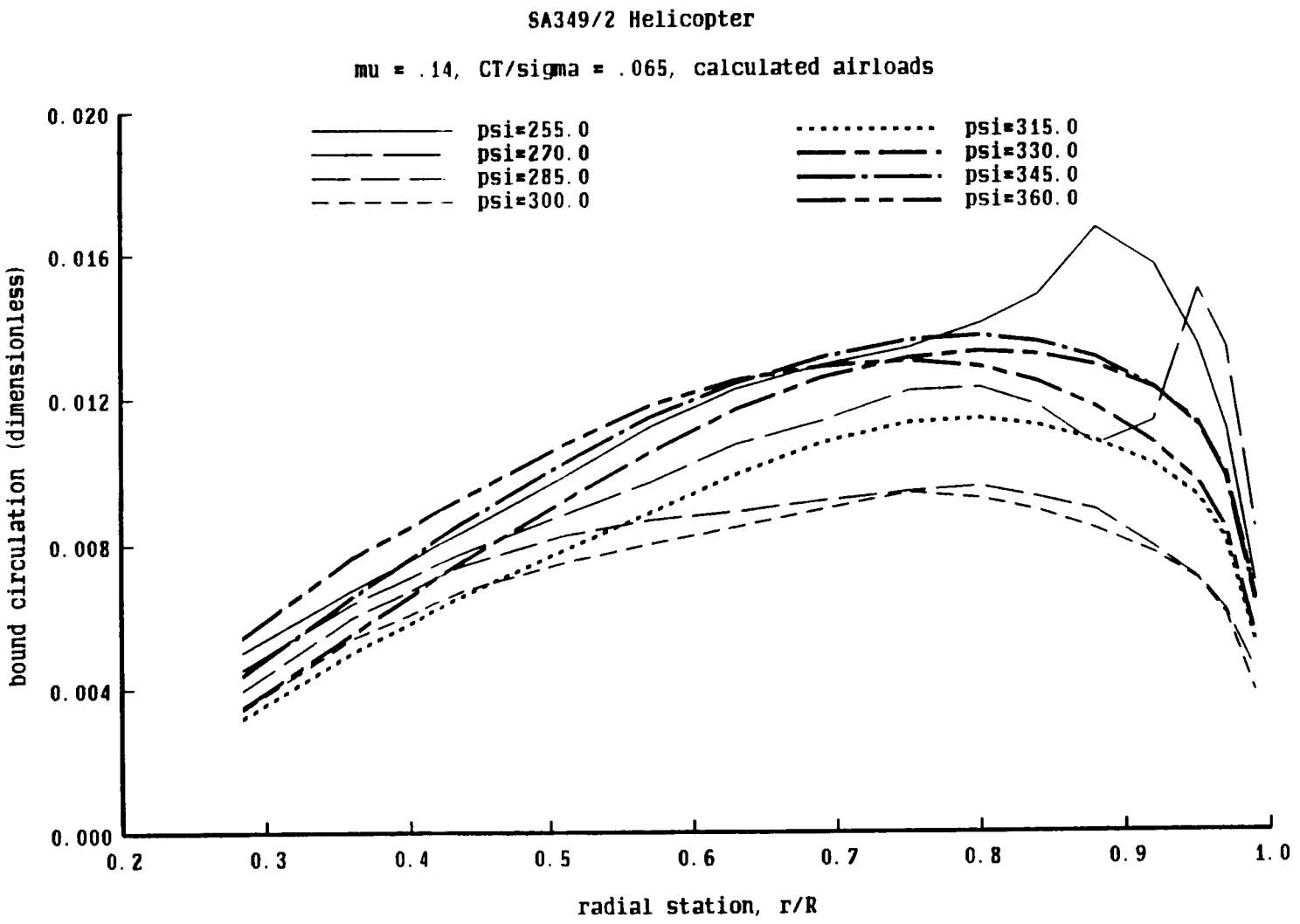

Figure 2-2a. Rotor blade loading at high speed

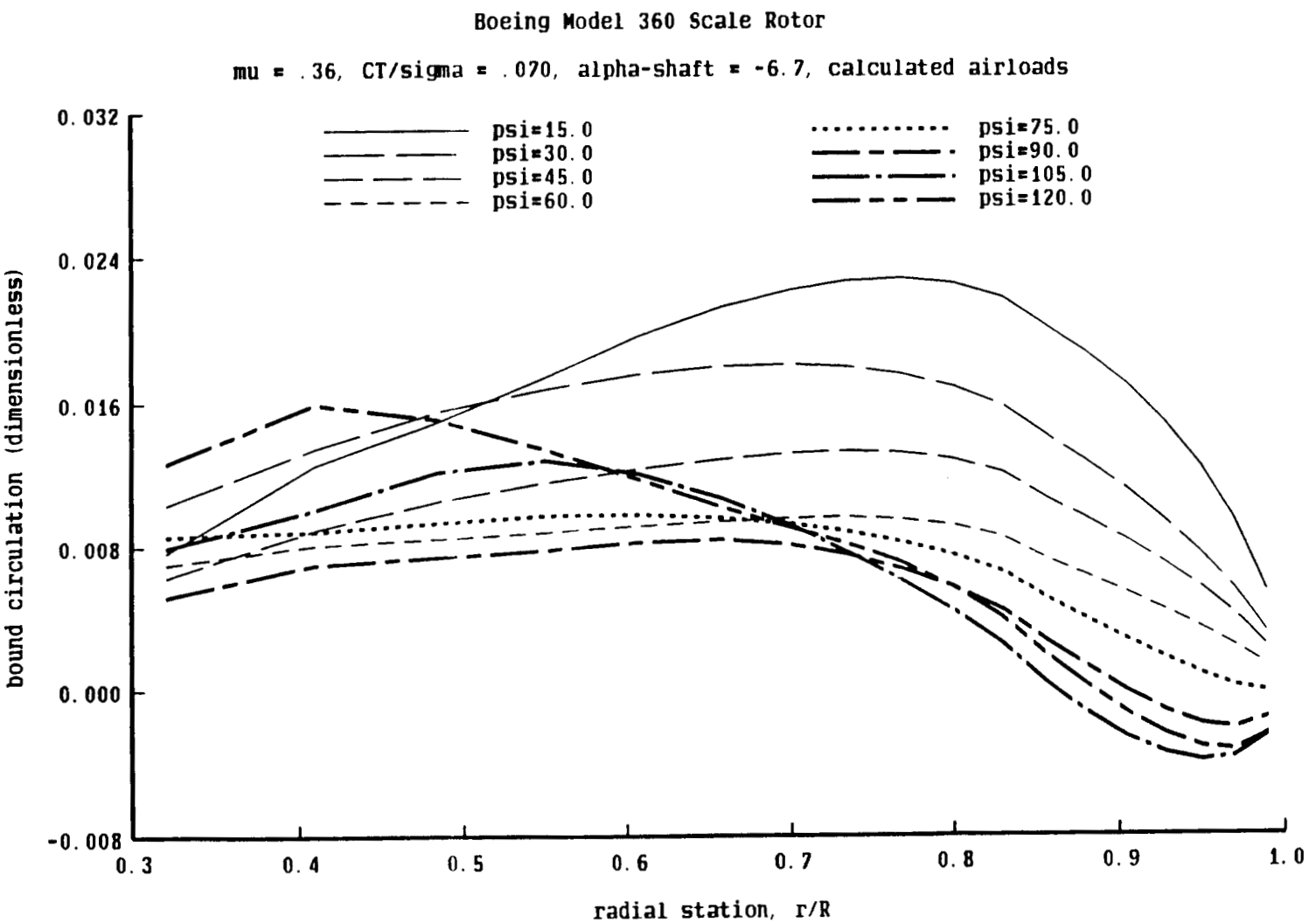

Figure 2-2b. Rotor blade loading at high speed

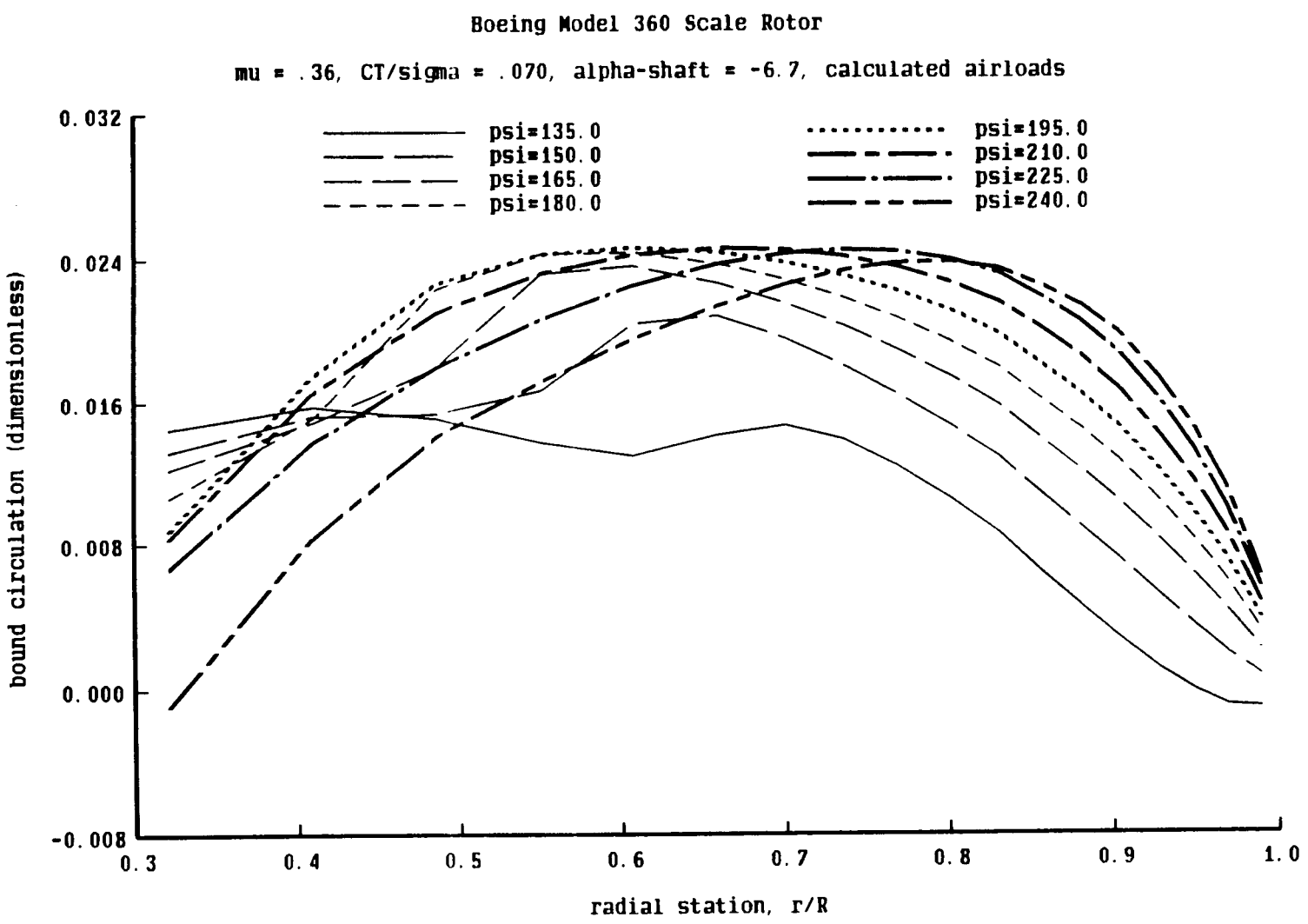

Figure 2-2c. Rotor blade loading at high speed

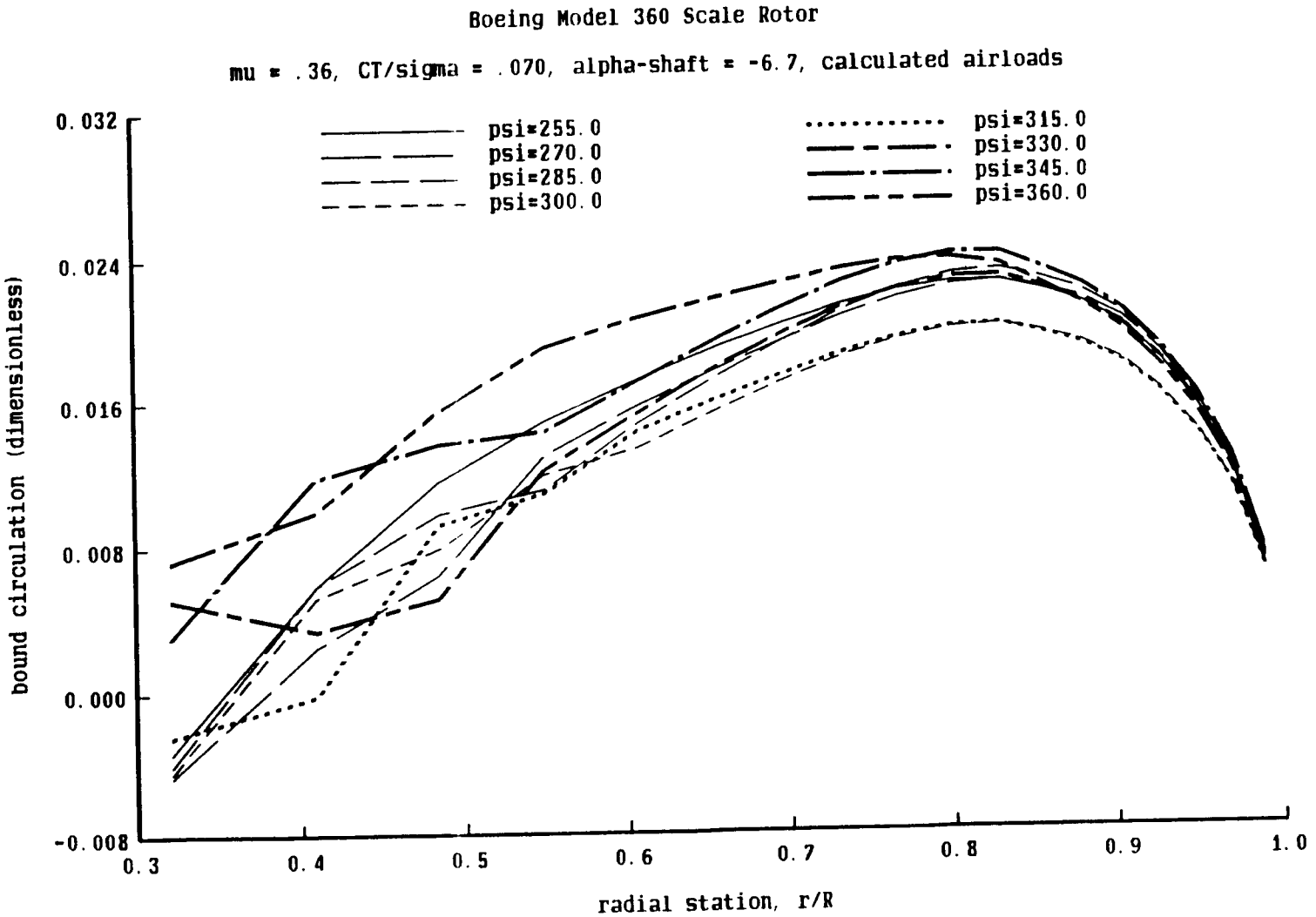

Figure 2-3a. Rotor blade loading at high speed

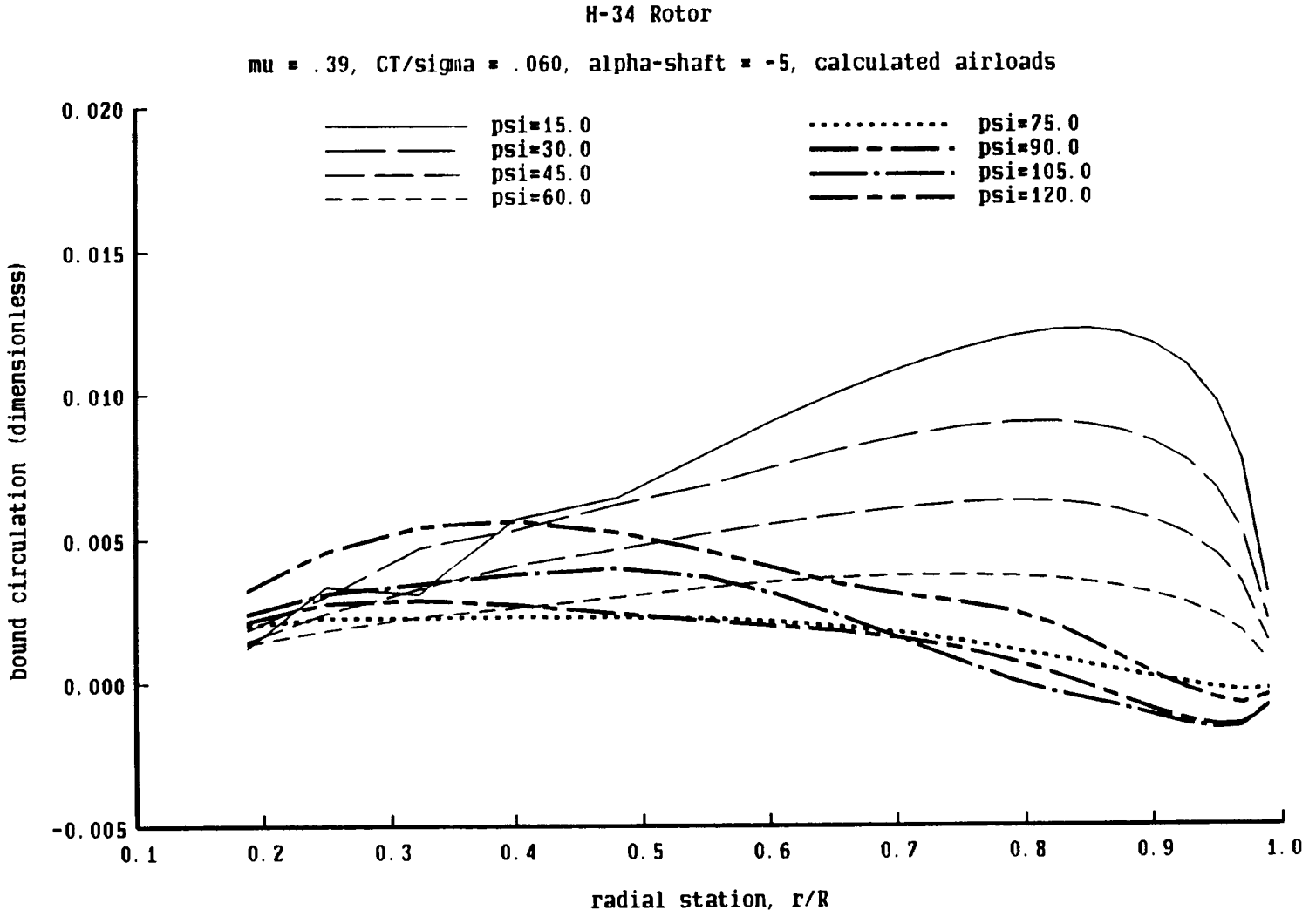

Figure 2-3b. Rotor blade loading at high speed

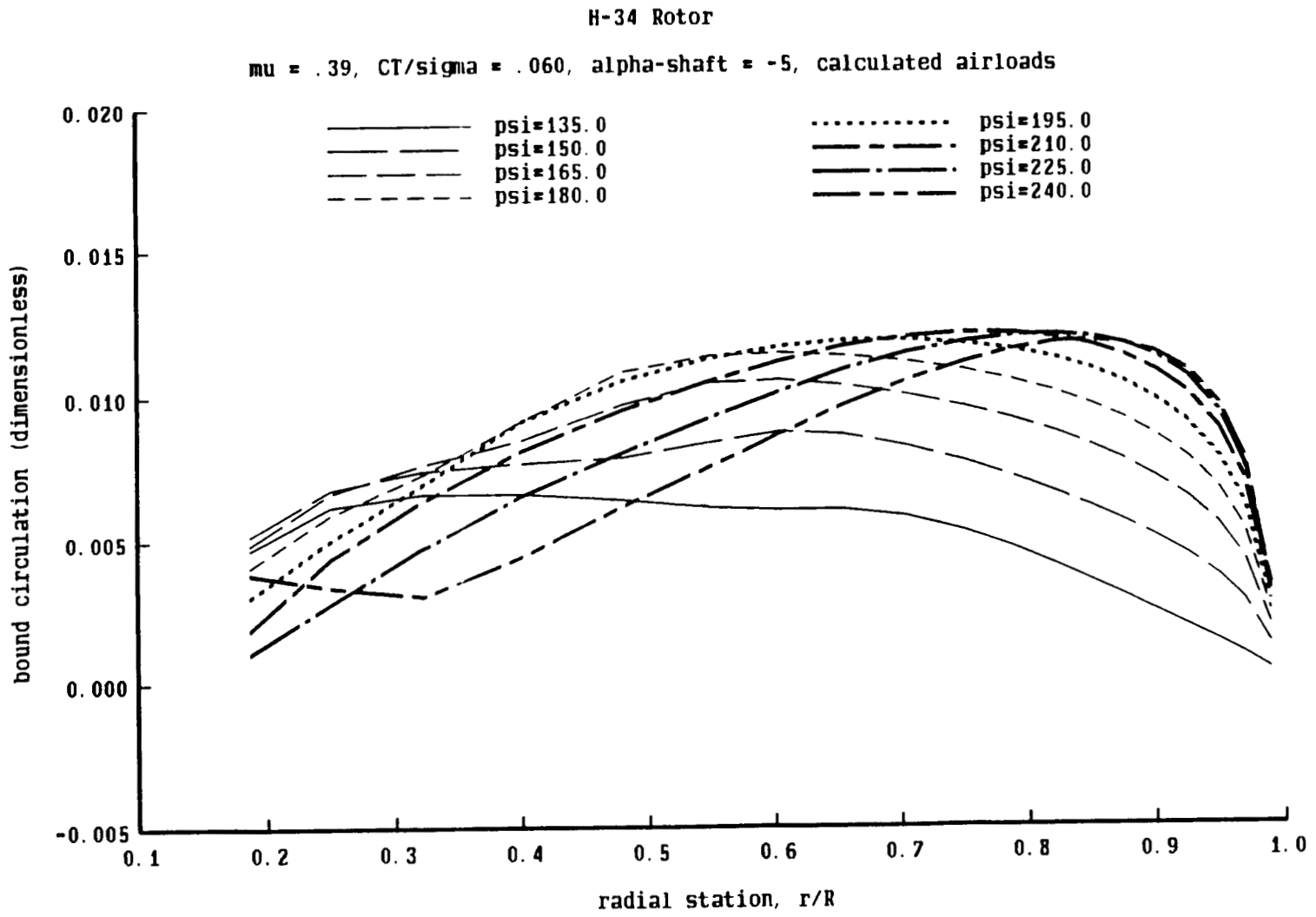

Figure 2-3c. Rotor blade loading at high speed

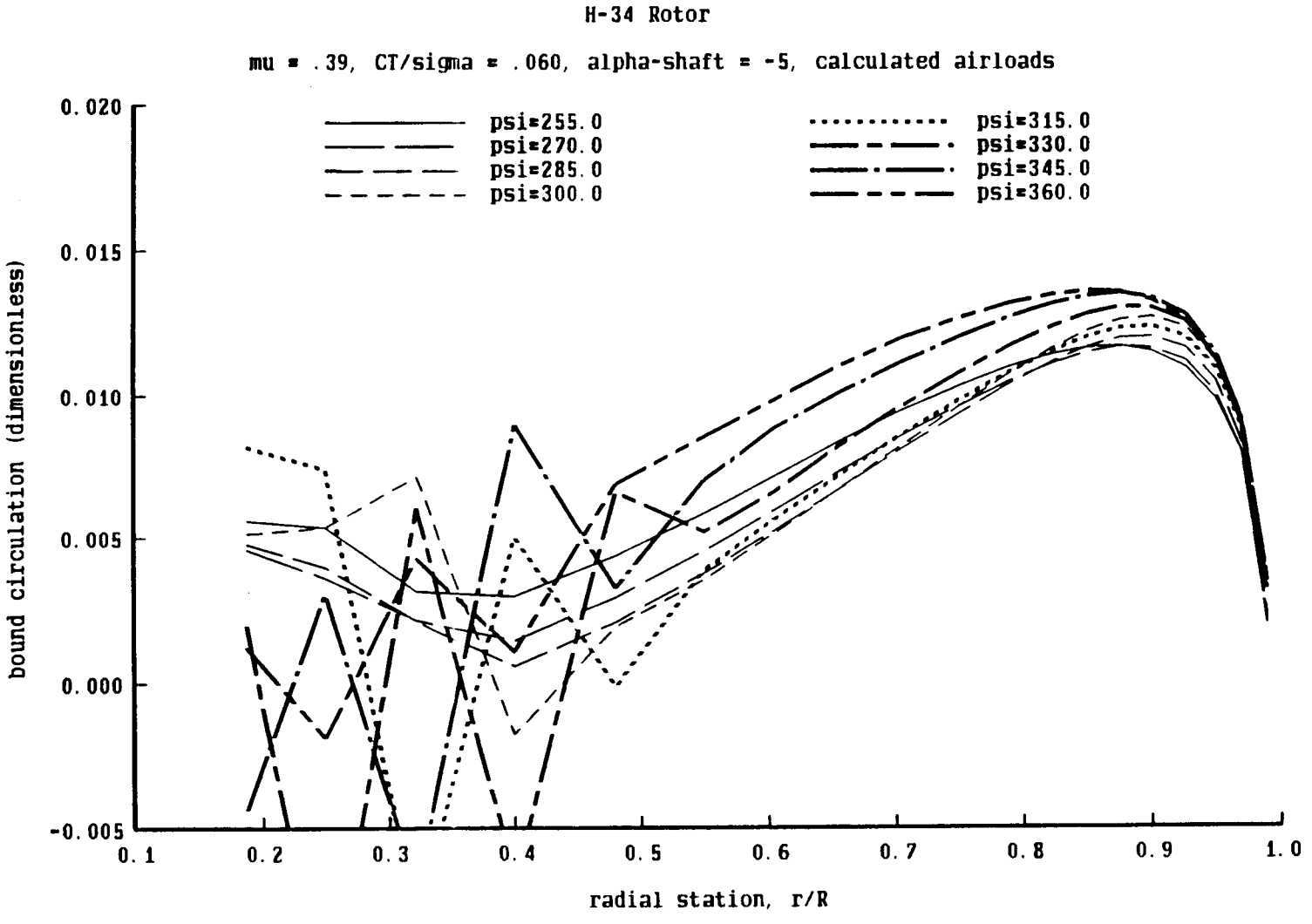

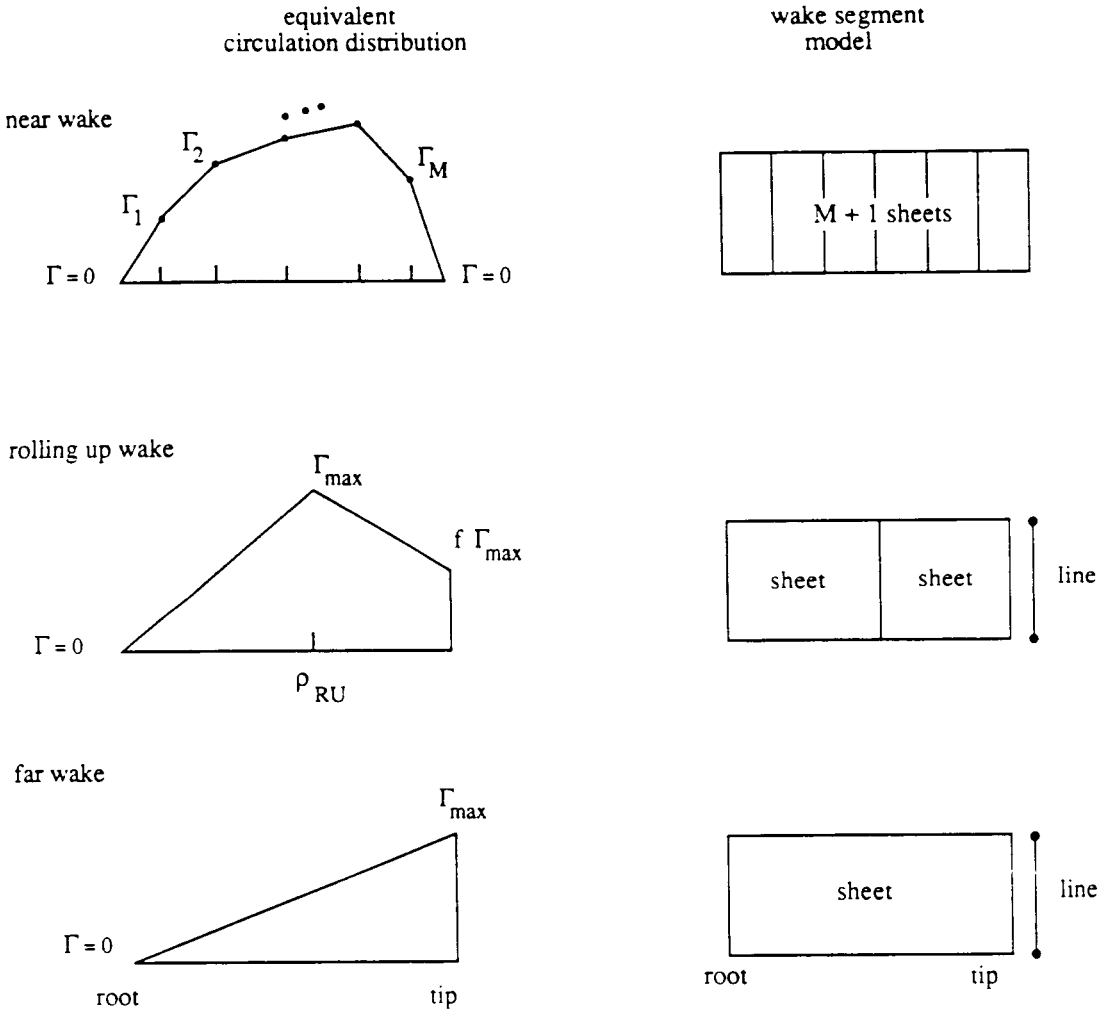

Figure 2-4. CAMRAD equivalent circulation distribution and resulting wake segment models

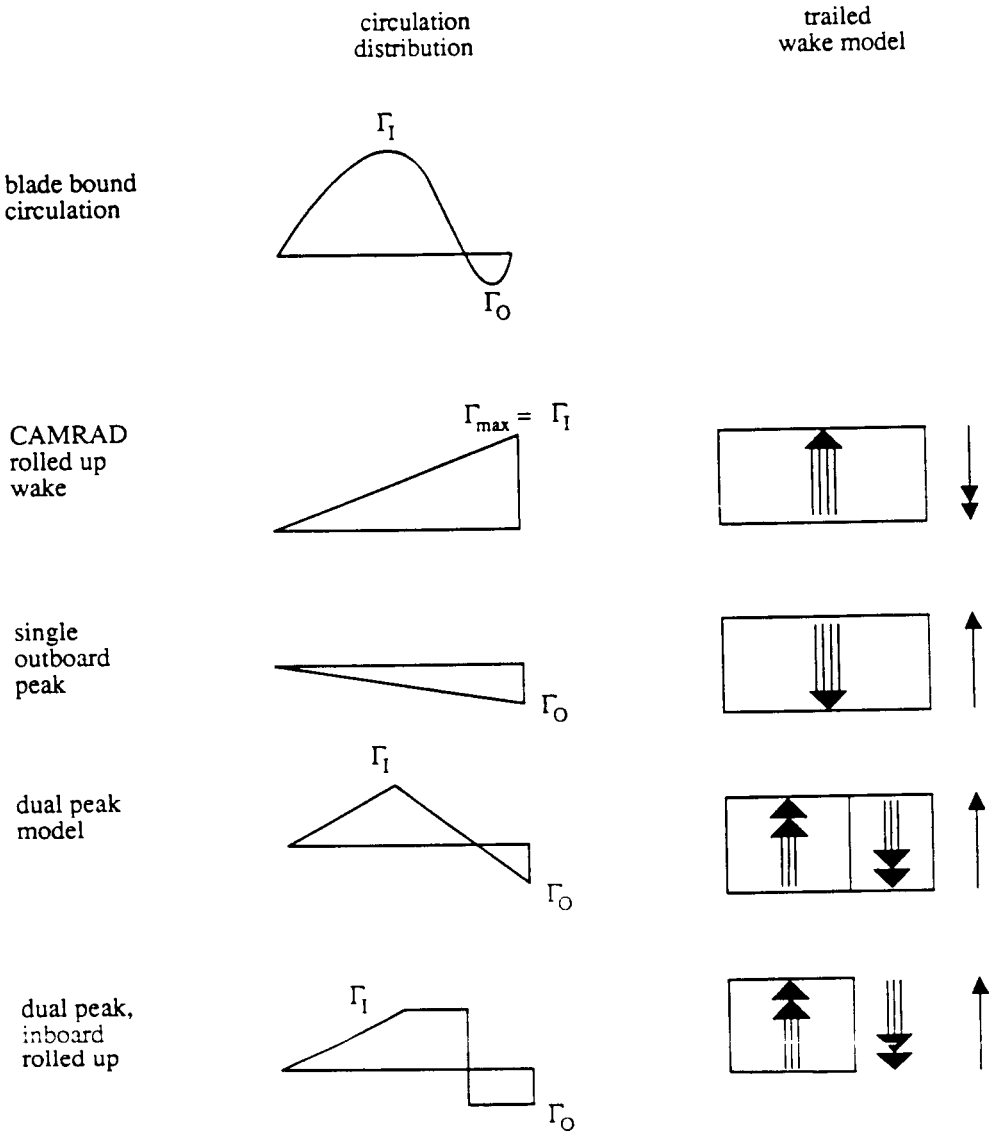

Figure 2-5. Possible wake models for dual-peak loading case.

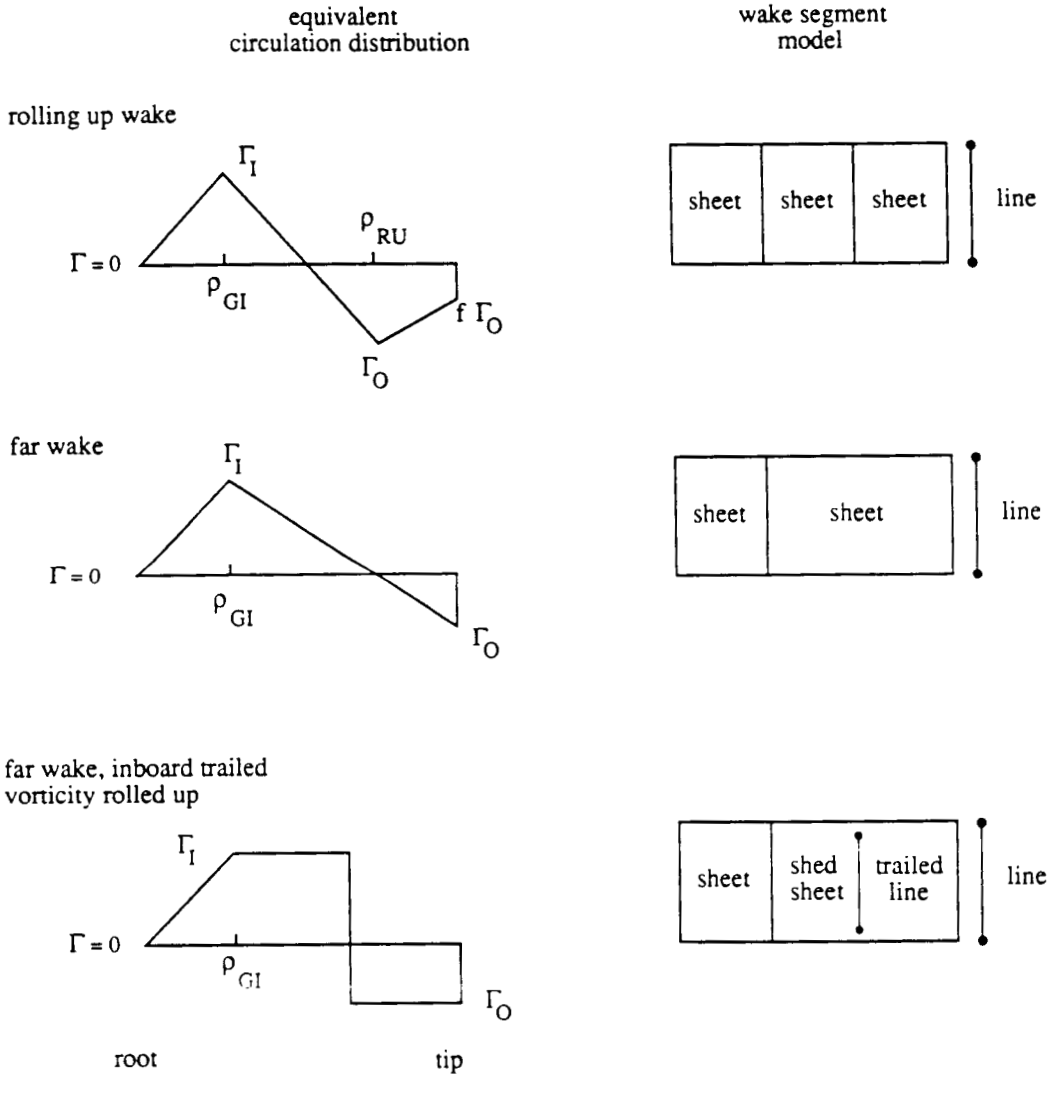

Figure 2-6. Dual-peak model: equivalent circulation distribution and resulting wake segment models

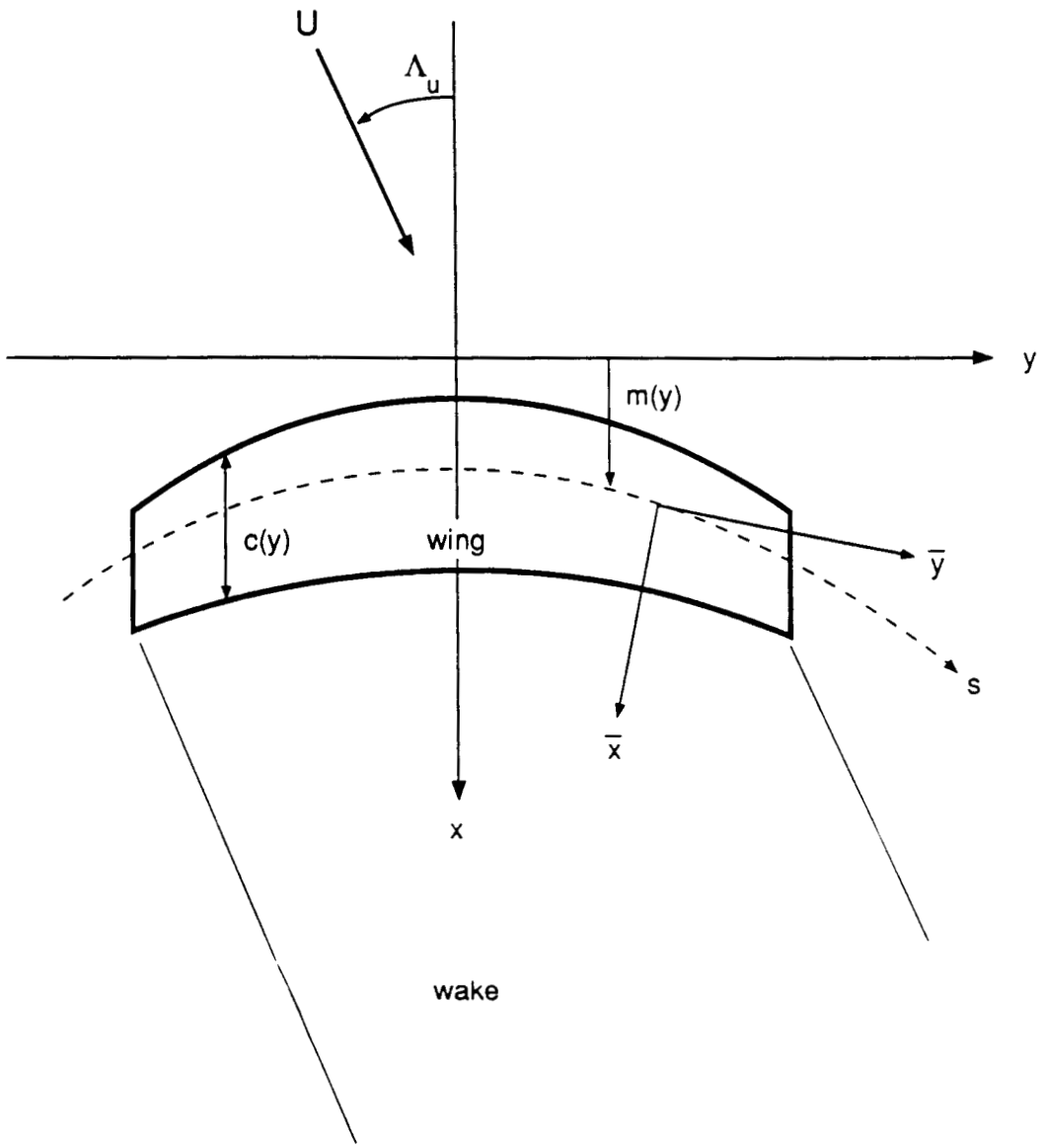

Figure 3-1. Fixed wing with sweep and yawed flow

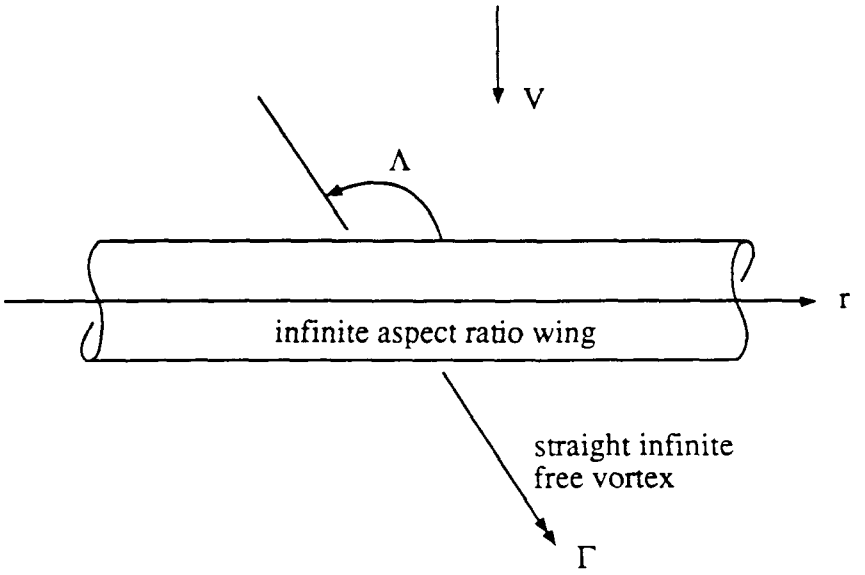

Figure 4-1. Lifting-surface theory model problem for vortex-induced loads

Figure 4-2. Lift deficiency function for perpendicular interaction

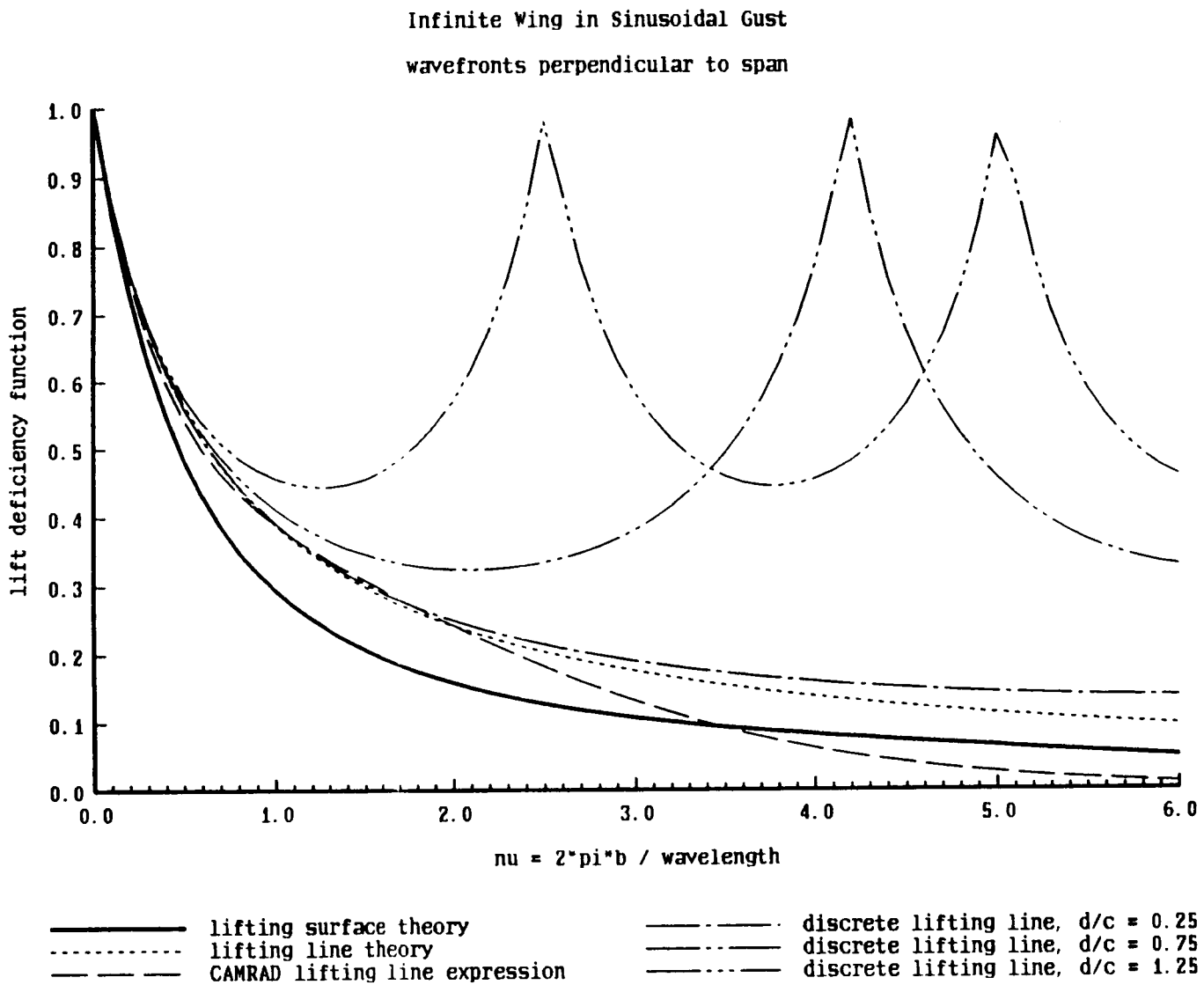

Figure 4-3. Vortex-induced downwash spectrum

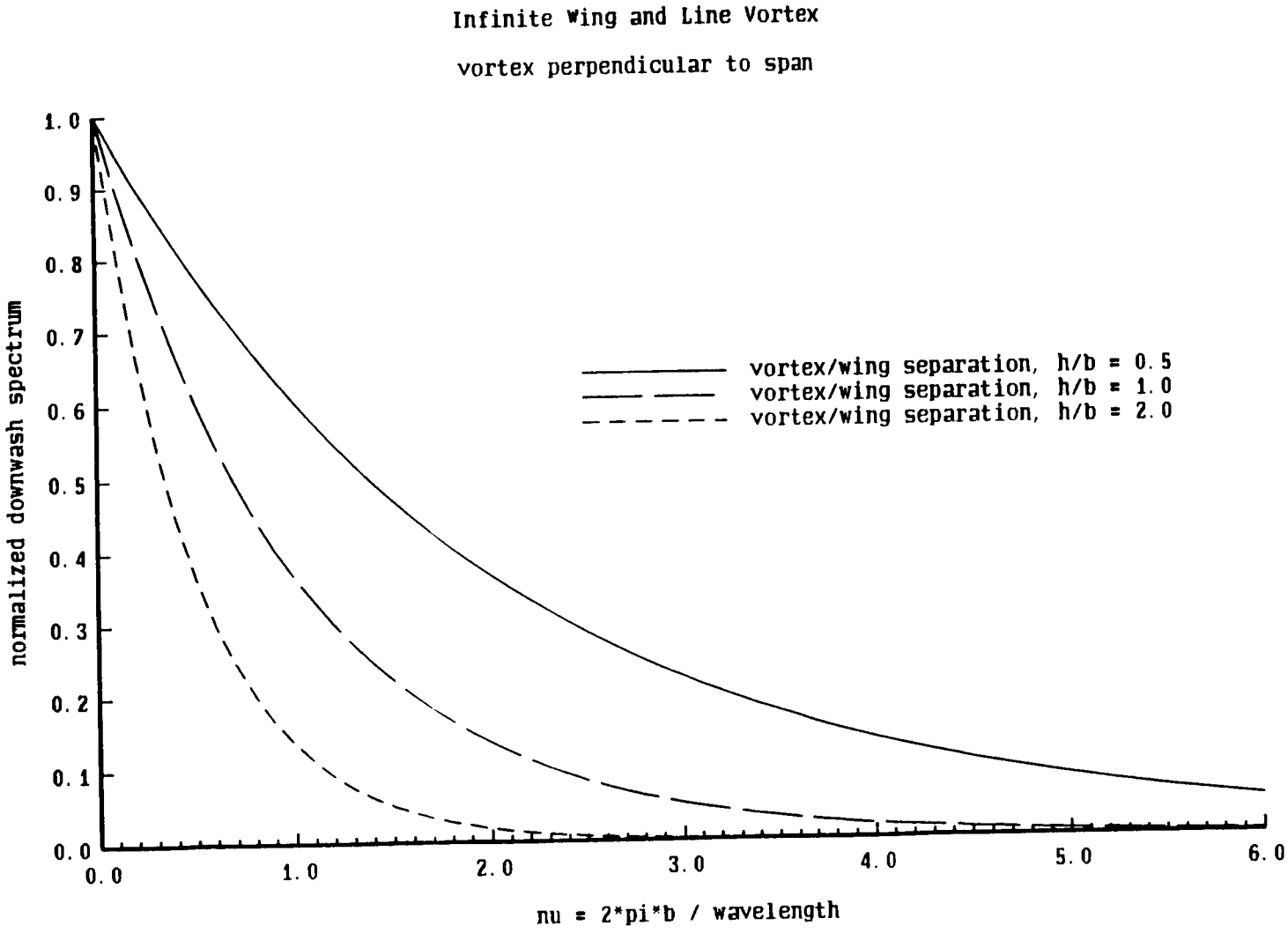

Figure 4-4. Vortex-induced load for perpendicular interaction

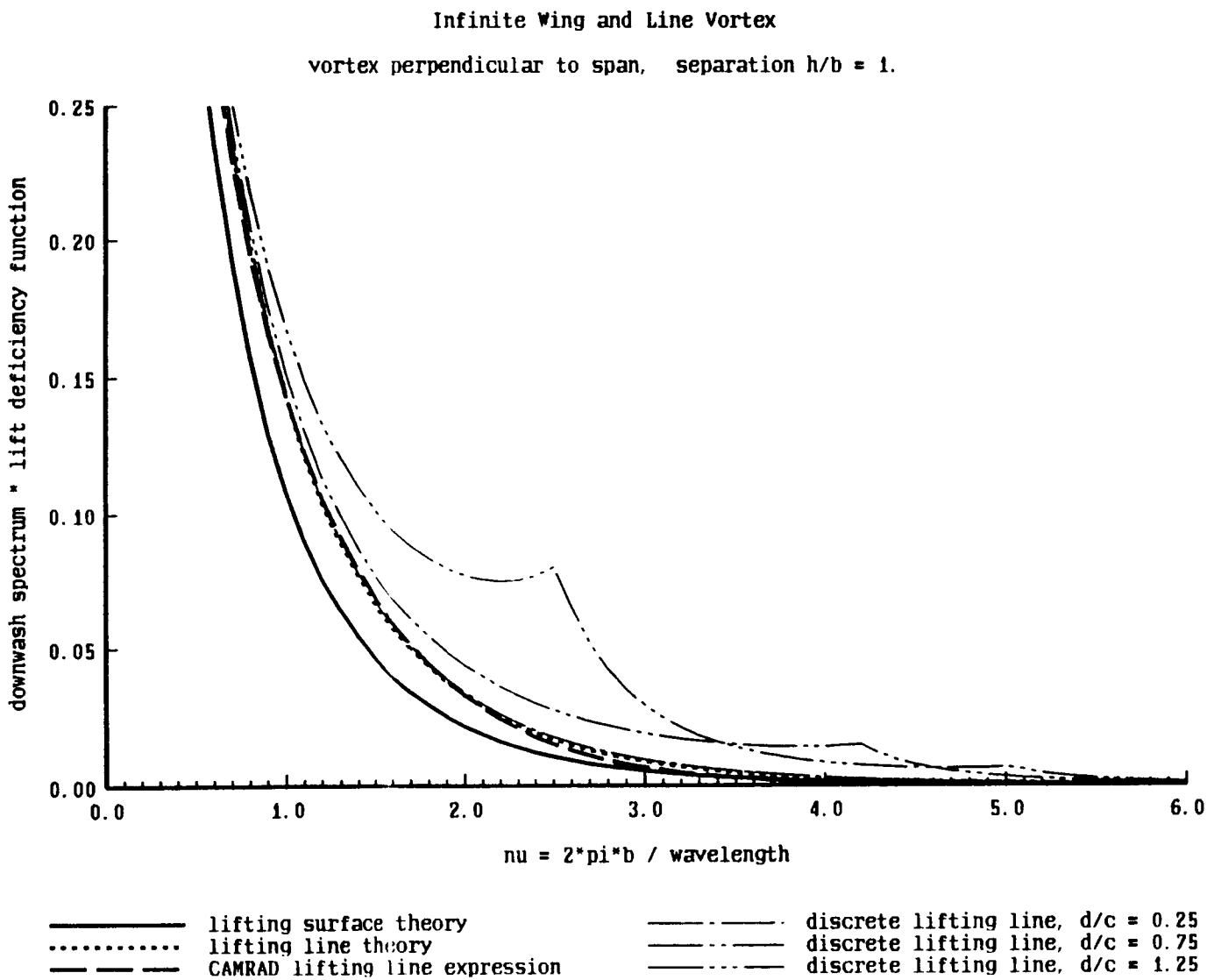

Figure 4-5. Revised lift deficiency function for perpendicular interaction

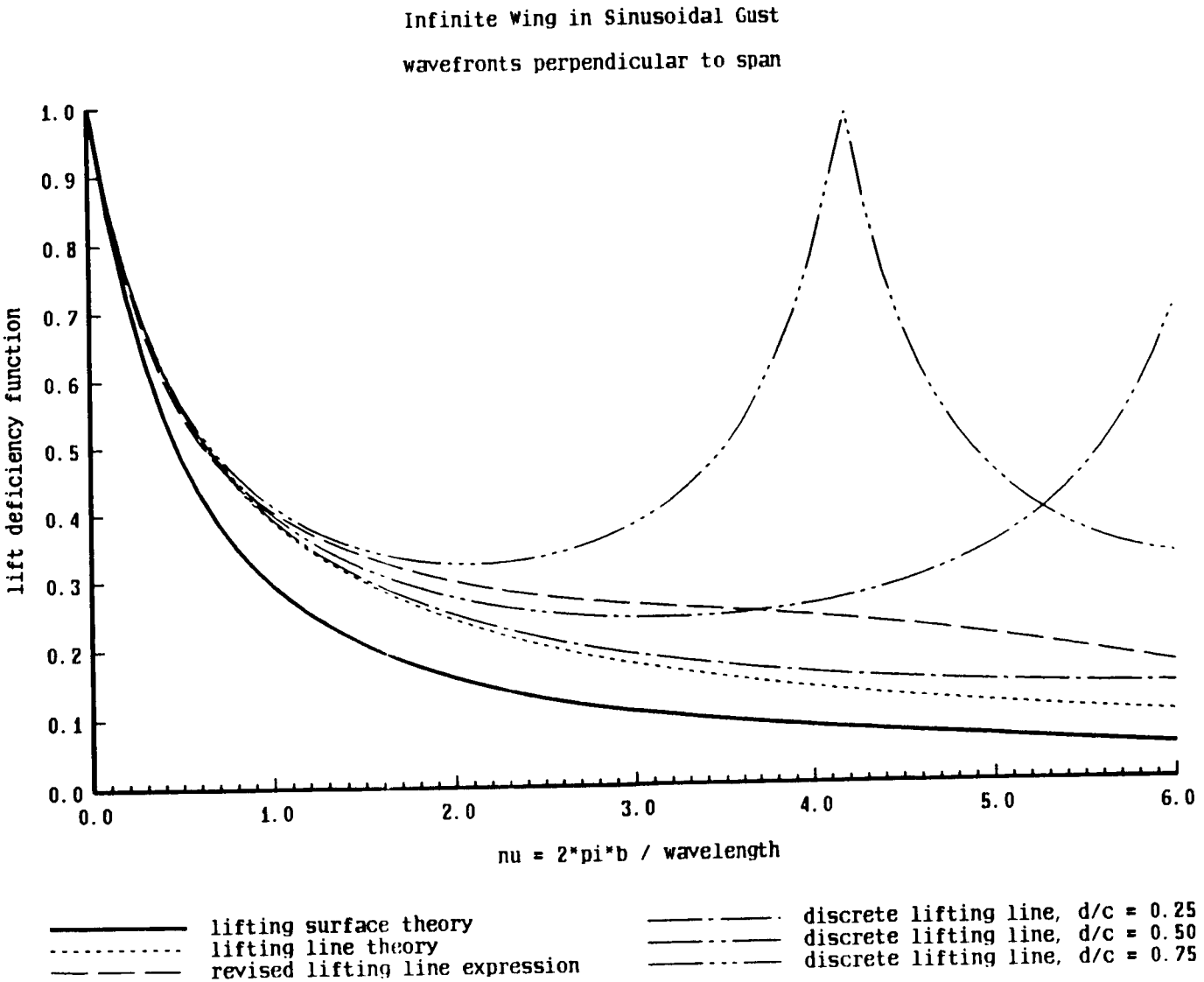

Figure 4-6. Revised vortex-induced load for perpendicular interaction

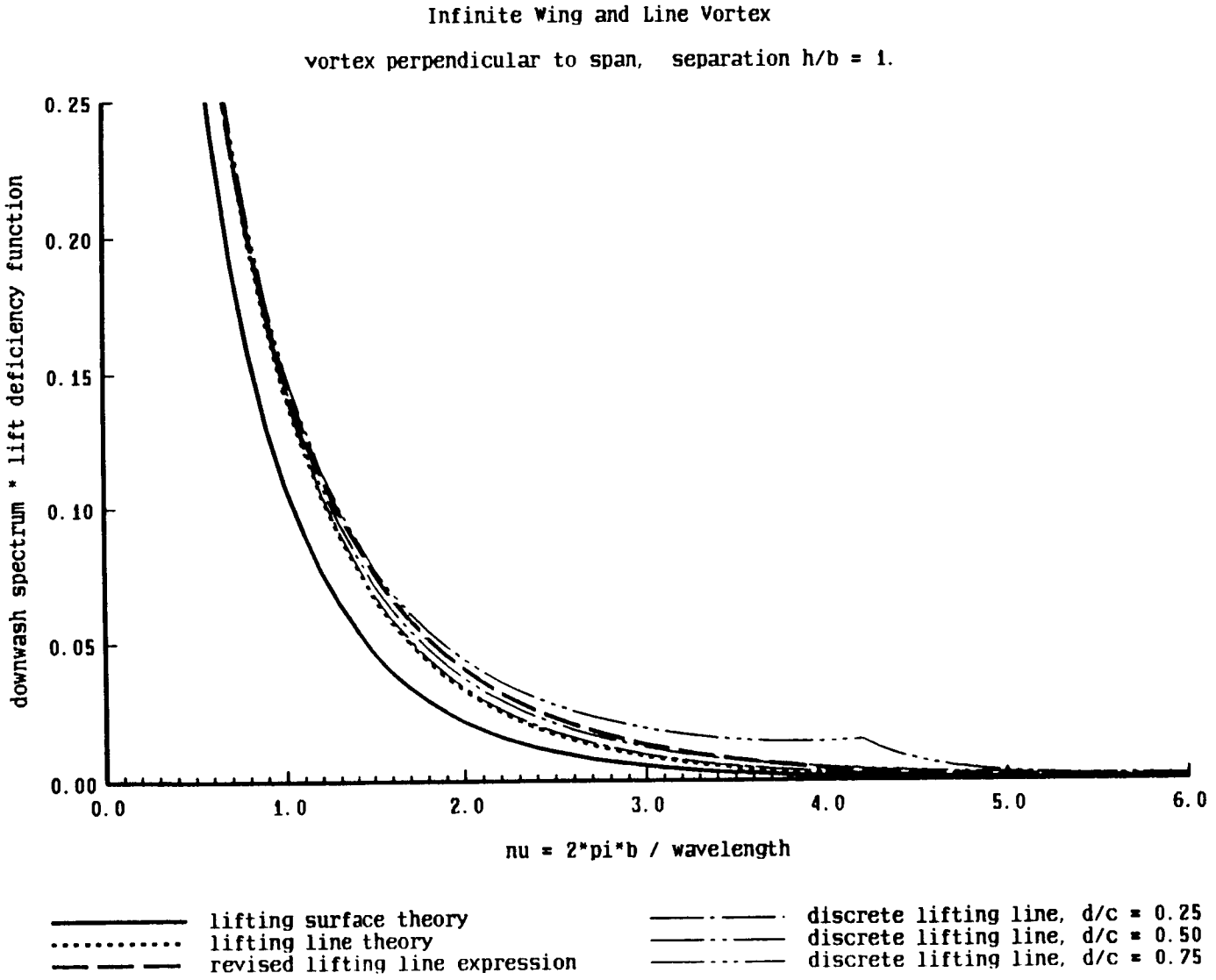

Figure 4-7a. Lift deficiency function for parallel interaction

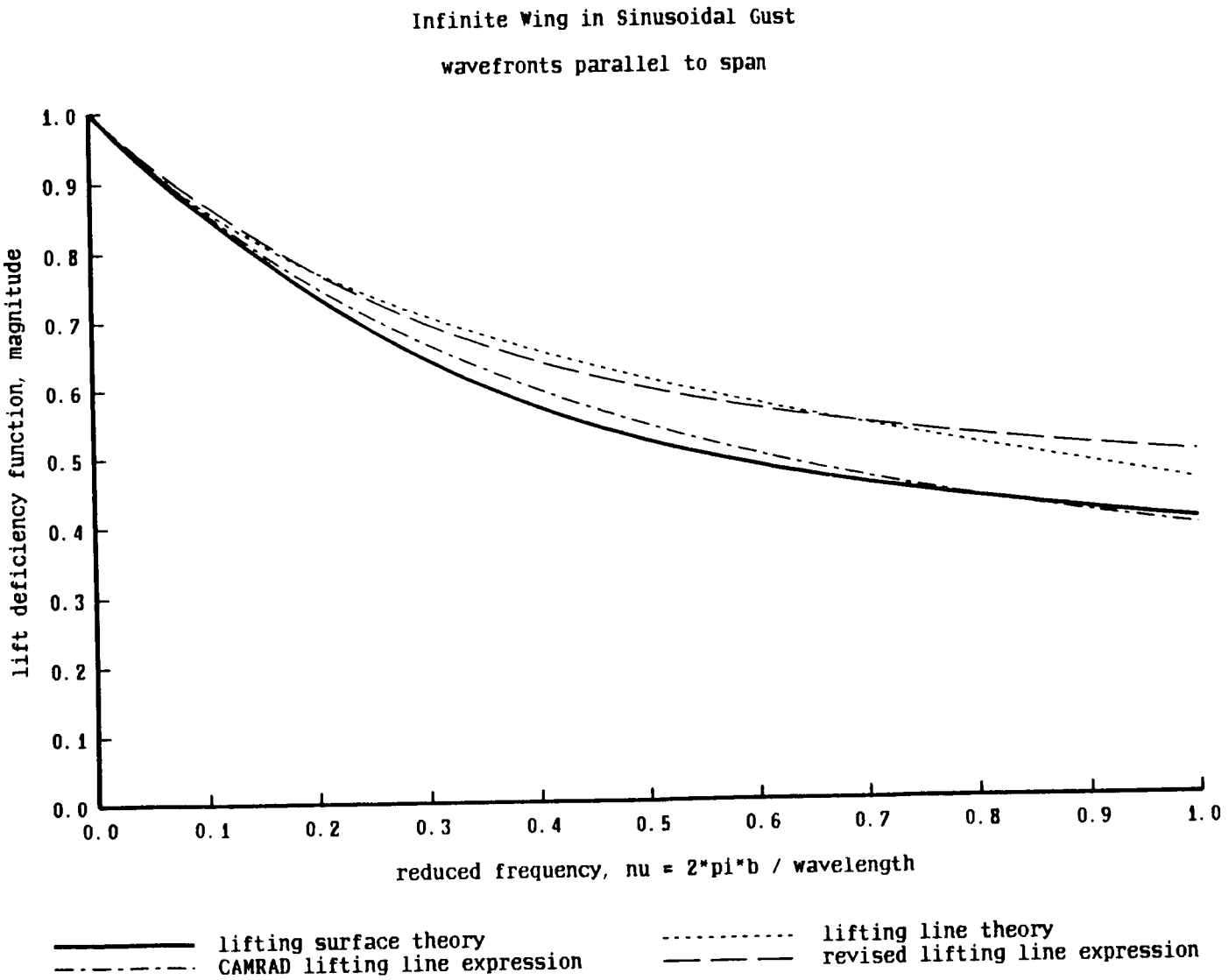

Figure 4-7b. Lift deficiency function for parallel interaction

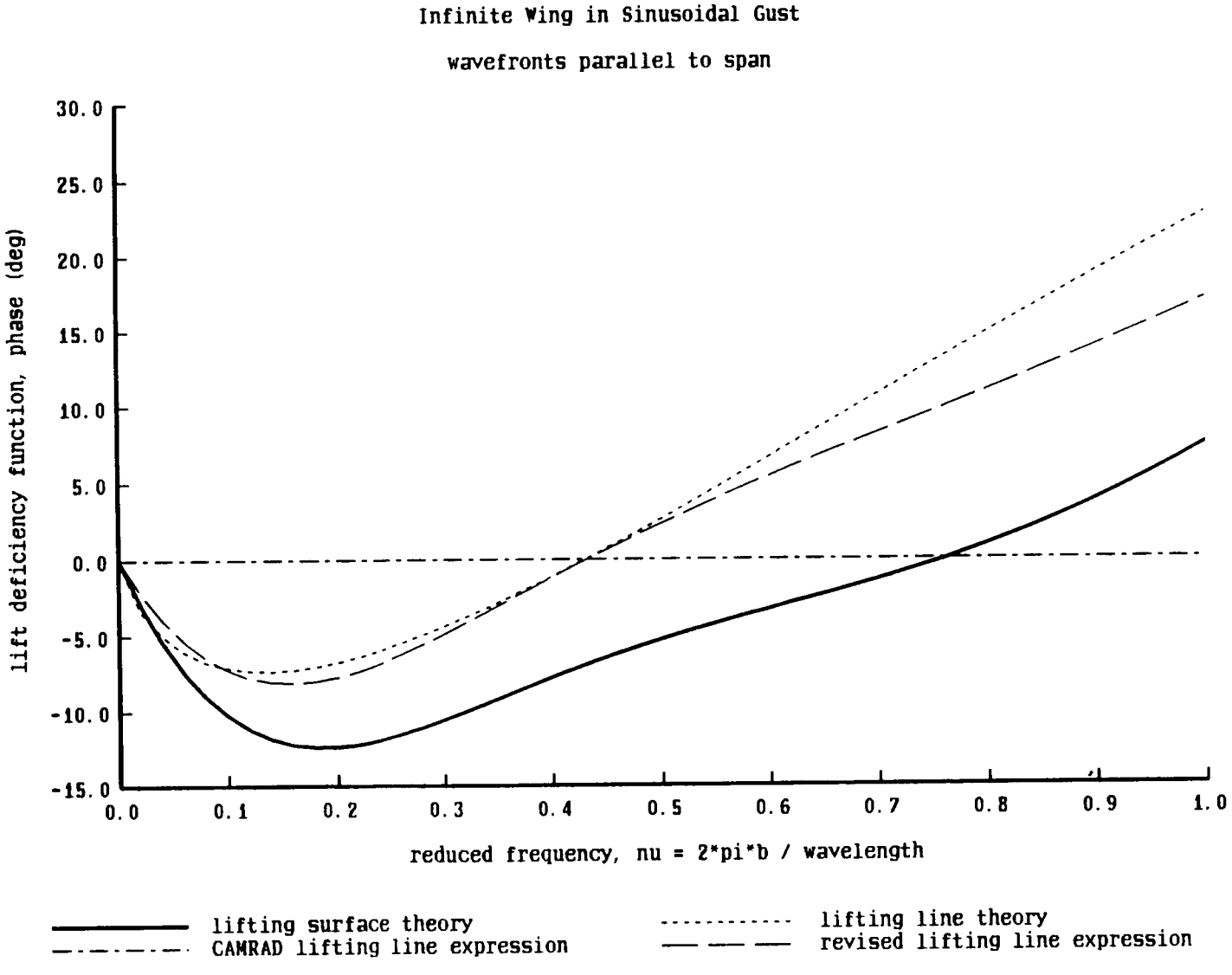

Figure 4-8a. Peak vortex-induced lift for perpendicular interaction

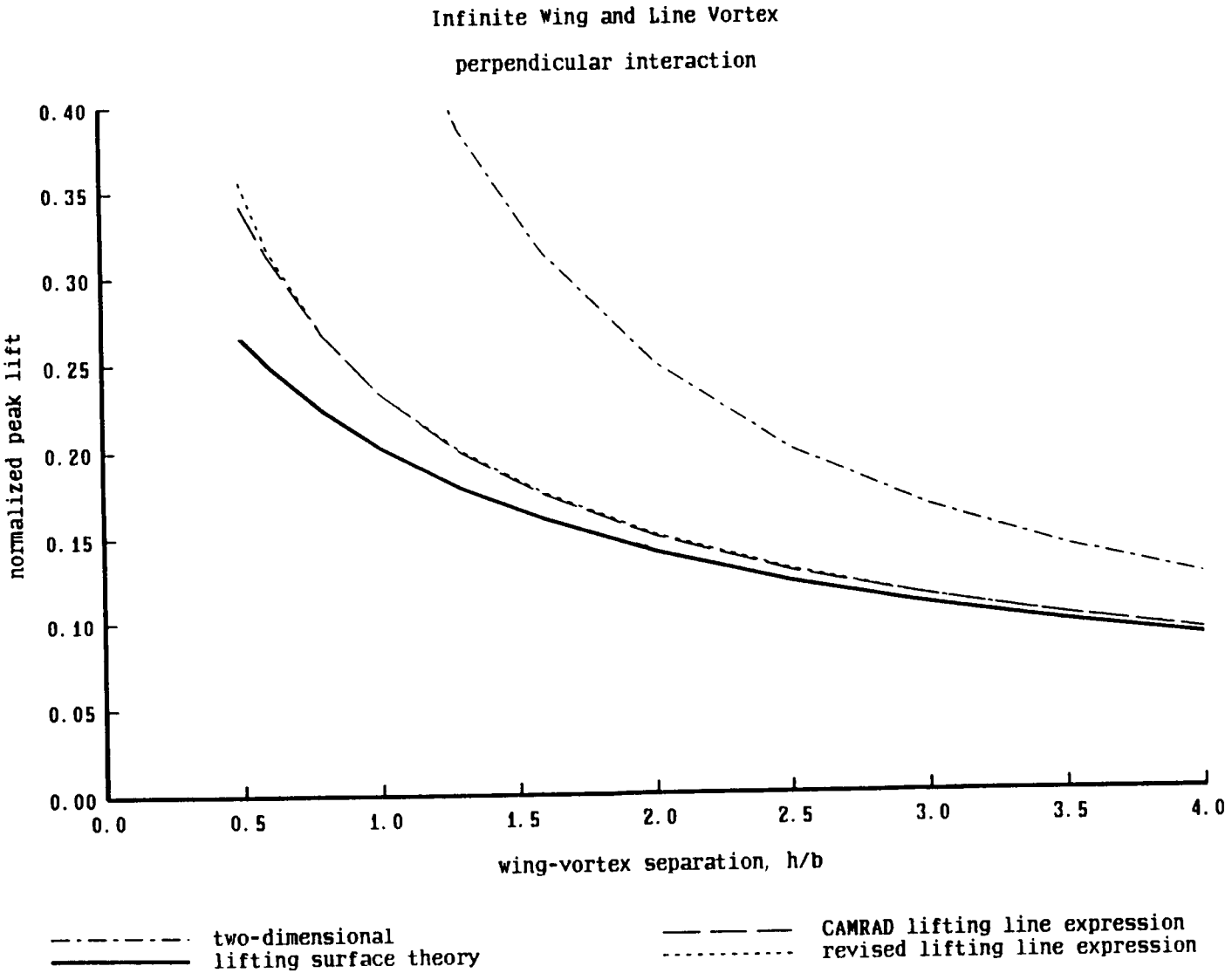

Figure 4-8b. Peak vortex-induced lift for perpendicular interaction

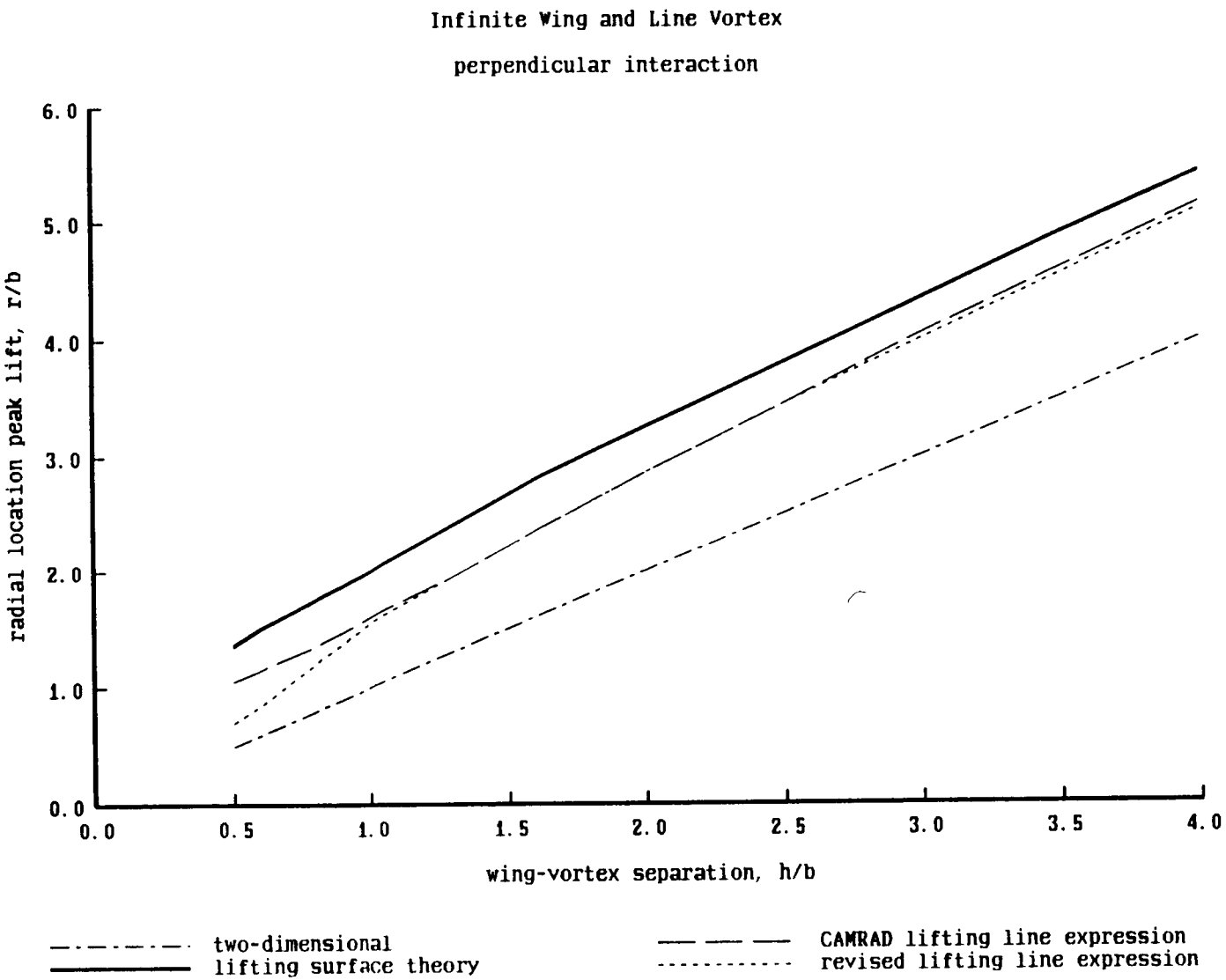

Figure 4-9. Peak vortex-induced lift for parallel interaction

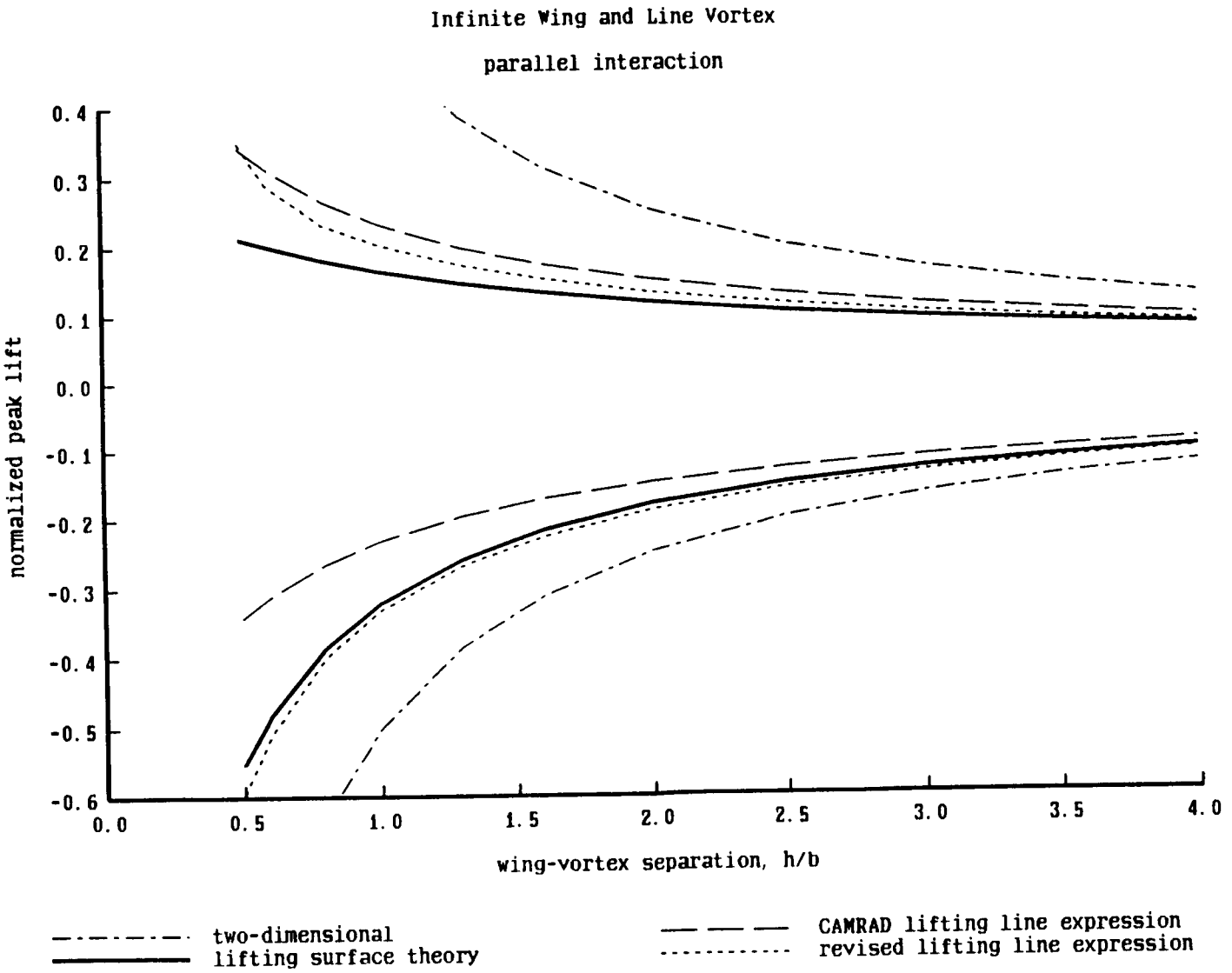

Figure 4-10. Peak vortex-induced lift for interaction 30 deg from perpendicular

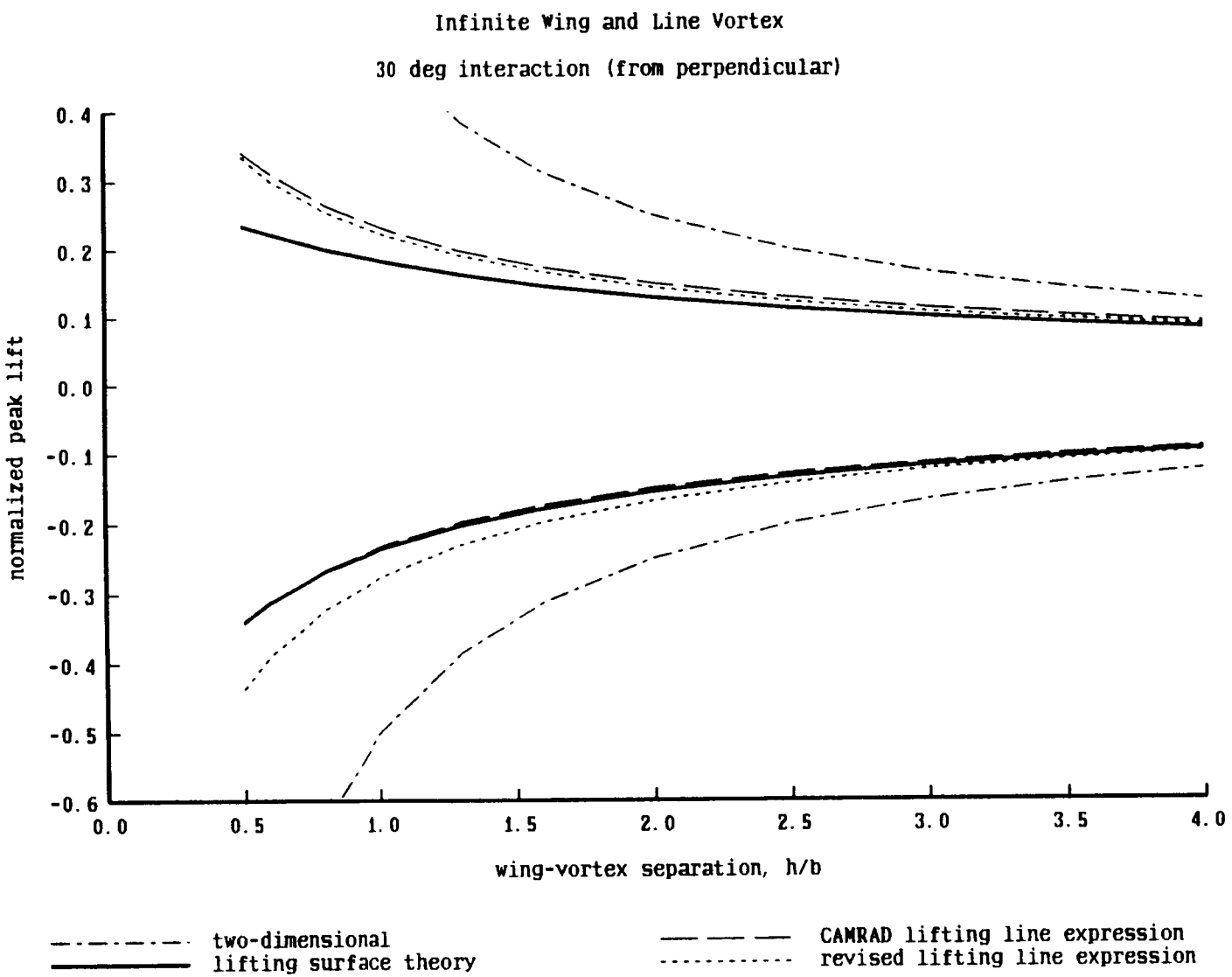

Figure 6-1a. Influence of tip vortex rollup position on loading

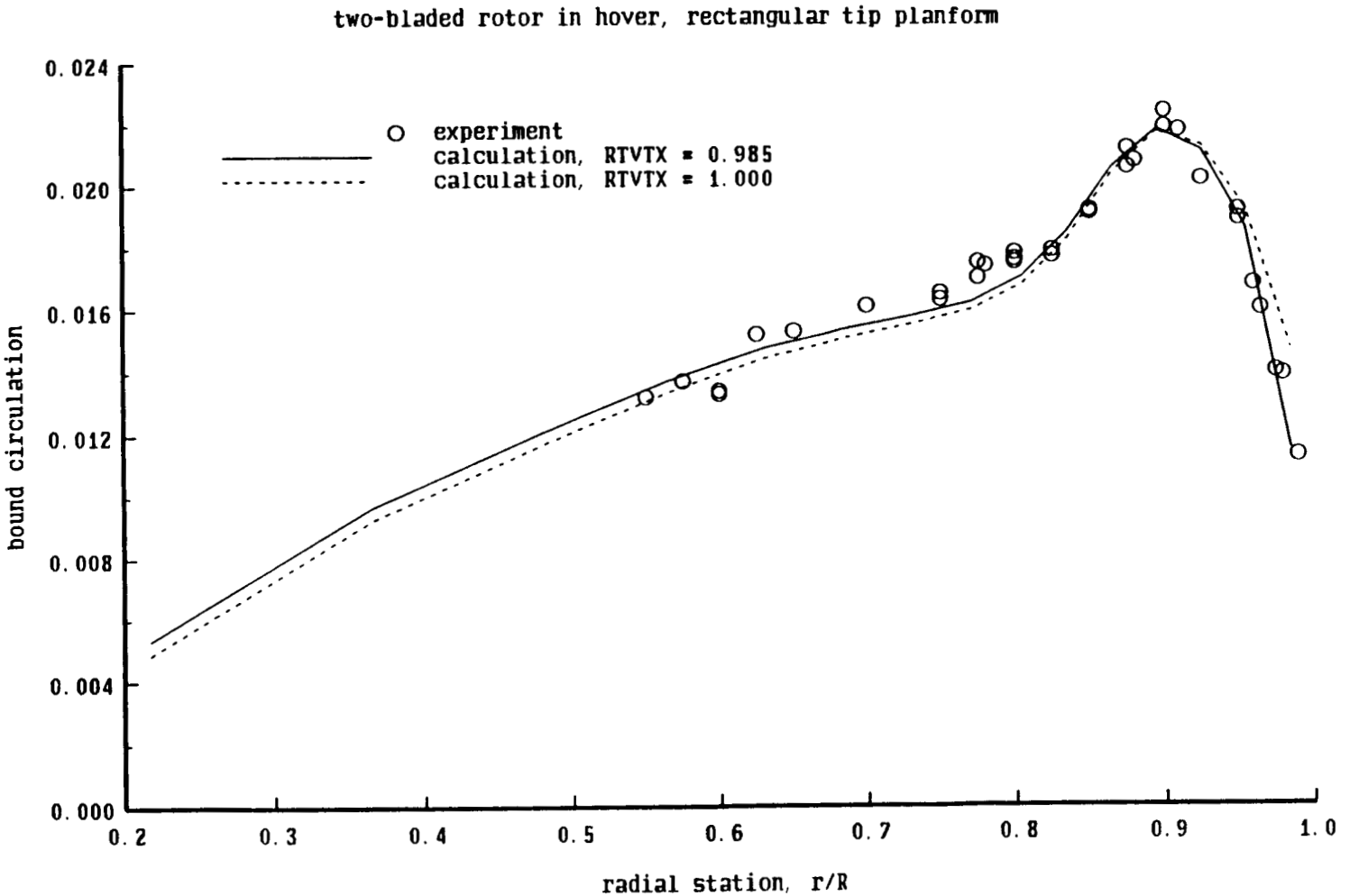

Figure 6-1b. Influence of tip vortex rollup position on loading

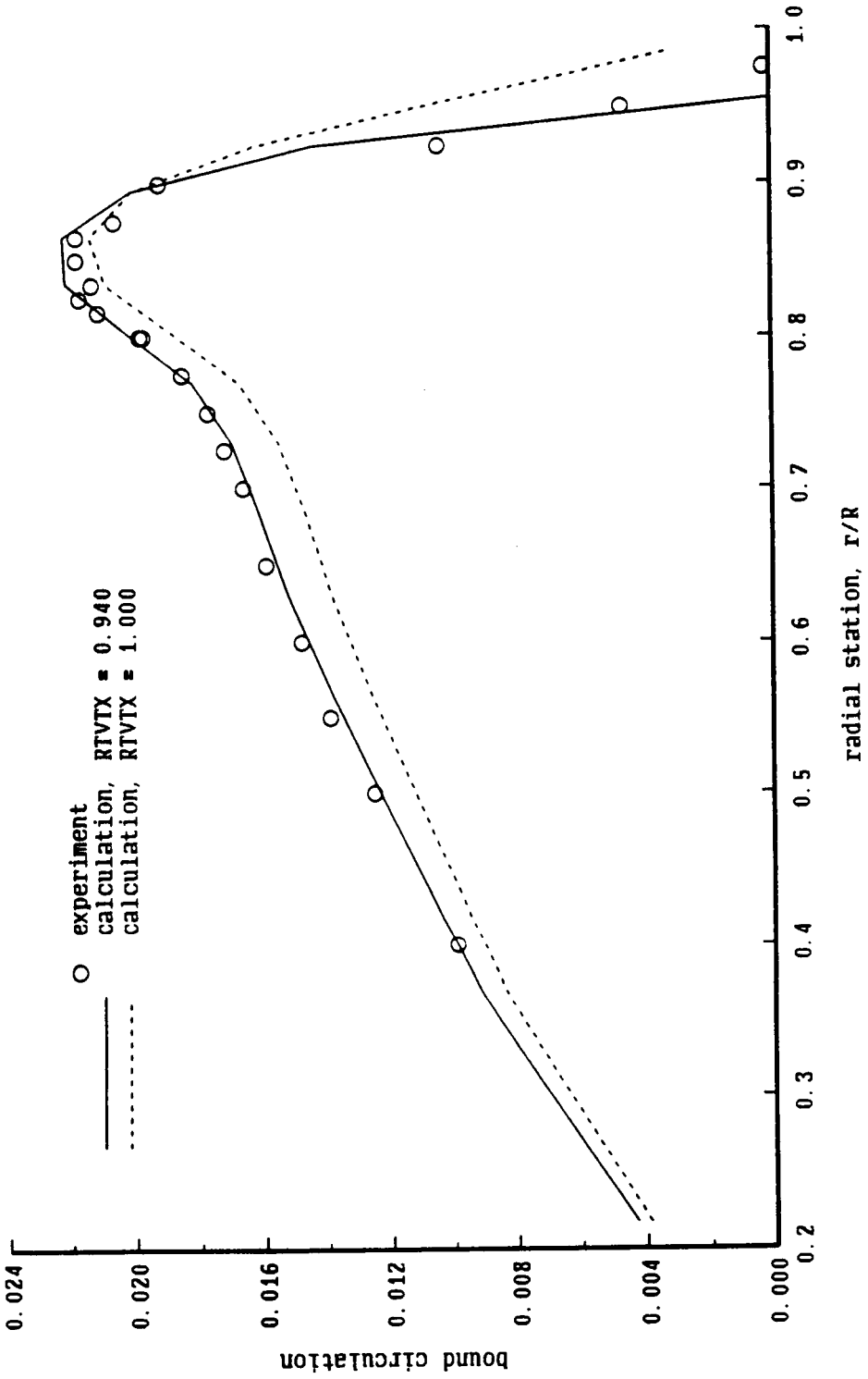

Figure 7-1a. Influence of near wake model on lateral flapping

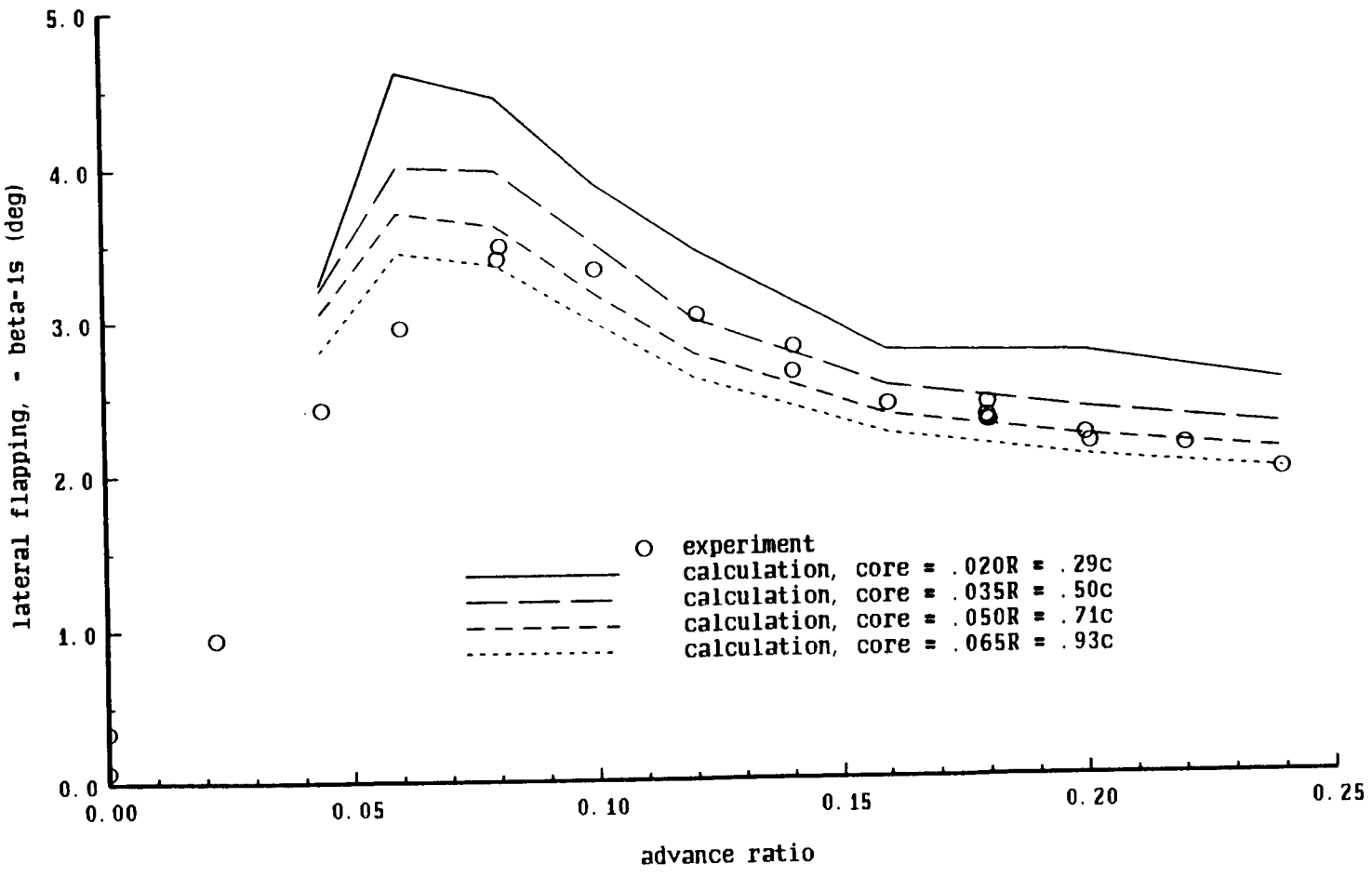

Figure 7-1b. Influence of near wake model on lateral flapping

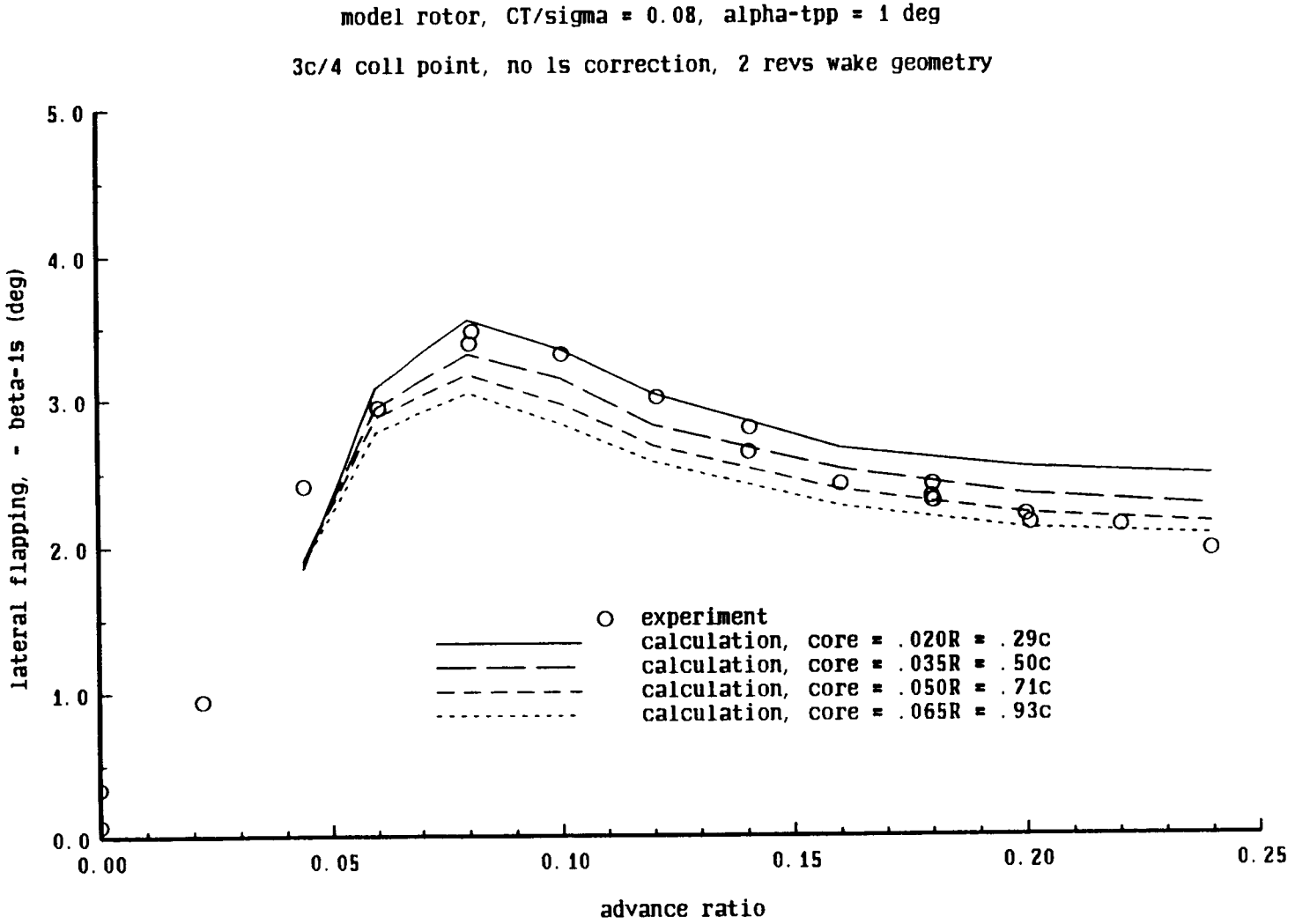

Figure 7-1c. Influence of near wake model on lateral flapping

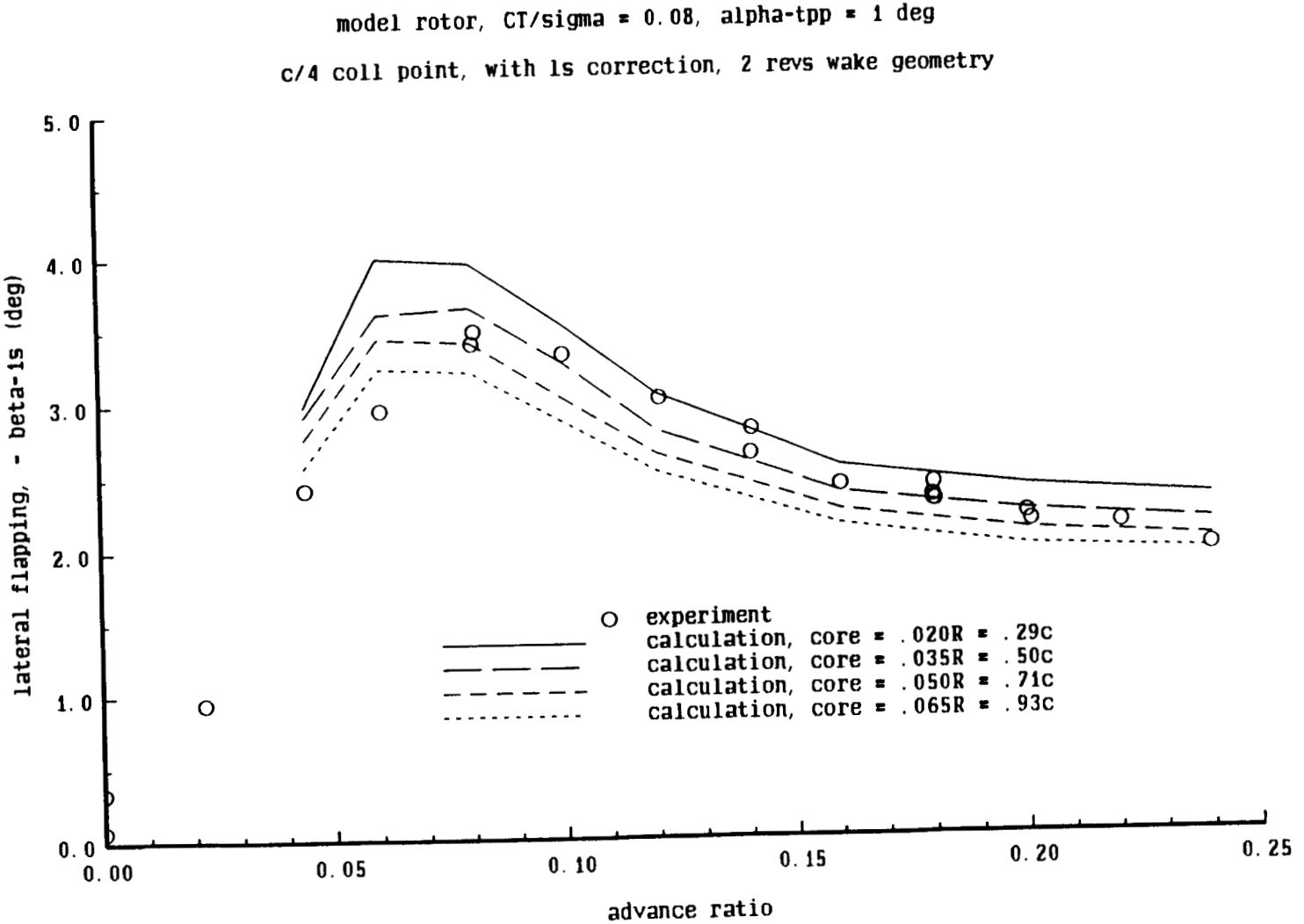

Figure 7-2a. Influence of near wake model on longitudinal flapping

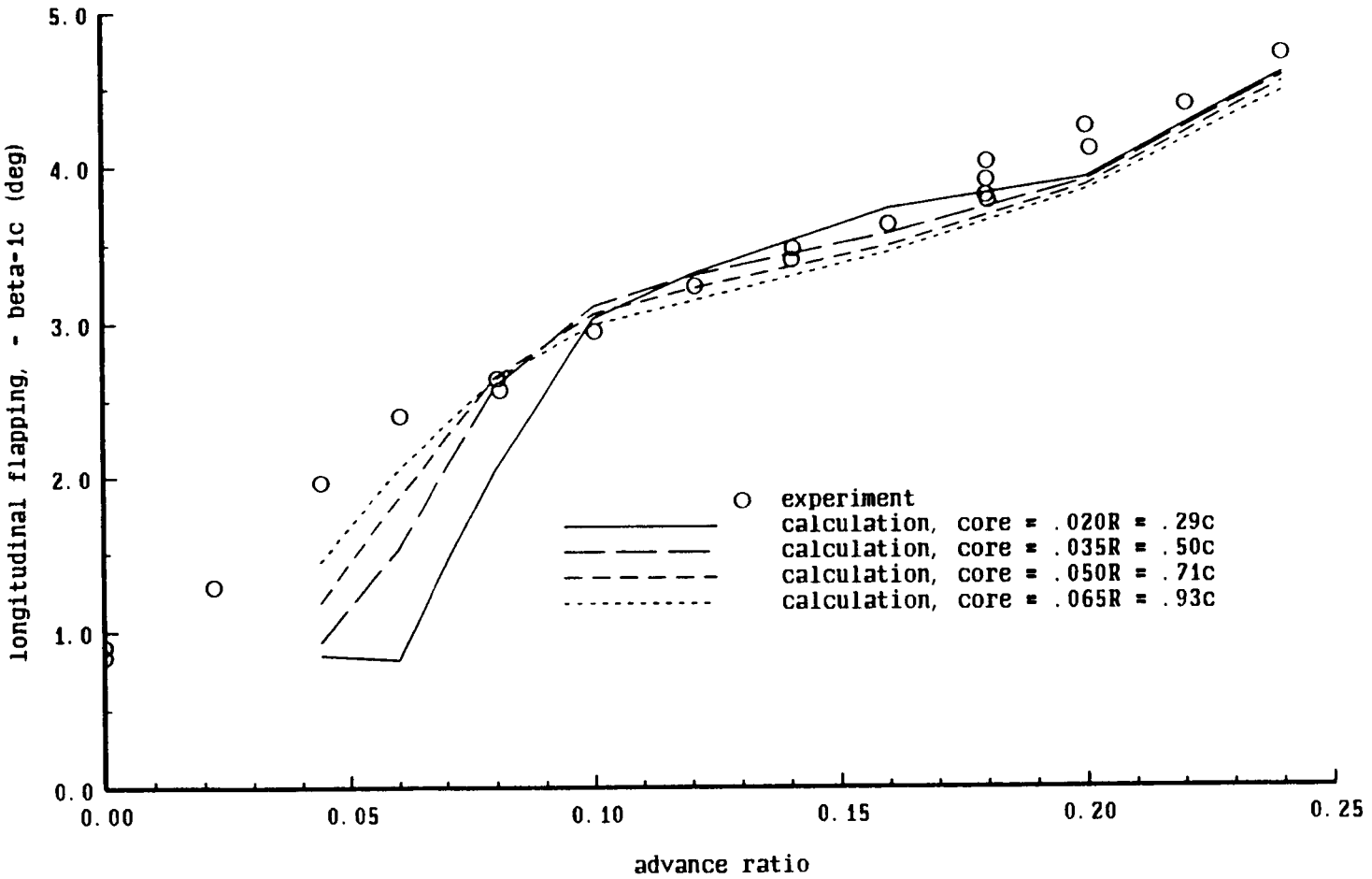

Figure 7-2b. Influence of near wake model on longitudinal flapping

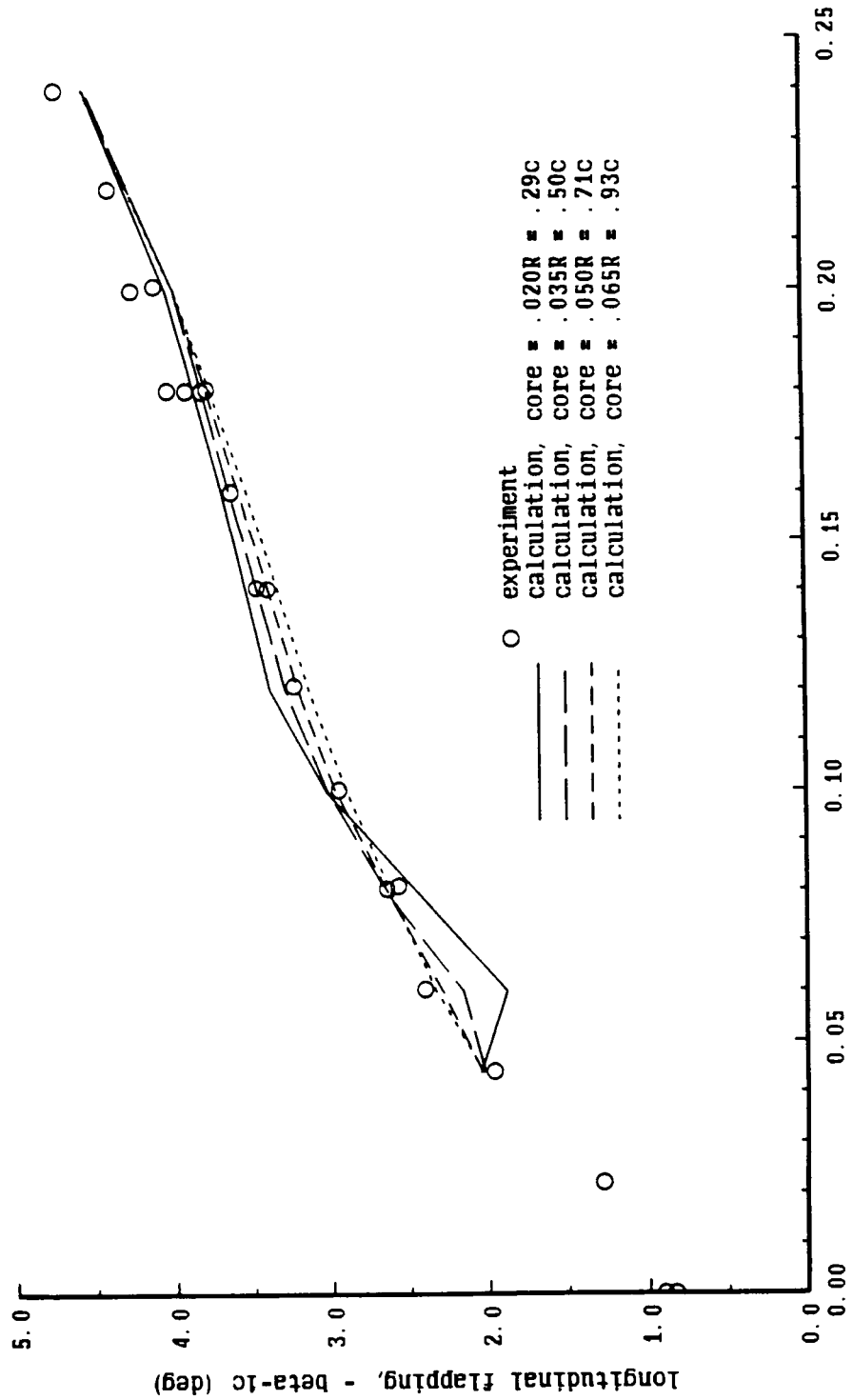

Figure 7-2c. Influence of near wake model on longitudinal flapping

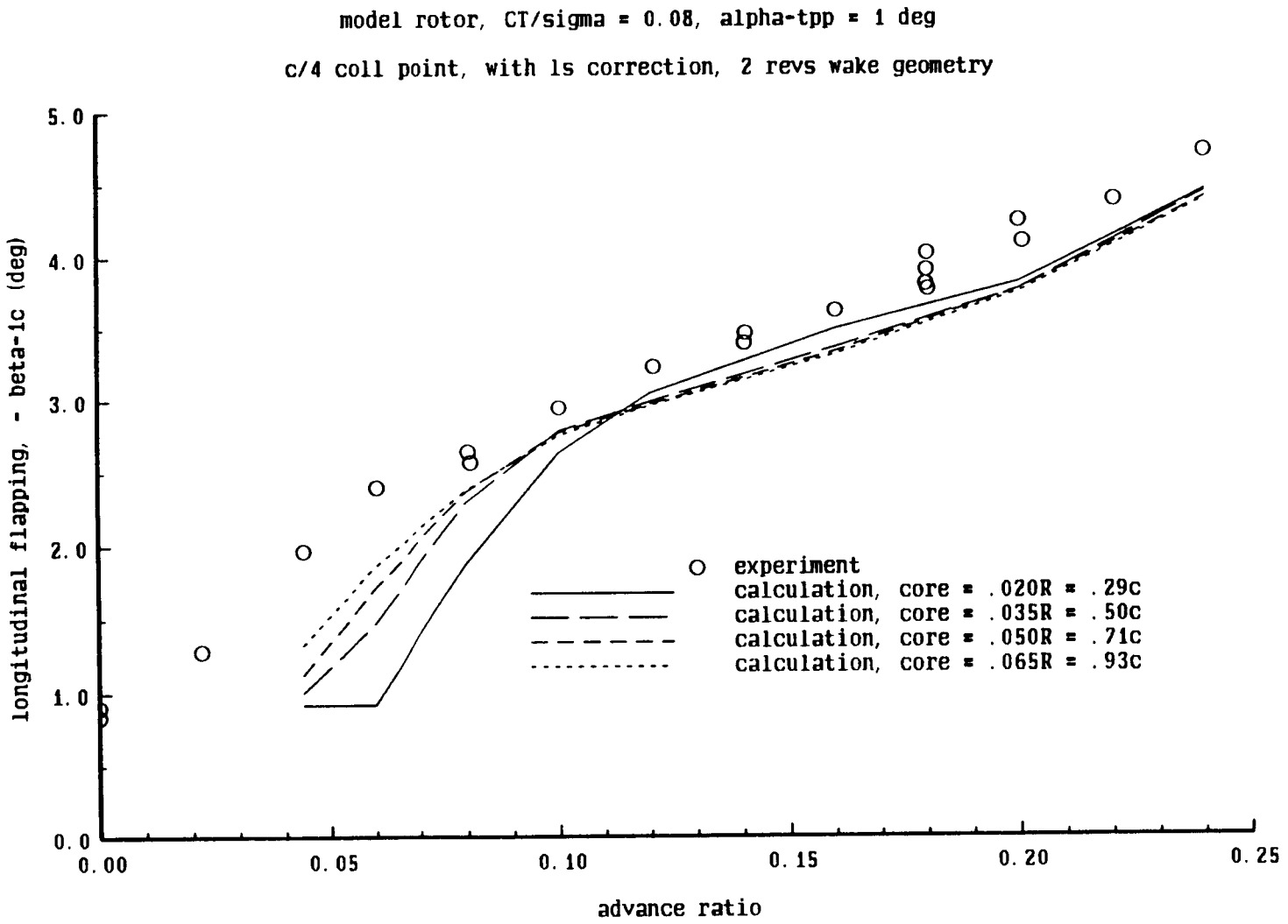

Figure 8-1a. SA349/2 helicopter: influence of nonuniform inflow and wake geometry

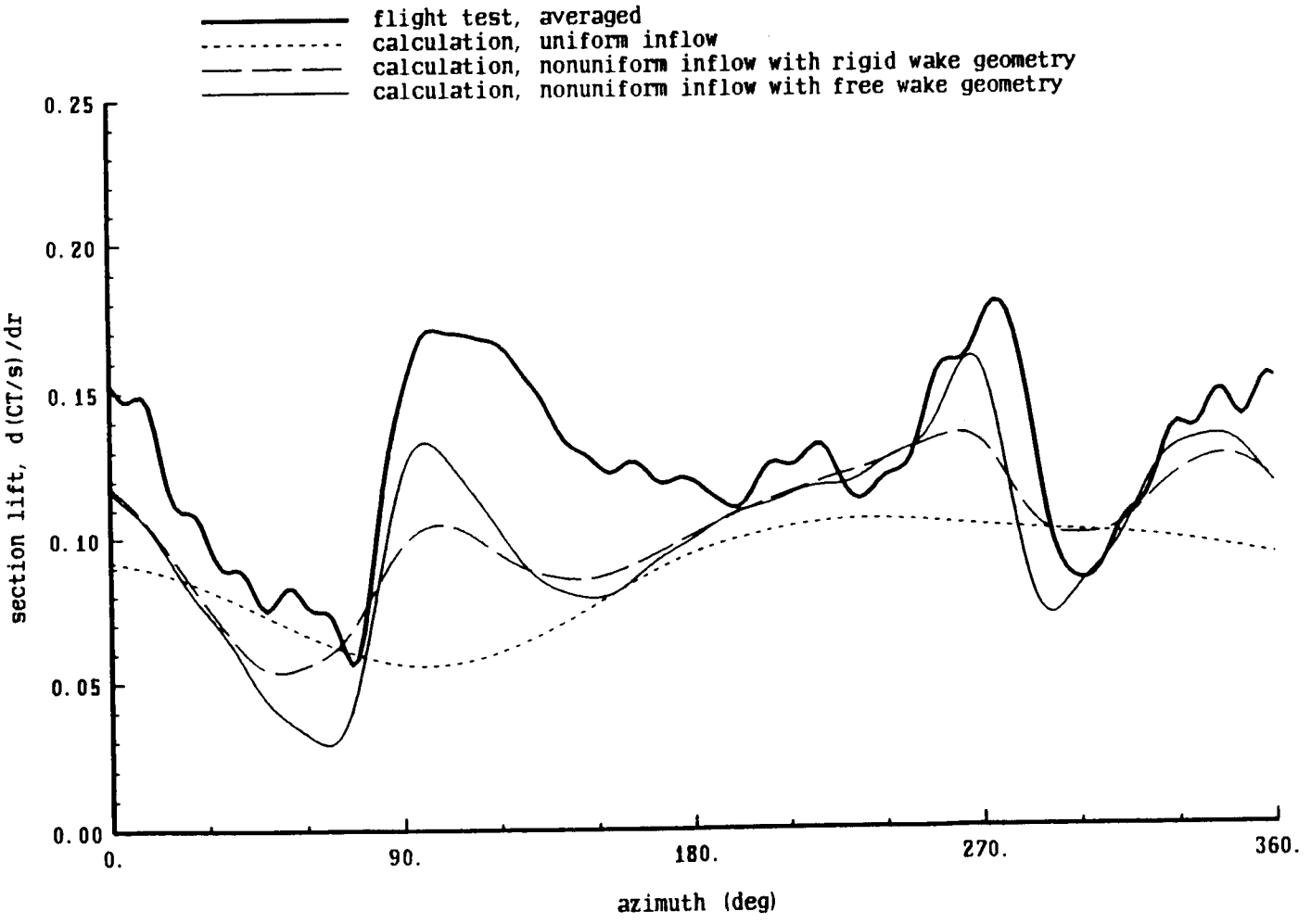

Figure 8-1b. SA349/2 helicopter: influence of nonuniform inflow and wake geometry

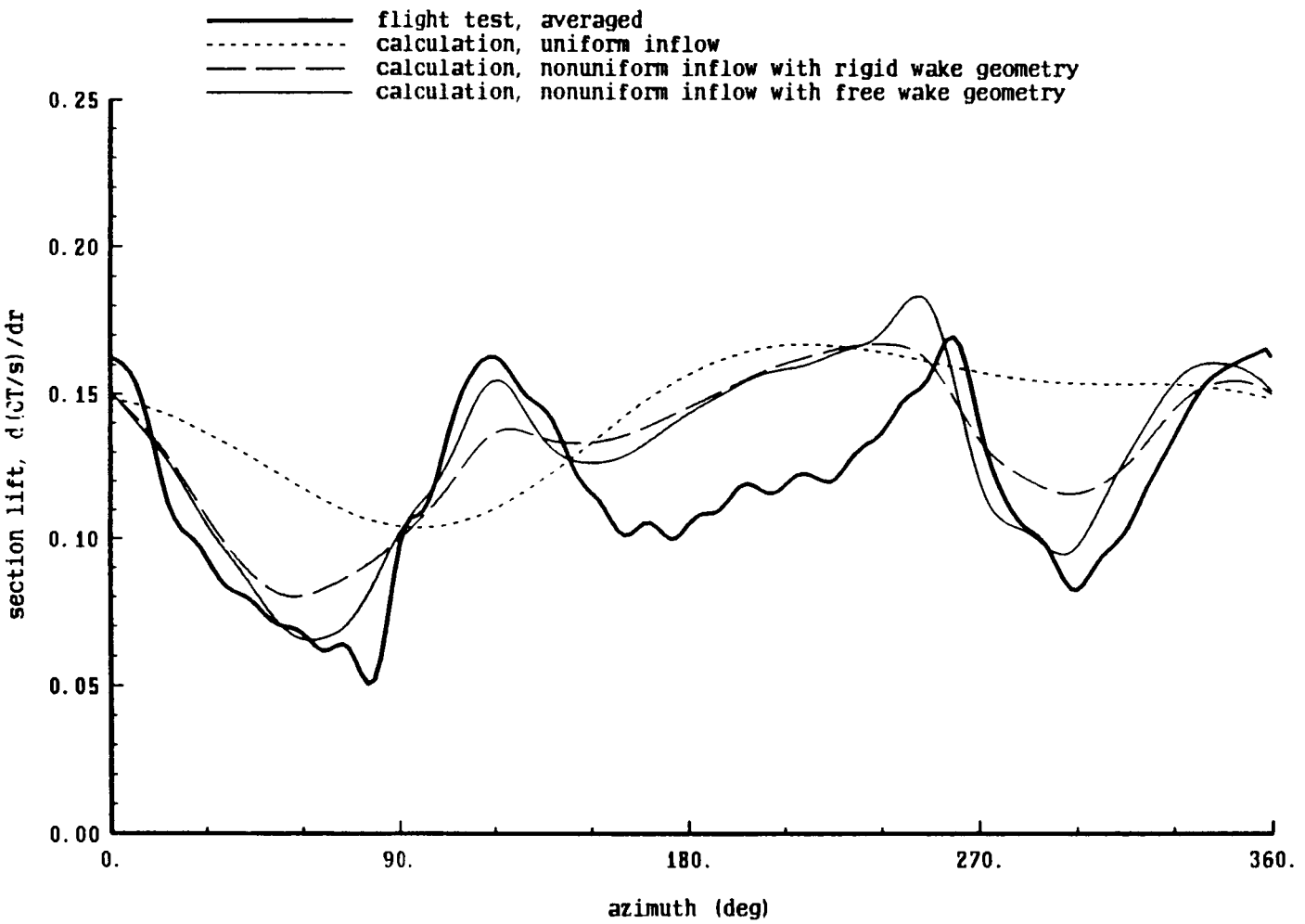

Figure 8-1c. SA349/2 helicopter: influence of nonuniform inflow and wake geometry

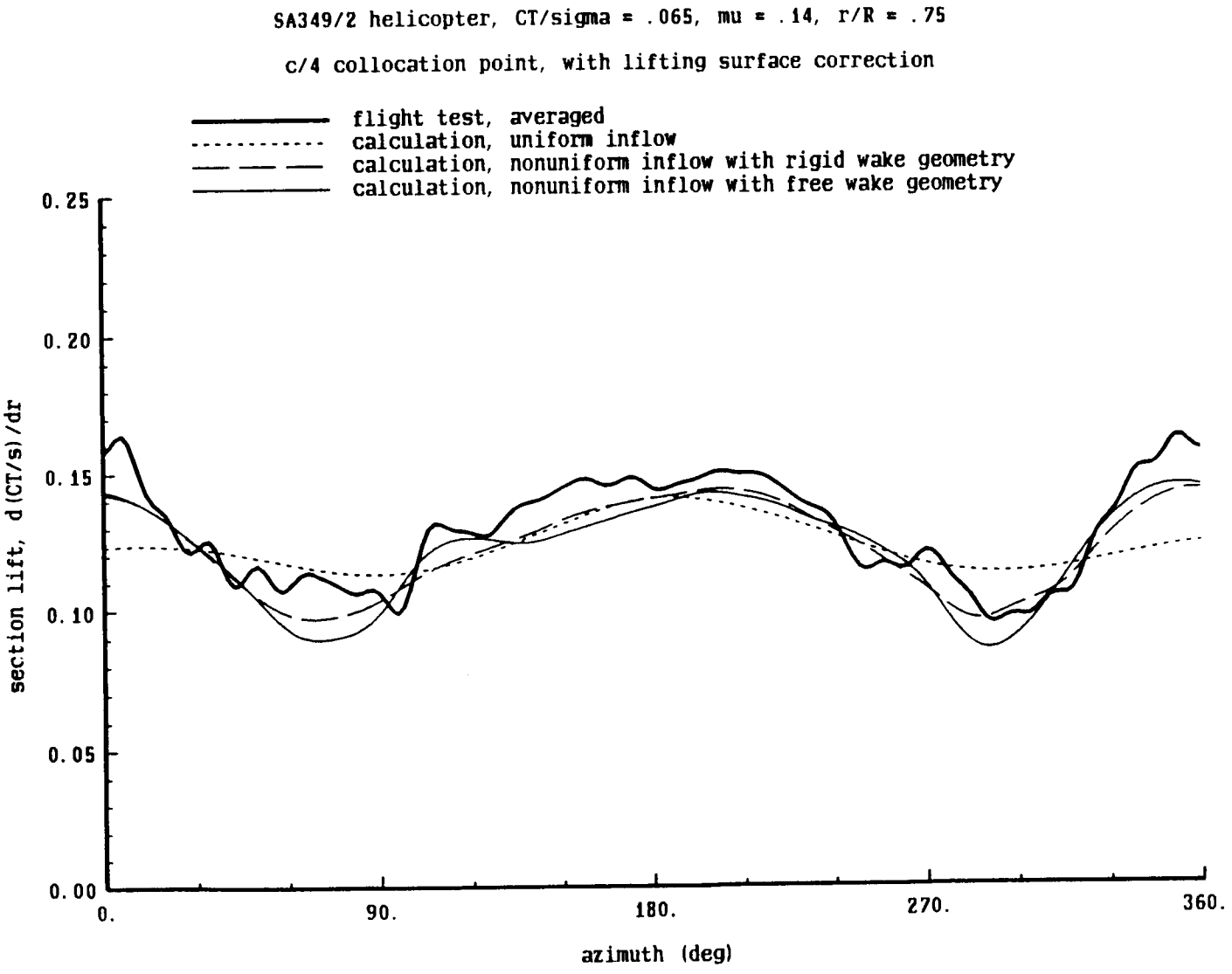

Figure 8-2. SA349/2 helicopter: calculated wake geometry

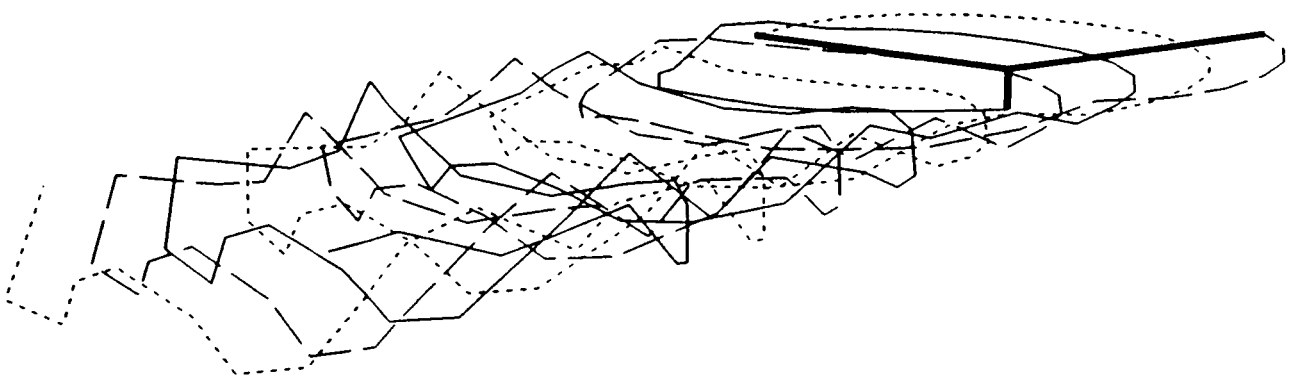

Figure 8-3a. SA349/2 helicopter: influence of tip vortex core size

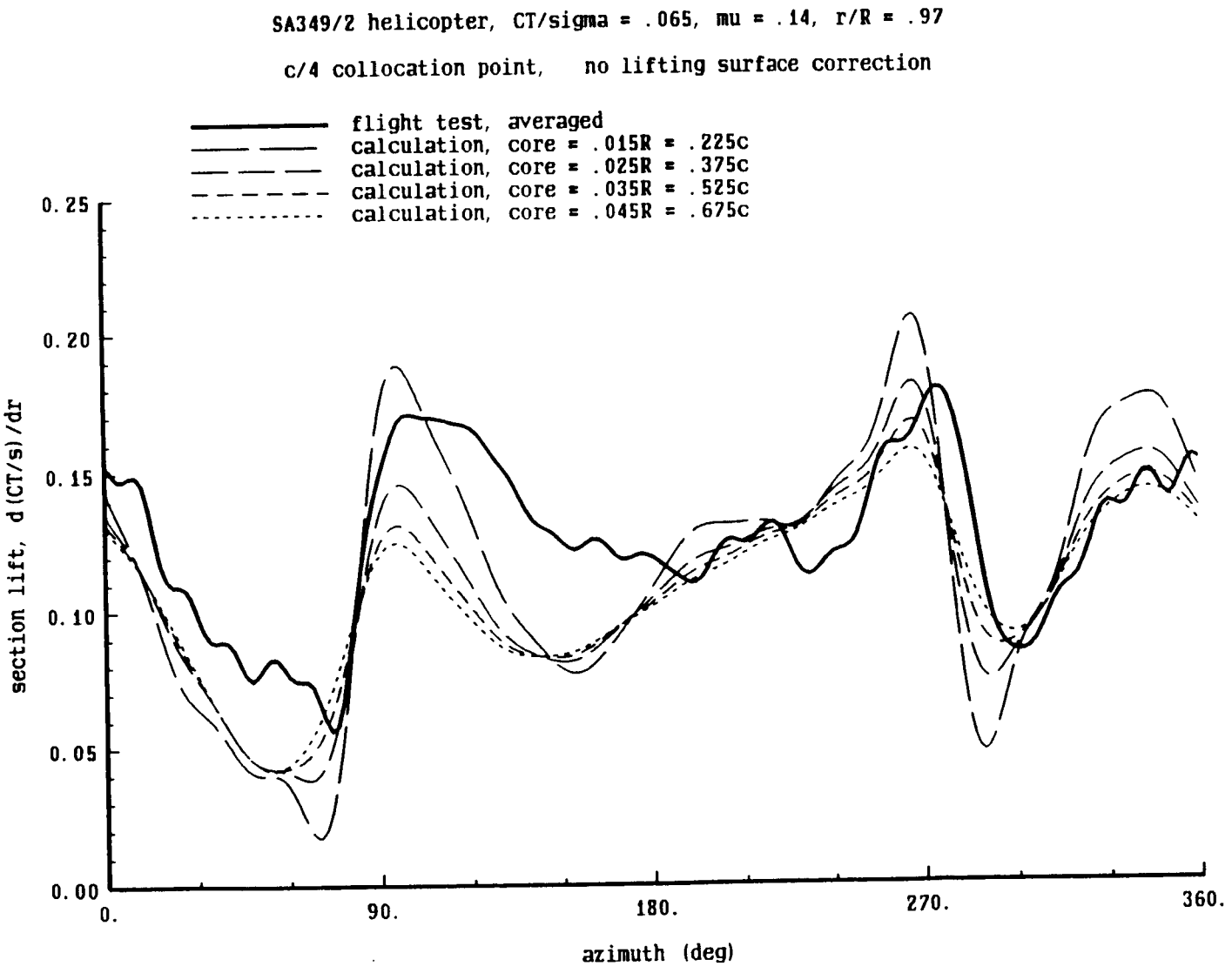

Figure 8-3b. SA349/2 helicopter: influence of tip vortex core size

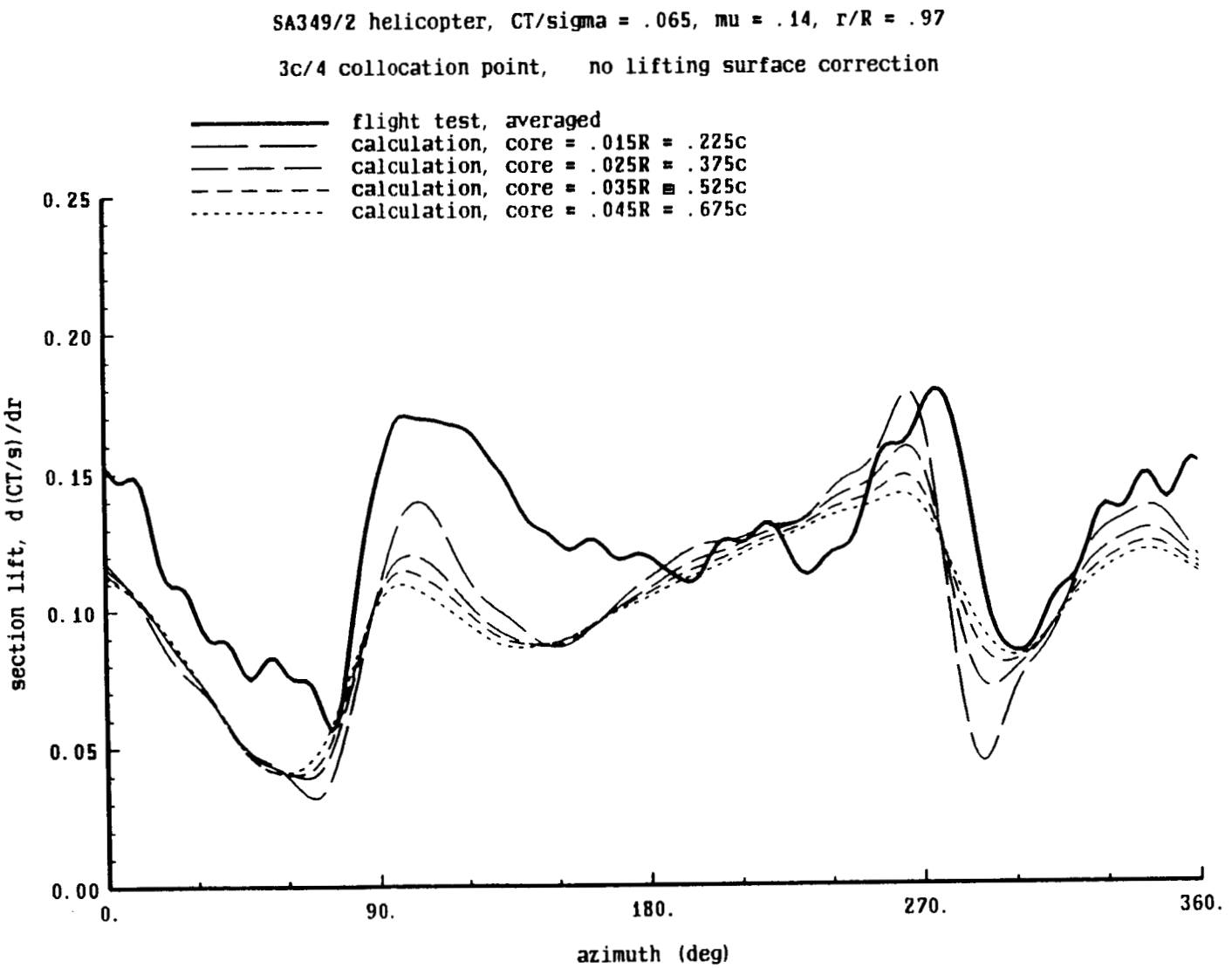

Figure 8-3c. SA349/2 helicopter: influence of tip vortex core size

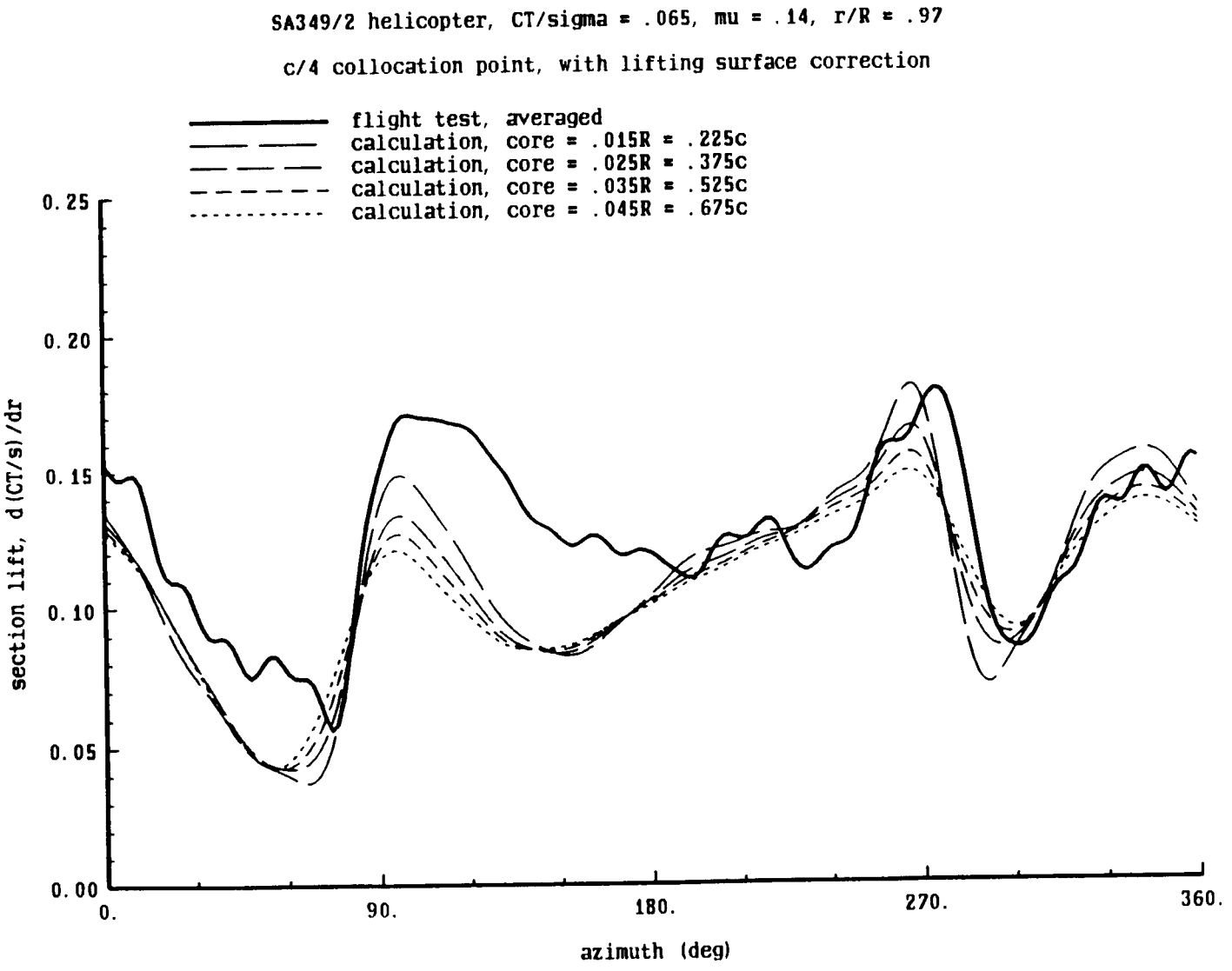

Figure 8-4a. SA349/2 helicopter: influence of tip vortex core size

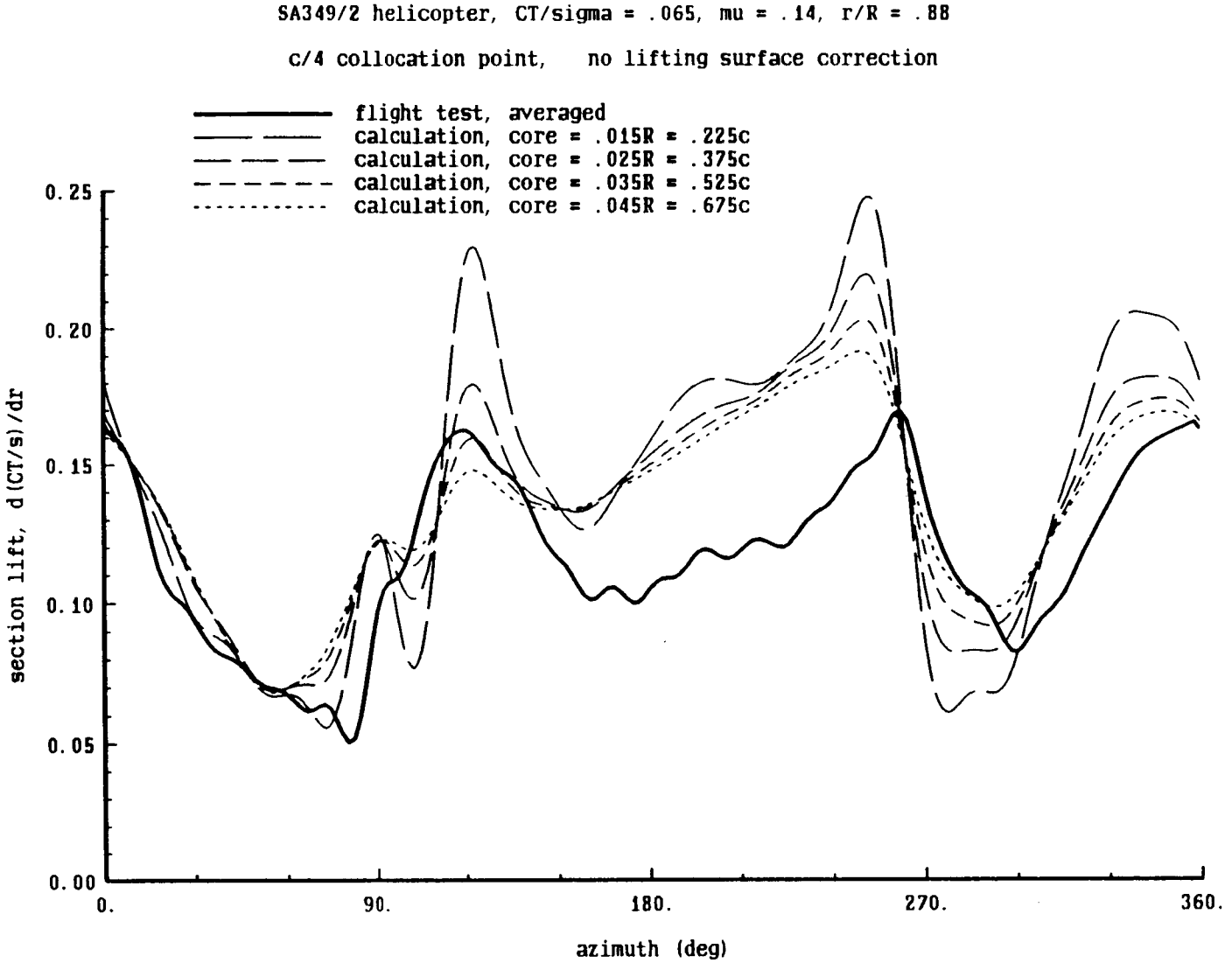

Figure 8-4b. SA349/2 helicopter: influence of tip vortex core size

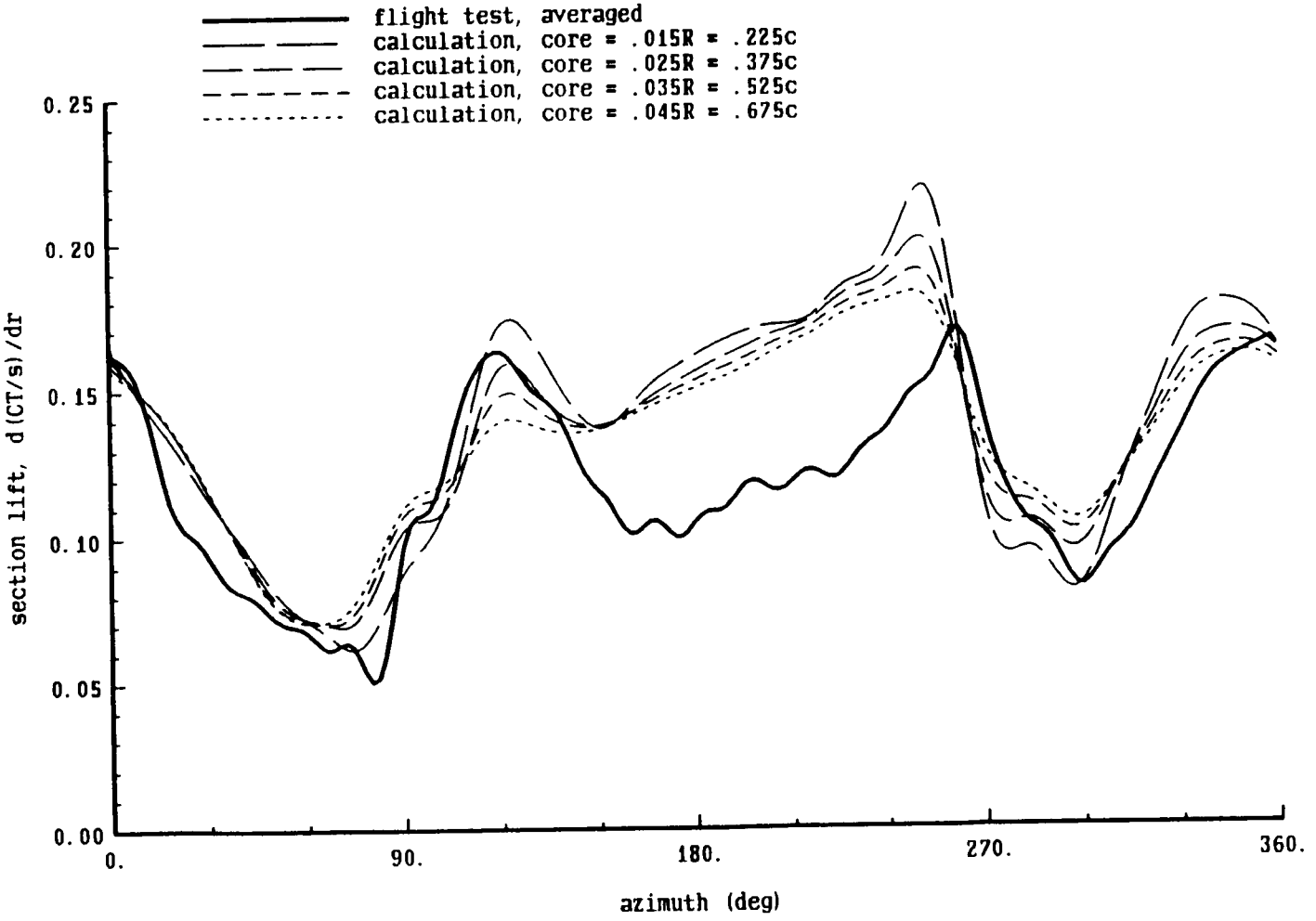

Figure 8-4c. SA349/2 helicopter: influence of tip vortex core size

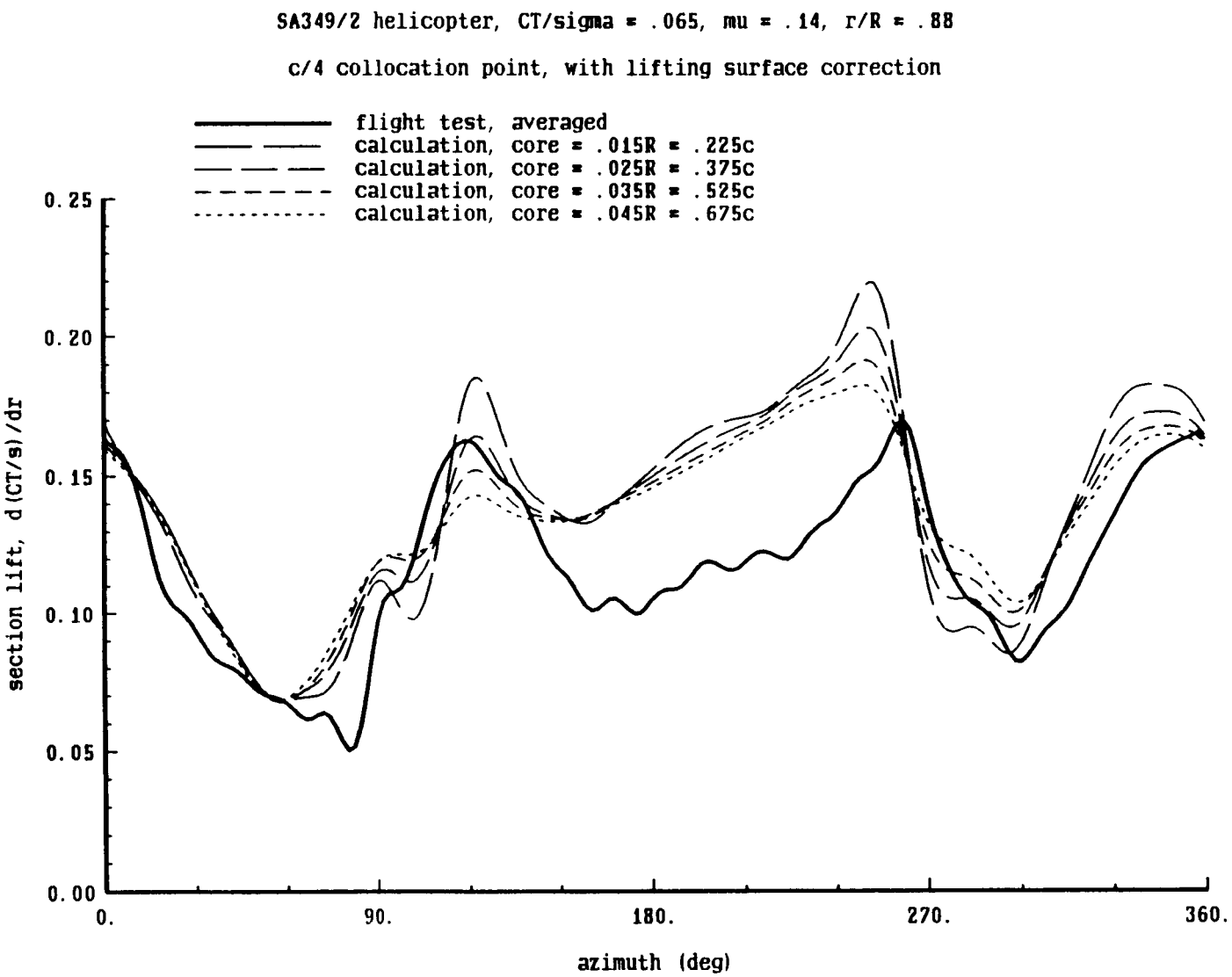

Figure 8-5a. SA349/2 helicopter: influence of tip vortex core size

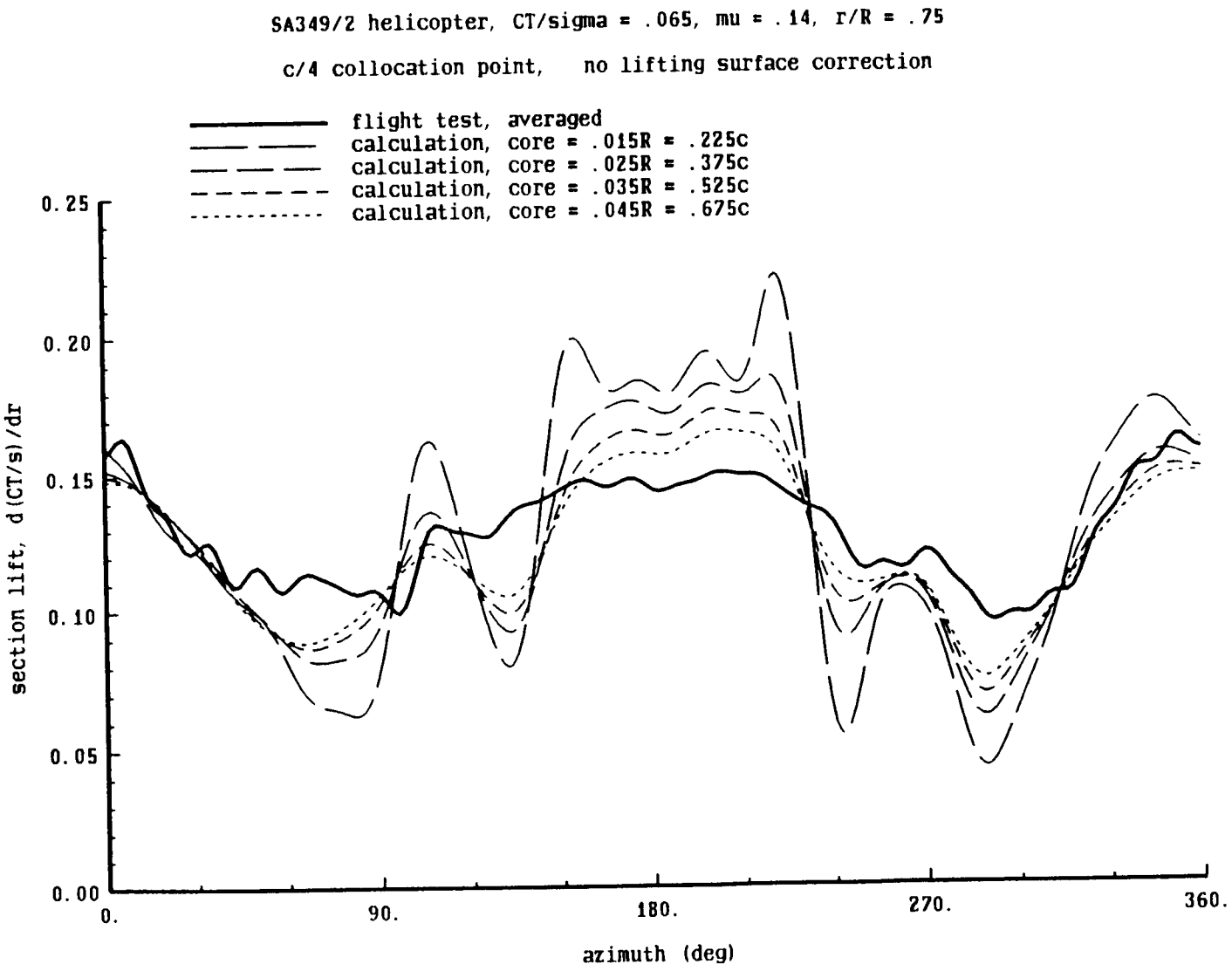

Figure 8-5b. SA349/2 helicopter: influence of tip vortex core size

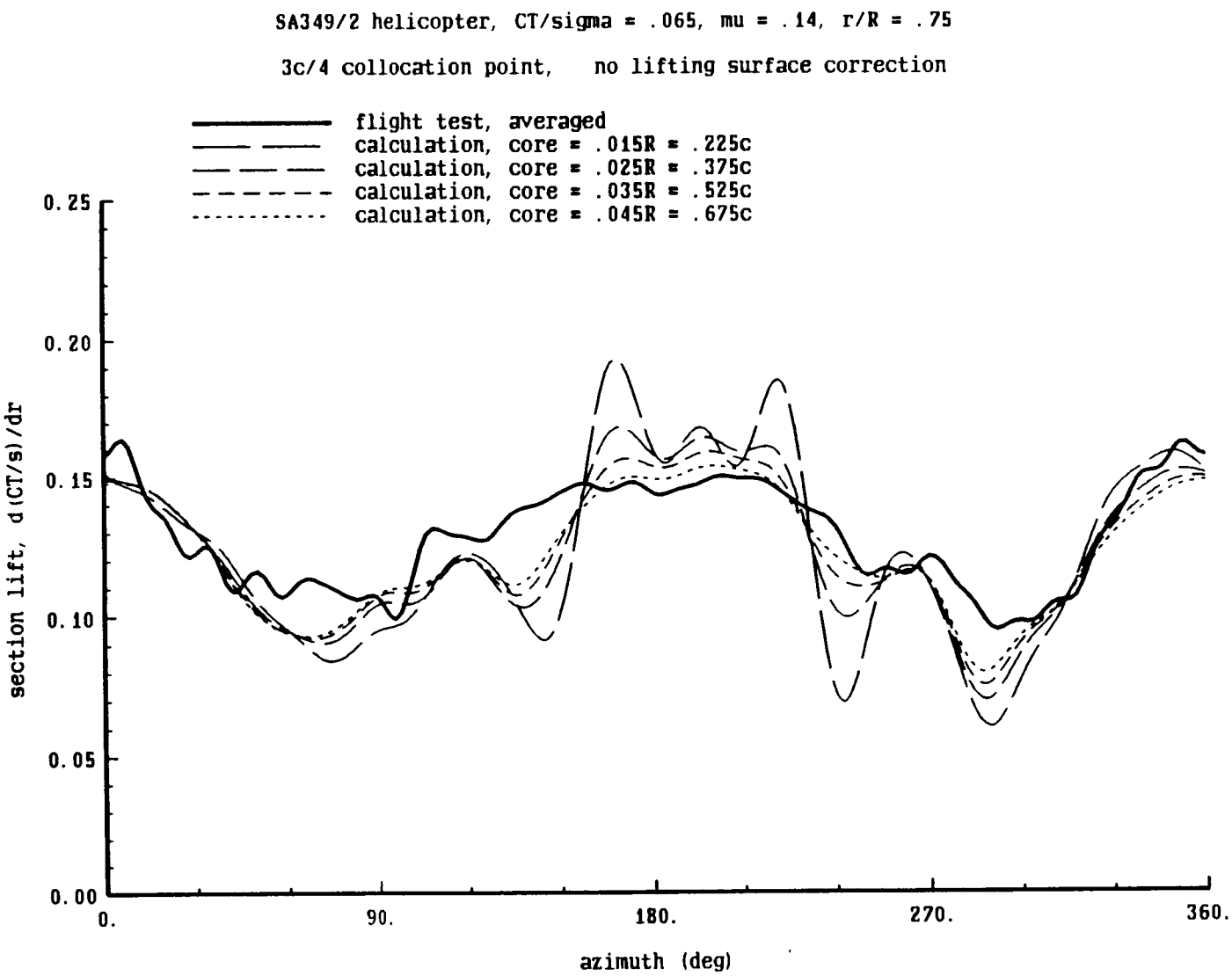

Figure 8-5c. SA349/2 helicopter: influence of tip vortex core size

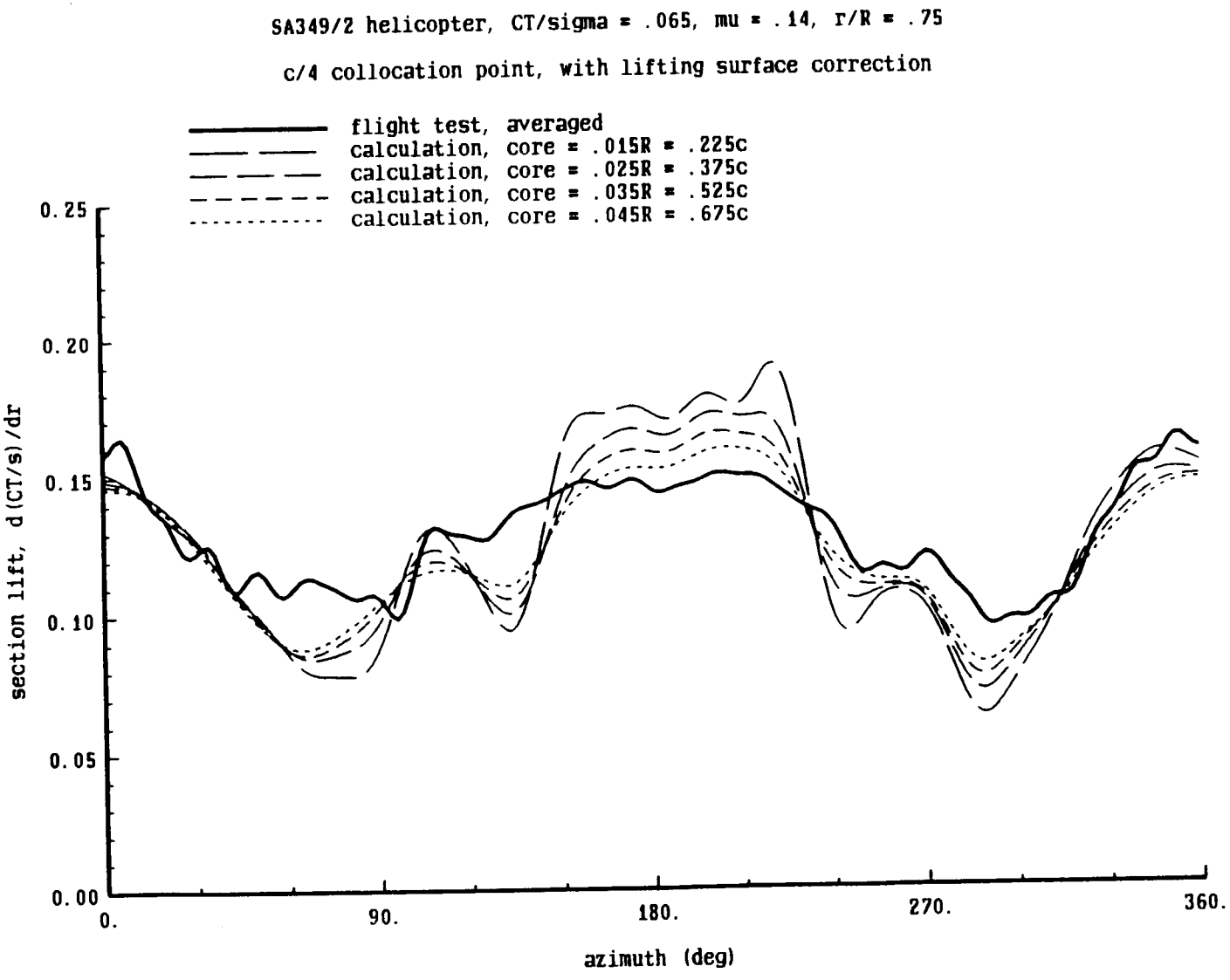

Figure 8-6a. SA349/2 helicopter: influence of near wake model

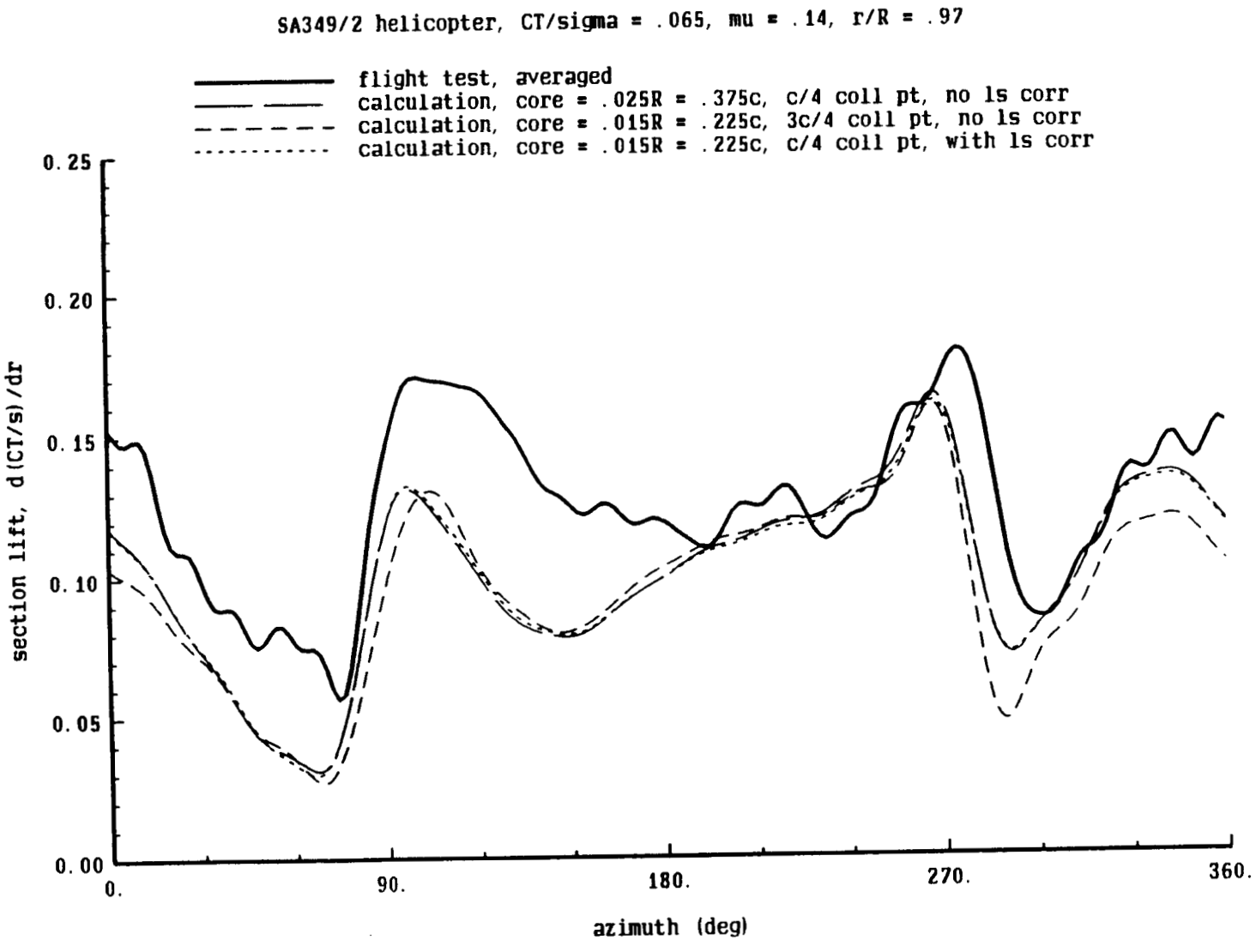

Figure 8-6b. SA349/2 helicopter: influence of near wake model

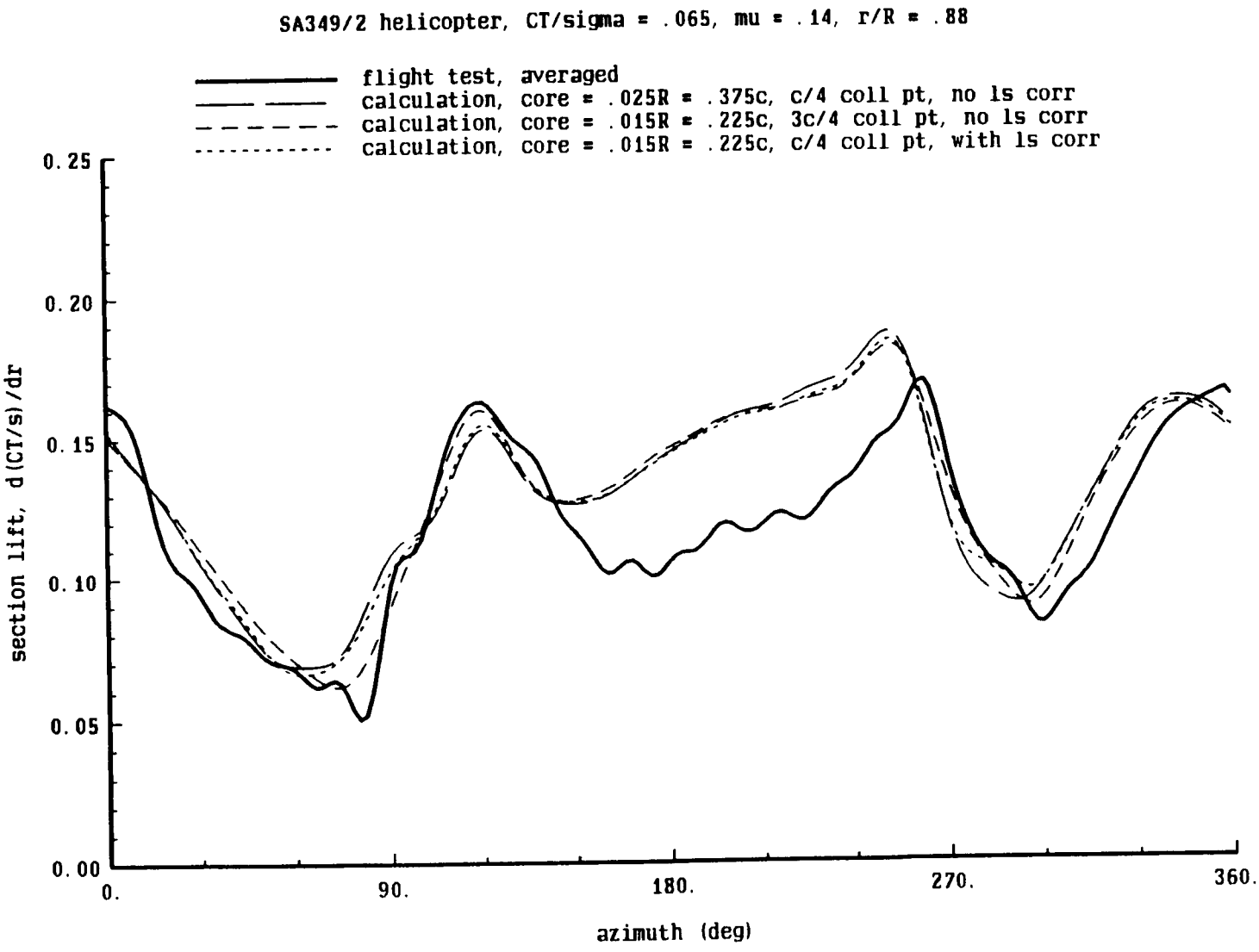

Figure 8-6c. SA349/2 helicopter: influence of near wake model

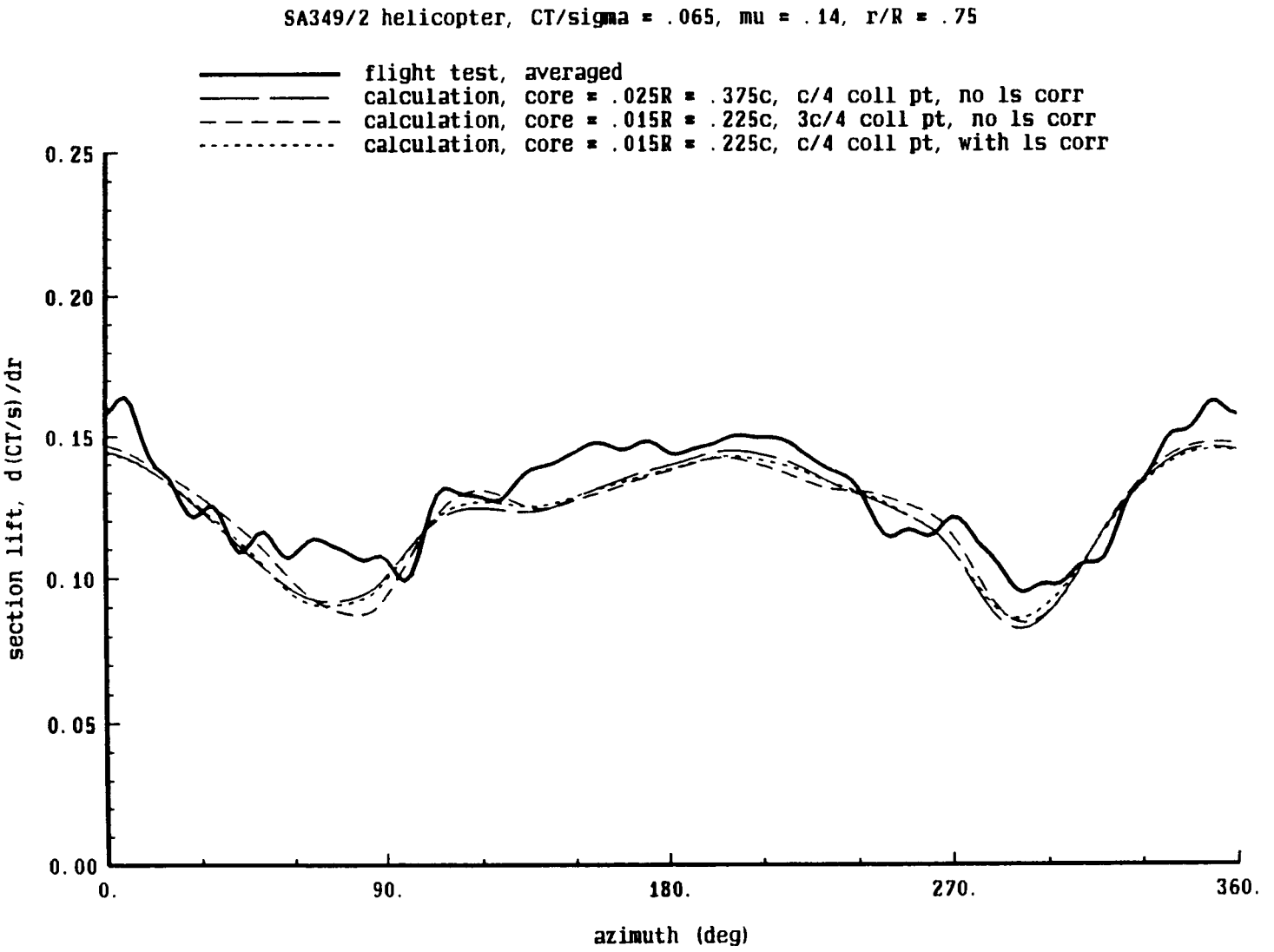

Figure 8-7a. SA349/2 helicopter: influence of inboard blade-vortex interaction

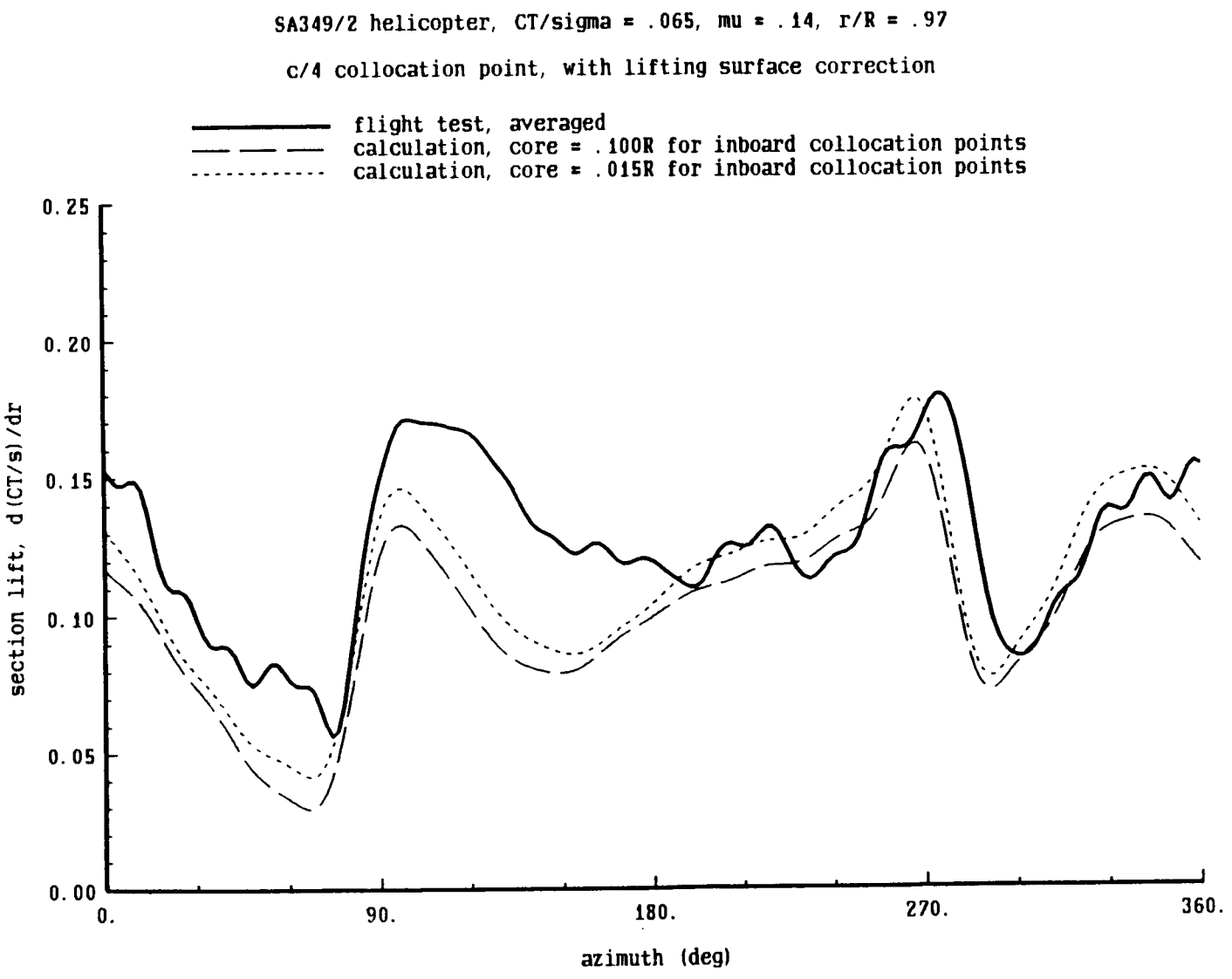

Figure 8-7b. SA349/2 helicopter: influence of inboard blade-vortex interaction

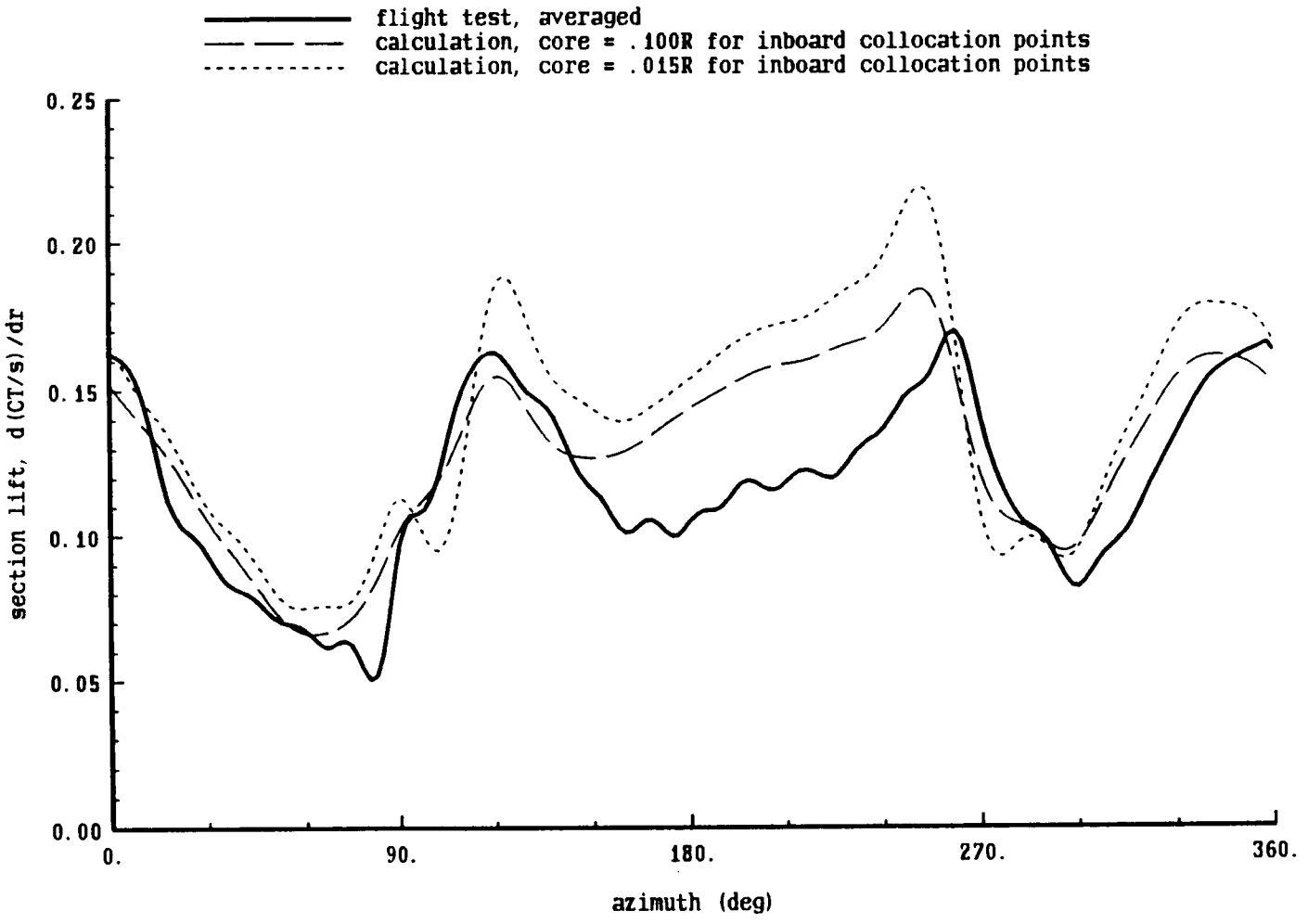

Figure 8-7c. SA349/2 helicopter: influence of inboard blade-vortex interaction

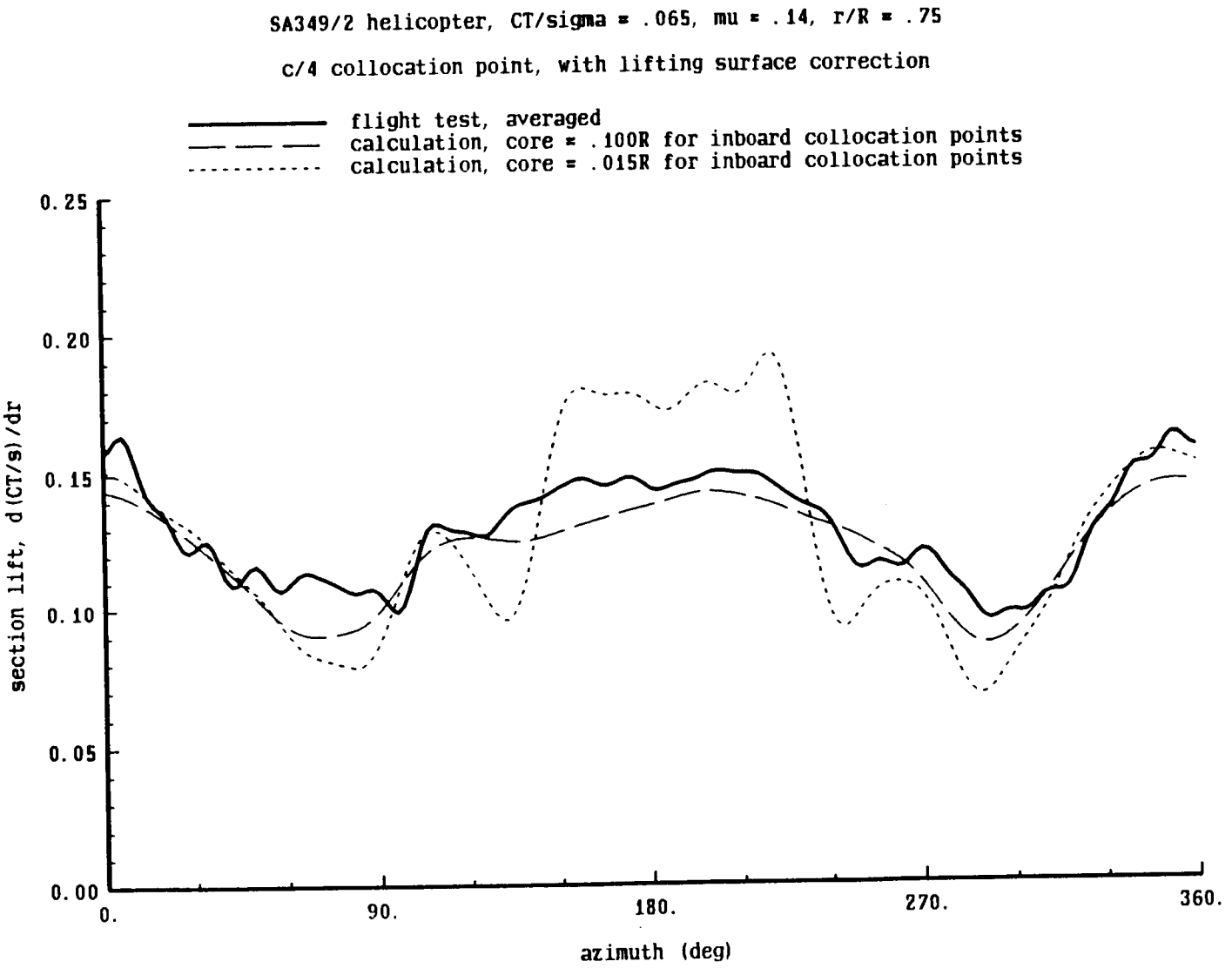

Figure 8-8a. SA349/2 helicopter: comparison with unaverged test data

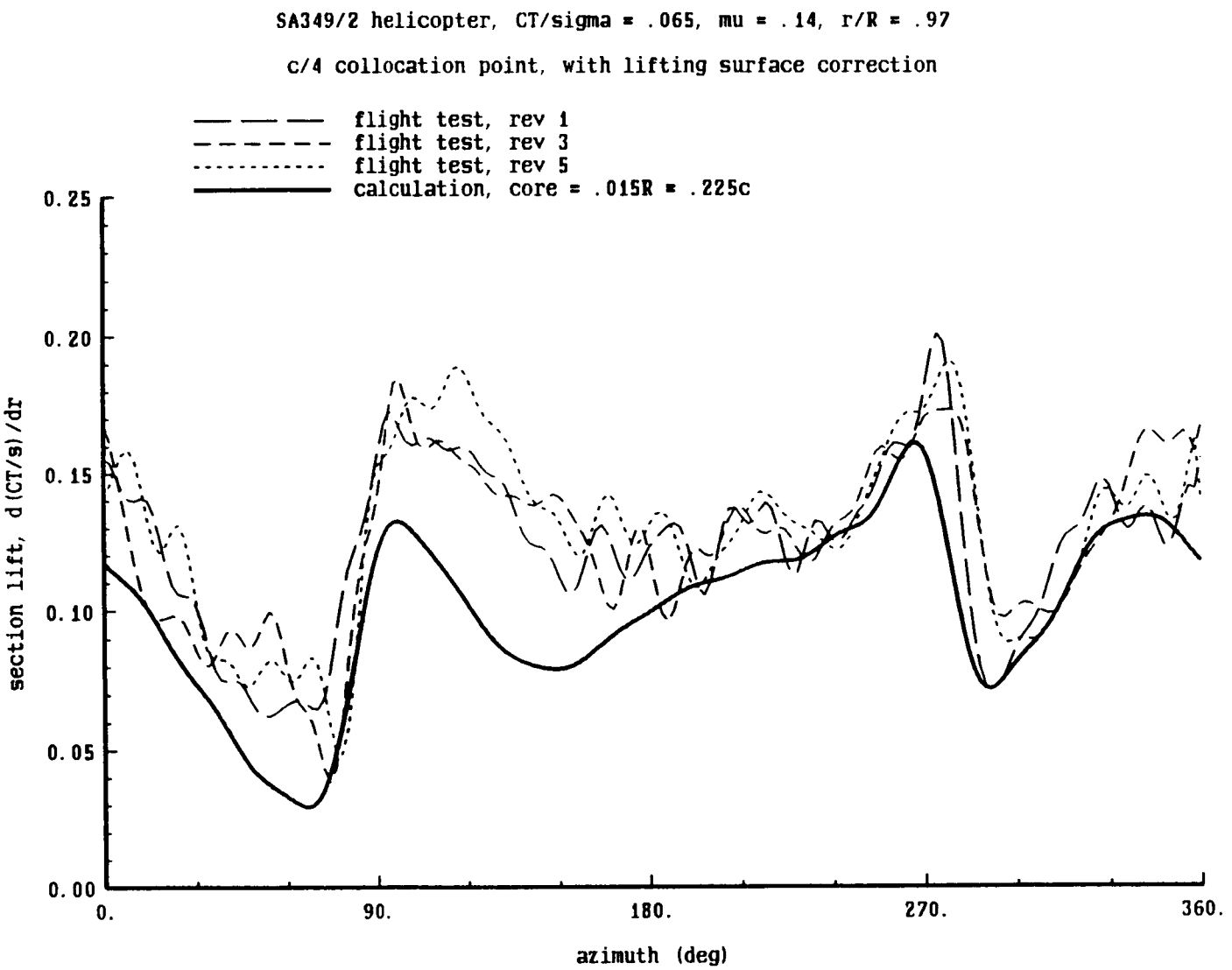

Figure 8-8b. SA349/2 helicopter: comparison with unaverged test data

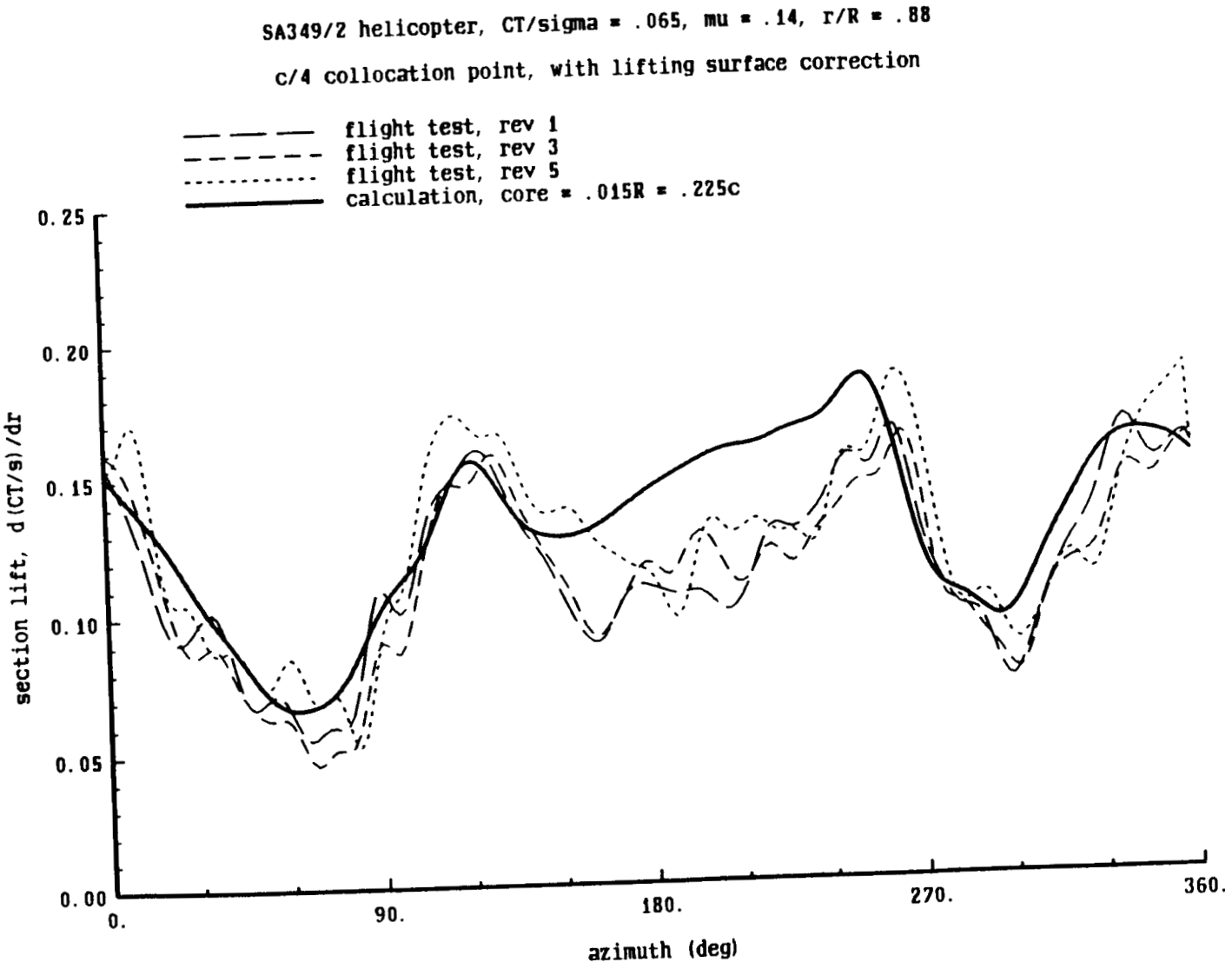

Figure 8-8c. SA349/2 helicopter: comparison with unaverged test data

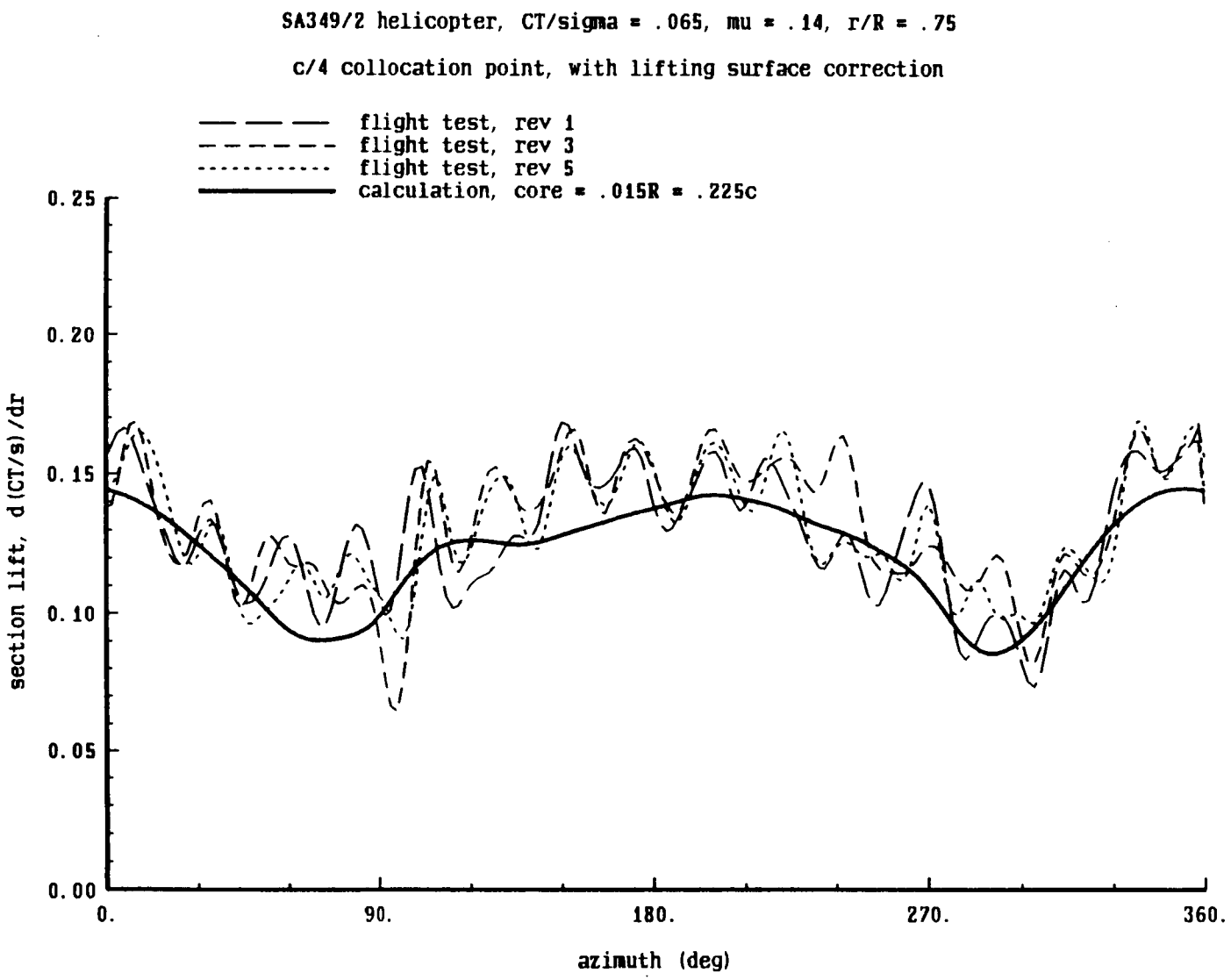

Figure 9-1a. Influence of wake and wing model for swept tips

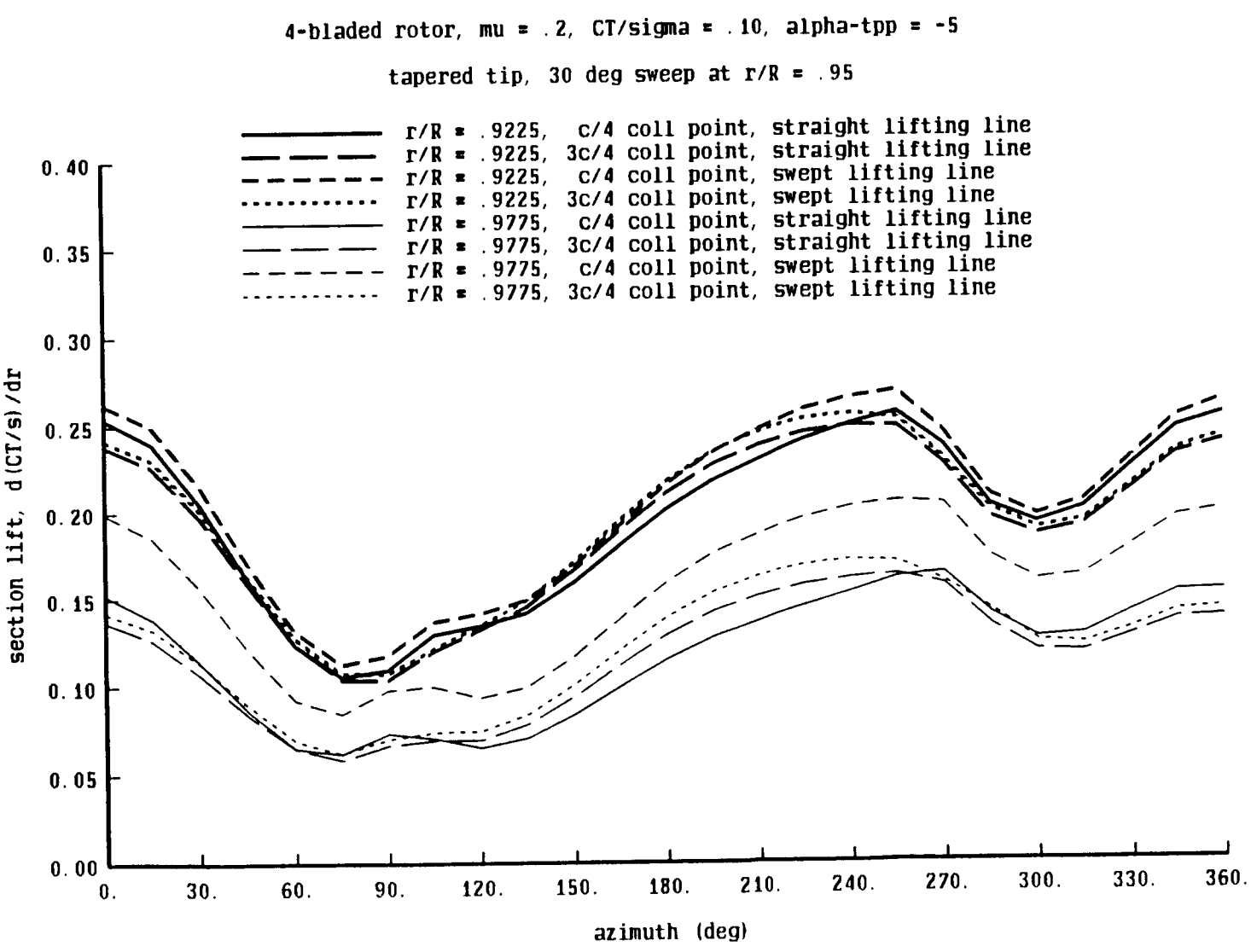

Figure 9-1b. Influence of wake and wing model for swept tips

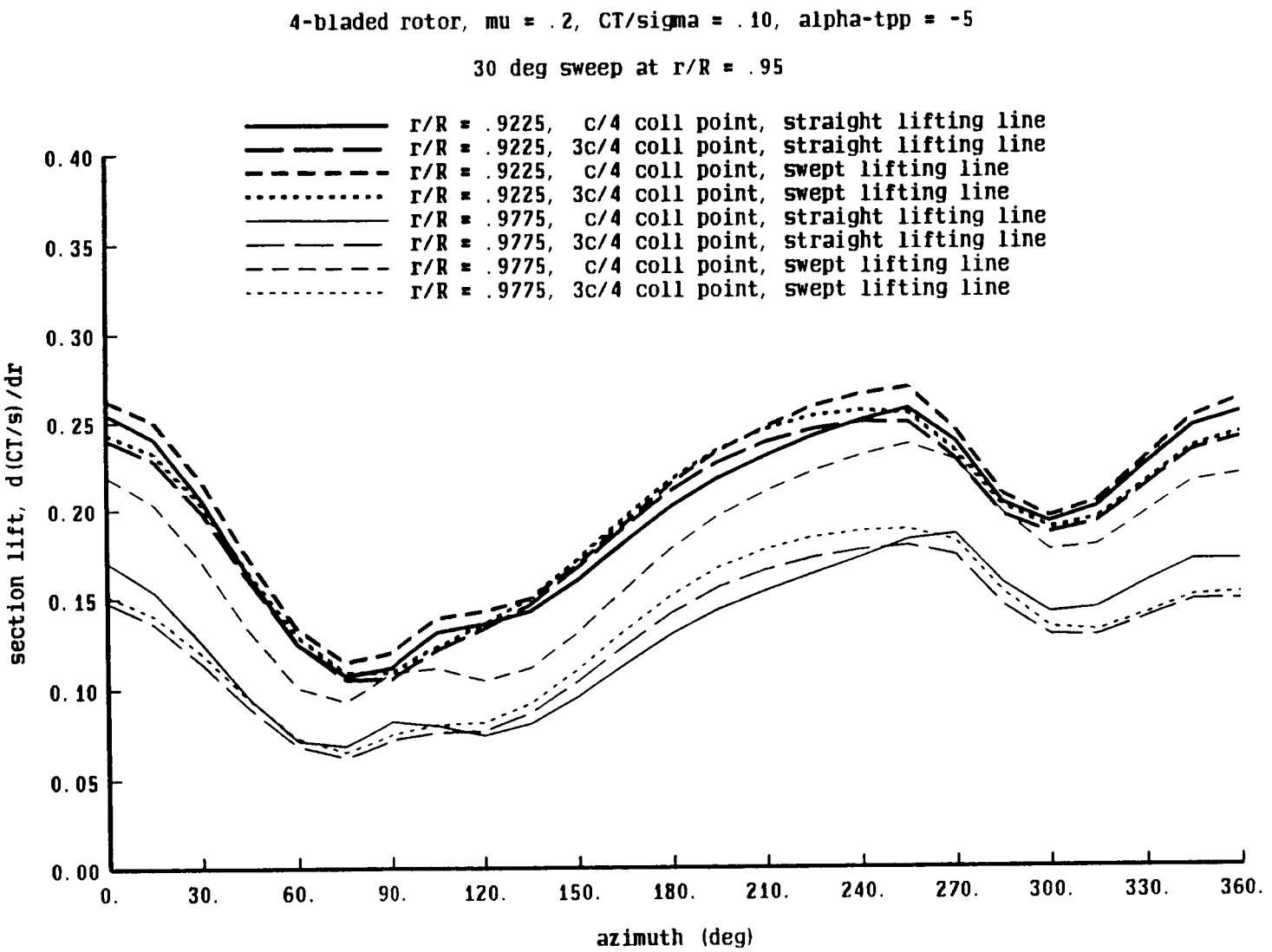

Figure 9-1c. Influence of wake and wing model for swept tips

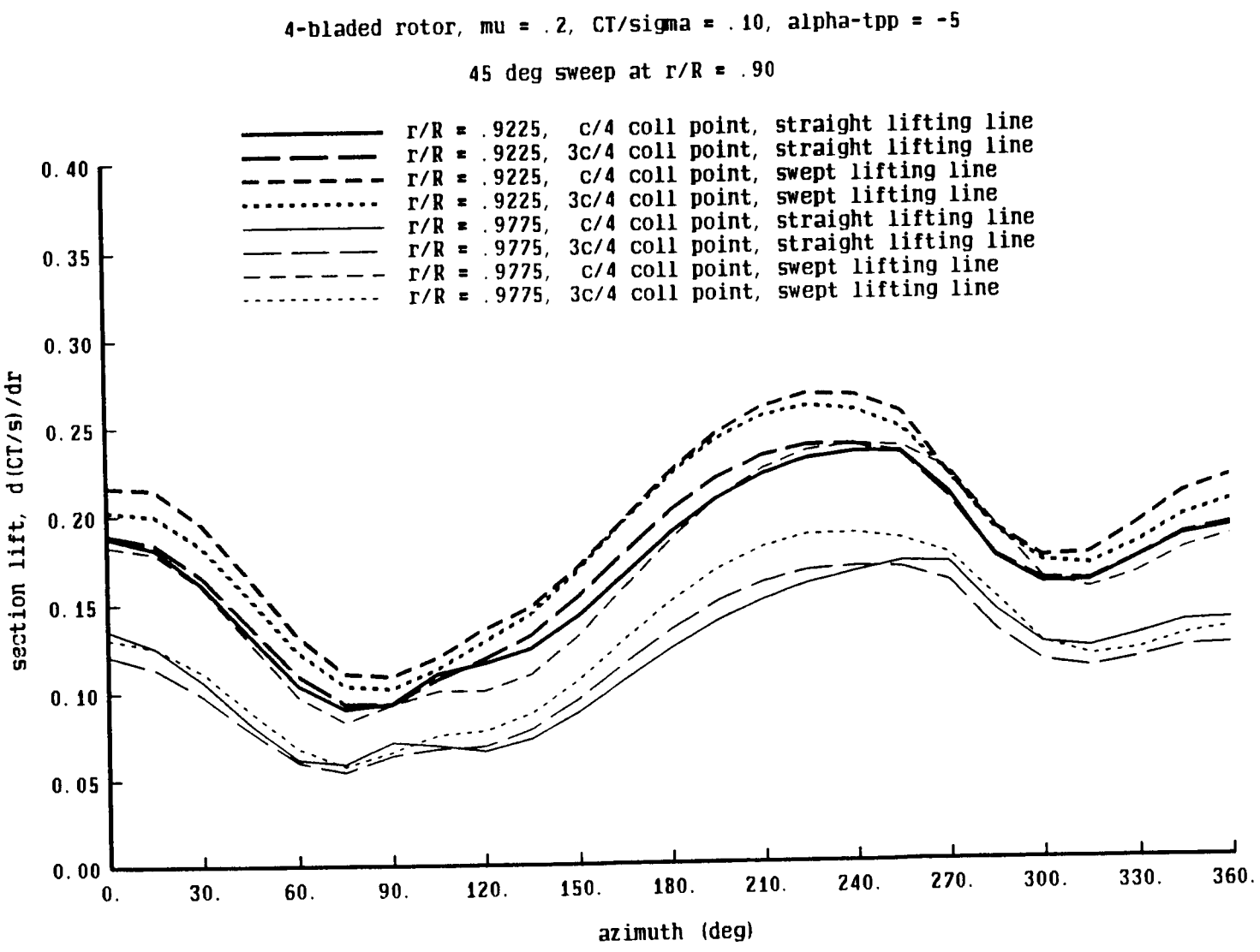

Figure 10-1a. Model 360 rotor: influence of far wake model

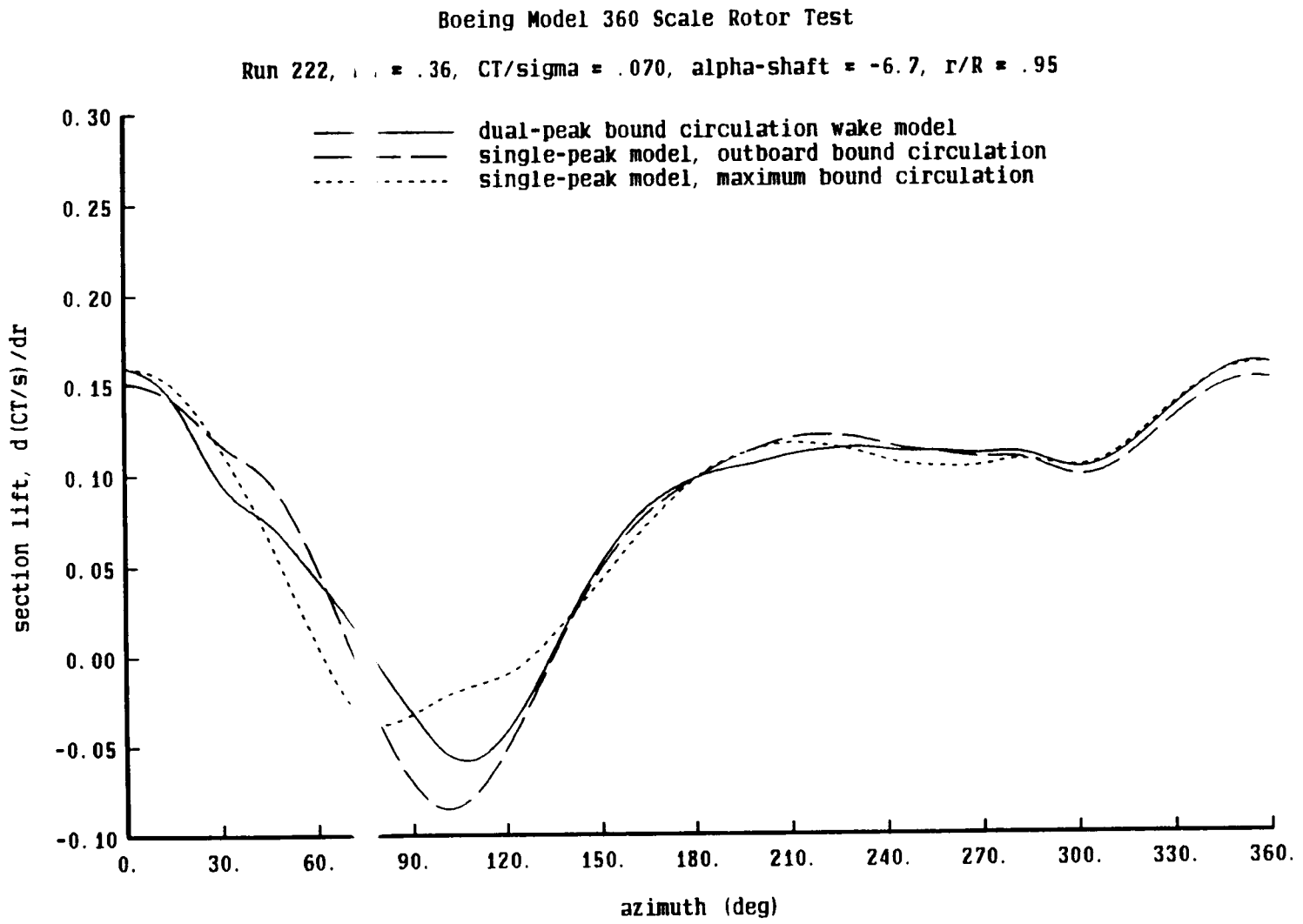

Figure 10-1b. Model 360 rotor: influence of far wake model

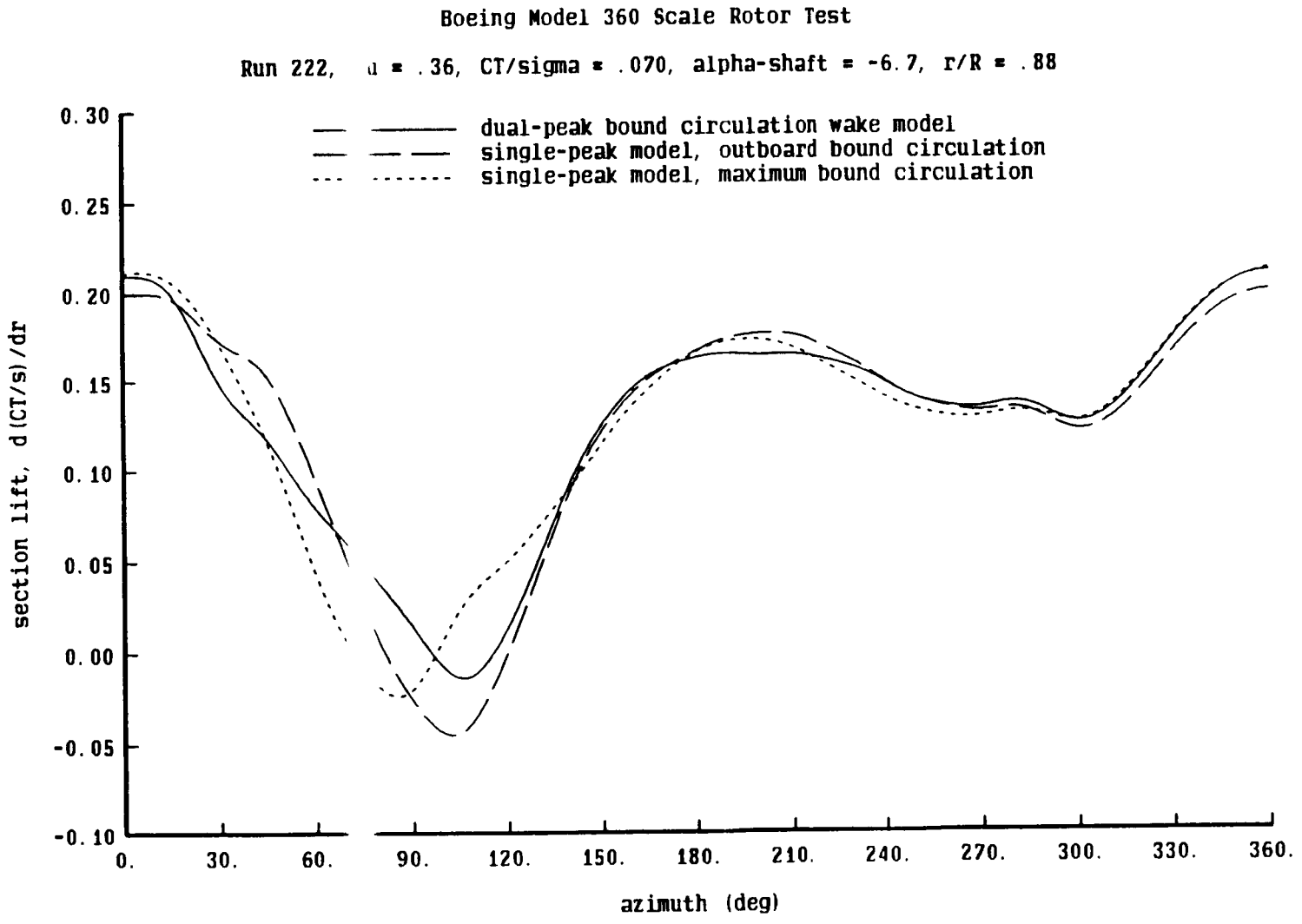

Figure 10-1c. Model 360 rotor: influence of far wake model

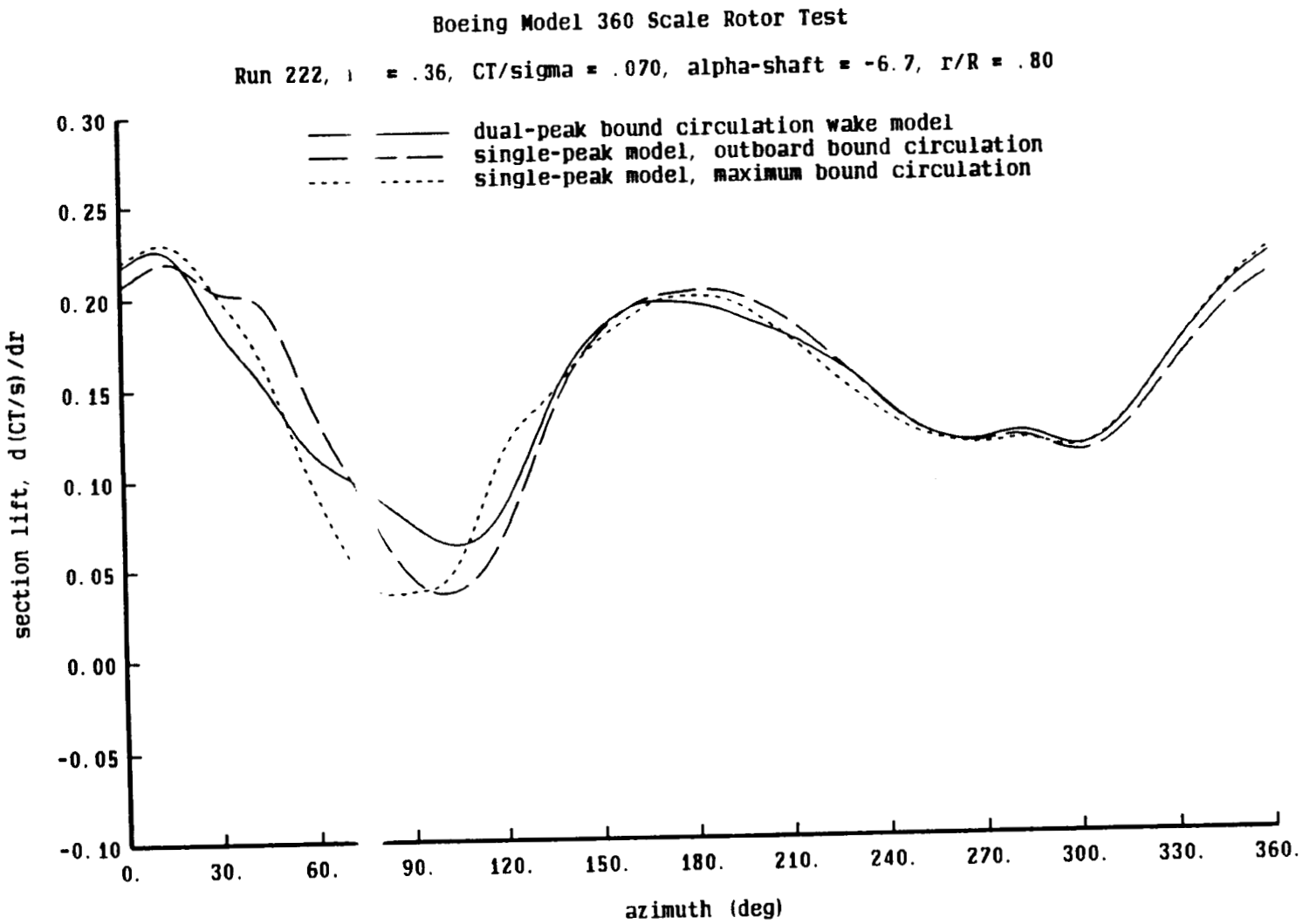

Figure 10-2a. ›del 360 rotor: convergence of wake geometry for ıal-peak model

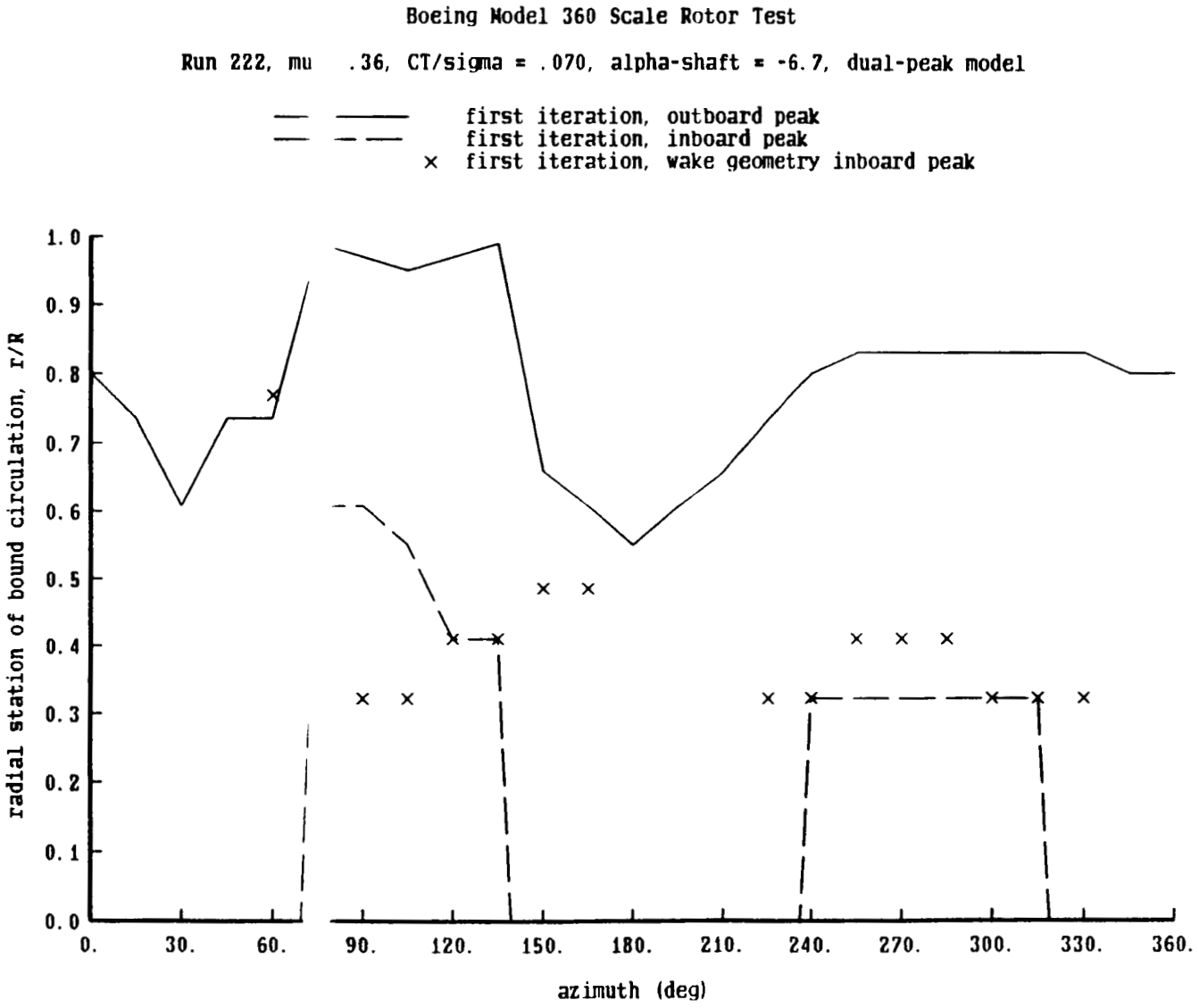

Figure 10-2b. Model 360 rotor: convergence of wake geometry for dual-peak model

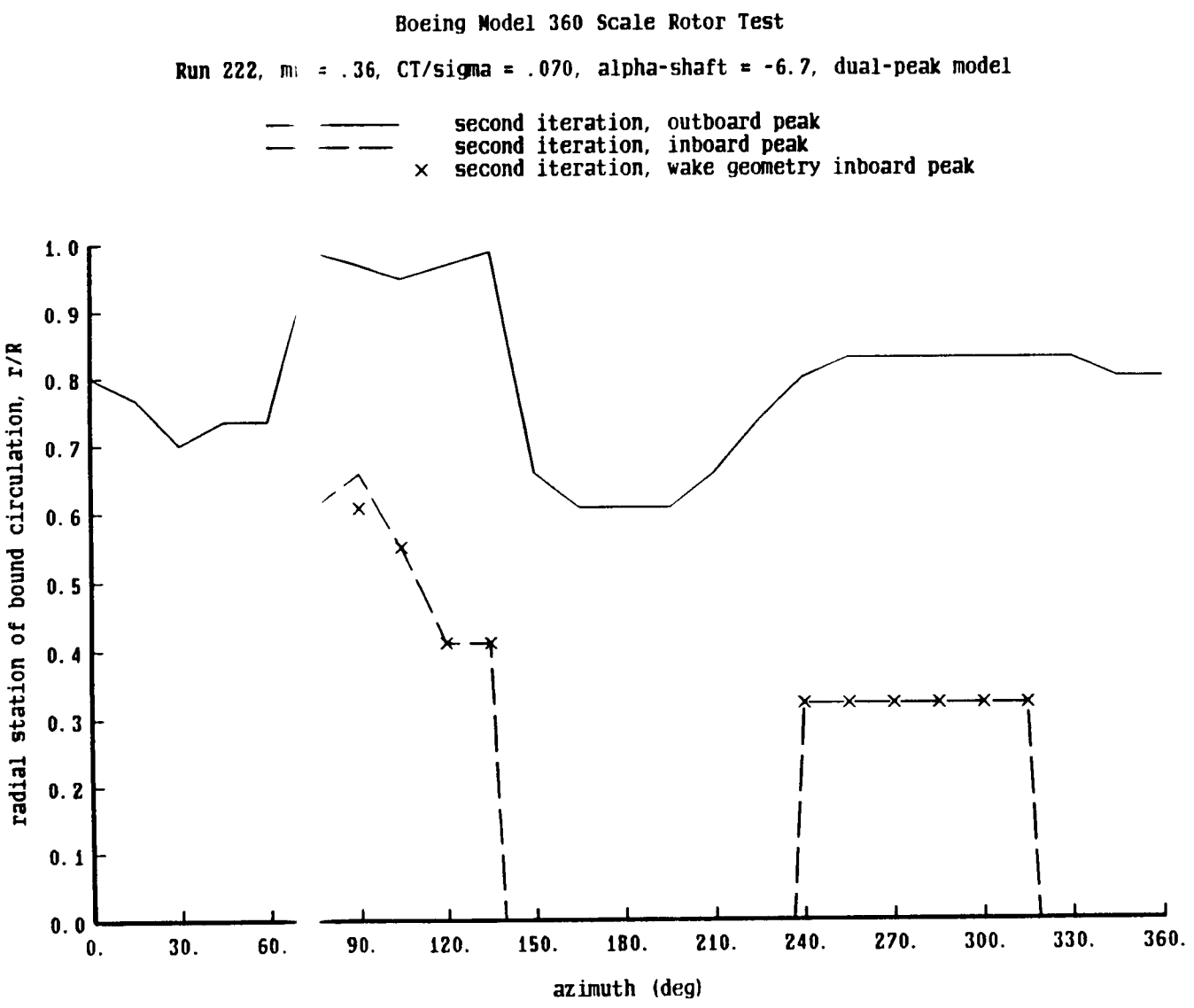

Figure 10-2c. Model 360 rotor: convergence of wake geometry for dual-peak model

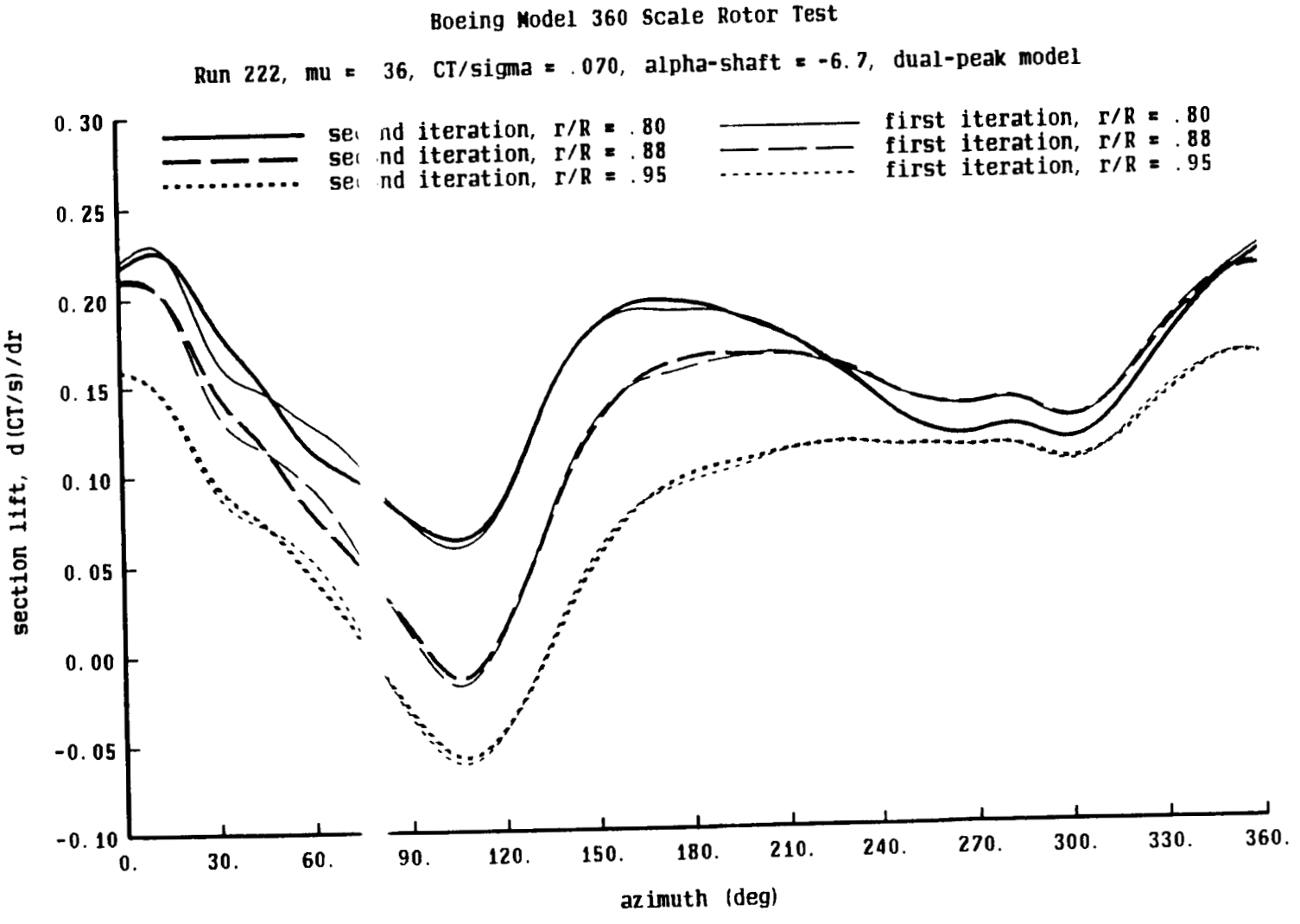

Figure 10-2d. Model 360 rotor: convergence of wake geometry for dual-peak model

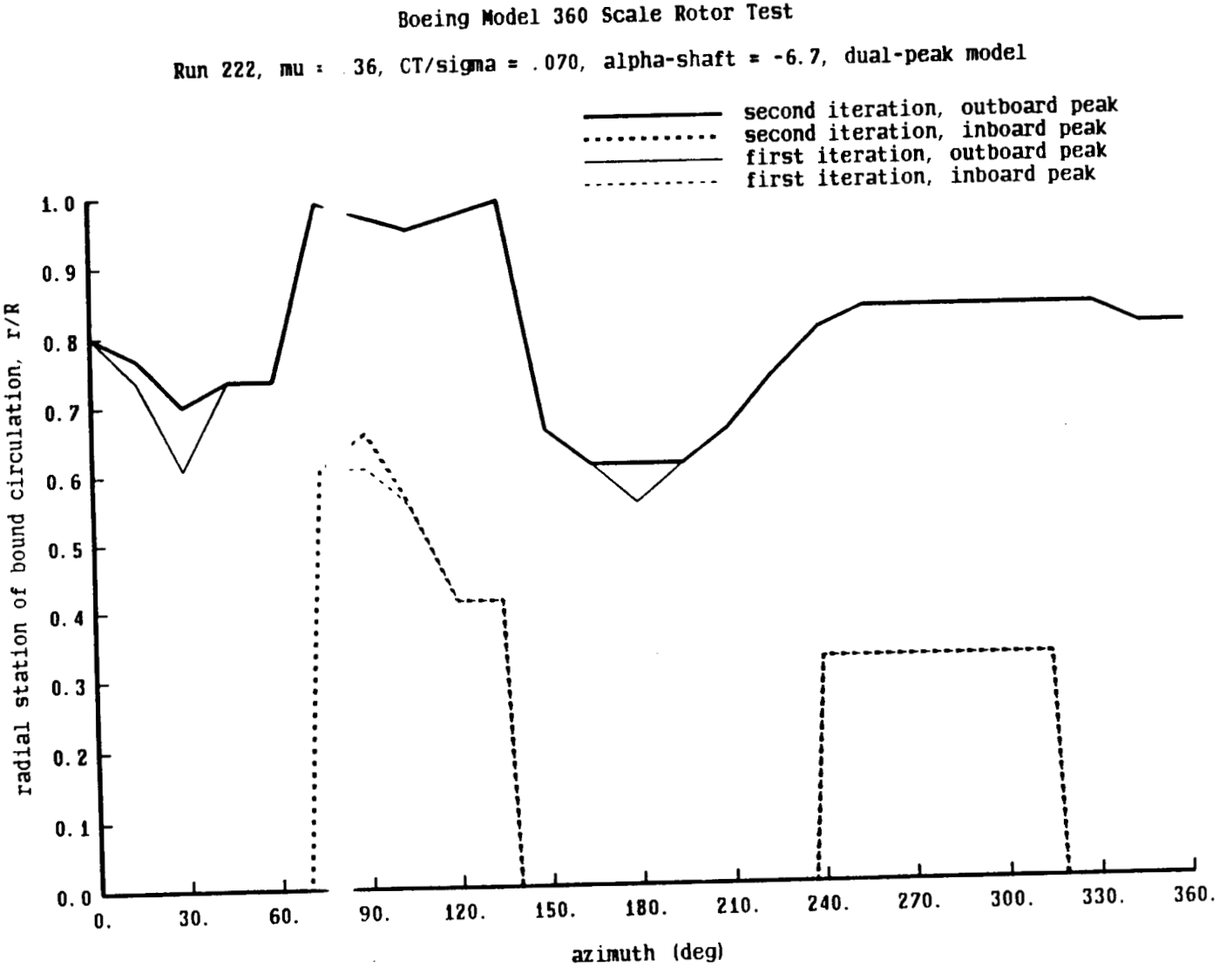

Figure 10-2e. Model 360 rotor: convergence of wake geometry for dual-peak model

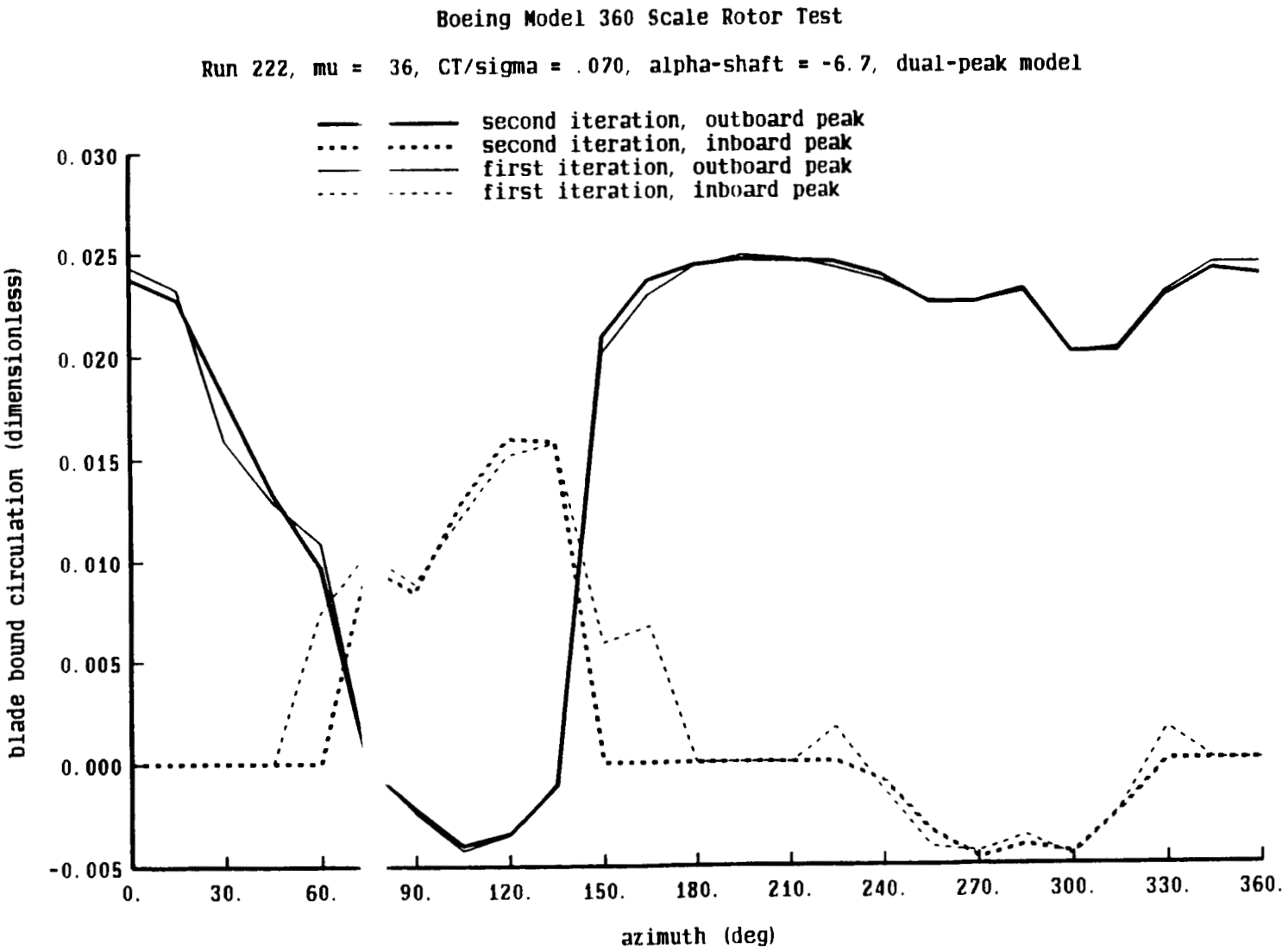

Figure 10-3a. odel 360 rotor: influence of far wake model

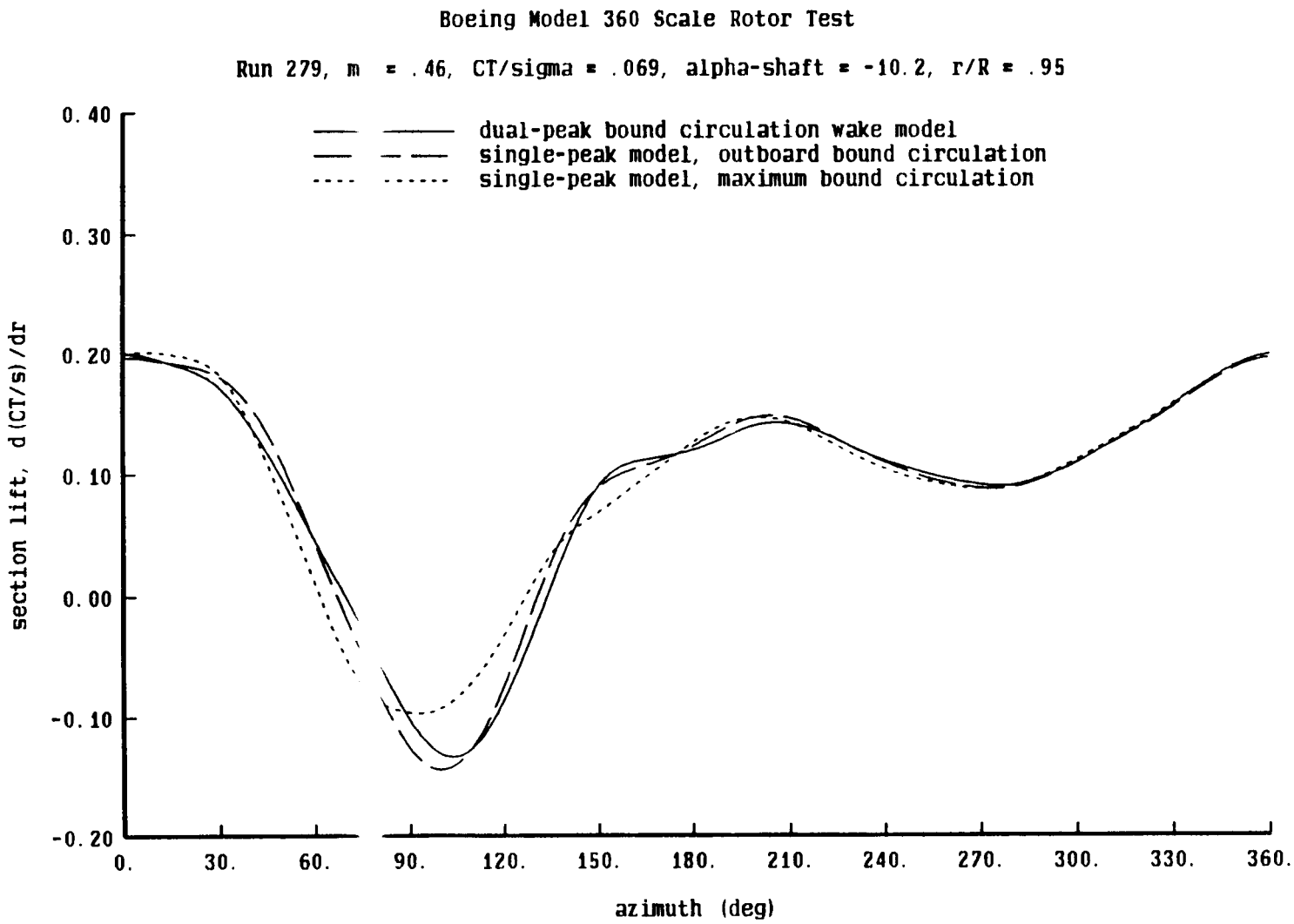

Figure 10-3b. Model 360 rotor: influence of far wake model

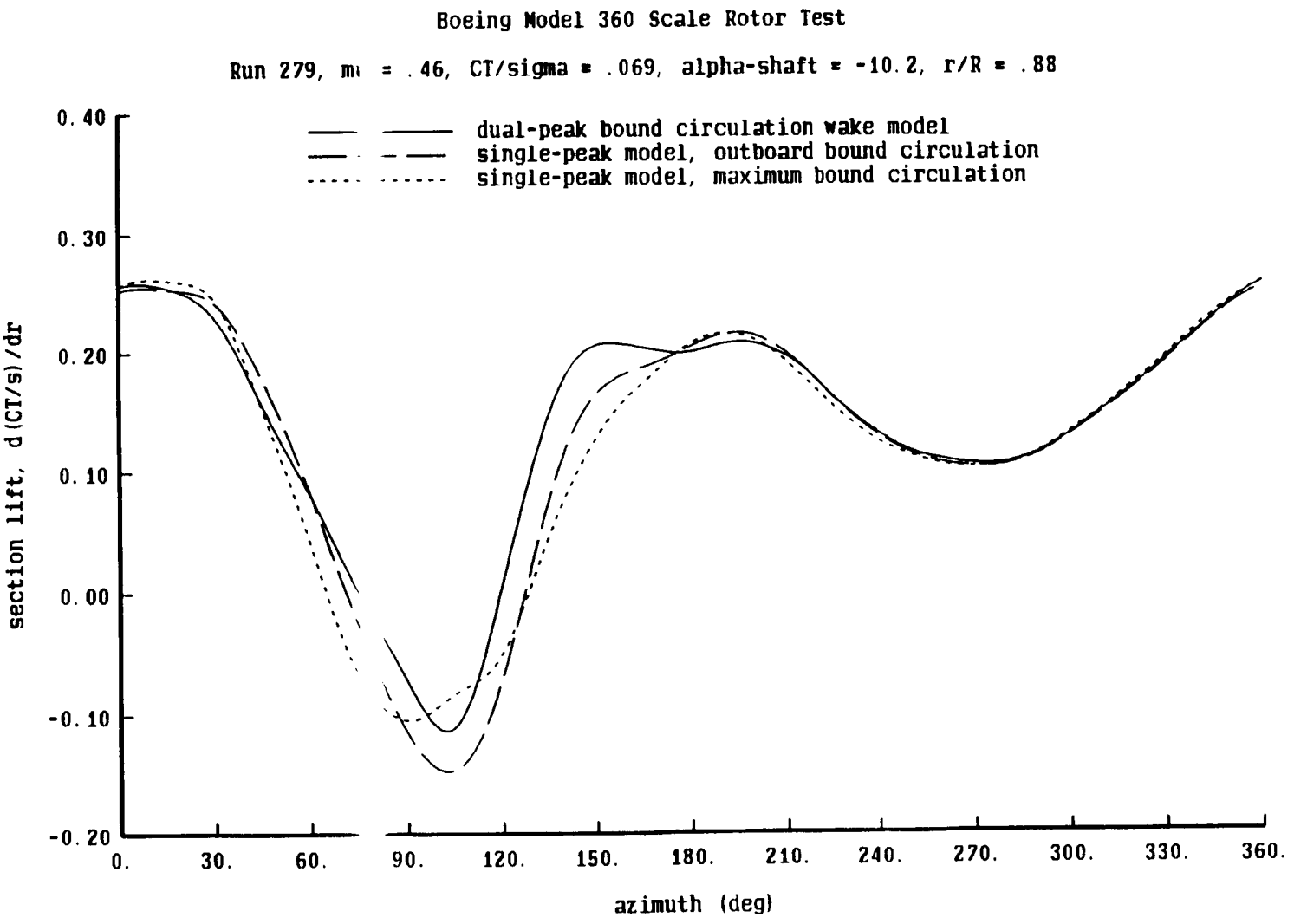

Figure 10-3c. Model 360 rotor: influence of far wake model

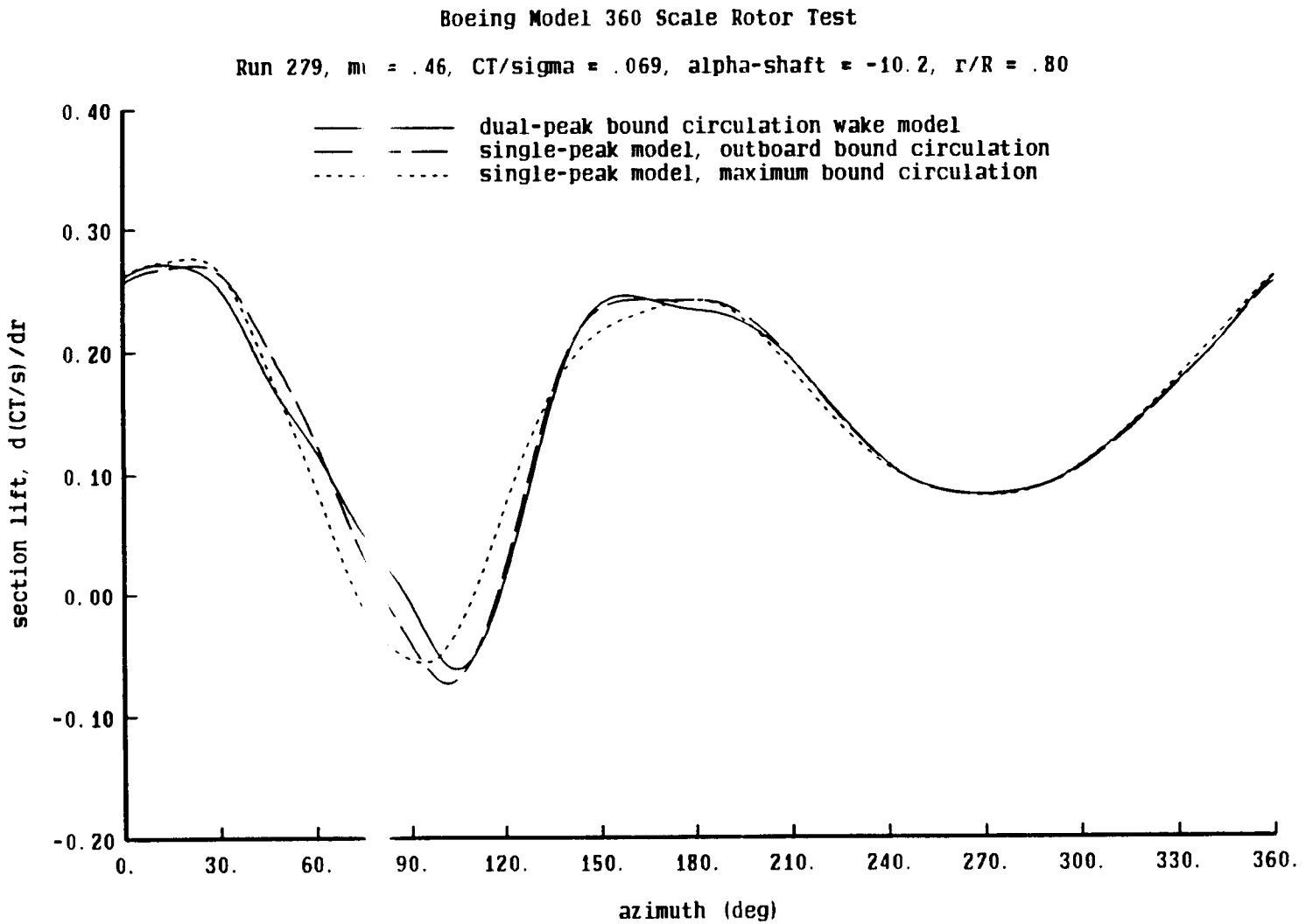

Figure 10-4a. Model 360 rotor: convergence of wake geometry for dual-peak model

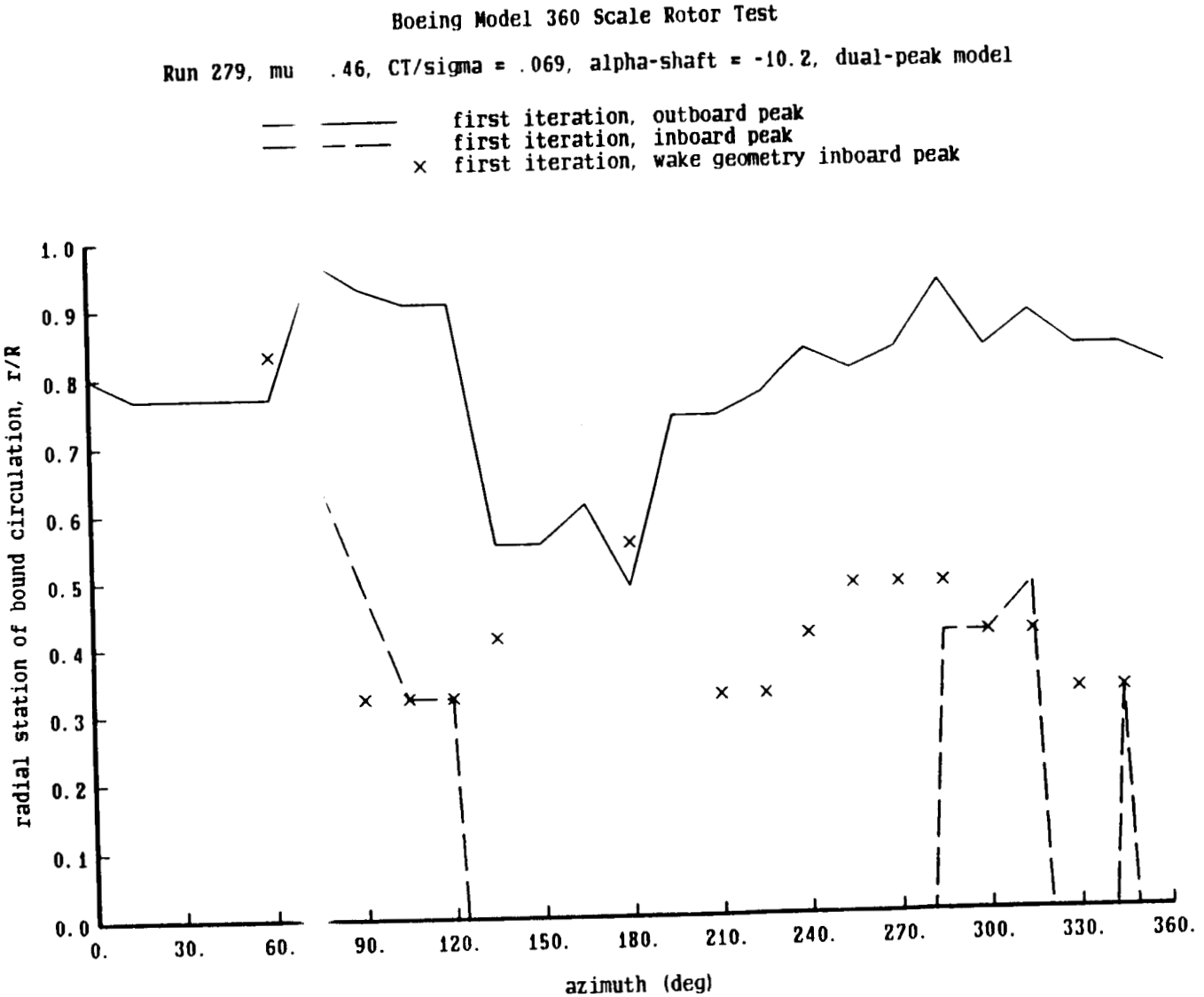

Figure 10-4b. Model 360 rotor: convergence of wake geometry for dual-peak model

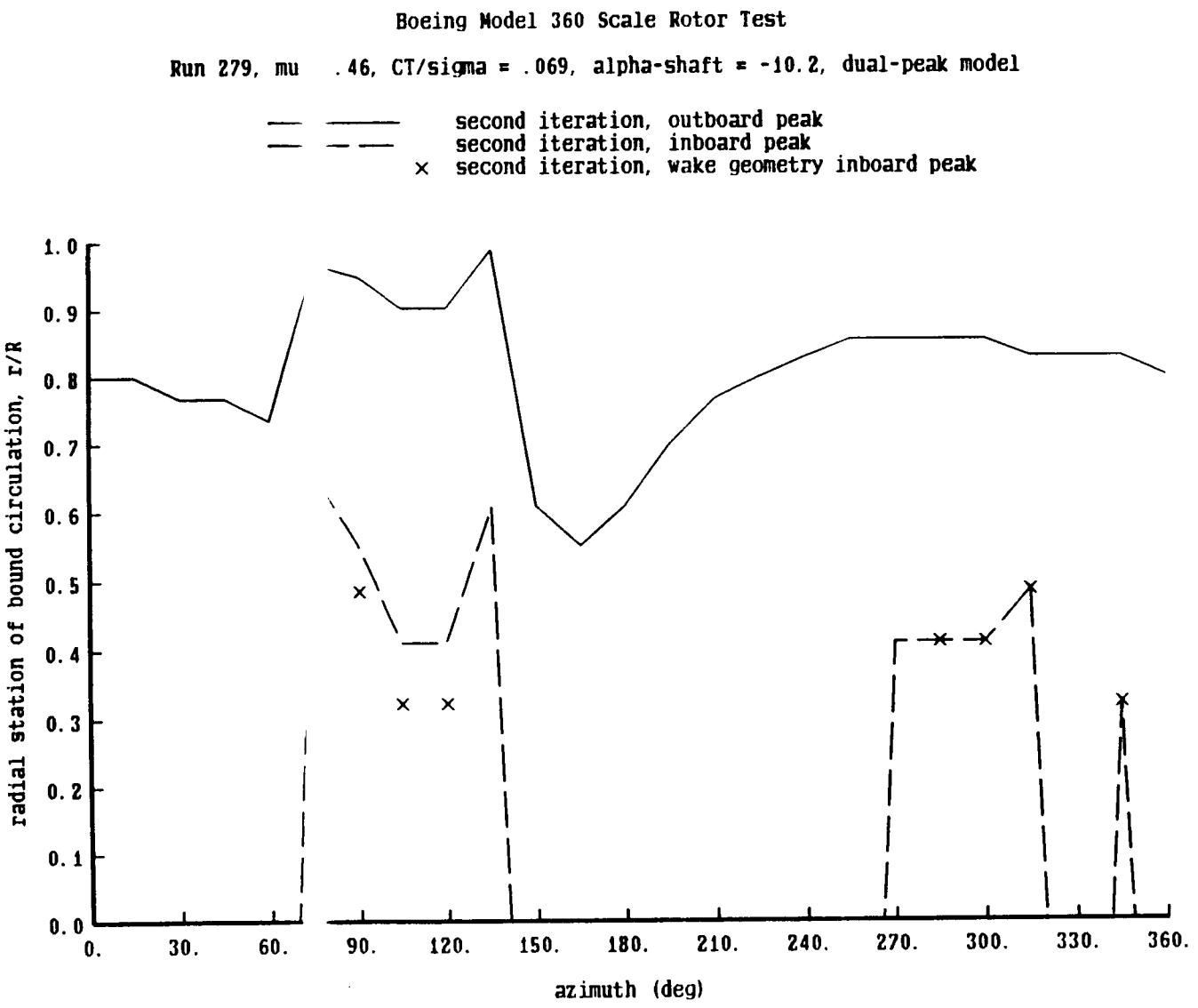

Figure 10-4c. Model 360 rotor: convergence of wake geometry for dual-peak model

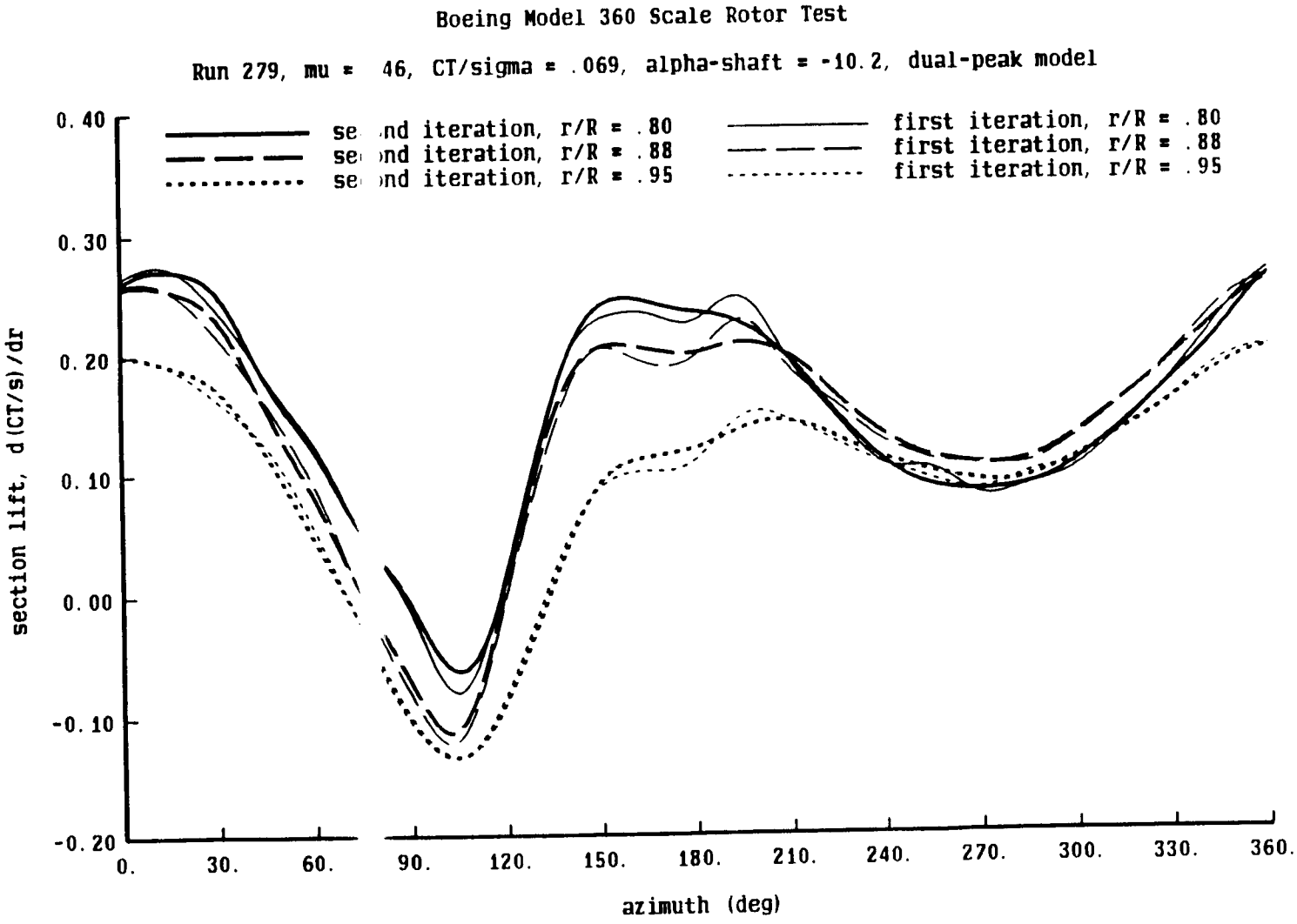

Figure 10-4d. Model 360 rotor: convergence of wake geometry for dual-peak model

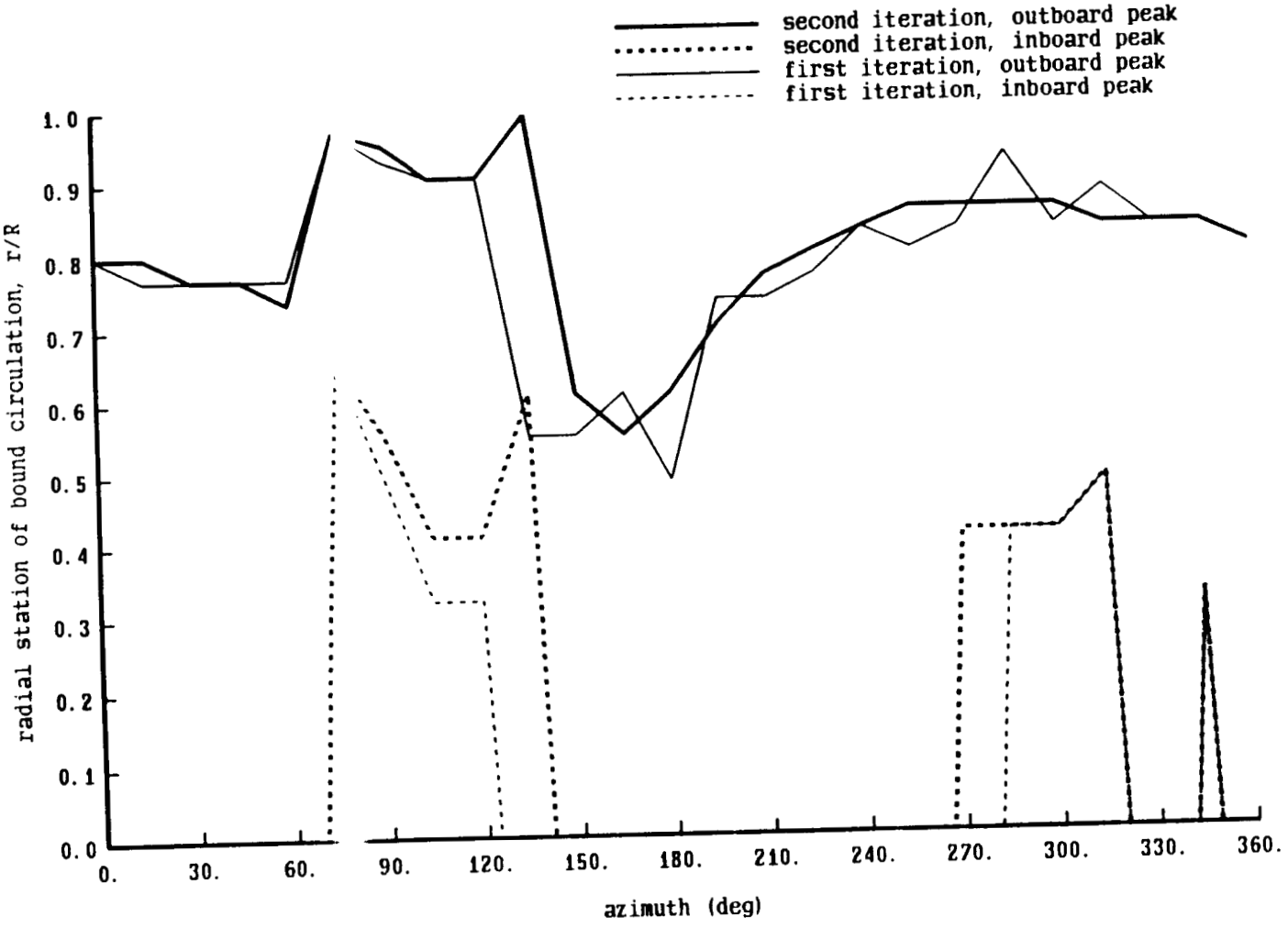

Figure 10-4e. Model 360 rotor: convergence of wake geometry for dual-peak model

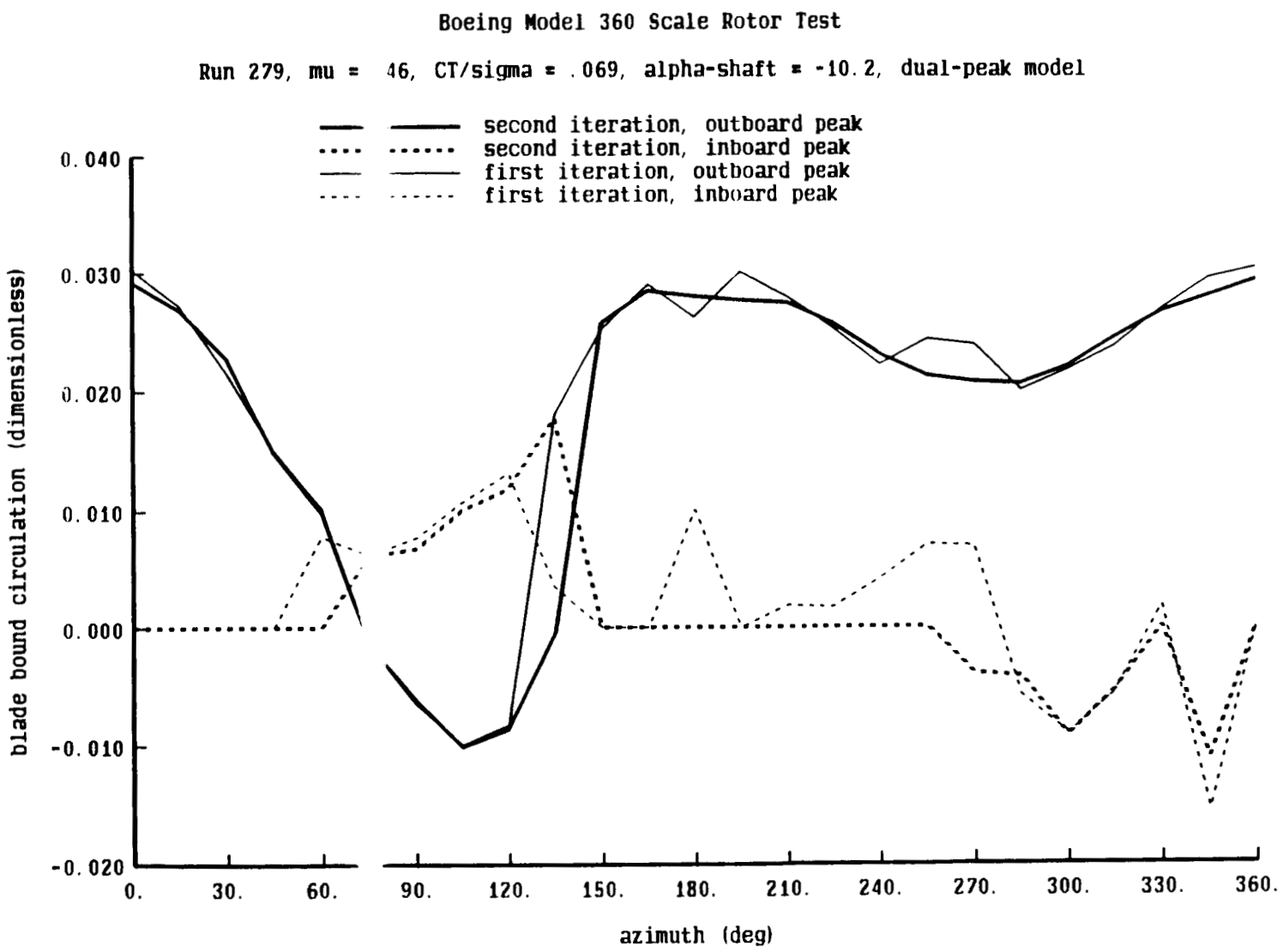

Figure 10-5a. Mc el 360 rotor: influence of near wake model

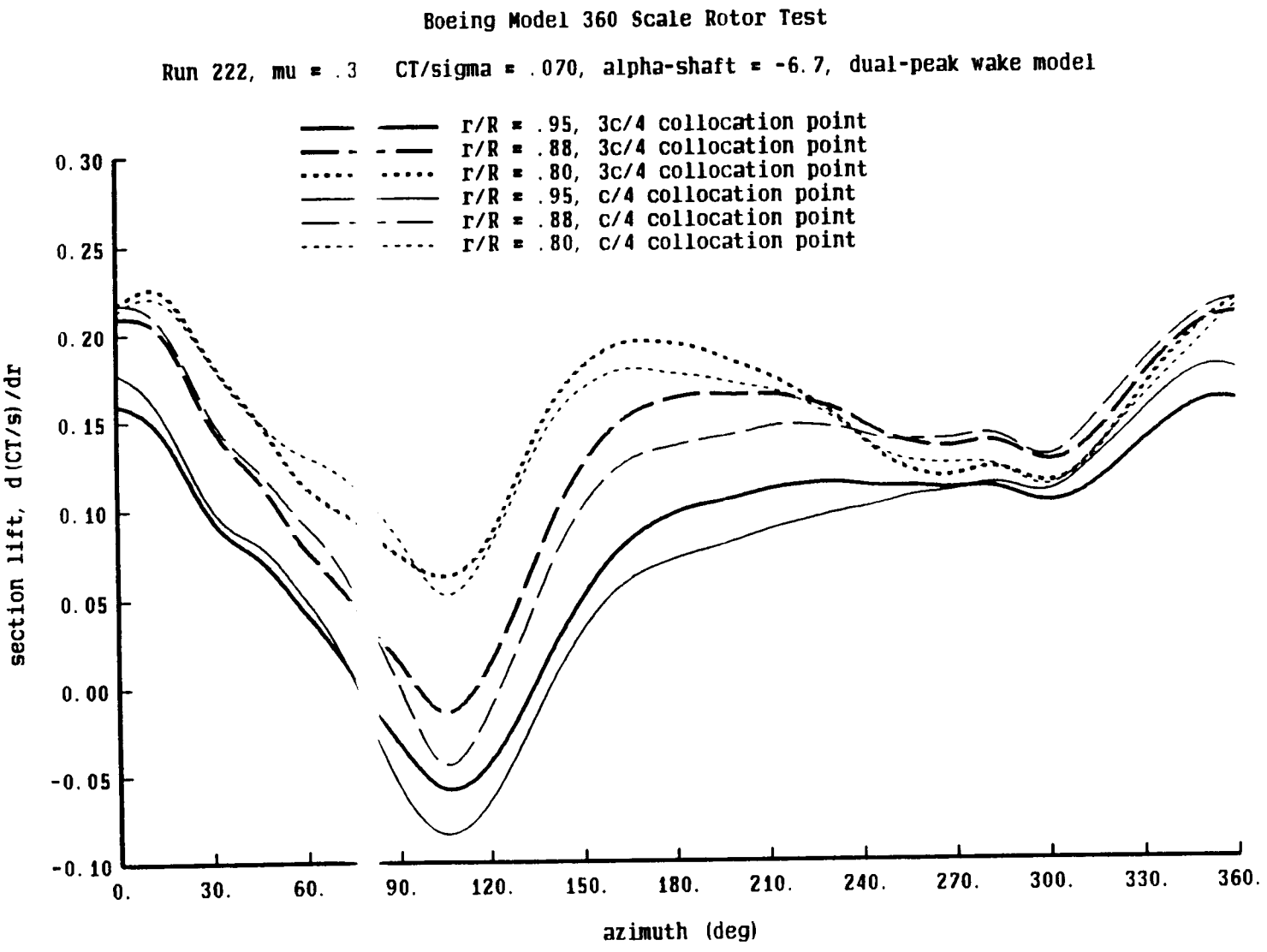

Figure 10-5b. Model 360 rotor: influence of near wake model

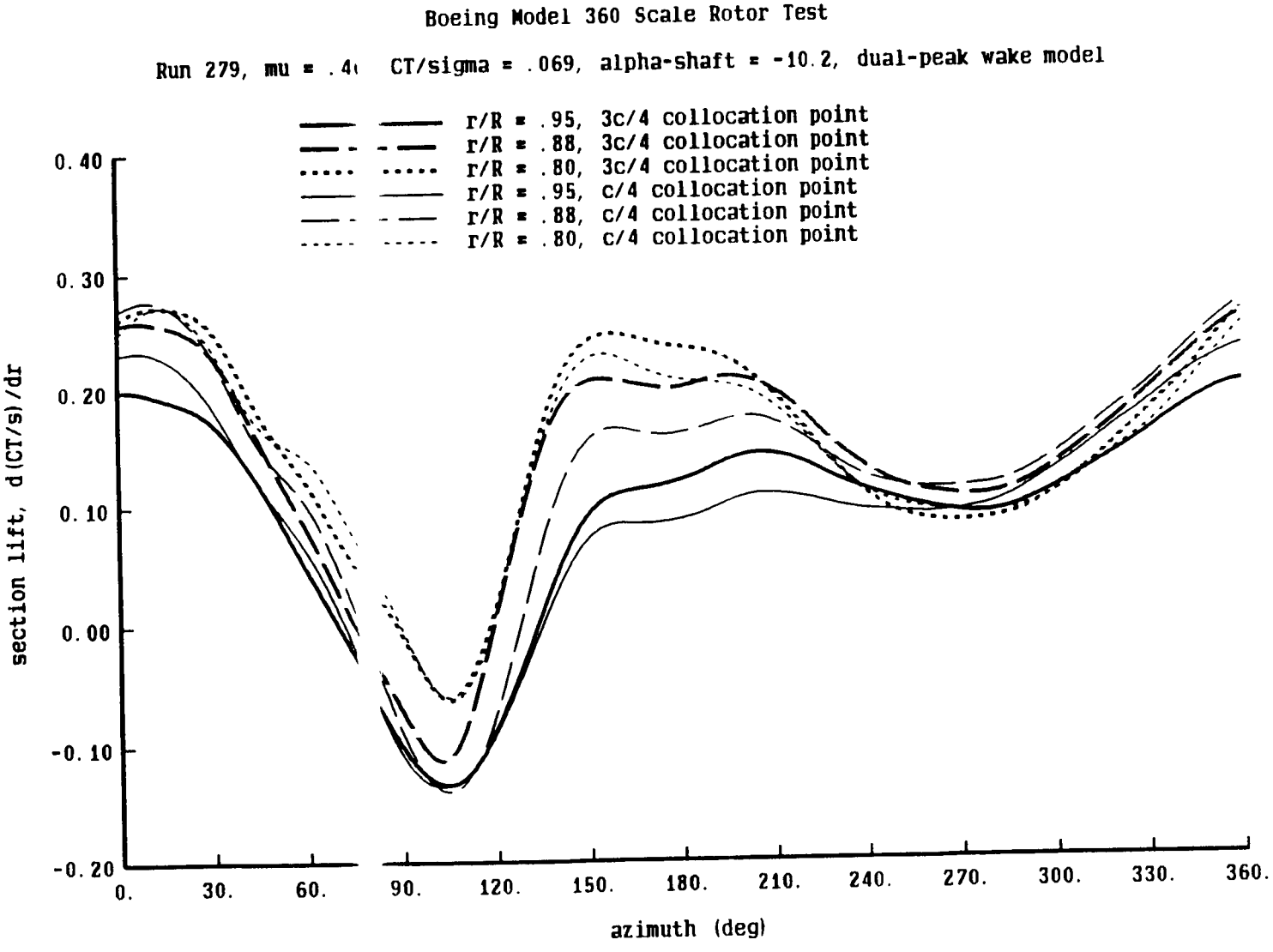

Figure 10-6a. odel 360 rotor: influence of inboard trailed ake rollup

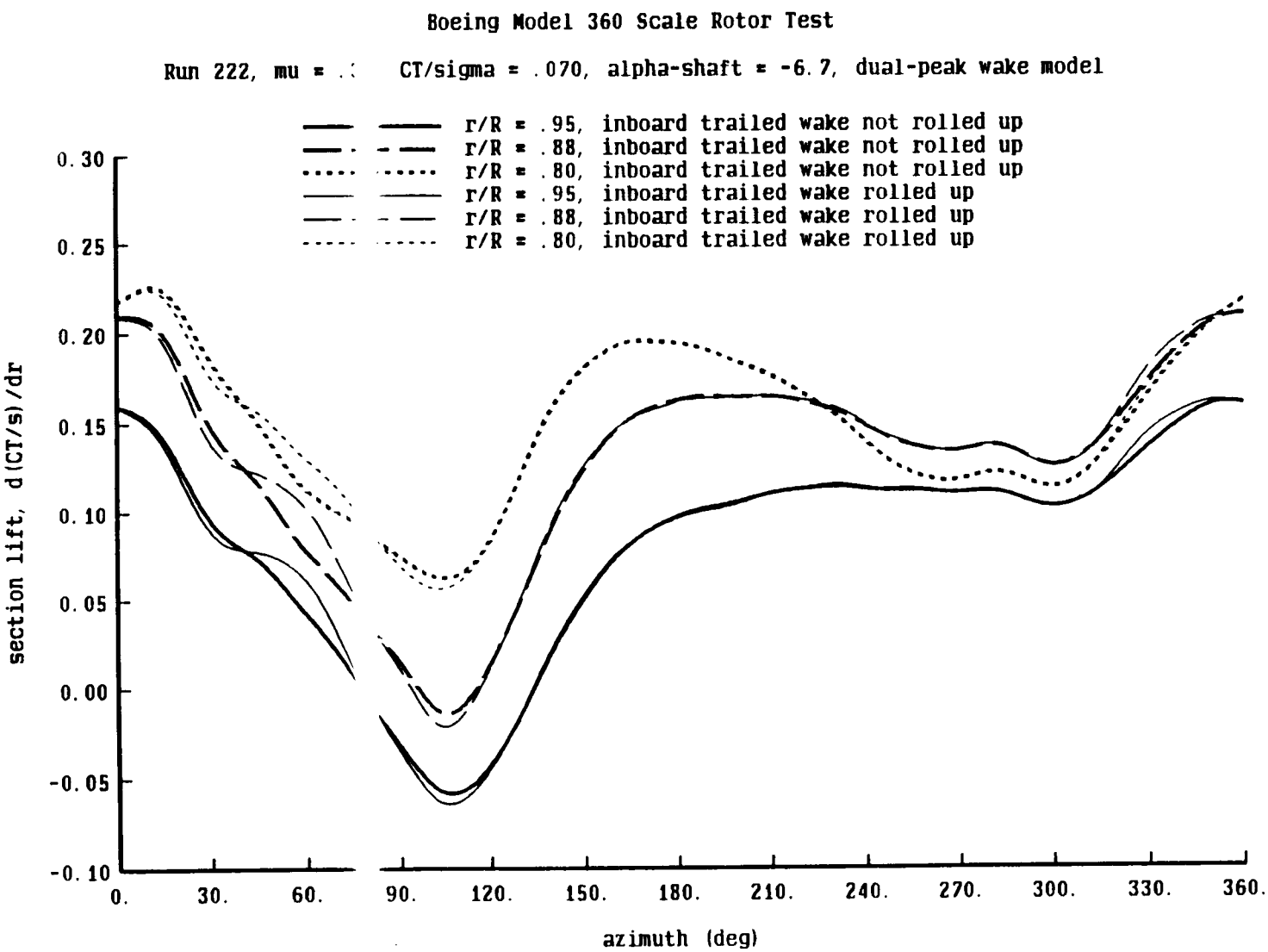

Figure 10-6b. Model 360 rotor: influence of inboard trailed wake rollup

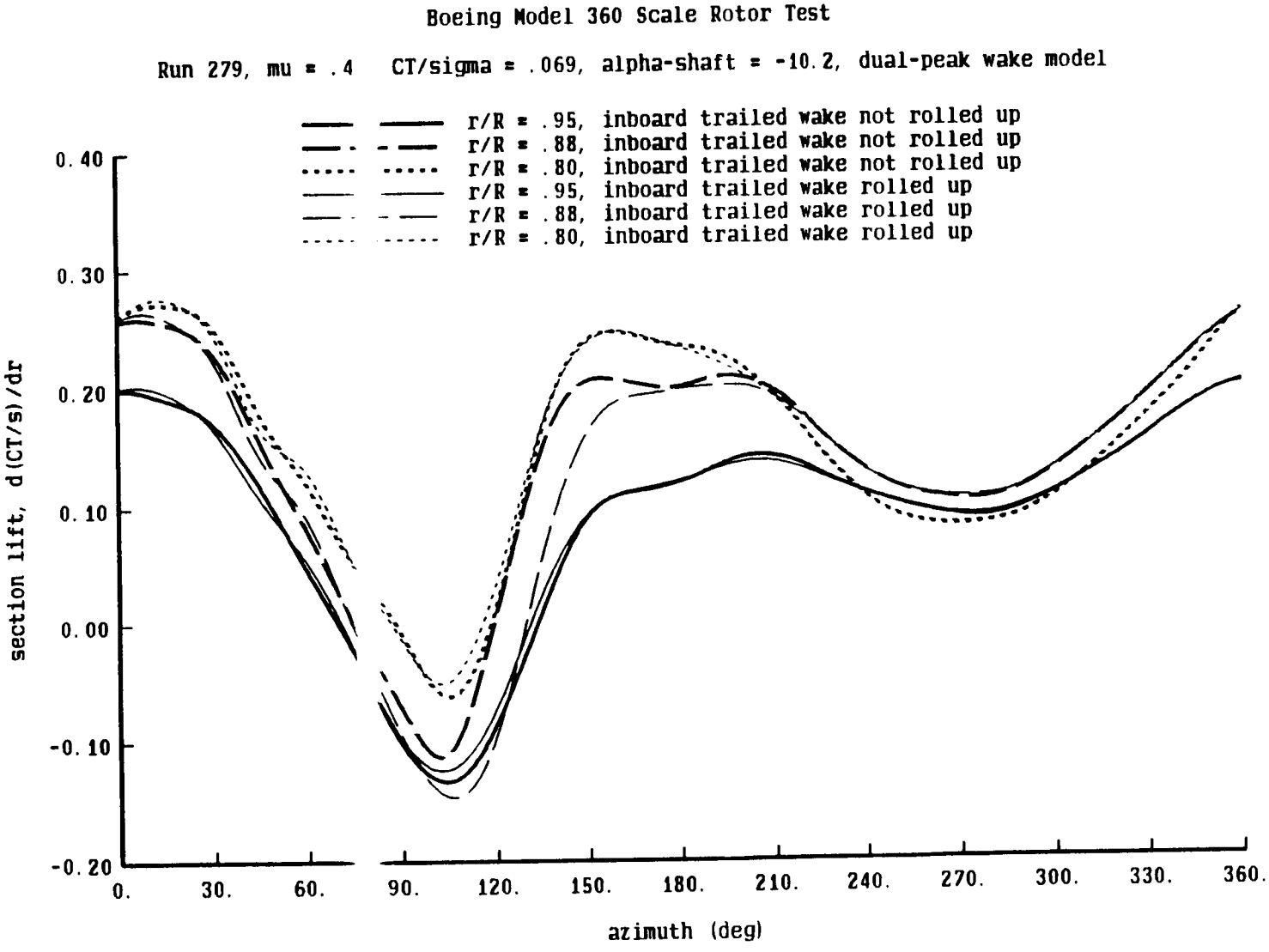

Figure 10-7a. Model 360 rotor: influence of blade elastic motion

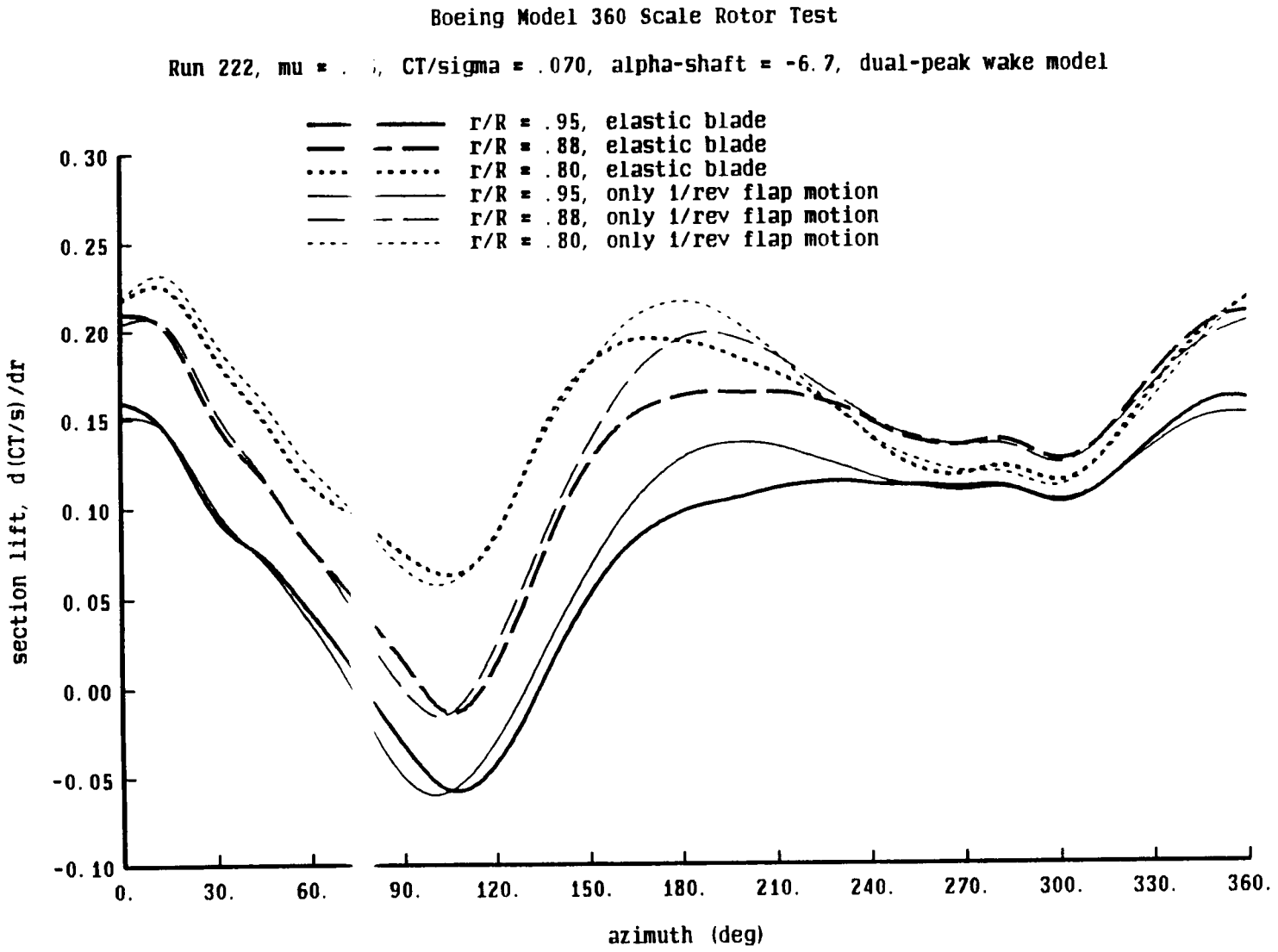

Figure 10-7b. odel 360 rotor: influence of blade elastic motion

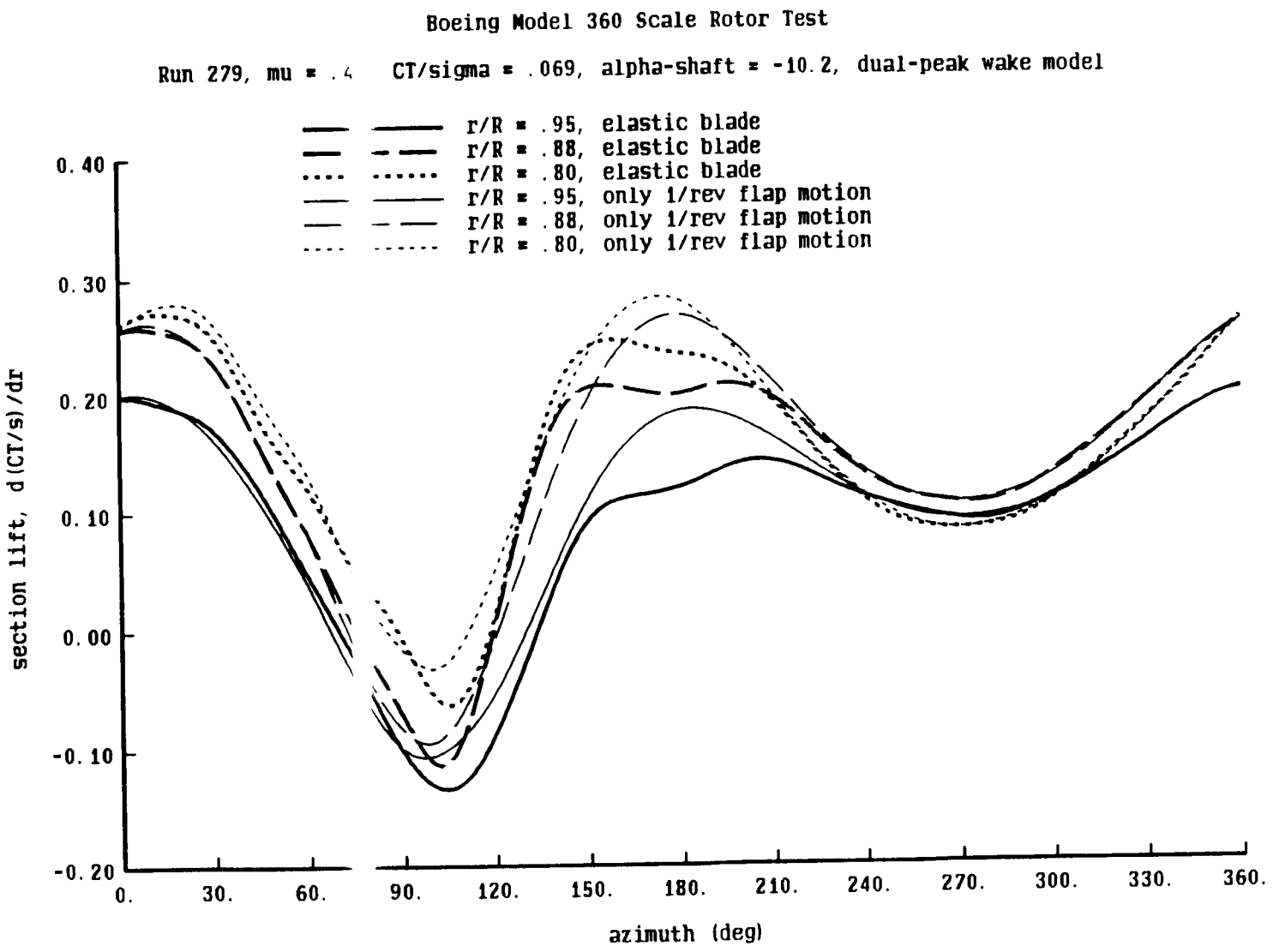

Figure 10-8. Model 360 rotor: blade elastic torsion motion

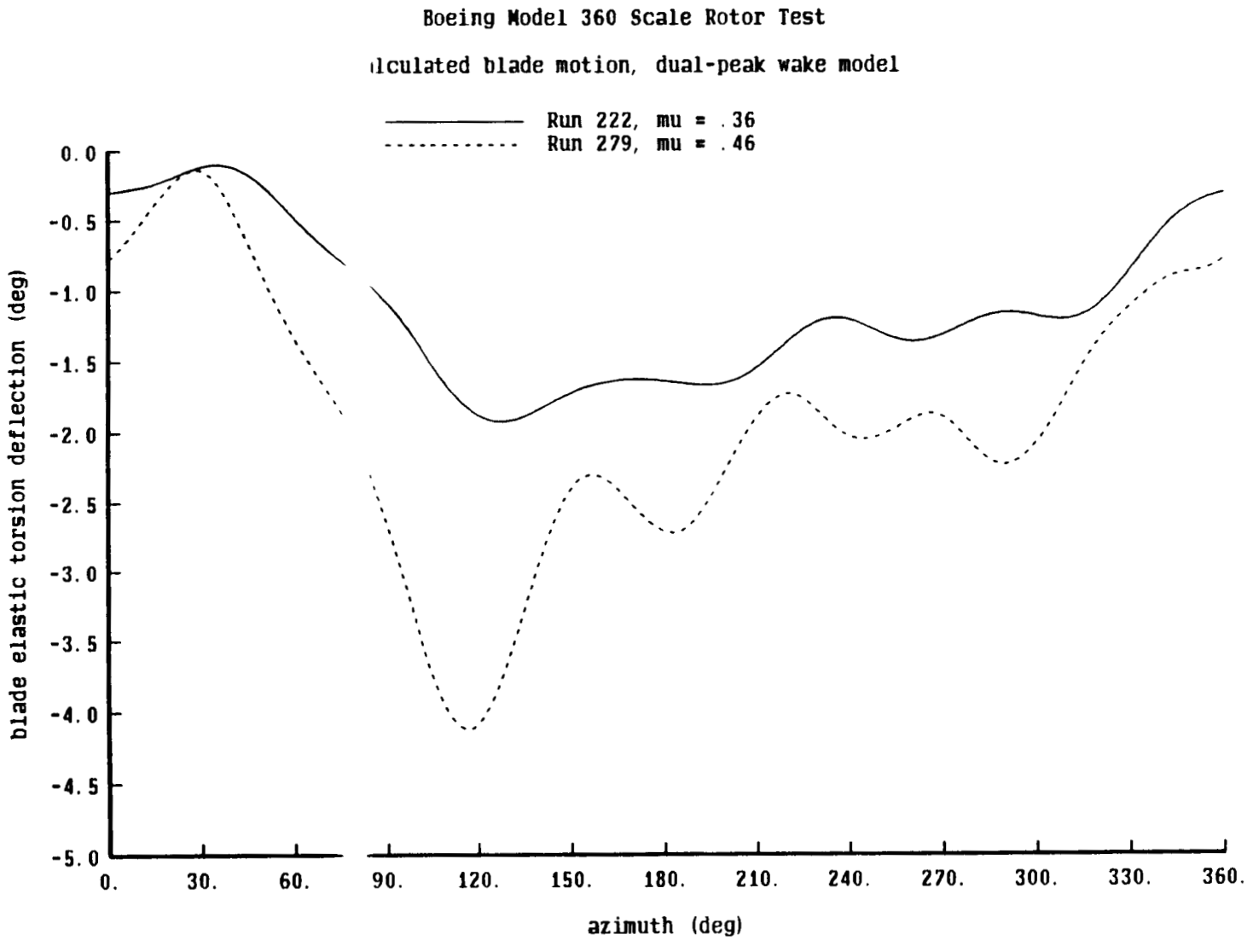

Figure 10-9a. Model 360 rotor: measured and calculated airloads

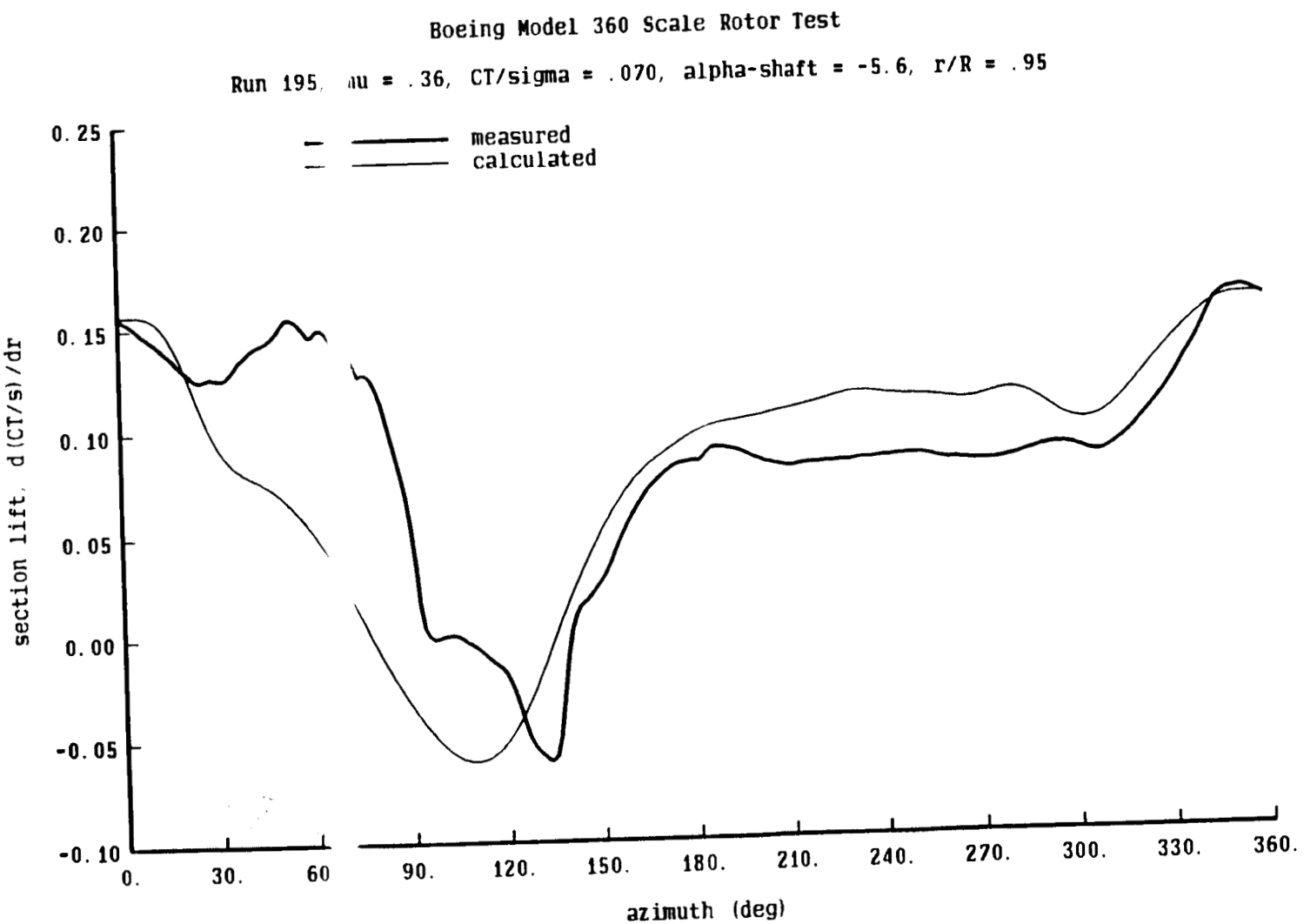

Figure 10-9b. Model 360 rotor: measured and calculated airloads

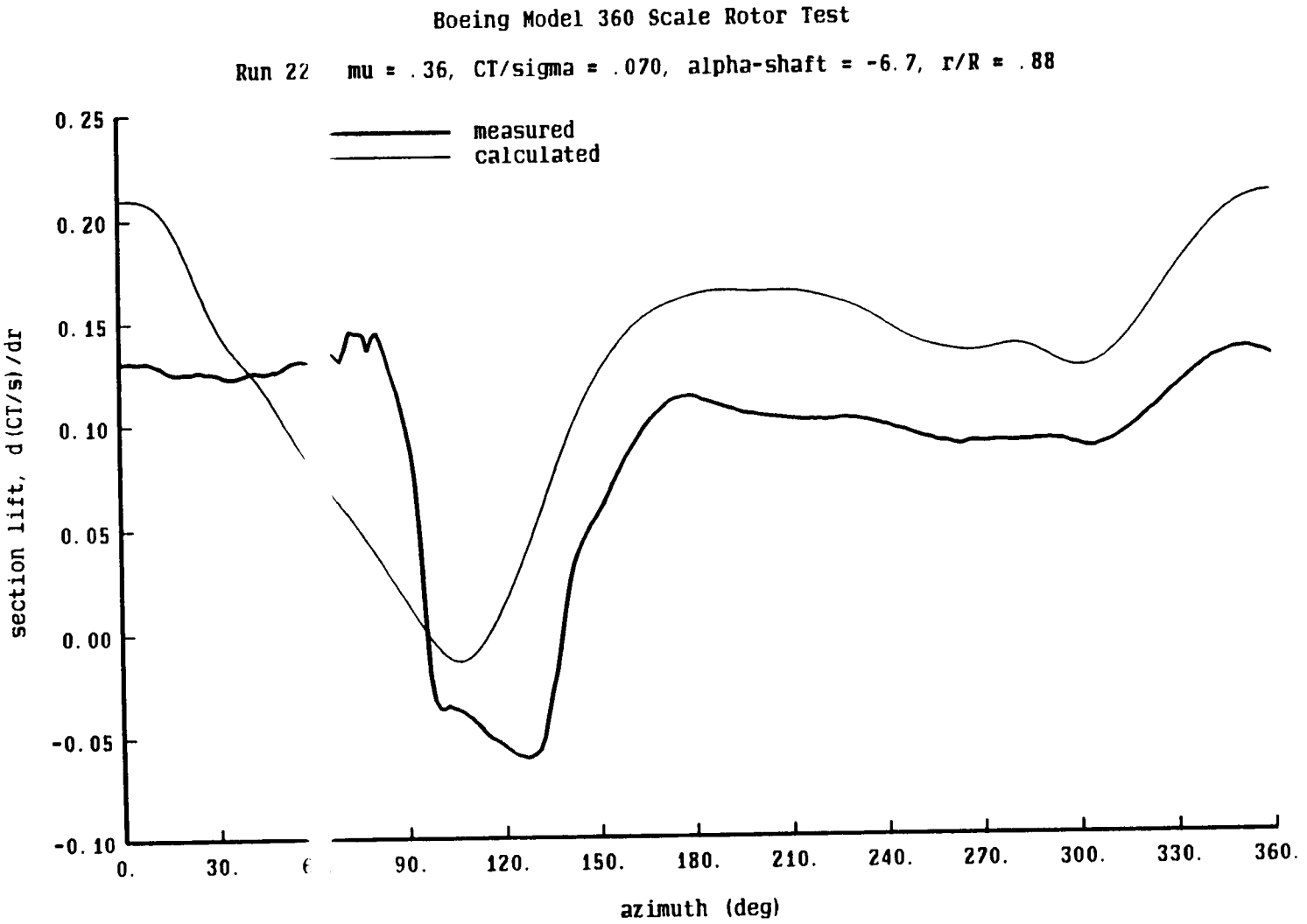

Figure 10-9c Model 360 rotor: measured and calculated airloads

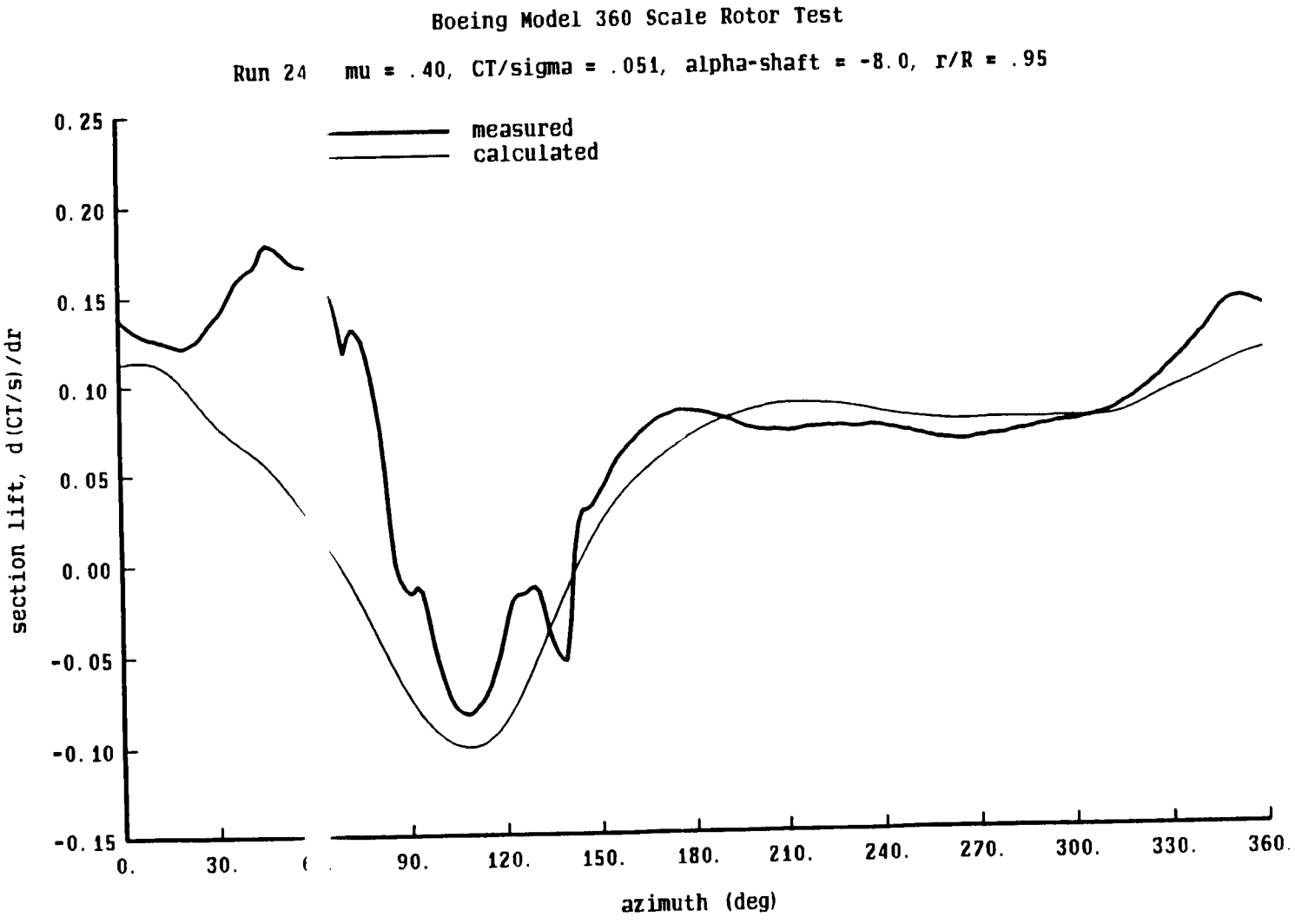

Figure 10-9d. Model 360 rotor: measured and calculated airloads

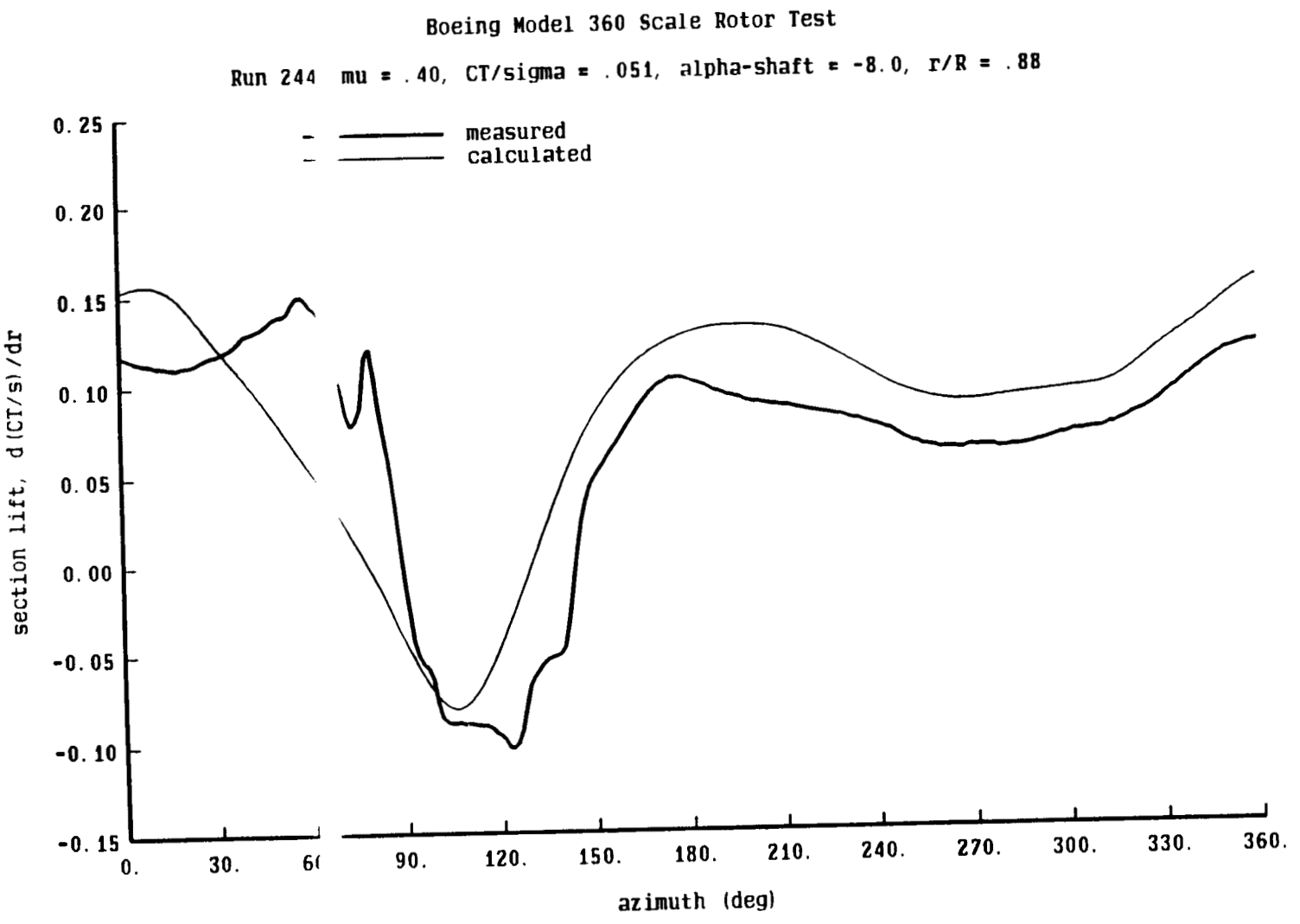

Figure 10-9e. odel 360 rotor: measured and calculated airloads

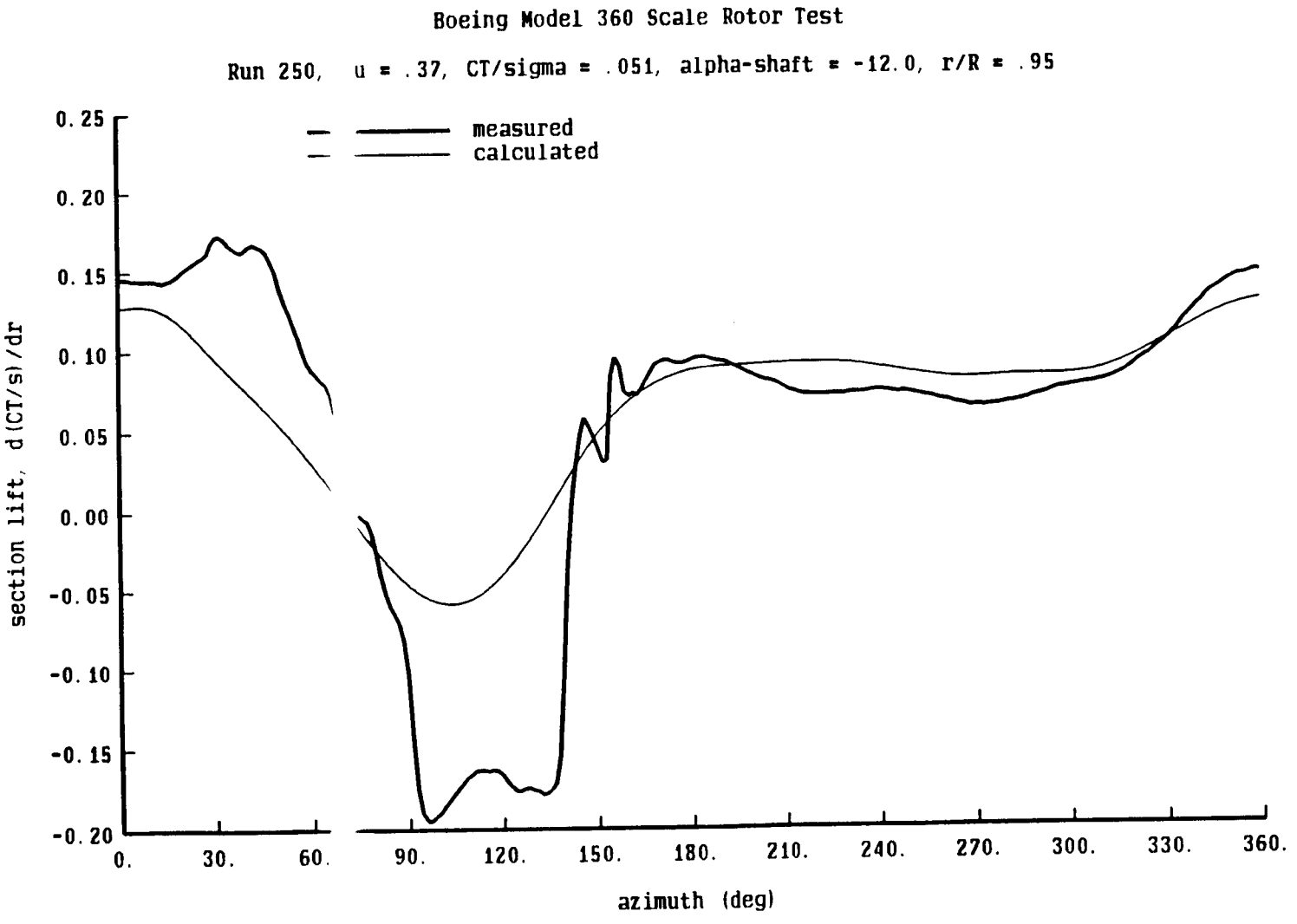

Figure 10-9f. Model 360 rotor: measured and calculated airloads

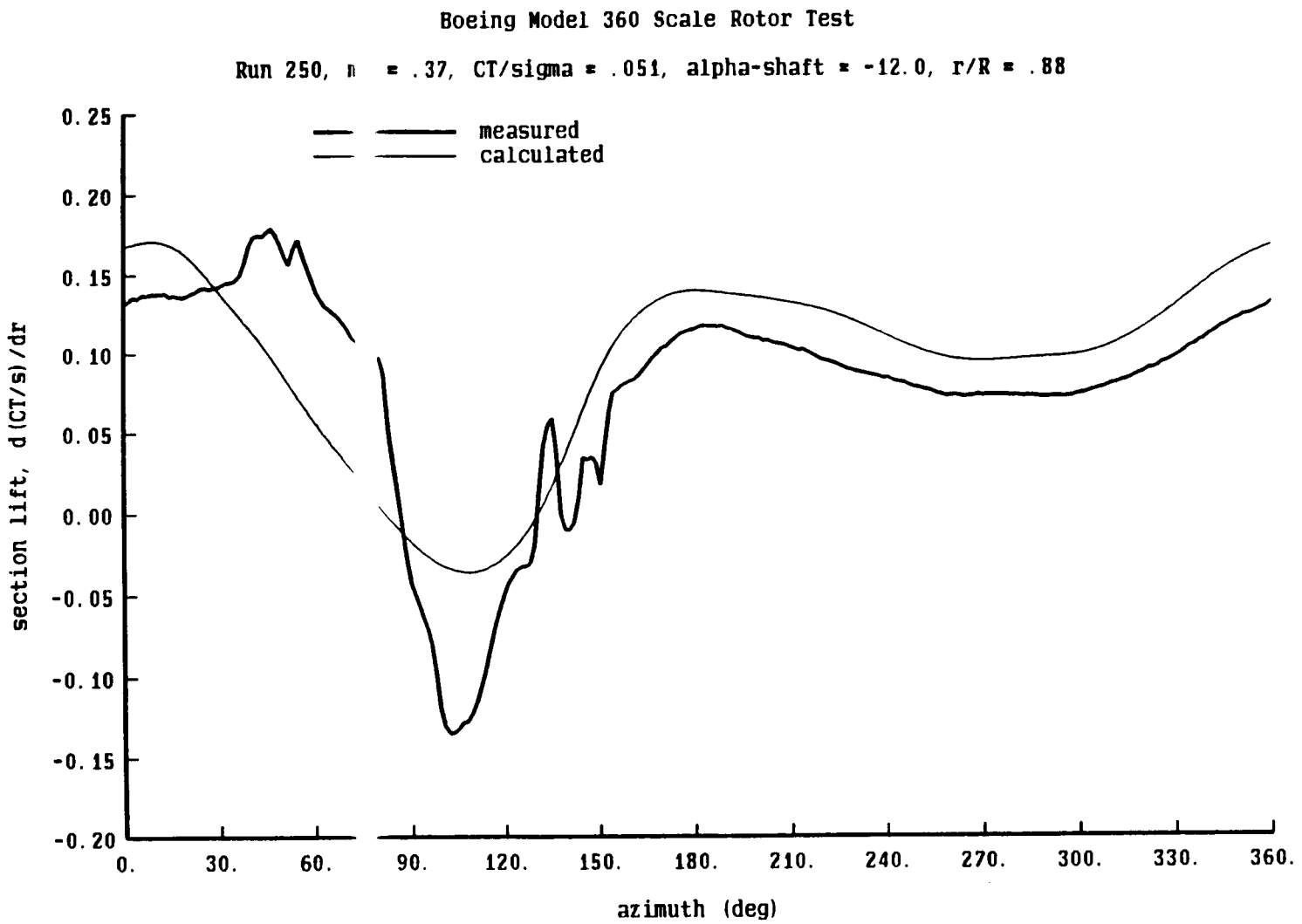

Figure 10-9g. Model 360 rotor: measured and calculated airloads

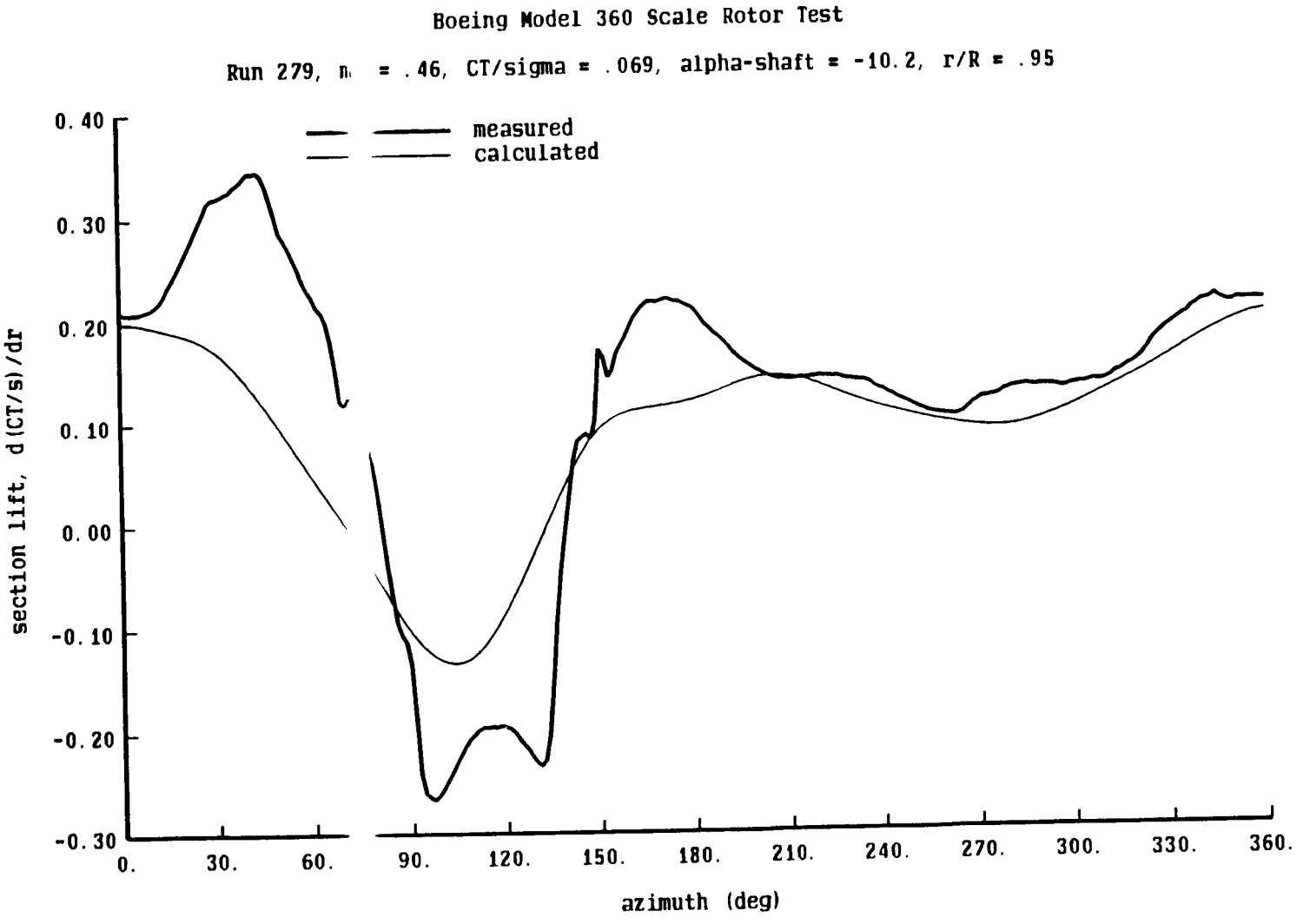

Figure 10-9h. Model 360 rotor: measured and calculated airloads

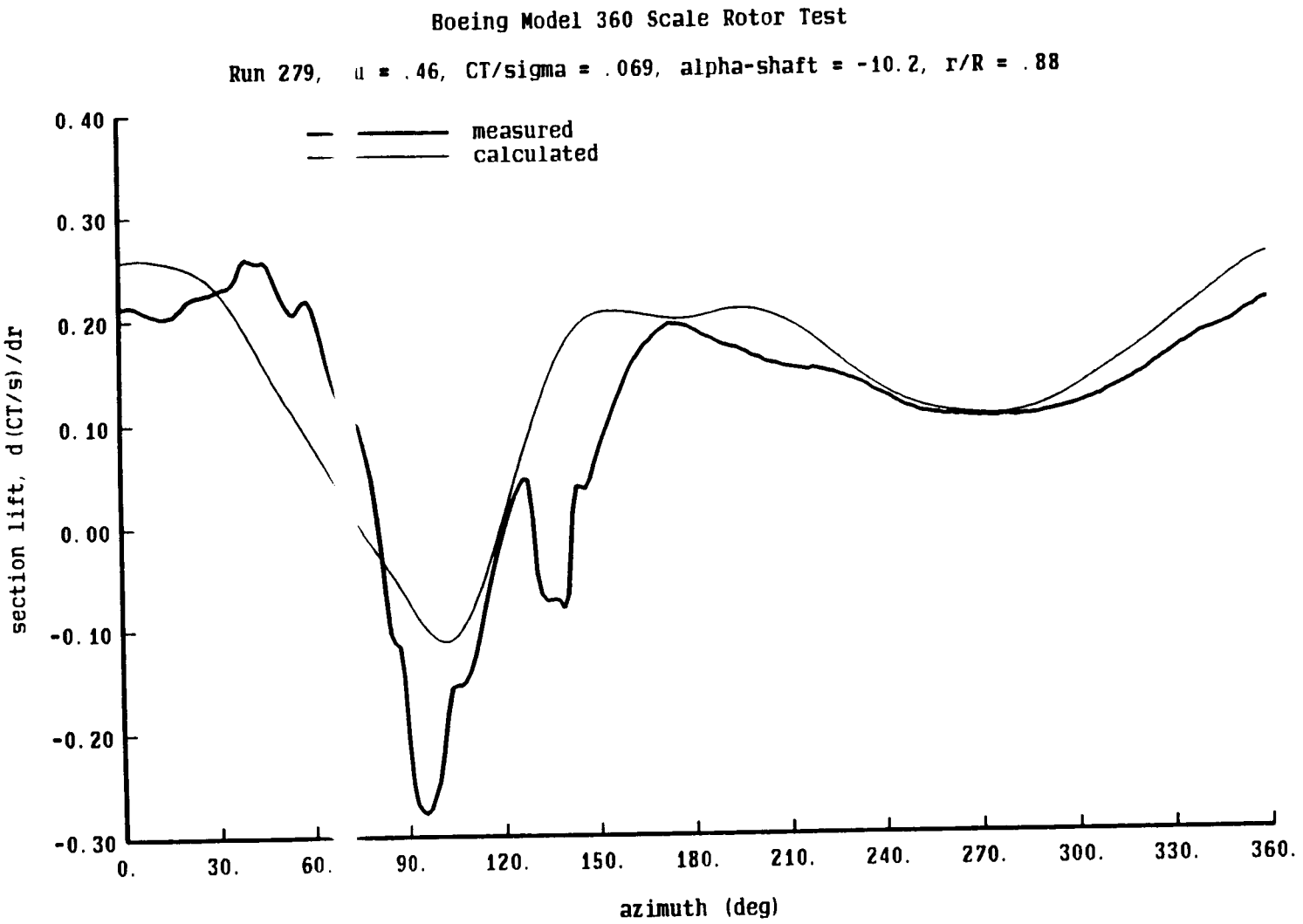

Figure 10-1 a. Model 360 rotor: airfoil table data

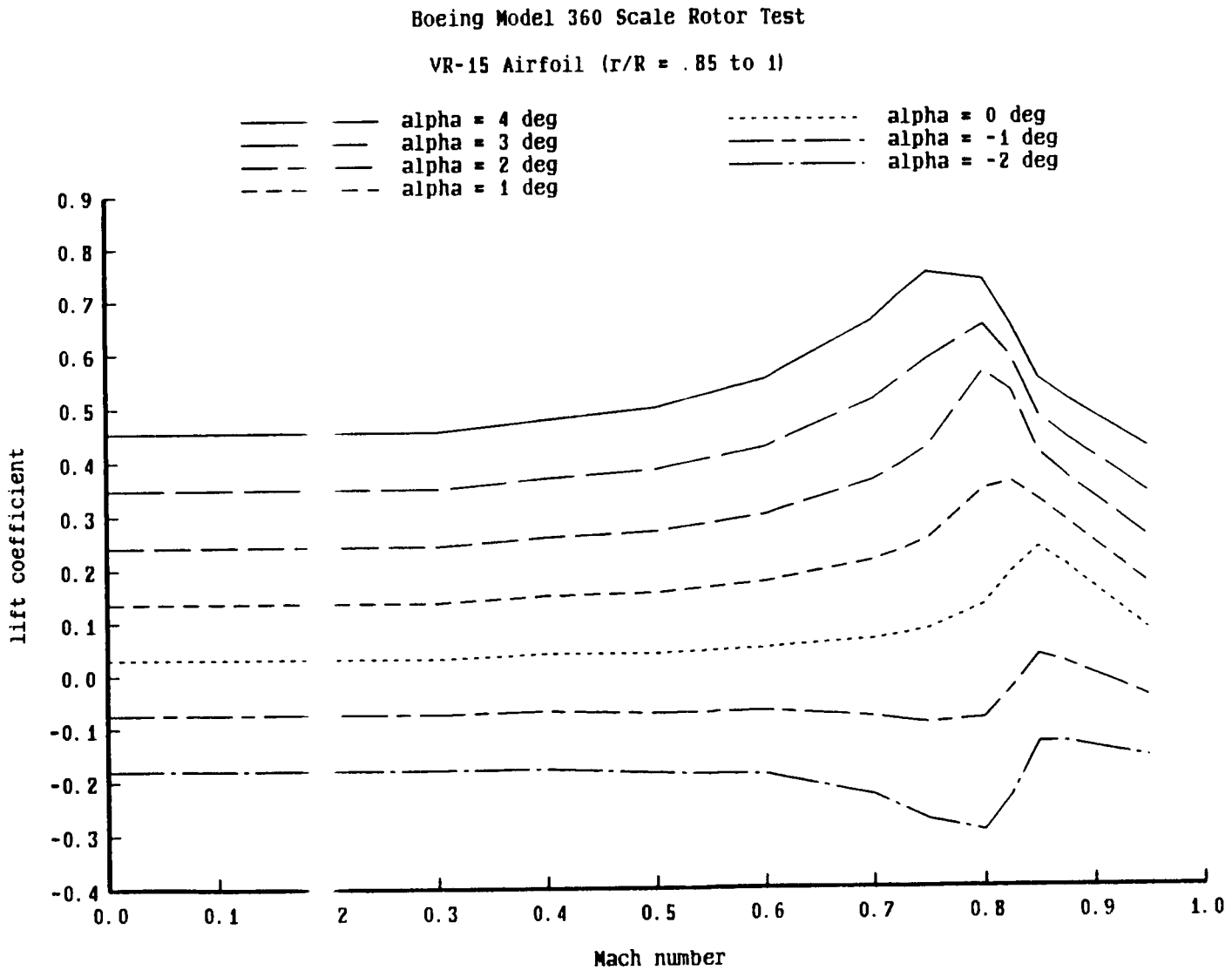

Figure 10b. Model 360 rotor: airfoil table data

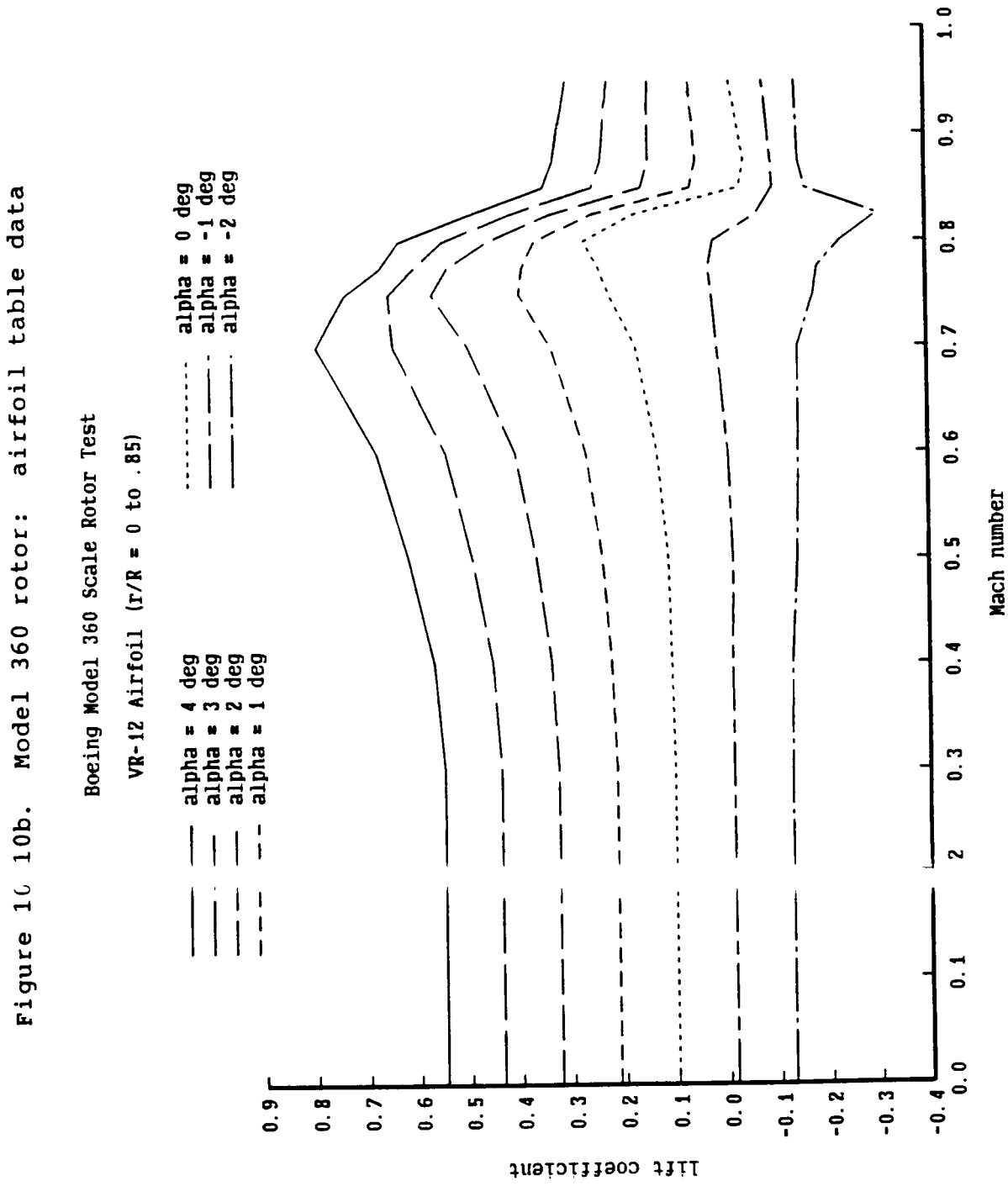

Figure 10-11a Model 360 rotor: measured and calculated torsion moment

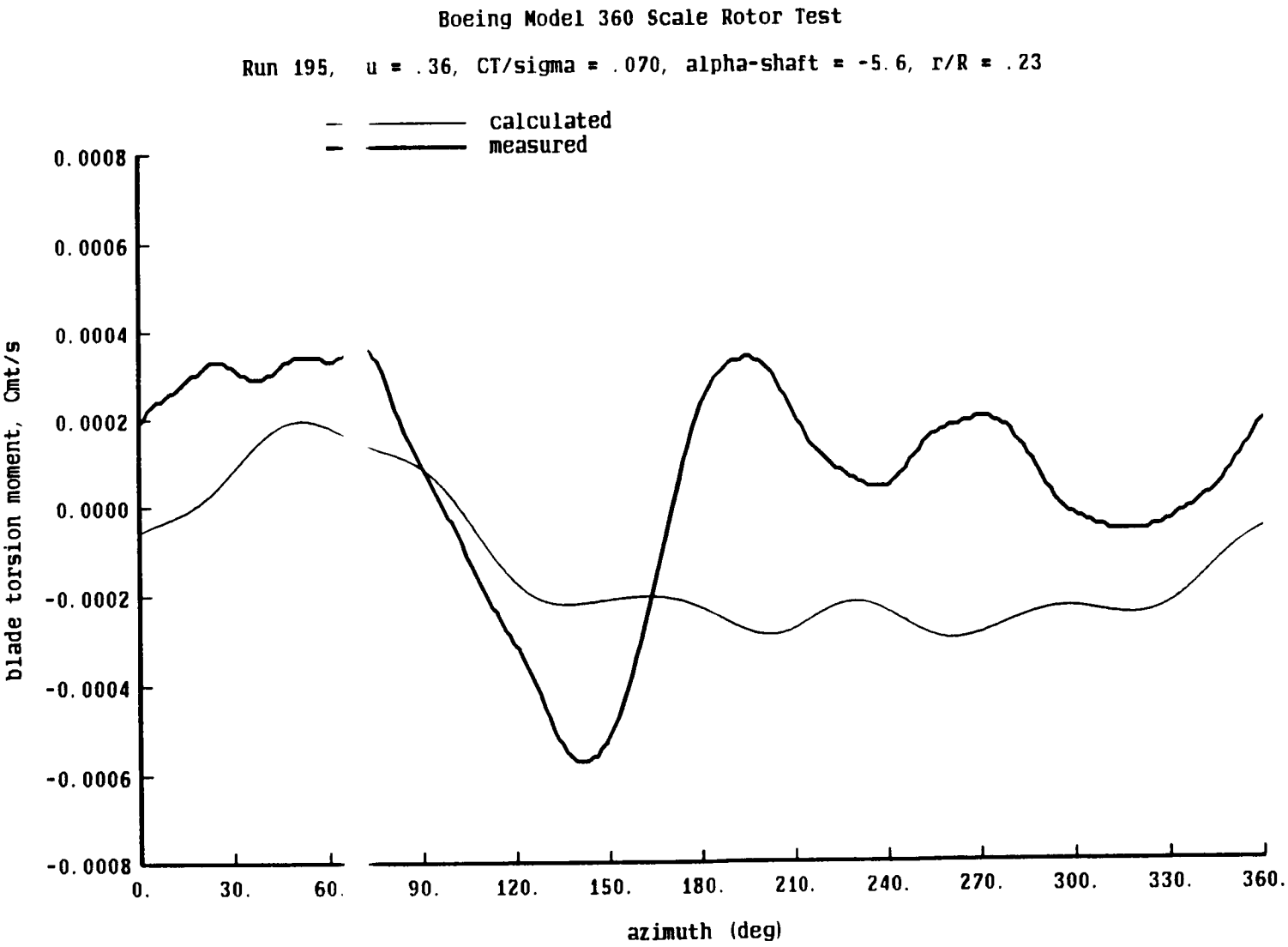

Figure 10-1 b. Model 360 rotor: measured and calculated torsion moment

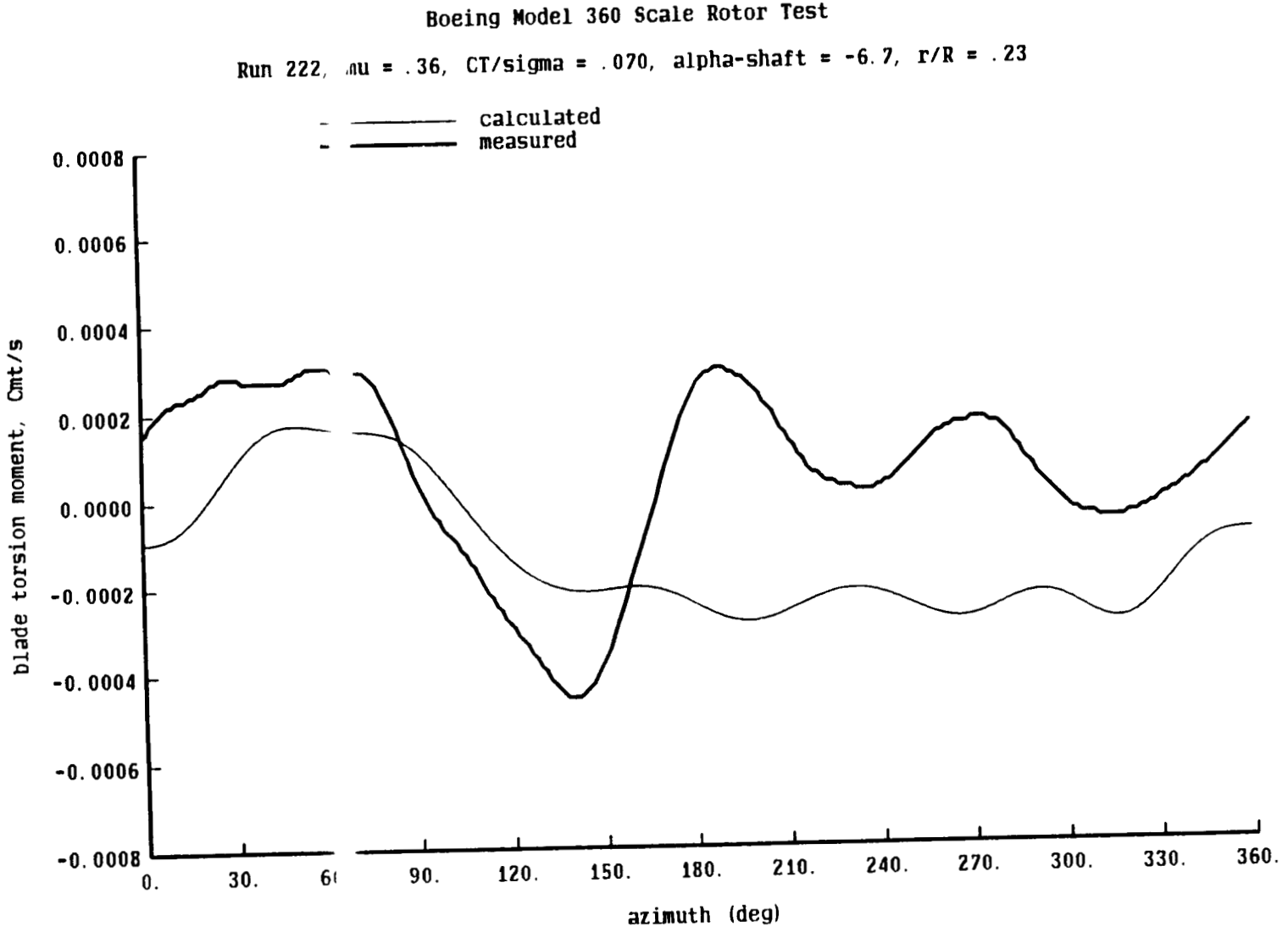

Figure 10-11c. Model 360 rotor: measured and calculated torsion moment

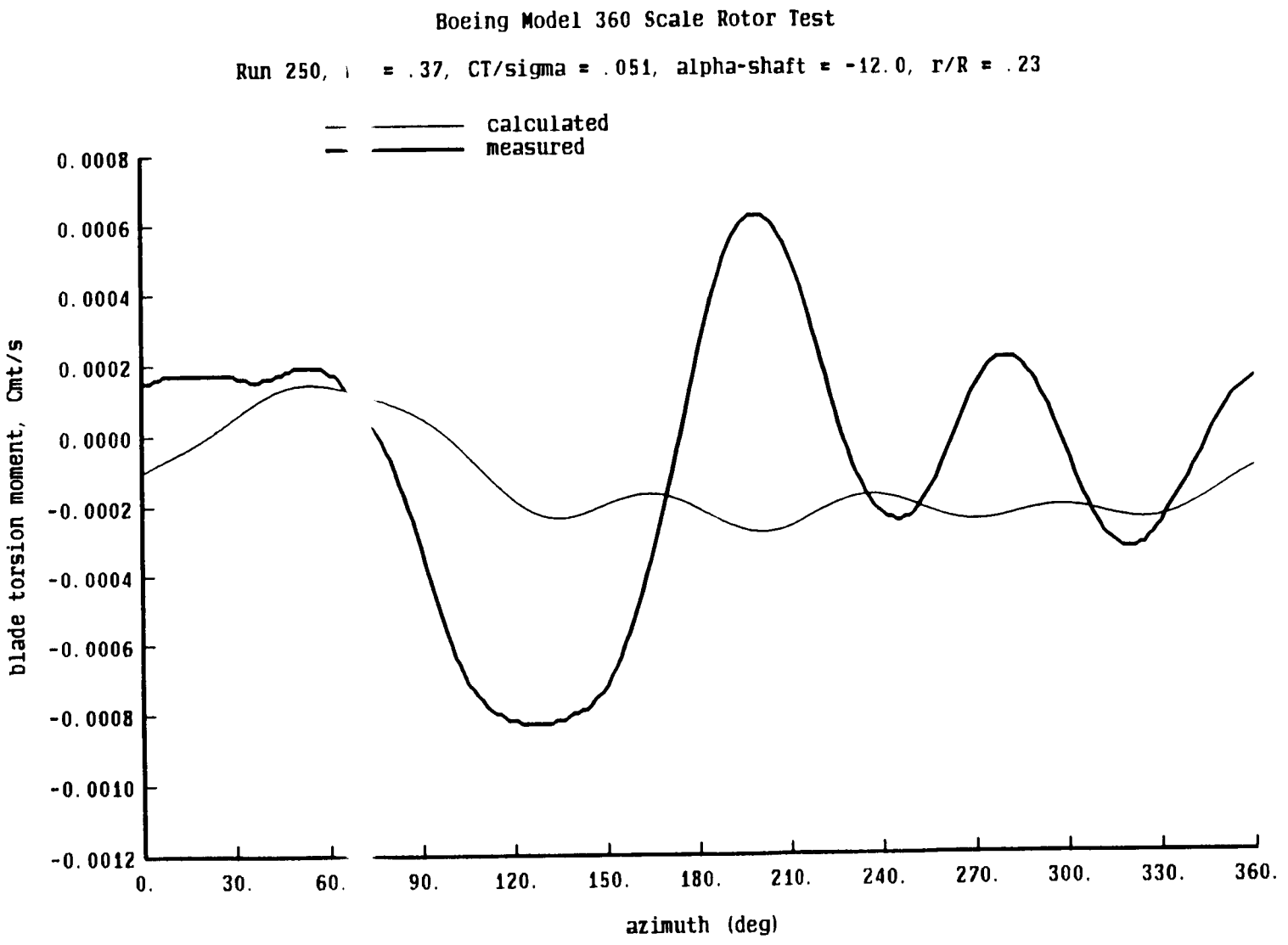

Figure 10-11d. Model 360 rotor: measured and calculated torsion moment

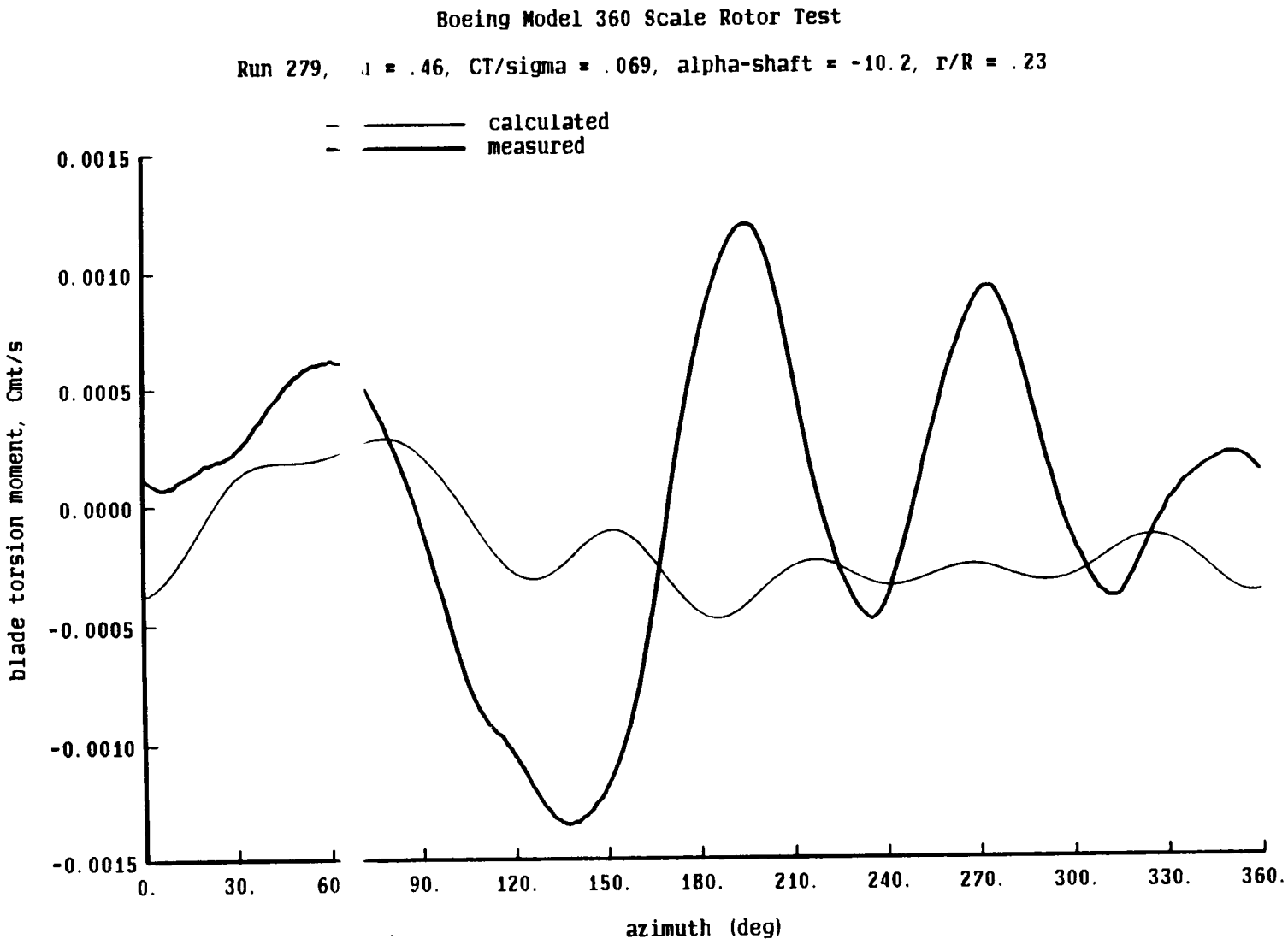

Figure 10-12 . Model 360 rotor: influence of torsion stiffness and center-of-gravity position

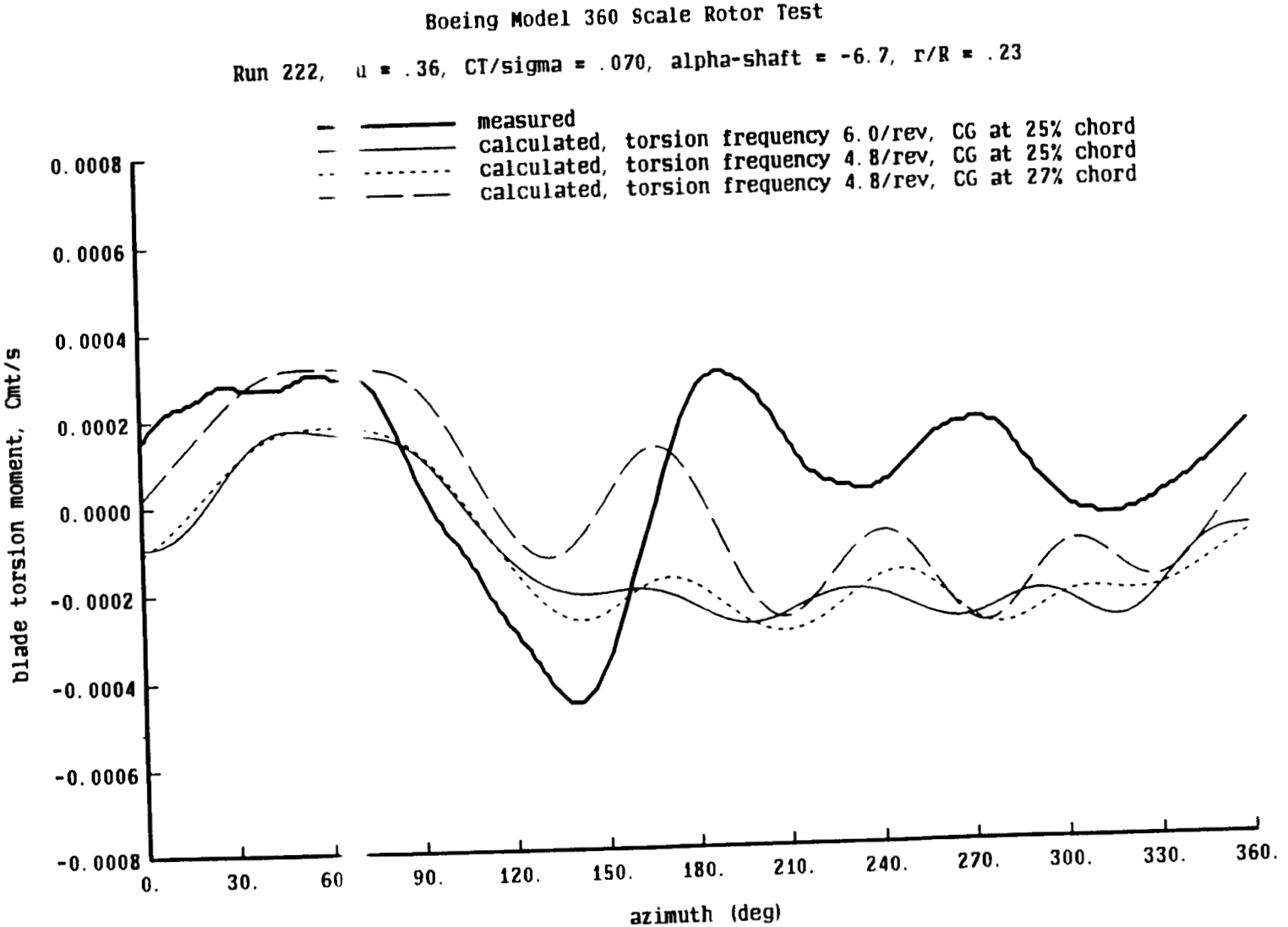

Figure 10-12b. Model 360 rotor: influence of torsion stiffness and center-of-gravity position

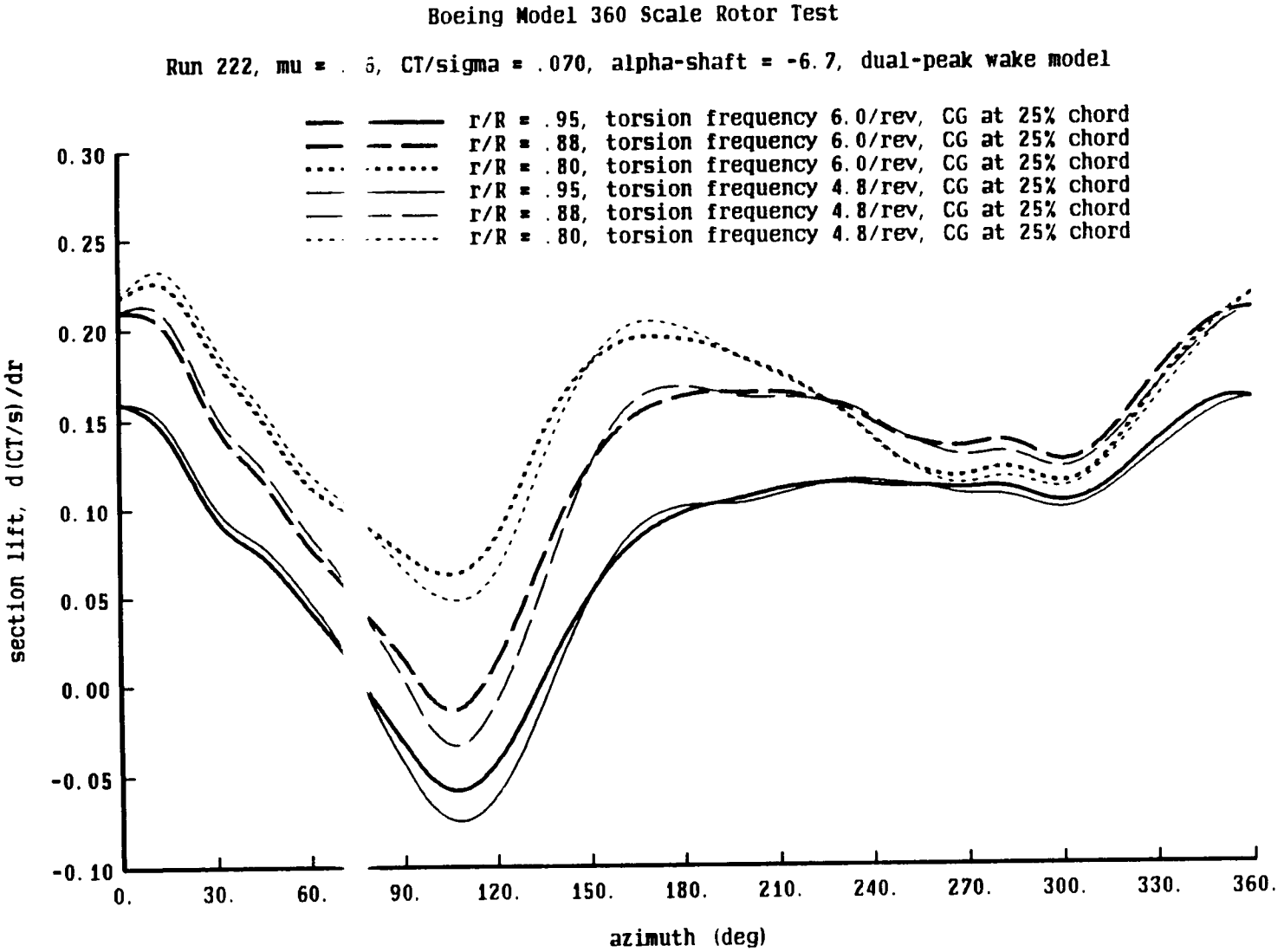

Figure 10-12c. Model 360 rotor: influence of torsion stiffness and center-of-gravity position

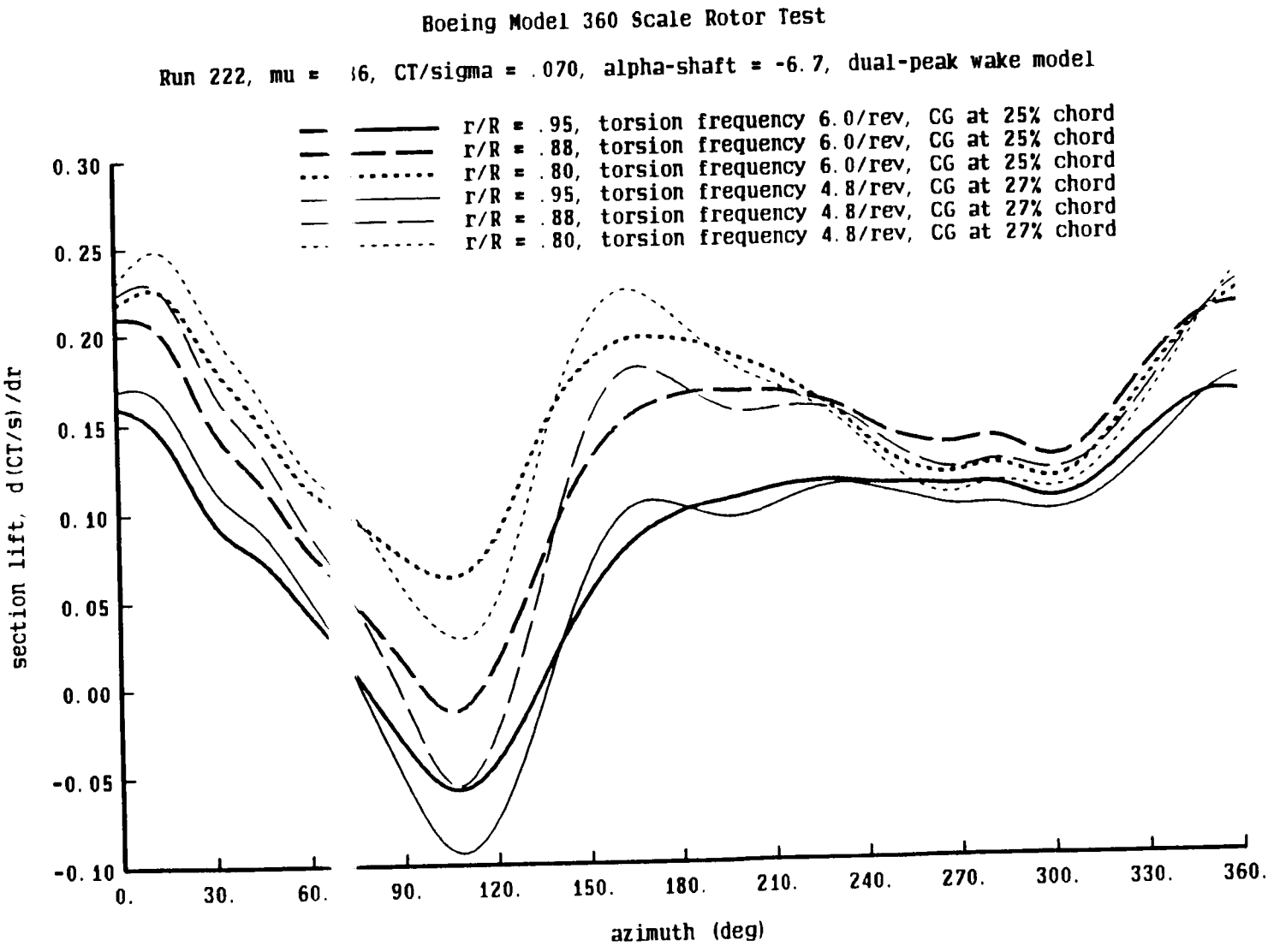

Figure 11-1a. H34 wind tunnel test: influence of far wake model

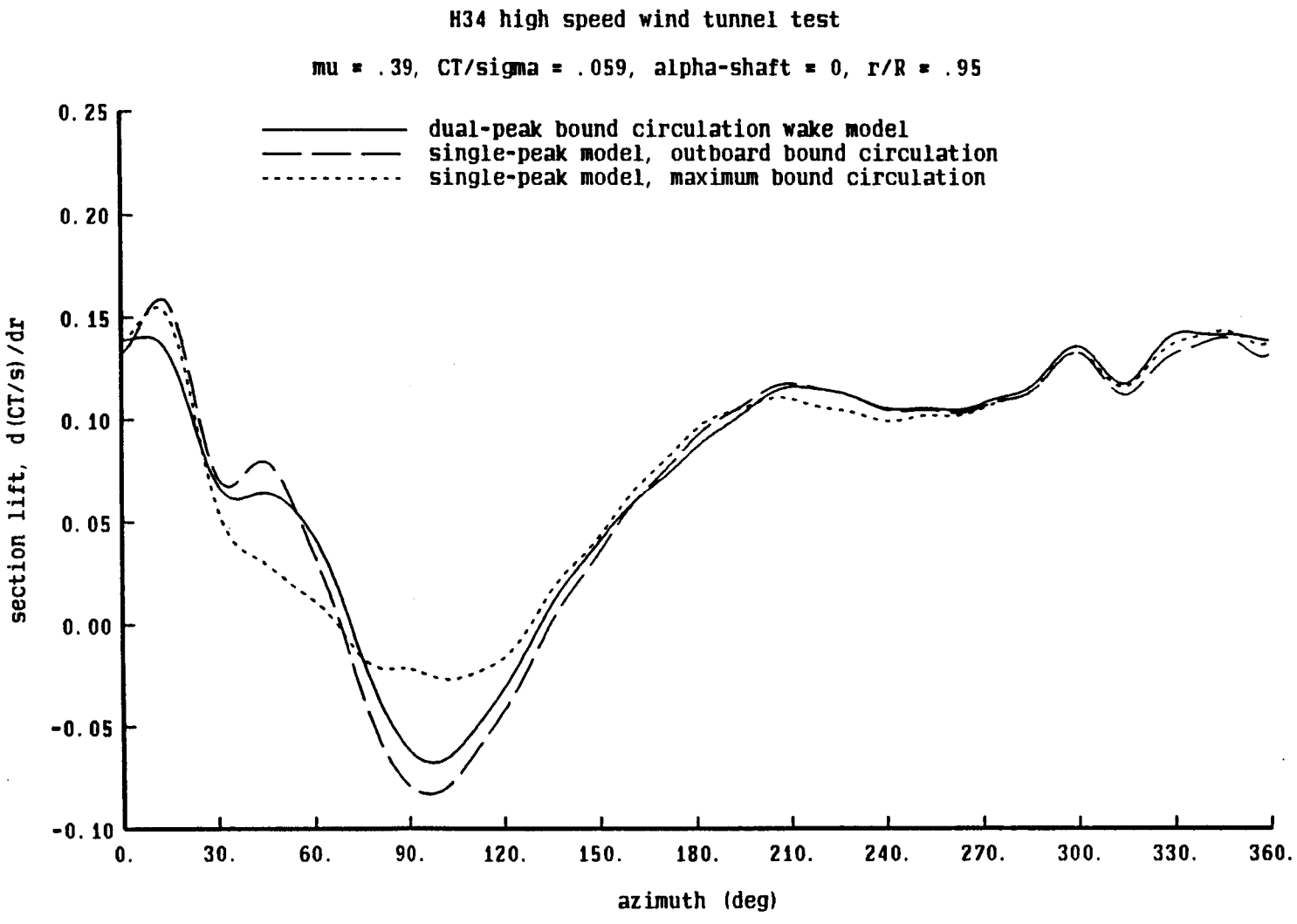

Figure 11-1b. H34 wind tunnel test: influence of far wake model

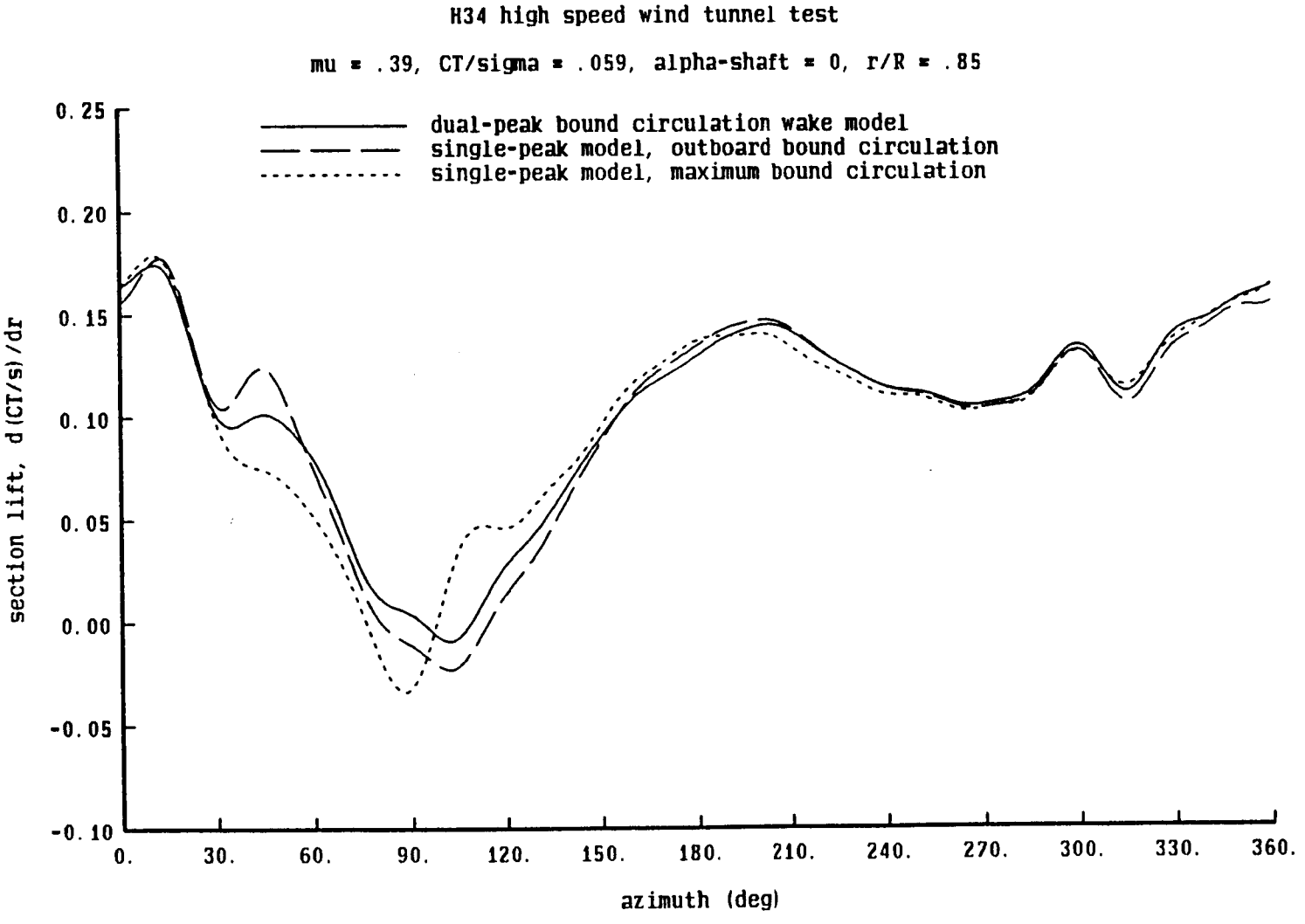

Figure 11-1c. H34 wind tunnel test: influence of far wake model

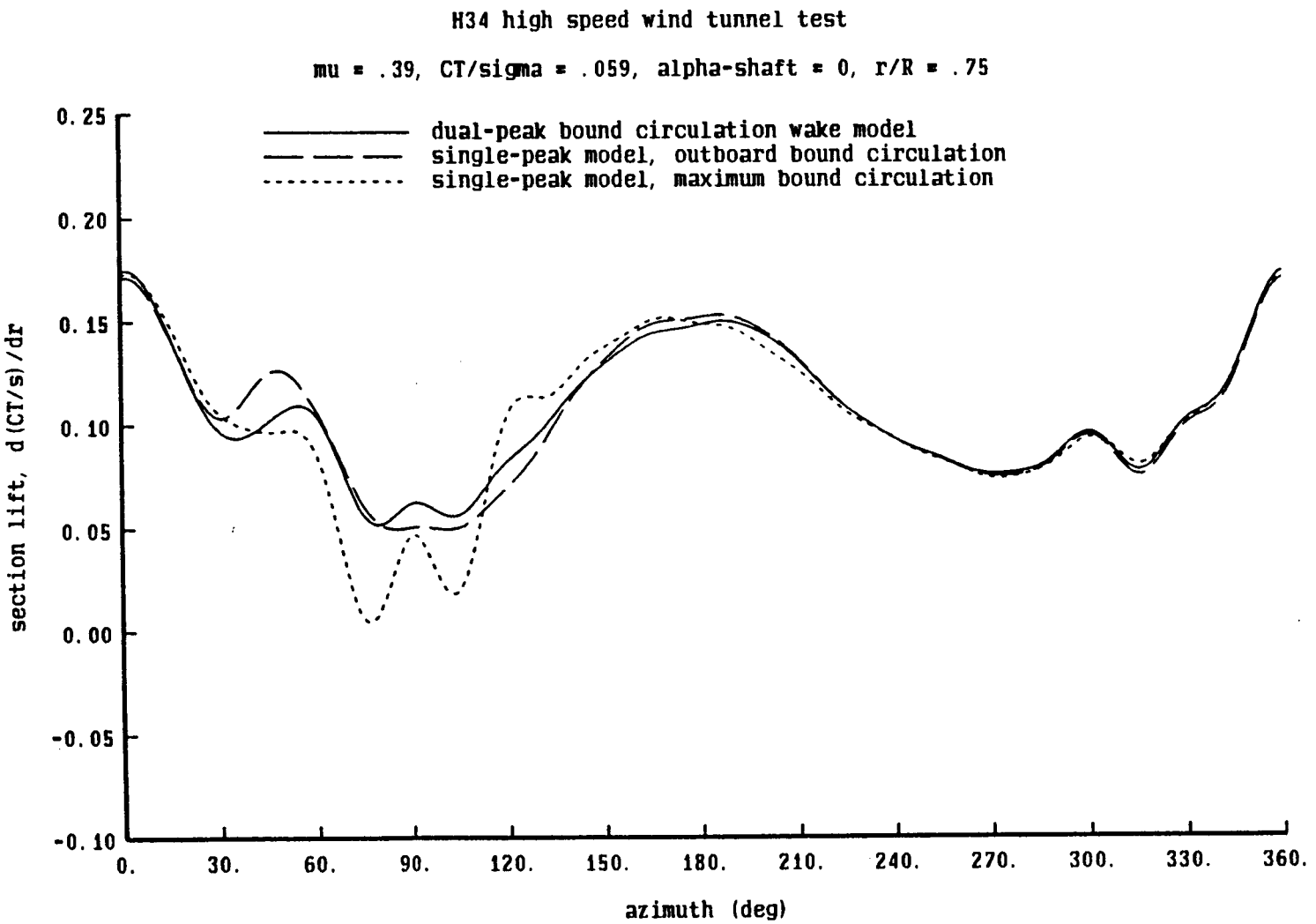

Figure 11-2a. H34 wind tunnel test: convergence of wake geometry for dual-peak model

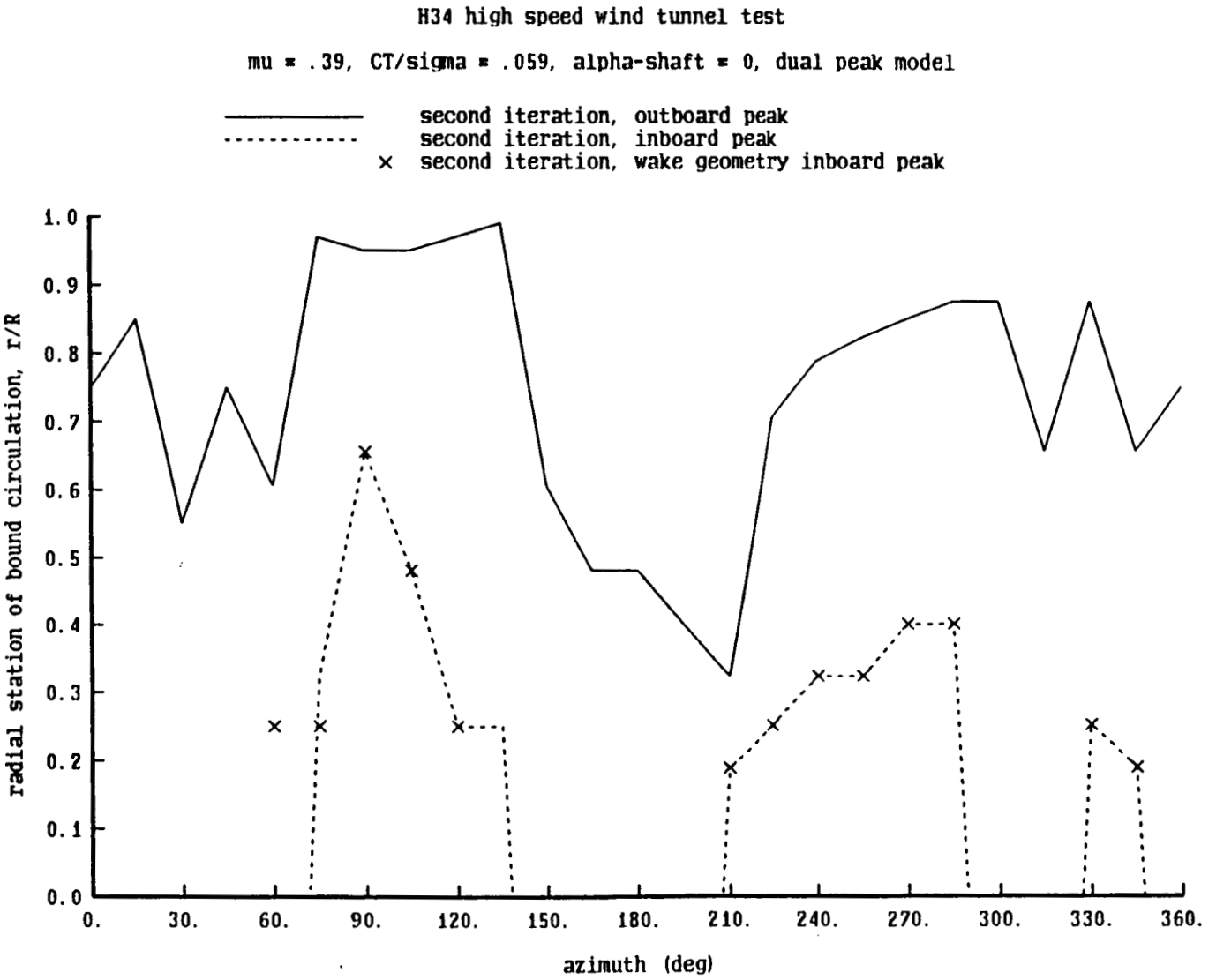

Figure 11-2b. H34 wind tunnel test: convergence of wake geometry for dual-peak model

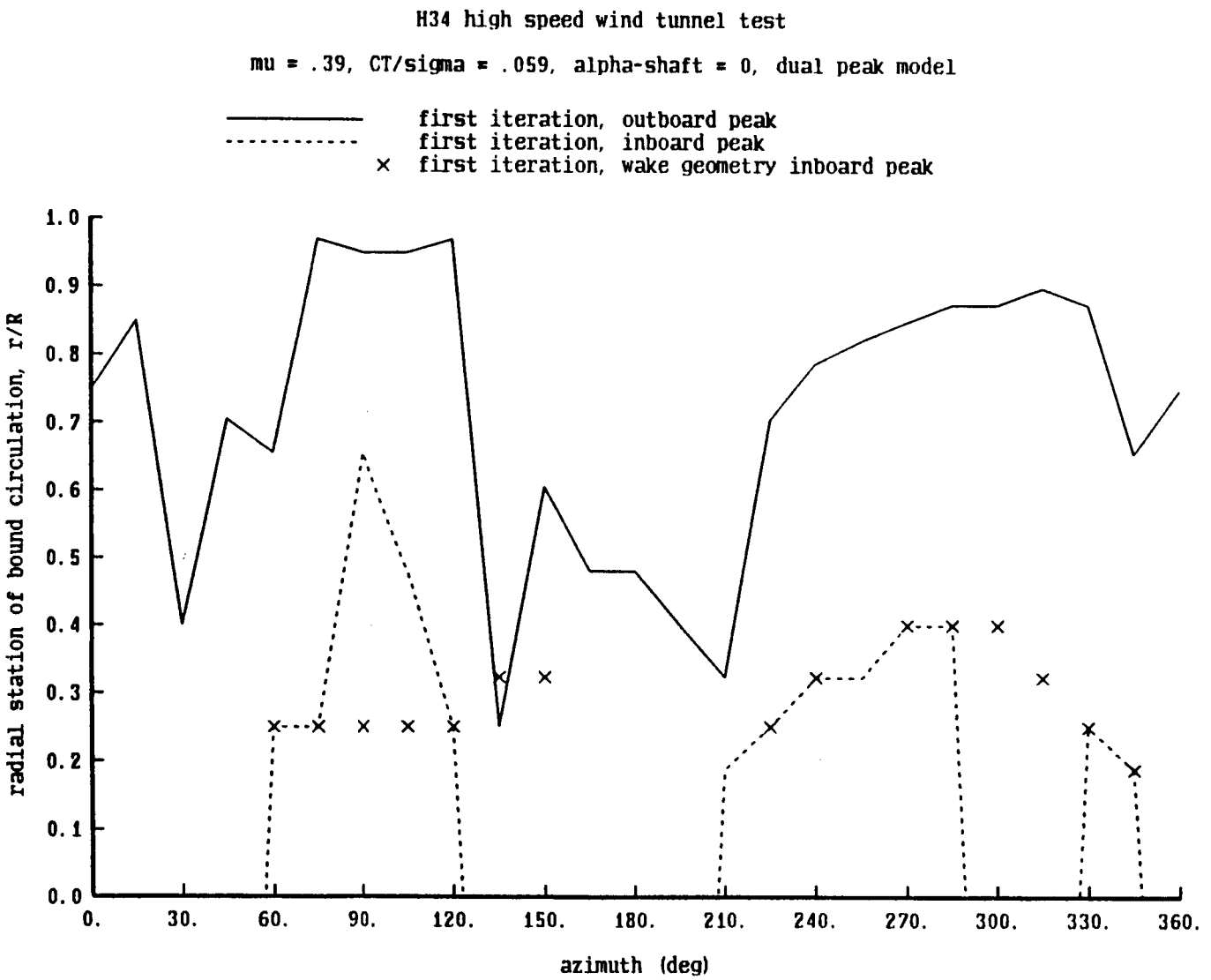

Figure 11-2c. H34 wind tunnel test: convergence of wake geometry for dual-peak model

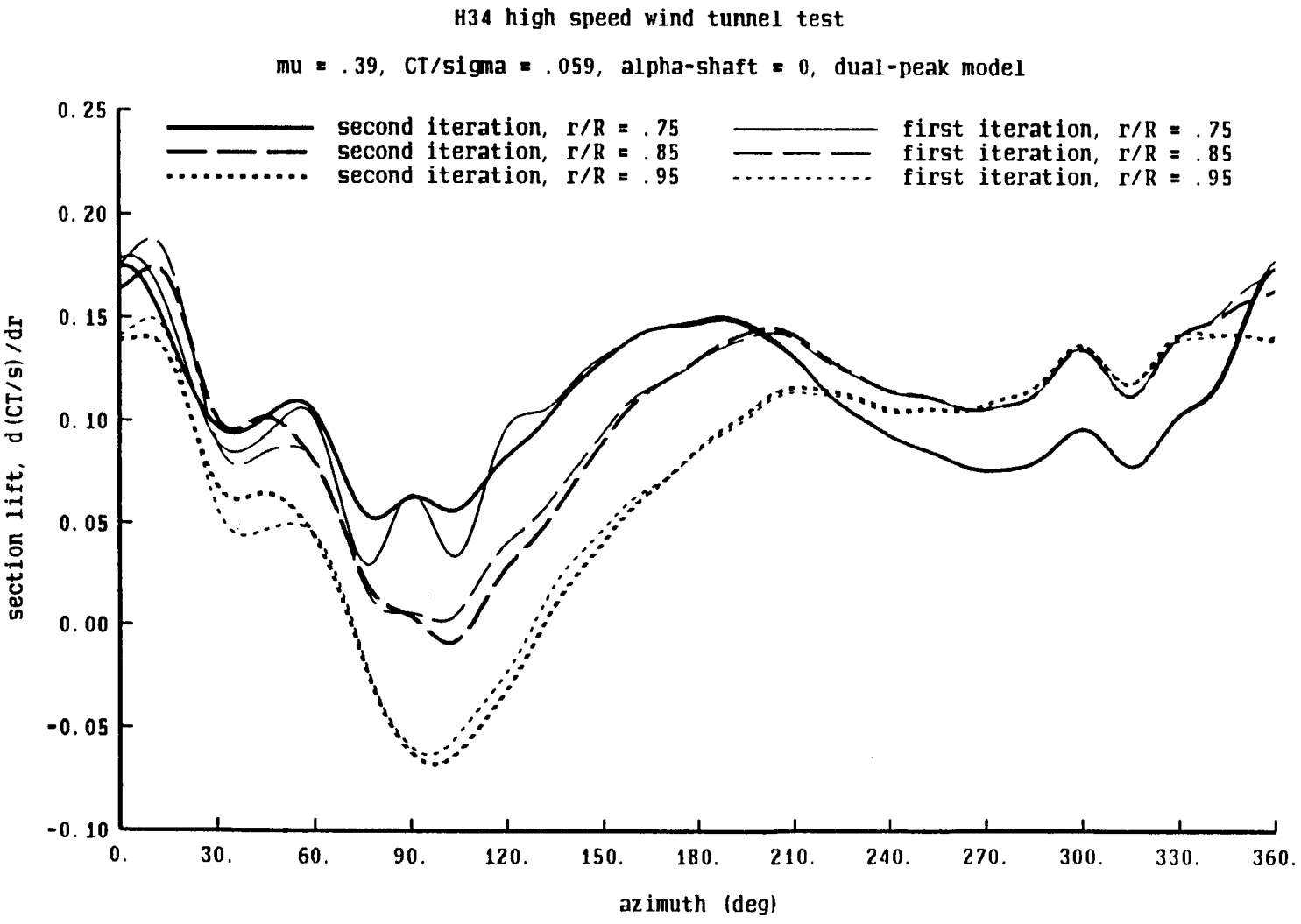

Figure 11-2d. H34 wind tunnel test: convergence of wake geometry for dual-peak model

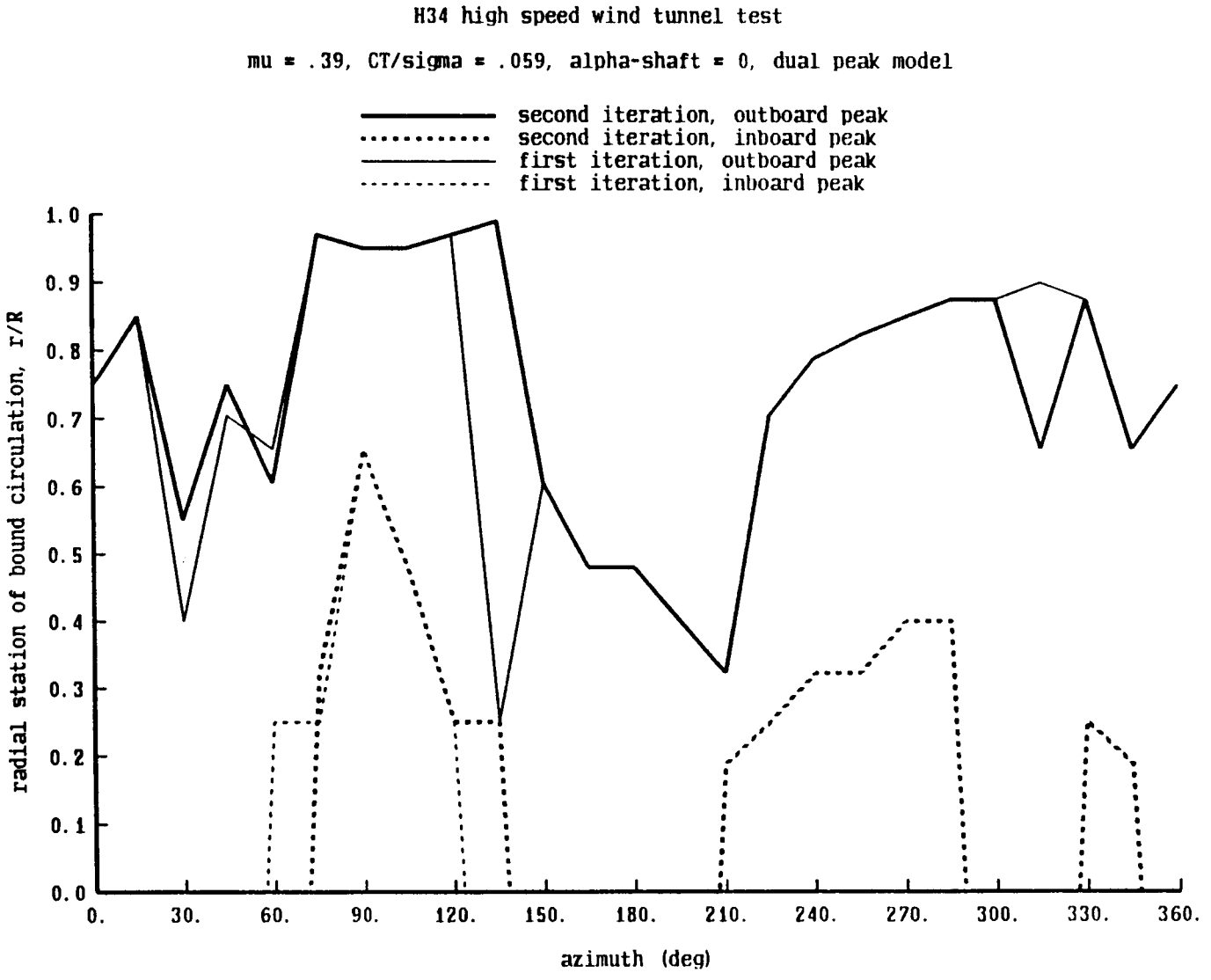

Figure 11-2e. H34 wind tunnel test: convergence of wake geometry for dual-peak model

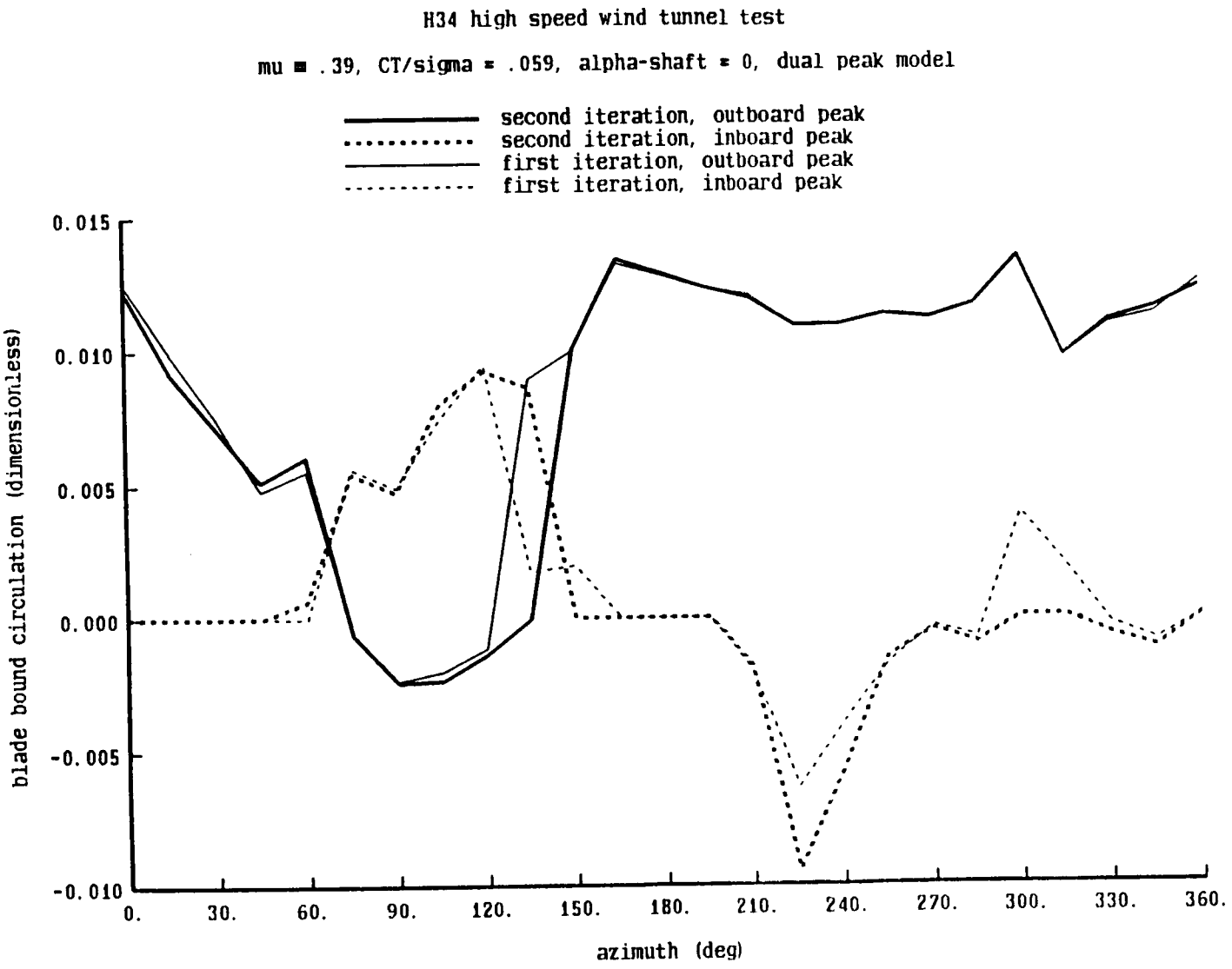

Figure 11-3a. H34 wind tunnel test: influence of near wake model and blade elastic motion

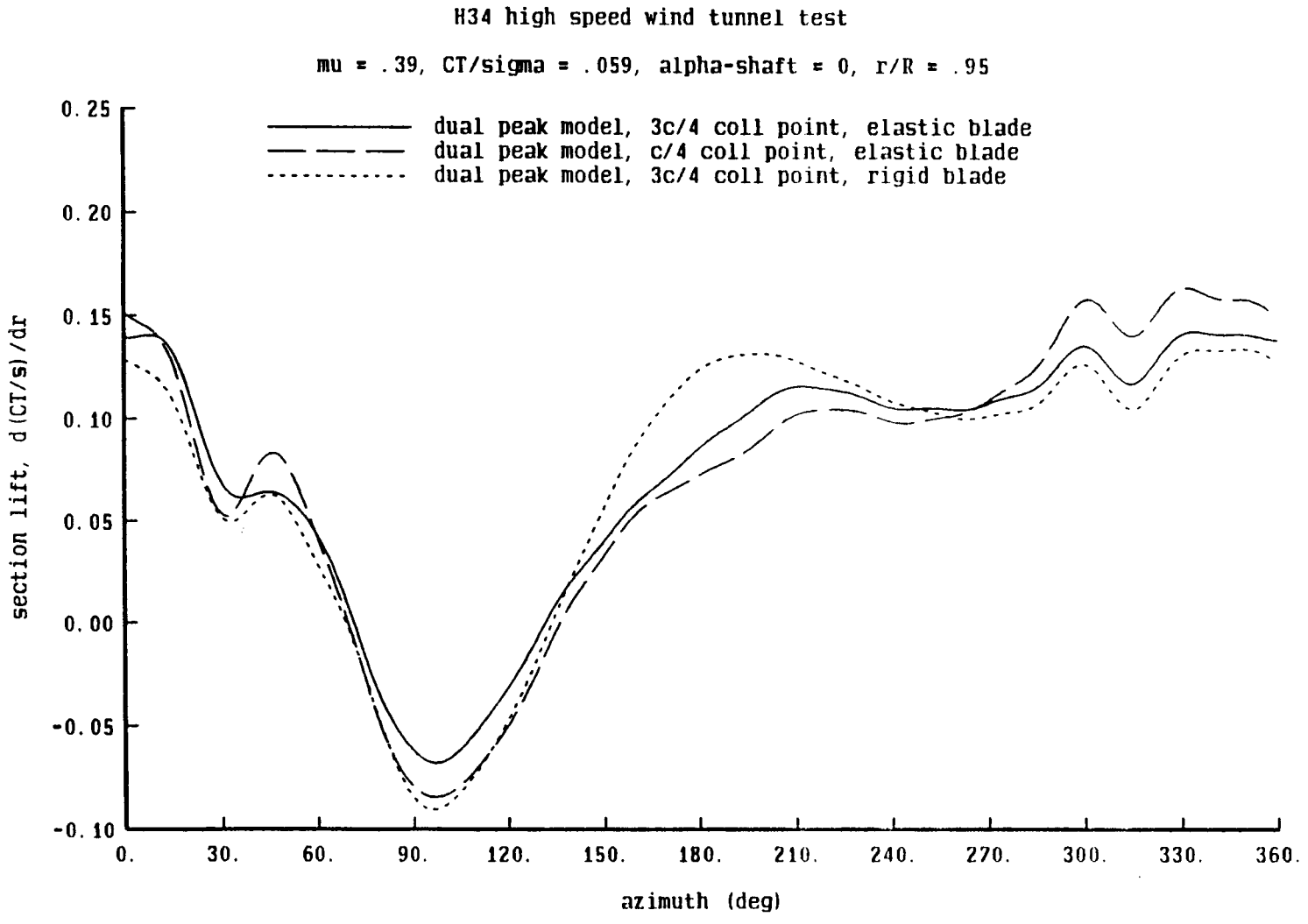

Figure 11-3b. H34 wind tunnel test: influence of near wake model and blade elastic motion

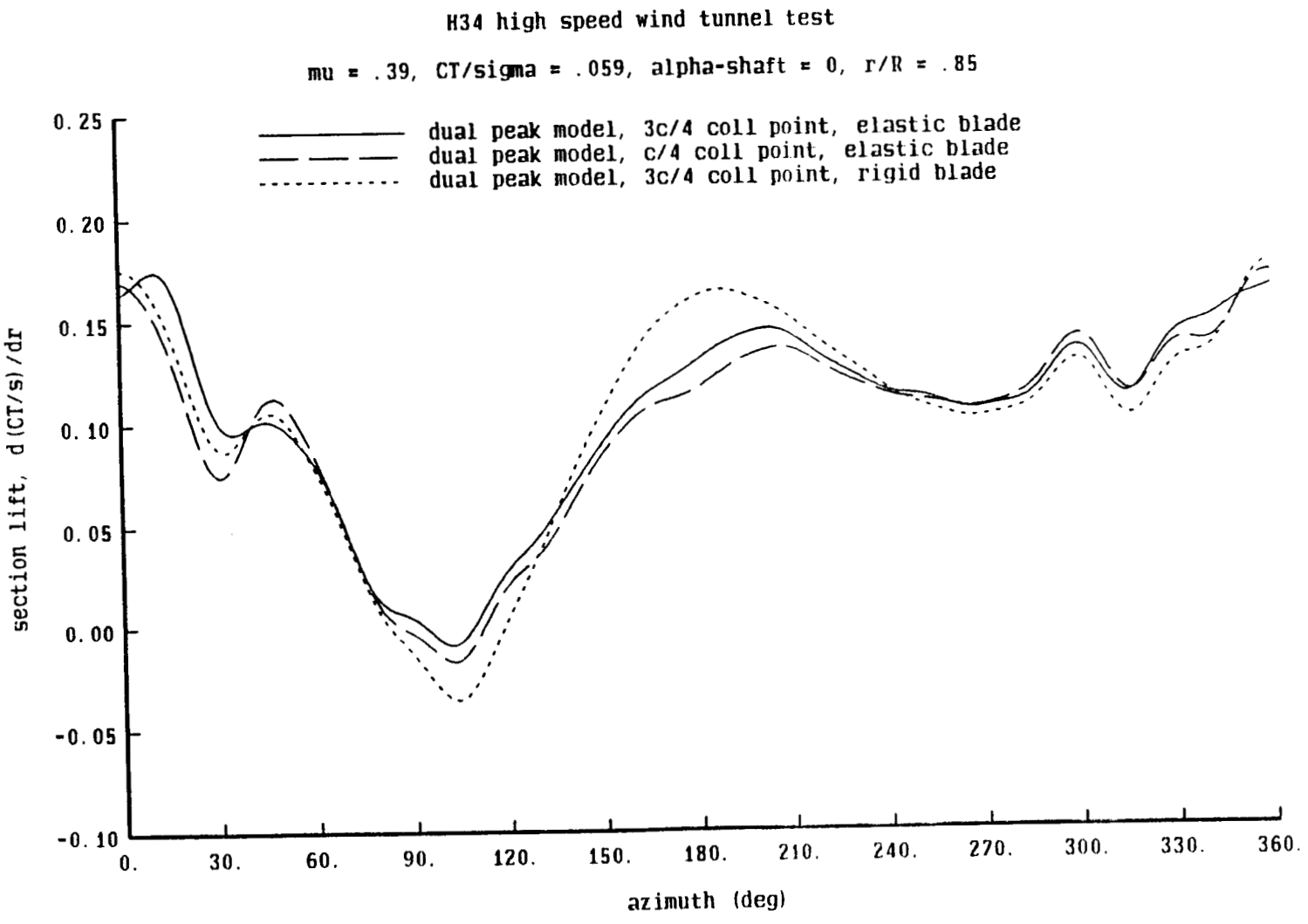

Figure 11-3c. H34 wind tunnel test: influence of near wake model and blade elastic motion

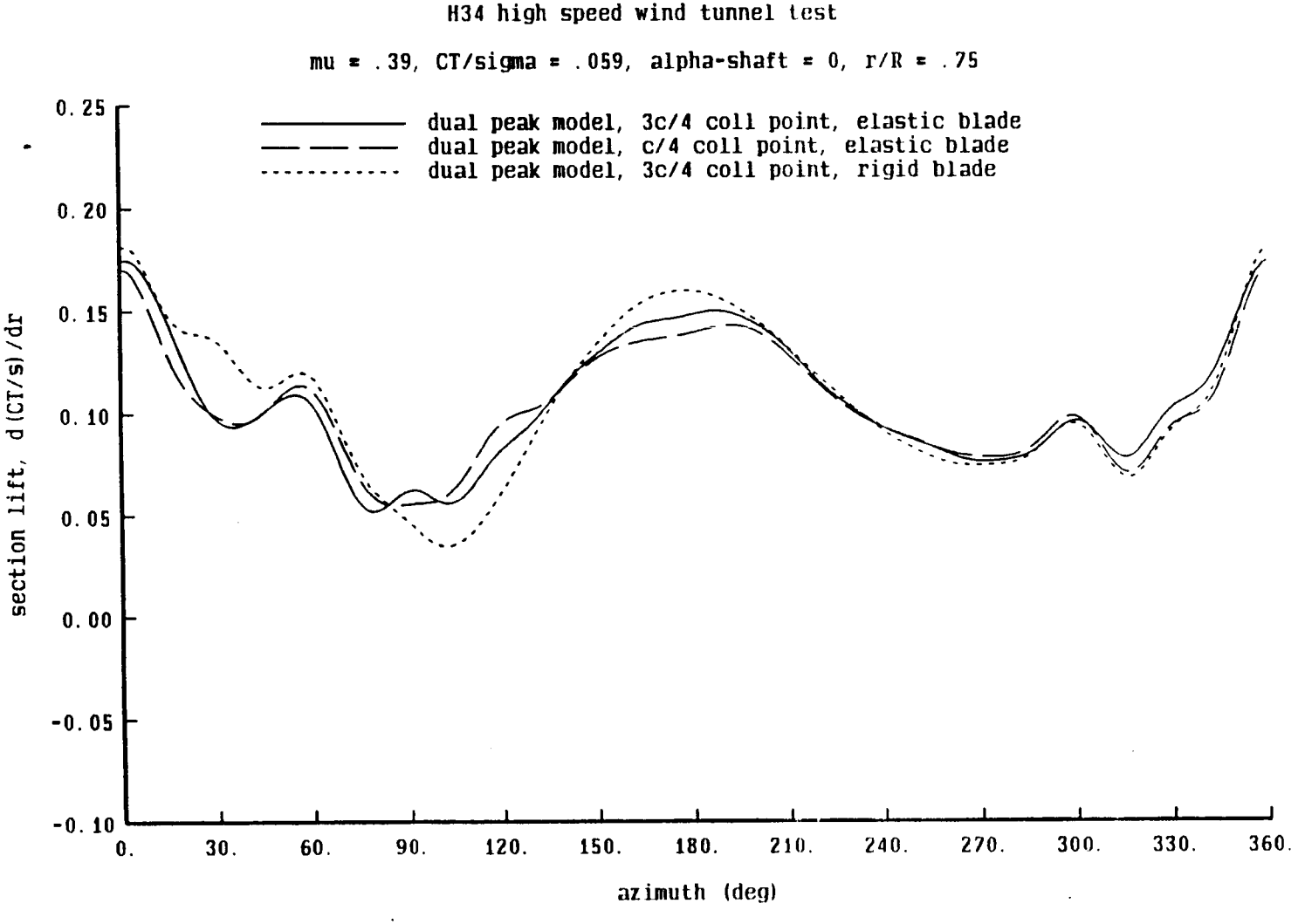

Figure 11-4a. H34 wind tunnel test: influence of tip vortex core and inboard rollup

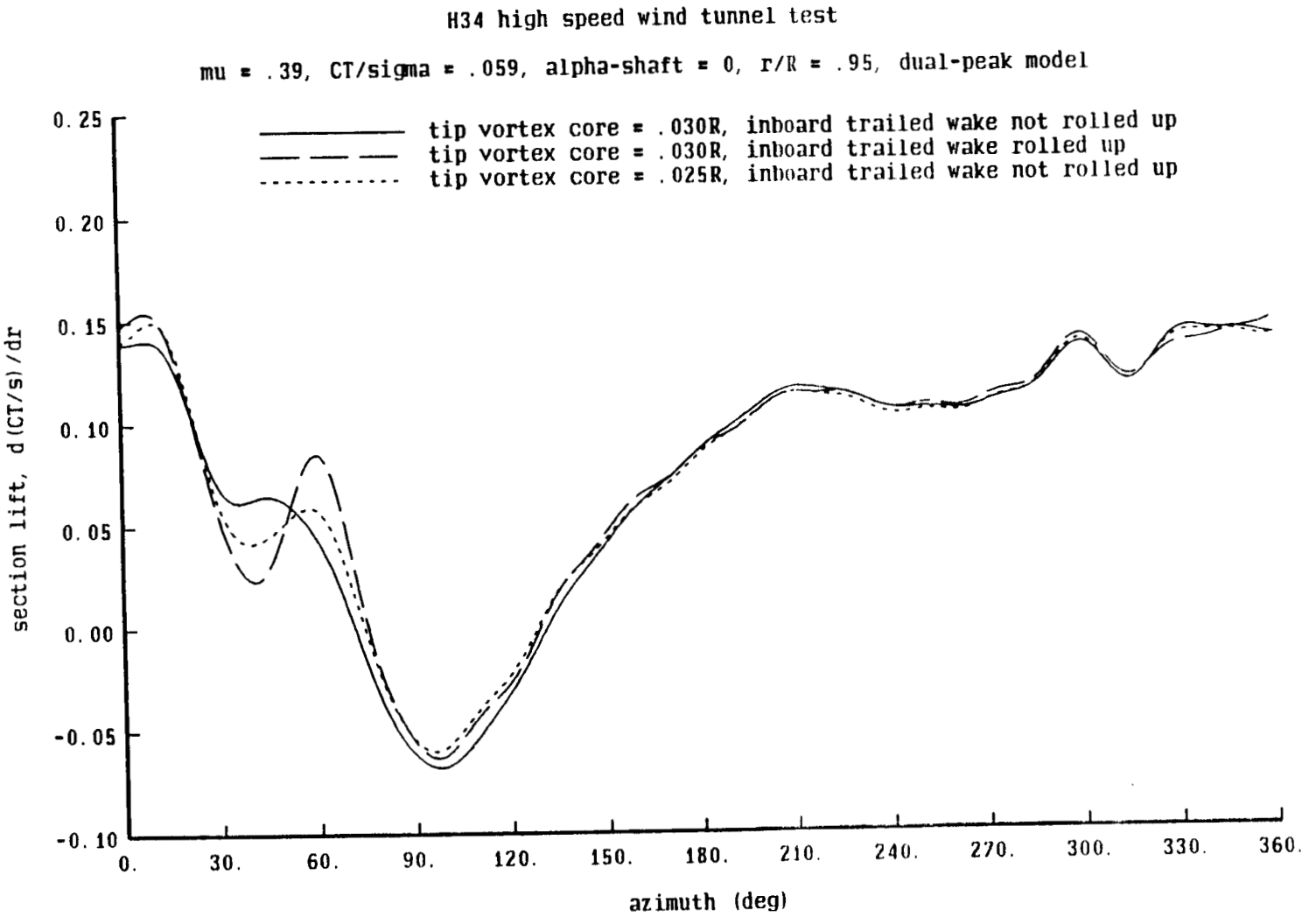

Figure 11-4b. H34 wind tunnel test: influence of tip vortex core and inboard rollup

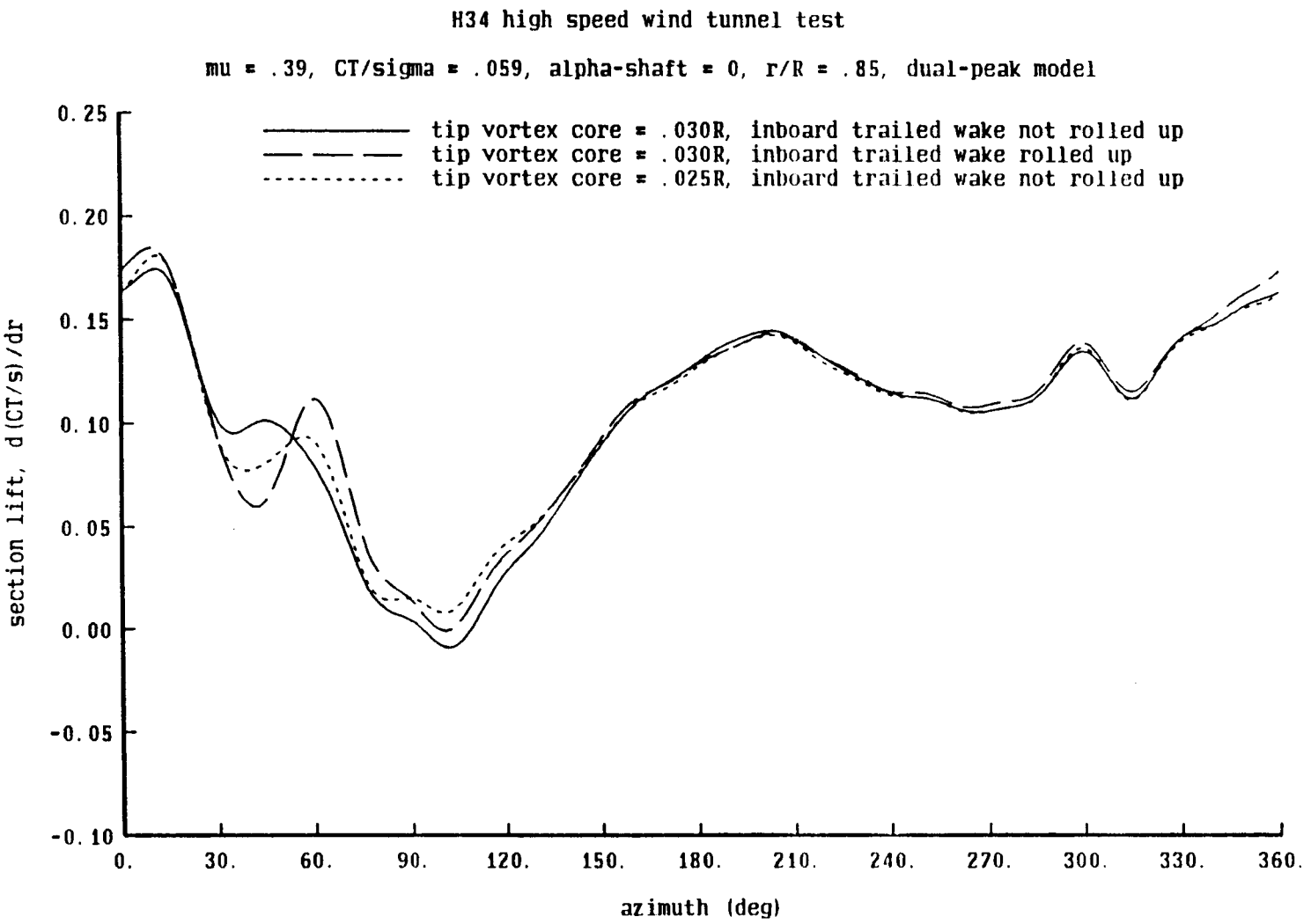

Figure 11-4c. H34 wind tunnel test: influence of tip vortex core and inboard rollup

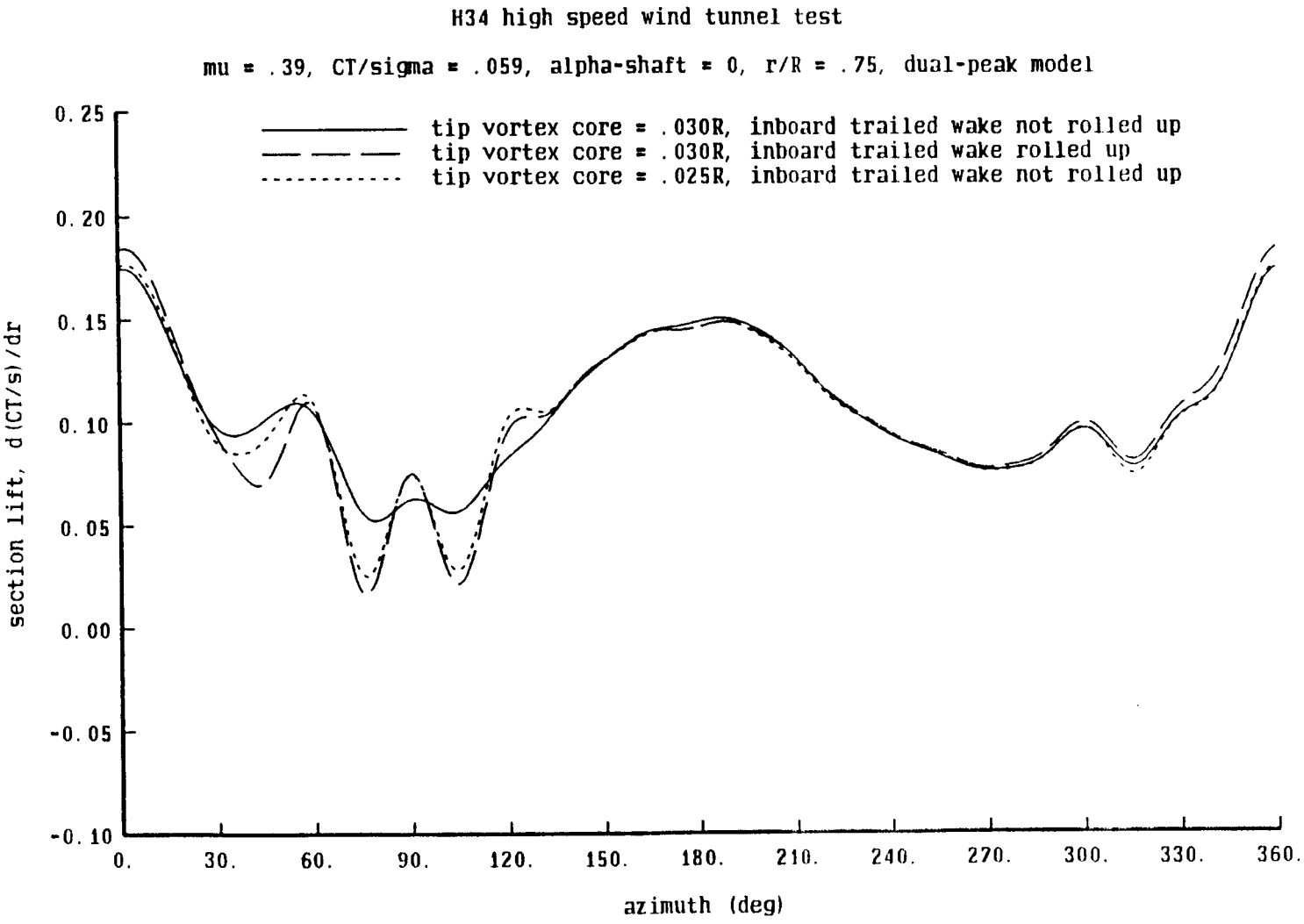

Figure 11-5a. H34 wind tunnel test: measured and calculated airloads

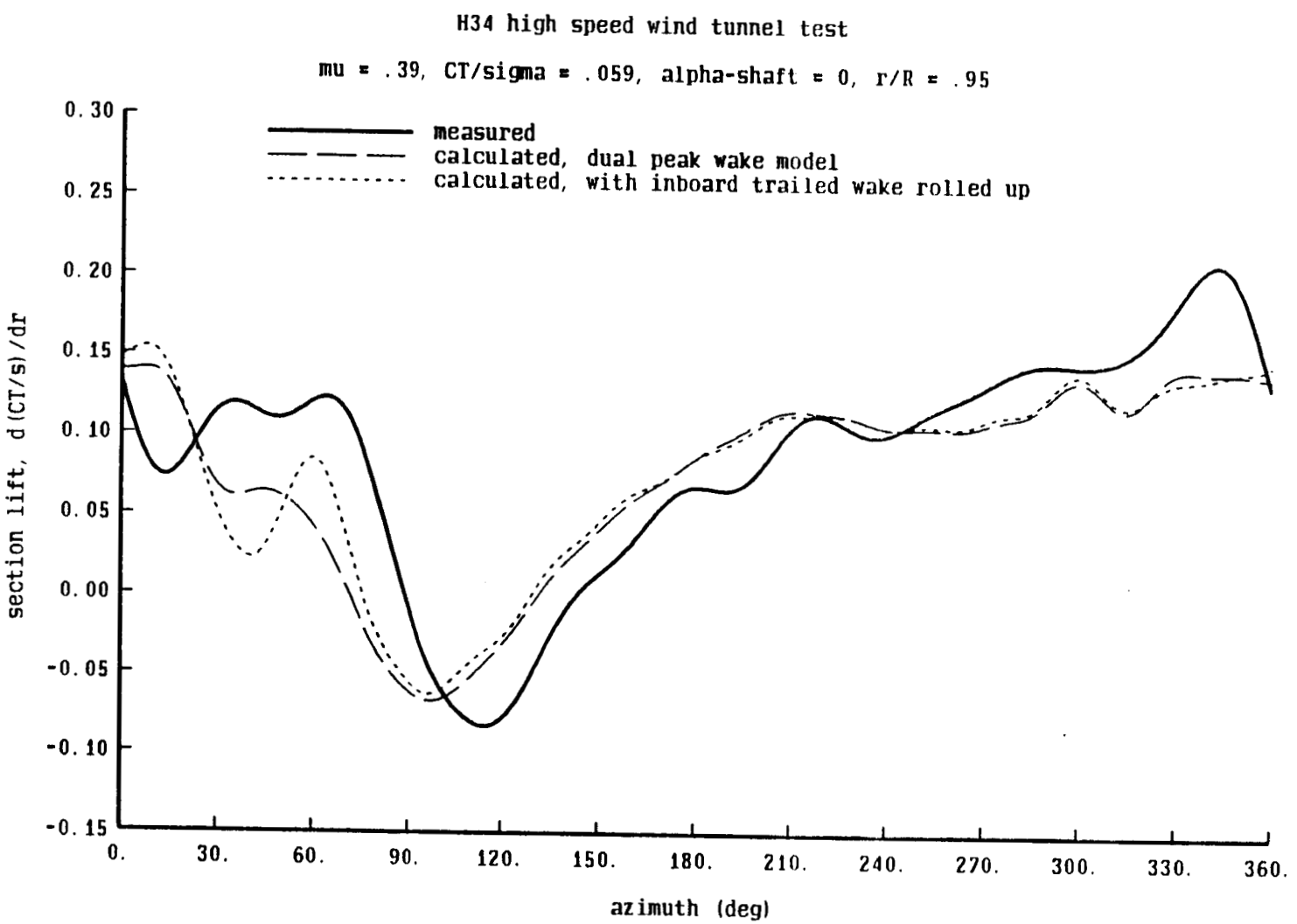

Figure 11-5b. H34 wind tunnel test: measured and calculated airloads

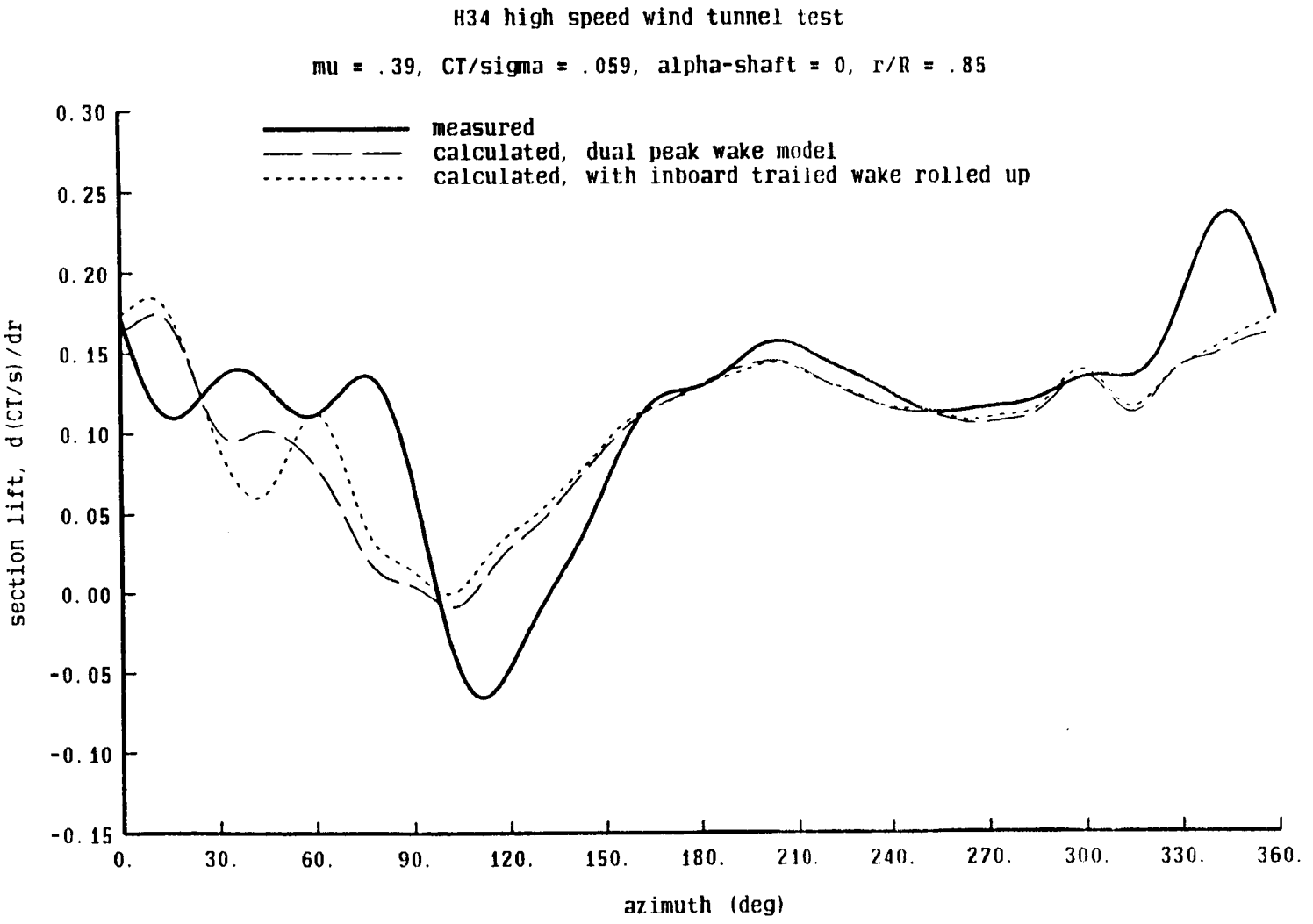

Figure 11-5c. H34 wind tunnel test: measured and calculated airloads

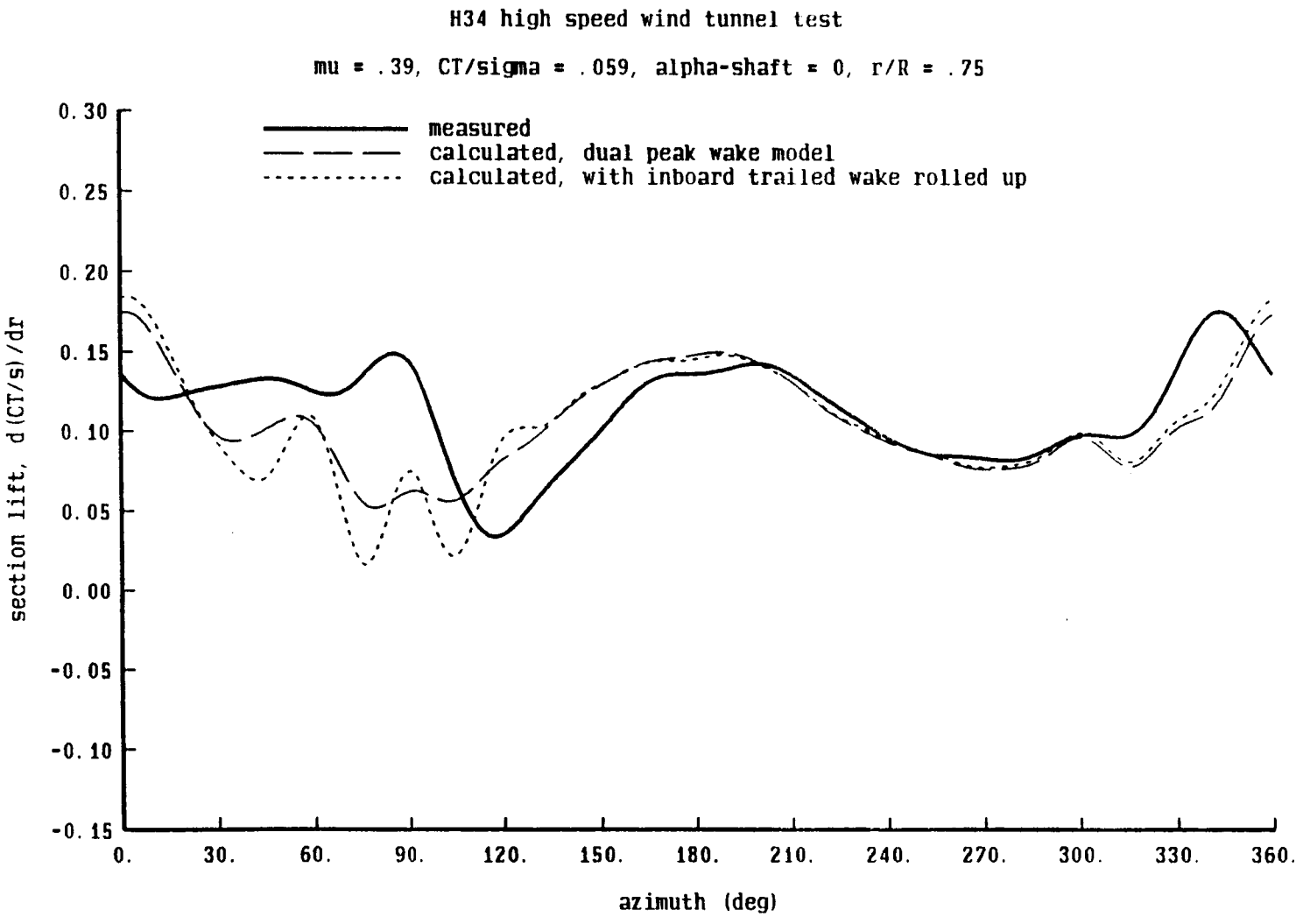

Figure 11-6a. H34 wind tunnel test: measured and calculated airloads

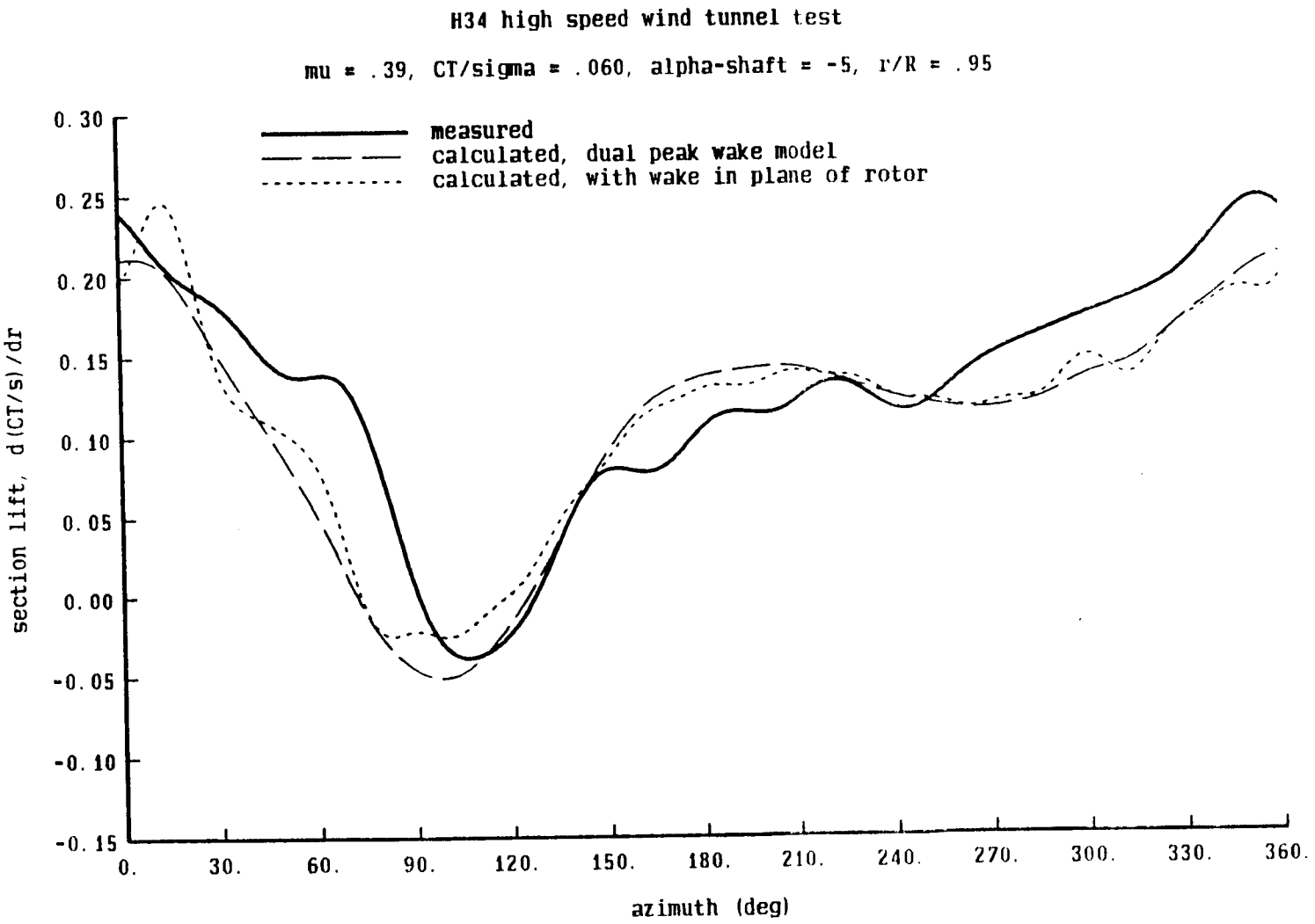

Figure 11-6b. H34 wind tunnel test: measured and calculated airloads

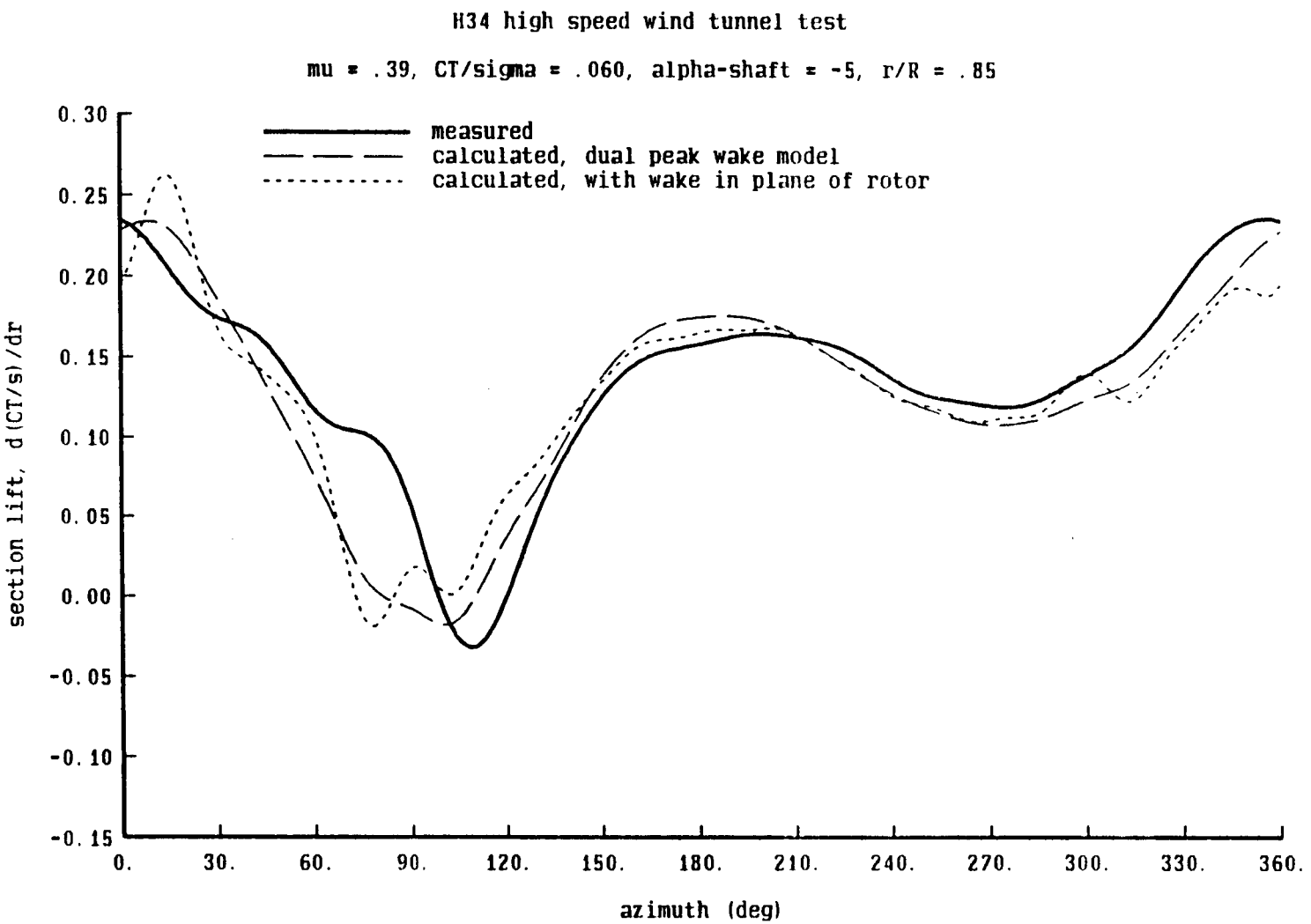

Figure 11-6c. H34 wind tunnel test: measured and calculated airloads

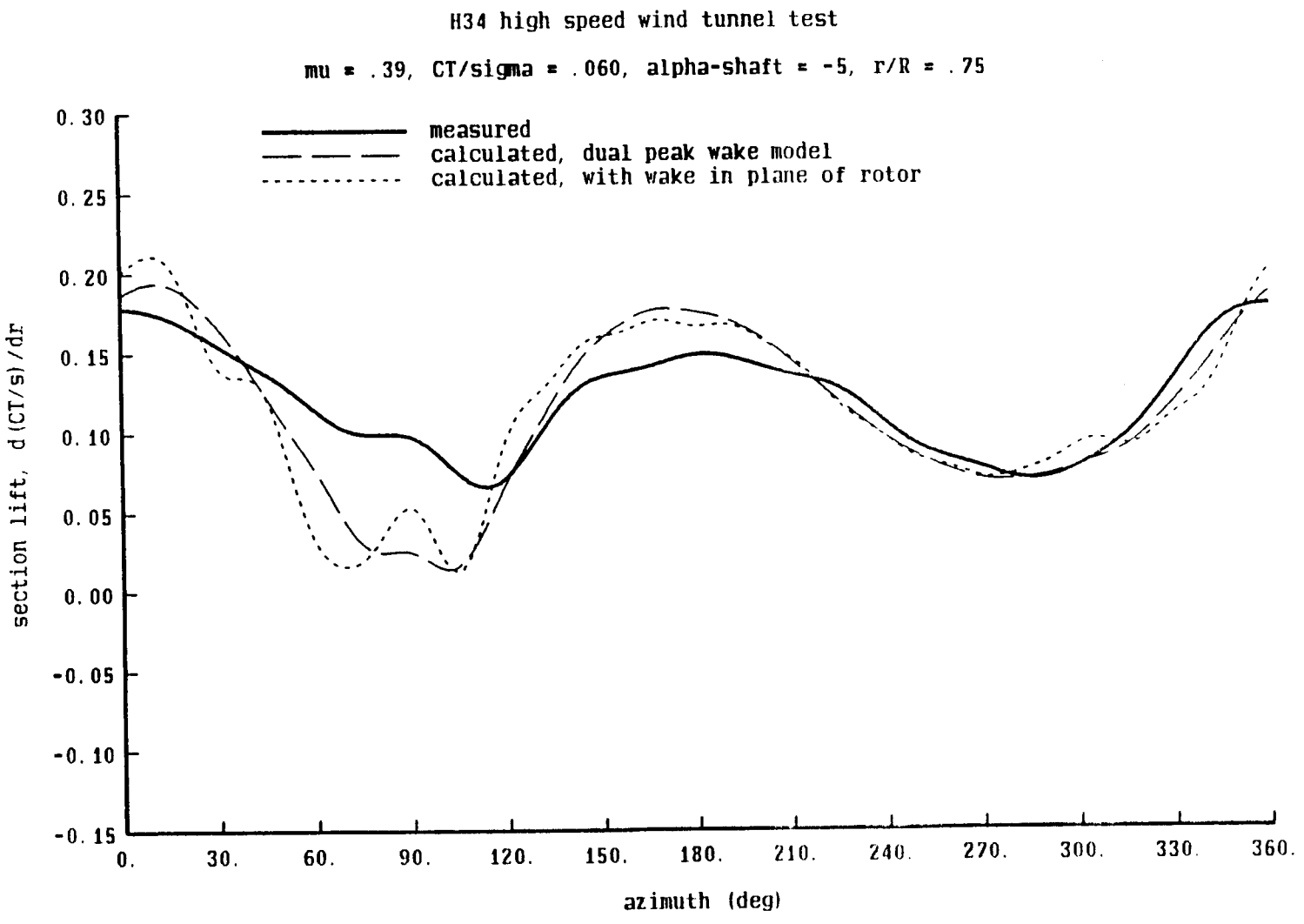

Figure 11-7a. H34 wind tunnel test: measured and calculated airloads

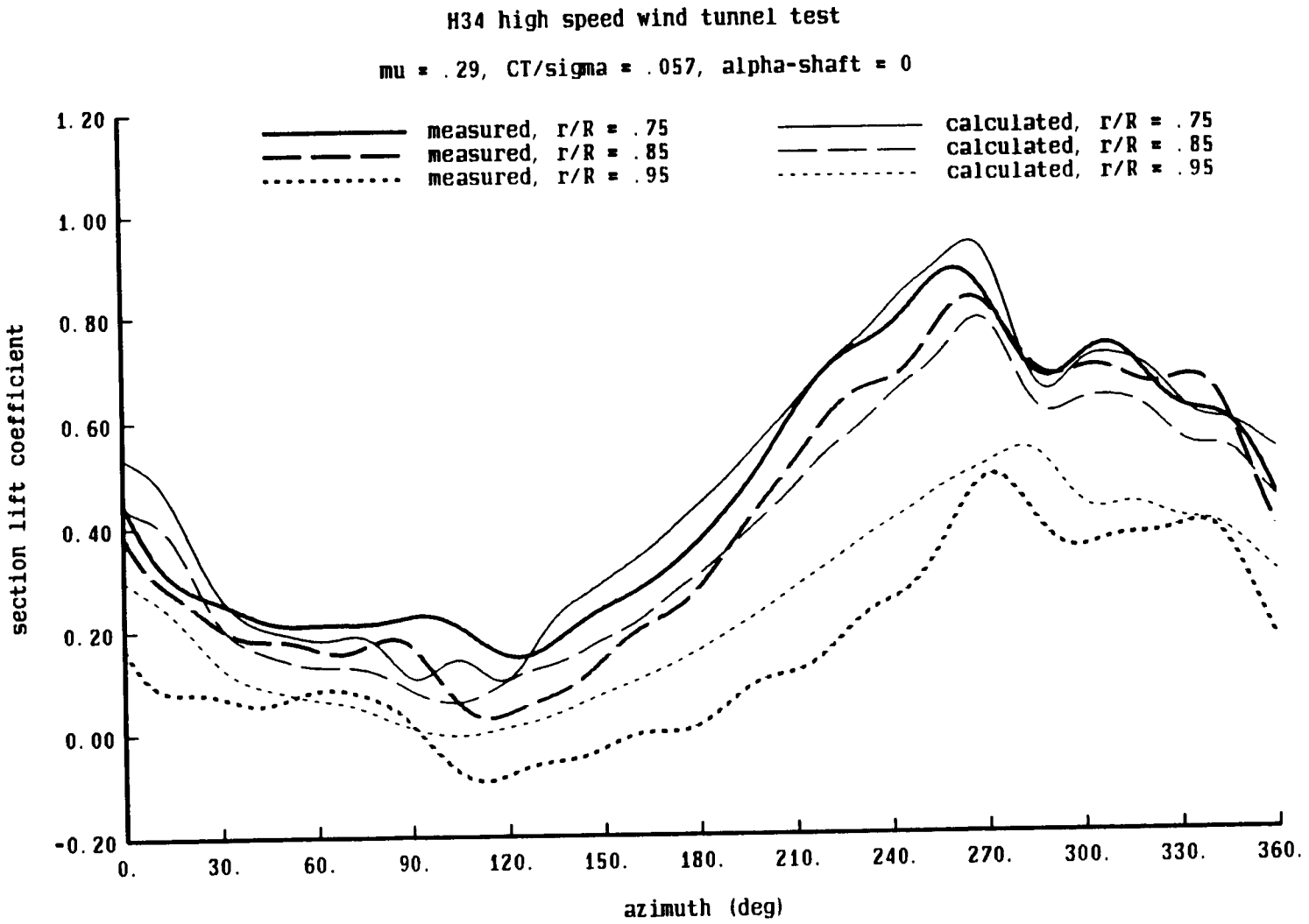

Figure 11-7b. H34 wind tunnel test: measured and calculated airloads

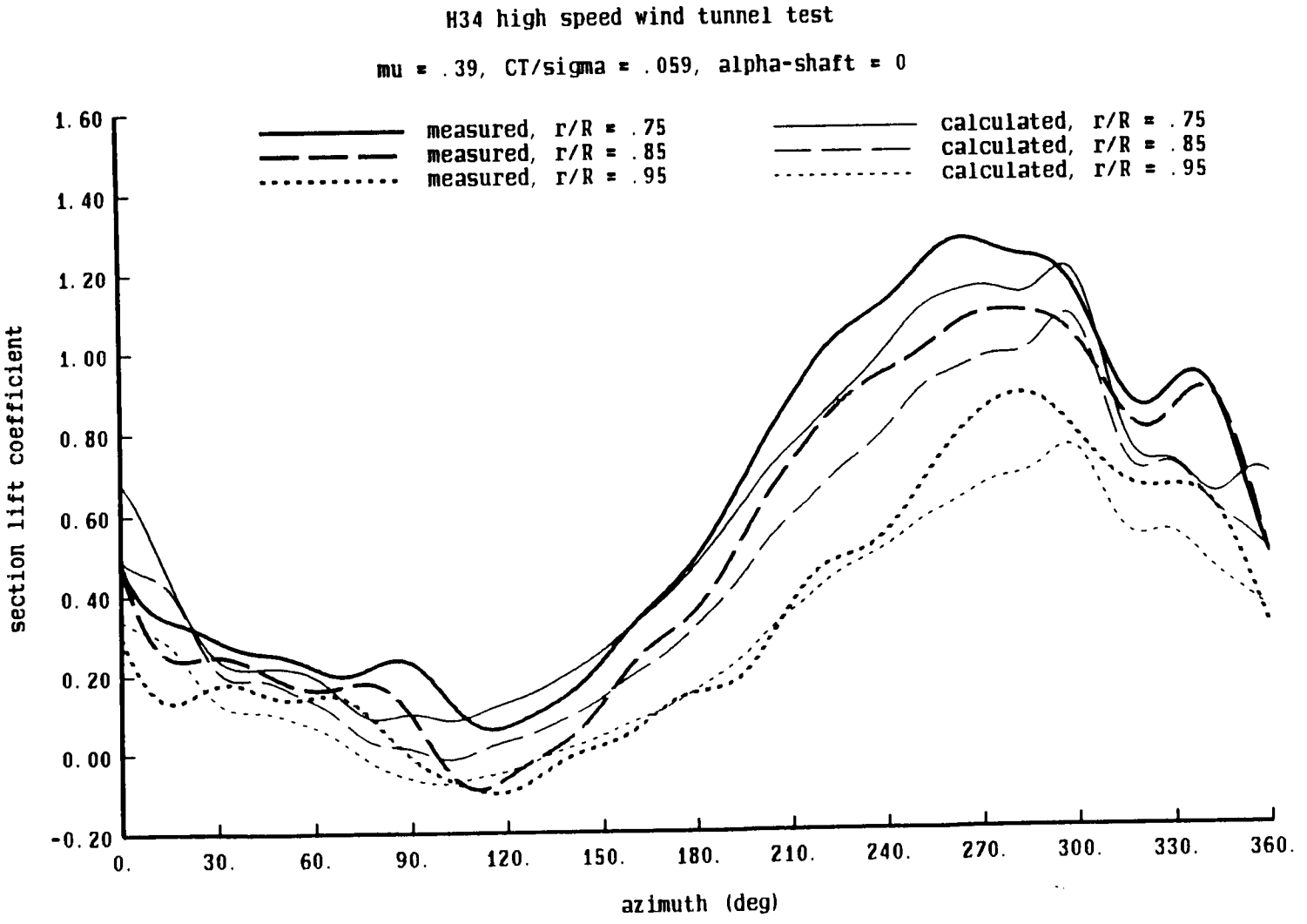

Figure 11-7c. H34 wind tunnel test: measured and calculated airloads

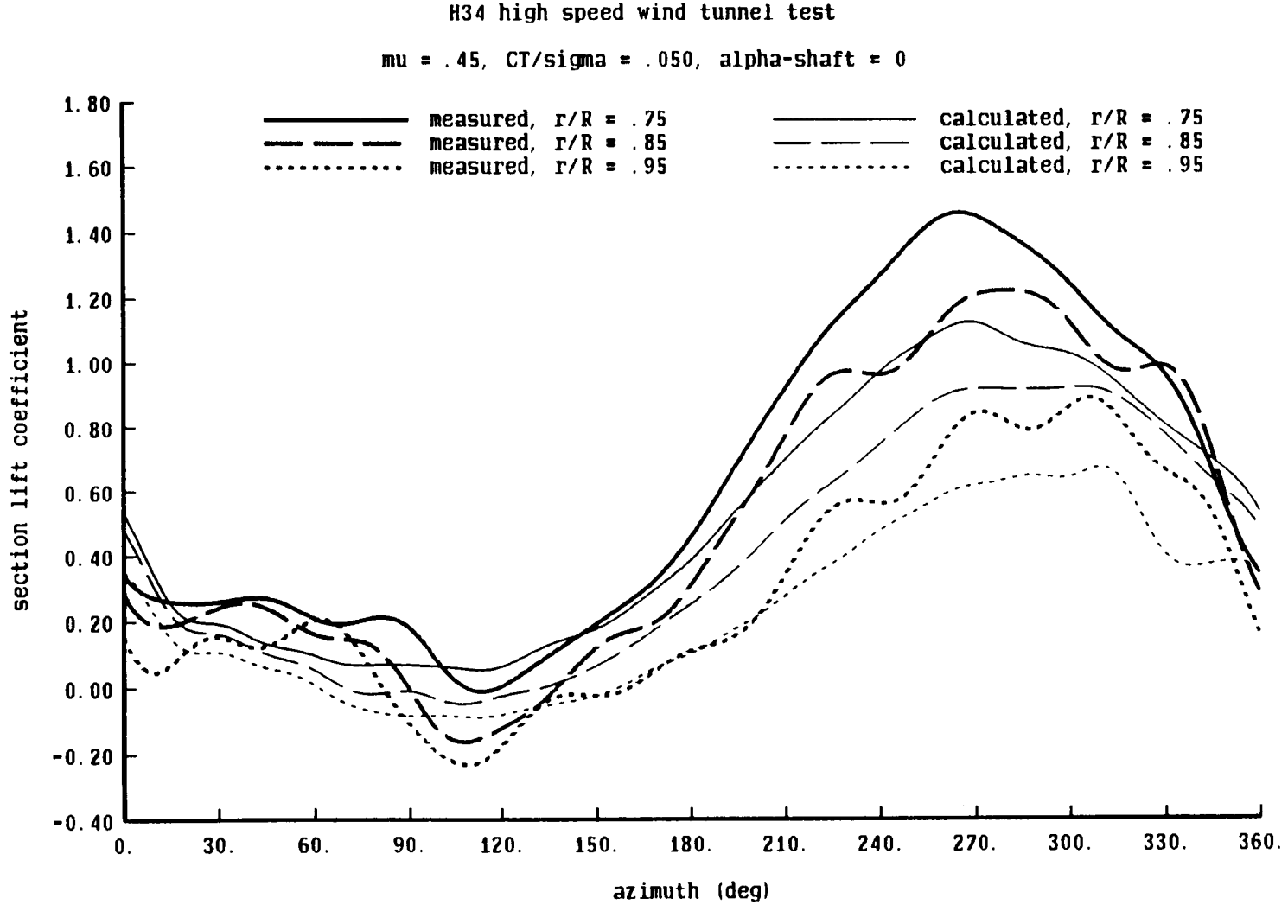

Figure 11-7d. H34 wind tunnel test: measured and calculated airloads

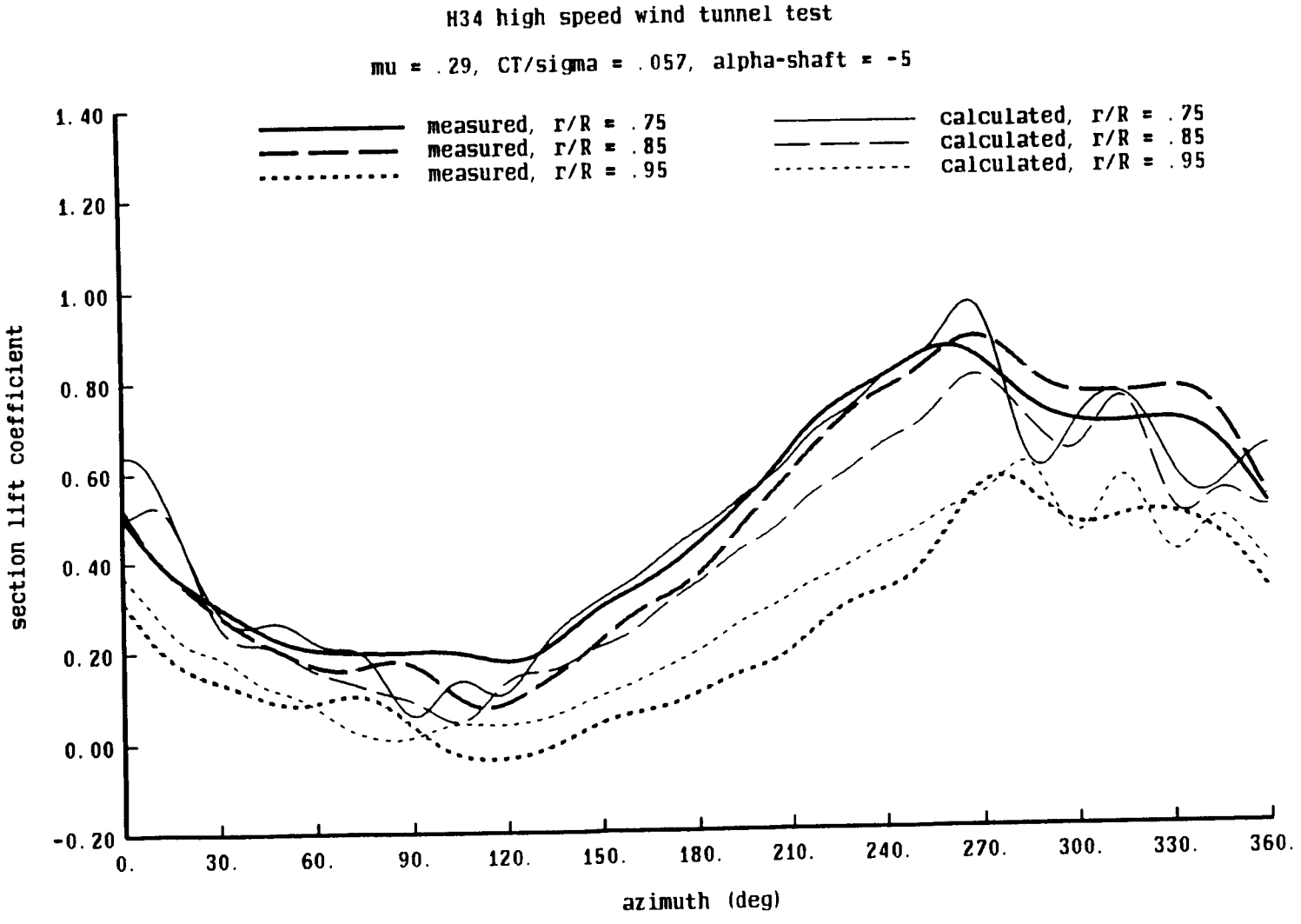

Figure 11-7e. H34 wind tunnel test: measured and calculated airloads

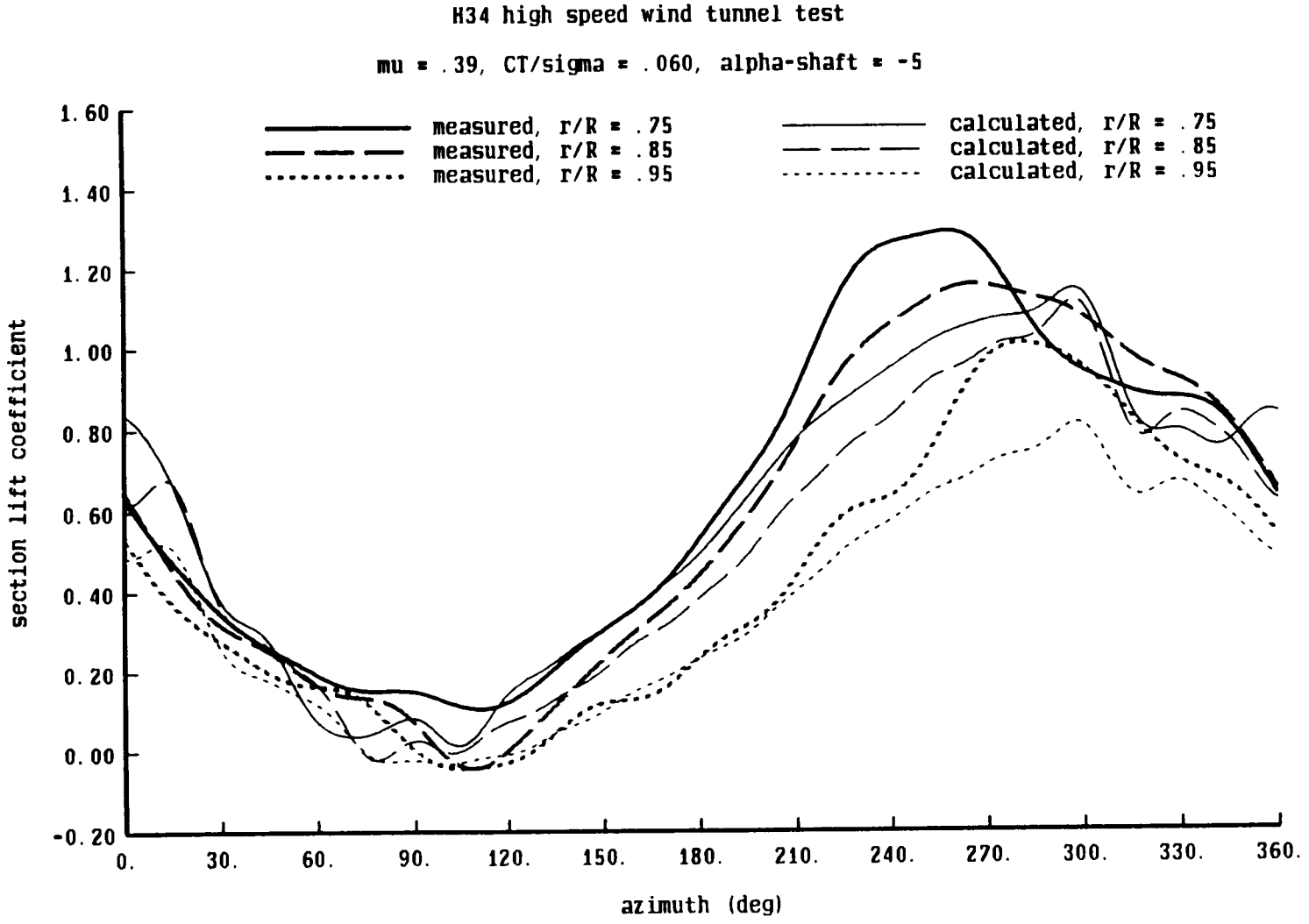

Figure 11-7f. H34 wind tunnel test: measured and calculated airloads

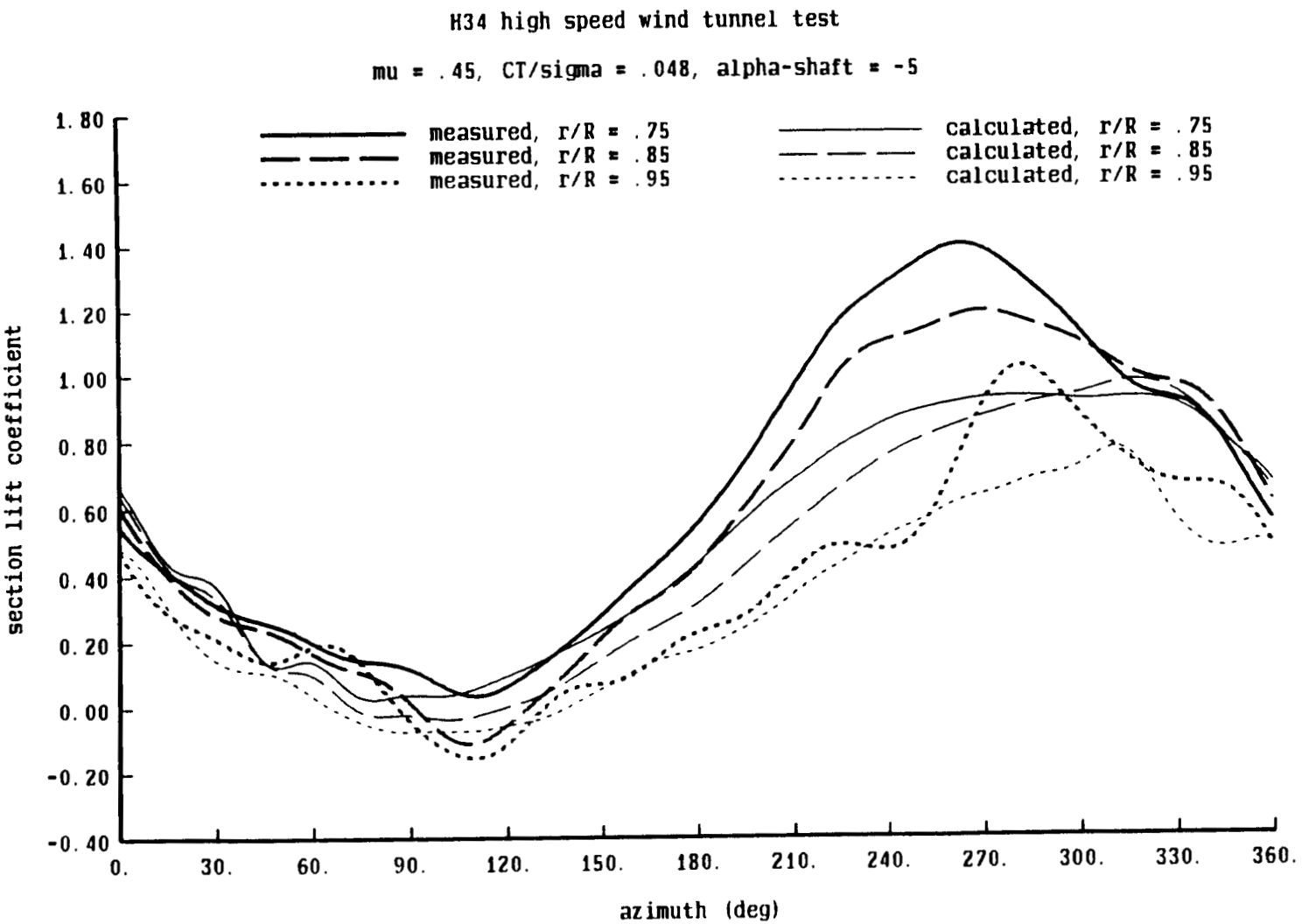

Figure 11-8a. H34 wind tunnel test: influence of shaft angle on measured loading

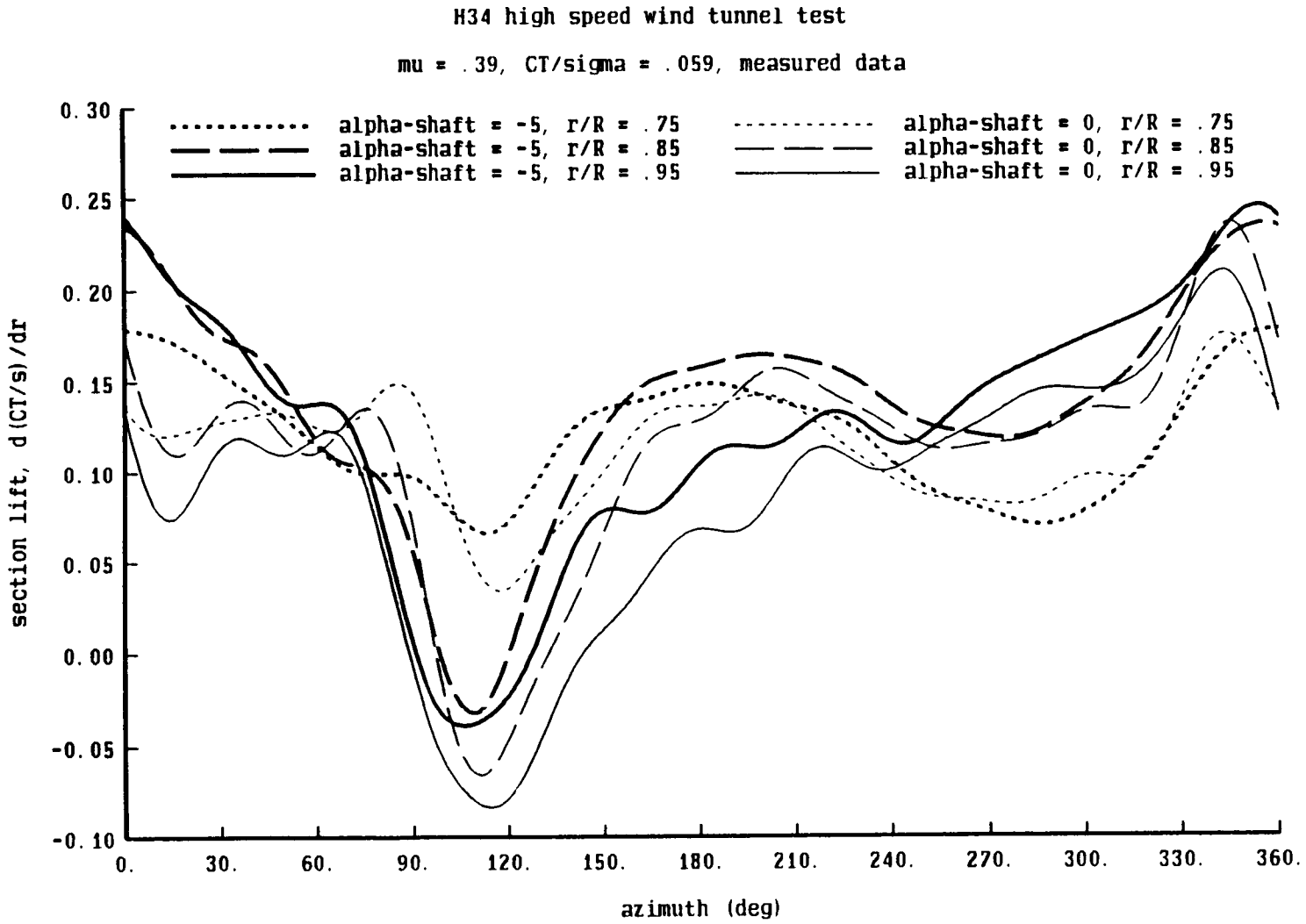

Figure 11-8b. H34 wind tunnel test: influence of shaft angle on measured loading

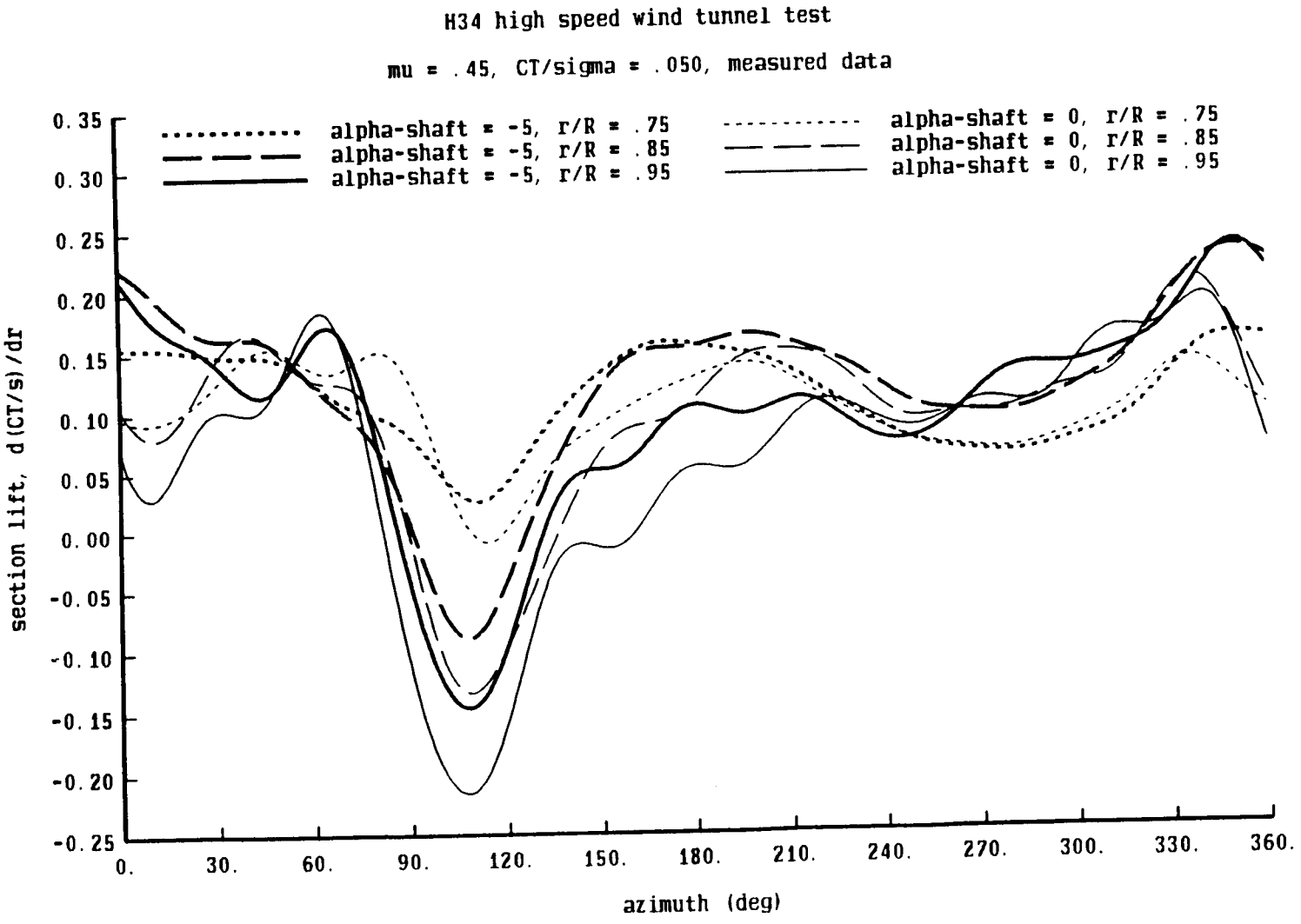

Figure 11-9a. H34 wind tunnel test: chordwise pressure distribution

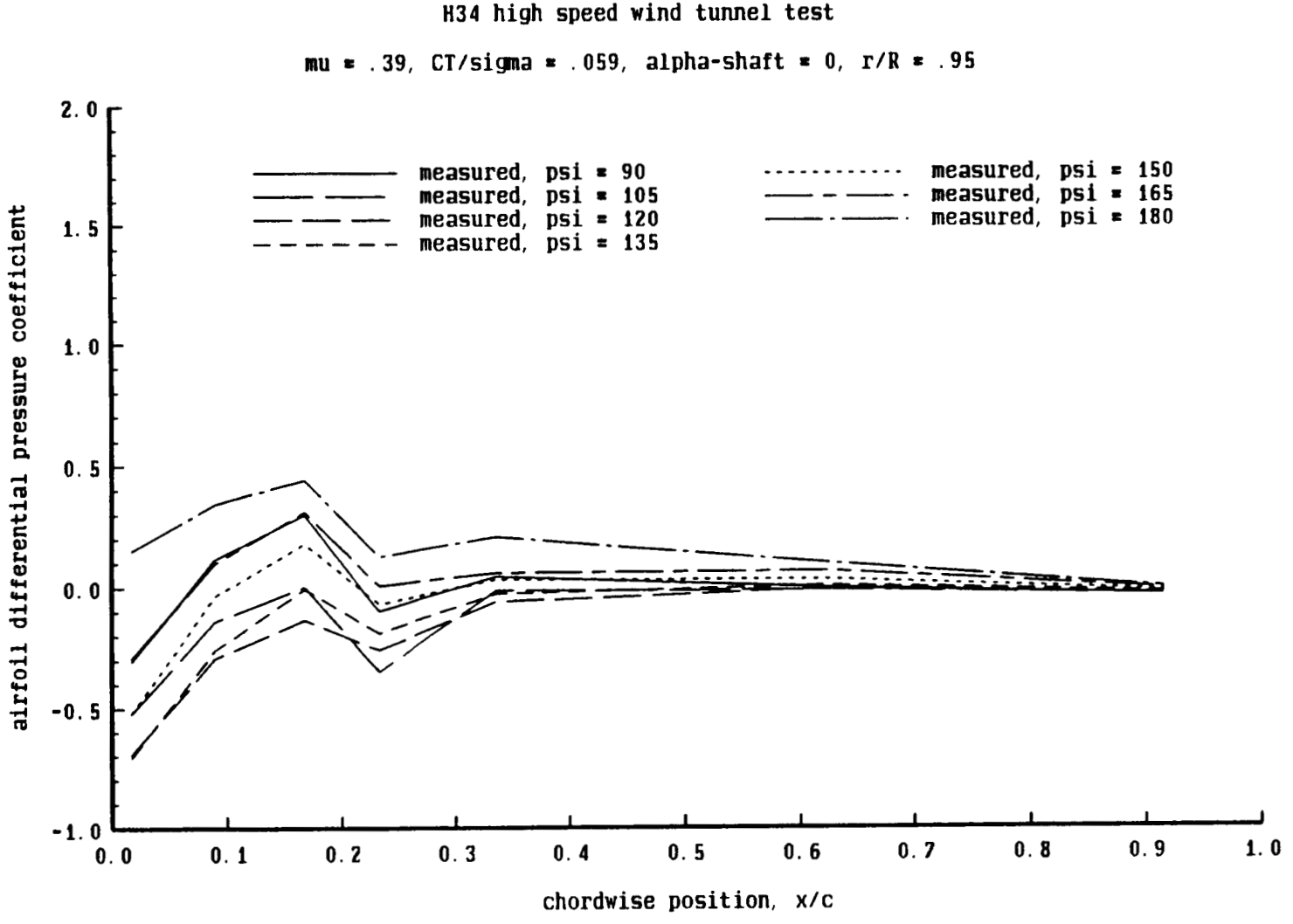

Figure 11-9b. H34 wind tunnel test: chordwise pressure distribution

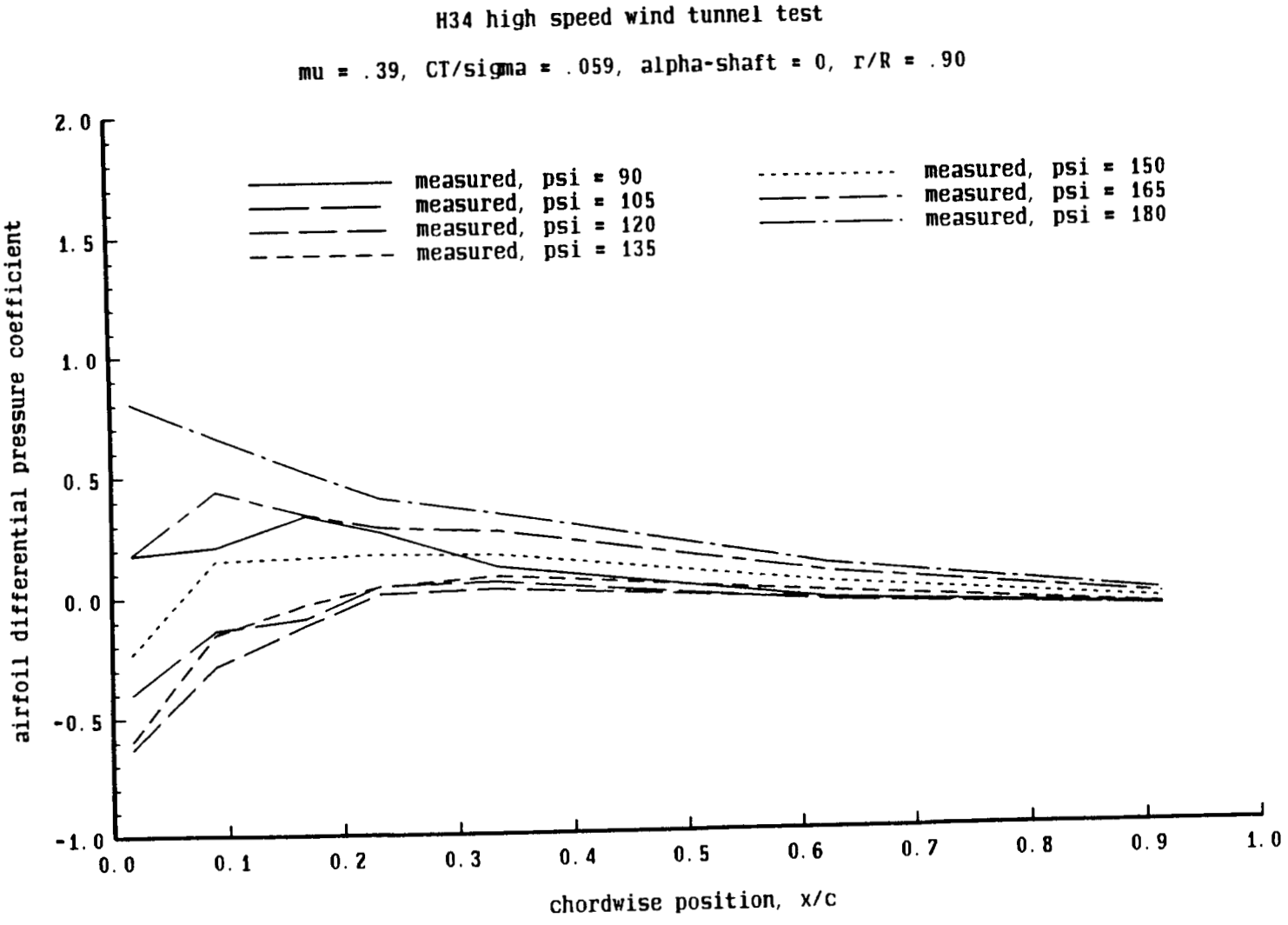

Figure 11-9c. H34 wind tunnel test: chordwise pressure distribution

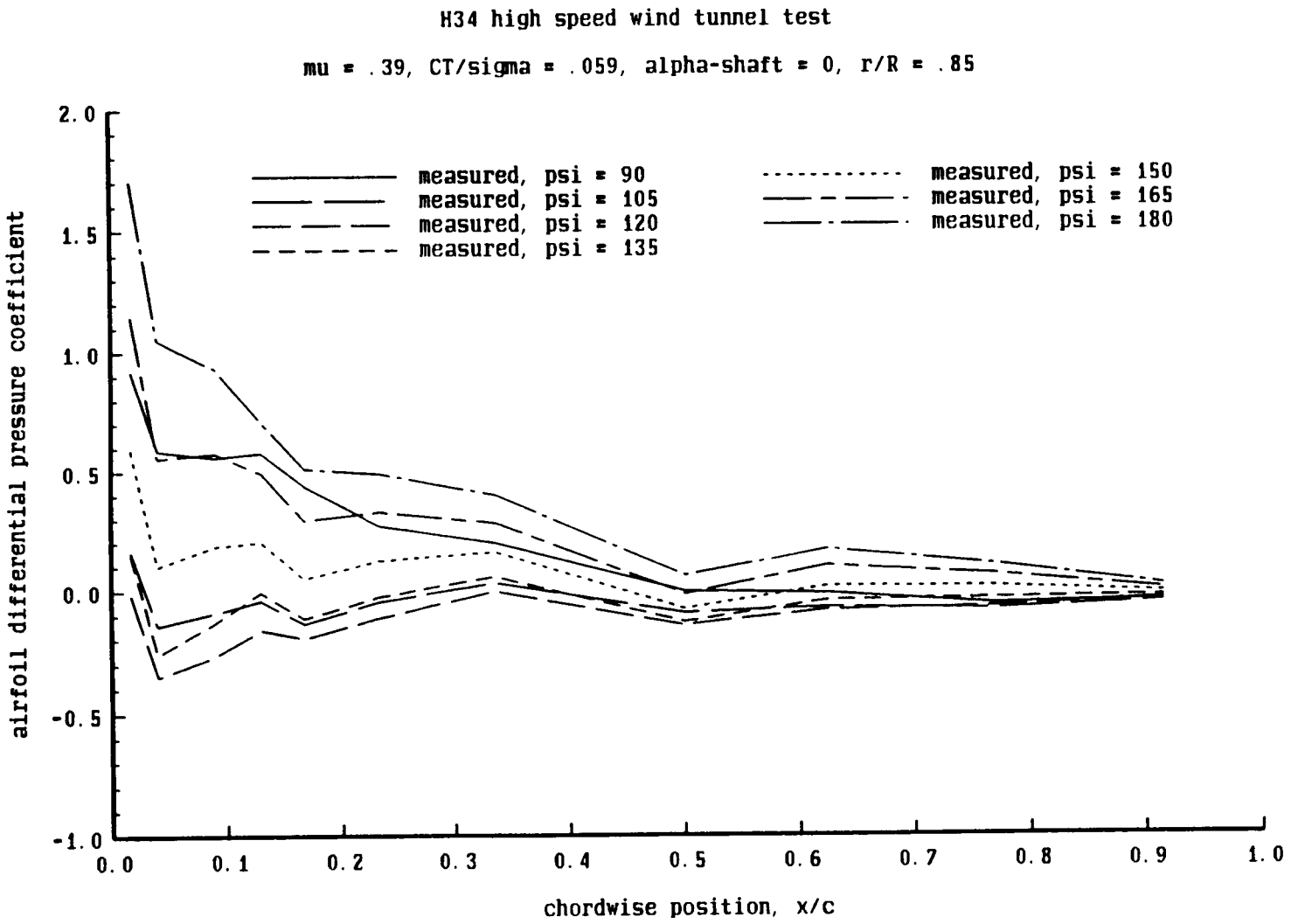

Figure 12-1a. AH-1G helicopter: measured and calculated airloads

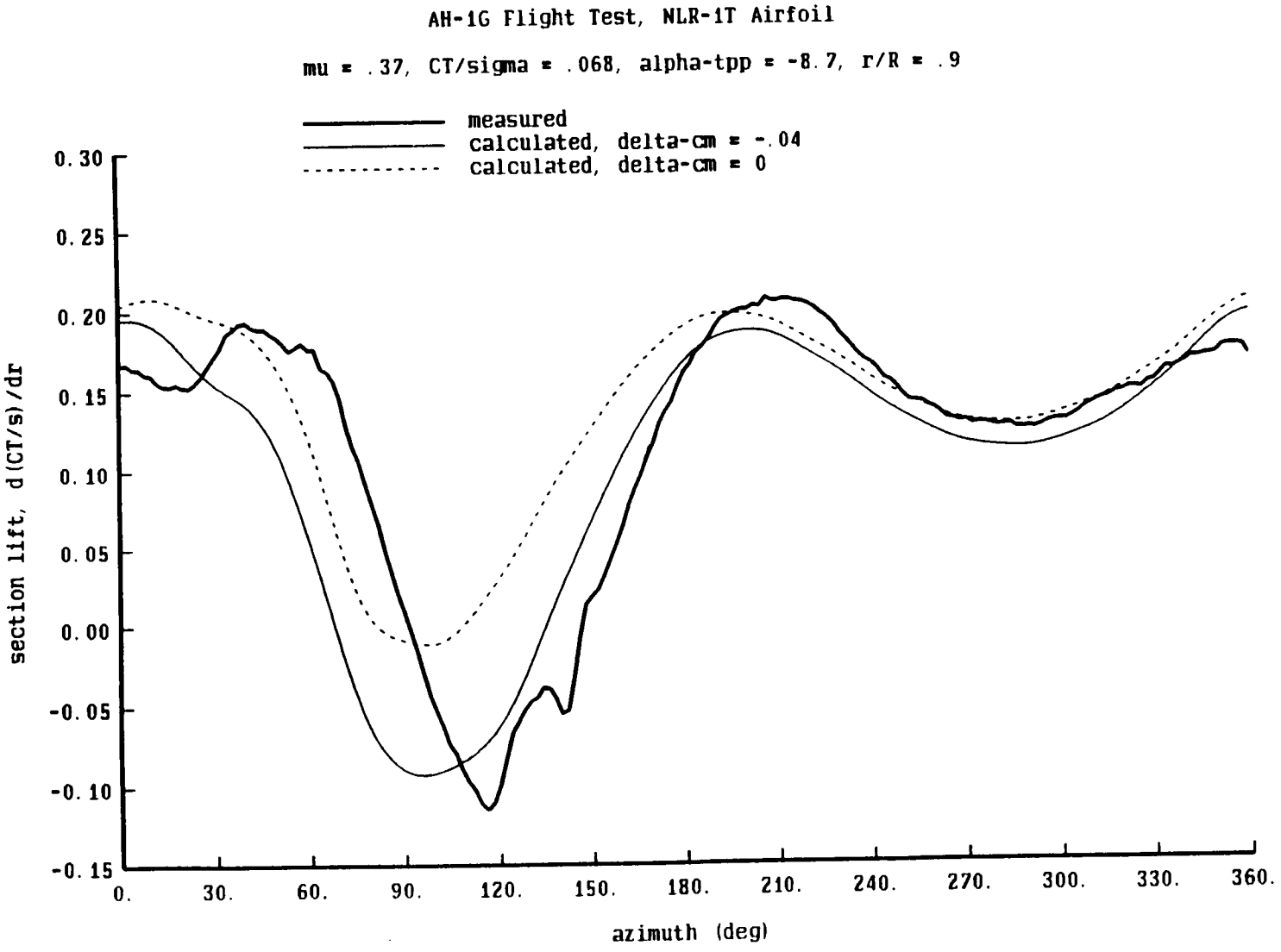

Figure 12-1b. AH-1G helicopter: measured and calculated airloads

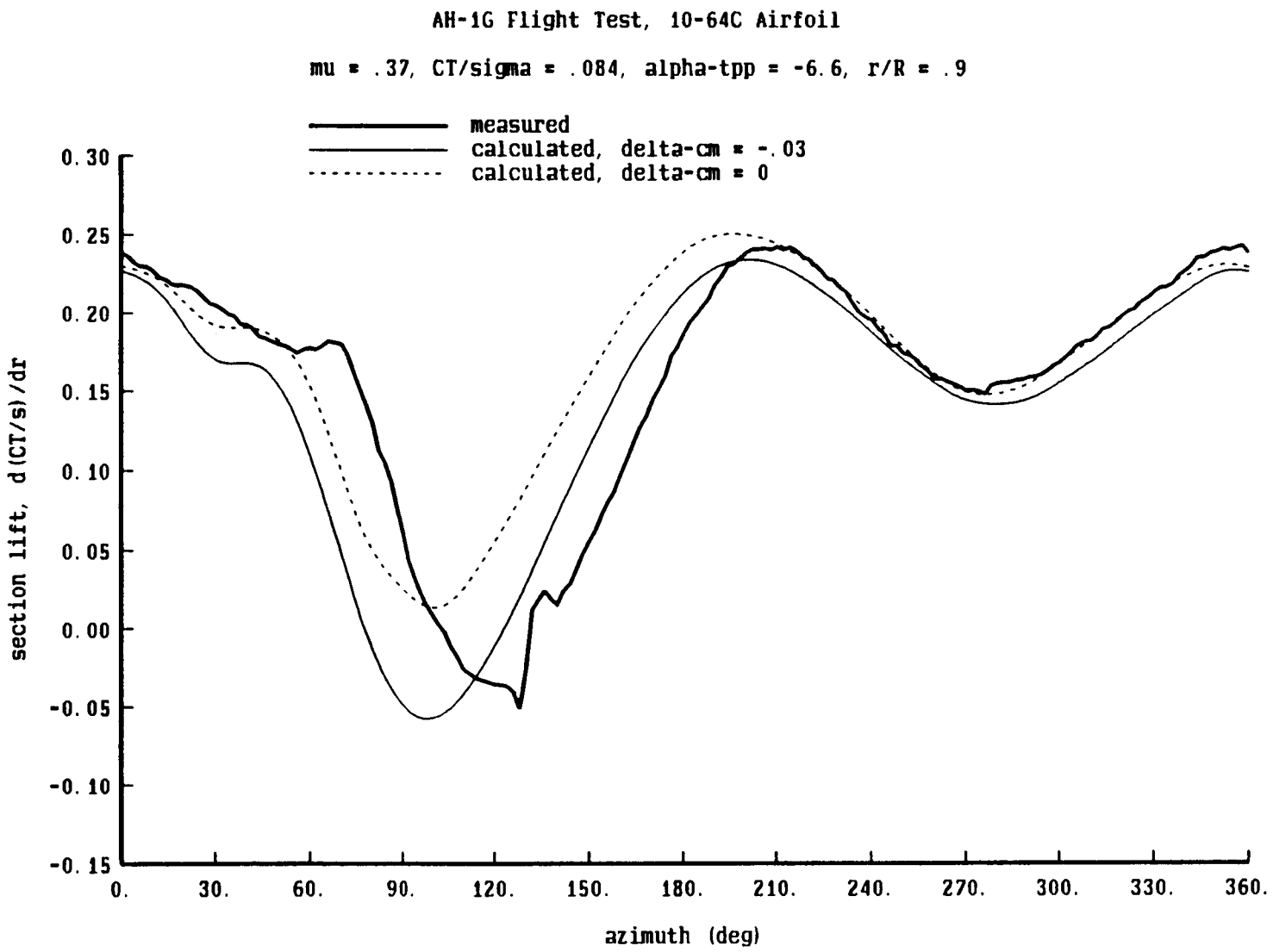

Figure 12-1c. AH-1G helicopter: measured and calculated airloads

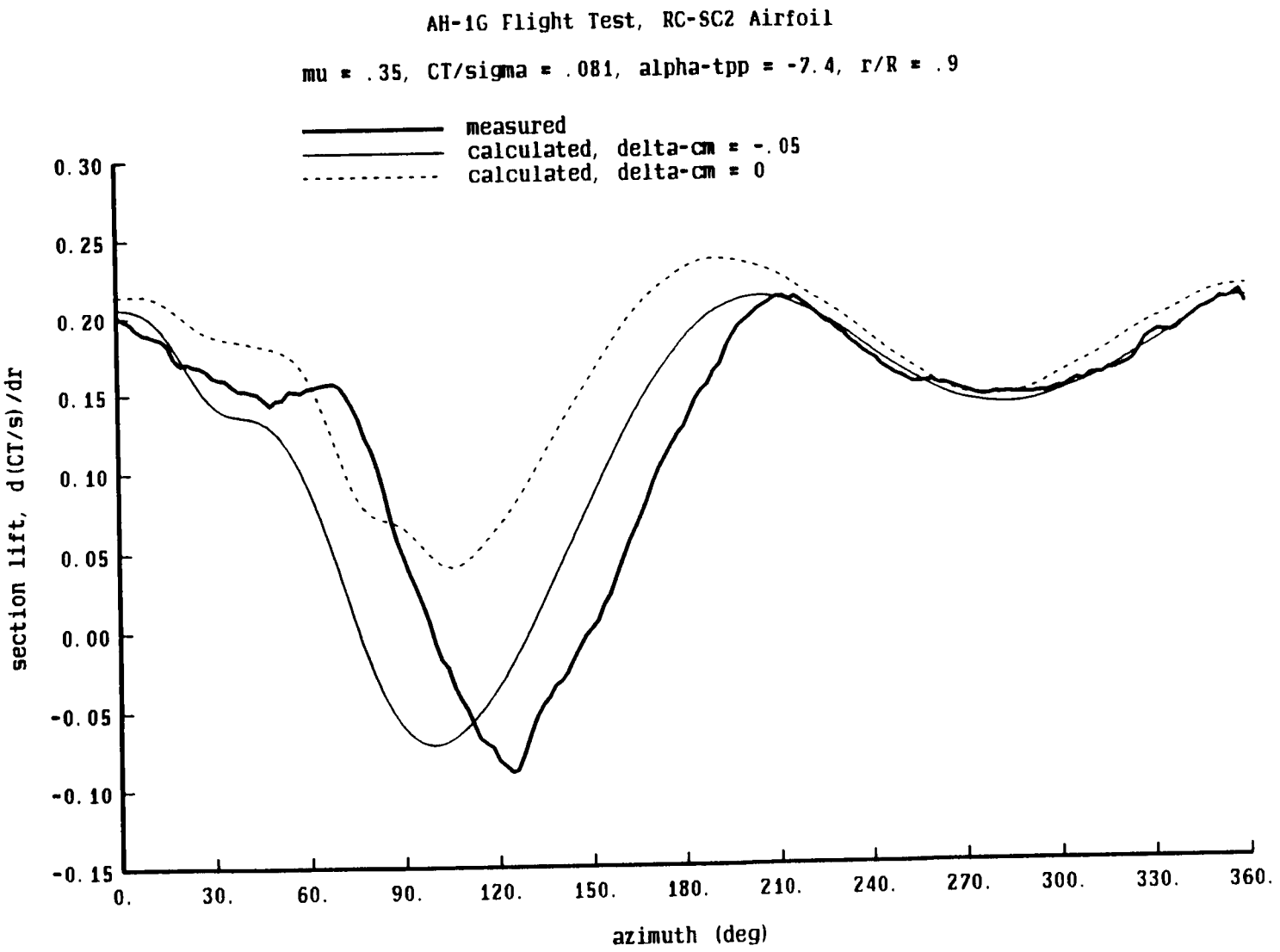

Figure 12-2a. AH-1G helicopter: influence of far wake model

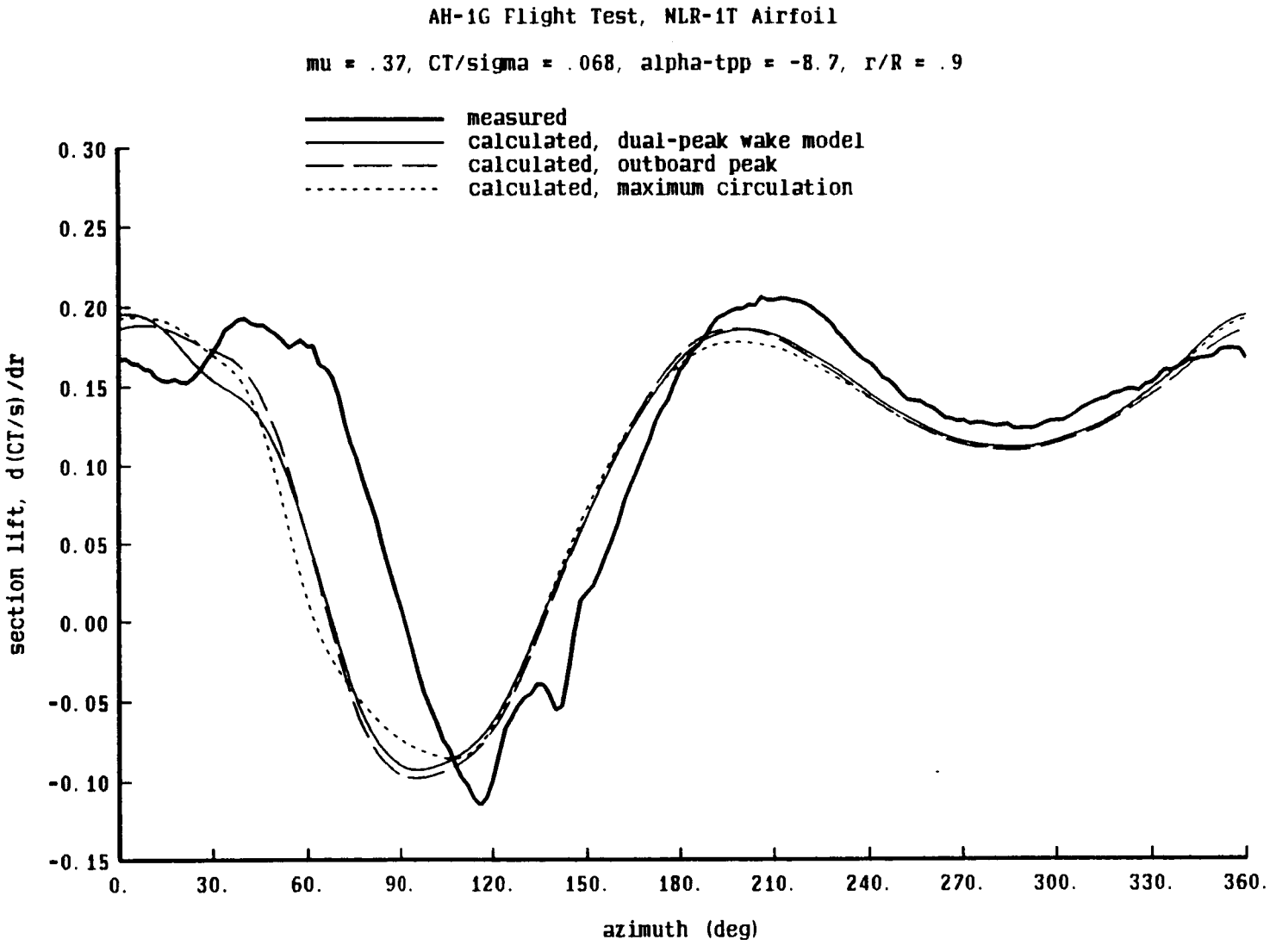

Figure 12-2b. AH-1G helicopter: influence of far wake model

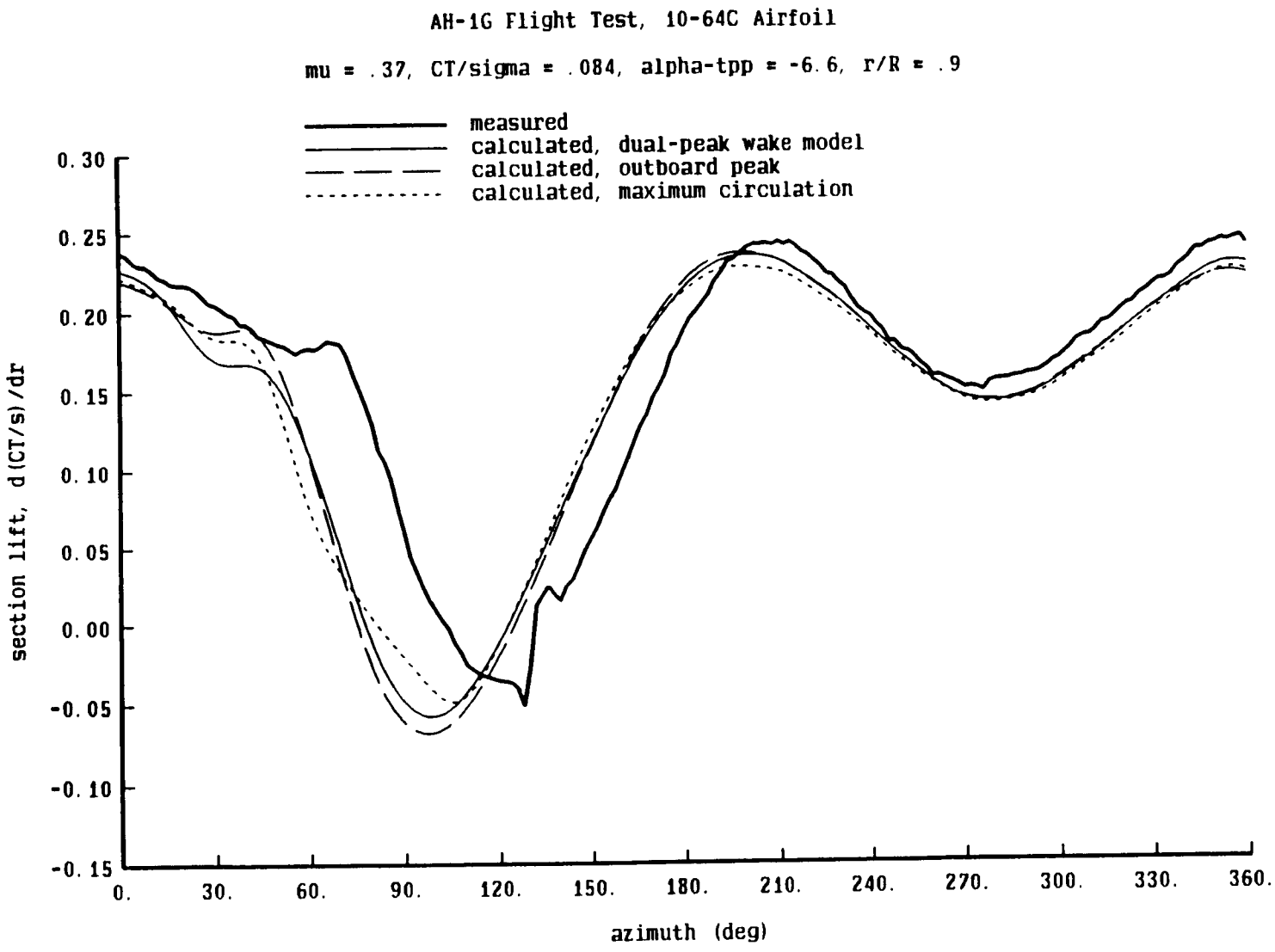

Figure 12-2c. AH-1G helicopter: influence of far wake model

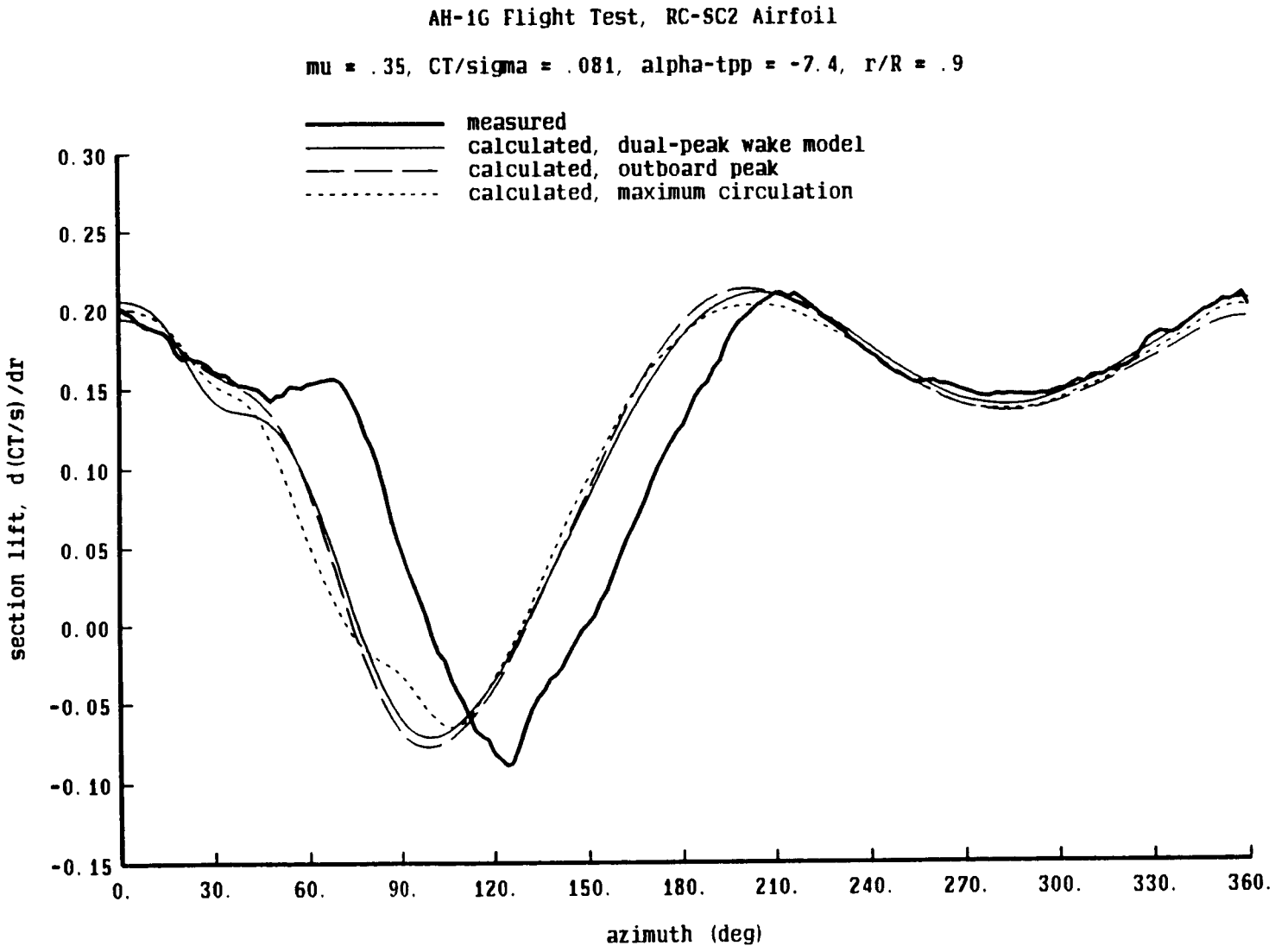

Figure 12-2d. AH-1G helicopter: influence of far wake model

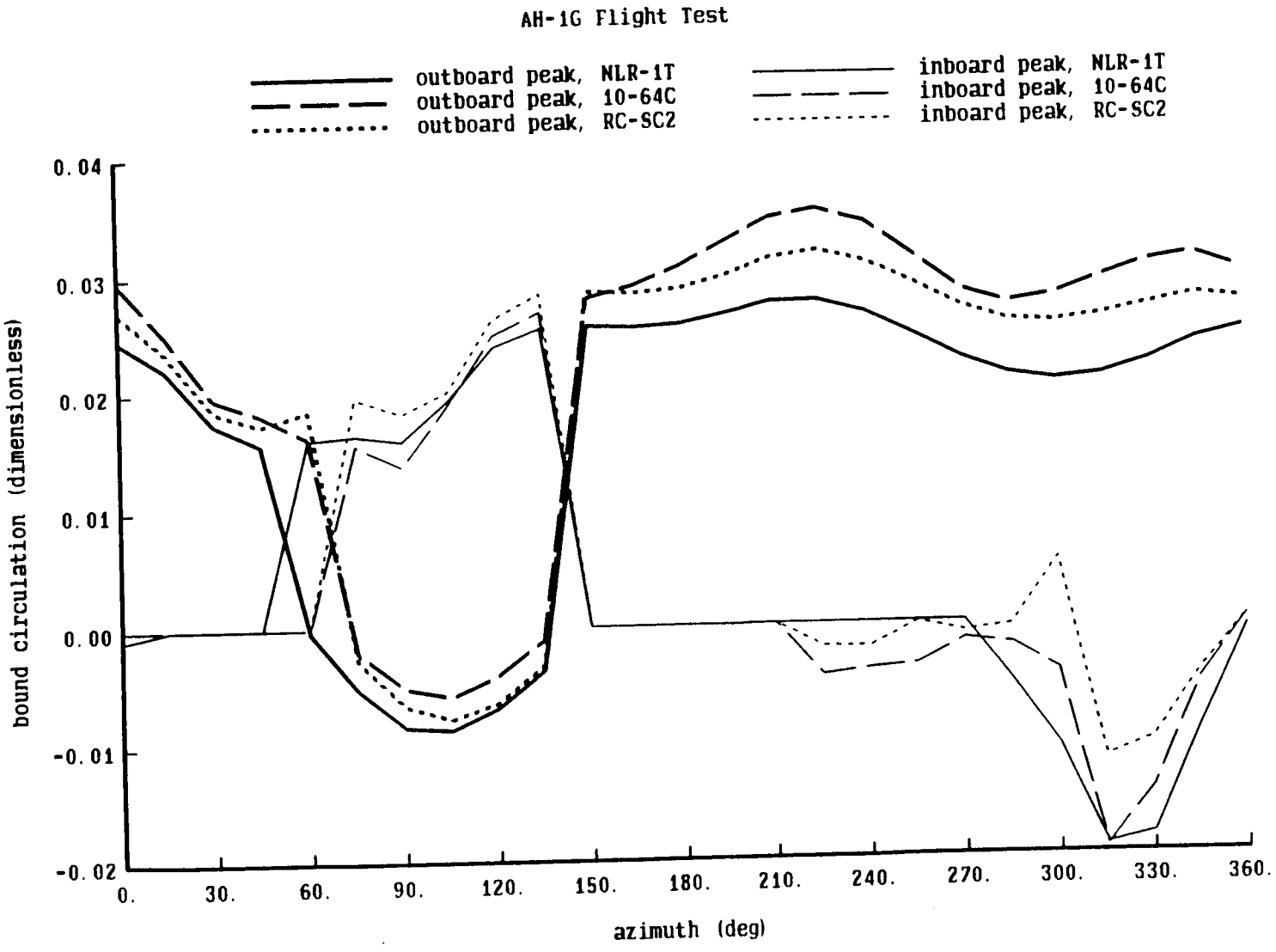

Figure 12-2e. AH-1G helicopter: influence of far wake model

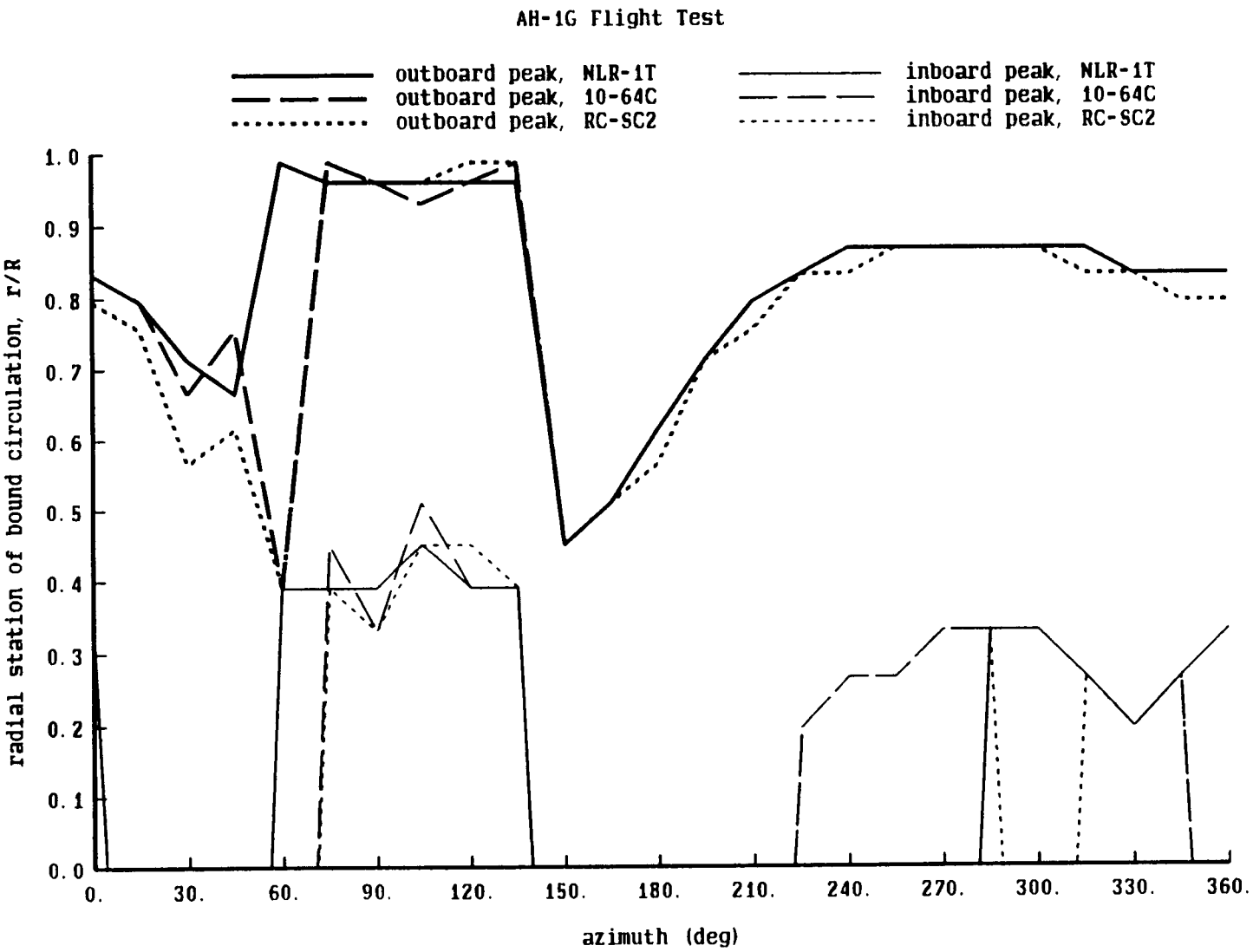

Figure 12-3a. AH-1G helicopter: influence of near wake model

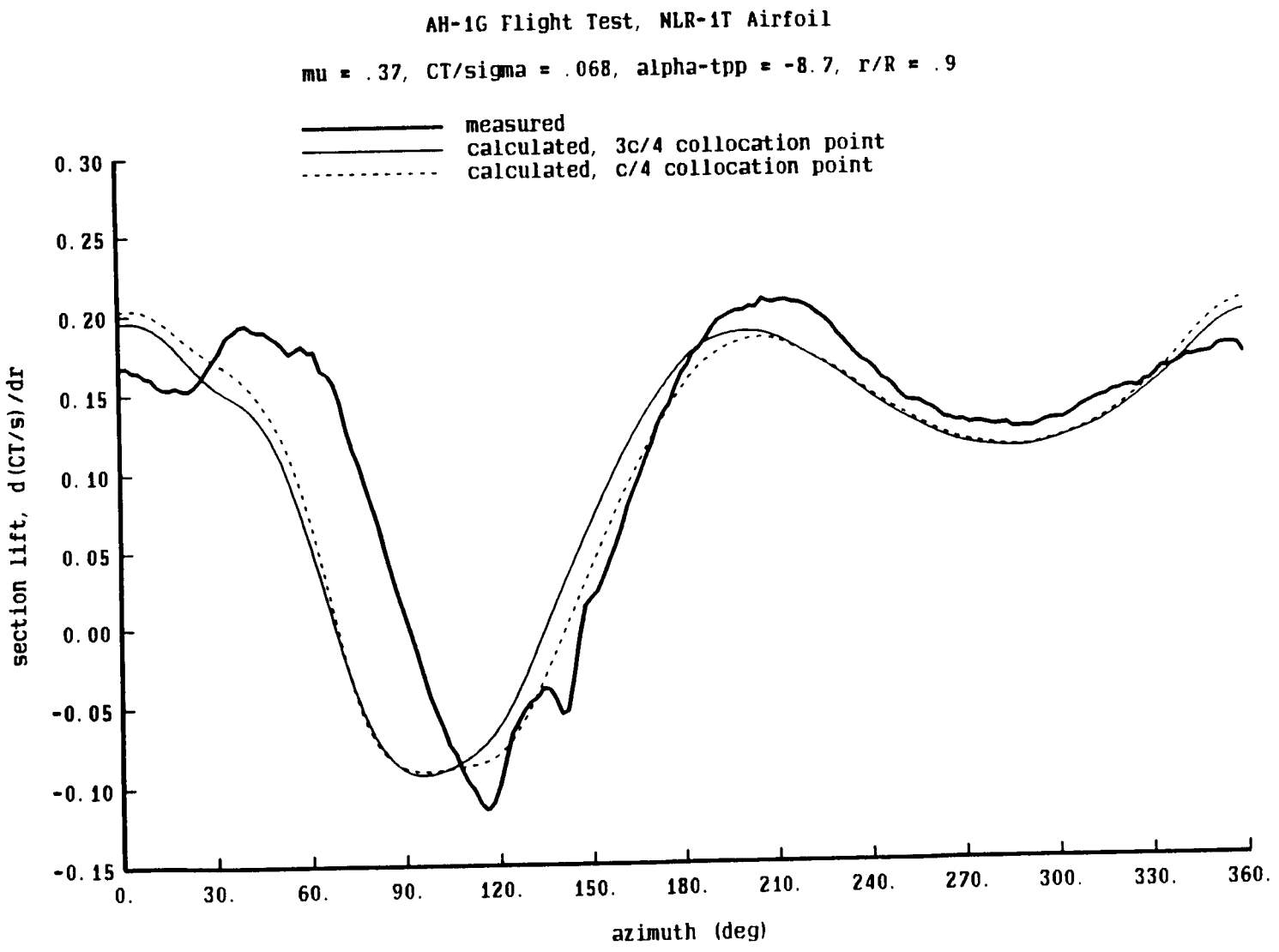

Figure 12-3b. AH-1G helicopter: influence of near wake model

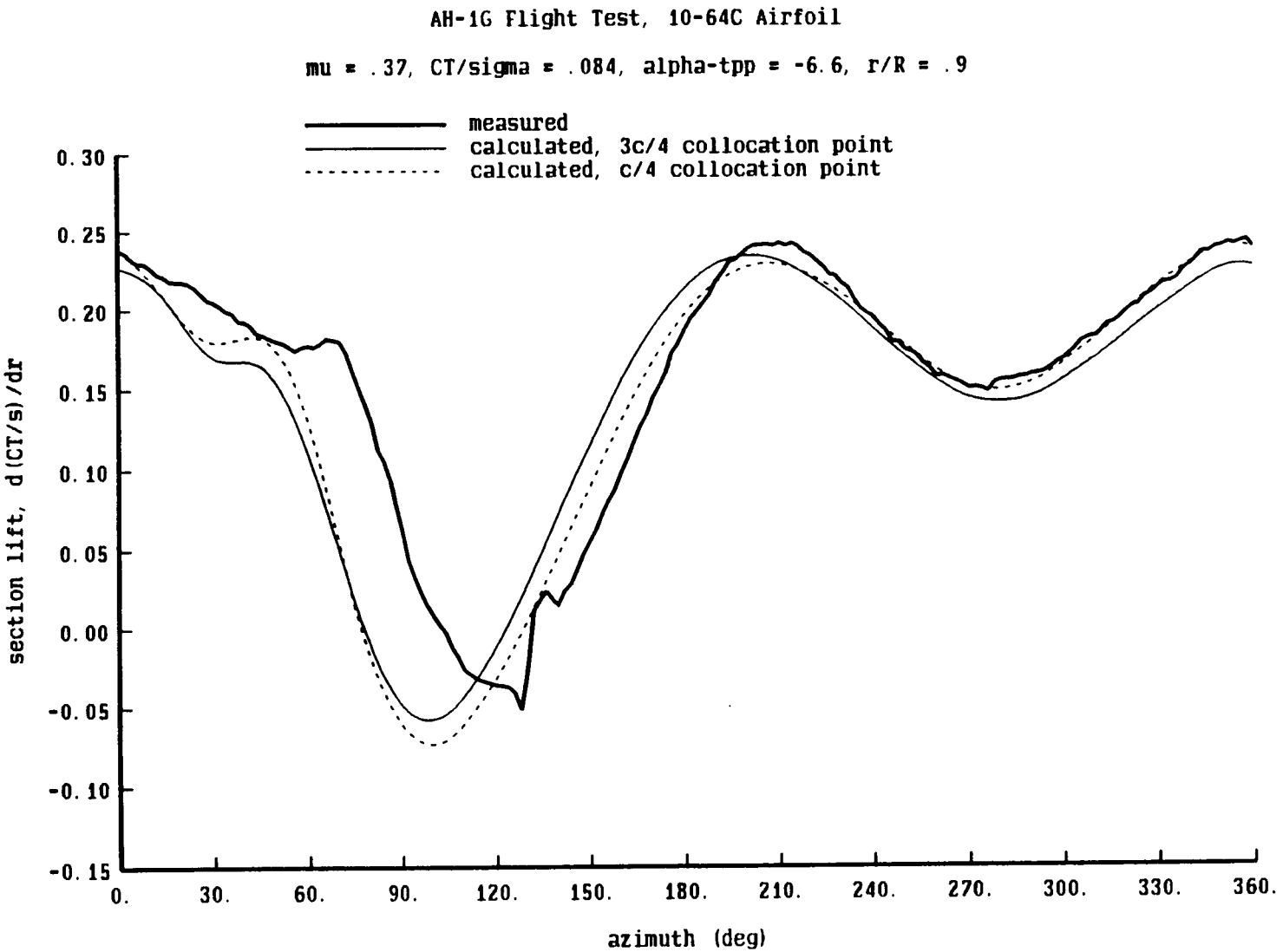

Figure 12-3c. AH-1G helicopter: influence of near wake model

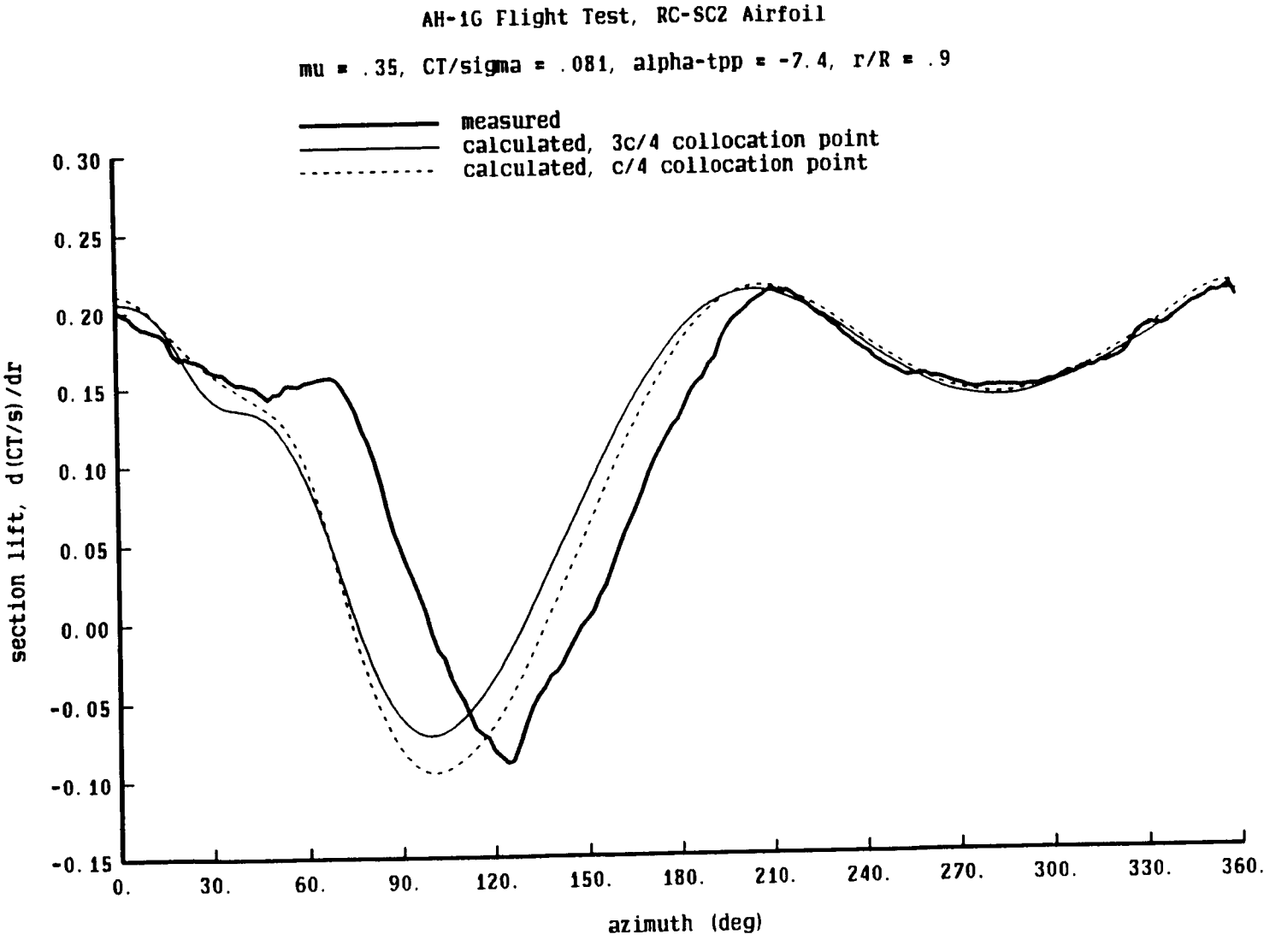

Figure 12-4a. AH-1G helicopter: influence of blade elastic motion

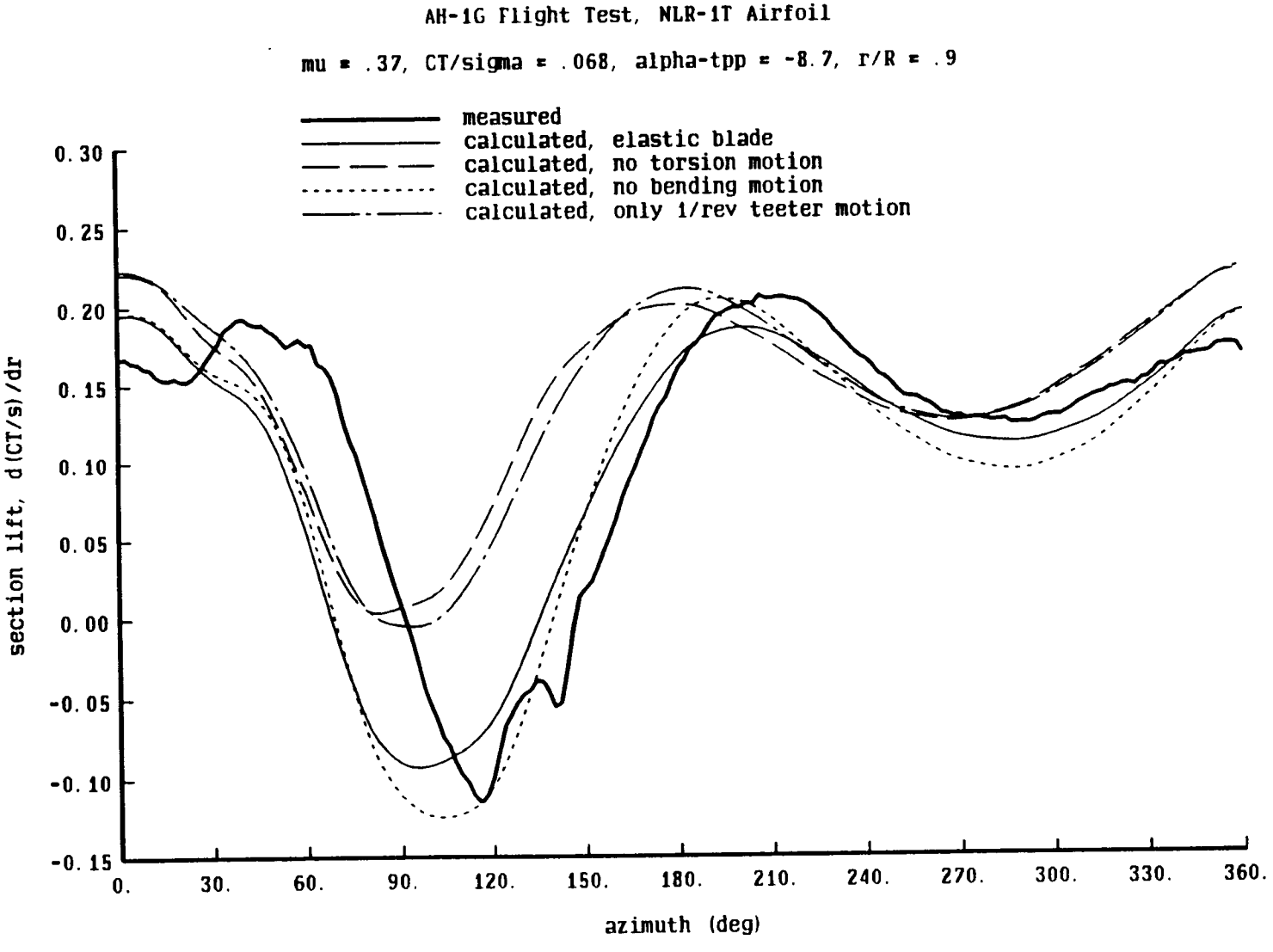

Figure 12-4b. AH-1G helicopter: influence of blade elastic motion

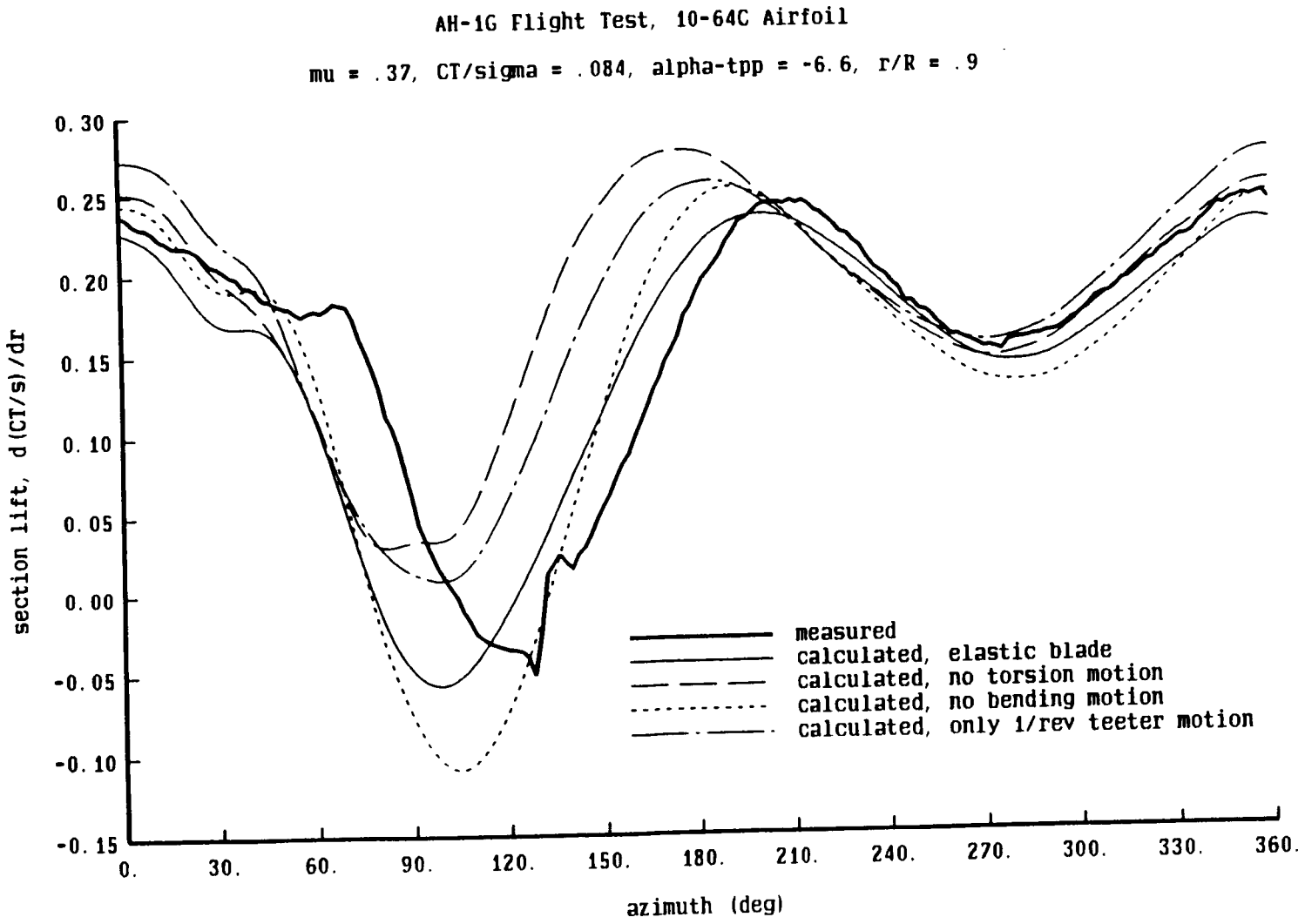

Figure 12-4c. AH-1G helicopter: influence of blade elastic motion

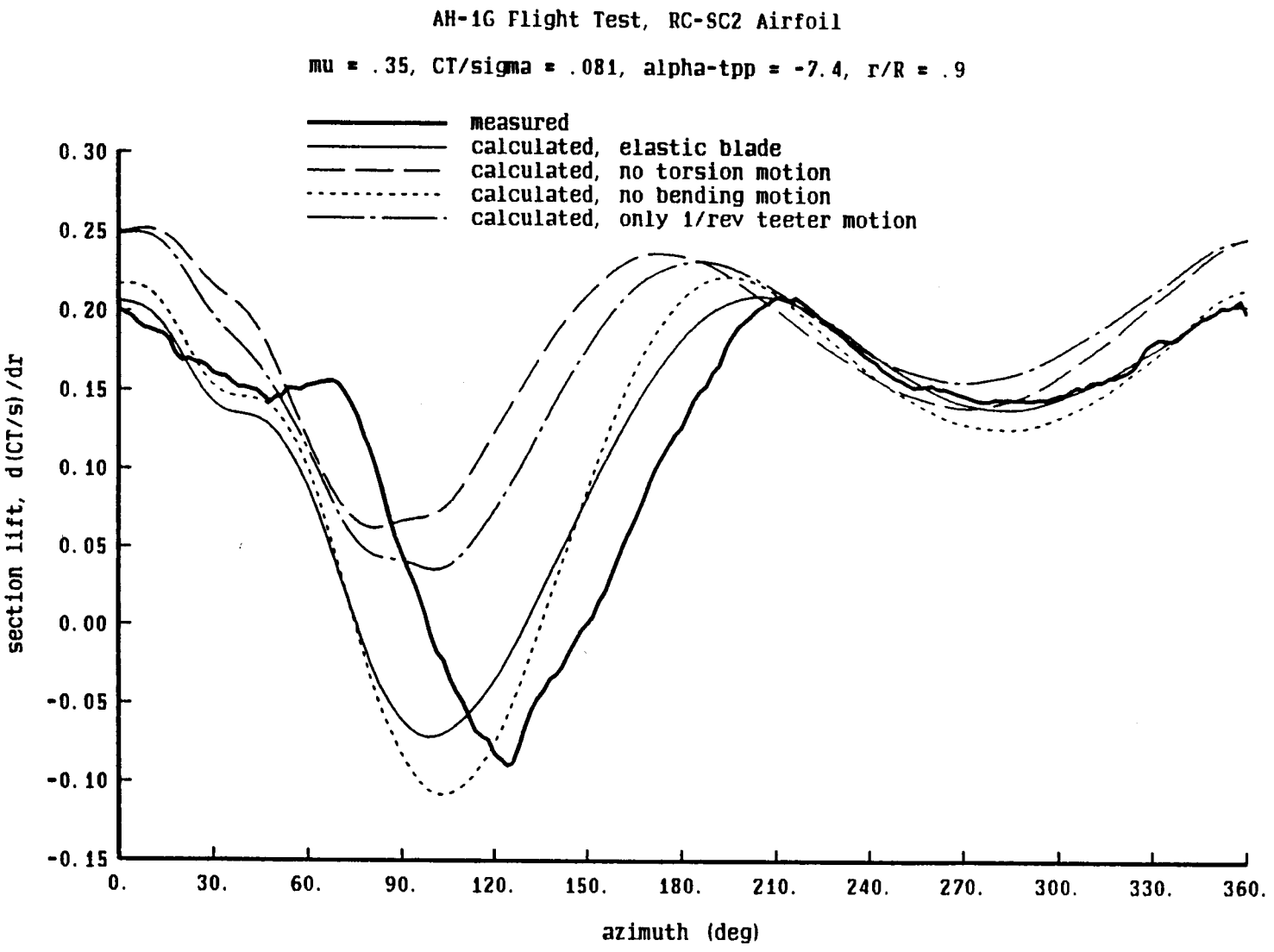

Figure 12-5. AH-1G helicopter: elastic torsion motion at tip

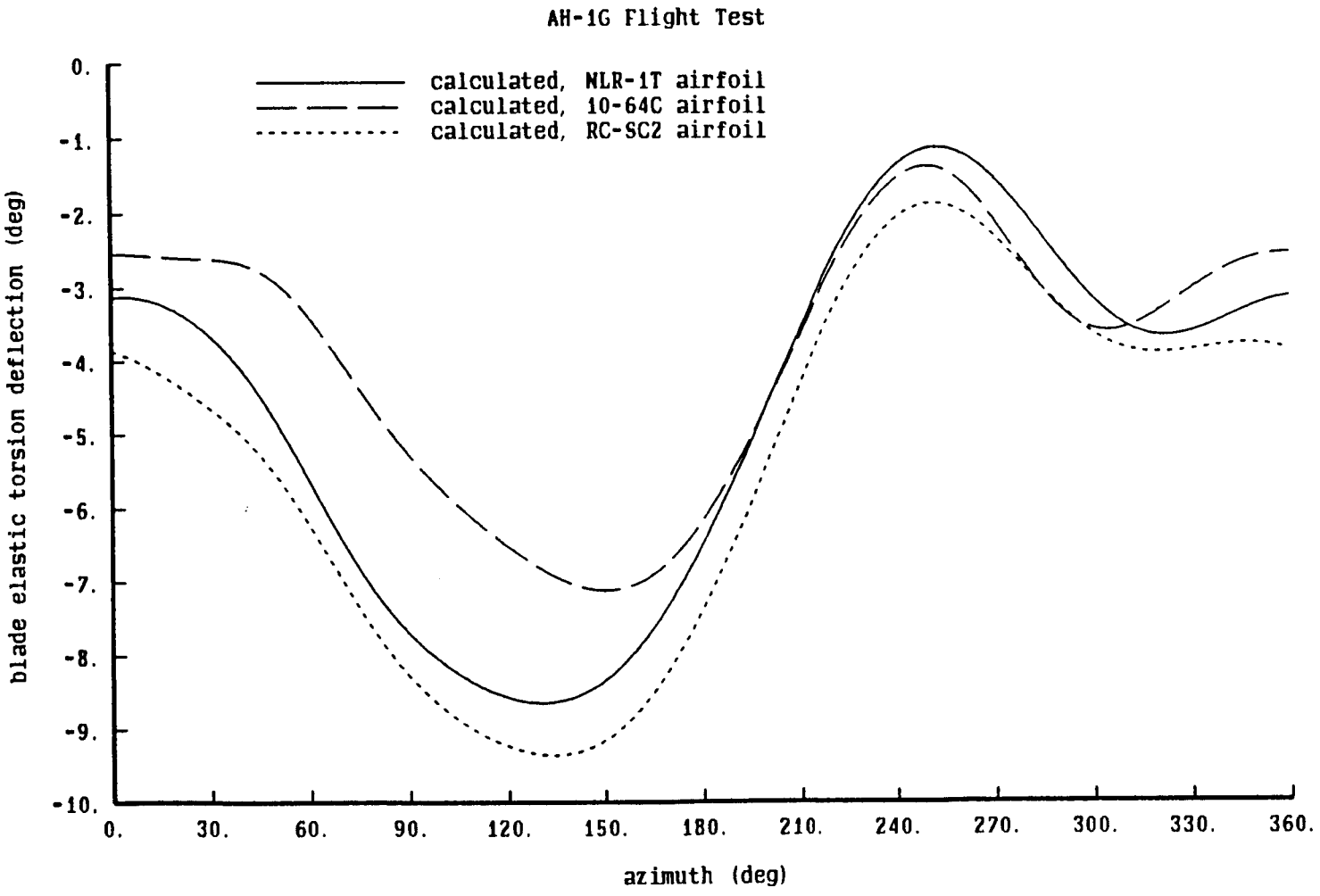

Figure 12-6a. AH-1G helicopter: measured and calculated pitch moment

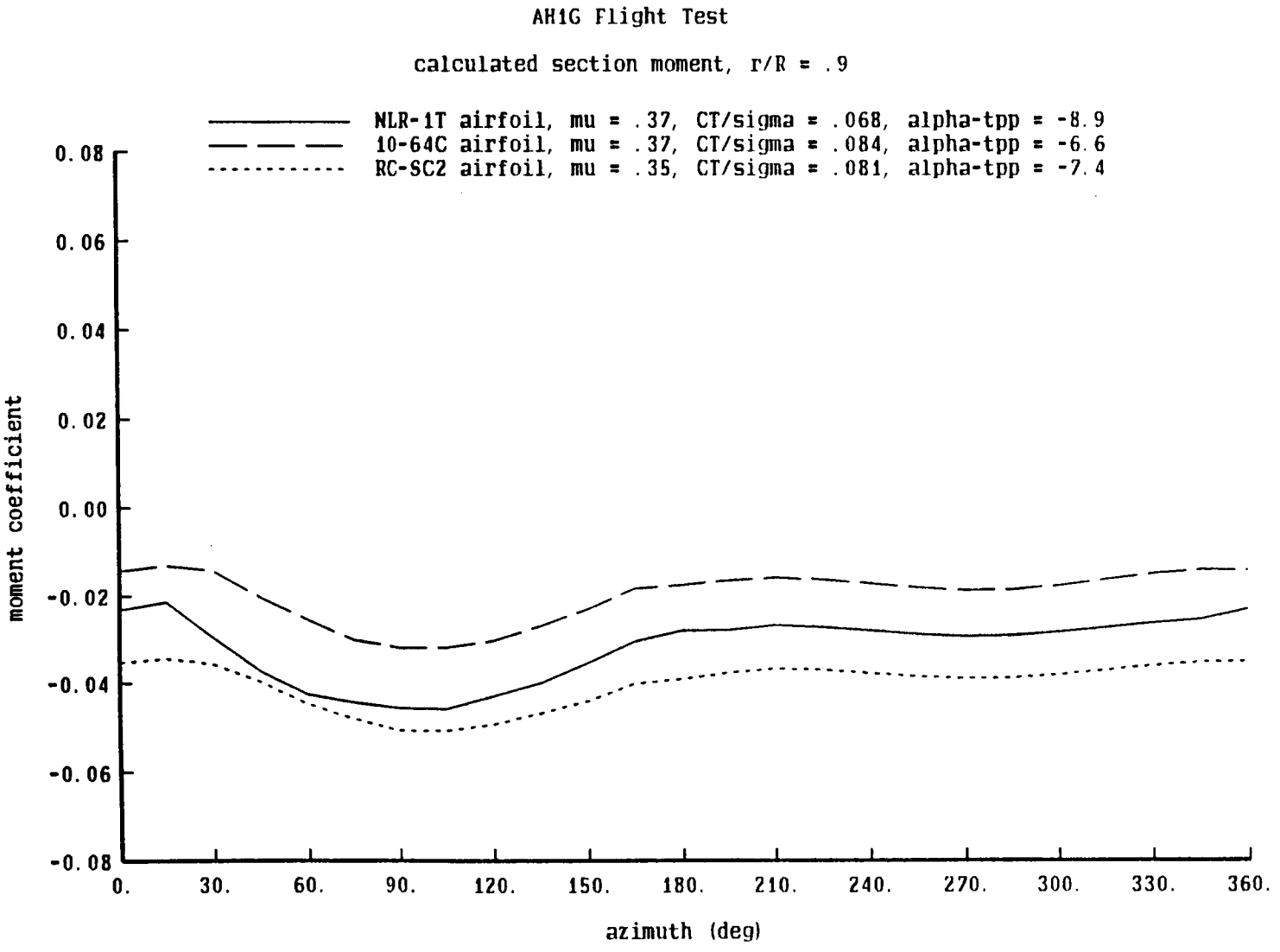

Figure 12-6b. AH-1G helicopter: measured and calculated pitch moment

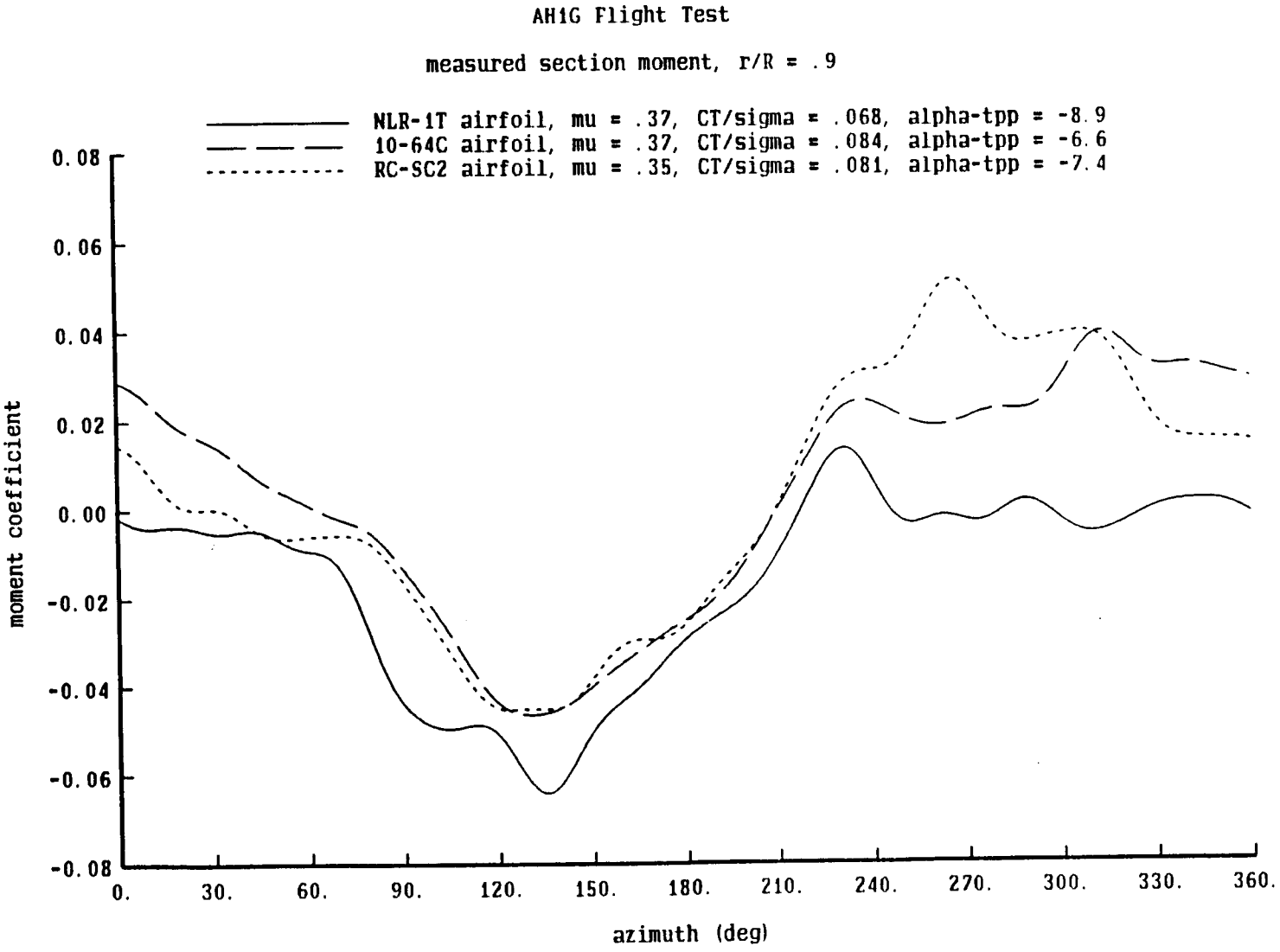

Figure 12-7a. AH-1G helicopter: chordwise pressure distribution

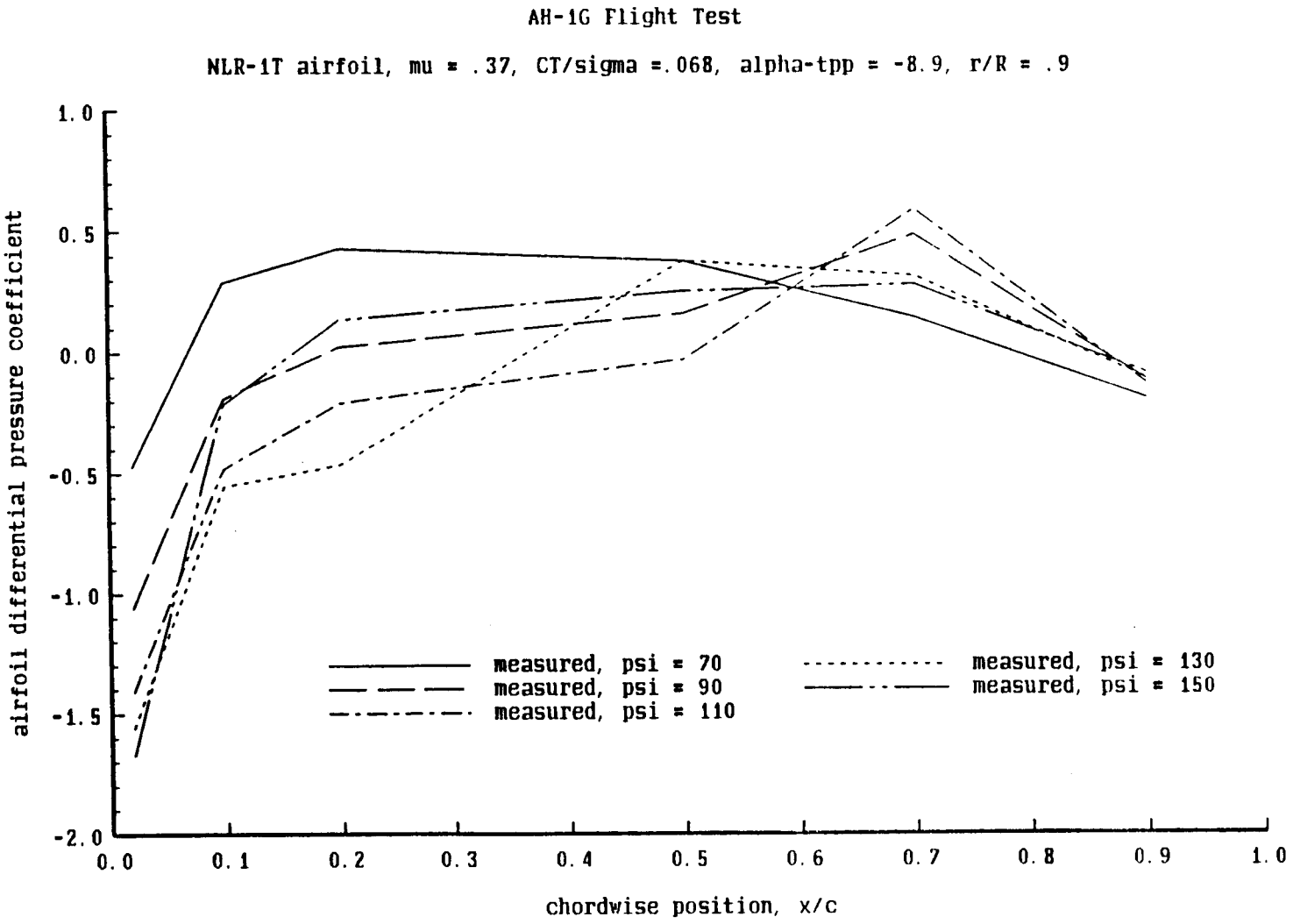

Figure 12-7b. AH-1G helicopter: chordwise pressure distribution

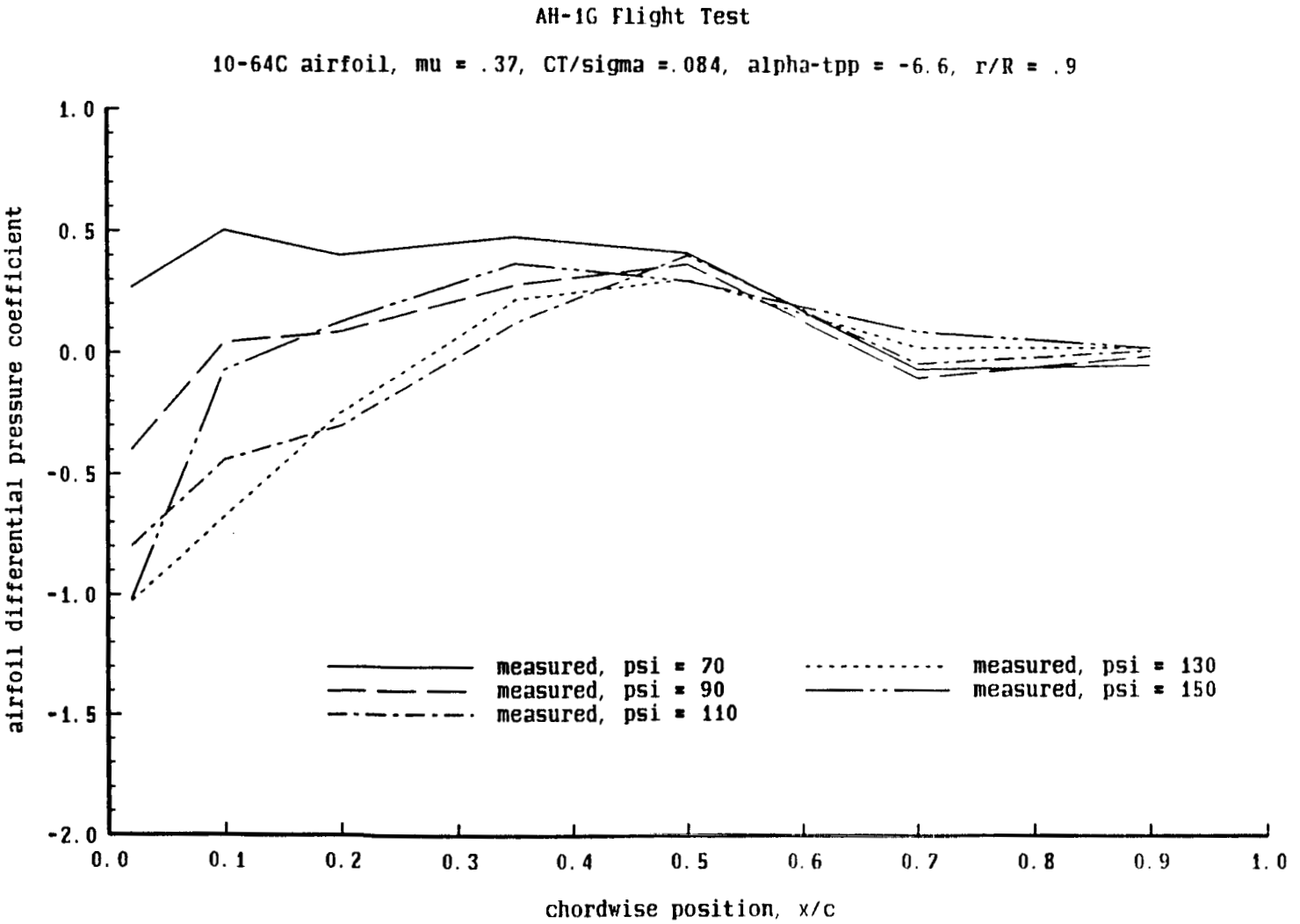

Figure 12-7c. AH-1G helicopter: chordwise pressure distribution

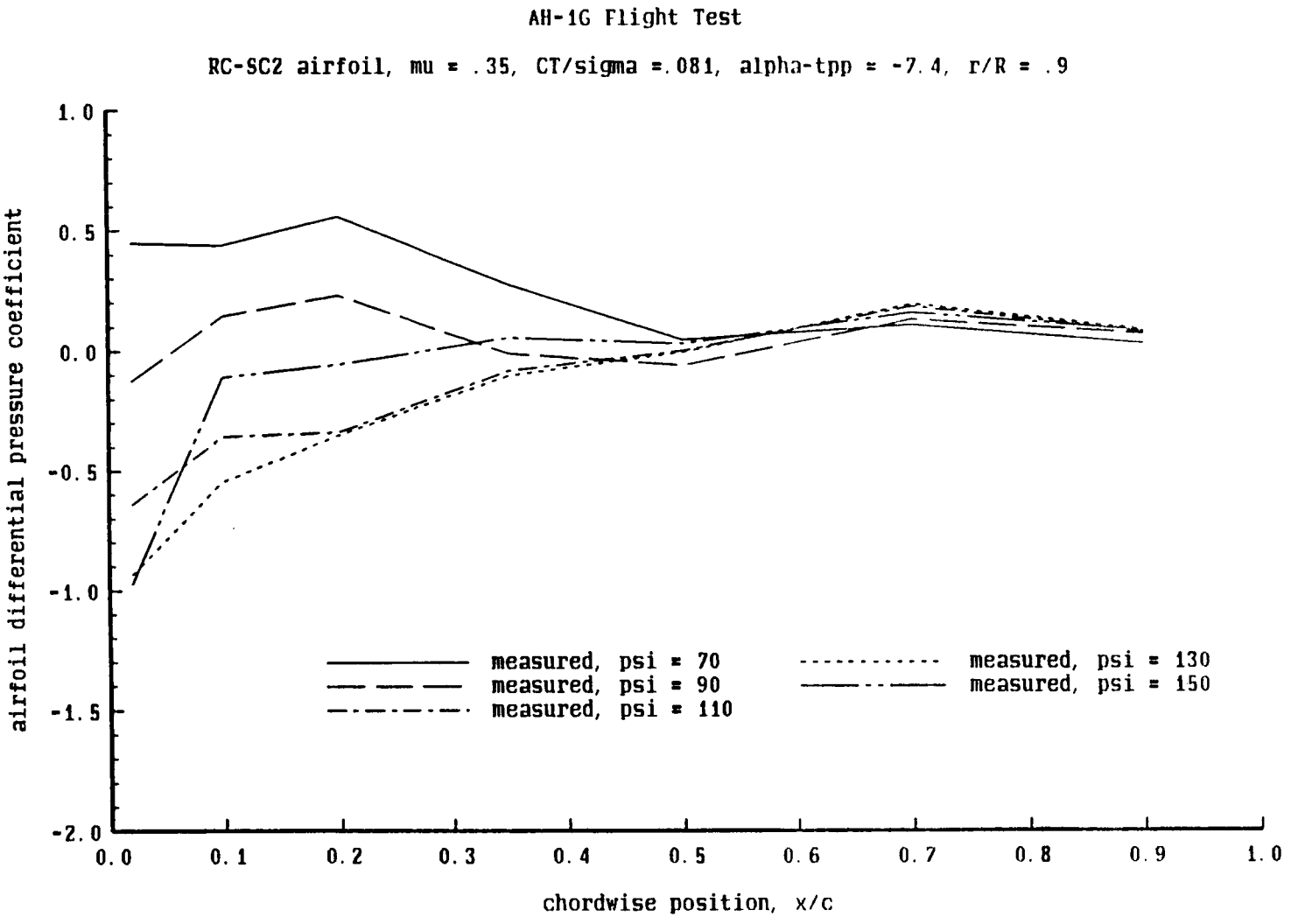

Figure 12-7d. AH-1G helicopter: chordwise pressure distribution

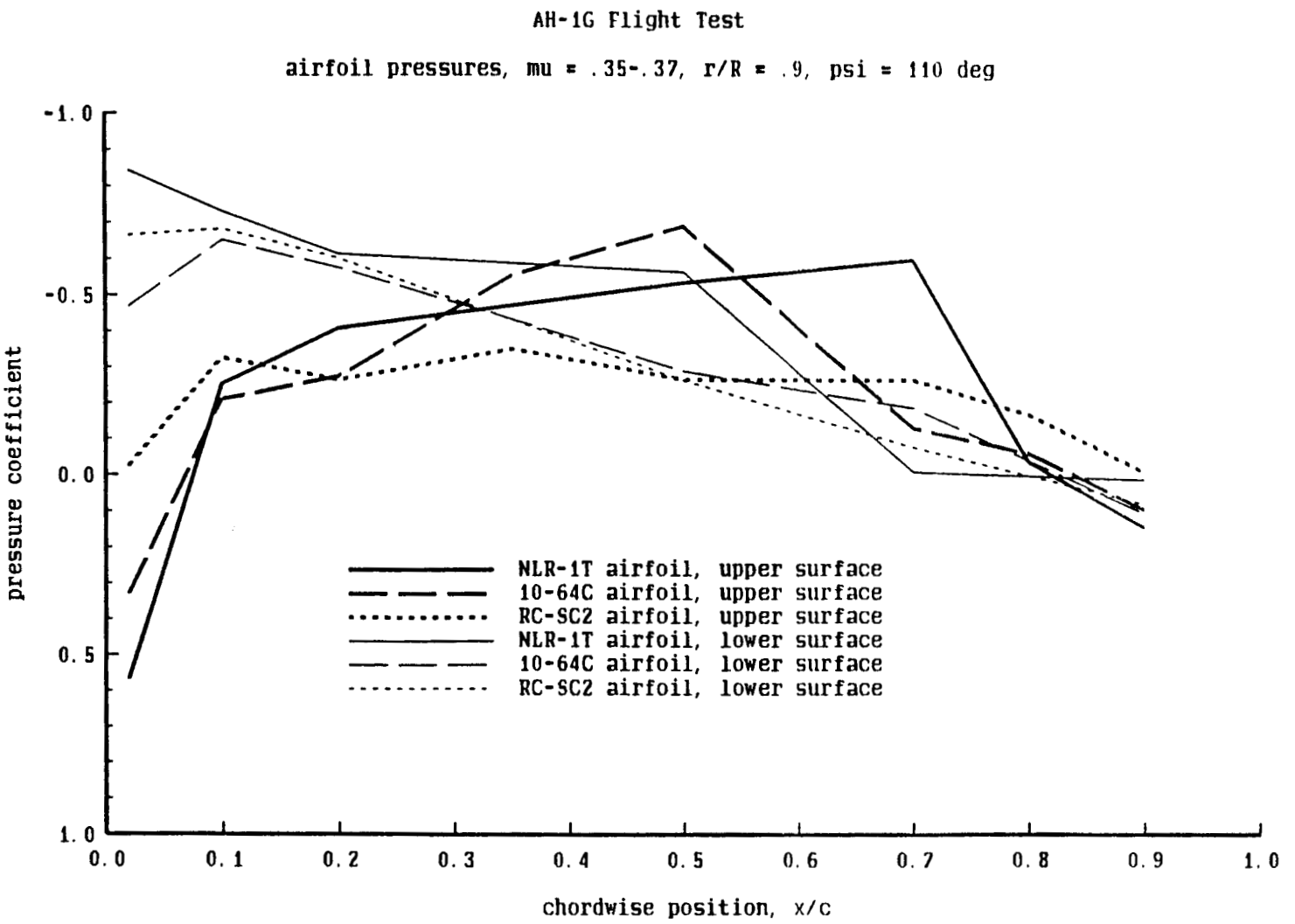

Figure 13-1a. H-34 flight test: influence of nonuniform inflow and wake geometry

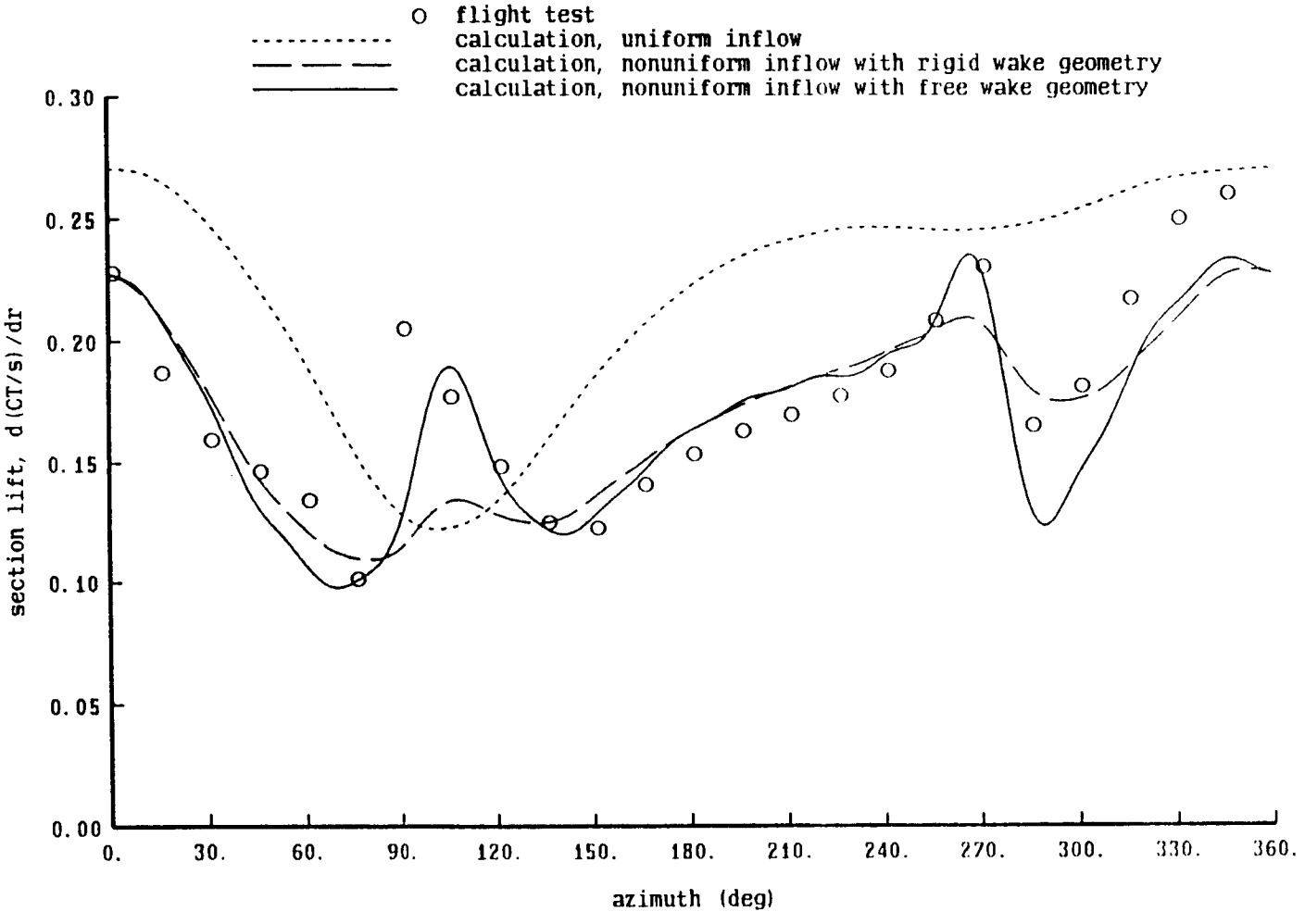

Figure 13-1b. H-34 flight test: influence of nonuniform inflow and wake geometry

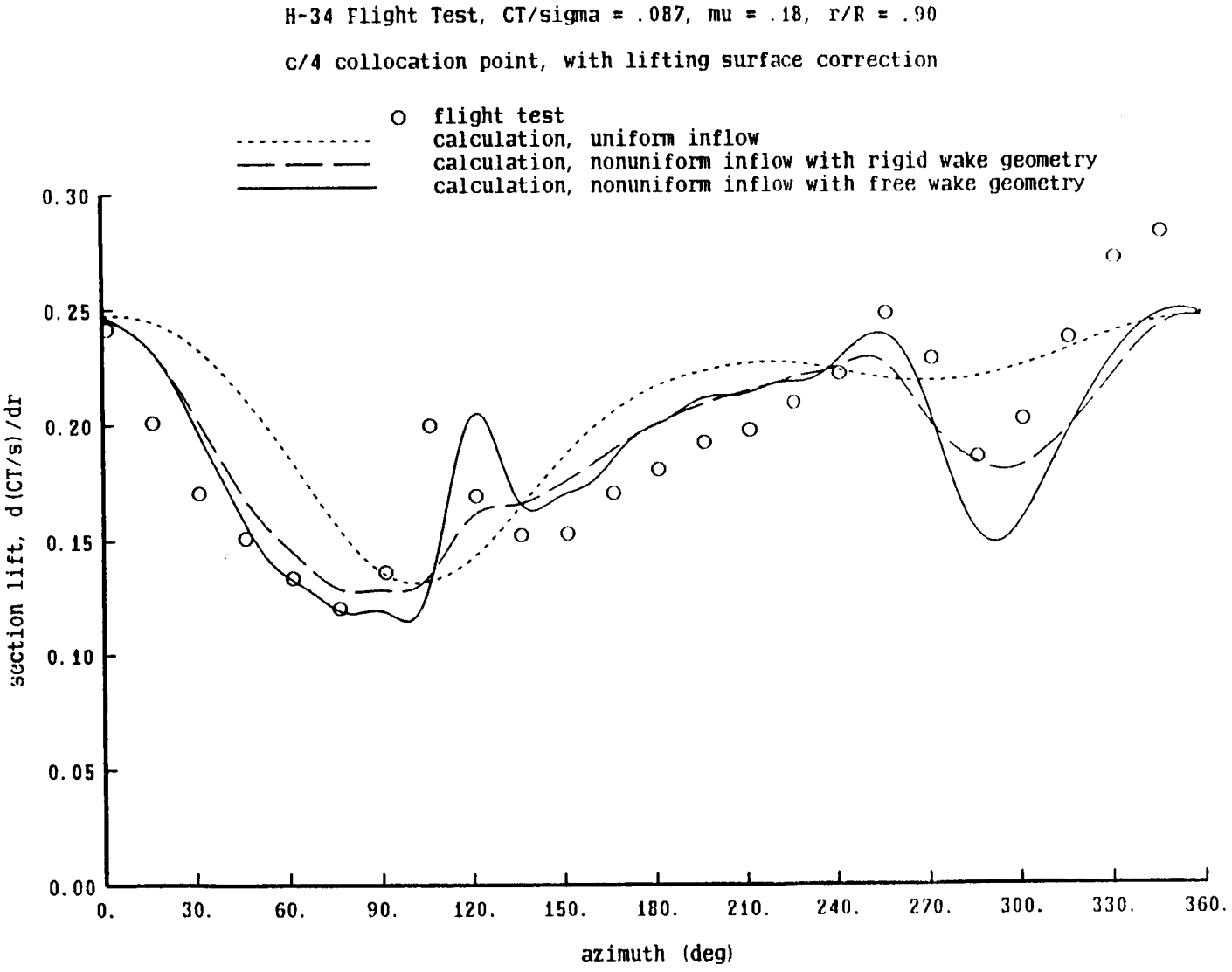

Figure 13-1c. H-34 flight test: influence of nonuniform inflow and wake geometry

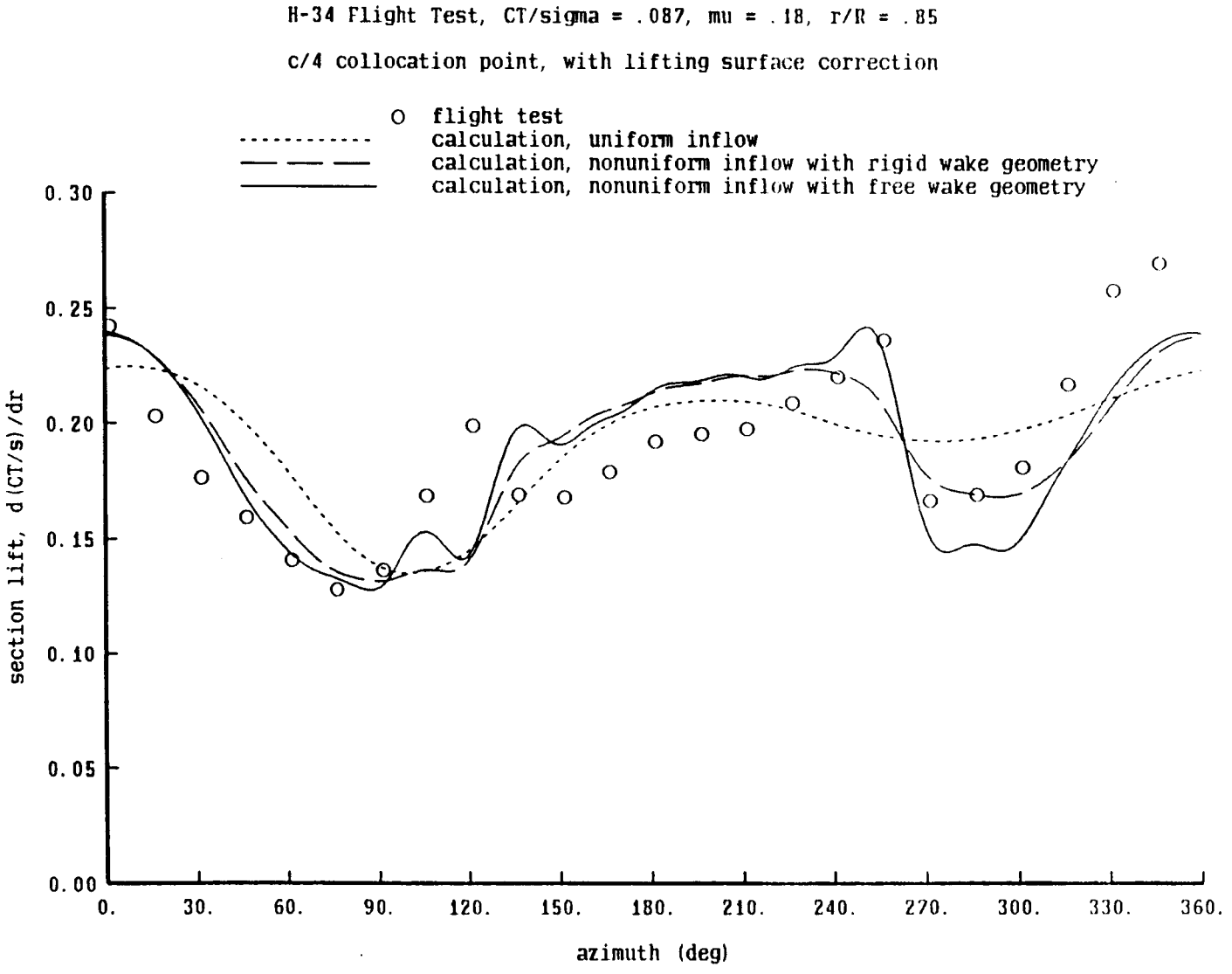

Figure 13-1d. H-34 flight test: influence of nonuniform inflow and wake geometry

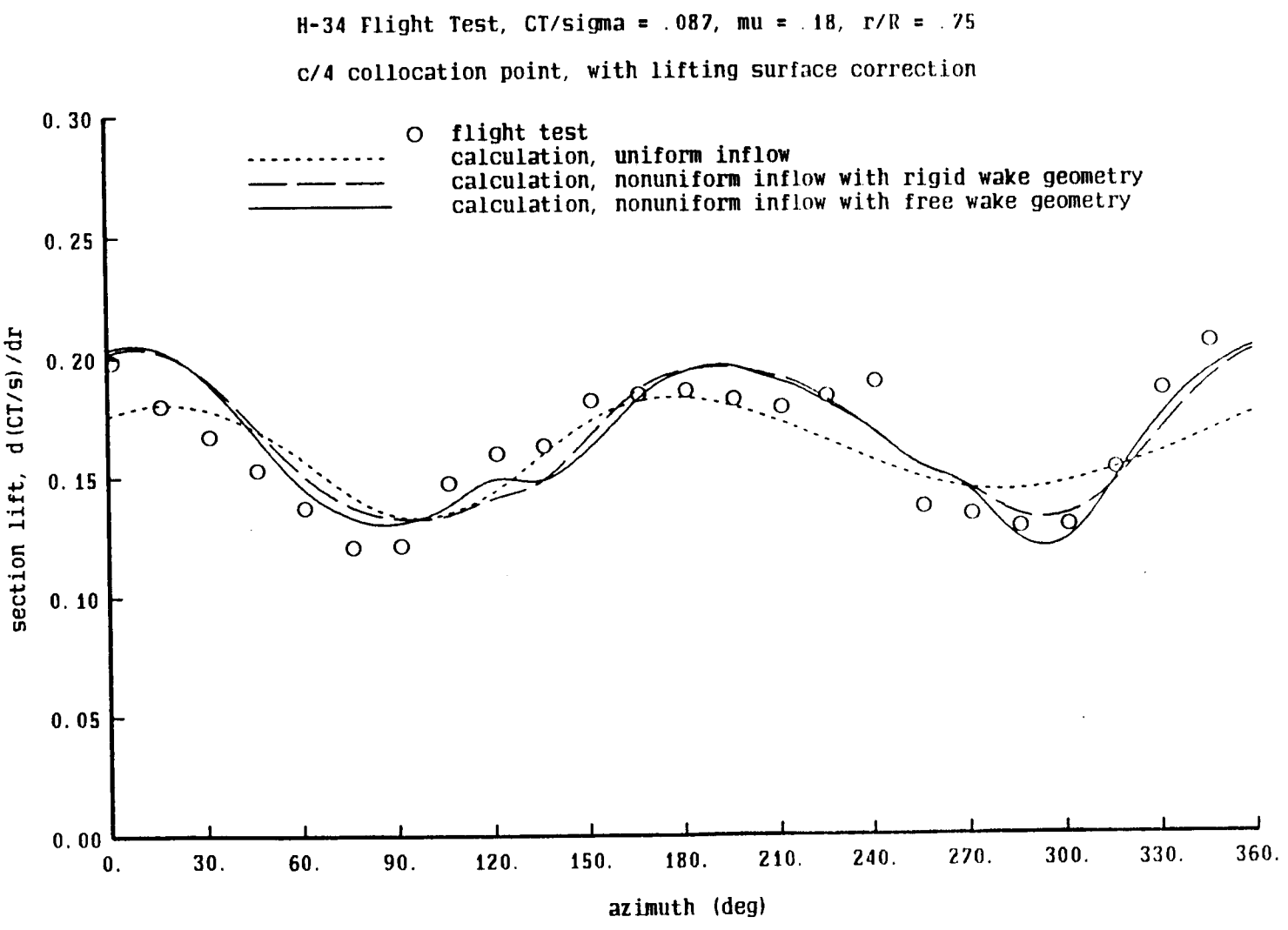

Figure 13-2. H-34 flight test: calculated wake geometry

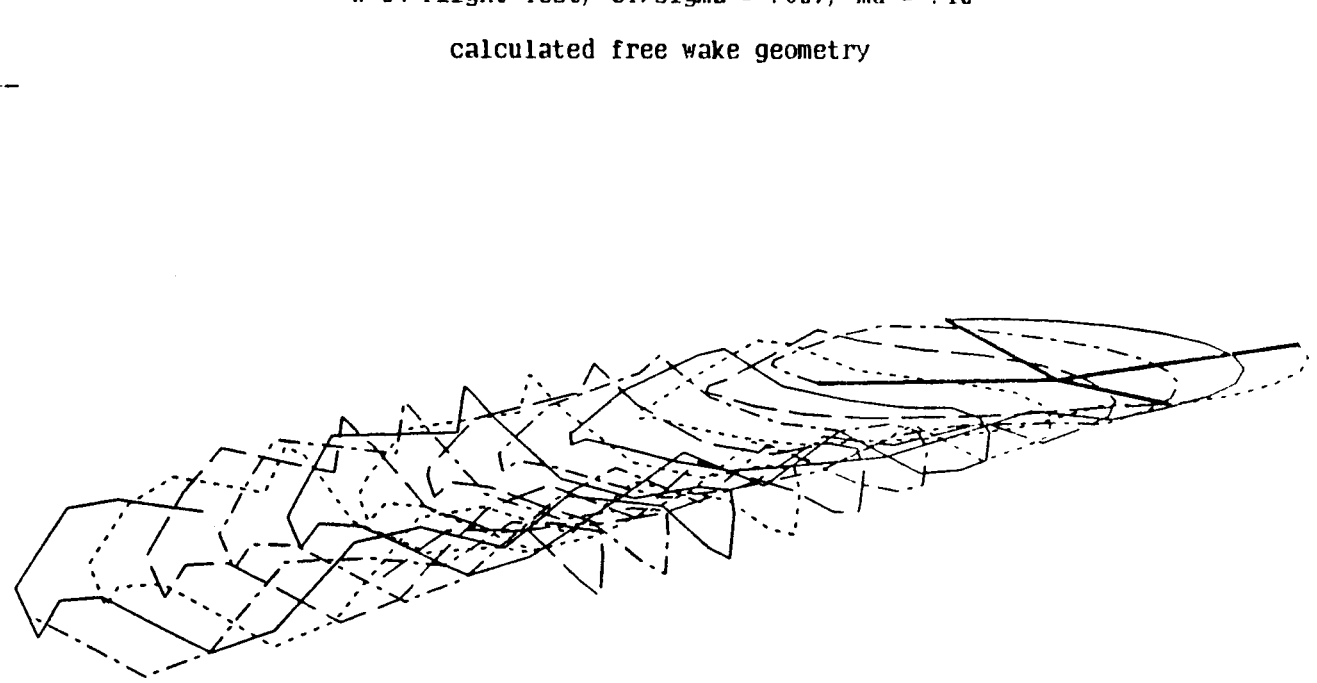

Figure 13-3a. H-34 flight test: influence of near wake model

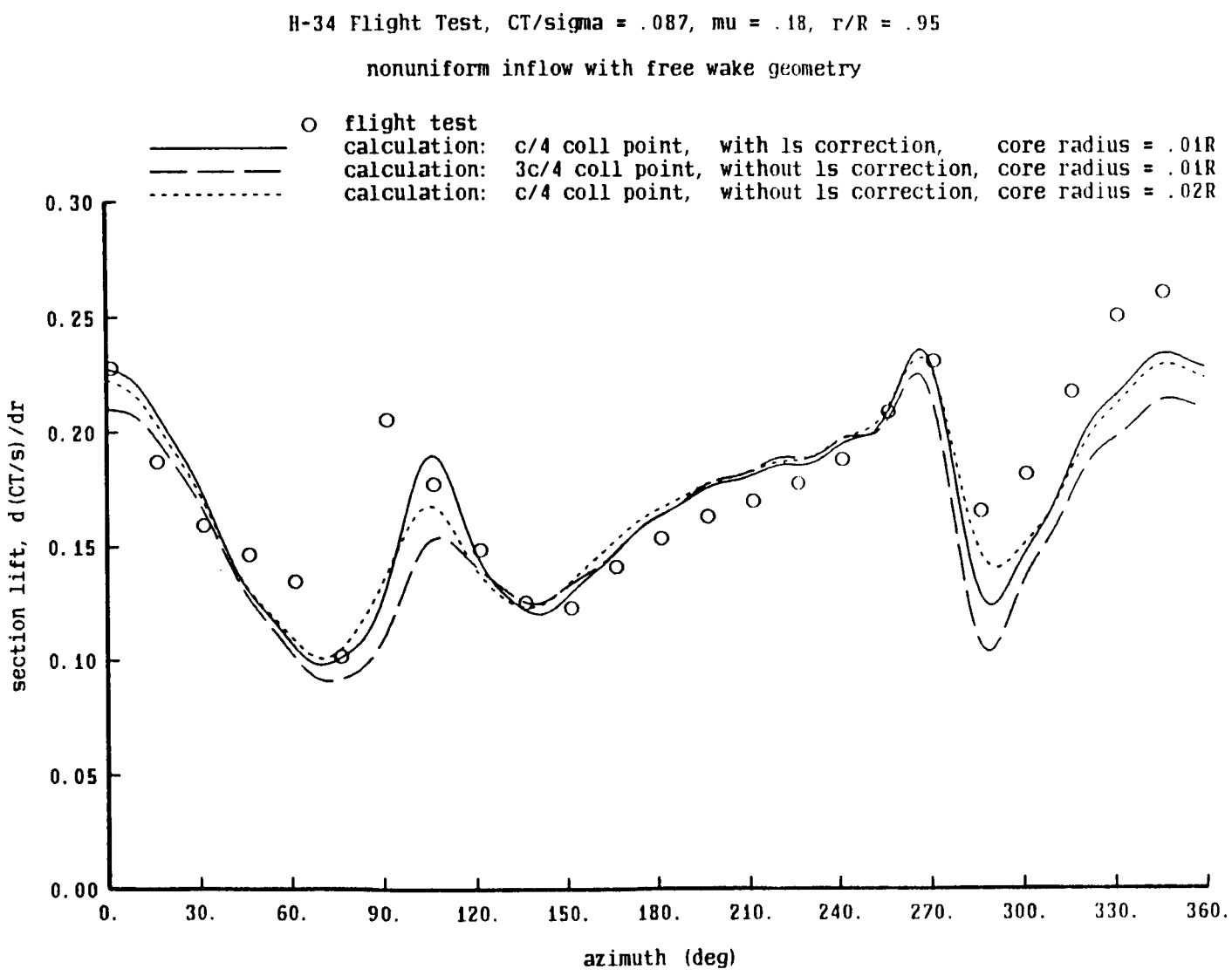

Figure 13-3b. H-34 flight test: influence of near wake model

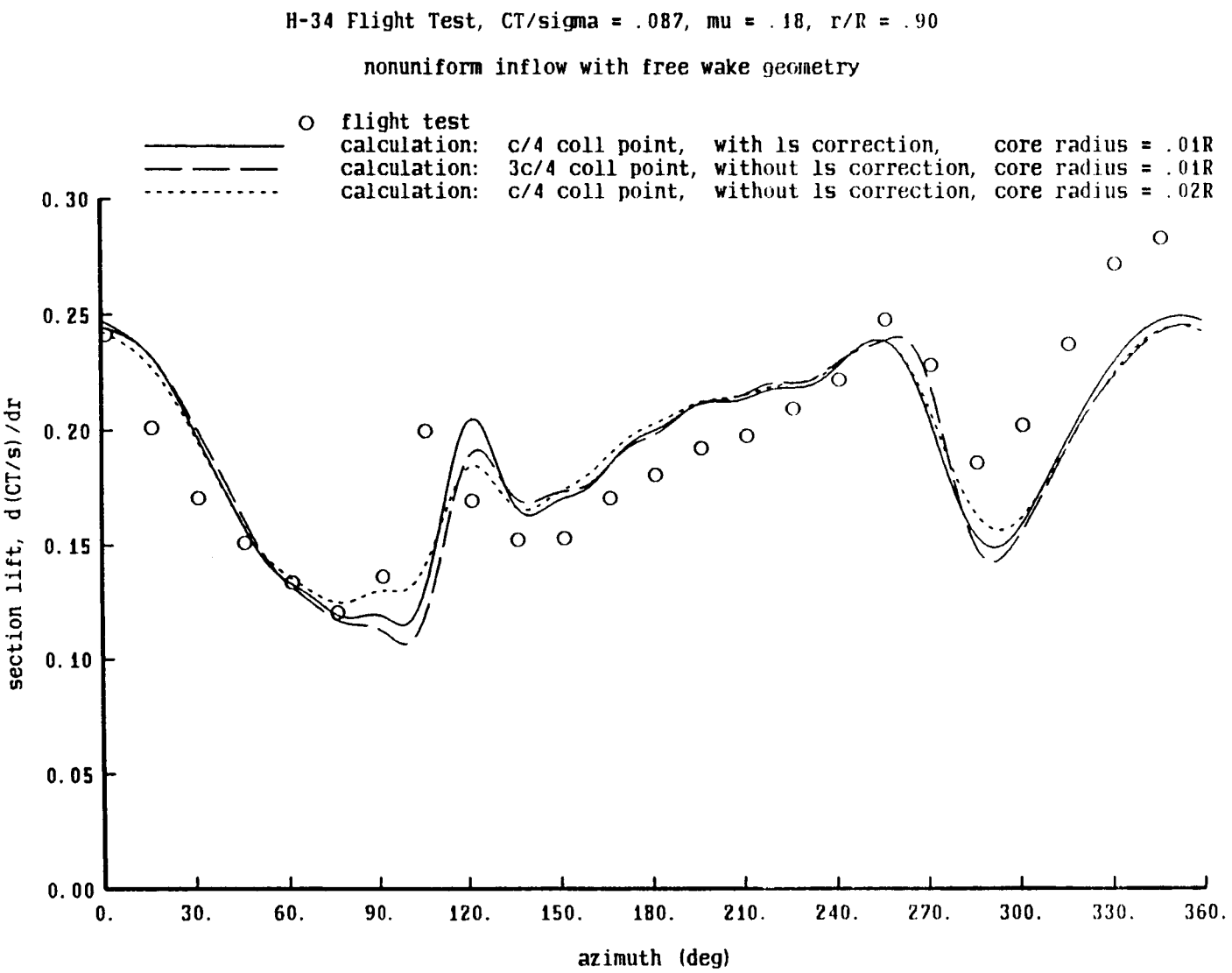

Figure 13-3c. H-34 flight test: influence of near wake model

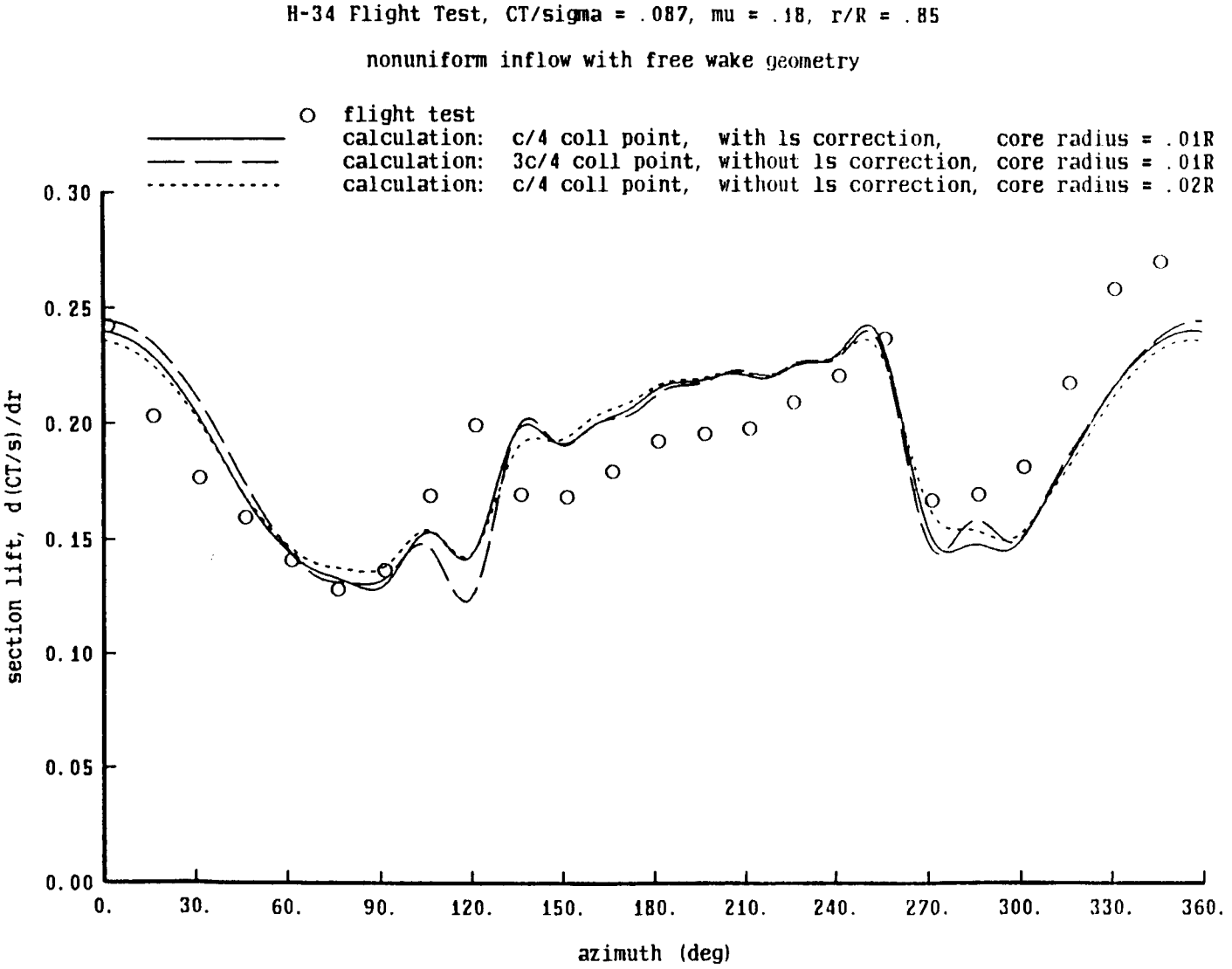

Figure 13-3d. H-34 flight test: influence of near wake model

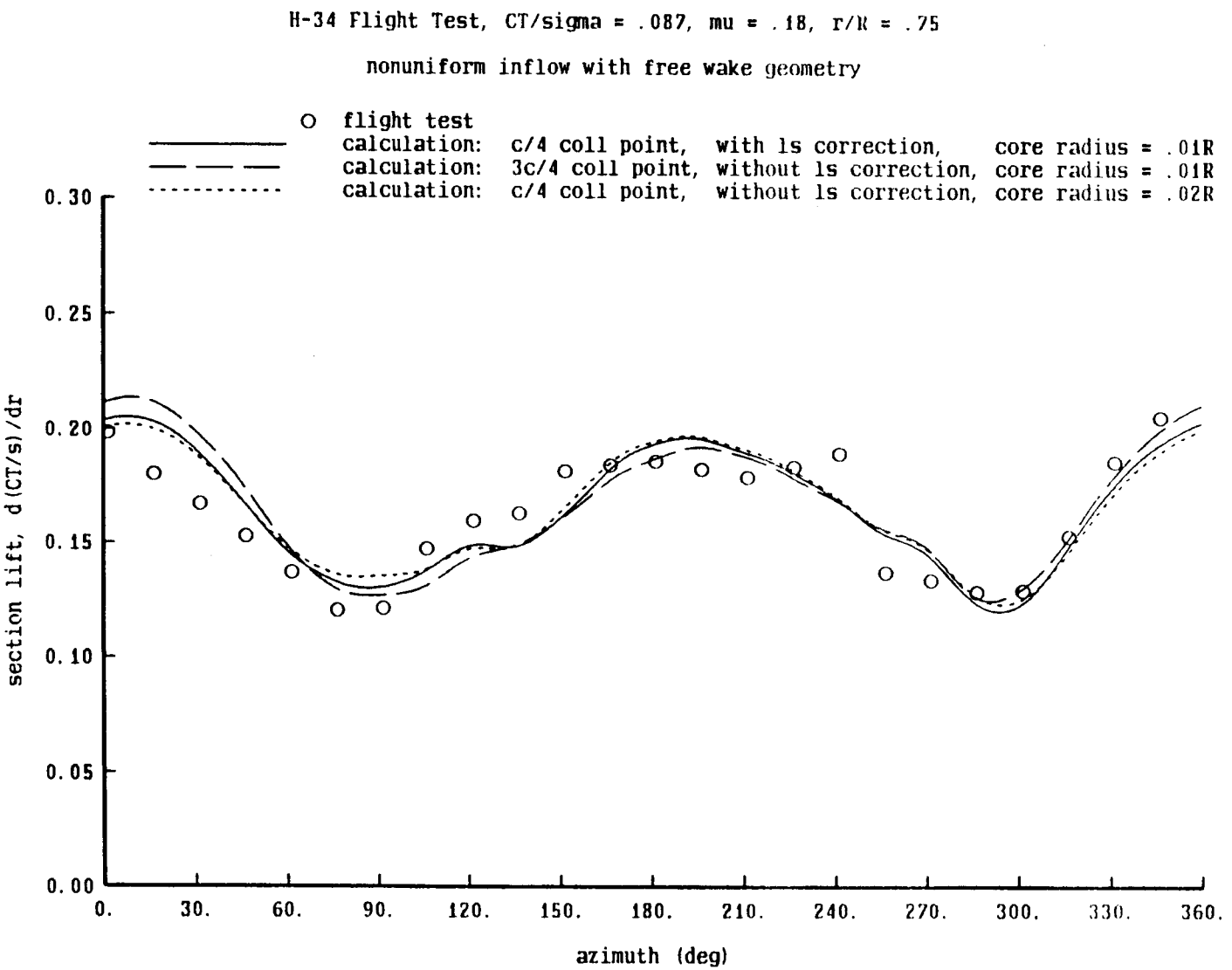

Figure 13-4a. H-34 flight test: influence of inboard blade-vortex interaction

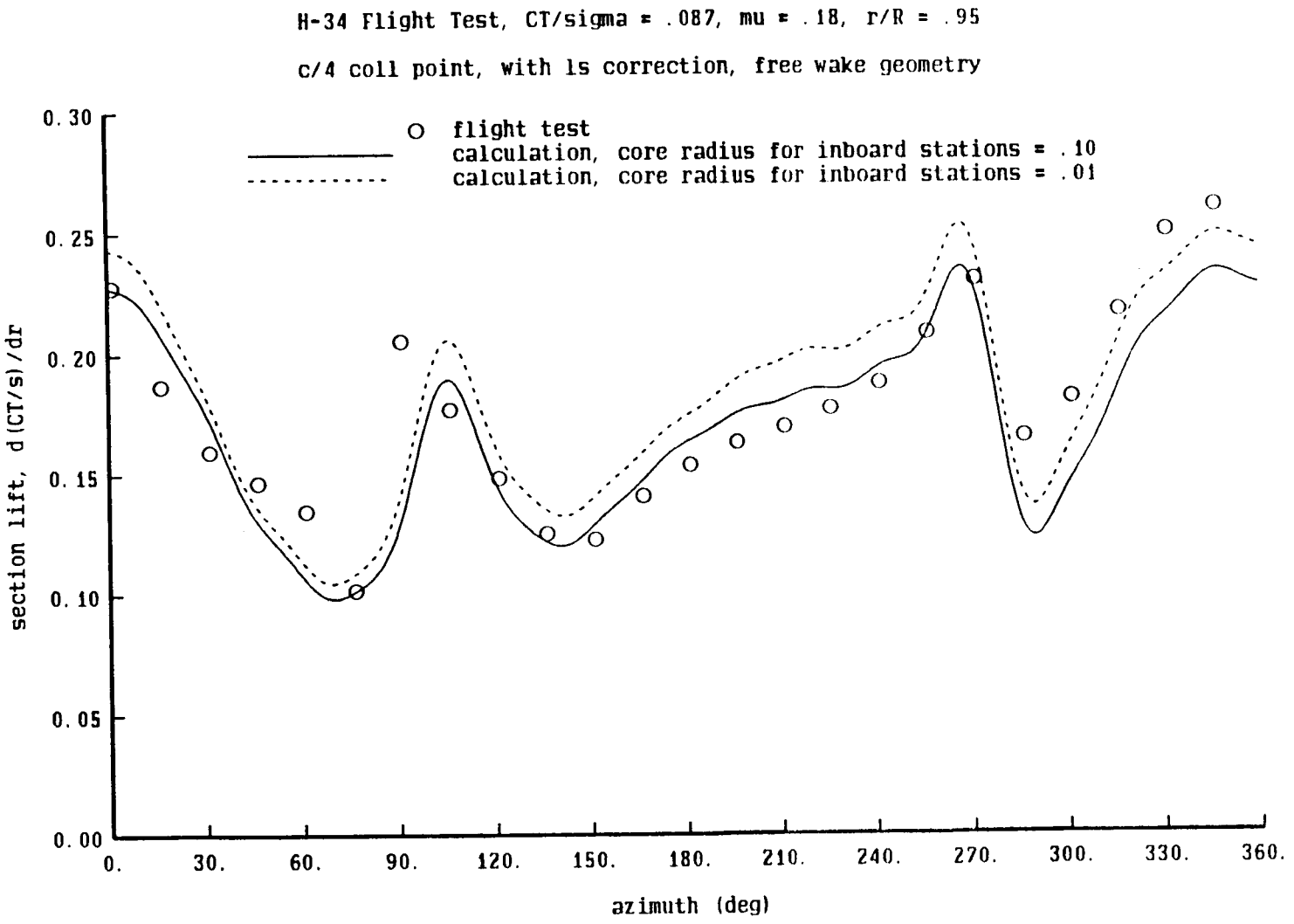

Figure 13-4b. H-34 flight test: influence of inboard blade-vortex interaction

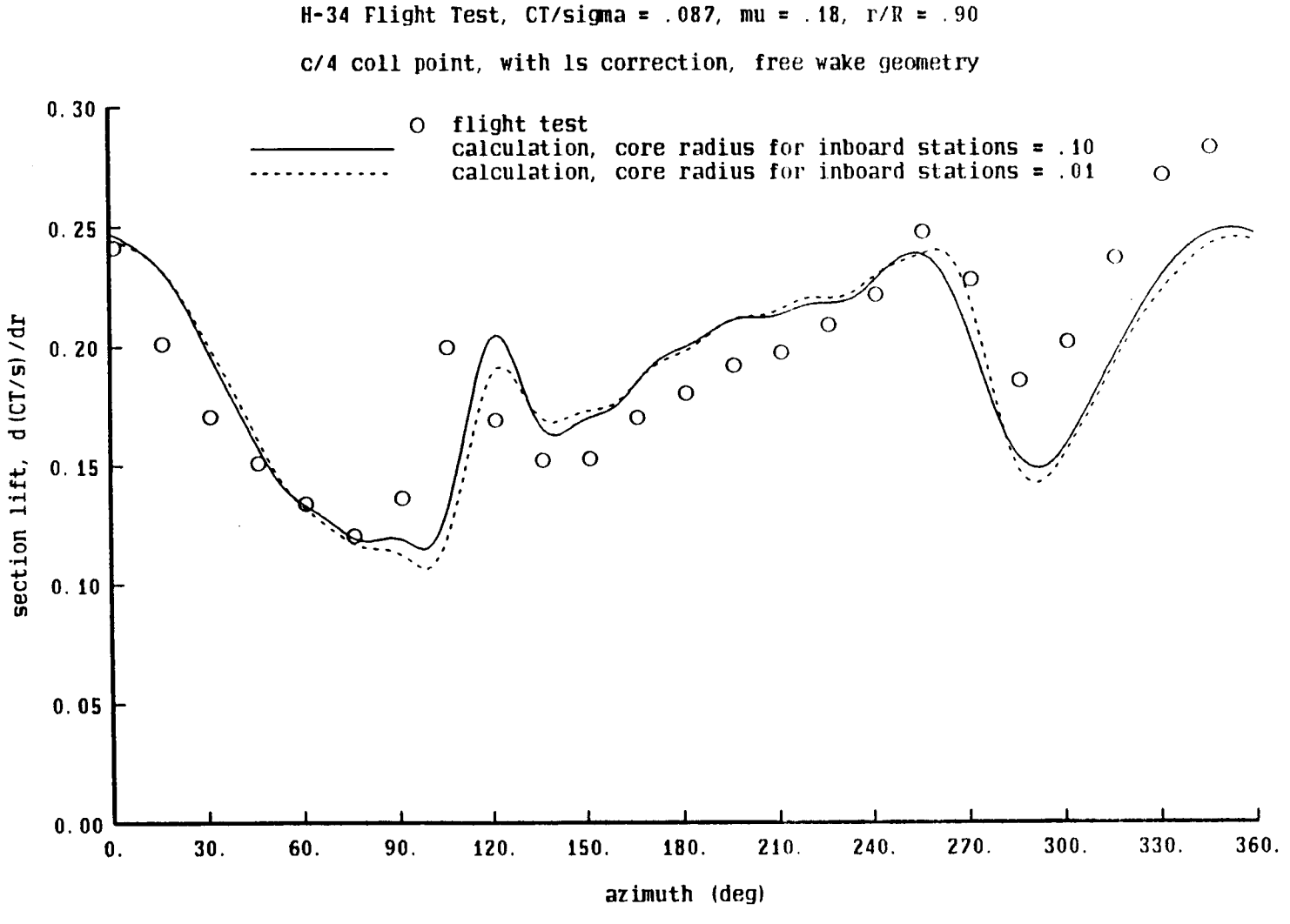

Figure 13-4c. H-34 flight test: influence of inboard blade-vortex interaction

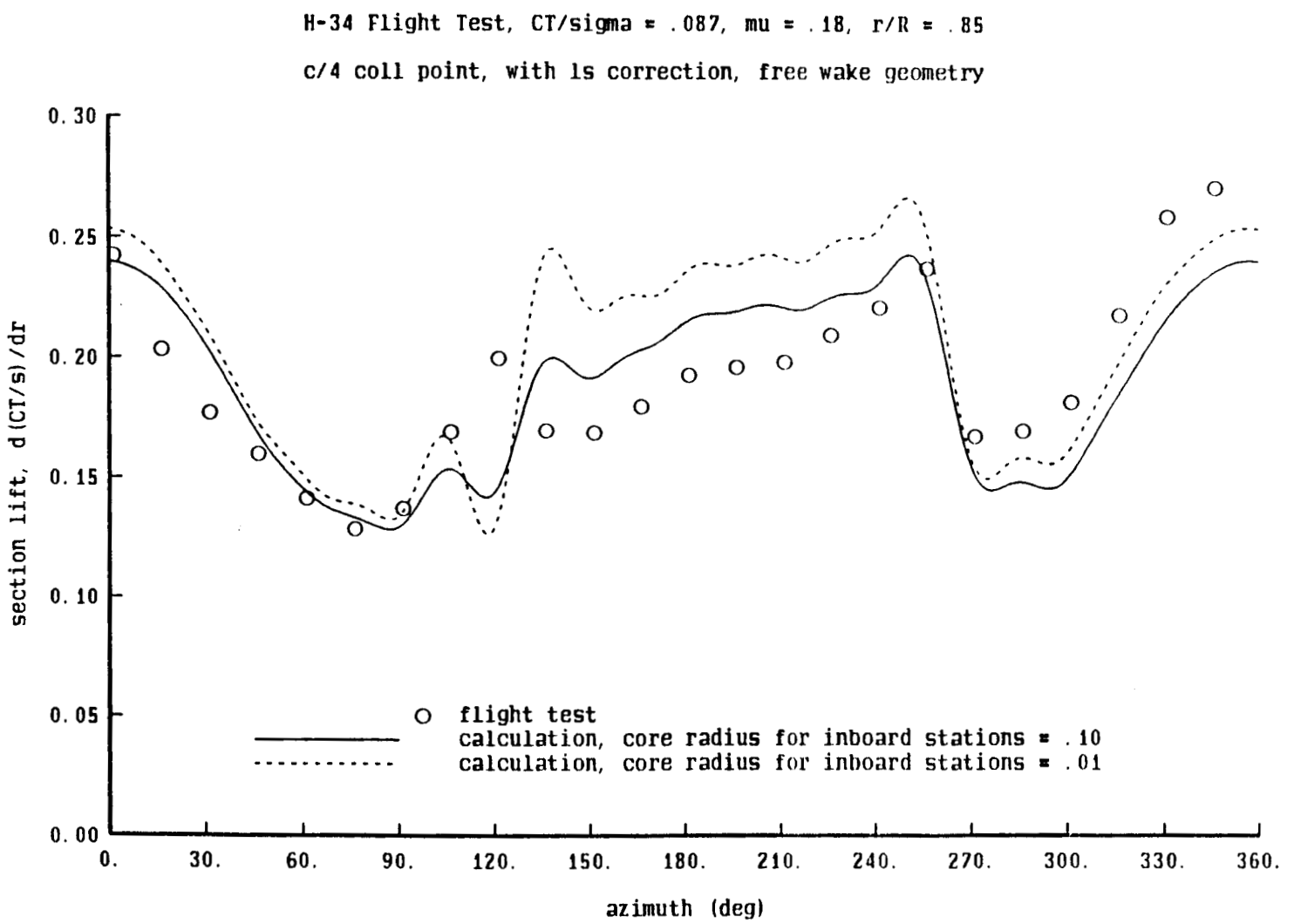

Figure 13-4d. H-34 flight test: influence of inboard blade-vortex interaction

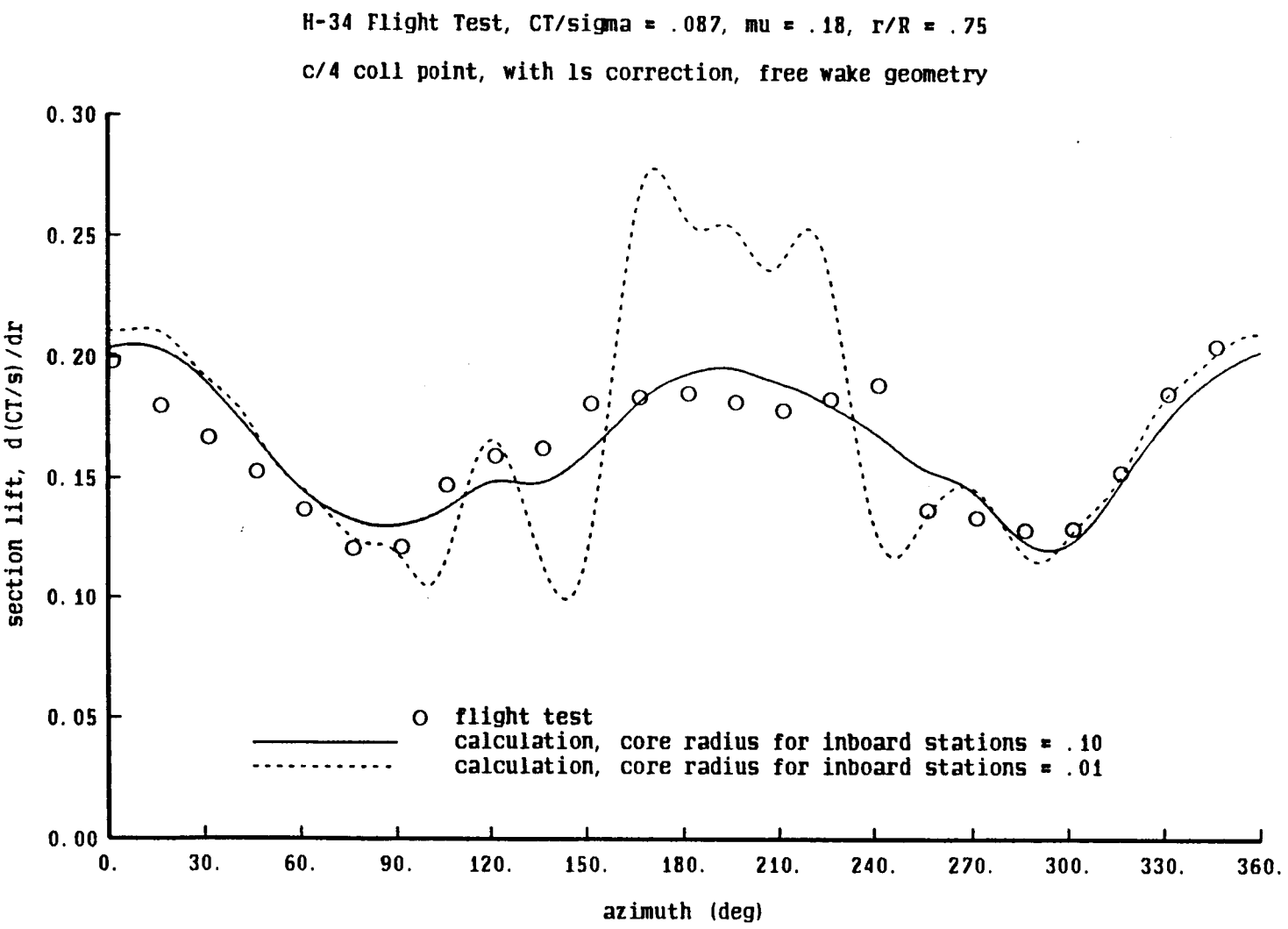

Figure 13-5a. H-34 flight test: influence of blade elastic motion

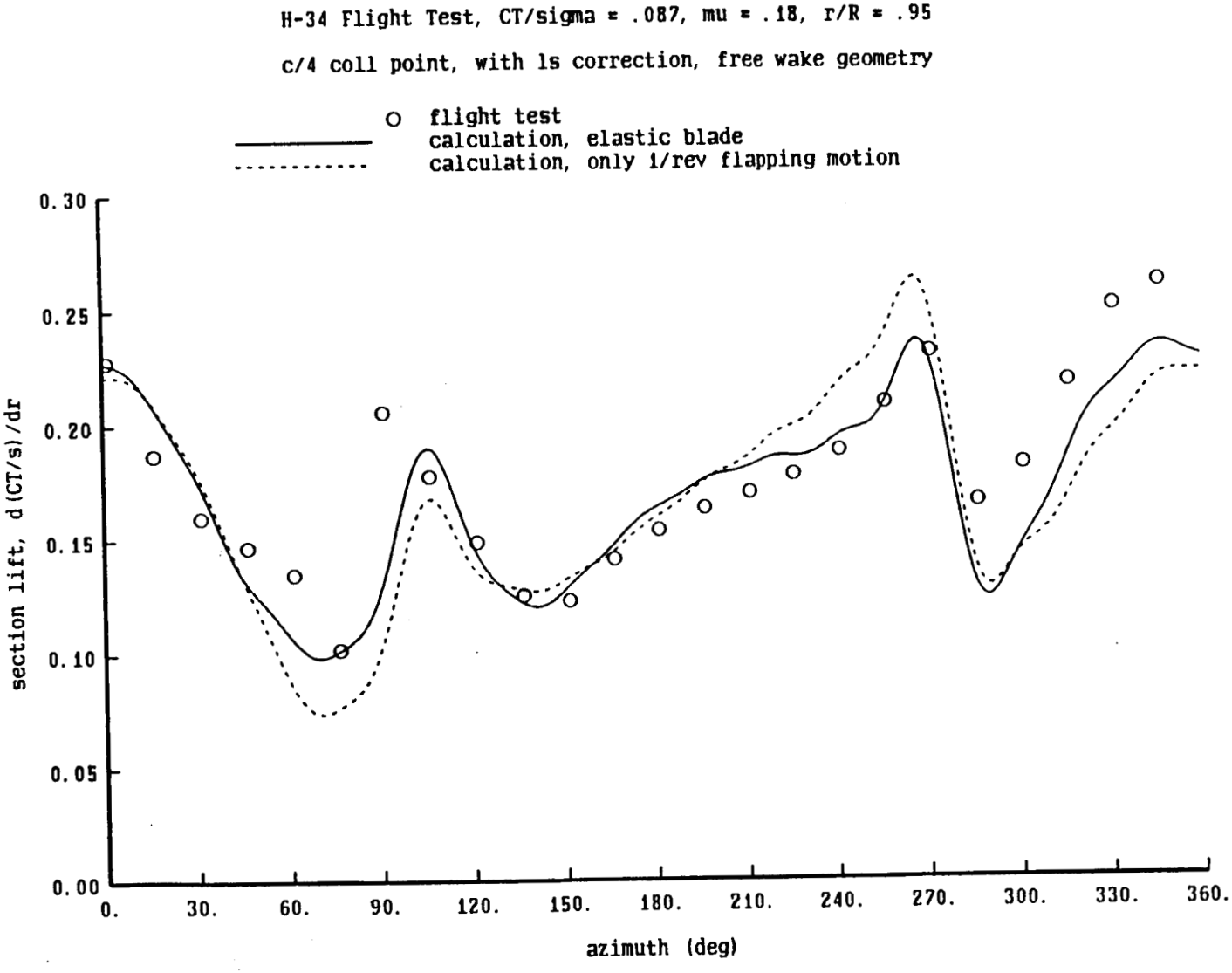

Figure 13-5b. H-34 flight test: influence of blade elastic motion

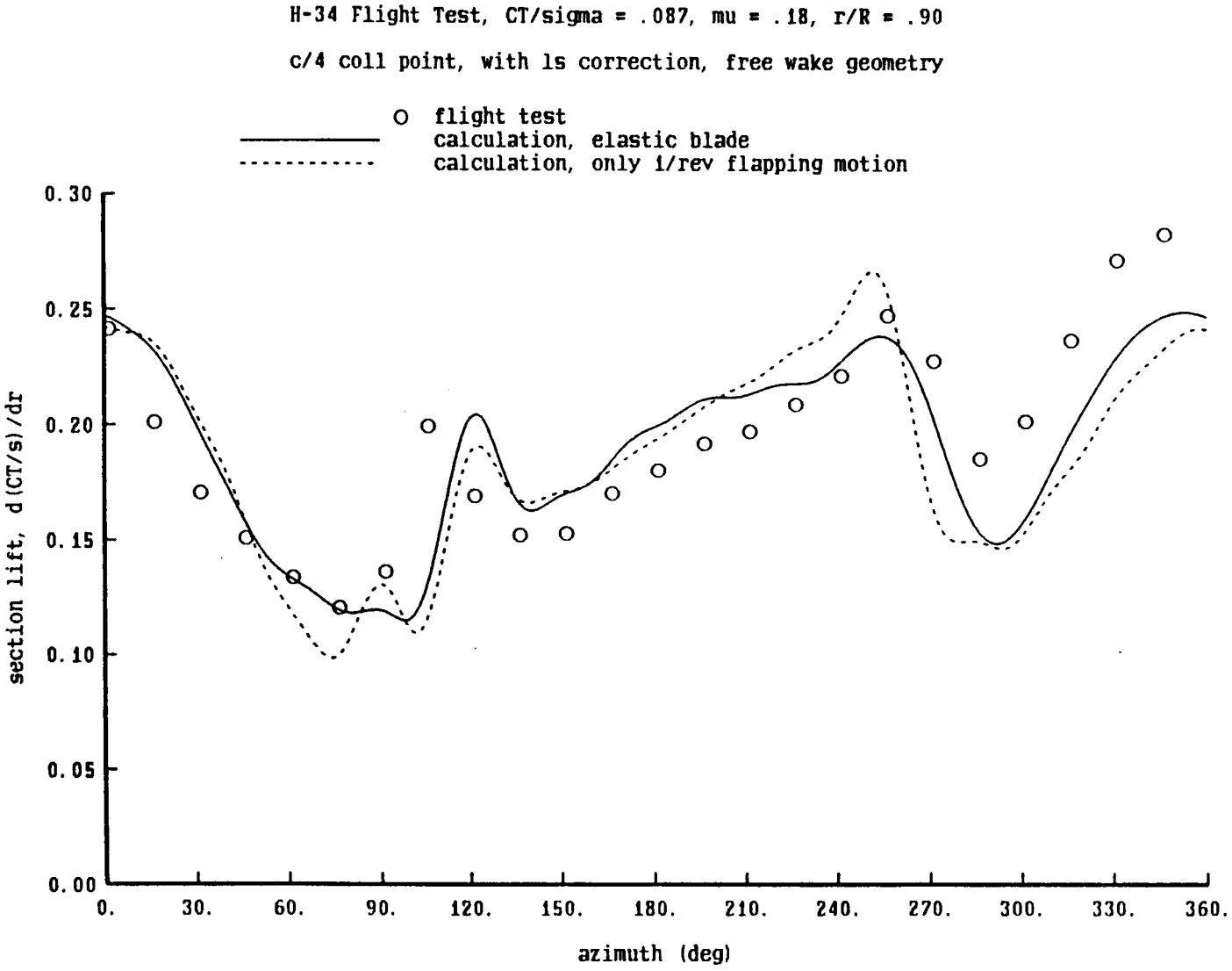

Figure 13-5c. H-34 flight test: influence of blade elastic motion

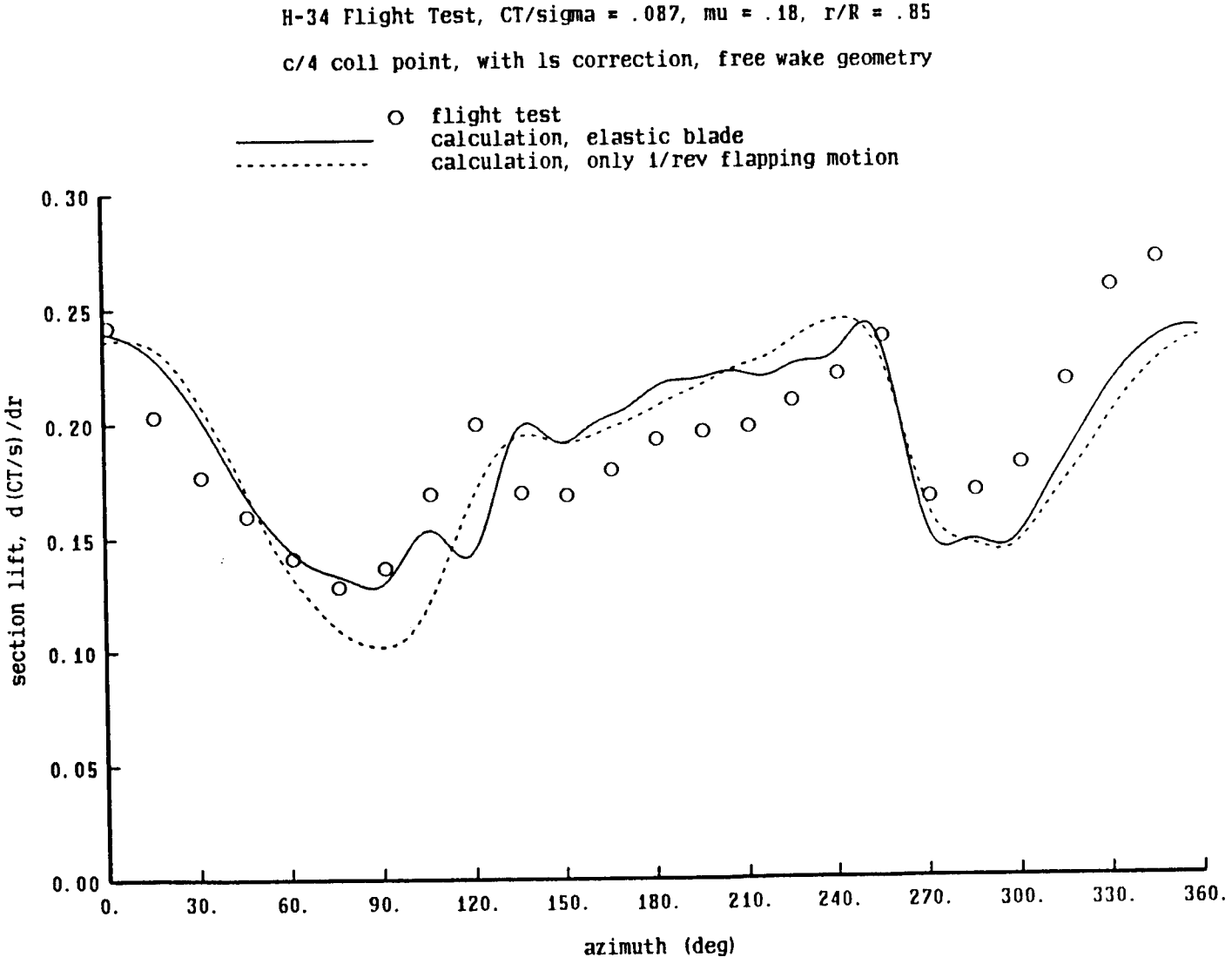

Figure 13-5d. H-34 flight test: influence of blade elastic motion

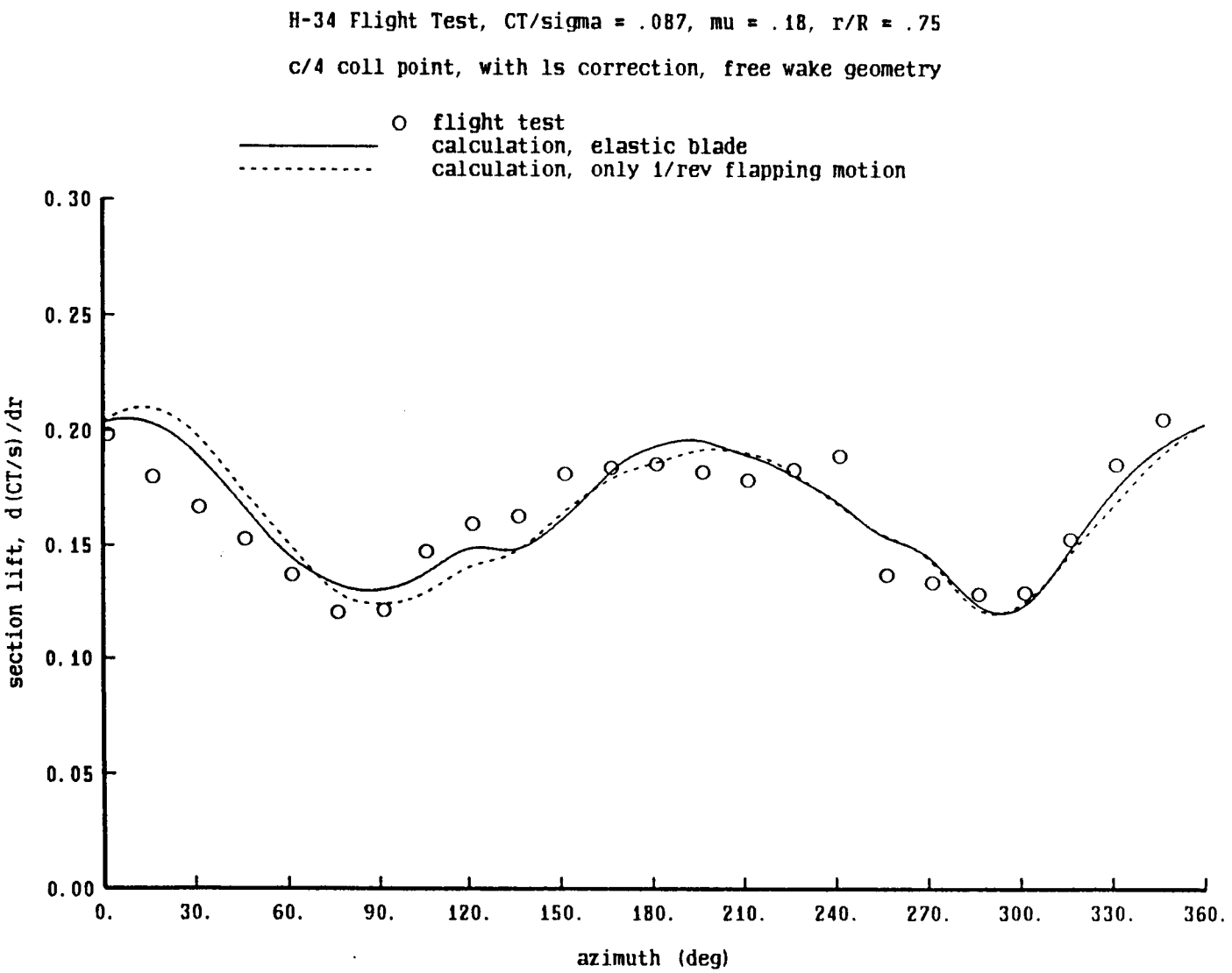

Figure 13-6a. H-34 flight test: influence of nonuniform inflow

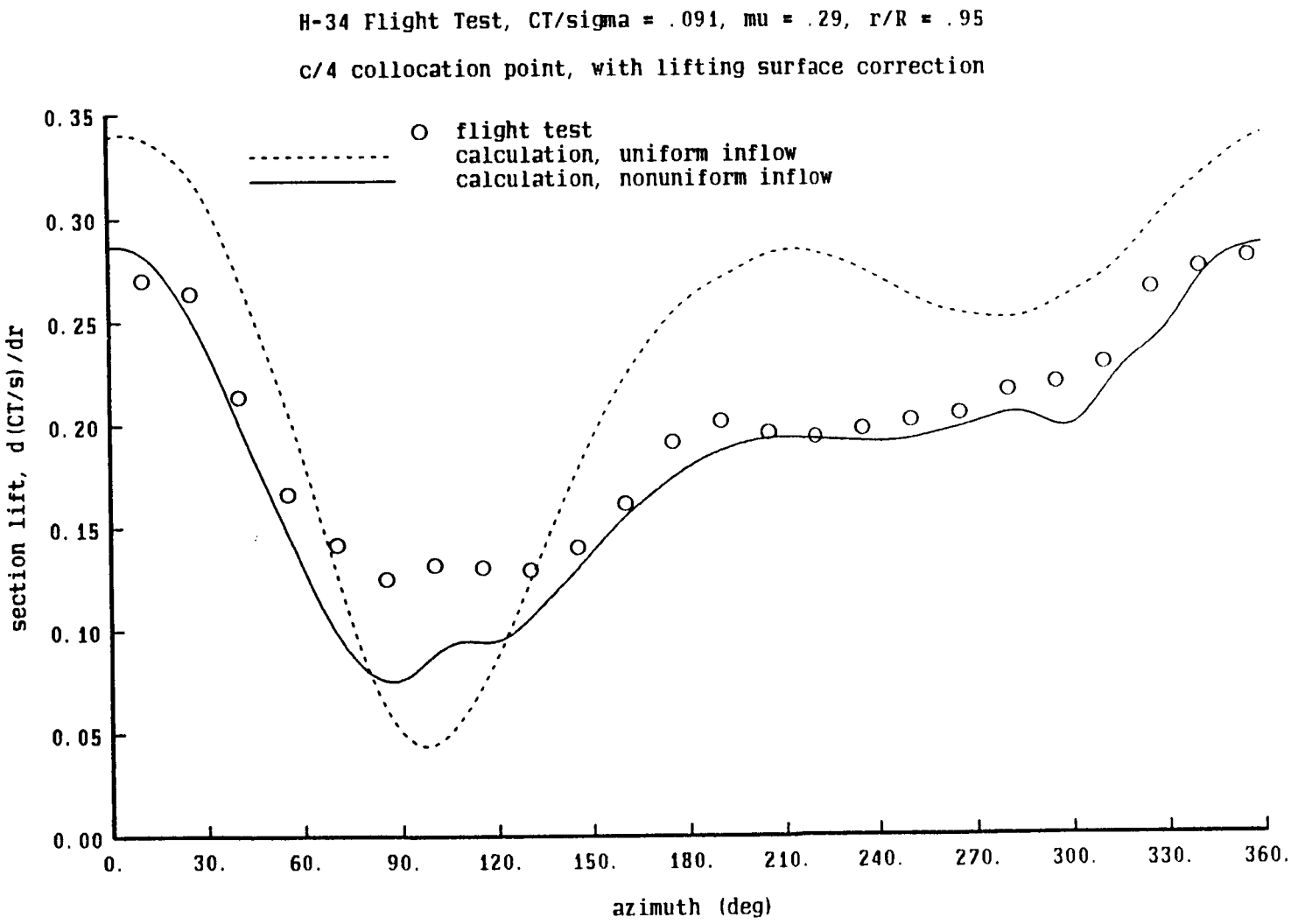

Figure 13-6b. H-34 flight test: influence of nonuniform inflow

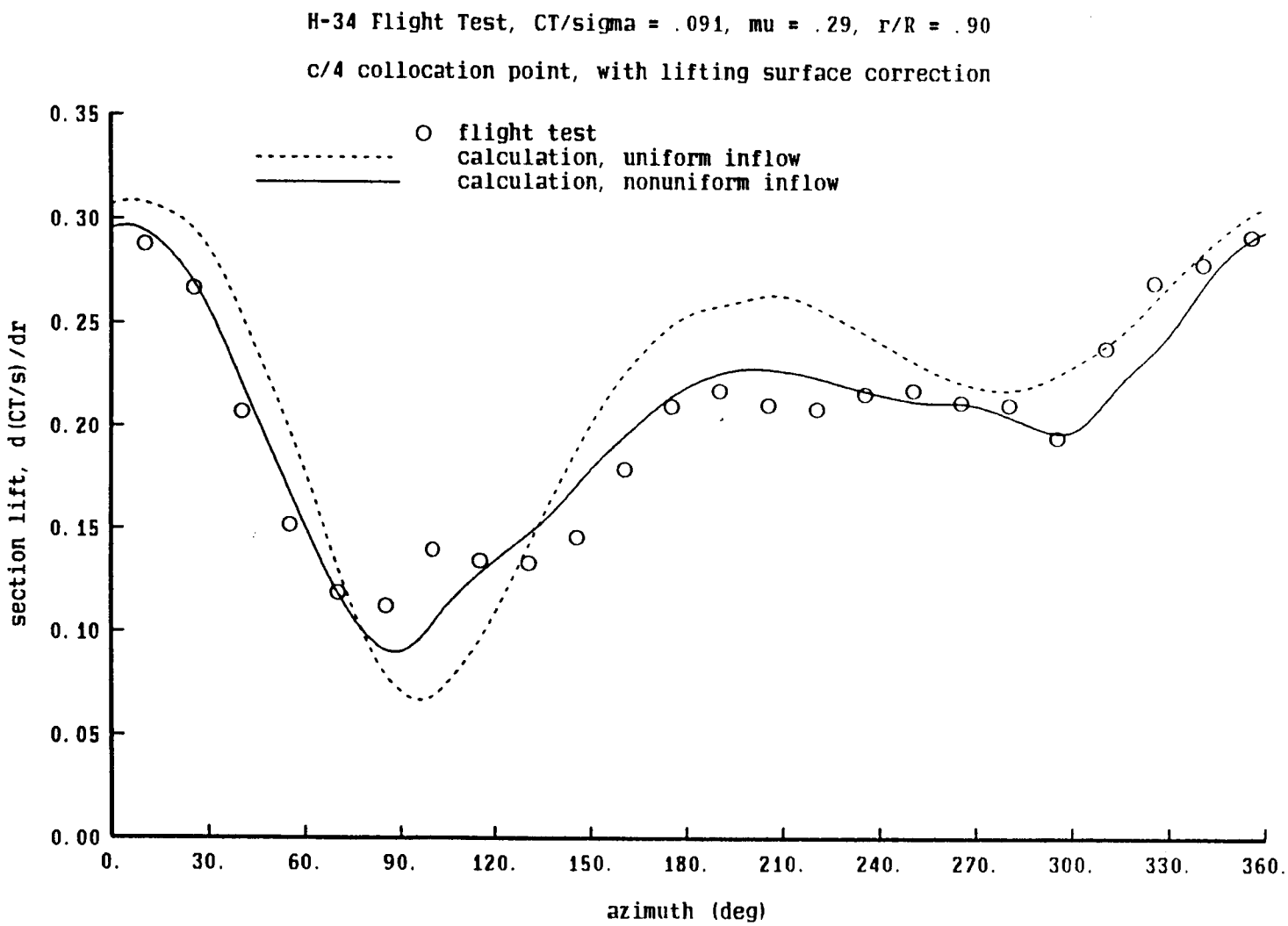

Figure 13-6c. H-34 flight test: influence of nonuniform inflow

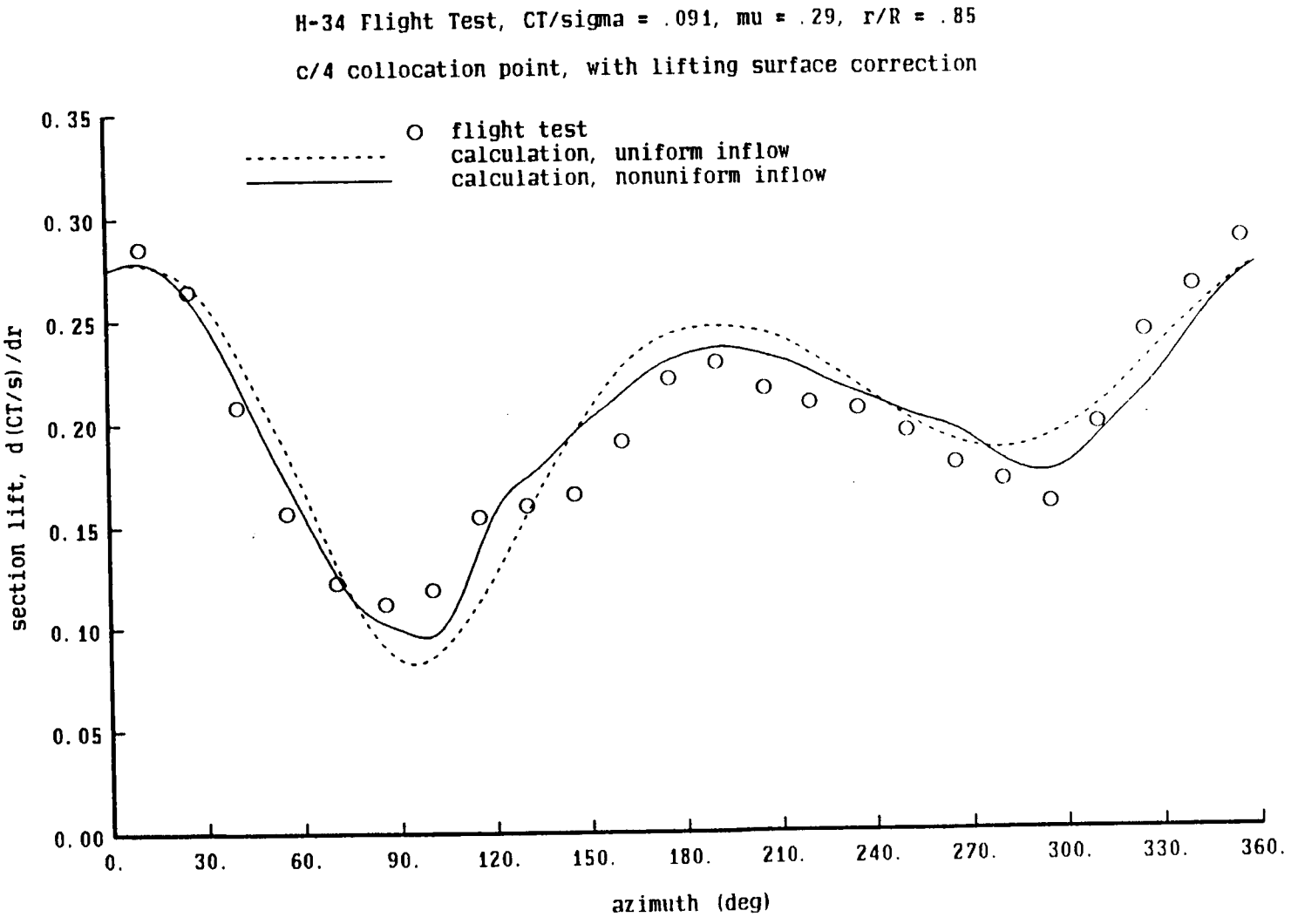

Figure 13-6d. H-34 flight test: influence of nonuniform inflow

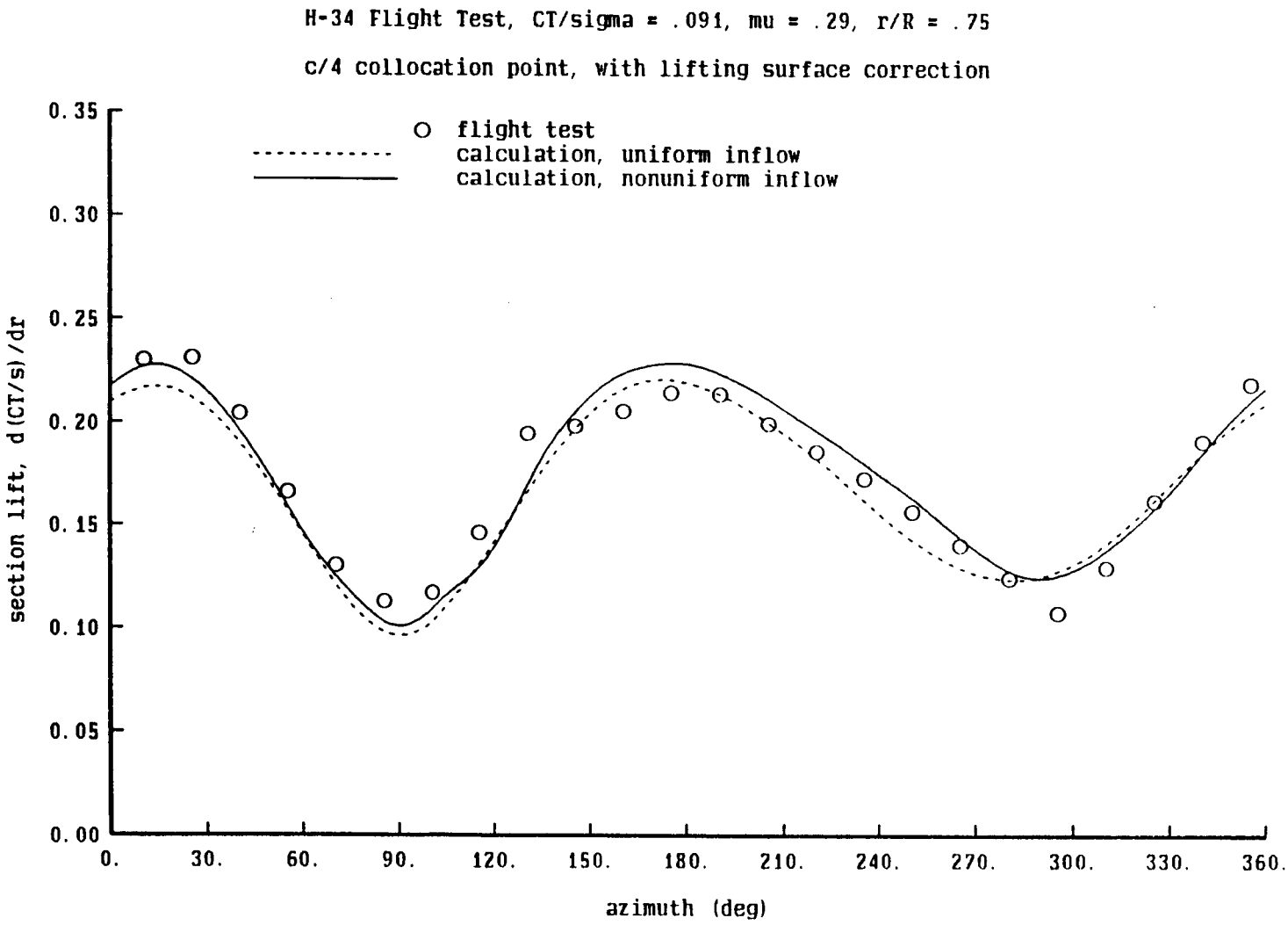

Figure 13-7a. H-34 flight test: influence of near wake model

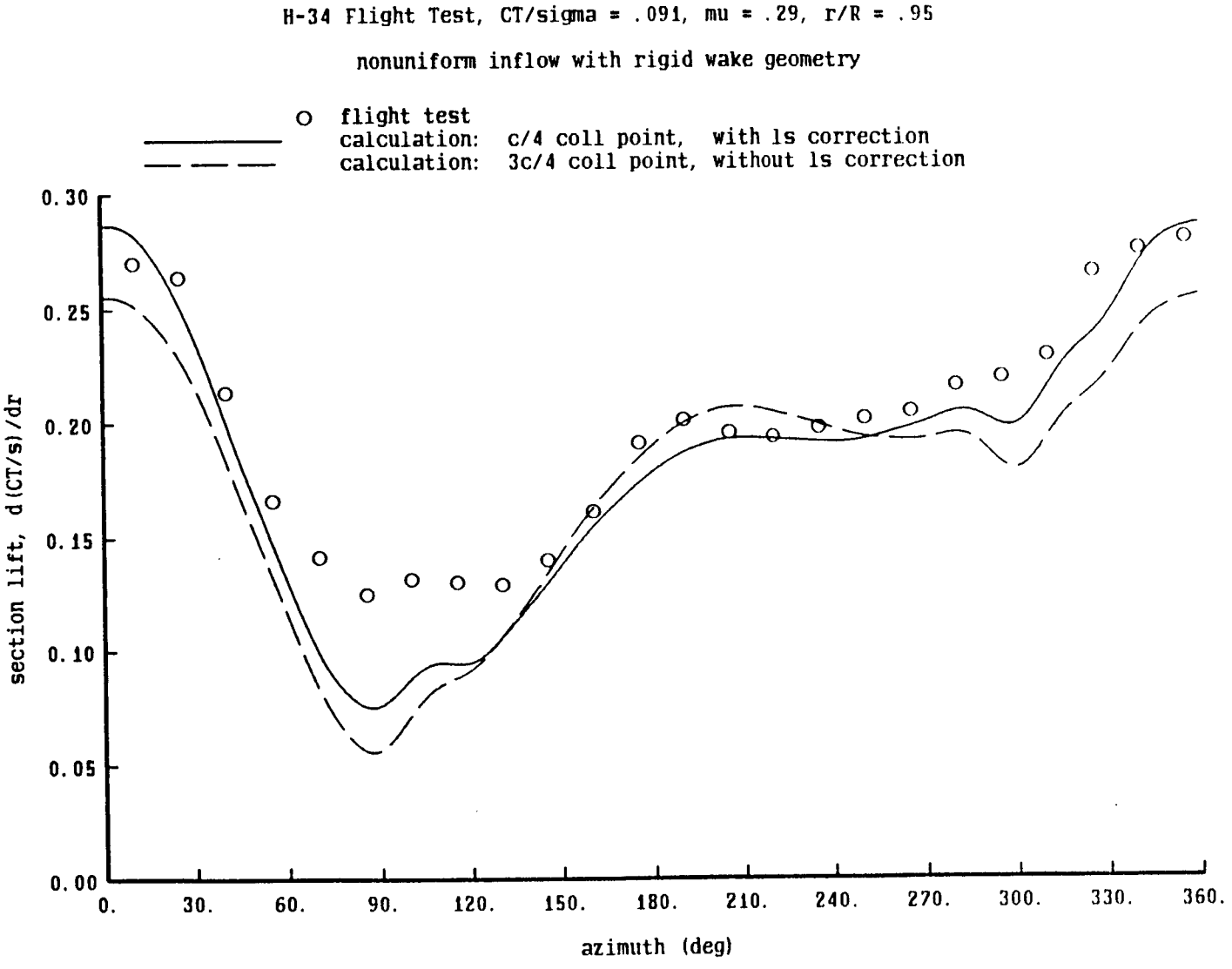

Figure 13-7b. H-34 flight test: influence of near wake model

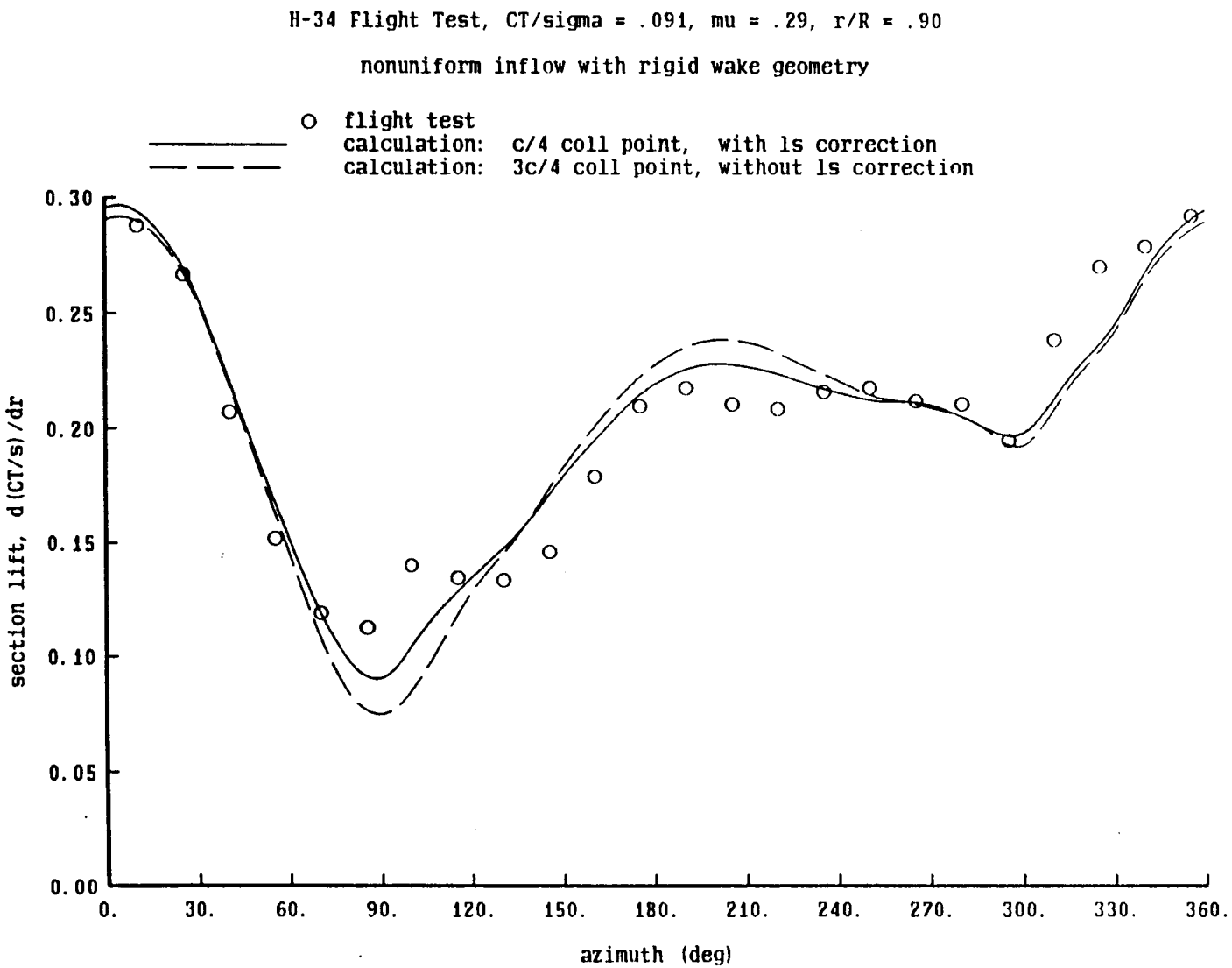

Figure 13-7c. H-34 flight test: influence of near wake model

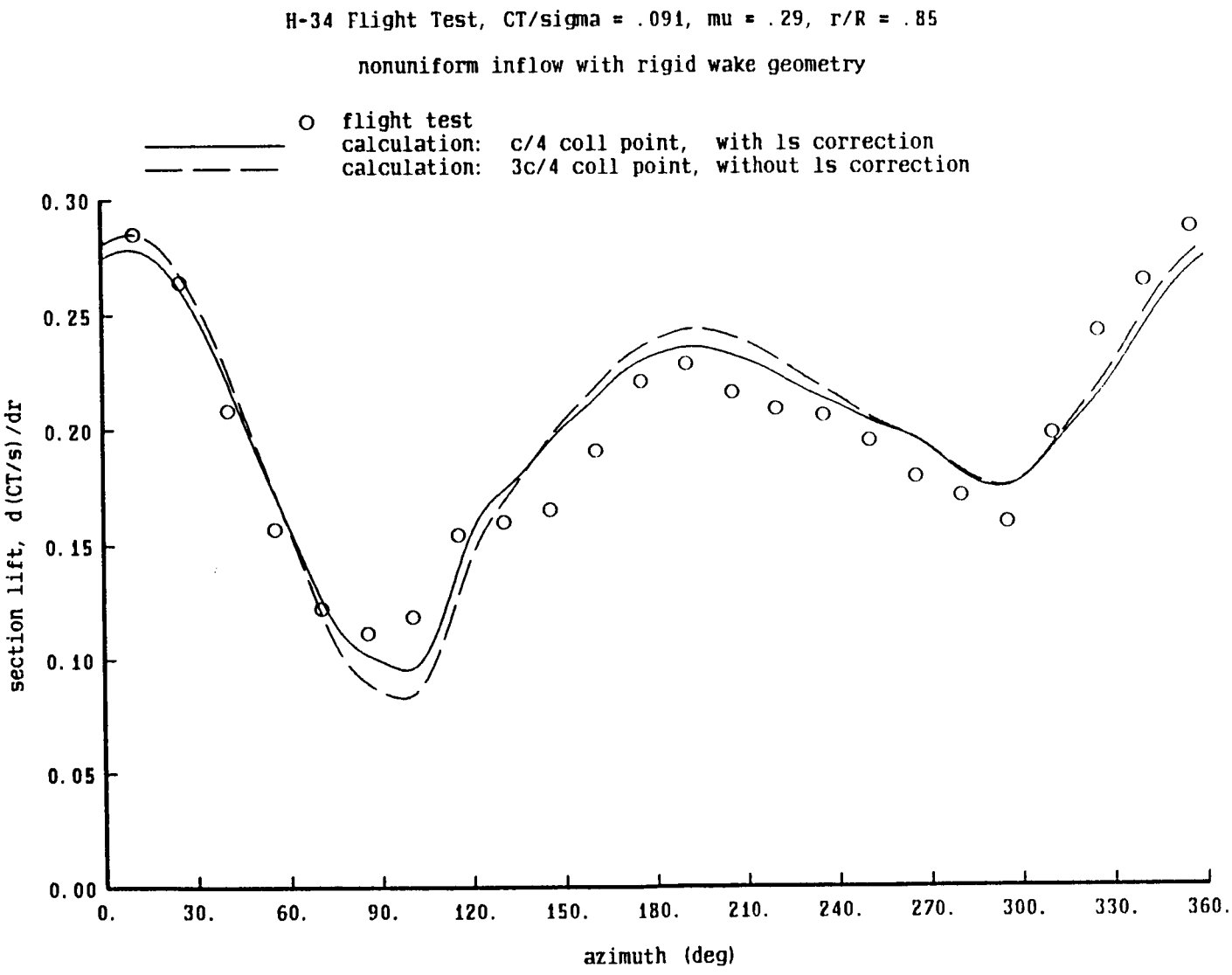

Figure 13-7d. H-34 flight test: influence of near wake model

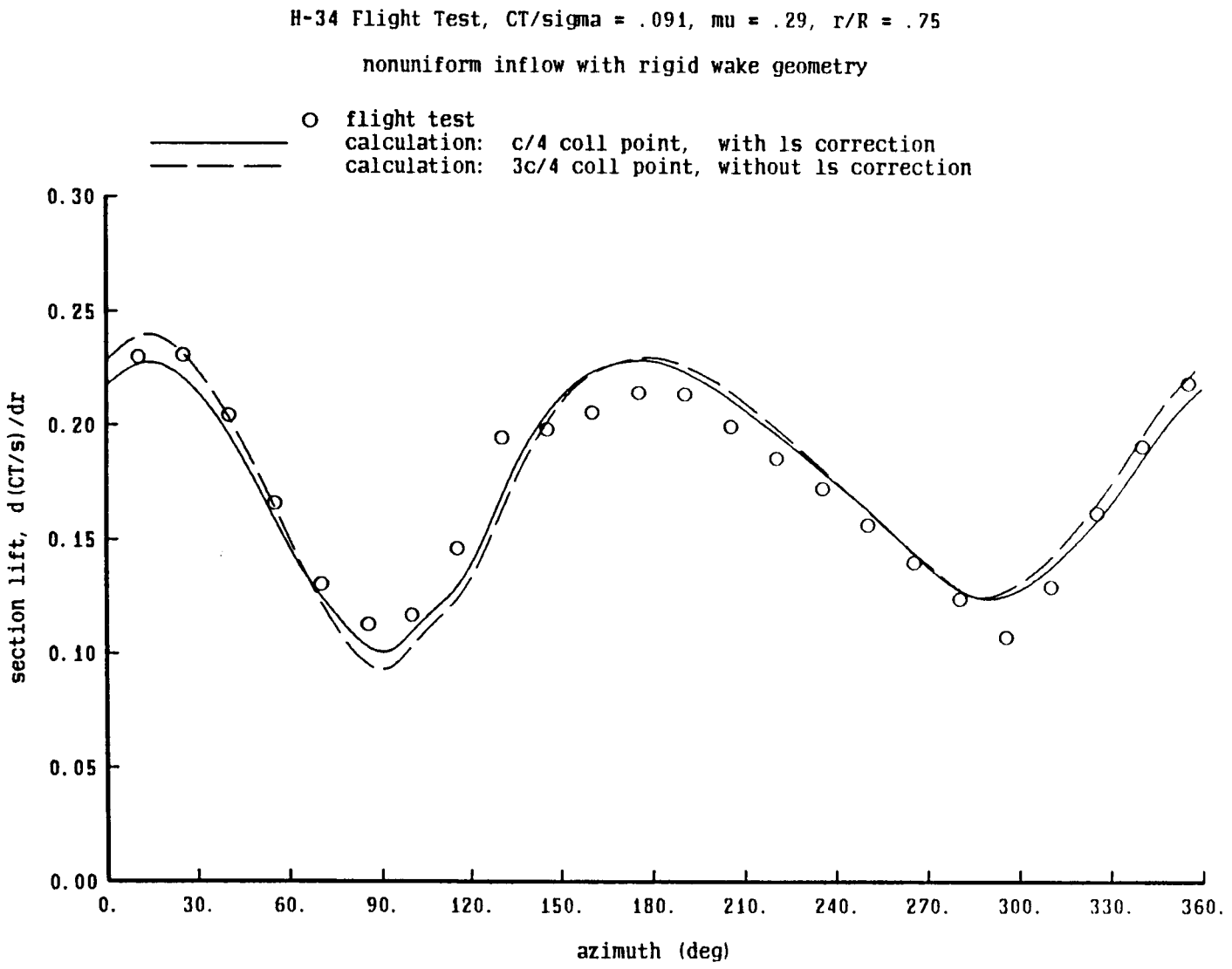

Figure 13-8a. H-34 flight test: influence of blade elastic motion

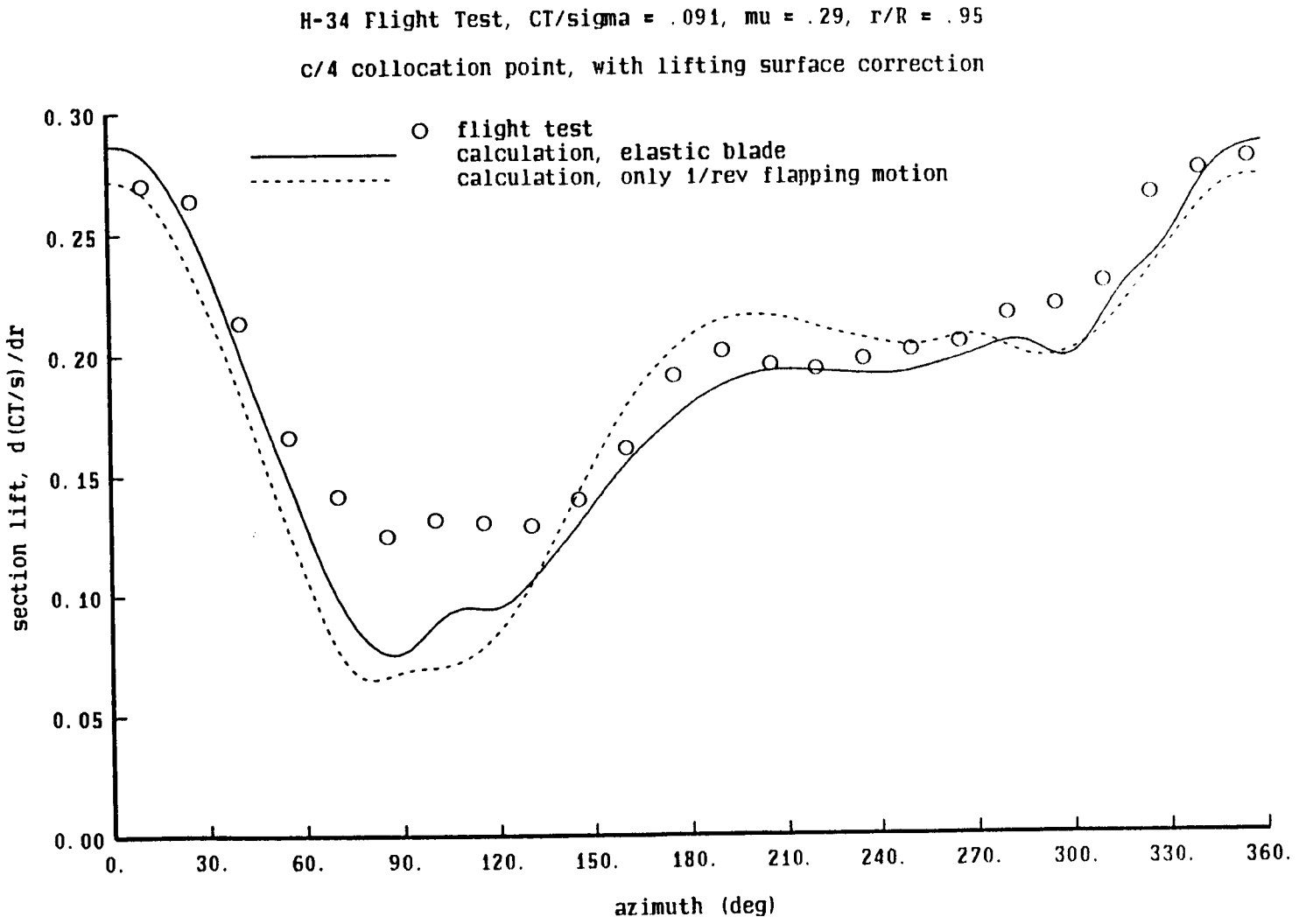

Figure 13-8b. H-34 flight test: influence of blade elastic motion

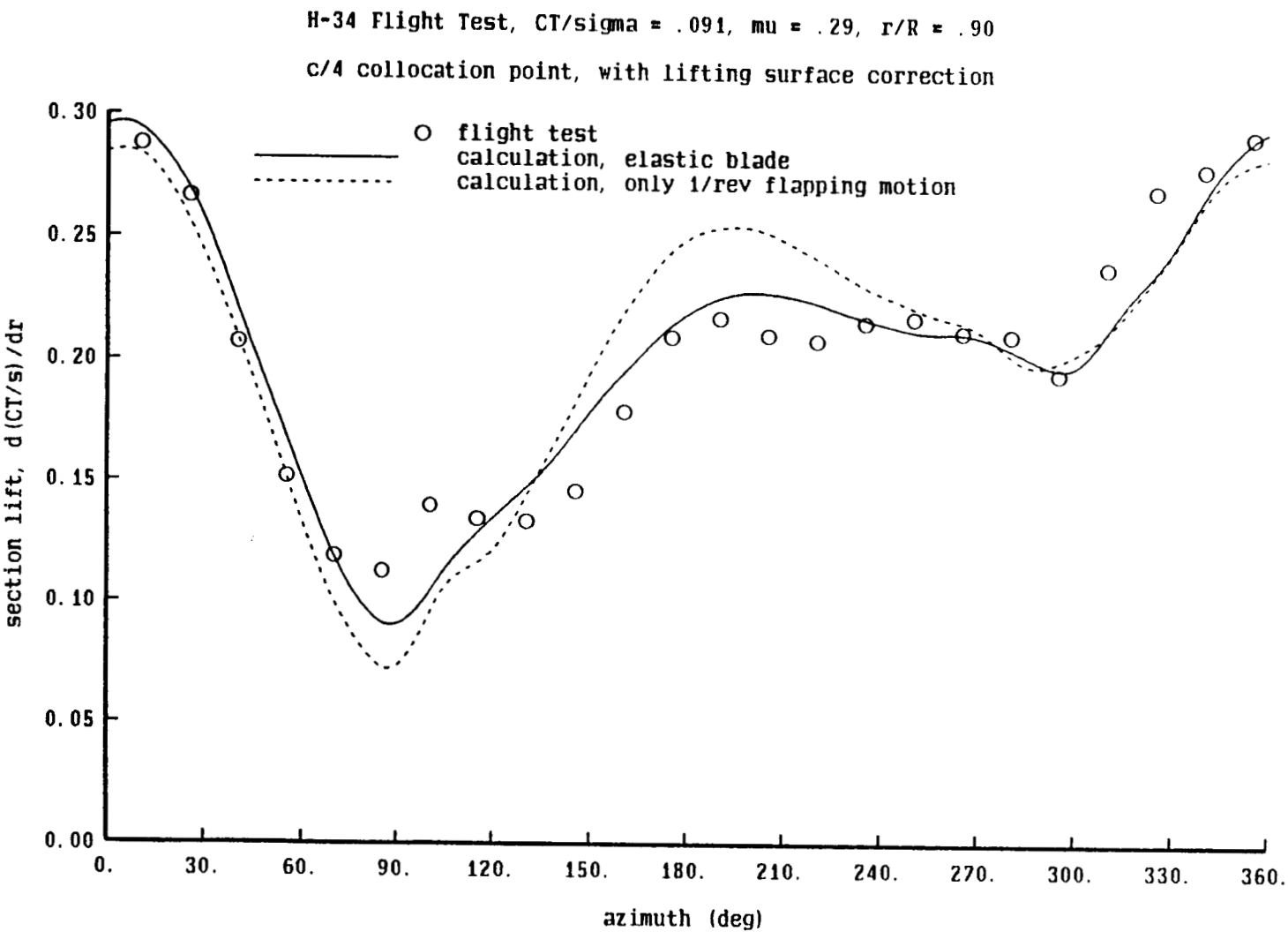

Figure 13-8c. H-34 flight test: influence of blade elastic motion

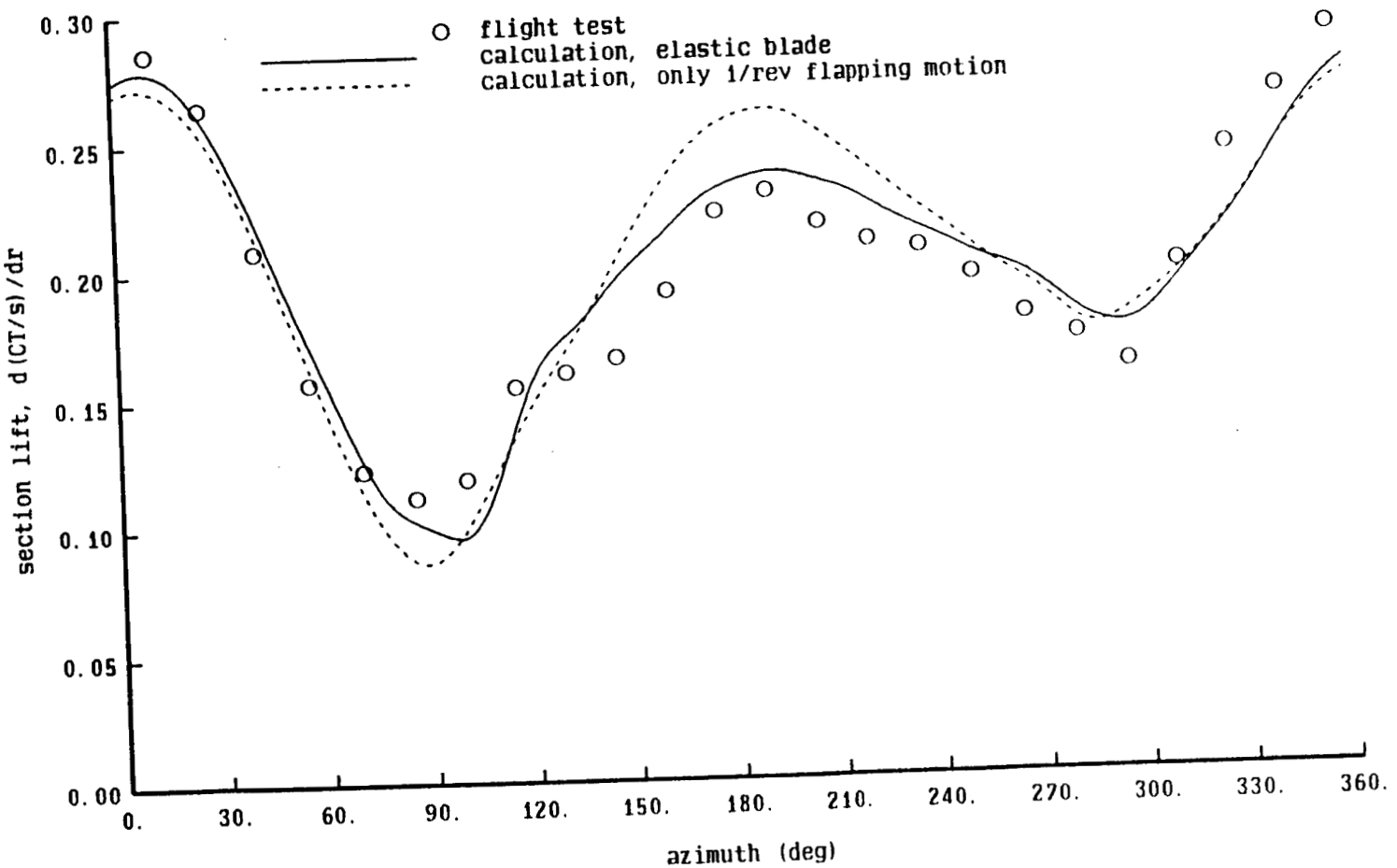

Figure 13-8d. H-34 flight test: influence of blade elastic motion

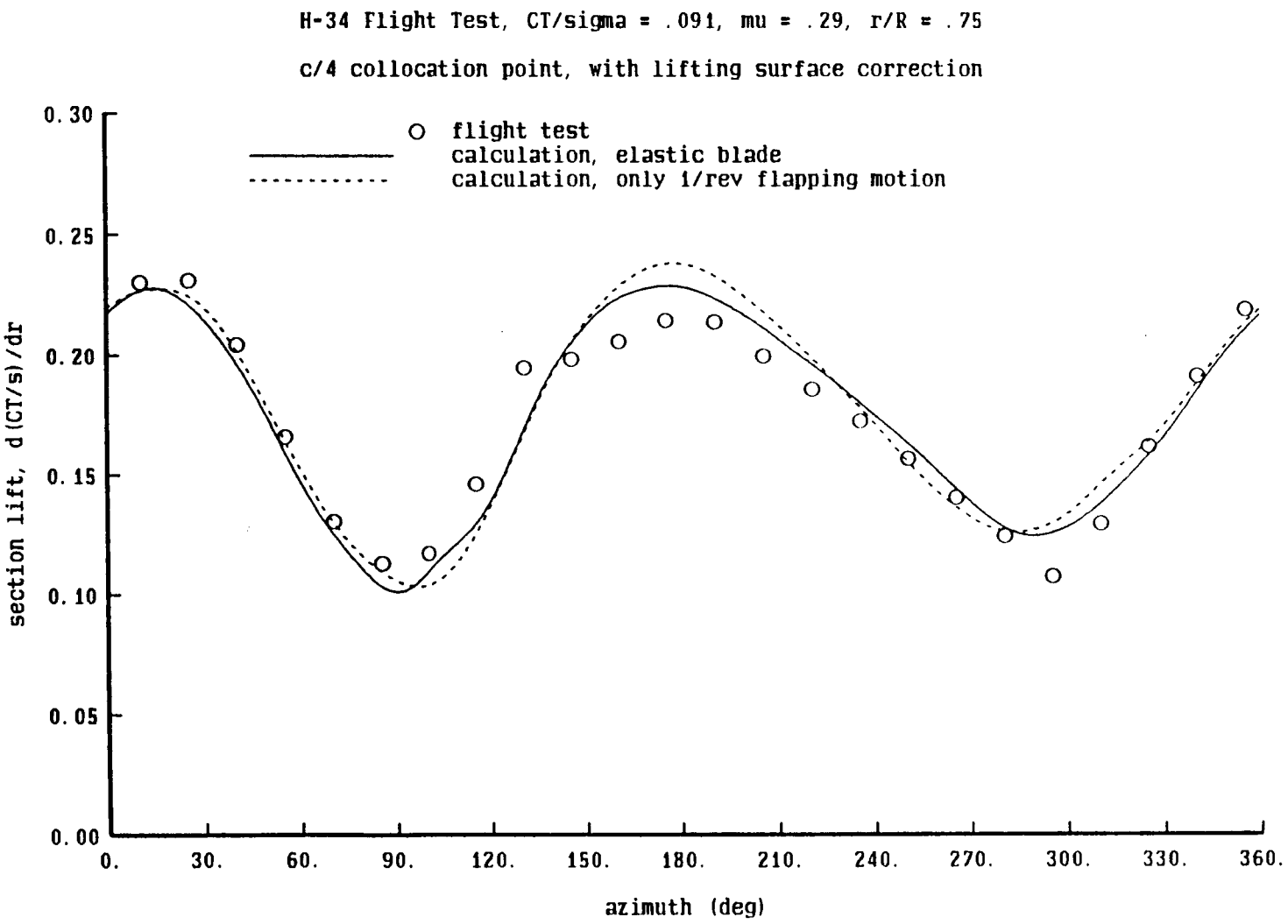

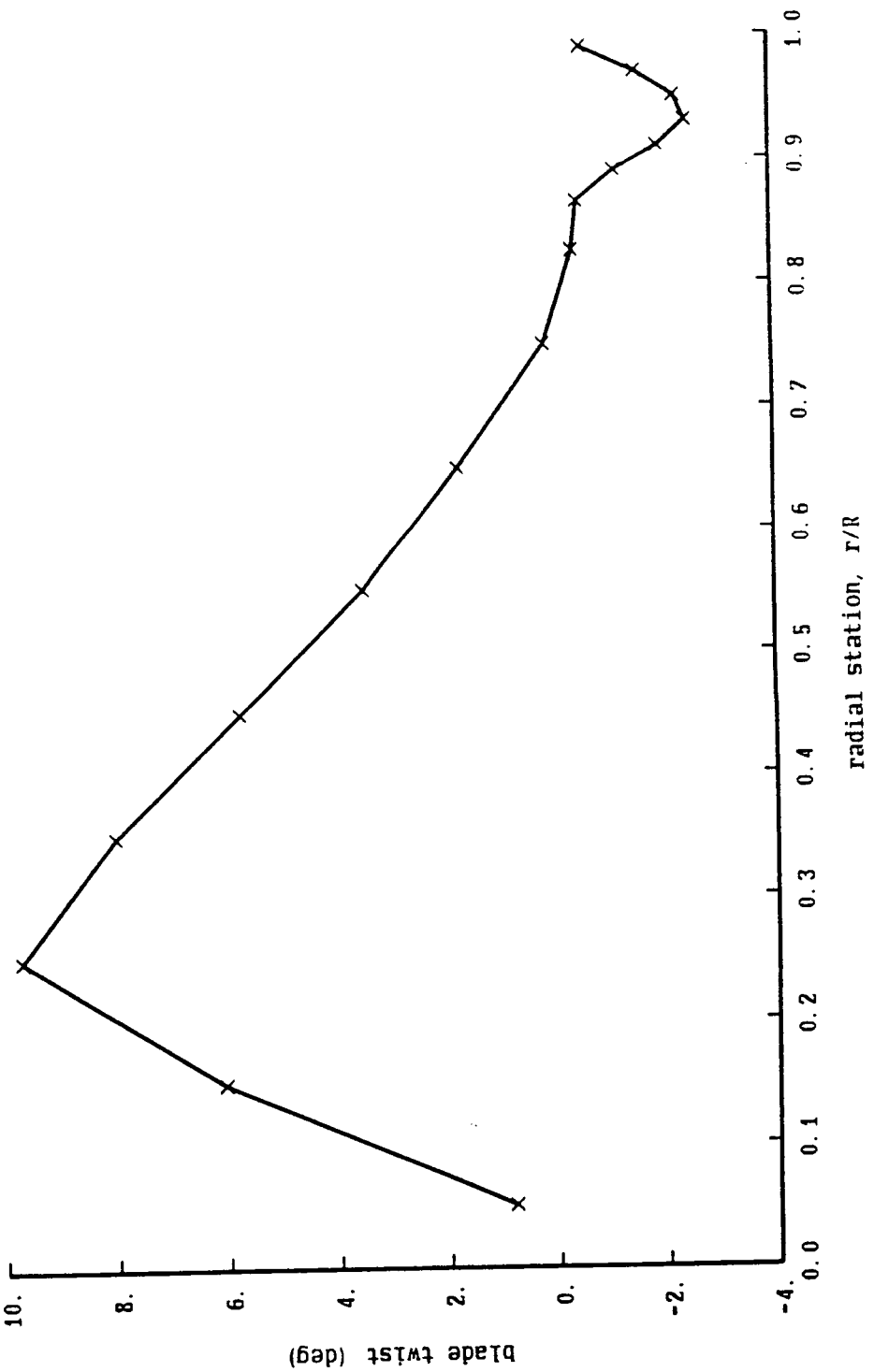

Figure 14-1. UH-60A rotor: blade built-in twist

Figure 14-2a. UH-60A rotor: influence of nonuniform inflow and wake geometry

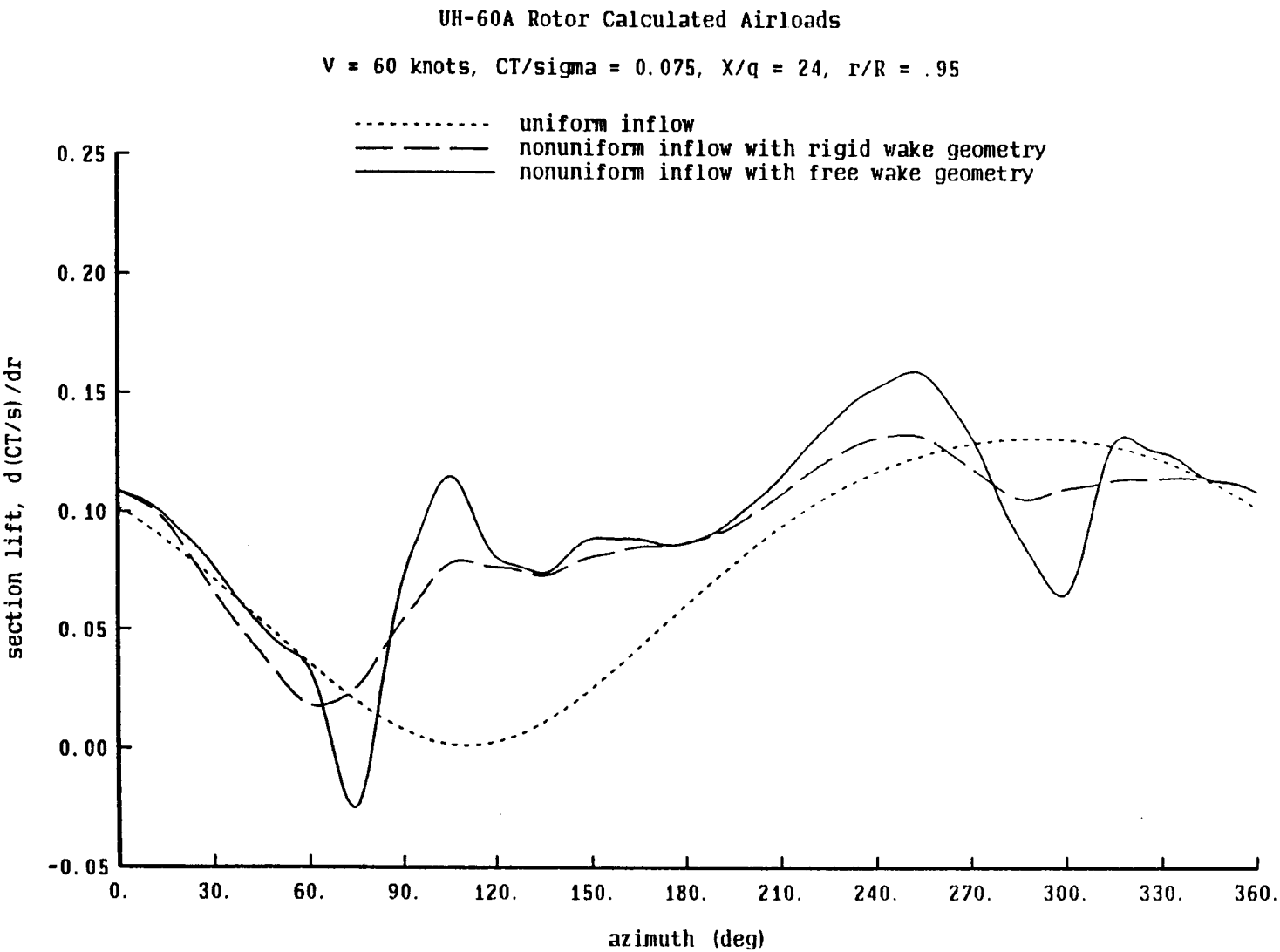

Figure 14-2b. UH-60A rotor: influence of nonuniform inflow and wake geometry

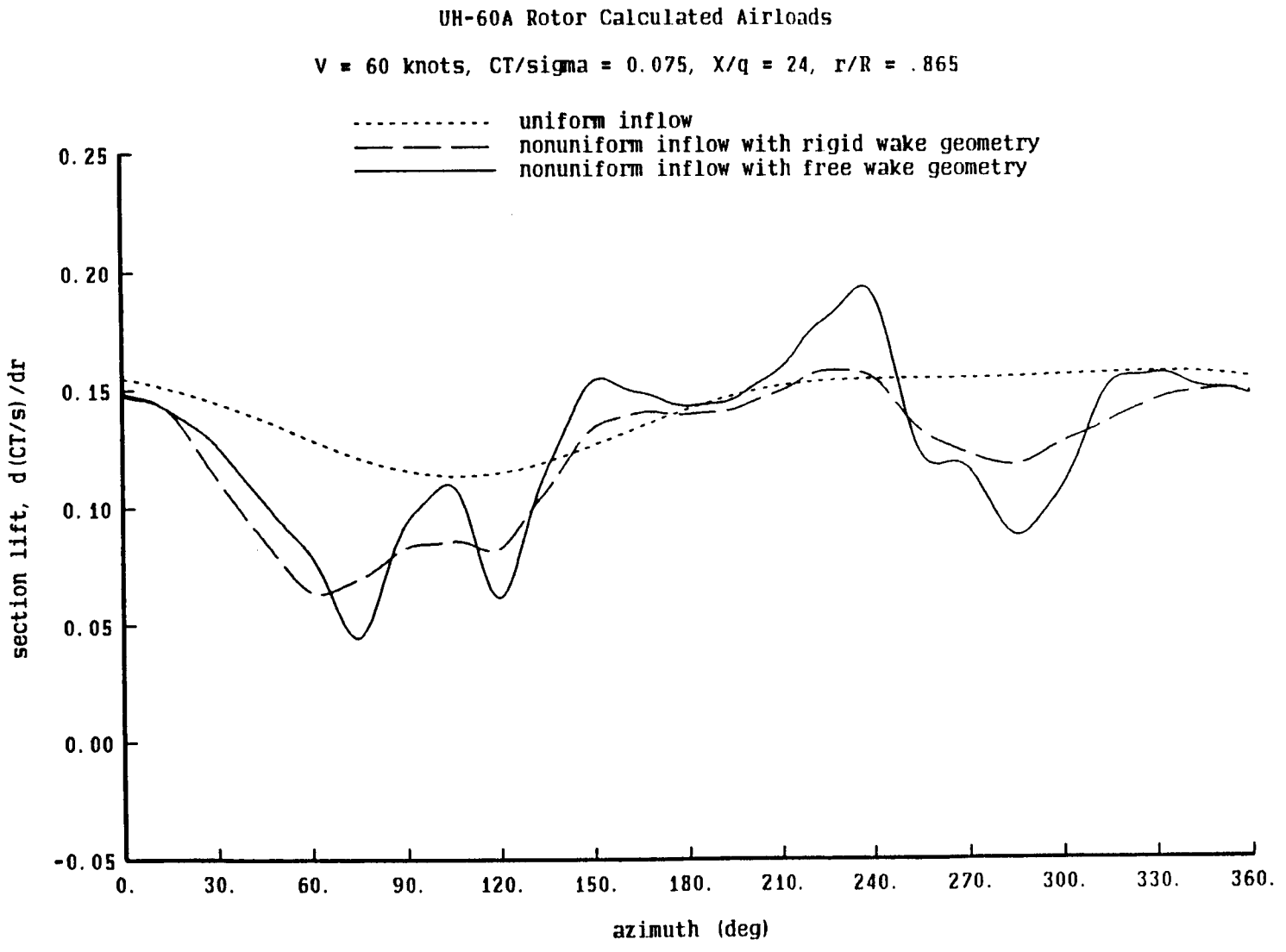

Figure 14-2c. UH-60A rotor: influence of nonuniform inflow and wake geometry

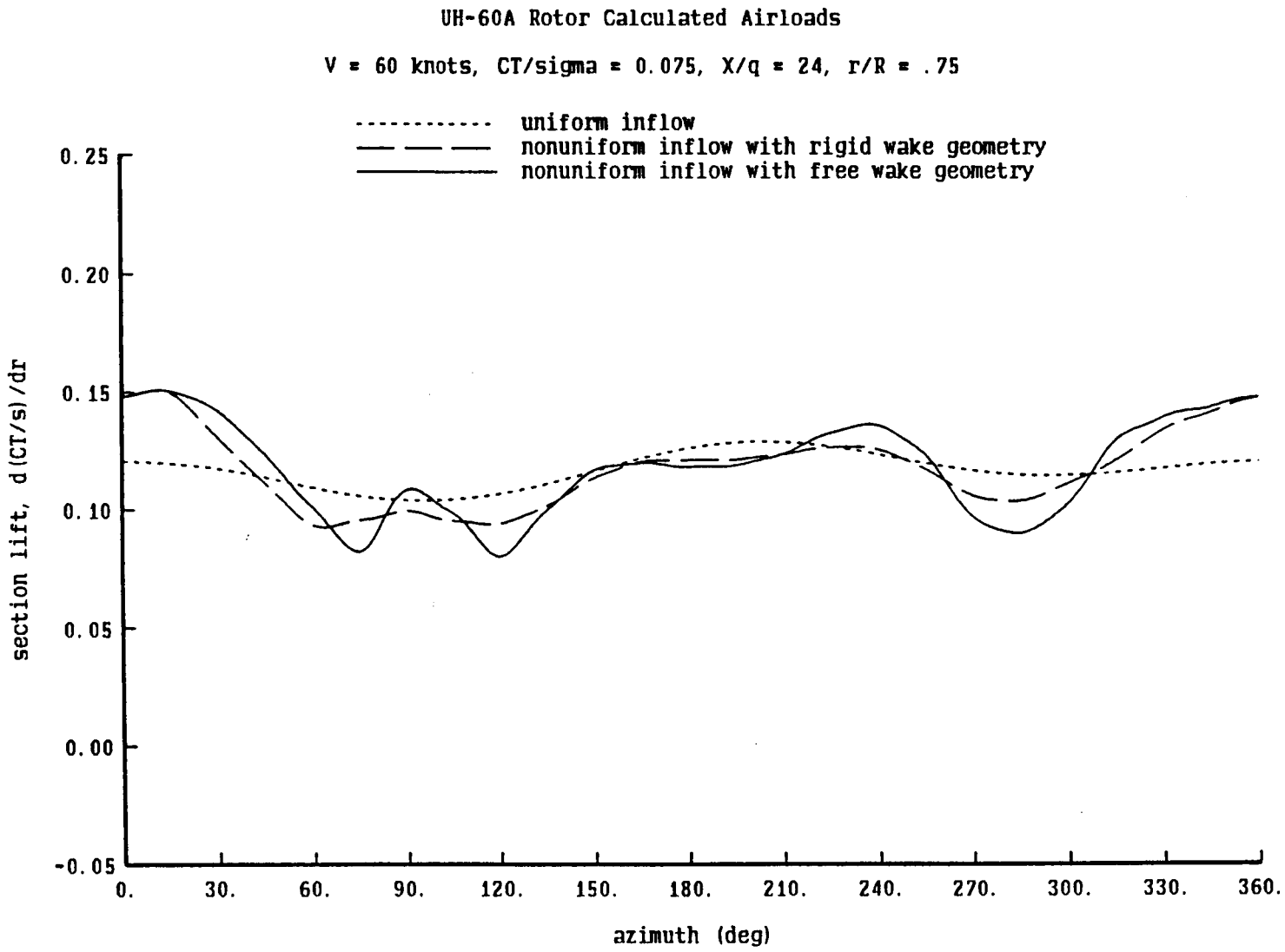

Figure 14-3a. UH-60A rotor: radial circulation distribution

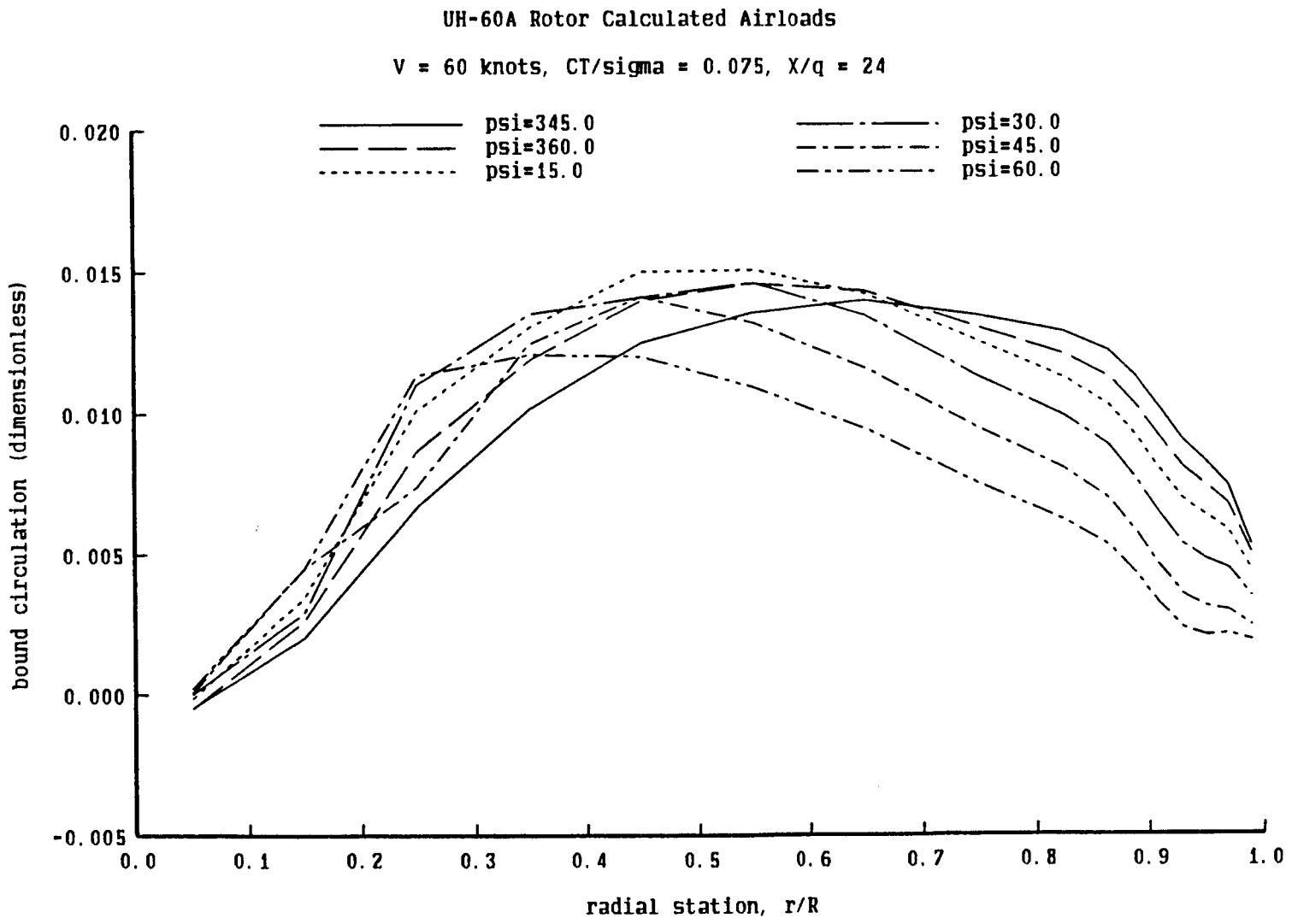

Figure 14-3b. UH-60A rotor: radial circulation distribution

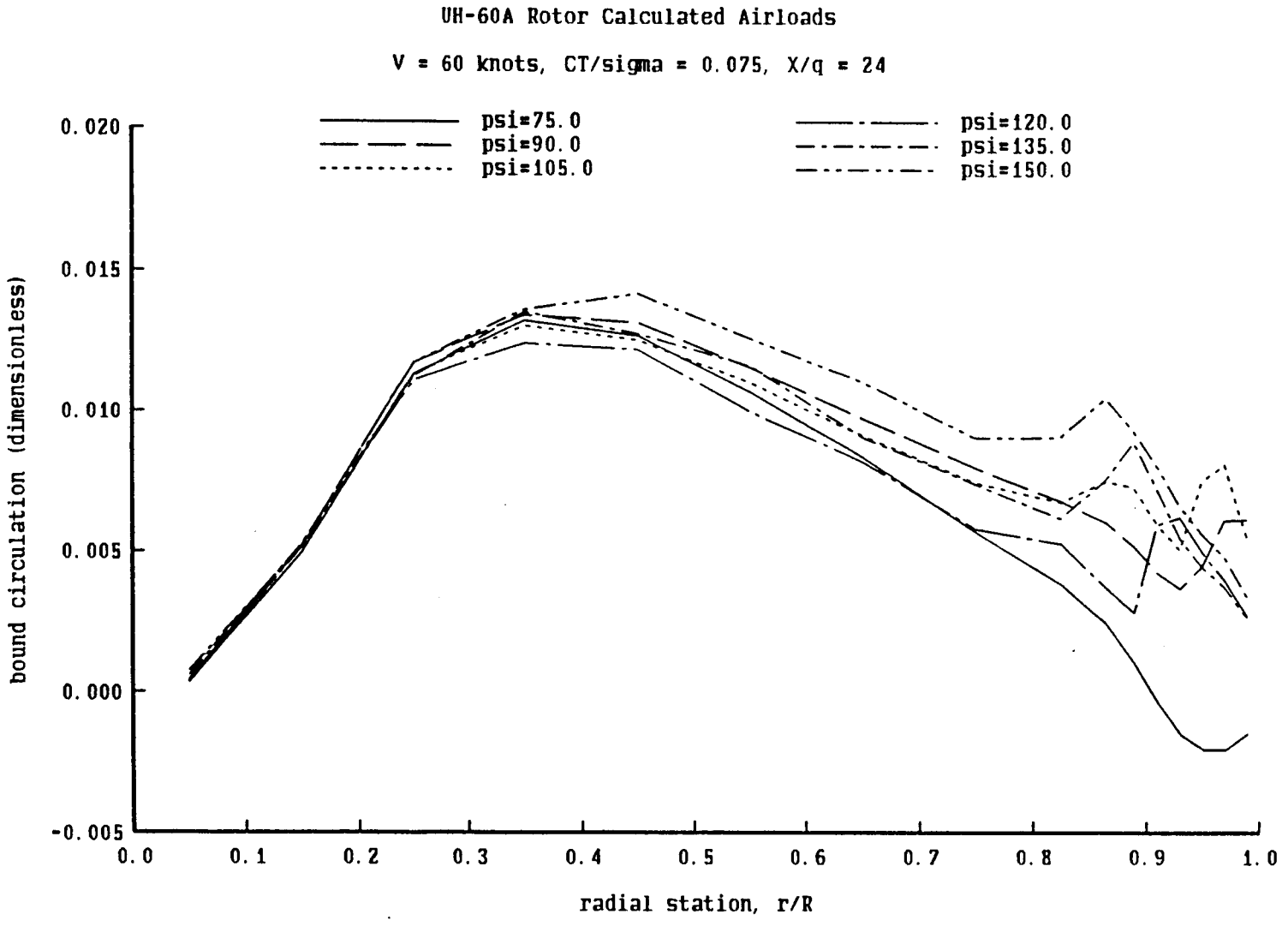

Figure 14-3c. UH-60A rotor: radial circulation distribution

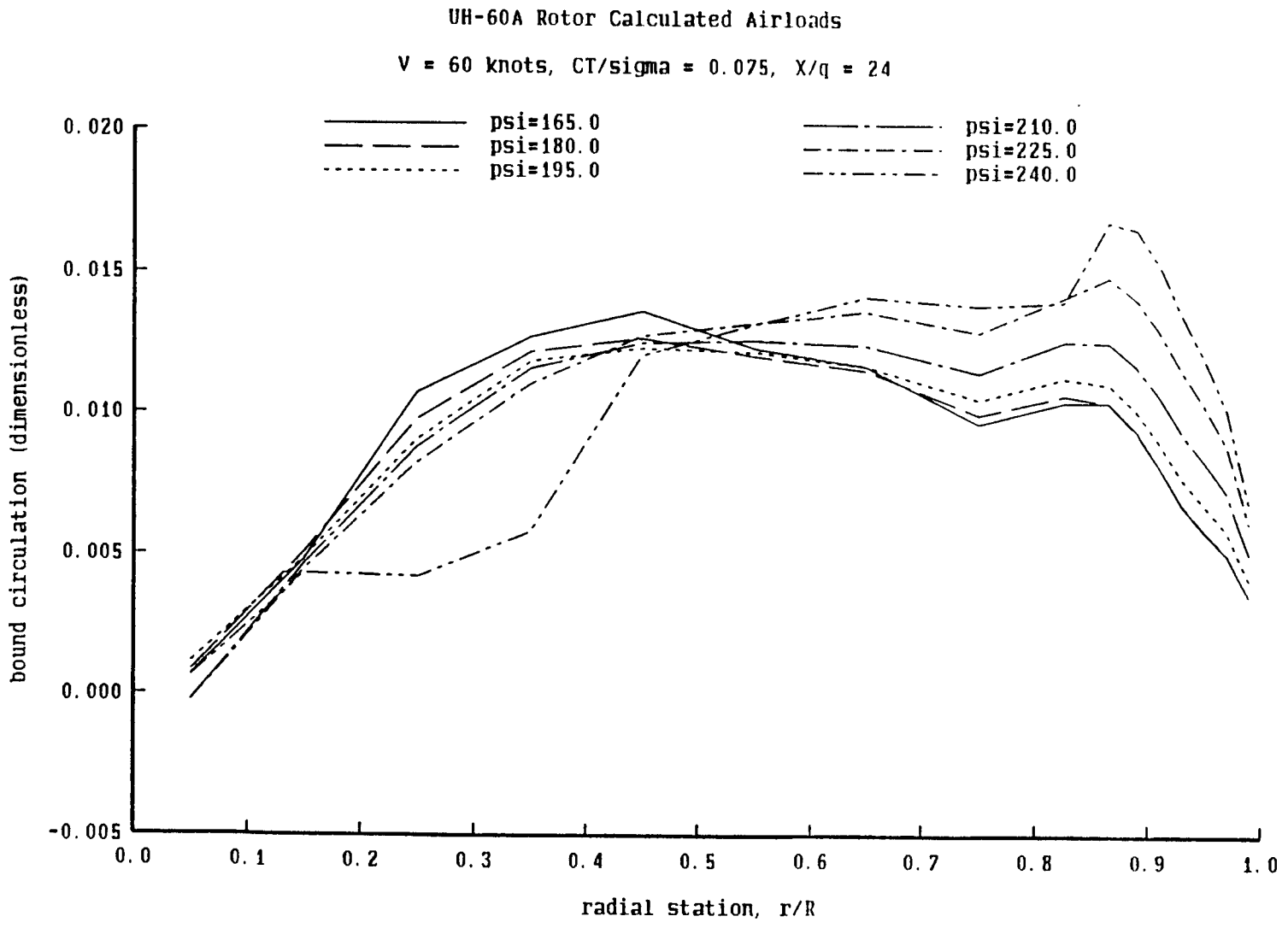

Figure 14-3d. UH-60A rotor: radial circulation distribution

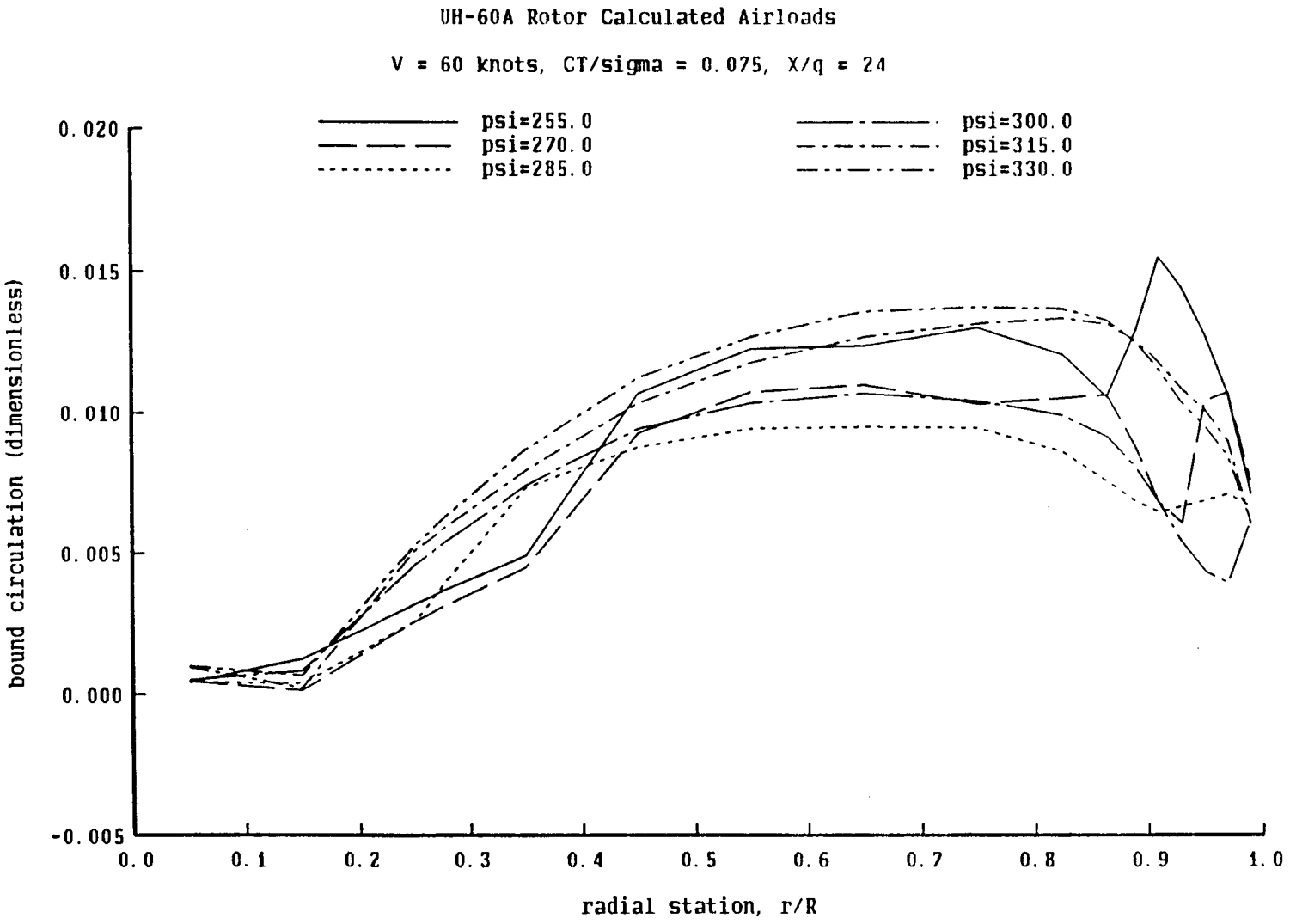

Figure 14-4a. UH-60A rotor: influence of far wake model

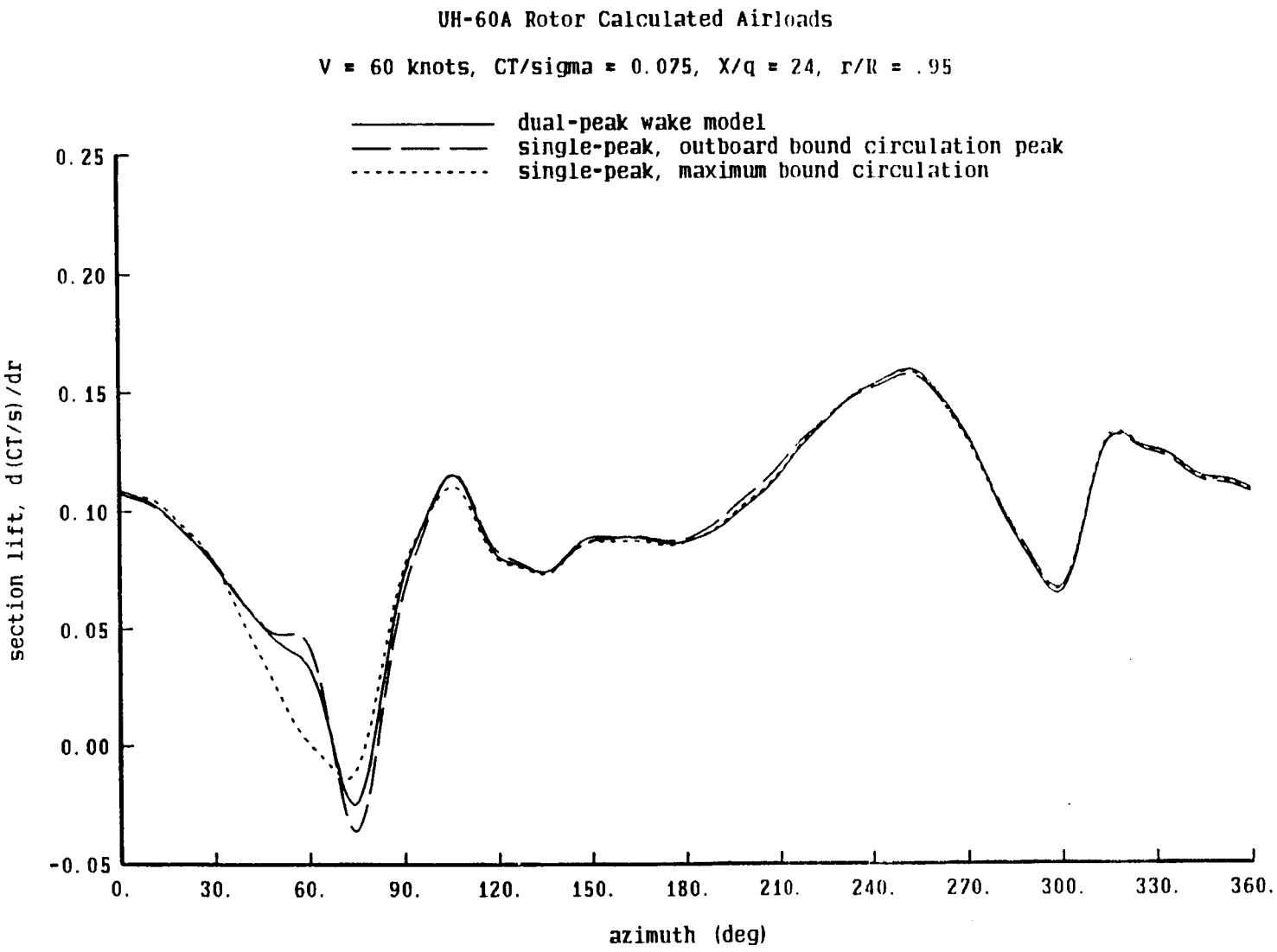

Figure 14-4b. UH-60A rotor: influence of far wake model

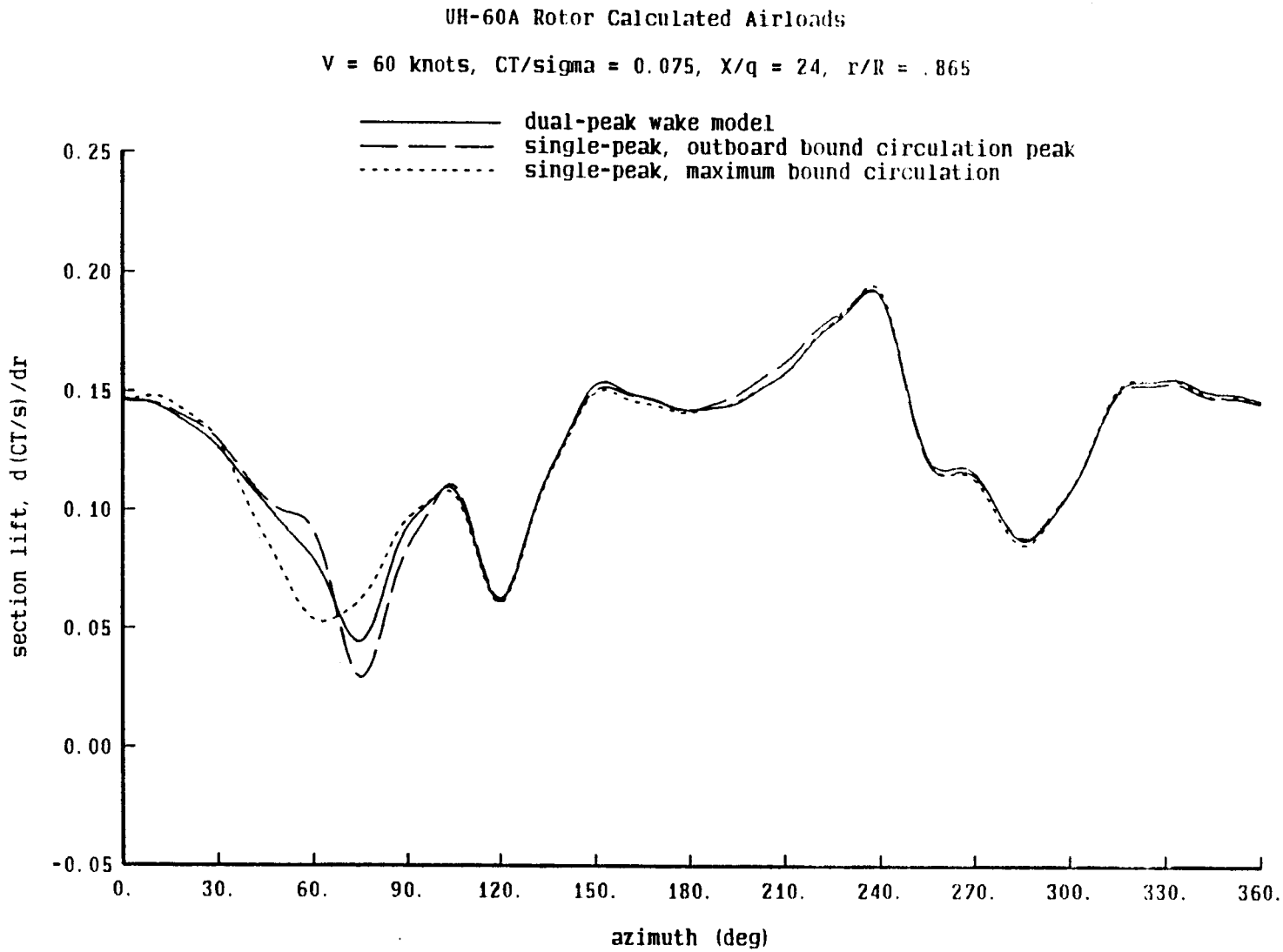

Figure 14-4c. UH-60A rotor: influence of far wake model

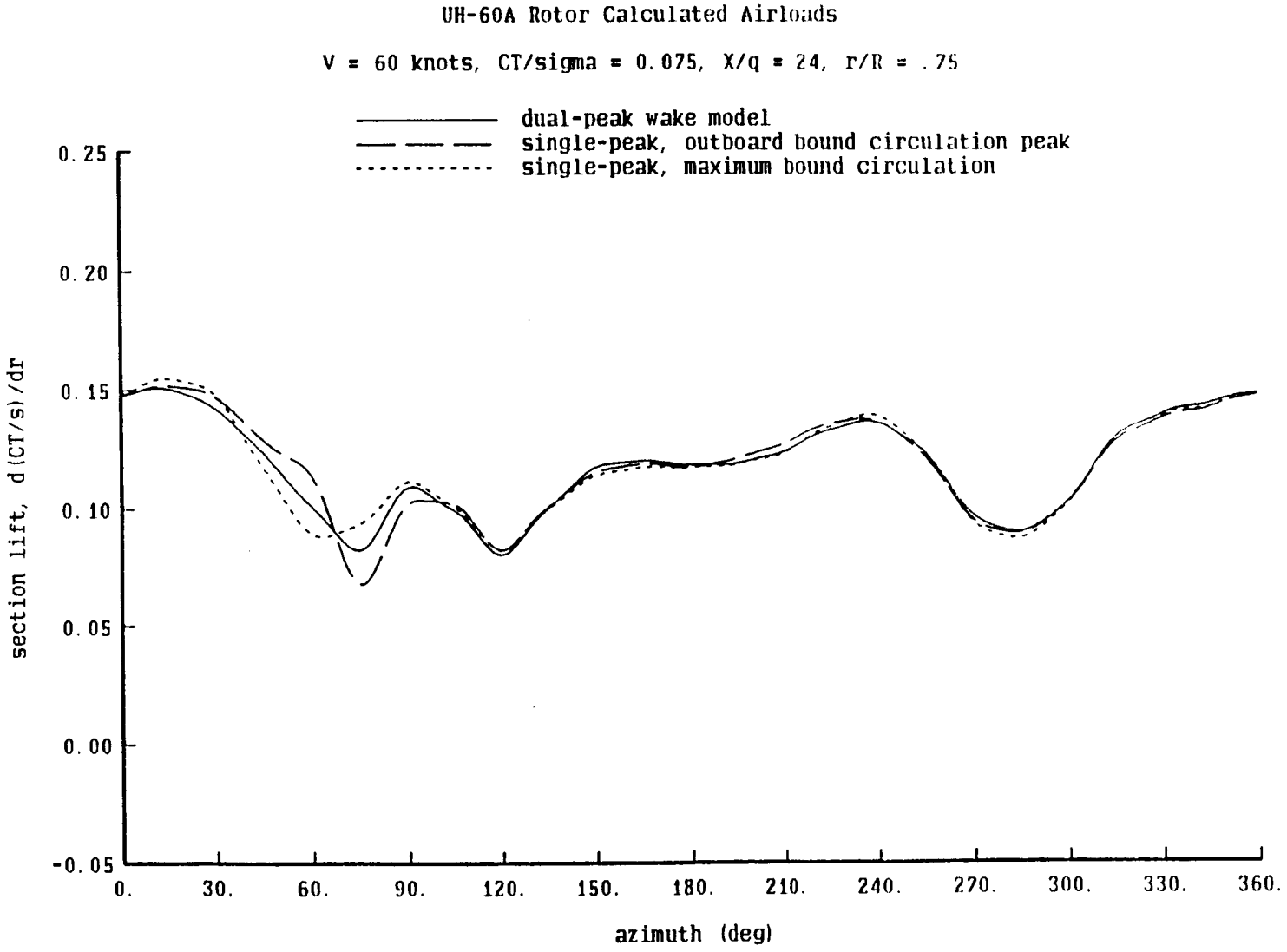

Figure 14-5a. UH-60A rotor: influence of blade motion

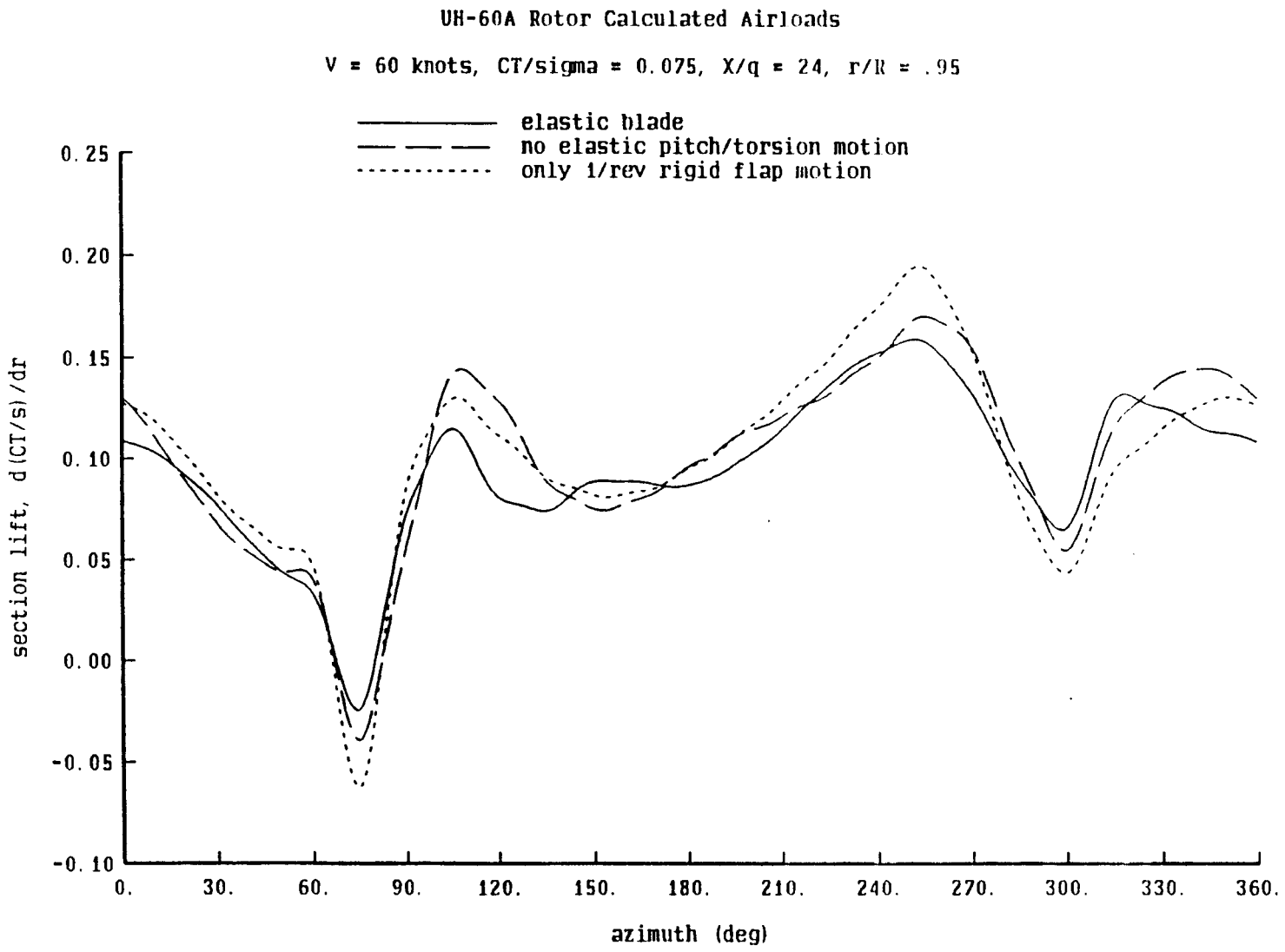

Figure 14-5b. UH-60A rotor: influence of blade motion

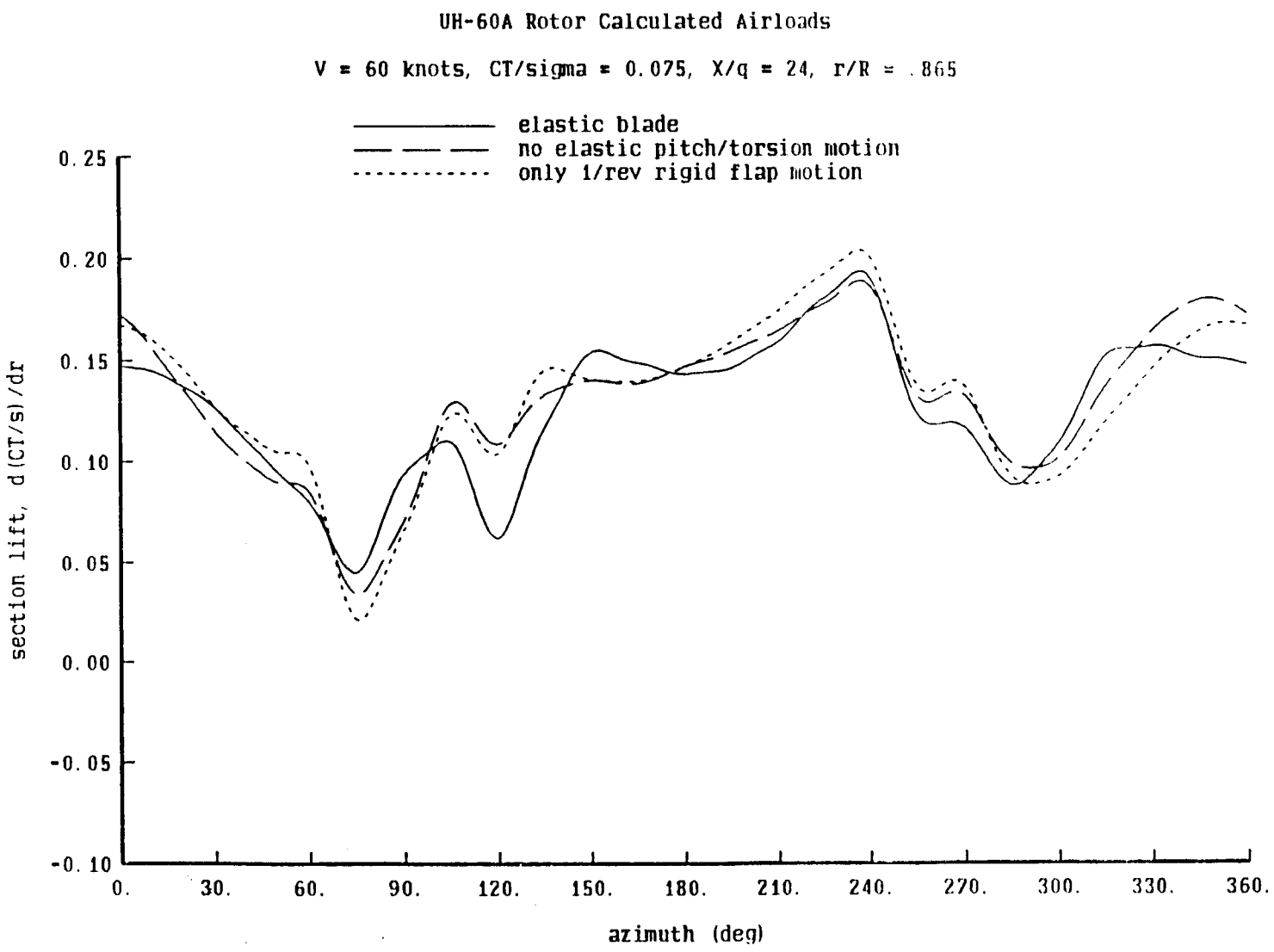

Figure 14-5c. UH-60A rotor: influence of blade motion

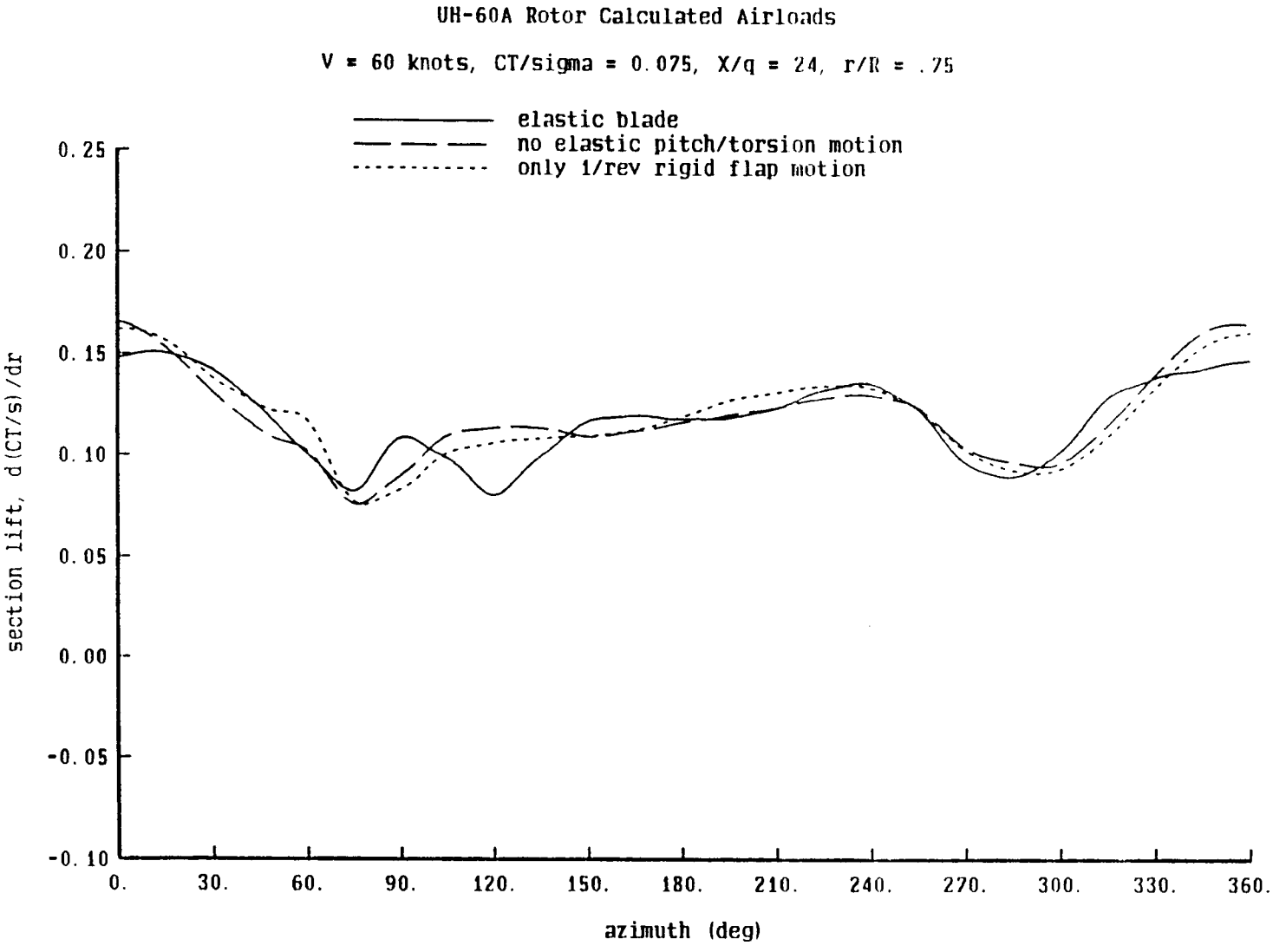

Figure 14-6a. UH-60A rotor: influence of swept tip aerodynamics model

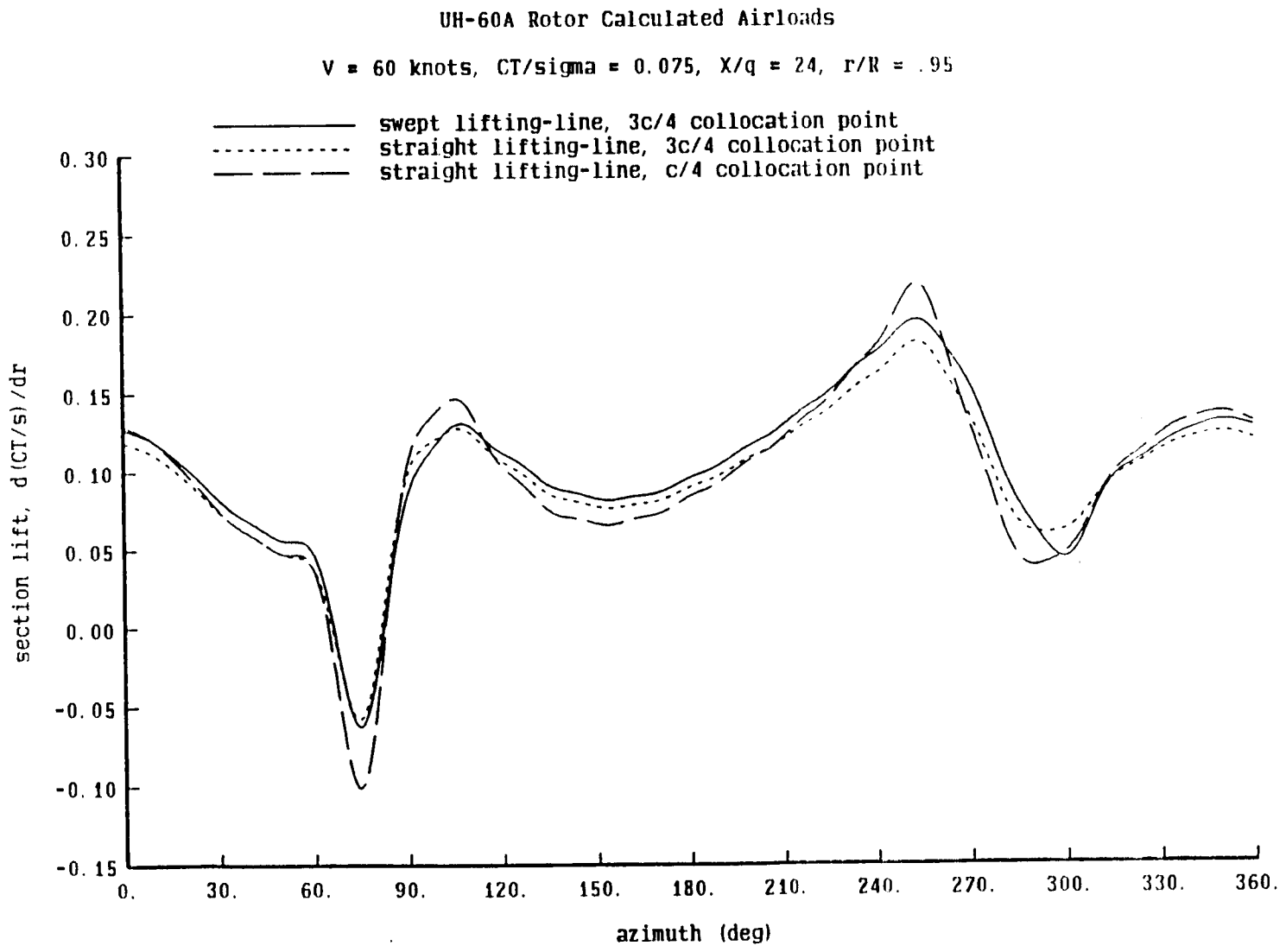

Figure 14-6b. UH-60A rotor: influence of swept tip aerodynamics model

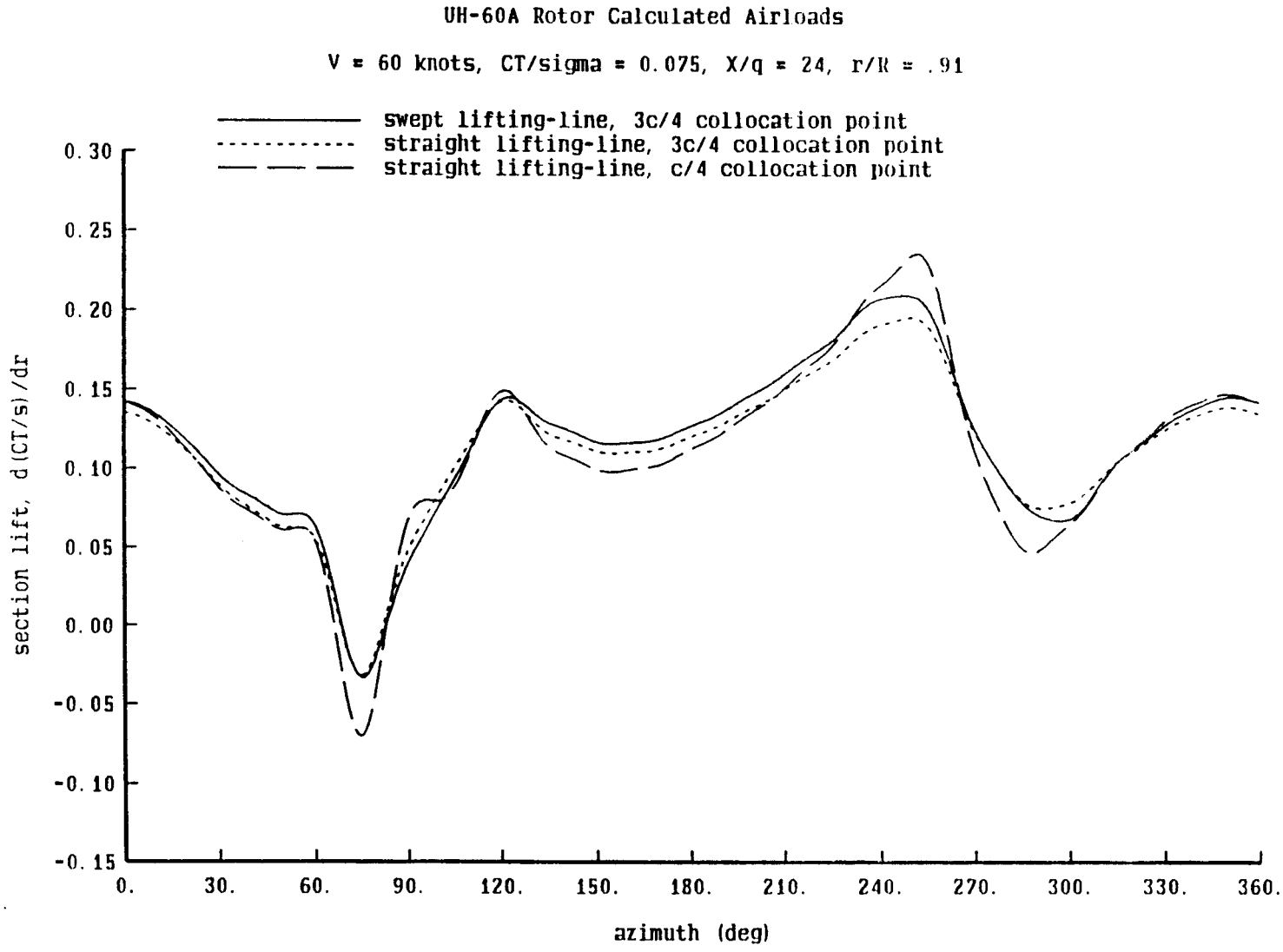

Figure 14-7a. UH-60A rotor: influence of nonuniform inflow

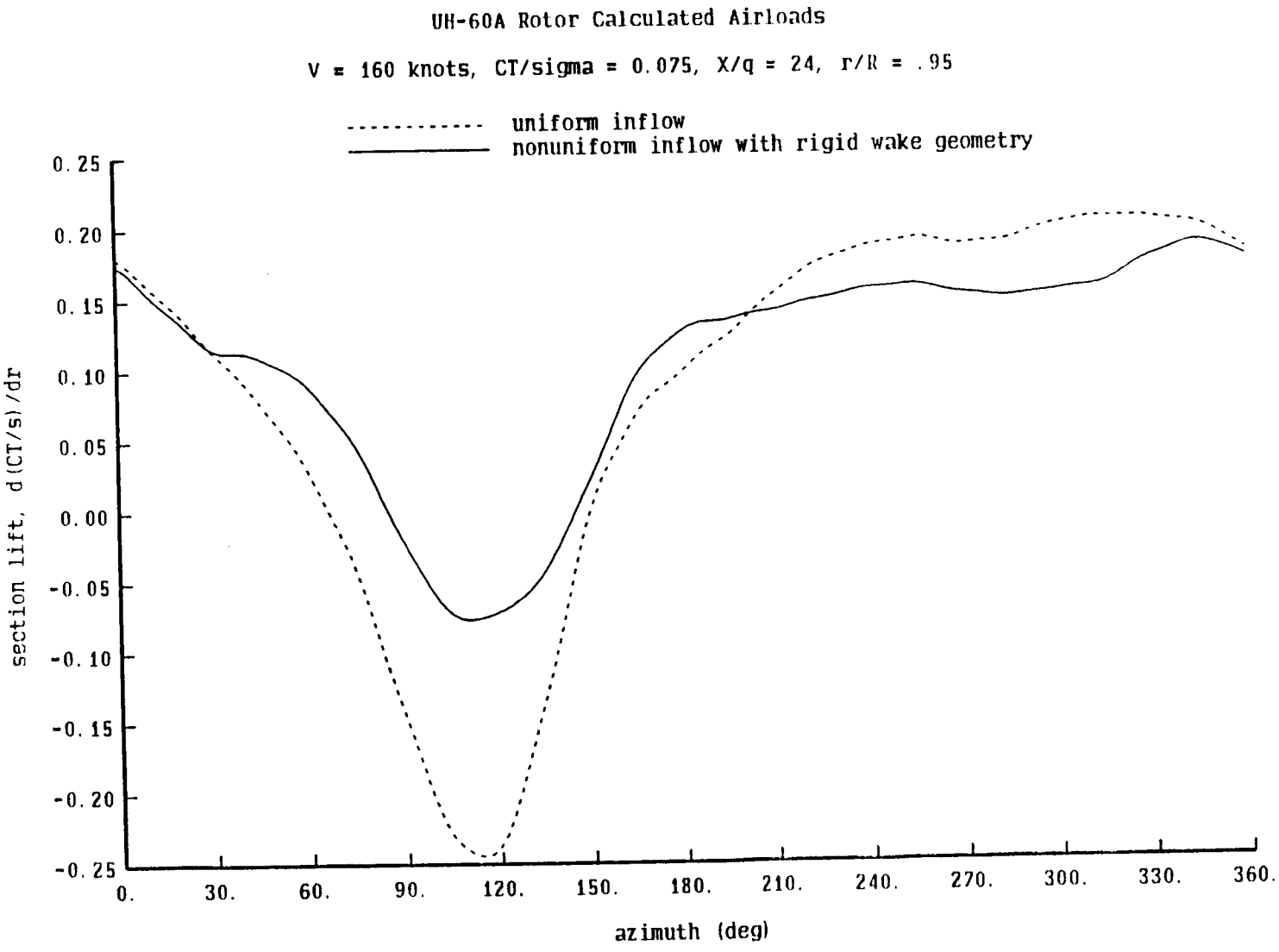

Figure 14-7b. UH-60A rotor: influence of nonuniform inflow

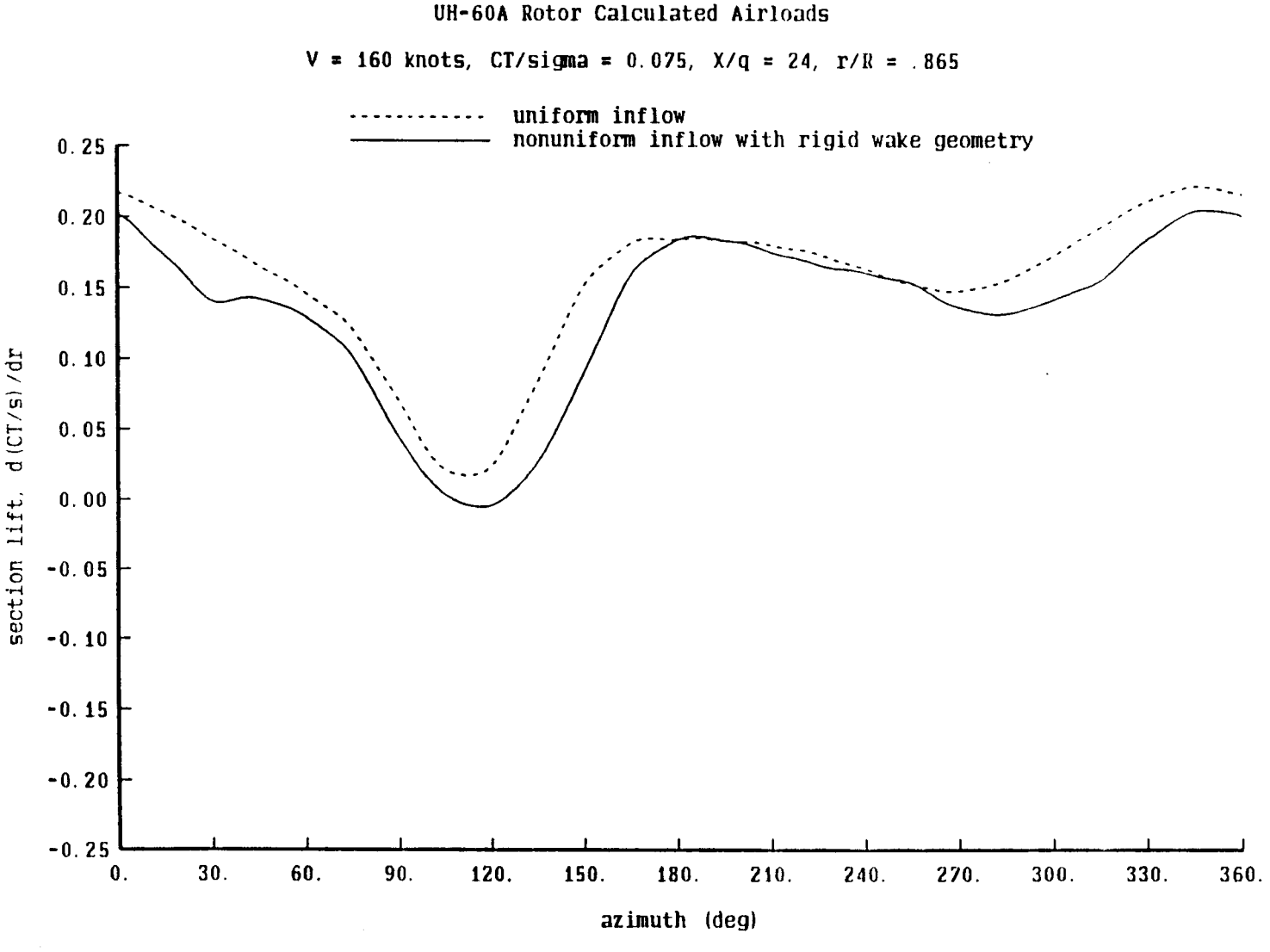

Figure 14-7c. UH-60A rotor: influence of nonuniform inflow

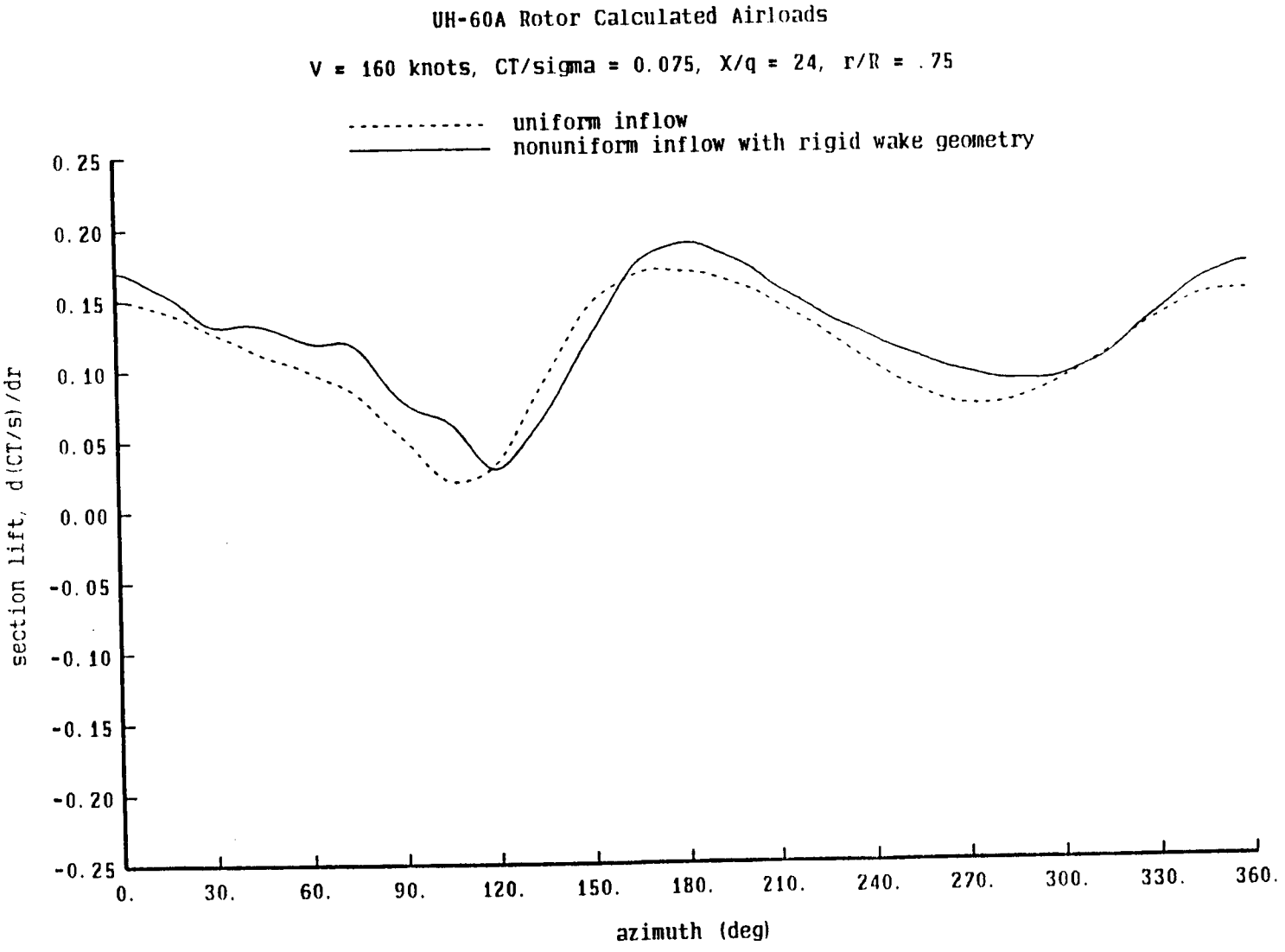

Figure 14-8a. UH-60A rotor: radial circulation distribution

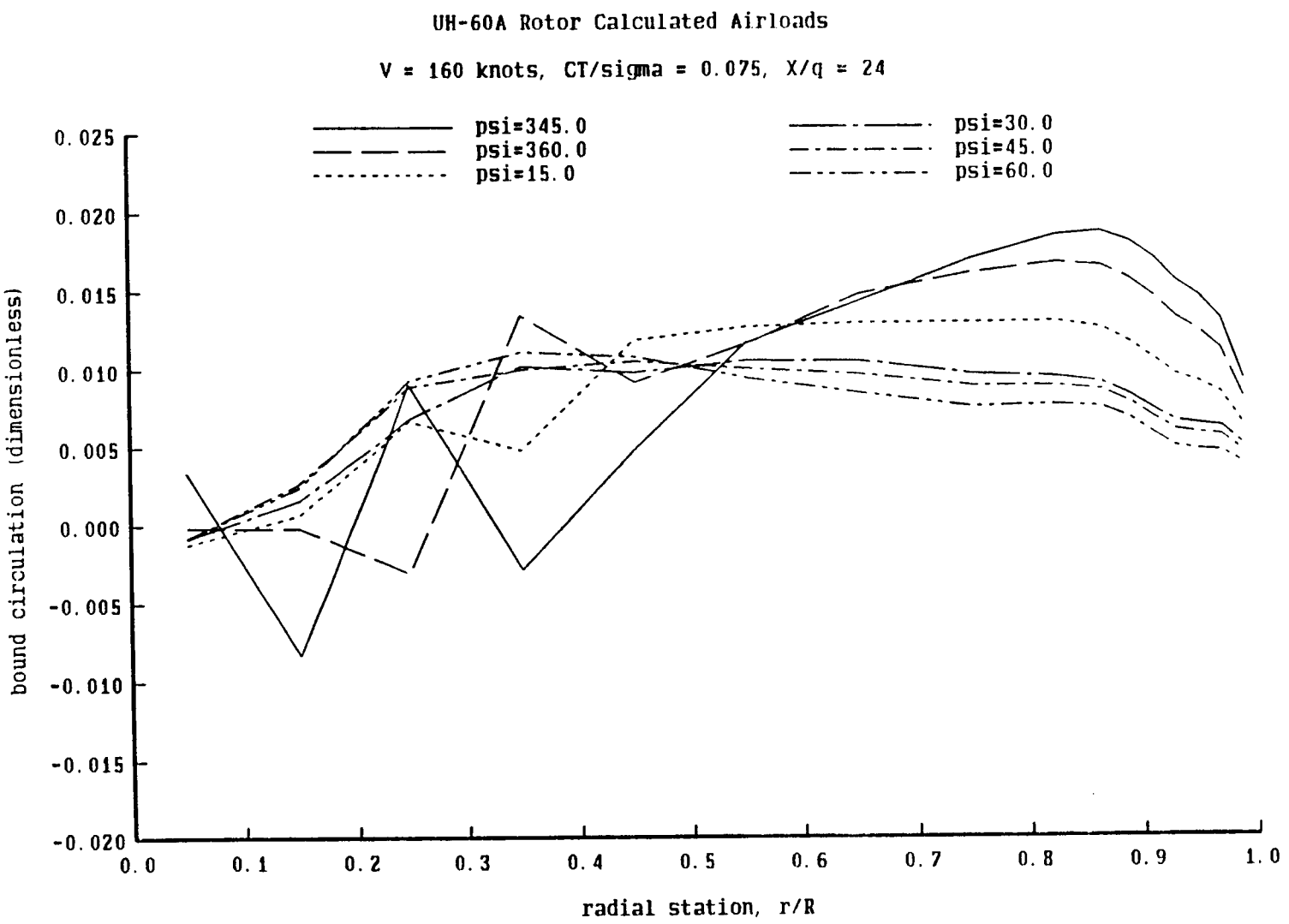

Figure 14-8b. UH-60A rotor: radial circulation distribution

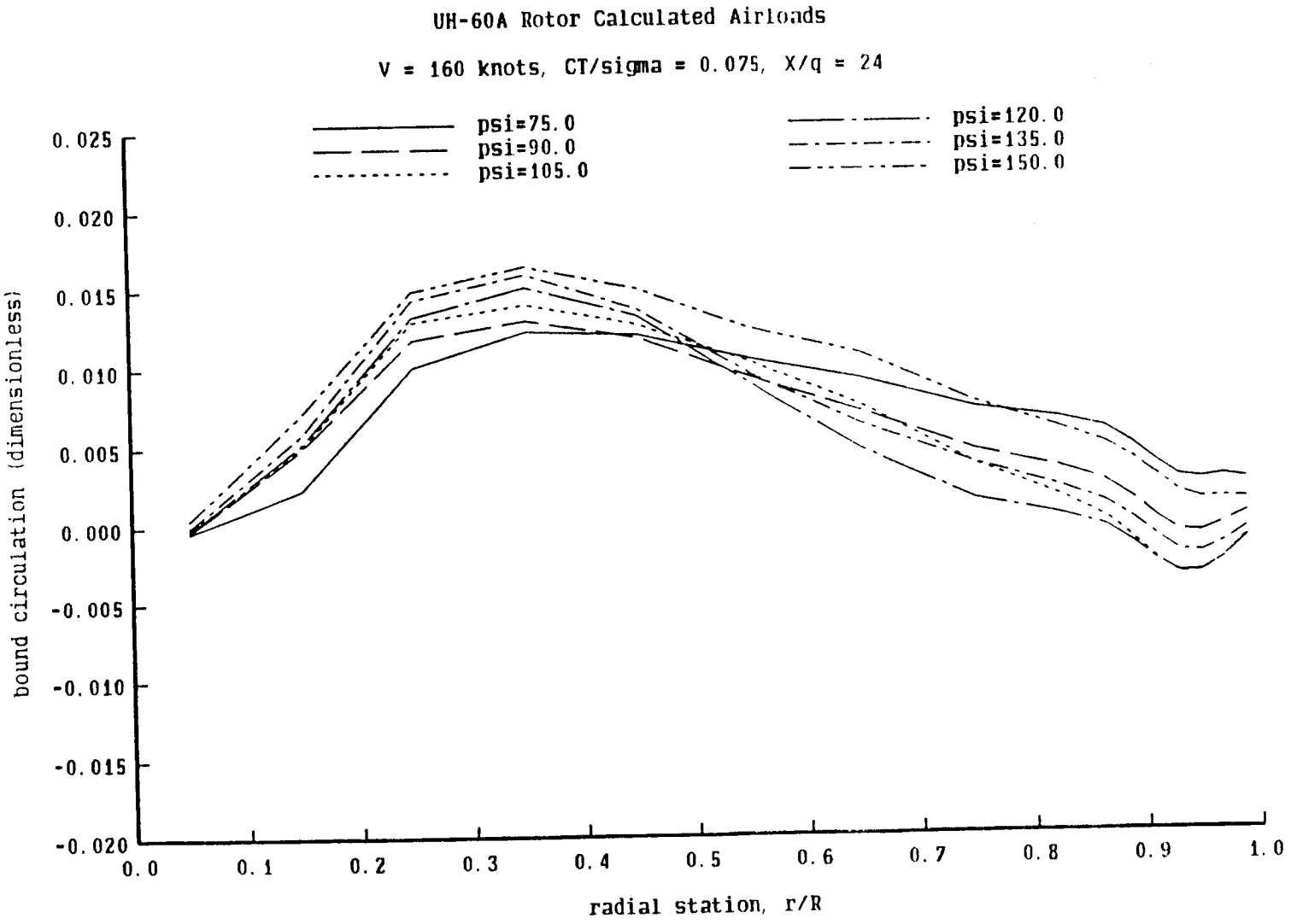

Figure 14-8c. UH-60A rotor: radial circulation distribution

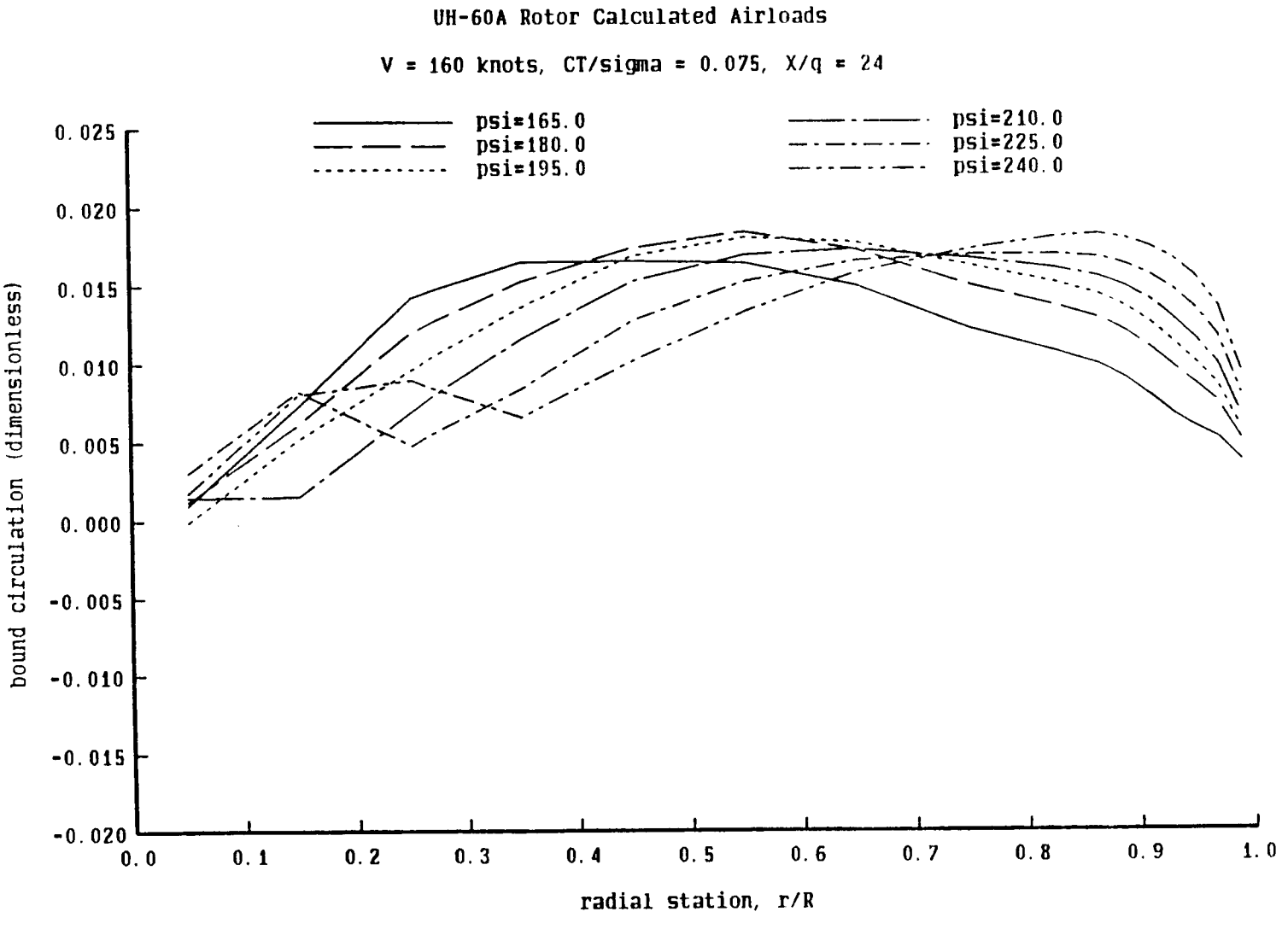

Figure 14-8d. UH-60A rotor: radial circulation distribution

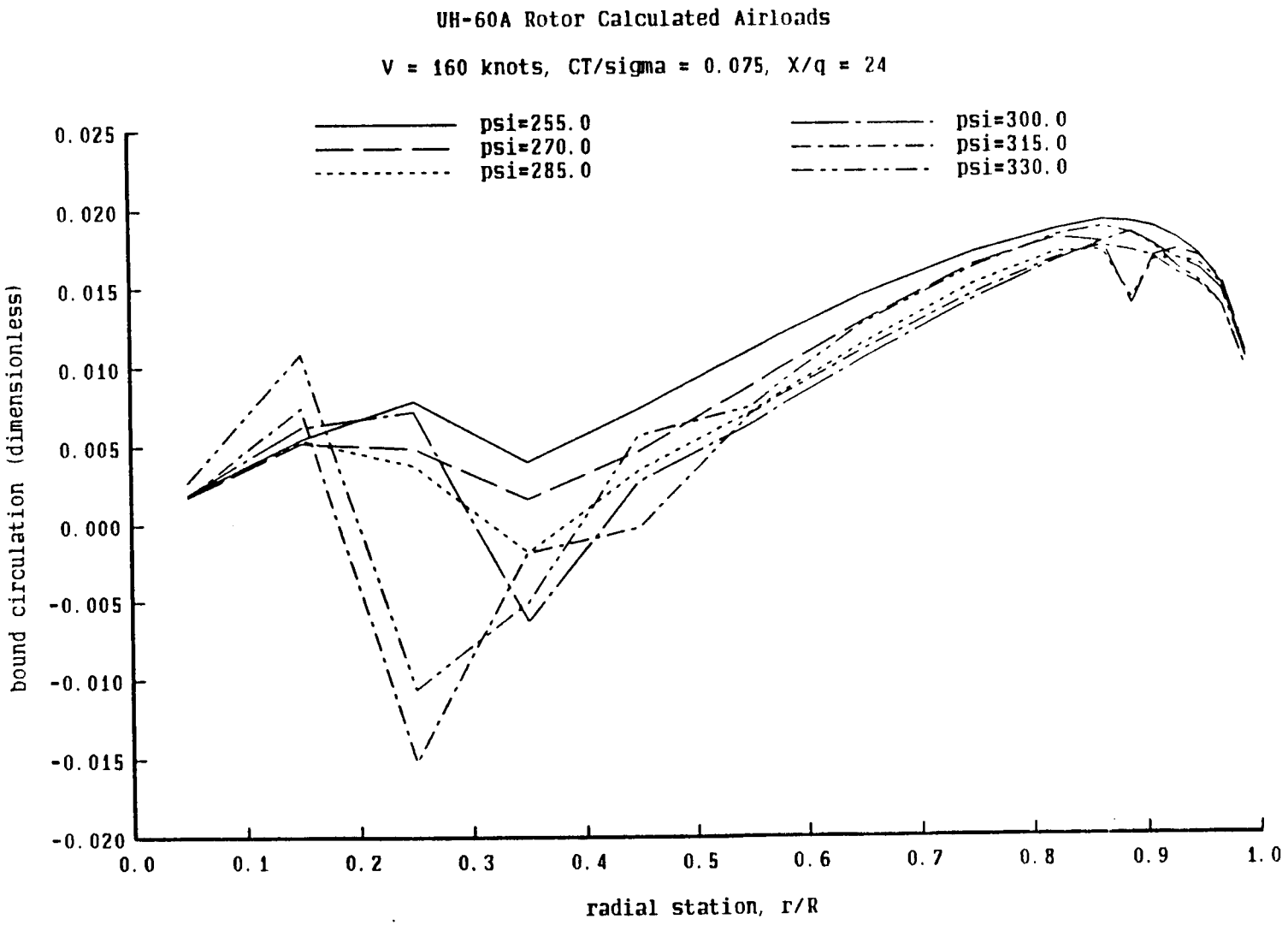

Figure 14-9a. UH-60A rotor: influence of far wake model

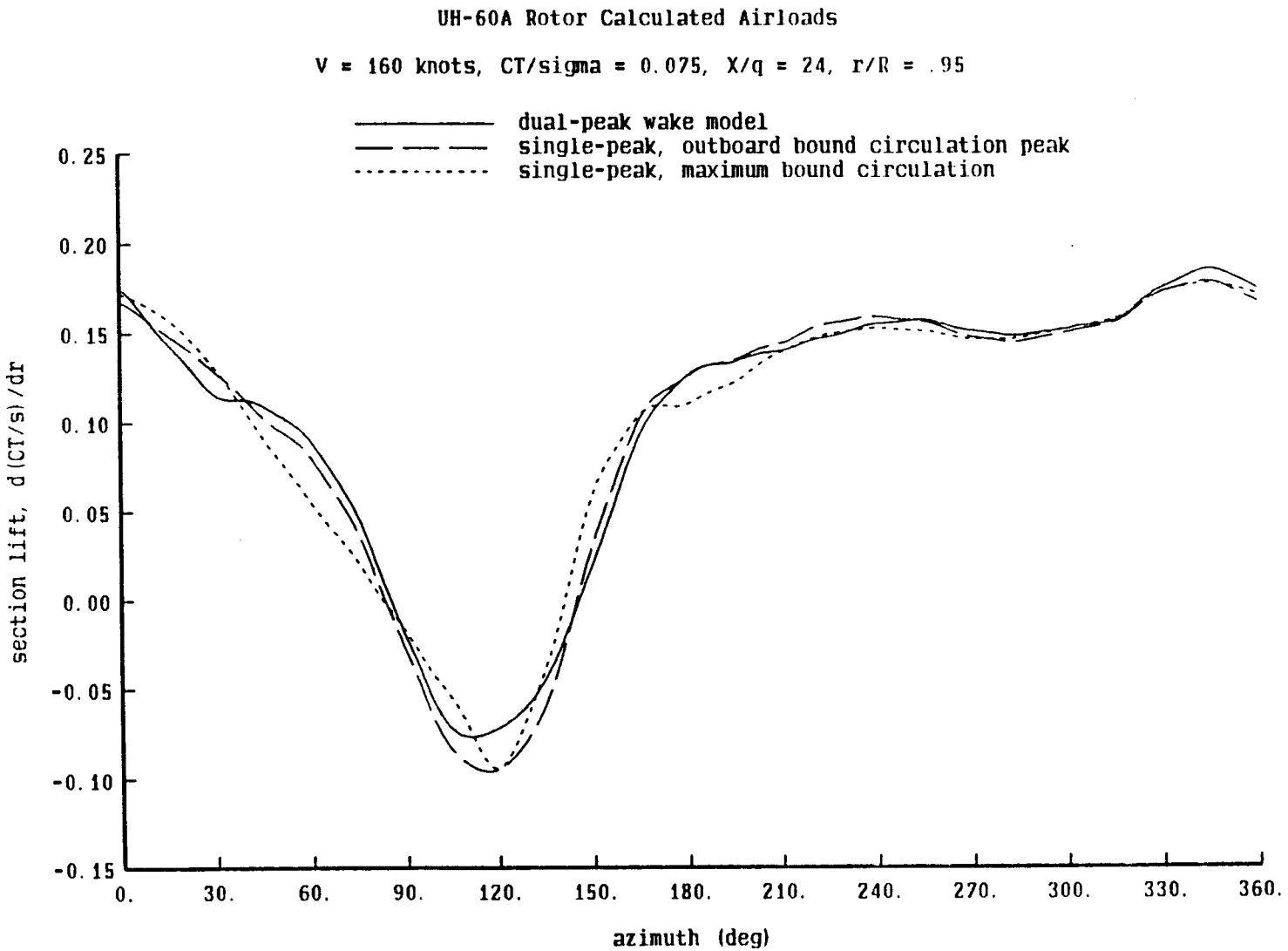

Figure 14-9b. UH-60A rotor: influence of far wake model

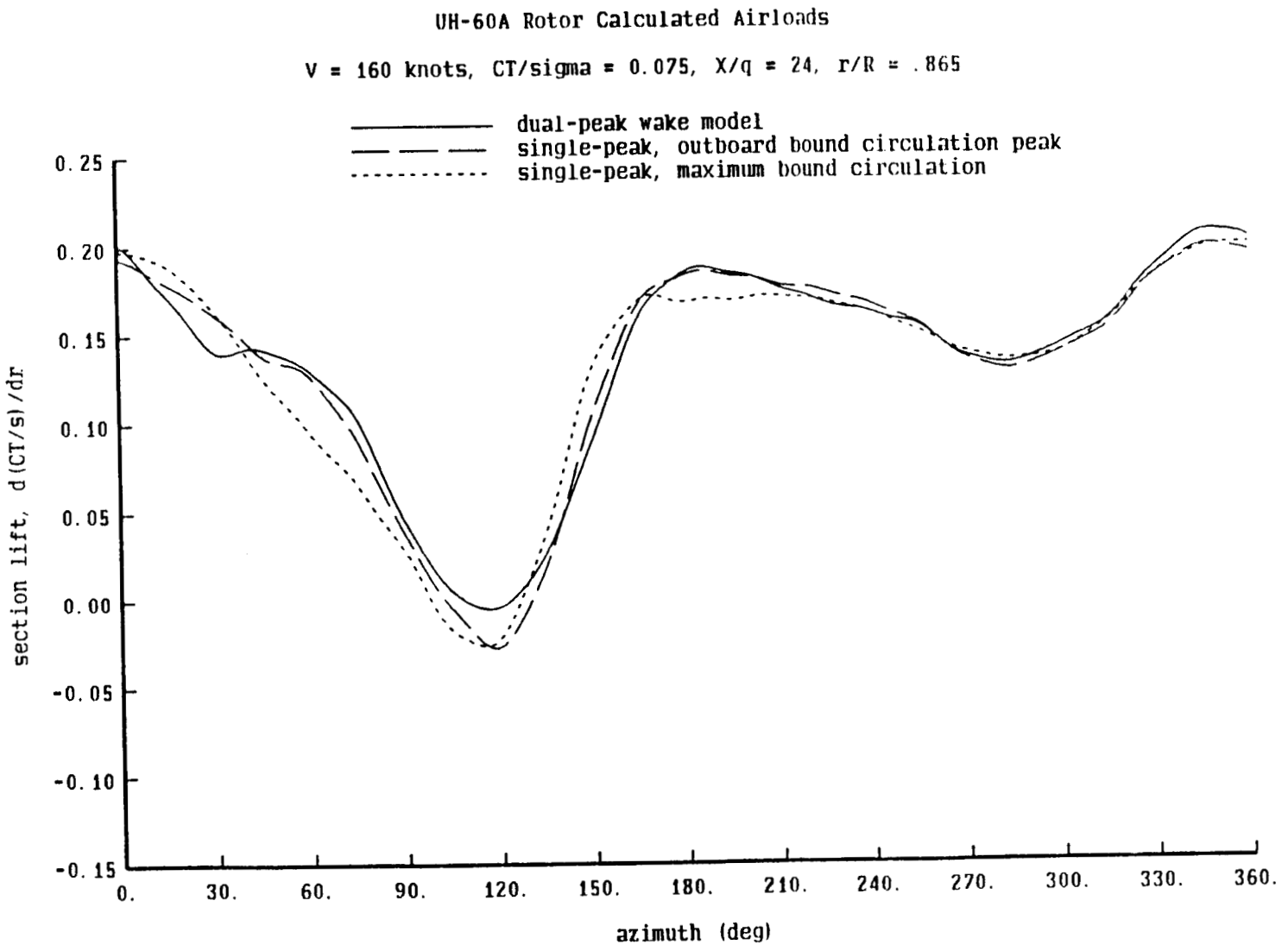

Figure 14-9c. UH-60A rotor: influence of far wake model

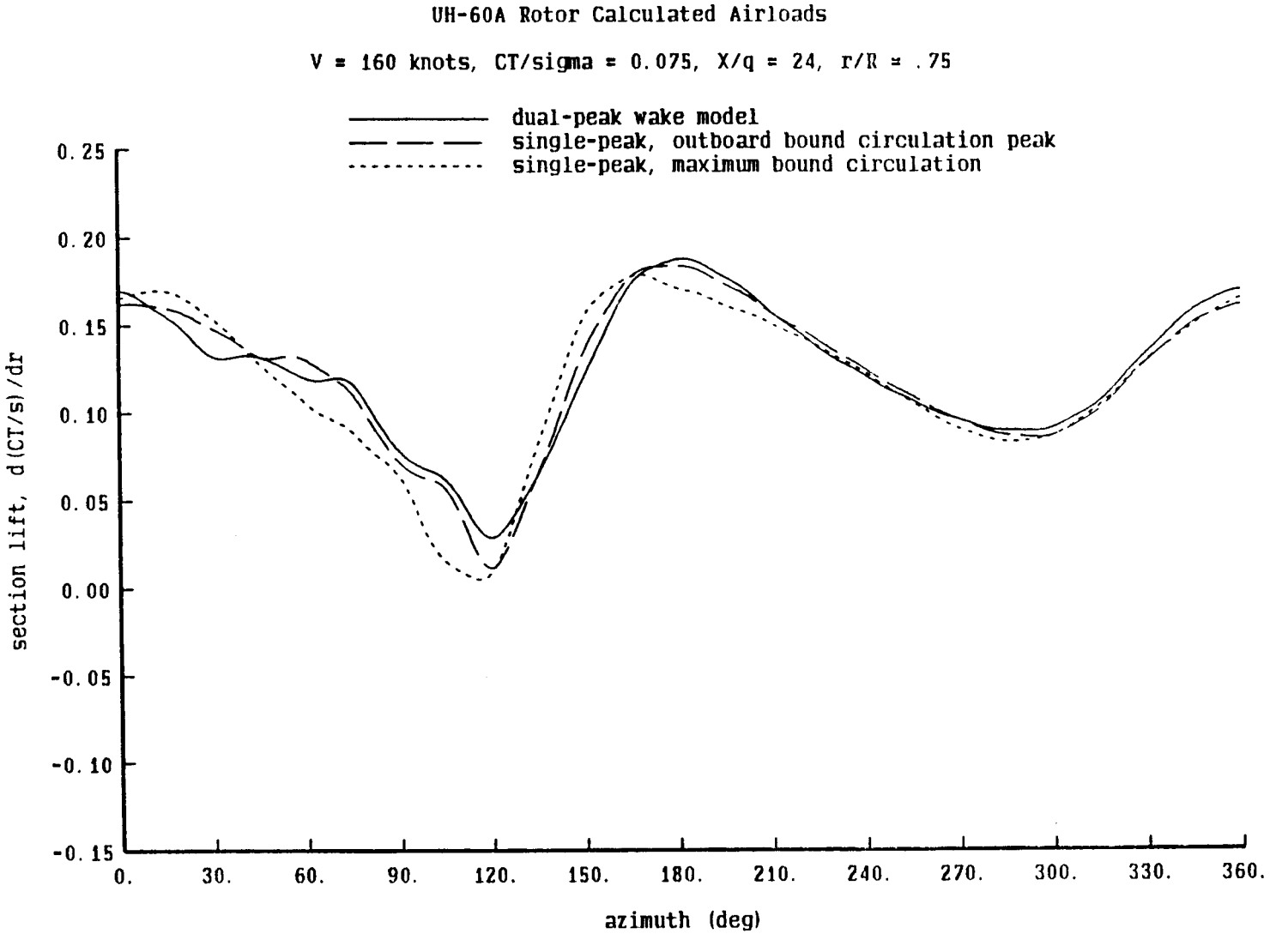

Figure 14-10a. UH-60A rotor: influence of blade motion

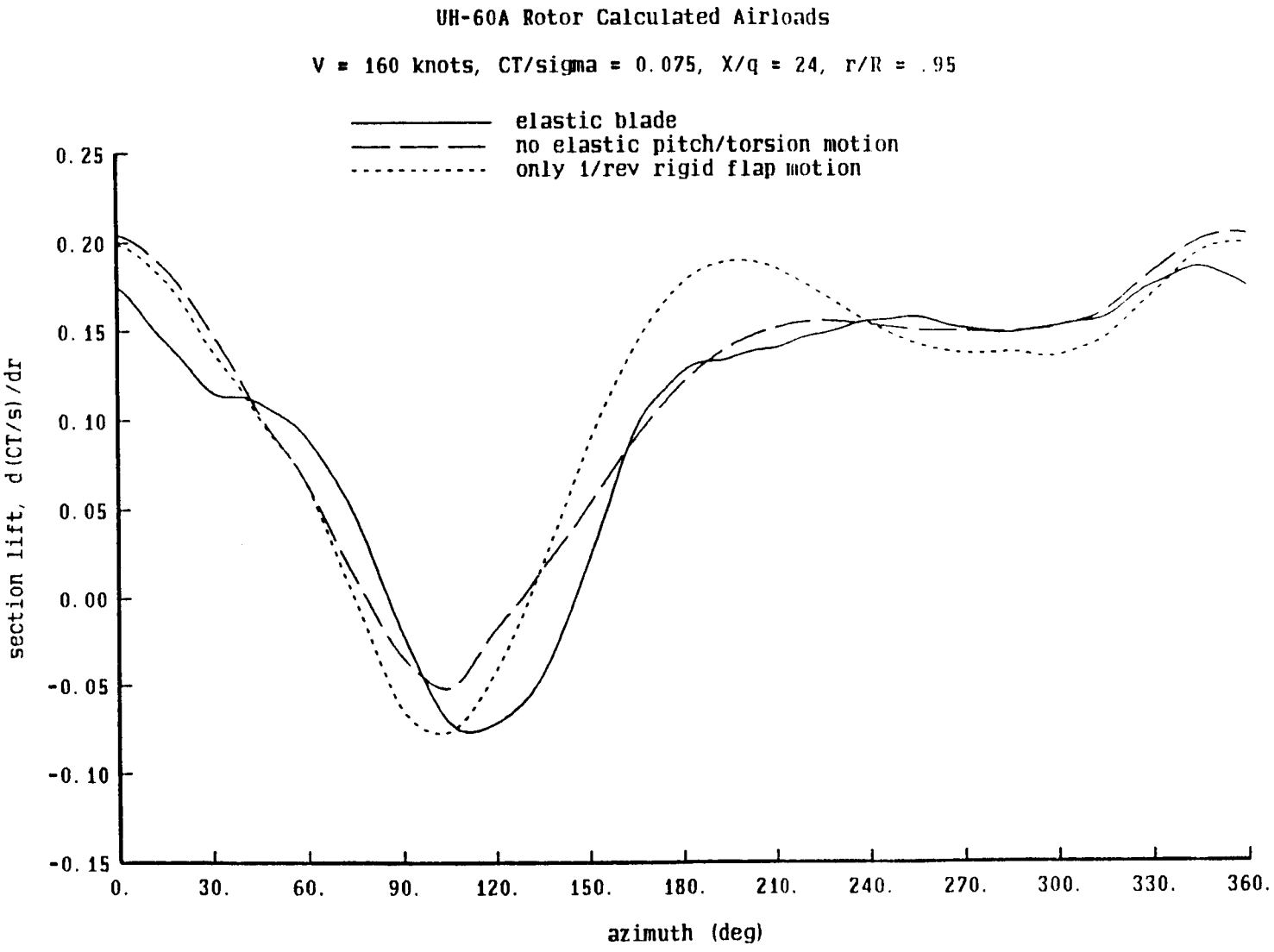

Figure 14-10b. UH-60A rotor: influence of blade motion

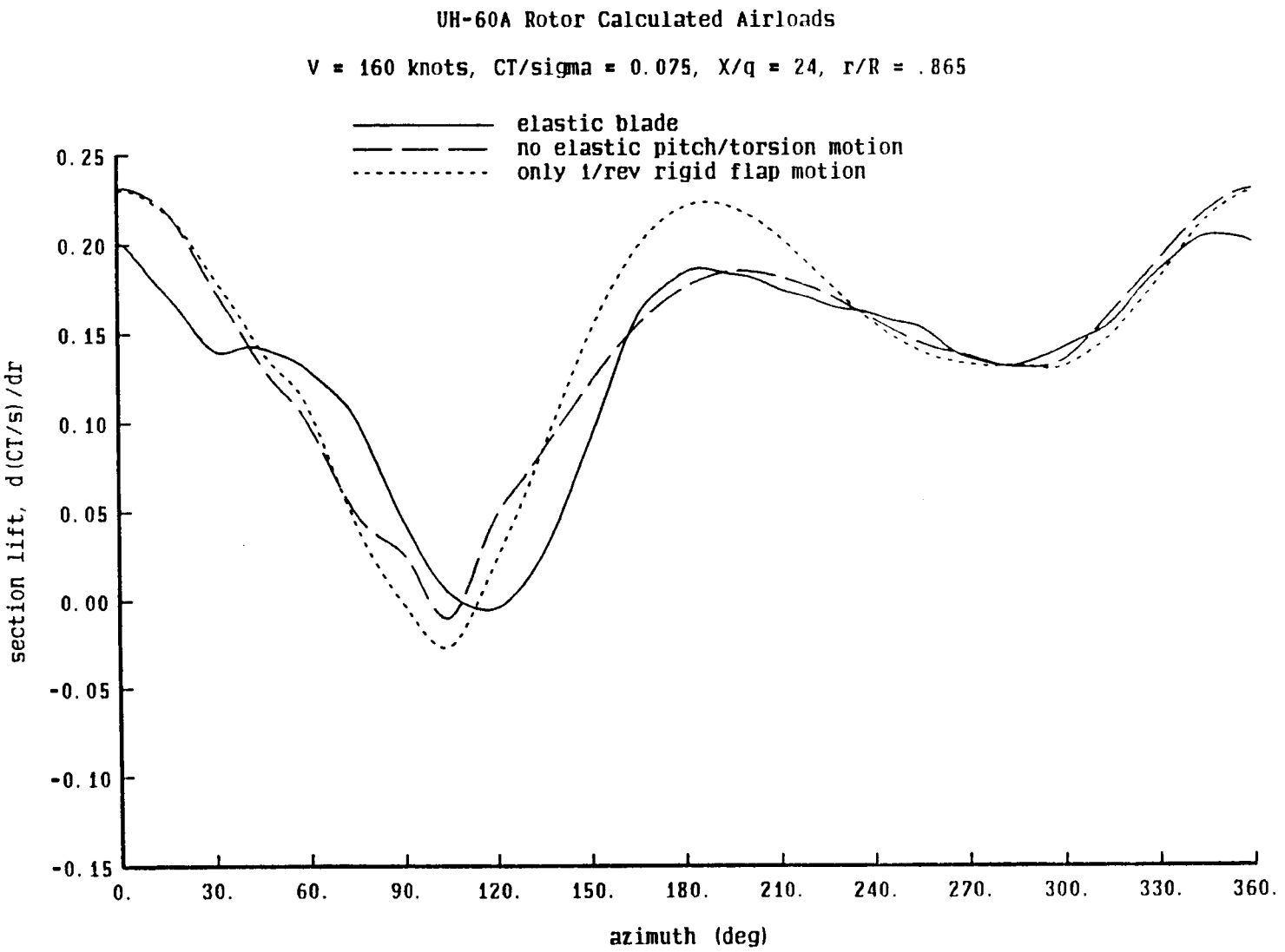

Figure 14-10c. UH-60A rotor: influence of blade motion

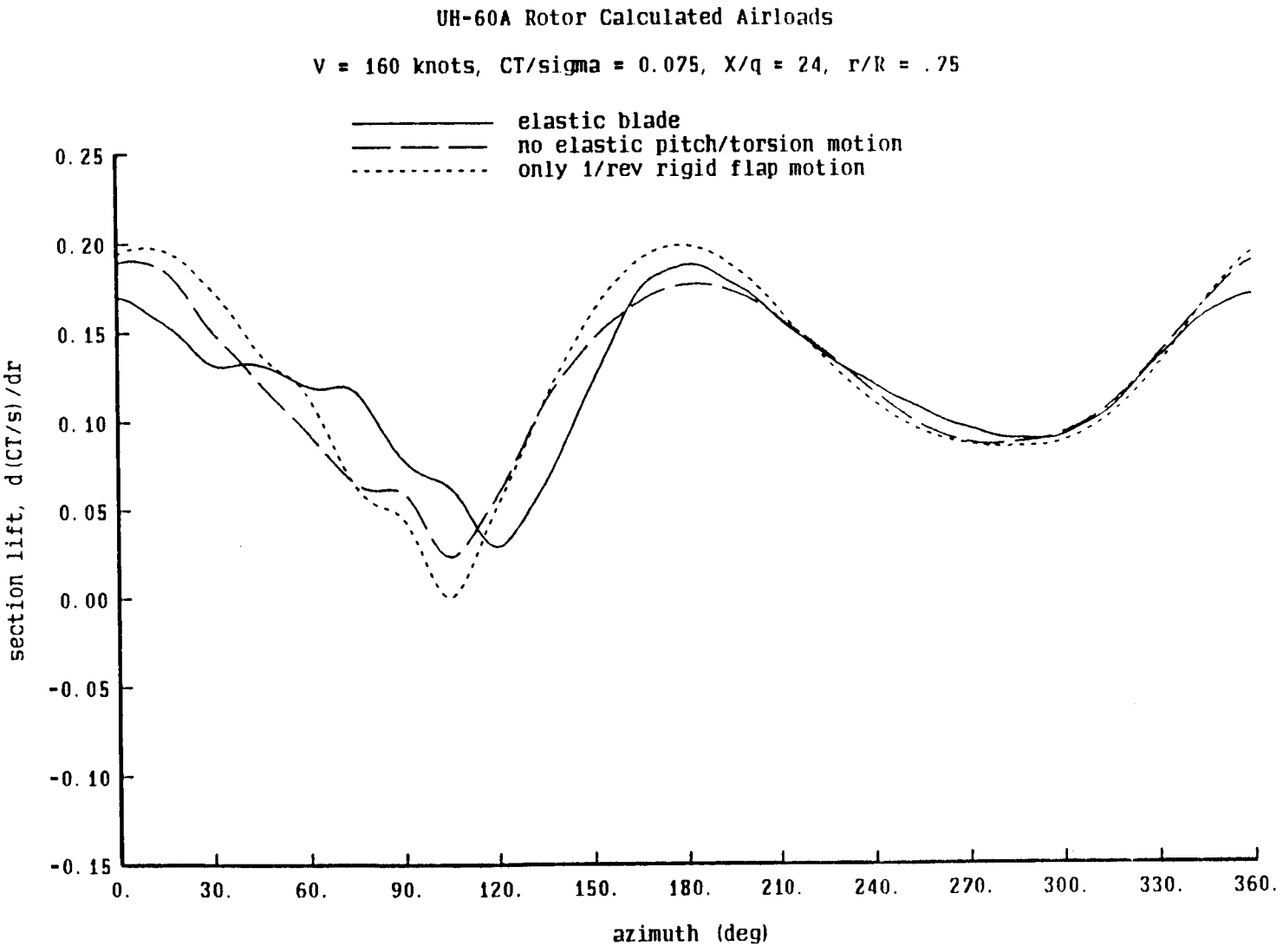

Figure 14-11a. UH-60A rotor: influence of swept tip aerodynamics model

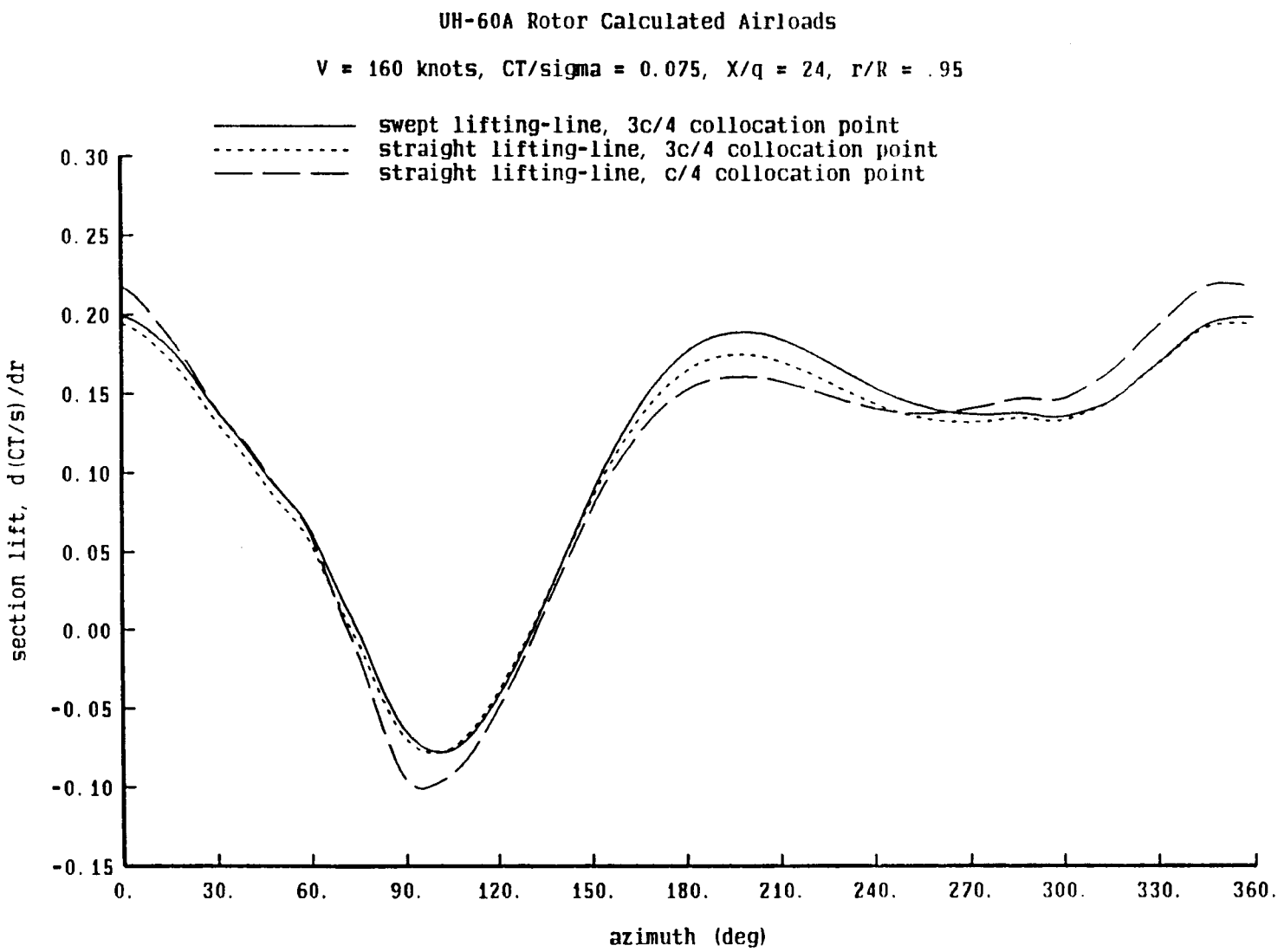

Figure 14-11b. UH-60A rotor: influence of swept tip aerodynamics model

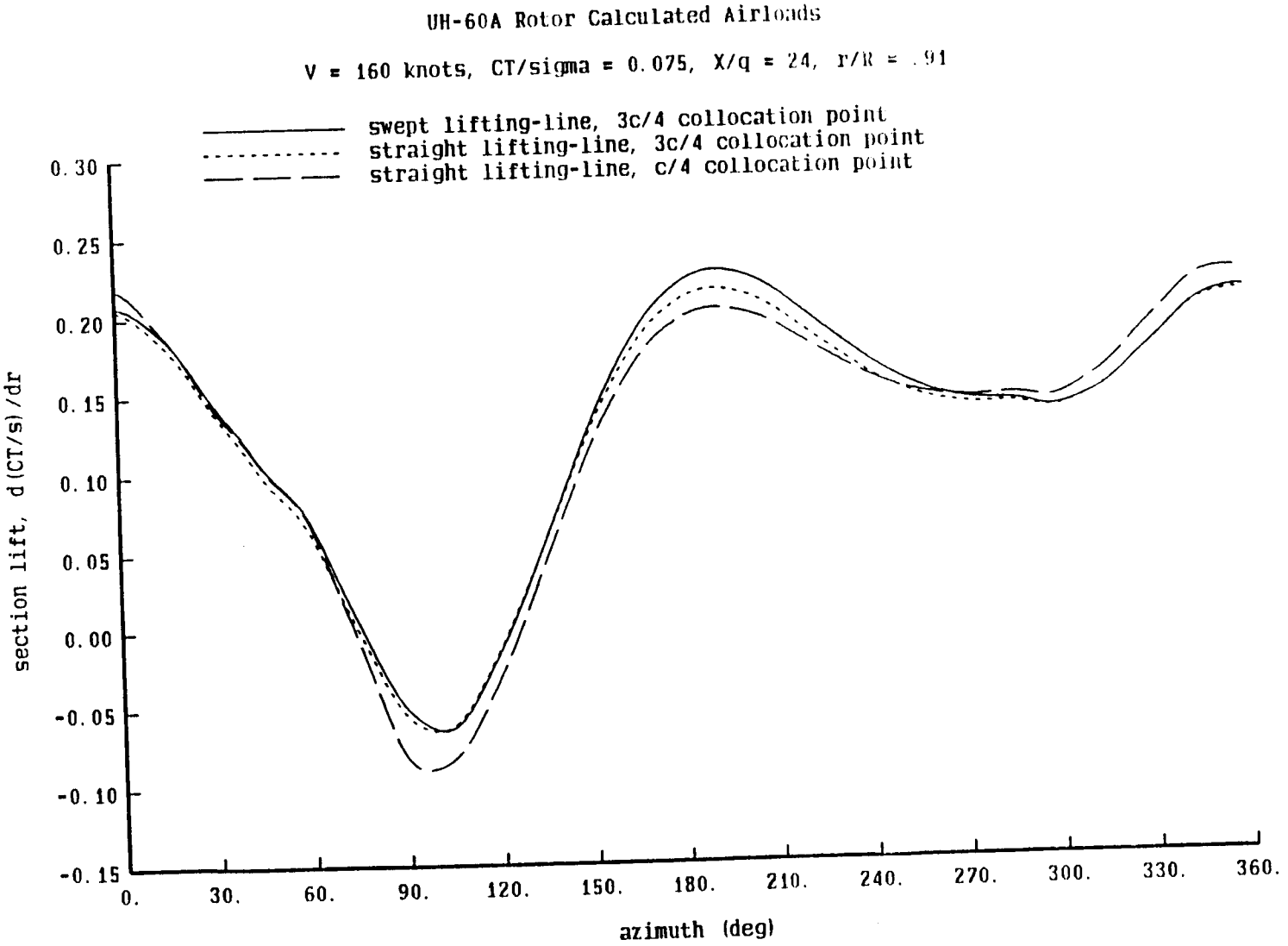

Figure 15-1a. SA349/2 helicopter: harmonic content of airloads

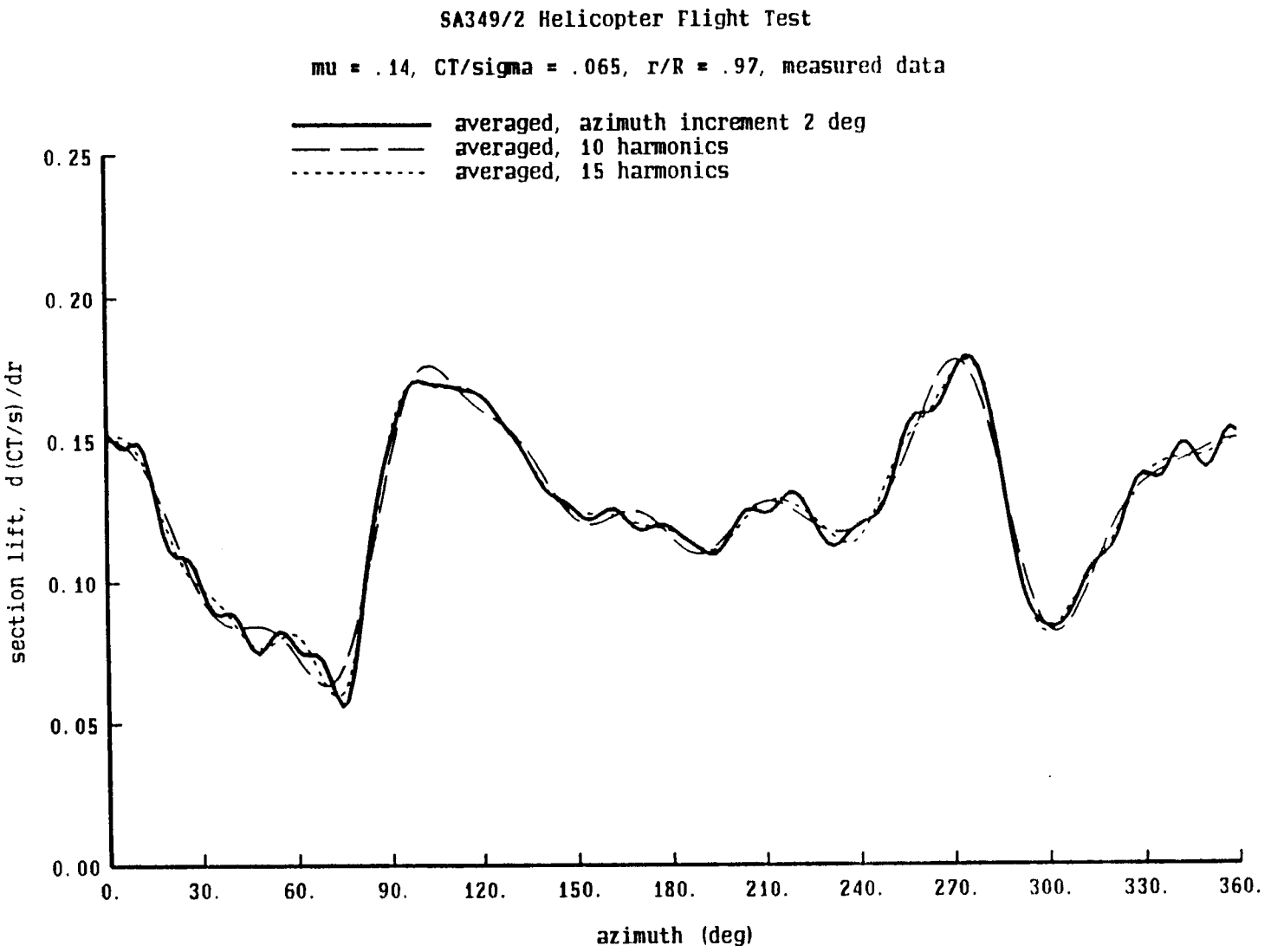

Figure 15-1b. SA349/2 helicopter: harmonic content of airloads

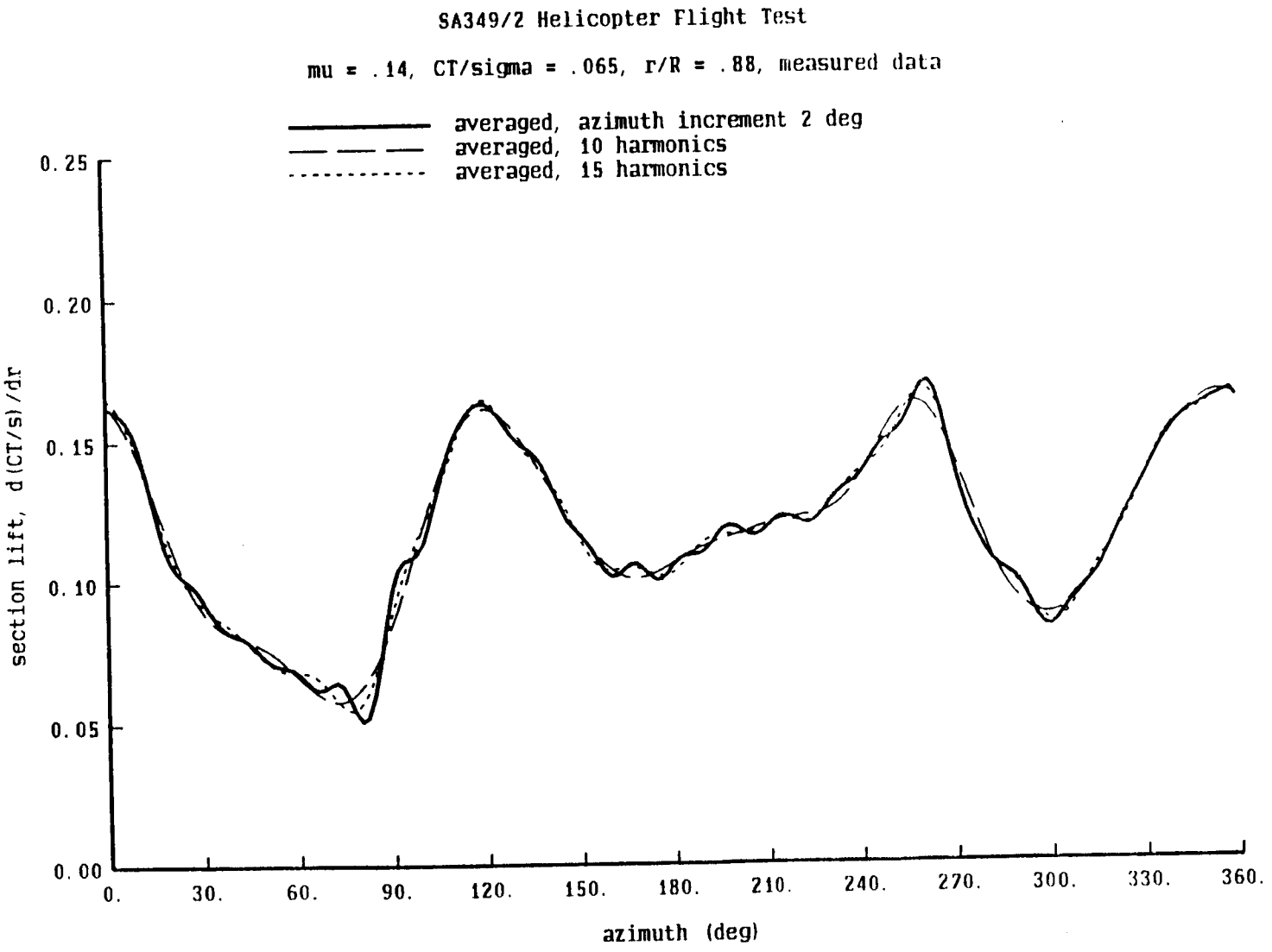

Figure 15-1c. SA349/2 helicopter: harmonic content of airloads

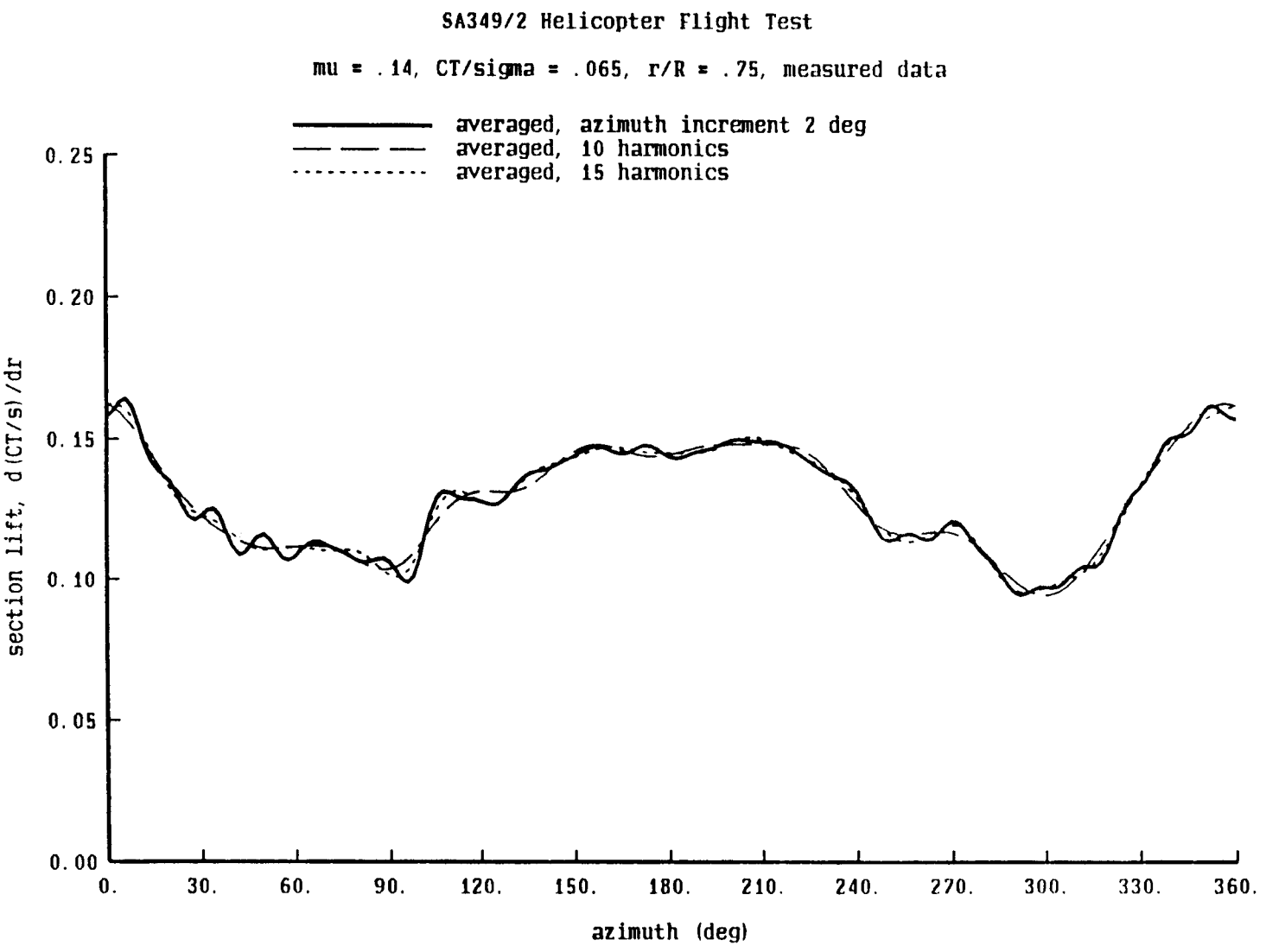

Figure 15-2. SA349/2 helicopter: harmonic content of airloads

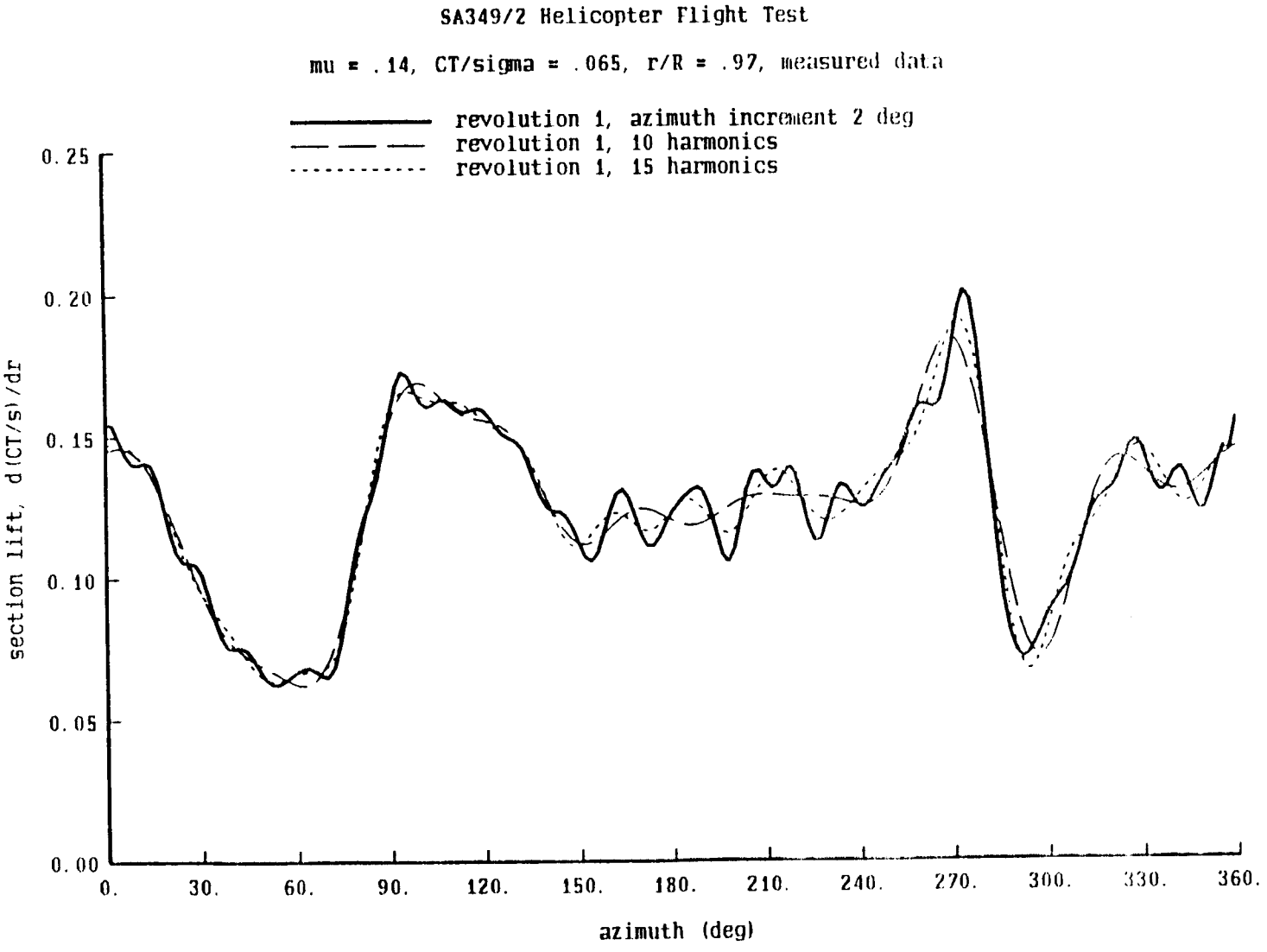

Figure 15-3a. SA349/2 helicopter: comparison of averaged and original data

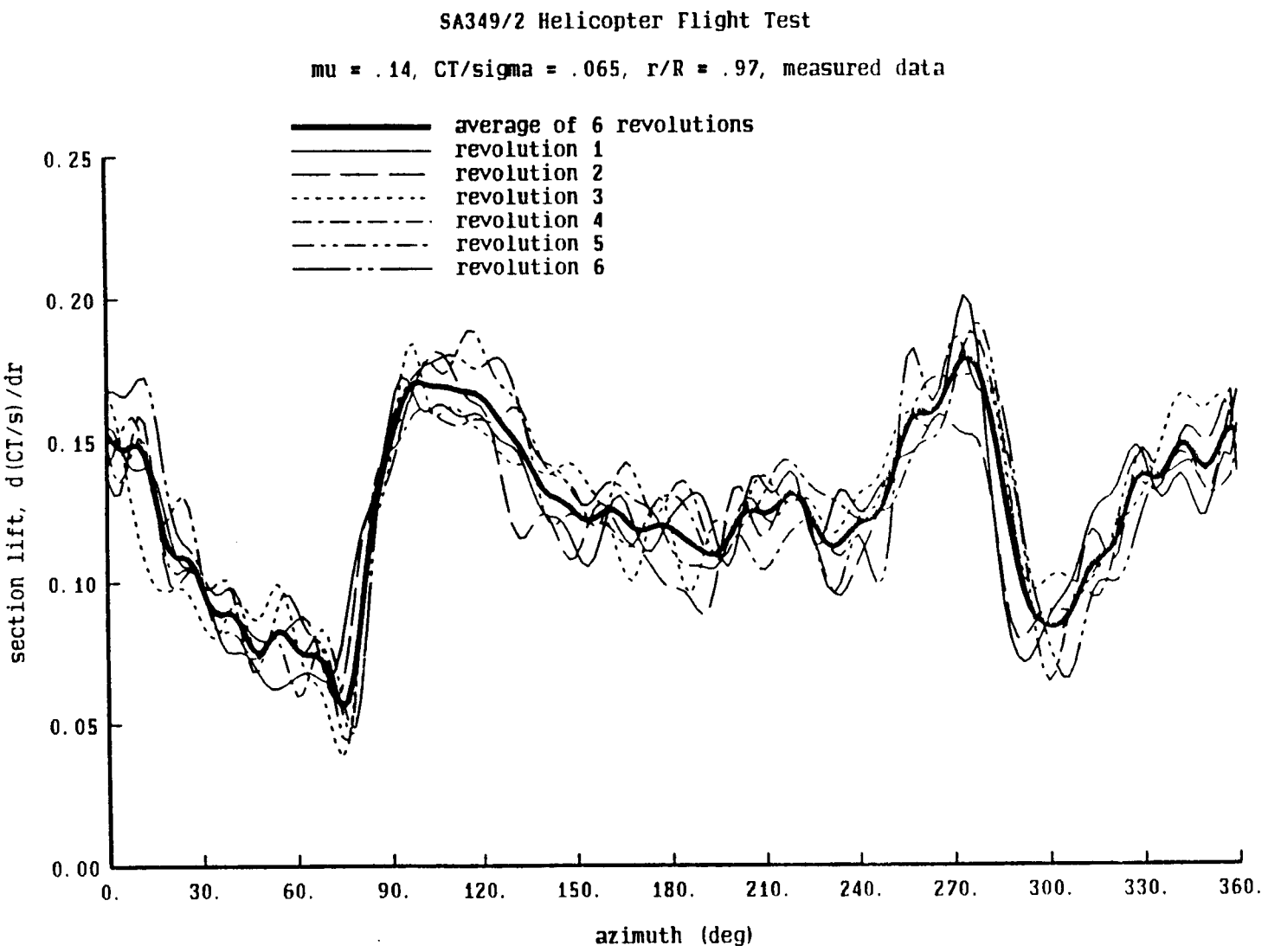

Figure 15-3b. SA349/2 helicopter: comparison of averaged and original data

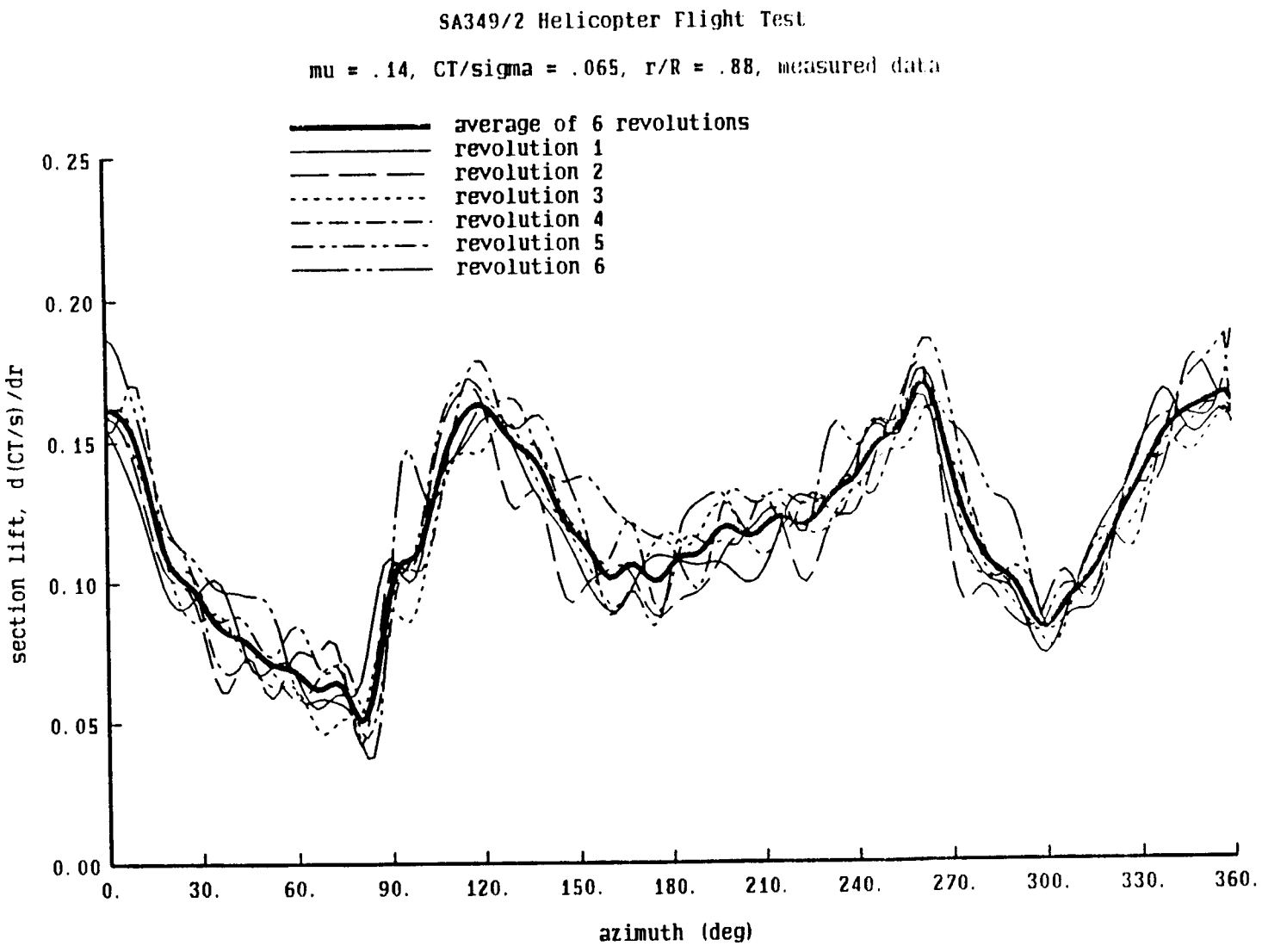

Figure 15-3c. SA349/2 helicopter: comparison of averaged and original data

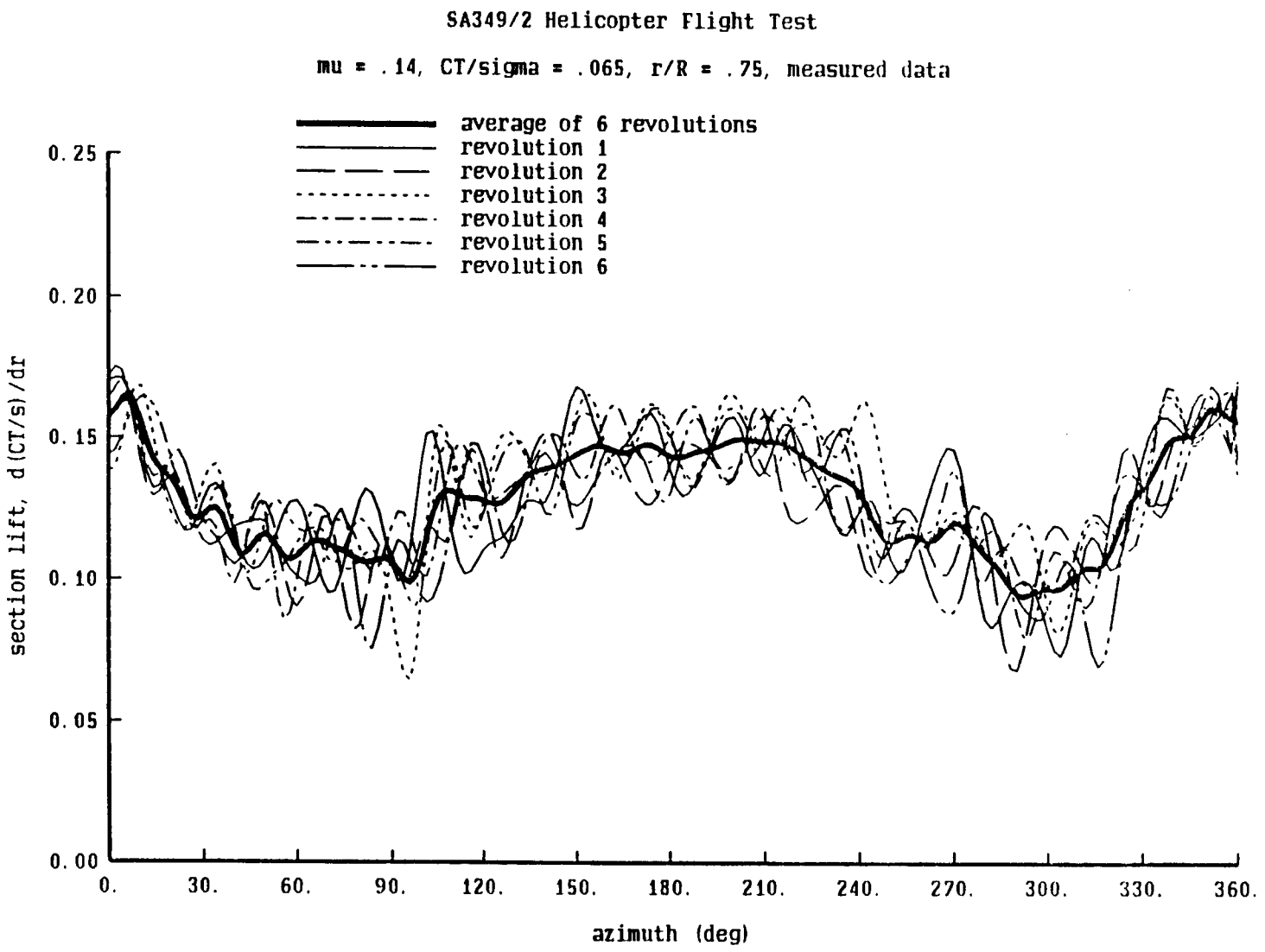

Figure 15-4a. Model 360 rotor: harmonic content of airloads

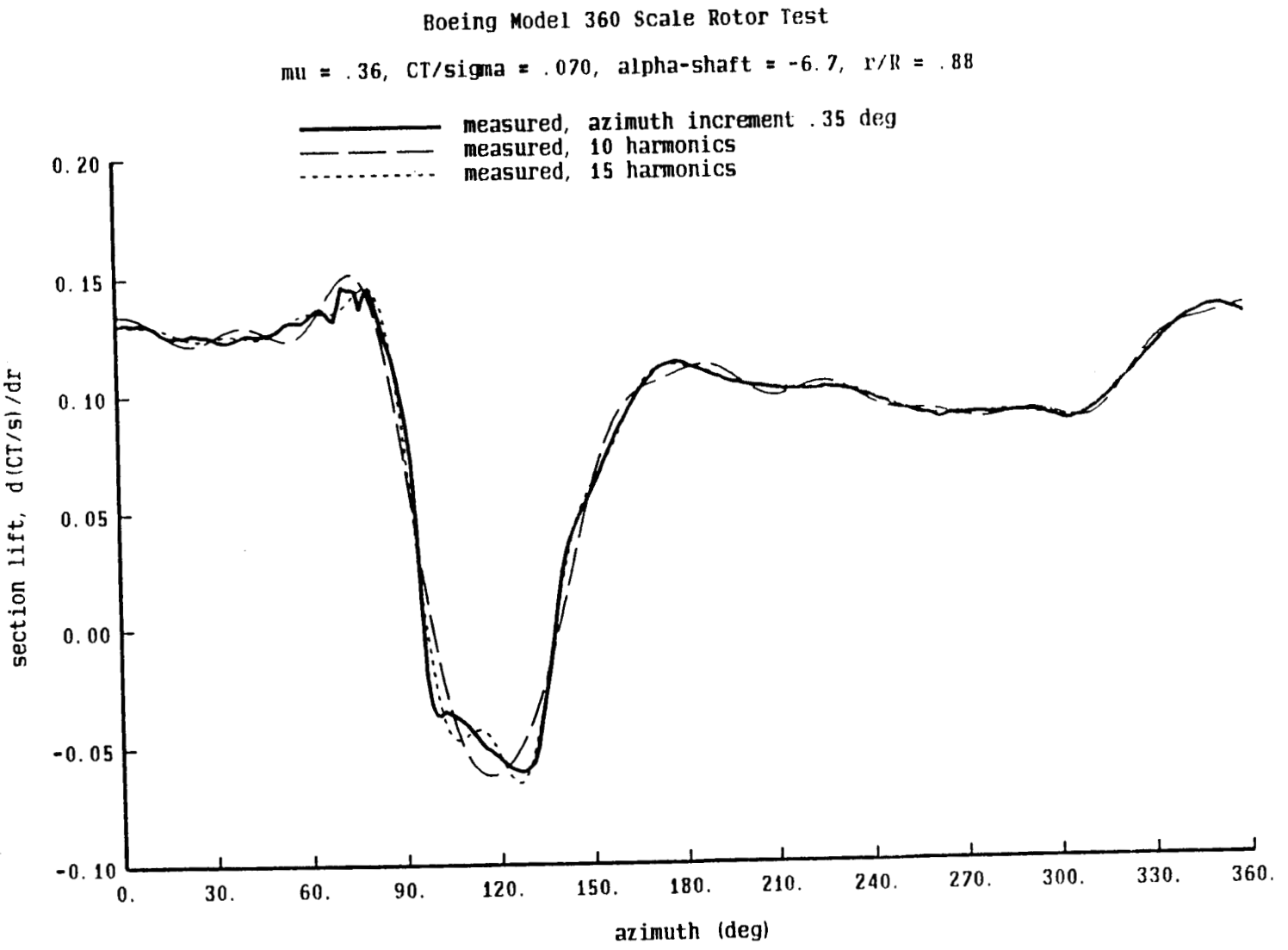

Figure 15-4b. Model 360 rotor: harmonic content of airloads

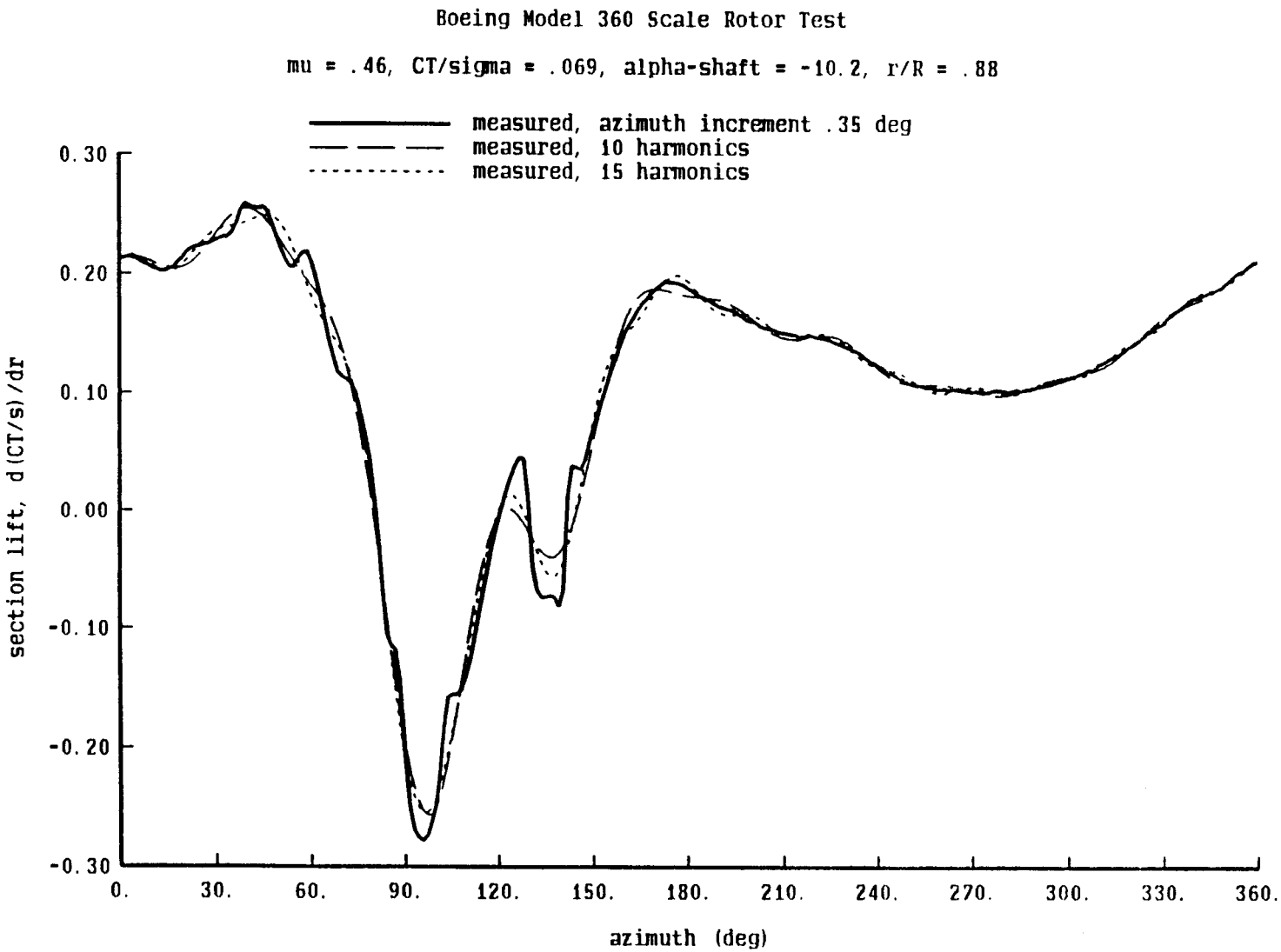

Figure 15-4c. Model 360 rotor: harmonic content of airloads

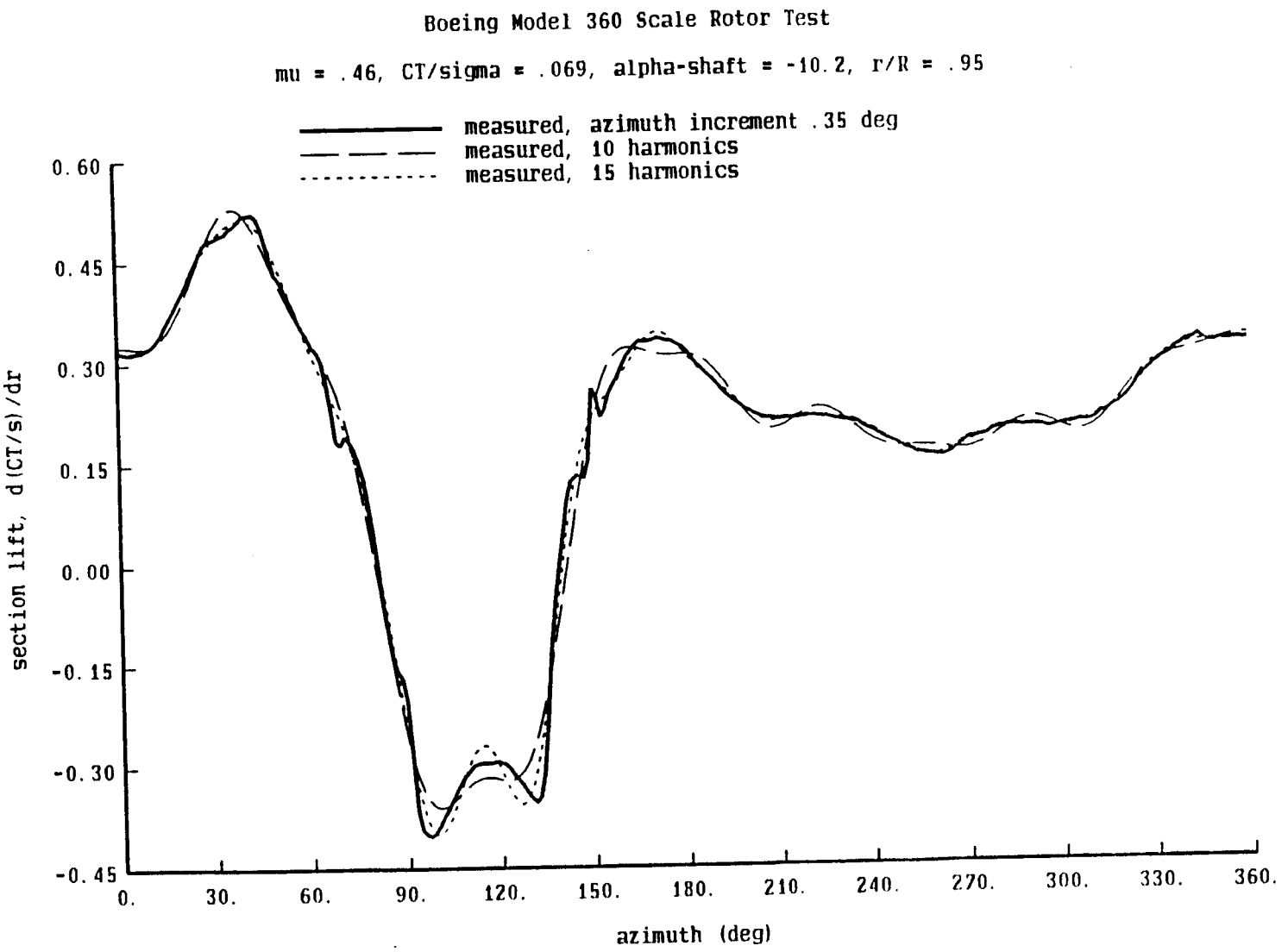

Figure 15-5a. AH-1G helicopter: harmonic content of airloads

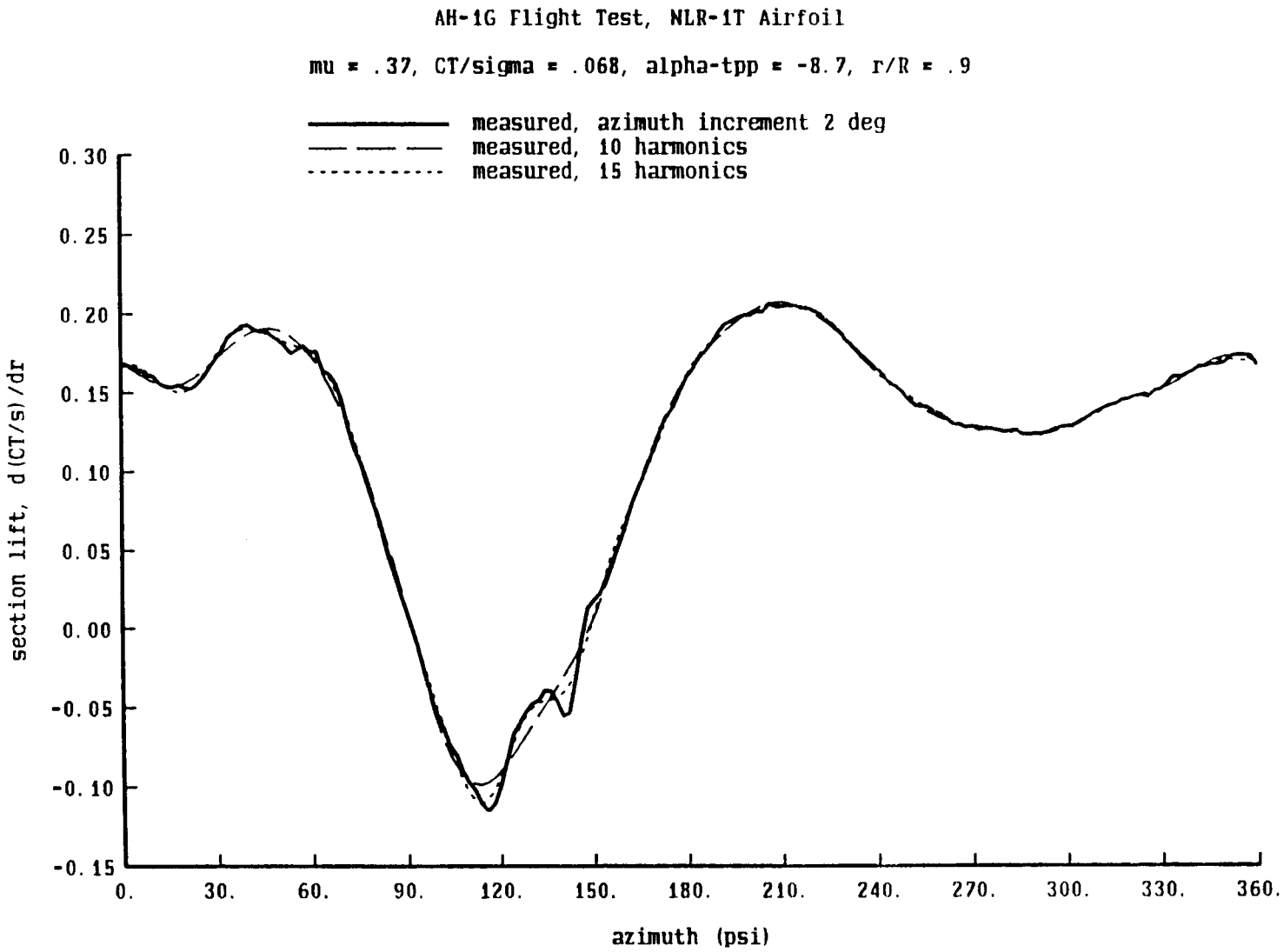

Figure 15-5b. AH-1G helicopter: harmonic content of airloads

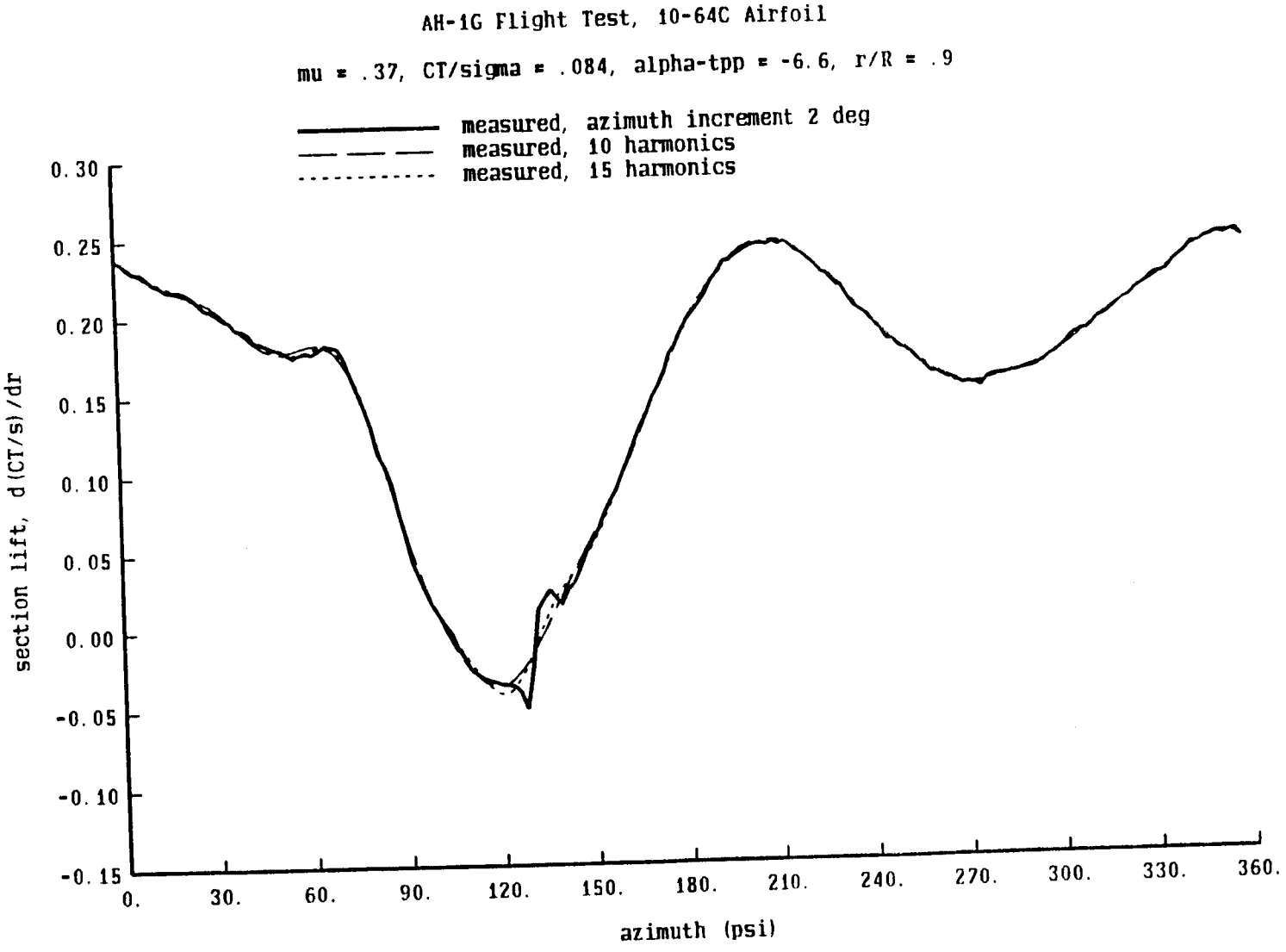

Figure 15-5c. AH-1G helicopter: harmonic content of airloads

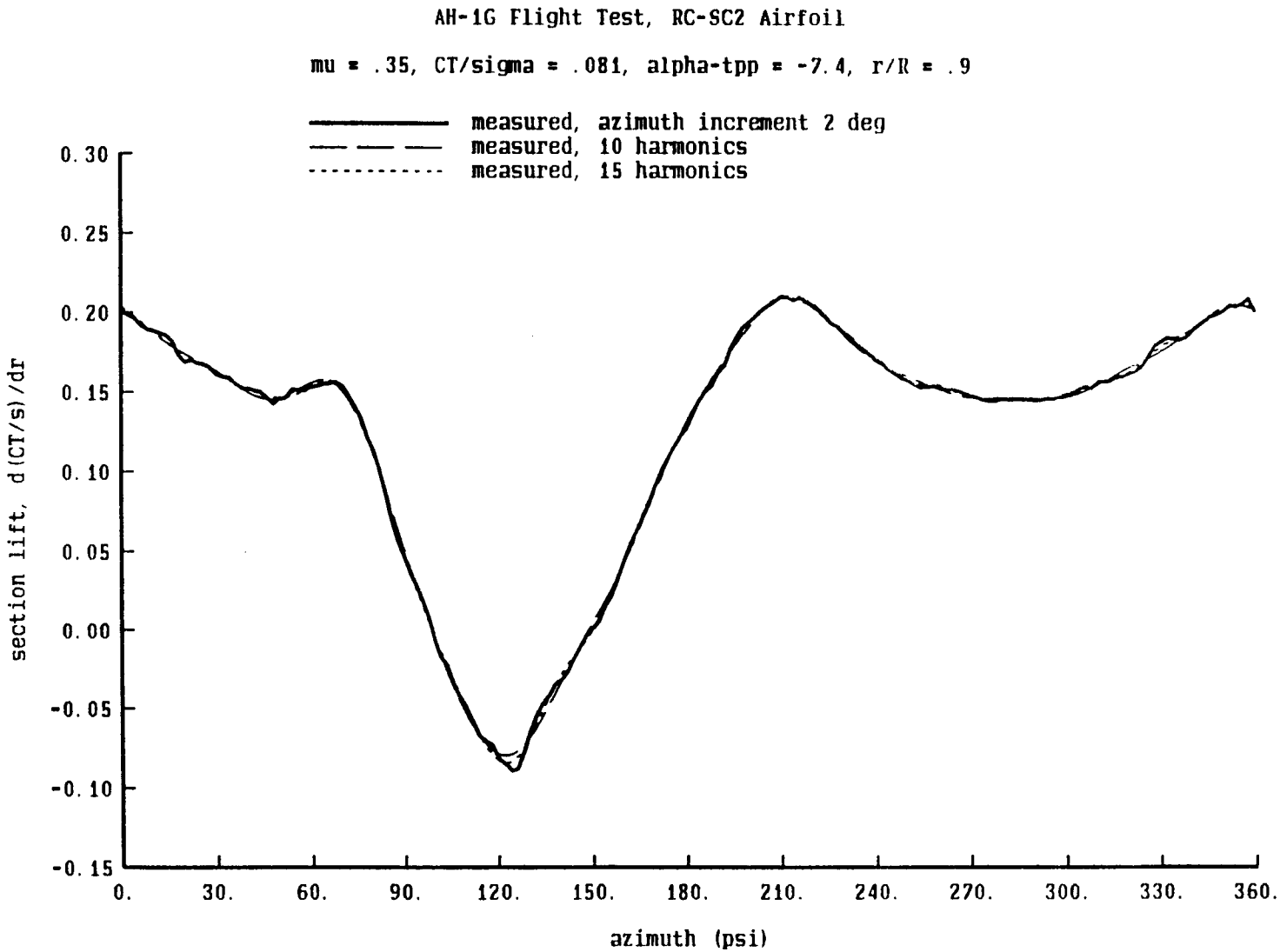

Figure 15-6a. H-34 helicopter: harmonic content of airloads

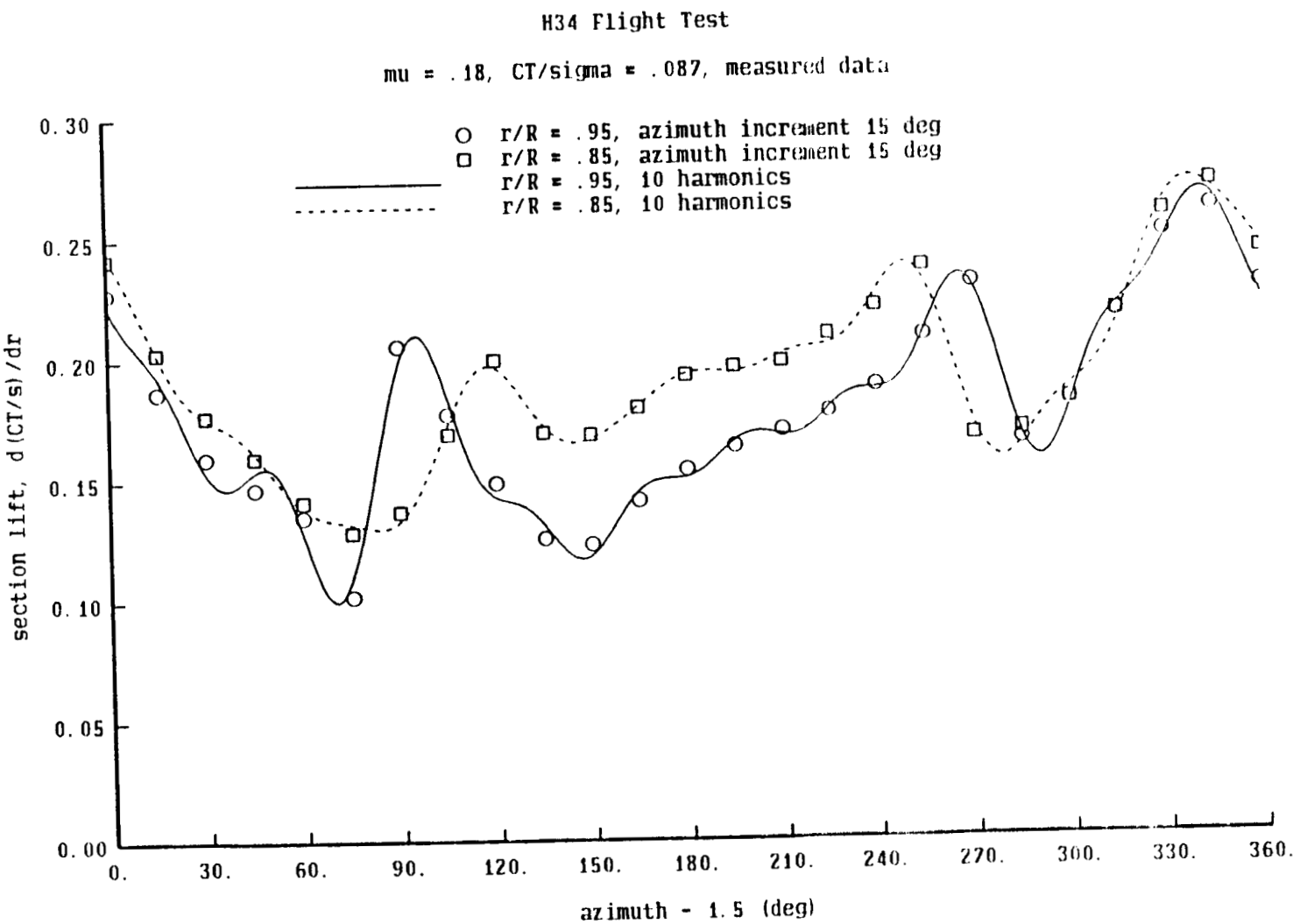

Figure 15-6b. H-34 helicopter: harmonic content of airloads

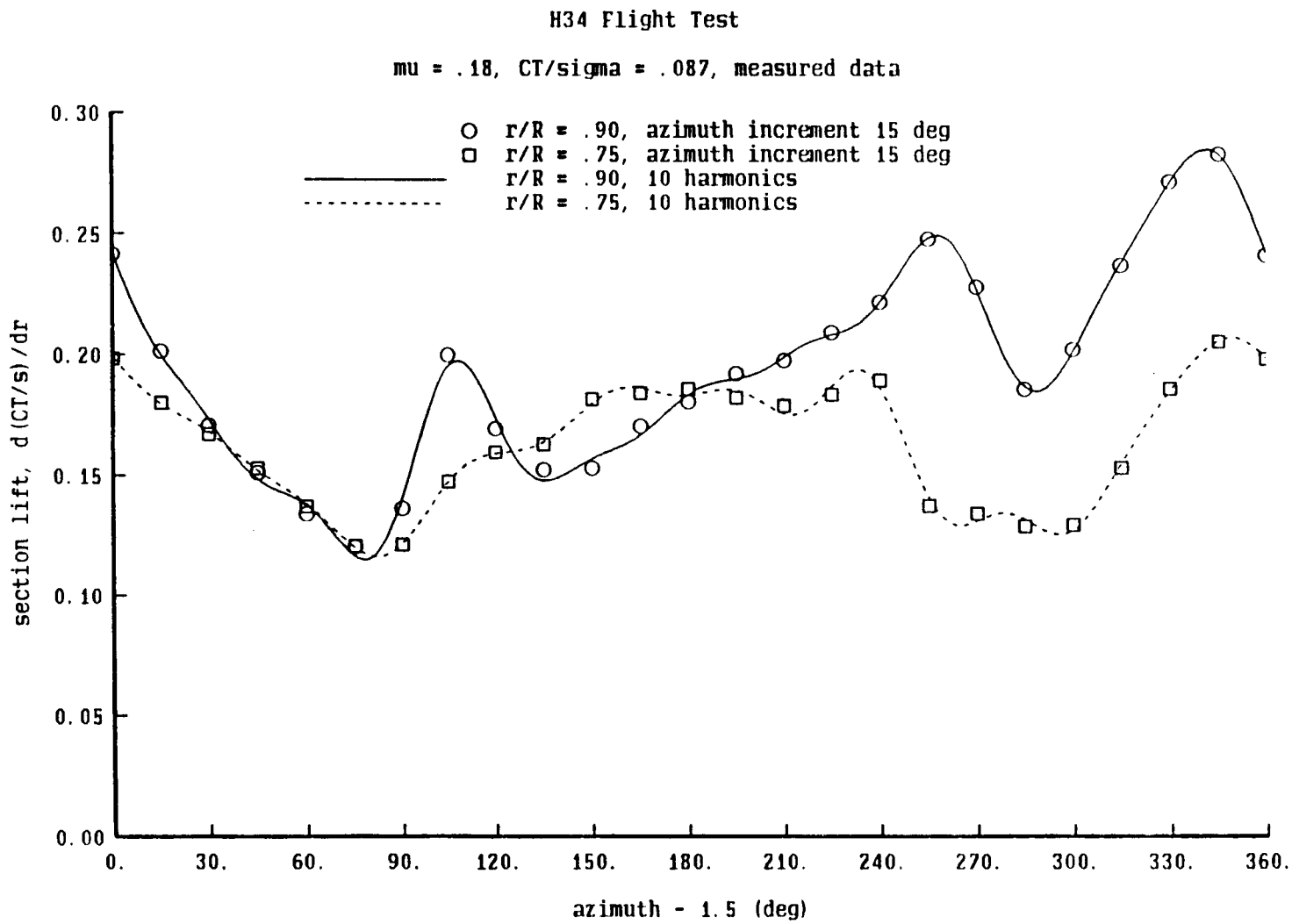

Figure 15-6c. H-34 helicopter: harmonic content of airloads

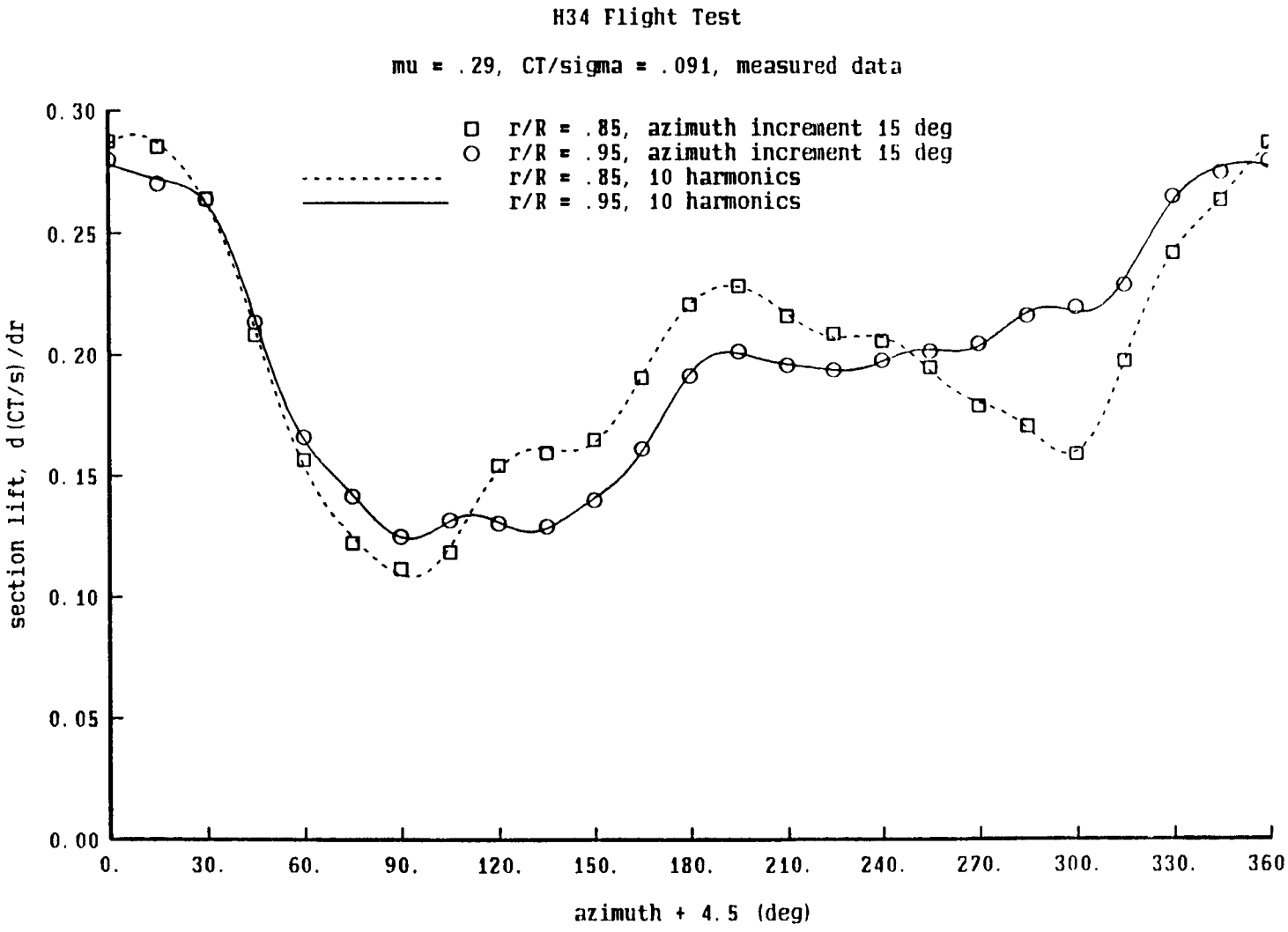

Figure 15-6d. H-34 helicopter: harmonic content of airloads

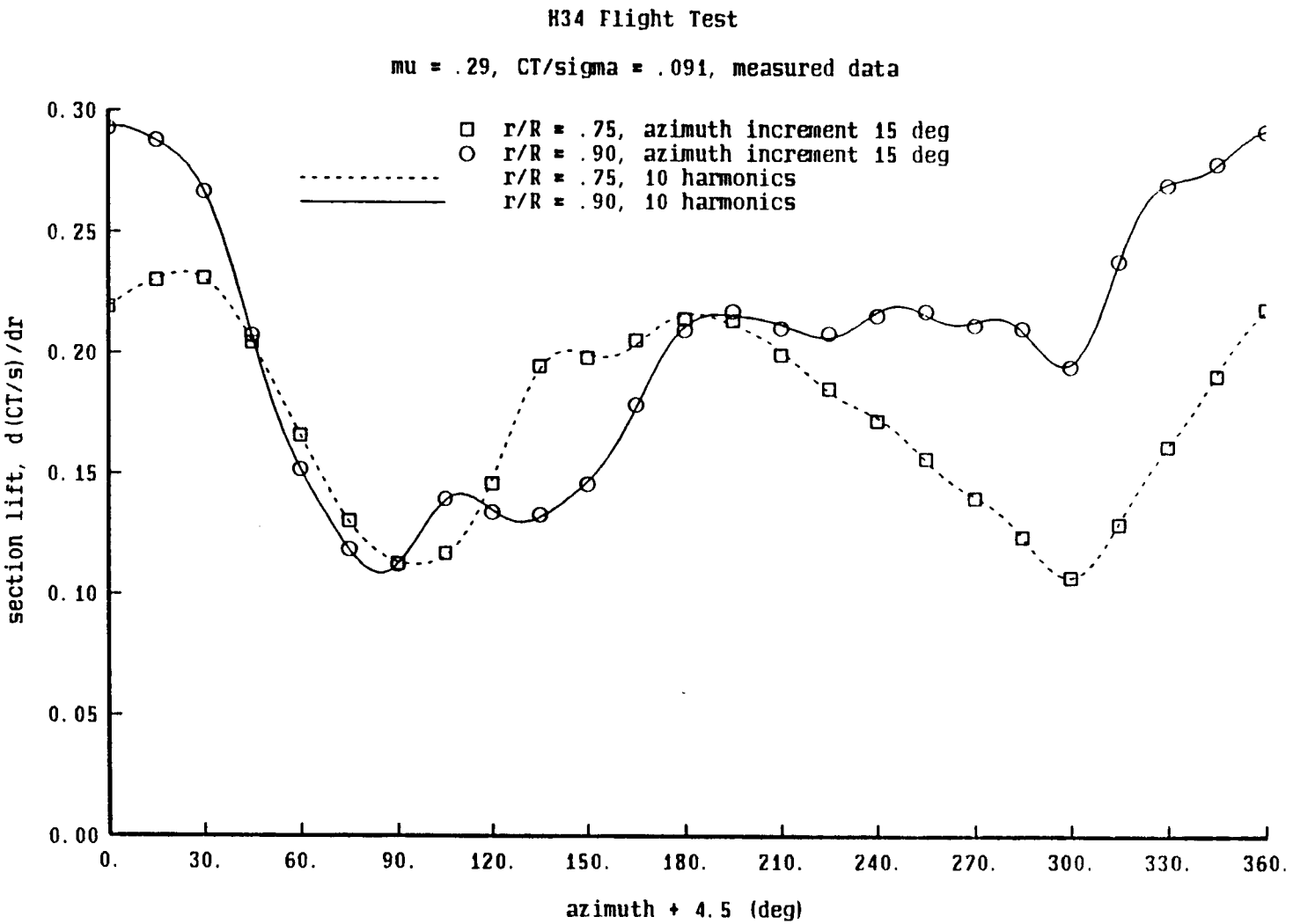

NASA National Aeronautics and Space Administration

Report Documentation Page

1. Report No.	2. Government Accession No.	3. Recipient's Catalog No.
NASA CR 177507 USAVSCOM TR-88-A-008		

4. Title and Subtitle	5. Report Date
Wake Model for Helicopter Rotors in High Speed Flight	November 1988
	6. Performing Organization Code

7. Author(s)	8. Performing Organization Report No.
Wayne R. Johnson	
	10. Work Unit No.
	RTOP #505-61-51

9. Performing Organization Name and Address	11. Contract or Grant No.
Johnson Aeronautics P.O. Box 1253 Palo Alto, CA 94302	NAS2-12767
	13. Type of Report and Period Covered
12. Sponsoring Agency Name and Address	Contract Report
Aeroflightdynamics Directorate NASA Ames Research Center Moffett Field, CA 94035	14. Sponsoring Agency Code

15. Supplementary Notes

Dr. Chee Tung
Aeroflightdynamics Directorate
NASA Ames Research Center
Moffett Field, CA 94035
415-694-5241

16. Abstract

Two alternative approaches are developed to calculate blade-vortex interaction airloads on helicopter rotors: second order lifting-line theory, and a lifting-surface theory correction. The common approach of using a larger vortex core radius to account for lifting-surface effects is quantified. The second order lifting-line theory also improves the modeling of yawed flow and swept tips. Calculated results are compared with wind tunnel measurements of lateral flapping, and with flight test measurements of blade section lift on SA349/2 and H-34 helicopter rotors. The tip vortex core radius required for good correlation with the flight test data is about 20% chord, which is within the range of measured viscous core sizes for helicopter rotors.

17. Key Words (Suggested by Author(s))	18. Distribution Statement
Rotor Wakes, Blade Vortex Interaction, Rotor Airloads	Unlimited - Unclassified

19. Security Classif. (of this report)	20. Security Classif. (of this page)	21. No. of pages	22. Price
Unclassified	Unclassified	148	A07